RL-80-026

Rutherford Laboratory
CHILTON, DIDCOT, OXON, OX11 0QX

Science Research Council
Central Laser Facility

Annual Report to the
Laser Facility Committee 1980

Laser Division
Rutherford Laboratory

RL-80-026

SCIENCE RESEARCH COUNCIL

CENTRAL LASER FACILITY

ANNUAL REPORT TO THE LASER FACILITY COMMITTEE, 1980

Preface

The report covers the work done at, or in association with, the Central Laser Facility during the year April 1979 to March 1980. It is arranged in seven chapters, compared with eight last year, reflecting the current scientific group structure: the Atomic and Radiation Physics Group and the XUV Laser Group have been combined. An appendix at the end of the report lists the publications based on work at, or in conjunction with, the Facility, which have appeared or been accepted for publication during the year.

The scientific groups using the glass laser are listed in the accompanying table together with the names of their chairmen and secretaries and the time allocated to them. In addition there is an E-beam programme committee concerned with the gas laser development programme. It will be noticed that the number of weeks allocated for work with or on the glass laser exceeds 52. This arises because of the introduction, during the year under review, of parallel working in the six and single beam target areas so that two groups can operate simultaneously. The degree to which parallel operation is possible depends on the actual experiments to be conducted and appears to be most fruitful when the two groups have common objectives or at least interests. Notwithstanding the increased productivity represented by parallel working demand for laser time still exceeds supply and the ratio of allocated time to requested time last year was less than 0.5.

Chapter 1 describes the work done during the year to improve the glass laser, the target facilities and diagnostic instrumentation. Notable here has been the commissioning of the six beam target chamber for compression studies and the conversion of the laser to phosphate glass.

Facility development is a continuing activity which must respond, as far as time and money permit, to user demand. For example, during the year it has become clear that increasing power will be demanded to generate X-rays for target backlighting and this has lead to a reconsideration of the optimum disposition of the newly available disc amplifiers, scheduled to be installed during the coming year.

Work on gas lasers is described in Chapter 2. Research here and elsewhere appears to confirm the need for short wavelength ($\sim$ 300 nm) lasers for compression and it now seems clear that one of the rare gas halides, probably KrF, will provide the basic element of any gas laser to replace glass. Though "Elf" has worked well and its successor, "Sprite" is in the design stage, there remain many major problems to solve, notably the determination of the best technique for pulse compression.

The expectation that laser wavelengths below 1 μm will be valuable has been partially confirmed by experiments using the second harmonic of the glass laser frequency, generated in phase matched KDP crystals. In particular Brillouin backscatter appears to be reduced (Chapter 3); ablation pressure, particularly at high irradiances, is significantly increased (see Chapter 4) and it has been known for some time that hot electron preheat is reduced. Another and novel method of reducing preheat by resistive inhibition is discussed in Chapter 4. In addition to these studies the interaction and transport groups have continued and extended their more traditional activities on harmonic generation in plasmas, on density profile determination and on exploding pusher targets, the latter in six beam geometry for the first time.

The commissioning of the six beam system, although as yet only at relatively low powers, has given considerable impetus to the work of the ablative compression group who have extended and refined the X-ray shadowgraphy technique described in previous reports. With more spherical irradiation, studies of target stability as a function, for example, of shell aspect ration can be undertaken and preliminary results are described in Chapter 5.

Relatively little work has been done at the central facility by the

Spectroscopy and XUV laser group in the past year but work has proceeded at Hull and Queen's Universities and it is hoped to give more time to this activity in the coming year. Chapter 6 describes this work, together with theoretical studies of line profiles conducted by the group at Imperial College which can provide diagnostic techniques for high density plasma. Most of the theoretical work associated with the Facility is, however, described in Chapter 7 which covers a wide and expanding range of activities from analytic modelling of implosions to the development of sophisticated particle-in-cell codes. Much of this work is carried out in Universities but is essential to the interpretation of experiments carried out at the facility.

A F Gibson
31 March 1980

GLASS LASER SCIENTIFIC PROGRAMME AND SCHEDULING COMMITTEE

SCIENTIFIC GROUPS

Group Title	Chairman	Secretary	Approx Time Allocated during year (weeks)
Laser Plasma Interactions	Mr T P Hughes Essex University	Dr D J Nicholas	10
Transport & Particle Emission	Dr J Kilkenny Imperial College	Mr W T Toner	7
Spectroscopy & XUV Lasers	Dr G Pert Hull University	Dr R G Evans	3
Ablative Compression	Prof M G Haines Imperial College	Dr P T Rumsby	18
Theory & Computational Modelling	Prof T J M Boyd Univ Coll of N Wales	Dr C Webb	-
Facility Development	Dr A F Gibson Rutherford Laboratory	Mr J E Boon	For development 12 For maintenance 6

CHAPTER 1 GLASS LASER FACILITY DEVELOPMENT

INDEX

CHAPTER EDITOR: J E Boon

CHAPTER 1 GLASS LASER FACILITY

1.1 Introduction

A number of important developments have been made during the year under review: in target facilities, in the laser and in diagnostic instrumentation.

Most important has been the extension of the laboratory area by about 265 m^2. Part of the extension houses capacitors for additional disc amplifiers to be brought into use during the coming year while the remainder provides two new target areas for single beam interaction studies and six beam compression respectively (see section 1.4). The position of one mirror in the laser area determines which target chamber receives power. Parallel operation in which one area receives shots while alignment, etc, is done in the other, has proved easier than the pessimistic feared. The six beam system, which provides reasonably spherical illumination (see section 5.2) has been used for both exploding pusher and ablative compression targets, as described in sections 4.4 and 5.4.

Last year's report described tests on commercially available samples of Nd doped phosphate glass. Following these the entire laser system was changed over to phosphate glass and the oscillator wavelength changed appropriately. The use of phosphate glass has given enhanced performance with fewer rods in the driver section, as discussed in 1.3 below. At the same time oscillator development has increased the range of pulse durations available for experiments including the simultaneous generation of a short probe pulse with a long pulse generated by stacking. Some experiments have called for both long and short pulses of green (530 nm) light (see, for example, 4.3) and these have been provided by harmonic generation.

All experimental physics is limited by measurement techniques and plasma physics is no exception. The on going programme of diagnostic development, much of it in UK Universities, is described in section 1.6. These instruments and techniques are in varying stages of development:

for example the X-ray microscope has been in routine use for much of the year and proved invaluable in the study of ablative compression by the X-ray backlighting technique while the use of coded zone plates for X-ray imaging was investigated only towards the end of the year under review. The use of these and other diagnostic developments are described in later chapters as appropriate.

A.F. Gibson

1.2 Glass Laser Operations

The start of this period saw two major changes to the laser systems. The first was the introduction of phosphate glass to replace the existing silicate glass and along with this the oscillator was modified to operate at wavelengths suitable for phosphate glass. The second was the introduction of six beam operations in the target area TA1 and this involved a passive splitting of the existing two beams into six. Fig.1.01 shows the laser system as used for the majority of the period of this report.

The year's programme covered 18 experiments over 33 weeks of actual operation time. The first half of this programme was marked by a high demand for changes of laser mode from experiment to experiment, modes required being a combination of long pulse/short pulse/stacked pulse, target areas TA1/TA2, fundamental/second harmonic, with/without probe beam/backlighting beam. As a result reliability problems were encountered and the resulting decision to minimise these changes of laser mode as well as institute an engineering programme to improve reliability led to a more efficient experimental programme during the latter half of the year. A total of 846 target shots have been provided for this year's experimental programme, of which only 6.5% have been lost due to faulty laser operation. During the experiments peak energies for nanosecond pulses have been 127 J per beam while peak powers for short pulses (100 ps) have been 0.5 TW per beam.

The year closed with the first experiment using a new oscillator. This

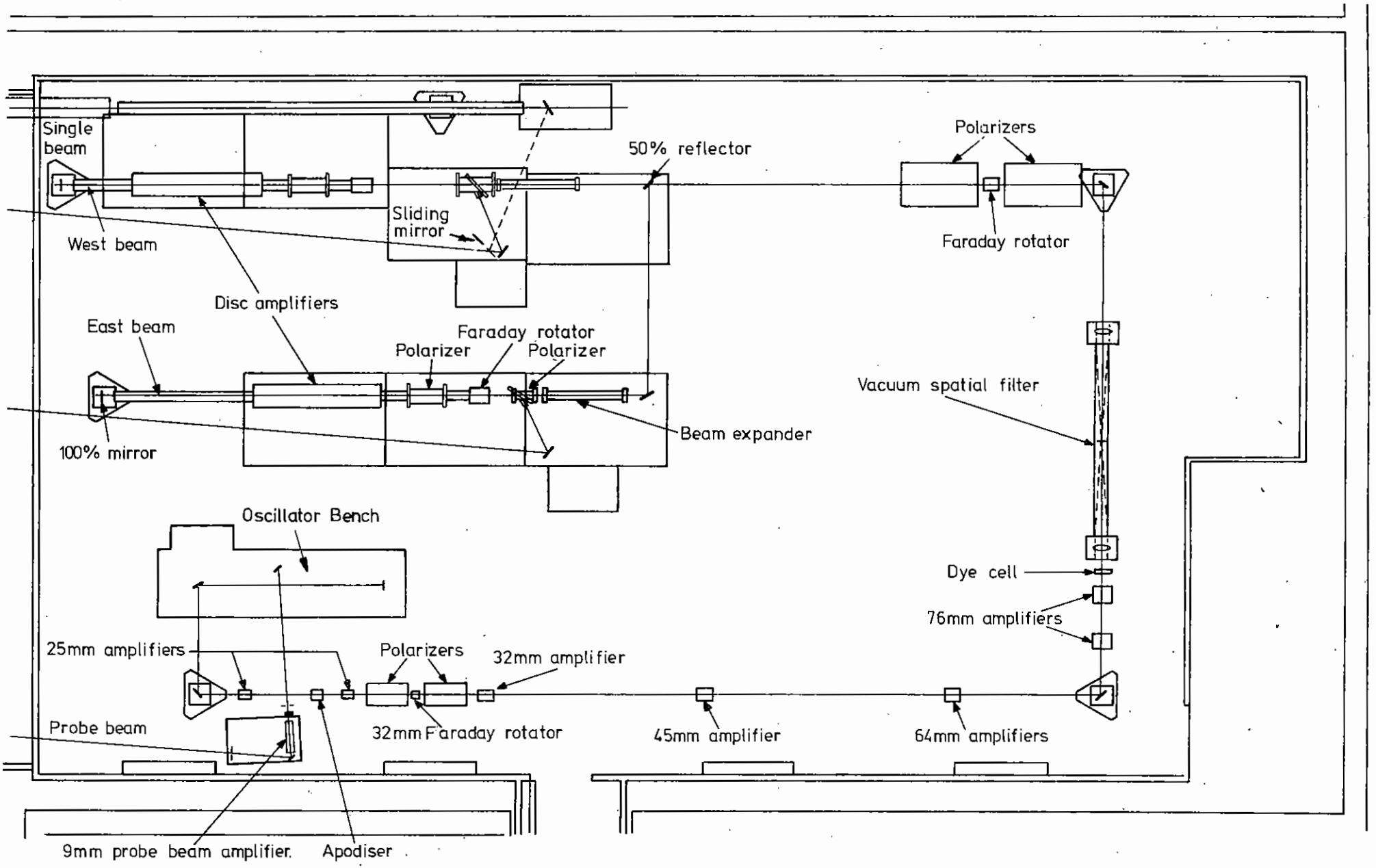
Single beam
West beam
50% reflector
Sliding mirror
Polarizers
Faraday rotator
Disc amplifiers
East beam
Faraday rotator
Polarizer
Polarizer
Vacuum spatial filter
100% mirror
Beam expander
Oscillator Bench
Dye cell
76mm amplifiers
25mm amplifiers
Polarizers
32mm amplifier
Probe beam
32mm Faraday rotator
45mm amplifier
64mm amplifiers
9mm probe beam amplifier
Apodiser

Fig 1.01

oscillator will improve reliability, give increased reproducibility of energy and pulse durations and give longer mode-locked pulses.

I.N. Ross

1.3 Glass Laser Development

1.3.1 Pulse Generator Development

Pulse generator development during this period has been largely concentrated on improving the performance and reliability of oscillators matched to the phosphate glass wavelength. At the beginning of the period the 1.052 μm tuned YAG oscillator was being used to generate both mode-locked and Q switched pulses, and a change of dye, cavity resonator, and switch-out unit was involved in changing between "short" and "long" pulse laser operation. In September 1979 this oscillator was devoted entirely to Q switched operation for long pulses, and improvements were made to rectify its earlier long term reliability problems. During February 1980 the new two-oscillator front end was commissioned, with an actively mode-locked glass oscillator providing short pulses over the range of 75 to 750 ps which complemented well the 600 ps to many nanosecond pulse duration capability of the fast switchout system following the Q switched oscillator. The new oscillator table layout is shown in Fig.1.02. Change over between short and long pulse operation now only involves the movement of the one mirror M_c.

Some time has also been devoted to the development of electro-optic gates and switchout systems. As well as the improvements to the reliability and flexibility of the long pulse gate out unit, encouraging preliminary results have been obtained with a mode-locked pulse selector based on a laser activated silicon switch.

M.S. White, I.N. Ross

1.3.1(a) 1.052 μm YAG Oscillator

The YAG oscillator, now dedicated to long pulse operation, is tuned to the 1.052 μm line of Nd in YAG with three Brewster angle prisms, to provide a close wavelength match to the phosphate glass of the amplifier chain. It is passively Q switched with BDN dye. A two etalon resonant reflector constrains the oscillation to single longitudinal mode to provide a temporally smooth pulse. During the year two improvements have been made to this oscillator.

The first was the addition of a 25 μm air spaced etalon (with 30% reflectivity faces) to greatly enhance the wavelength selection by the prisms of the comparatively weak 1.052 μm line against parasitic misaligned 1.064 μm modes. Previously the prisms' discrimination had been just adequate to run the oscillator mode-locked or Q switched up to moderate power levels. Mode pulling degraded the beam quality and there were problems with long term reliability. Installation of the etalon has completely eliminated the problem of parasitic 1.064 μm modes, and allowed the oscillator to be run at higher power levels using a stronger Q switching dye, with a resultant improvement in shot to shot repeatability. It now produces typically 9 mJ in a 35 ns pulse with an energy standard deviation of 6.5% without having reached any fundamental limit, whereas without the etalon the figures were limited at around 4 mJ, 60 ns, and 10% respectively.

The other improvement involved reconfiguring the output resonant reflector, which now consists of a 150 mm and a 5 mm fused silica etalon separated by an 80 mm air gap, with the 150mm component outermost. The incidence of shots producing a modulated temporal pulse envelope due to mode beating is now down to $\lesssim$ 1%. Even when mode beating does occur, it now has a period of 9 ns and is unlikely to significantly perturb the switched out fraction with its 0.6 - 2 ns timescale, except in the rare event of a very deeply modulated pulse.

The long pulse gating system following the Q switched oscillator has been brought to fully operational status, and has worked extremely reliably

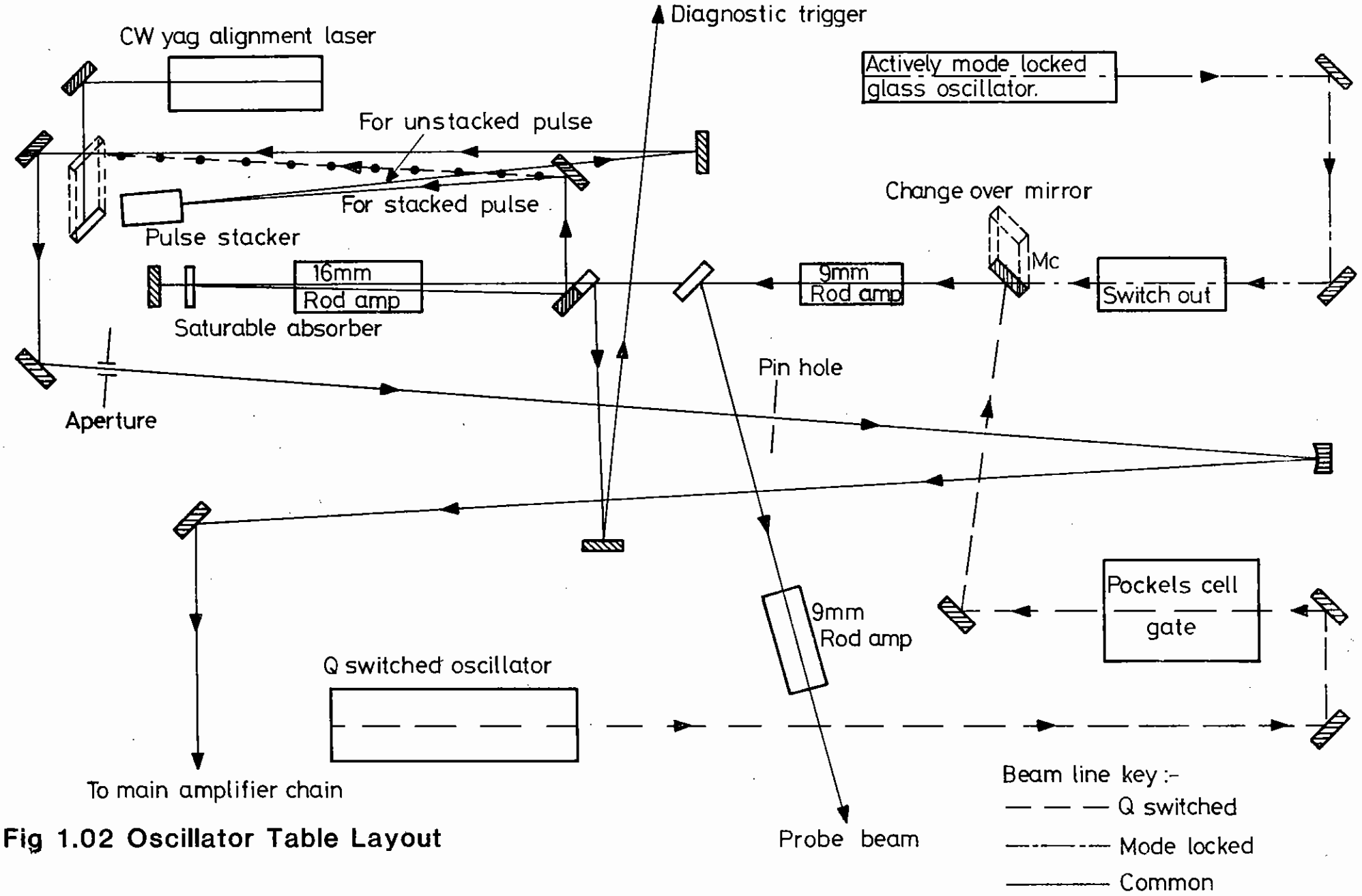

Fig 1.02 Oscillator Table Layout

over the many months of long pulse operation during this period. Very clean pulses as short as 580 ps (fwhm) have been generated with risetimes around 400 ps and a power contrast ratio of nearly 10^4.

M.S. White

1.3.1(b) Actively Mode-locked Glass Oscillator

An actively mode-locked phosphate glass oscillator has been installed as part of the new two-oscillator system front end. It has shown a reliability and shot to shot reproducibility far superior to the previous passively mode-locked system as well as the capability to produce a much wider range of pulse durations. The oscillator was produced as part of a development contract with J.K. Lasers Ltd. It is based on a 5" x 3/8" EV4 glass rod mode locked by a Bragg angle tuned temperature controlled acousto optic modulator. The Q switching is passive, using BDN dye. Invar bars support the optical resonator.

The oscillator delivers a mode locked train of about 45 pulses with a total energy of 5 to 6 mJ. The shot to shot repeatability is very good, with the peak pulse in the train showing an energy standard deviation of better than 5% and a pulse duration standard deviation of better than 10% (at around 100 ps). The power could be increased and the reproducibility improved still further by the use of a stronger Q switching dye, but after experiencing long term damage accumulation in the original loss modulator crystal, the present device is being run in a very conservative fashion. By using different intra-cavity etalons in conjunction with varying the modulator drive level, the oscillator has reliably produced pulses over the range 75 - 750 ps, and less reliably up as far as 1.2 ns. However, in a brief trial using Pockels cell Q switching instead of the dye, trains of mode locked pulses as long as 1.8 ns (fwhm) have been reliably obtained. This approach shows promise and is being pursued.

I.N. Ross, M.S. White, J.K. Wright, T.B. Read and N.C. Cole

1.3.1(c) Photoconductive Silicon Switches

Photoconductive semiconductor switches offer an attractive alternative to more conventional high voltage switches (krytrons, laser triggered spark gaps, avalanche transistors, etc.) in view of their essentially zero inherent jitter and their capability of producing very fast risetimes.

During this reporting period we have assembled a silicon switch single mode locked pulse selector whose longer term reliability is currently under test. A silicon switch prepulse monitor is ready for trial in parallel with the existing photodiode system, as is a diagnostic trigger pulse generator. A 76 mm aperture Pockels cell is being tested in conjunction with a silicon switch, with a view to replacing the mid-chain saturable absorber dye cell for the control of amplified spontaneous emission.

Two designs of switch have been investigated. Both are constructed by modifying HN series through connectors to switch pulses in coaxial cables. In the first design (due to Mourou et.al., ref.1.01) part of the central conductor of the through connector is replaced by a silicon bar. A gap of a few mm is left between silver paint electrodes, and the structure is strengthened and protected against surface tracking by a thin layer of clear epoxy. A stub on one side of the connector is pulse charged (to avoid thermal avalanche breakdown) with a krytron pulse generator (1.02). When a laser pulse is applied photoconductive switching occurs between the charged stub and the output line. This switch design is very fast, normally laser pulse limited in its risetime, because of the excellent impedance matching continuity. But it is not voltage efficient in the sense that switching one cable into another produces a voltage pulse of amplitude only half the stub charging voltage, and in only one output cable.

The alternative switch design avoids this voltage halving. Although the construction is basically similar, the inner conductor is left complete and shorted to the ground (the outer casing) by the photoconductive switching of the silicon gap. A voltage edge of magnitude equal to the full charging voltage is then launched down both cables leading from the

switch. Both voltage edges can be used to open Pockels cell gates and (depending on the details of the layout) at least one of them can be reflected from a short or open circuited stub to shut the gate after the pulse.

The oscilloscope trace in Fig.1.03 illustrates the exceptionally clean and fast high voltage waveforms obtainable from the photoconductive silicon switch. Here a $\underline{\sim}$ 1.5 kv $\underline{\sim}$ 1.7 ns pulse from a "straight through" type switch has been displayed on a direct access Tektronix 7912 transient digitizer protected by coaxial attenuators. The pulse rise and fall times were instrument limited at around 350 ps, whilst the duration was controlled by the length of the charged stub. The amplitude was dictated only by the voltage handling capability of the attenuators, and in fact the switches of this design produced to date have switched up to 7 kv (i.e. 3.5 kv pulses). Improvements to the switch construction techniques are in hand which may allow this to be raised nearer the 7 kv target.

The switches have been used to activate an optical gate based on a 6 mm aperture Pockels cell. A single 100 ps mode locked pulse from a passively mode locked Nd:YAG oscillator was divided on a beamsplitter. Half activated the silicon switch while the other was taken through an optical delay trombone to the Pockels cell gate. Varying the optical delay to sweep the probing pulse through the rising edge of the gate's temporal profile gave a total turn on time of 300 ps. This represents a convolution of the 100 ps probe pulse with the electrical switching time of the silicon switch and the Pockels cell risetime (with the latter expected to dominate for the comparatively large aperture cell) and thus only provides an upper bound to the electrical switching time. However, it is clear that the use of photoconductive semiconductor switches enables the switching edge of a single mode locked pulse selector to be brought an order of magnitude closer to the pulse leading edge than, for example, in a krytron or transistor driven system, with great resultant benefit to the overall contrast ratio.

Preliminary results have recently been obtained from the new switches, of the "short to ground" geometry. They are not as fast as the straight

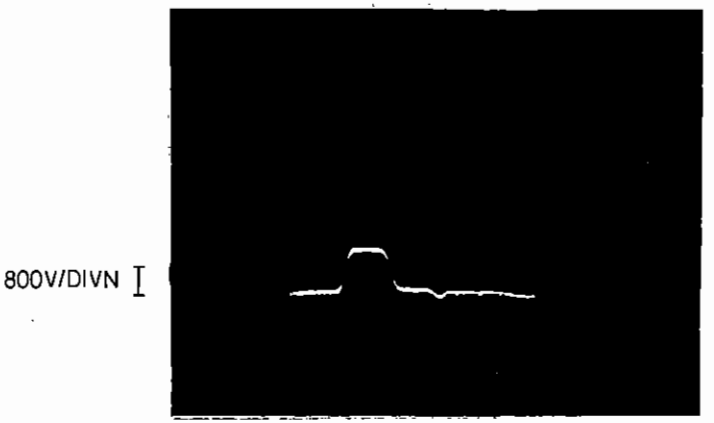

a) Voltage waveform from laser activated silicon switch.

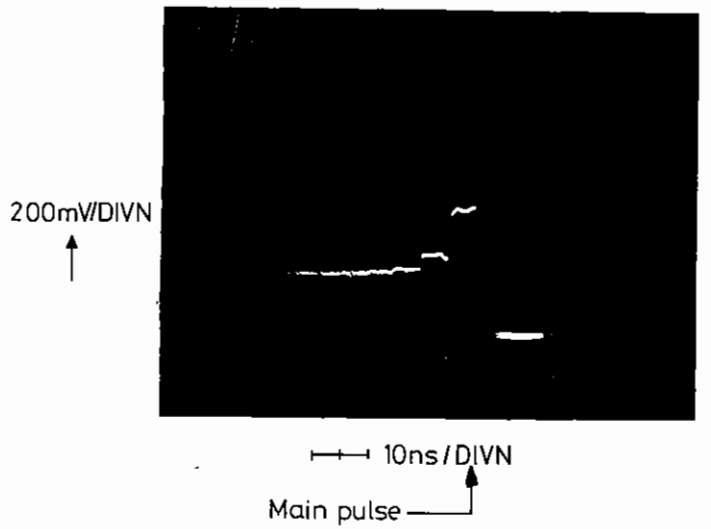

b) Voltage waveform generated by the switch as a prepulsemonitor

Fig 1.03

through design because impedance matching cannot be maintained to the same extent in this format. Even so, risetimes of less than 500 ps were obtained from the prototype, with room for further improvement. Its advantage in voltage efficiency was as expected - so far up to 8 kv pulsed edges down both cables have been obtained without having reached any fundamental limit. For applications not requiring ultra fast risetimes, but where the second channel of output and the extra ease of obtaining high voltage would be advantageous, this design may well be more attractive. Pockells cells controlling ASE in the amplifier chain are a good example.

Finally, Fig.1.03 shows a waveform produced by the photoconductive switch set up as a prepulse monitor. In this application its advantages over a photodiode are twofold. Its much faster risetime allows prepulse monitoring much closer to the leading edge of the main pulse. And, secondly, the long relaxation time of the silicon integrates the prepulses to an energy proportional "staircase" waveform which is far less ambiguous in interpretation than a photodiode record. In the photograph the switchout unit following a mode locked oscillator has been deliberately misaligned to give a leakage rising to 2×10^{-3} in power just before the main pulse. Each successive mode locked pulse caused additional partial switching of the silicon to give another step on the "staircase", before the trace disappeared upward on arrival of the main pulse. Responsivities were typically several volts per microjoule of prepulse energy with the switch conveniently DC biased to 50 volts.

M.S. White, E. Hodgson.

1.3.2 Phosphate Glass Performance

Initial measurements on the laser system following the introduction of phosphate glass were of its peak power capability under short pulse (100 ps) operation. Restriction of the uniformity of the output beam intensity profile to less than 2 to 1 modulation depth yielded a maximum output energy per beam of 65 joules in 80 ps, representing a peak power of 0.81 TW. This was thought to be limited to less than one terawatt by

break up due to significant scattering in the apodiser and Faraday isolators. However, despite this limitation achieved powers were a factor of 2 higher than those obtained using silicate laser glass.

The phosphate system has seen an extended period of long pulse operation, with pulses from 1 to 3 ns. To date expected maximum energies (more than 200 Joules per beam) have not been achieved primarily as a result of unexpectedly low damage thresholds on some large polarizers. Aside from this temporary limitation the system has performed as expected and particularly reliably following the introduction of an improved 1.052 μm selection technique in the Nd:YAG oscillator.

Measurements have been made of gain achieved by individual rod amplifiers (the gain of phosphate discs in the disc amplifiers was reported in the 1979 annual report). Table 1.01 presents the results of these measurements and a comparison with silicate glass in the same amplifiers. The larger rod amplifiers are limited by parasite oscillation but achieve very good values of α D in the region of 0.45. For smaller diameter amplifiers the phosphate to silicate ratio of gain coefficients approaches the expected ratio of cross sections. The gain of the ϕ76 mm rod was unexpectedly low and suggests that the system would achieve slightly higher power using ϕ64 mm rod amplifiers instead of the ϕ76 mm amplifiers.

The optical quality of the phosphate system is good and, as hoped, there has been no evidence of thermal lensing due to the rods. Dynamic output beam quality is still restricted by distortions in the disc modules and for a good quality beam to be maintained over many shots it is necessary to restrict the repetition rate to once every hour.

No major problems have arisen as a result of the use of phosphate glass. However, greater surface cleanliness is required on phosphate glass to prevent surface pitting in use, and it has proved somewhat more difficult to clean.

I.N. Ross, M.S. White, N.A. Allen

TABLE 1.01

Small Signal Gain Measurements on Phosphate and Silicate Glass Rod Amplifiers

Rod diameter (mm)	76	64	45	32	25
Rod length (mm)	135	135	135	135	230
Phosphate gain	1.9	2.6	3.7	5.0	25
Phosphate gain coefficient					
α_p	0.048	0.071	0.097	0.119	0.140
αD	0.36	0.45	0.44	0.38	0.35
Silicate gain coefficient					
α_s	0.041	0.058	0.068	0.076	0.085
α_p/α_s	1.17	1.22	1.43	1.57	1.65

1.3.3 Alignment

Laser alignment has proved reliable and adequately stable to meet the experimental requirements to date. The future experimental programme places more stringent requirements on beam alignment and the enhancement of the laser to six beams increases the need for more automatic systems for setting up and running the laser.

An automatic alignment monitoring station has been designed and a prototype tested. Fig.1.04 shows a schematic of this device. The system uses two quadrant detectors to measure simultaneously the error in both the position and angle of the beams. The system can be used with HeNe, CW Nd:YAG or pulsed beams, but is principally intended to monitor using the main CW Nd:YAG alignment laser. The station was required to have a sensitivity in position of 1% of beam diameter and in angle of better than 100 μrad when using a CW Nd:YAG laser having about 1 watt output power.

The testing of the alignment station showed a positional sensitivity of 0.1% and an angular sensitivity of 50 μrad more than meeting the above requirement. Experience has been gained with the alignment station installed to monitor the single beam leaving the laser room for target area TA2. This has shown, for example, that our CW Nd:YAG laser has short time instabilities greater than the required tolerances on the main laser beam. It is therefore necessary to time average the error signal to reduce the instability to an acceptable level. We also plan to make improvements on the CW laser itself.

I.N. Ross, E. Hodgson, J. Watson.

1.3.4 Six Beam Enhancement - Progress

Almost all the necessary hardware has now been procured for this enhancement programme. This includes four extra disc amplifiers, Faraday isolators, and all the necessary optics including laser glass discs (EV4), Faraday discs and multilayer polarisers. Laser Applications Ltd. have nearly completed installation of the capacitor banks, ignitron switches

and associated components for the disc amplifiers and Faraday rotators. Work on the control and monitoring systems has started. Manufacture of the CAMAC flash tube monitor units is proceeding, and a Faraday rotator interlock unit has been built. Components for the extended PILC supply have been delivered. The power supplies at 20 KV for disc amplifier flash tubes, and 6 KV for the Faraday rotators will be upgraded to provide a charging time for the complete 6 beam installation of about 2 minutes.

The majority of effort is now being concentrated on the design layouts for both laser areas, involving the rearrangement of existing components together with the installation of the new components. The aim is to make the best use of the available equipment for the likely requirements of the users, and to allow for future developments to be installed with the minimum of disturbance.

The major change from our original concept of six parallel amplifiers, in the short term, has been caused by the need to dedicate one disc amplifier for the backlighting beam and the beam into the single beam target area. It is likely that the backlighting beam will be required to be of short duration compared to the main beam, and must therefore be driven through a separate driver and disc amplifier.

The beams for the six beam target area will be derived by splitting the beams from three double passed disc amplifiers, driven in turn by a fourth double passed disc amplifier, but arranged in a manner that three further disc amplifiers can be added to the system with minimal disturbance.

It is also intended that all seven output beams be fitted with three diagnostic units; an energy monitor, an alignment station, and a means for recording near and far field distribution. The installation of second harmonic crystals on the six beams for Target Area I will form an integral part of the system for forseeable experiments.

I.N. Ross, P. Gottfeldt, M. Forster

1.4 Target Areas - Parallel Operation

After Target Area I had been commissioned, parallel operation with Target Area II was attempted as an experiment by manually placing a mirror to deflect the beam into TAII between shots into TAI. The change over mirror has now been fitted to a precision slide, operated from the control room, which enables the beam to be directed into either area with no alignment problems. The laser is now scheduled to operate using both areas in this manner, which increases the number of experiments that can be accommodated.

J E Boon

1.4.1 New Six Beam Target Area TA1

Commissioning experiments in the new six beam target area commenced in June 1979 with a series of exploding pusher implosions. The number of beams used to drive these implosions was increased in stages from two to four to six and a dramatic improvement in implosion symmetry noted (section 4.4). Exploding pusher experiments were followed by several successful six beam ablative compression experiments (section 5) some of which used an additional seventh laser beam to produce a backlighting X-ray source for radiography. In addition to compression experiments the new facility has been used to study interferometrically the symmetry of the plasma corona surrounding targets illuminated by four laser beams.

Fig. 1.05 is a general view of the experimental area showing the target chamber with attached Kirkpatrick-Baez X-ray microscope and streak camera system. The seventh laser beam, used for X-ray backlighting experiments, is introduced into the top of the target chamber as shown. Also shown is the three level optical reference and alignment platform where the six incoming beams from the laser area are intercepted to allow local CW alignment lasers to be injected. This system allows the beams transmitted through and retroreflected from targets in the chamber to be monitored. This alignment system is operated independently to the main laser area and has proved very efficient in allowing maximum utilization of laser time. Experiments can be prepared and targets aligned while the laser system is being maintained or delivering shots to the other target area. When the

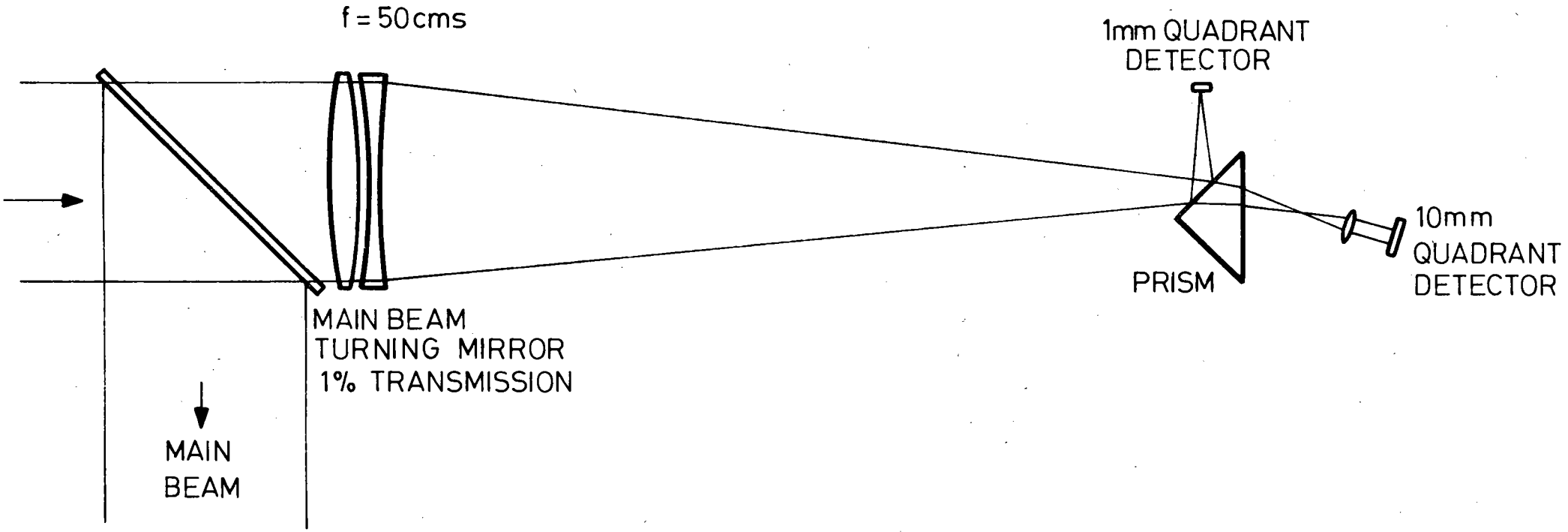

Fig 1.04 ALIGNMENT STATION

six beam chamber is ready to receive shots, shutters are opened and mirror adjustments made to align the incoming CW laser beams from the laser area with the target area near and far field reference monitors.

Fig. 1.06 is a view inside the target chamber showing the stepper motor driven lens and target mounts. At present, due to lens supply problems, six beam implosion experiments are conducted using a combination of two f/1 doublet lenses and four f/1.5 singlets. This situation will be rectified by the middle of 1980 when new aspheric lens production techniques that are being developed lead to quantity deliveries of new lenses. After this time all implosions will be conducted using six f/1 lenses with a consequent improvement in illumination uniformity. In addition to the main target mount shown in the figure a second mount is available for placing backlighting targets within a fraction of a millimeter of the shell target. These backlighting targets are irradiated, via an f/2.5 lens, with a seventh laser beam which has a similar alignment and reference table to the 6 main beams and in addition has an optical delay section to enable the time of arrival of the beam at the centre of the chamber to be varied.

At present replacement of targets and removal of some diagnostic devices requires that the vacuum chamber be let up to air and ports removed. A complete let up and pump down cycle can take as little as 5 minutes and consequently this practice does not significantly slow the laser shot rate which is dictated by the disc amplifier cooling time to roughly one per hour. However, for reasons of lens and alignment stability, chamber cleanliness and ultimate vacuum an airlocked target insertion mechanism has been designed and built. Two such systems will be installed on the chamber in mid 1980.

Our present X-ray streak camera was designed to mount on the original two beam target chamber and consequently is too large to mount other than on the outside of the new six beam chamber. Target to cathode spacings of less than 55 cm are unattainable and for most streak work a Kirkpatrick-Baez microscope with x15 magnification (section 1.6.2(b)) has been used to relay the image outside the chamber. To overcome this limitation and to

allow streaked high energy X-ray pinhole imaging and streaked X-ray spectroscopy of six beam implosions a new miniature streak tube has been developed (section 1.6.2(a)). This system inserts inside the chamber and allows target to cathode spacings of down to 18 cm to be achieved. This system will become operational in early 1980.

Approximately 100 successful, fully diagnosed, compression shots have been carried out in the 10 experimental weeks scheduled during the period of this report. In addition a roughly similar number of shots have taken place for purposes of ASE and prepulse checks, diagnostic test and interferometry experiments.

C. Hooker, S. Knight and P.T. Rumsby

1.4.2 Single beam target area TAII

Target Area II was used extensively throughout the year, often in parallel with Target Area I. The basic layout in TAII proved to be convenient to operate and remains unchanged. The energy monitoring system was studied and its operation is now a routine matter. Almost routine pulse length measurements can now be made using the EPL streak camera coupled to a two dimensional OMA and read-out through the GEC 4080 (section 1.6.6(a)).

The only significant change in the optical alignment system was the replacement of the refractive beam expander by a cassegrain telescope. Since all the input alignment lasers are defined by the same pinhole, the telescope produces colinear, confocal, expanded beams at all wavelengths. This greatly simplifies the procedures for operation at .53 μm.

The tuning characteristics of the frequency doubling crystal were studied using an auxiliary laser and improvements were made to its mounting so that effects due to ambient temperature changes could be corrected without any need for further optimisation during a run. There was a very successful series of green beam irradiations in the autumn. The peak power which could be used was limited by damage to the anti-reflection coatings on the windows of the cell containing the crystal. New windows

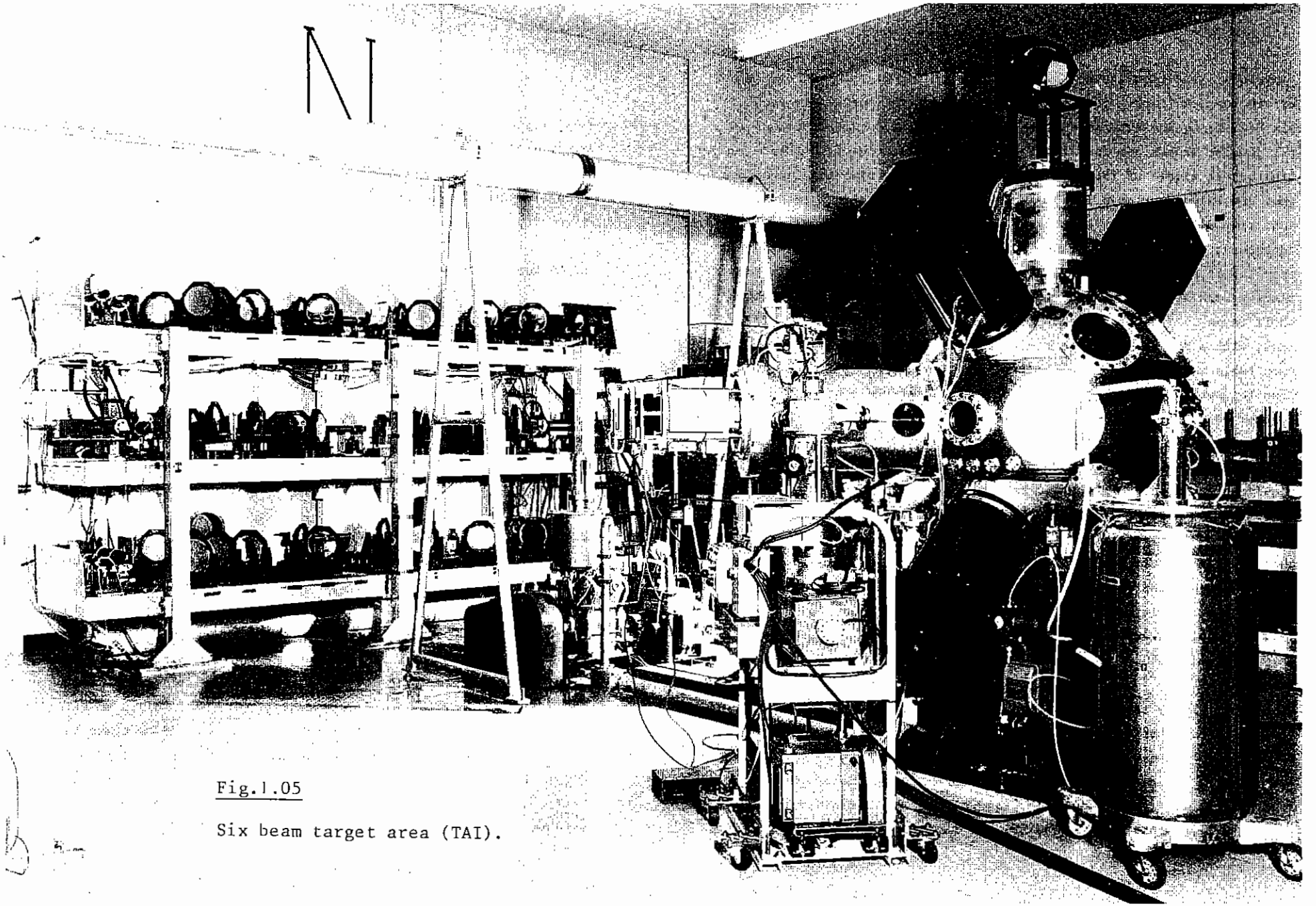

Fig.1.05

Six beam target area (TAI).

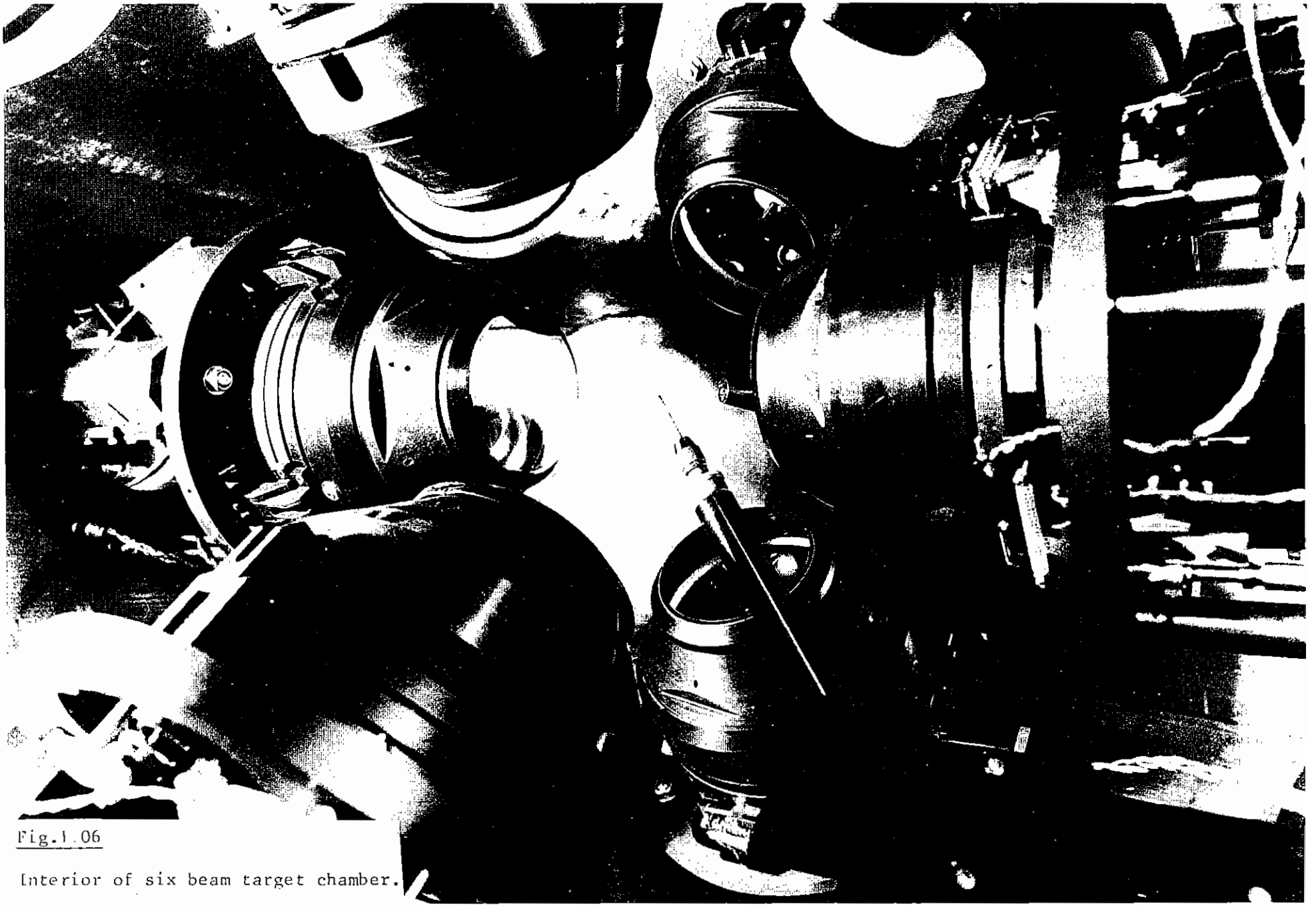

Fig.1.06

Interior of six beam target chamber.

without AR coatings have now been procured. During the green runs, some damage to the ICOS lens resulted from back-reflection from the pellicle used to protect the lens from target debris. In the green there is a ghost image just outside the lens surface. A new angled pellicle mount has been made which ensures that pellicle back-reflections miss the lens completely.

W.T. Toner, J. Szechi and D. Pepler

1.5 Target Fabrication

Once again both the number and complexity of targets required for the experimental programme have increased compared with previous years. All single beam experiments have required targets consisting of either thick or thin foil substrates coated with at least two layers of various materials. In addition most compression experiments have used shells coated with various layers.

X-radiography experiments are now performed in the new six beam chamber where two independent target mounts are available. Consequently, these experiments now require the preparation of two targets per implosion shot. For streaked radiography experiments targets consisting of 10-25 μm thick, 0.5 to 1 mm wide strips of brass or aluminium attached to suitable bases are used. For pulsed X-radiography experiments large numbers of 125 μm thick, 1 mm wide mylar strips coated with 2 μm thick layers of potassium chloride have been prepared.

Layered target preparation techniques have been simplified by the installation of a multi-turret evaporationhead in one coating plant allowing sequential deposition of up to four different materials. In addition a 3 kW electron beam evaporation unit has been installed in another coating plant enabling high melting point materials to be deposited.

Many multi-layered targets have required one or two intermediate layers of plastic separating high Z materials. Plasma polymerization techniques for

Fig.1.07

50 μm thick gold coating having a density of less than 0.2 gm/cm^3.

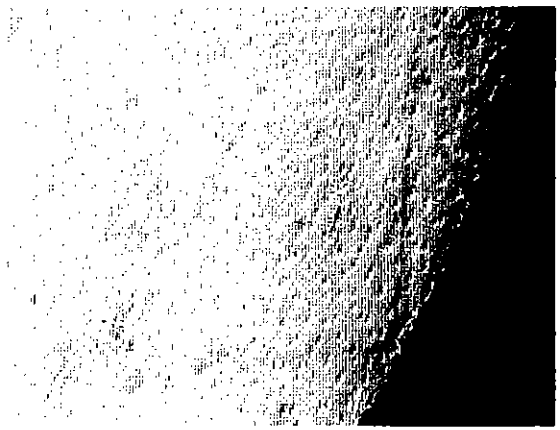

Fig.1.08

Gold lolipop target of 300 μm diameter and 3 μm thick with gold perturbations of 8 μm periodicity.

applying such coatings would require transfer of the targets to and from another coating plant with consequent possibility of contamination and would involve more complex measurement methods. To allow rapid preparation of such targets using the multi-turret evaporation head we have developed techniques for the thermal evaporation of polythene. Using a large molybdenum boat, filled with finely ground polythene powder, and pepper pot lid we have found the best heating cycle and deposition rate in order to avoid 'spluttering' of the molten polythene. By this technique high quality layers of polythene up to 3 μm thick have been deposited on various substrates and incorporated into targets. Measurements of such coatings have shown that they have a density of 0.7 $gm.cm^{-3}$.

Experiments to study the resistive inhibition of fast electron preheating have required the development of techniques for the deposition of gold layers having densities as low as 0.5% of solid density. Fig. 1.07 shows an example of such a coating showing scale size less than 1 μm. Layer thickness up to 100 μm have been deposited on flat substrates in a special vacuum plant where pressures around 10 torr of argon and high flow rates are carefully maintained. At these high pressures convection currents and gas flow dominate the deposition process and consequently care has to be taken to avoid substrate heating by suitable choice of deposition geometry. It has been found that coating density scales roughly inversely with chamber pressure, densities of about 10% of solid being produced at pressures of about 1 torr and densities less than 1% at pressures above 10 torr.

Coating techniques have also been developed for the controlled deposition of perturbations onto lollipop targets for Rayleigh-Taylor instability growth experiments. Fig. 1.08 shows a section of a 300 μm diameter, 3μm thick gold lollipop onto which 1 μm high gold perturbations with periodicity of 8 μm have been deposited. By placing many unmounted lollipop targets on the rear of electroformed grids of the required periodicity and transparency and coating various materials through the grid we have found it possible to fabricate targets with perturbation amplitudes up to a few μm and periodicity from a few to several tens of μm.

The total number of targets produced by the target fabrication group during the year has increased due mainly to increasing periods of parallel target area operation. Over 500 microsphere targets have been prepared for compression experiments and alignment purposes and a similar number of foil targets, lollipops and layered targets produced for single beam experiments.

G. Arthur, B. Child, S. Hallewell and P.T. Rumsby

1.6 Diagnostic Development

1.6.1 Optical Probe Beams

A new optical probe beam system was installed during the last year to facilitate alignment and to achieve certain experimental requirements, for example a long stacked heating pulse and, simultaneously, a short diagnostic pulse.

The layout of the probe beam is shown in Fig.(1.09). A fraction (∿ 1 mJ) of the oscillator pulse is split off by a 50% beamsplitter and amplified by a high repetition rate amplifier. A gain of up to 80 can be obtained if only every second oscillator pulse is amplified. The beam is then passed through a multipass delay line in order to achieve an approximate synchronization with the main beam. The probe beam is next directed to one of the two target areas where a further adjustable optical delay allows fine tuning between the heating and the diagnostic pulse and makes a time separation of up to 6 ns of the two pulses possible. To spatially filter the probe pulse, a 500μm diameter pinhole follows a 1 m focal length positive lens. A 50 cm focal length positive lens collimates the beam and reduces it to half its original size. The 1052 nm light is then converted to green (526 nm) in CDA-crystal cut for type I non-critical phase matching. At accurate phase matching approximately 10% energy conversion to the second harmonic is achieved giving 1.5 to 2 mJ of green output. The unconverted 1052 nm light is absorbed in a heat absorbing glass filter. If a UV probe beam (263 nm) is needed, the green beam is further doubled in a type I critical phase matched ADP-crystal. Again a 10% conversion efficiency from the second to the fourth harmonic

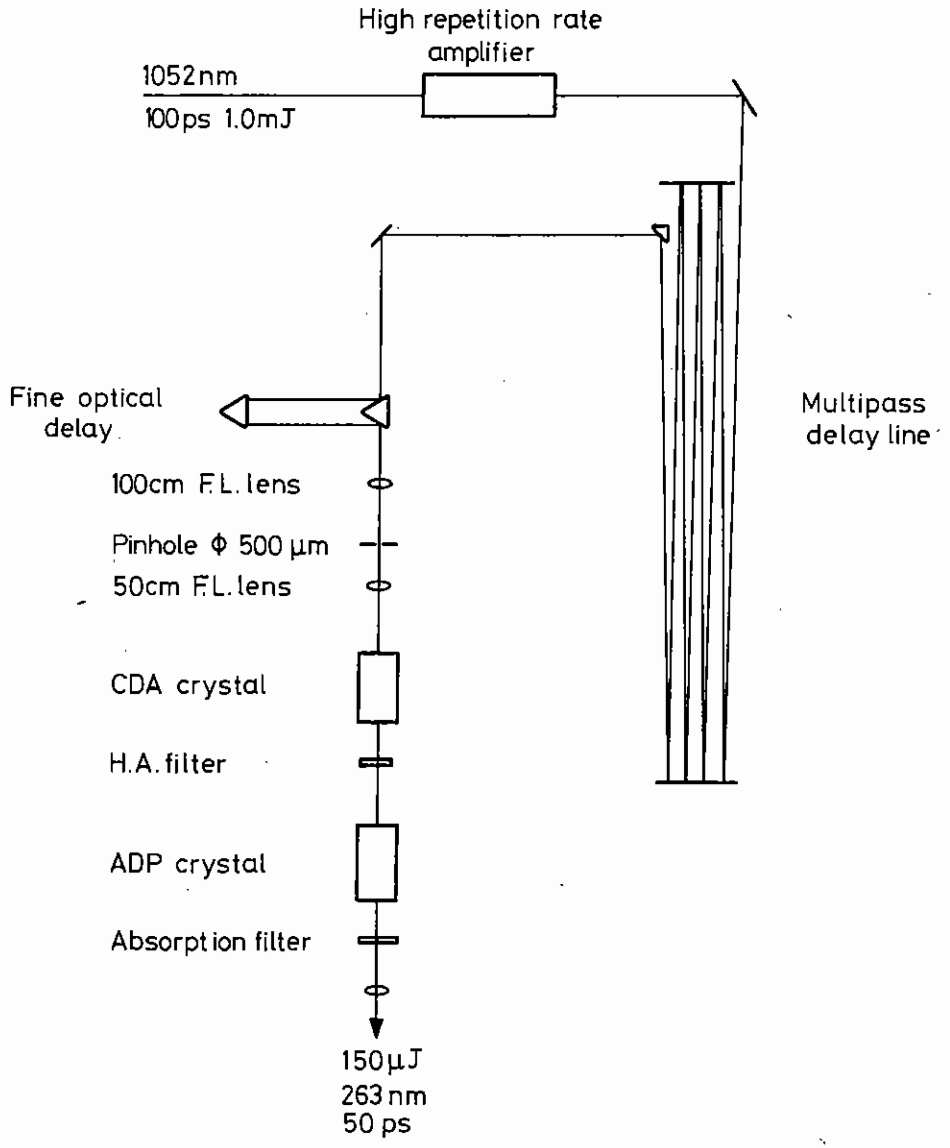

Fig 1.09 **OPTICAL PROBE BEAM SYSTEM**

is obtained for optimal phase matching resulting in 150 to 200µ mJ of UV light, which is sufficient for interferometry and holography. The second harmonic can also be shifted to the red (633 nm) using Raman cell (1.03), should it be required by the experimental programme.

Although all mirrors in the probe beam system have reflectivities of 99.9%, there is an energy loss of about 30% in the system, but this is of no importance due to the high gain in the probe beam amplifier.

The generation of the probe beam by means of a split off portion of the oscillator pulse has the great advantage that the remaining heating pulse can be stacked to a long pulse (see section 1.2) and therefore electron density profile measurements and magnetic field studies of ablatively driven targets can be made. Also a great flexibility of the main beam energy is achieved due to the possible gain variation in the amplifier chain. The probe beam system further proved easy to align due to the high repetition rate of the probe beam amplifier.

Different probe wavelengths can now be provided in both target areas at all times for experiments, such as shadowgraphy, interferometry, and or Faraday rotation measurements.

C. Duncan, A. Raven and O. Willi.

1.6.2 X-ray Imaging

1.6.2(a) New X-ray Streak Camera

A new X-ray streak camera has been designed and is under construction for use in the six beam interaction chamber. This is a compact instrument which can be located close to the target without obstructing either the focusing lenses or other diagnostic ports. It can therefore be left permanently in position to provide routine diagnostic information.

The main features of the new X-ray streak camera are shown in Fig.1.10. A modified version of the existing image tube is used. The photocathode and mesh are mounted on an insulating cylindrical extension to the cone electrode as shown in the figure. This new arrangement maintains the cathode and mesh parallel with a separation of 0.5 mm and also ensures that their surfaces are normal to the axis of the tube. This assembly is of a demountable construction which can readily be removed from the image tube allowing easy interchange of photocathodes. The photocathodes will typically consist of low density CsI deposited on a 15 μm beryllium substrate.

A second major change to the image tube is the shortened glass envelope which results in the photocathode mesh assembly projecting out in front of the main body of the tube. This has allowed the design of a compact housing which also incorporates the streak electronics. An additional pumping route has been provided to aid evacuation of the rear of the tube.

The X-ray calibration source (section 1.6.4) will be used to test the static operation of this new camera and time calibration of the streak speeds will be carried out at Queen's University, Belfast.

M. Lamb

1.6.2(b) Kirkpatrick-Baez X-ray Microscope/Streak Camera Coupling

In last year's Annual Report (1.03) the design and testing of an X-ray microscope was discussed. Recently the magnification of the microscope has been increased from 10 to 15 to allow the device to be coupled to the X-ray streak camera. The spatial resolution of the 15 x microscope has been measured using back-lit grids and glass microballoons and results show that the instrument is capable of a resolution of $\sim$ 5 μm at the object plane.

To facilitate alignment of the microscope the image can be recorded on polaroid film via an aluminized phosphor screen and intensifier. This recording system, being completely ex-vacuum, offers a higher shot repetition rate than conventional X-ray film recording.

The microscope/streak camera pair has recently been used to obtain streaked shadowgraph images of ablatively driven implosions using six beam illumination. Here the "dynamic" spatial resolution of the system is estimated to be $\sim$ 15 μm. Fig. 1.11 shows a schematic representation of the system.

R.L. Cooke, C.L.S. Lewis, P.T. Rumsby and C. Hooker

1.6.2(c) Zone Plate Coded Imaging of X-rays (ZPCI)

This technique has been developed during the last year and is now in use on the six beam irradiation facility. It provides a moderate resolution, two dimensional, X-ray imaging diagnostic.

The zone plates which were used, see Fig. 1.12 , were manufactured in 10μm thick copper using precision photolithography and electroforming techniques. They were supplied by Graticules Ltd., according to our specifications. The zone plates had 120 zones and a minimum zone width of $\sim$ 15μ which limited the resolution to $\sim$ 20 μm. Their large collection area ($\sim 10^{-1}$ sr) means that they can be used for relatively weak sources

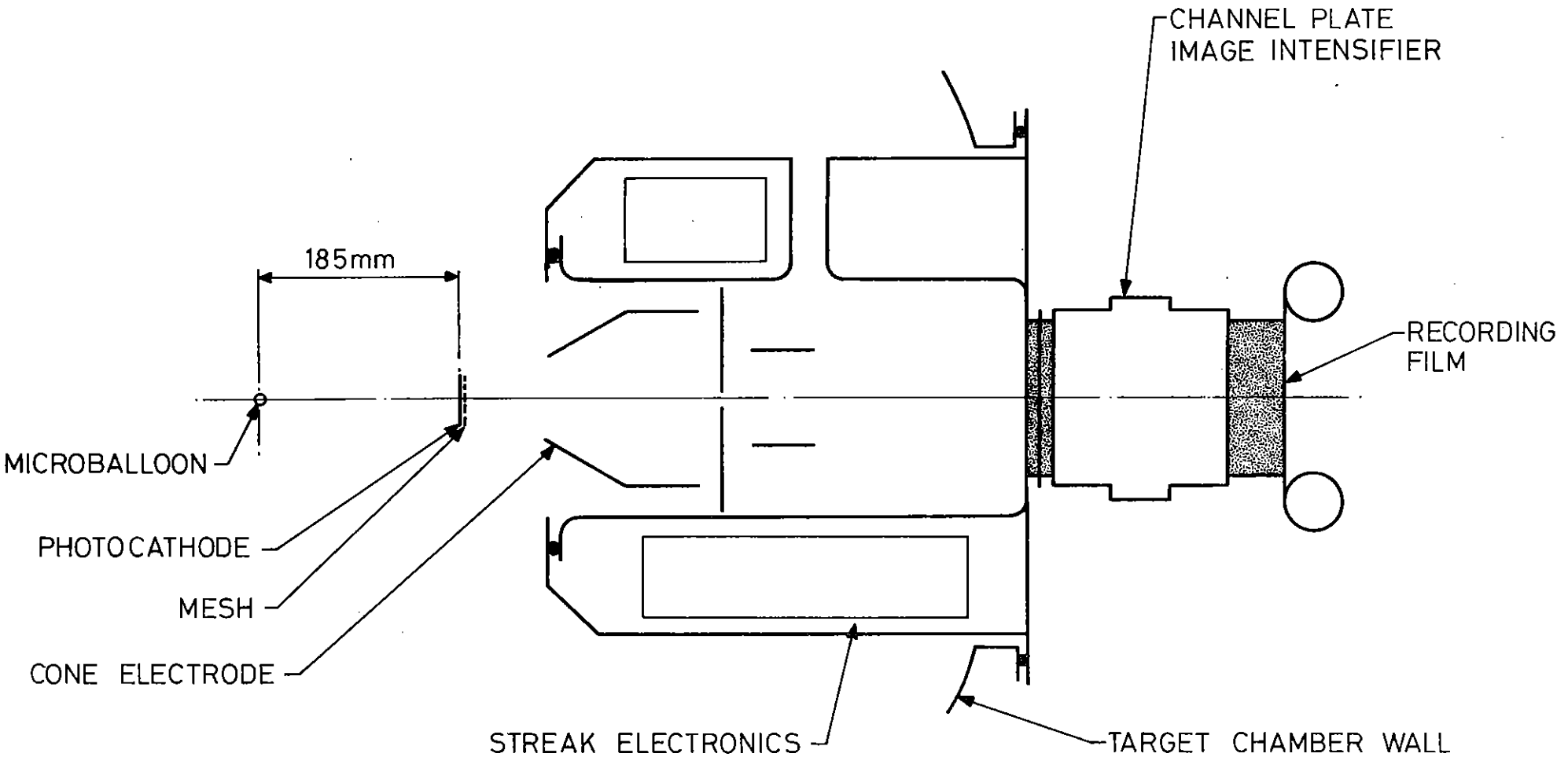

NEW X-RAY STREAK CAMERA

Fig 1.10

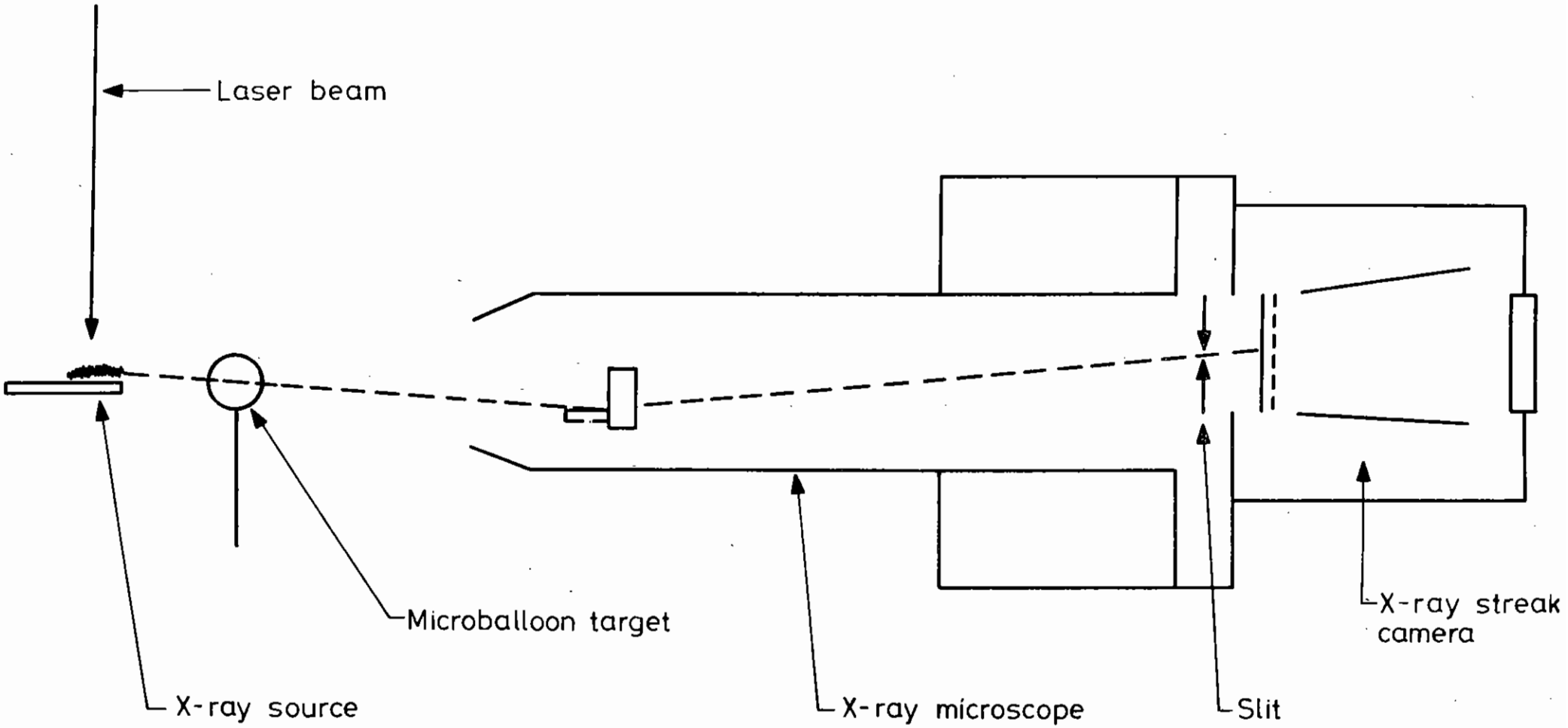

Fig 1.11 Schematic of Kirkpatrick–Baez X-ray Microscope/Streak Camera

of X-rays which are beyond the sensitivity of the pinhole camera and the Kirkpatrick-Baez X-ray microscope (section 1.6.2(b)). They can also be used to obtain images in the X-ray energy range above 10 keV by using thicker material for the zone plates.

ZPCI is a two stage process; the image is first encoded by the zone plates to form a pseudo-hologram which is then reconstructed using a He/Ne laser. In the encoding stage, Fig. 1.13 , the zone plate acts as a shadowcasting mask with negligible diffraction effects. Each point of emission on the object casts a shadow of the zone plate on the film. The size and position of the shadow is uniquely defined by the position of the source relative to the zone plate. The coded image of the object is therefore a superposition of zone plate shadows corresponding to the superposition of point sources which forms the object.

This image is developed and is then contact printed onto Kodak High Resolution Plates. The contact print may then be reconstructed. The reconstruction stage uses the diffractive properties of the zone plate to form the image. Diffraction theory shows that light incident on a Fresnel zone plate is diffracted into orders having real or virtual foci. The 'focal length' of the first order is given by the expression

$$f = \frac{r_1^2}{\lambda}$$

where r_1 is the radius of the first zone of the zone plate and λ is the wavelength of the reconstruction radiation. The dependence of the focal length upon the shadow size results in a three dimensional reconstruction of the original object, but the tomographic resolution is much poorer than the transverse resolution.

The reconstruction must be carried out with radiation of much longer wavelength than that used in encoding so that the coded image will give appreciable diffraction effects.

The system used for reconstruction is shown in Fig. 1.14 , it uses a 5 mW,

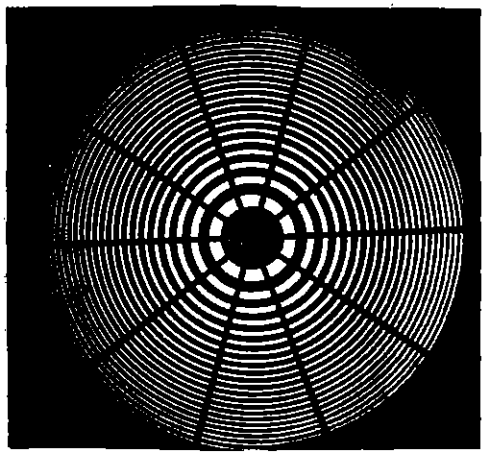

Fig 1.12 10x Magnified shadow of a zone plate.

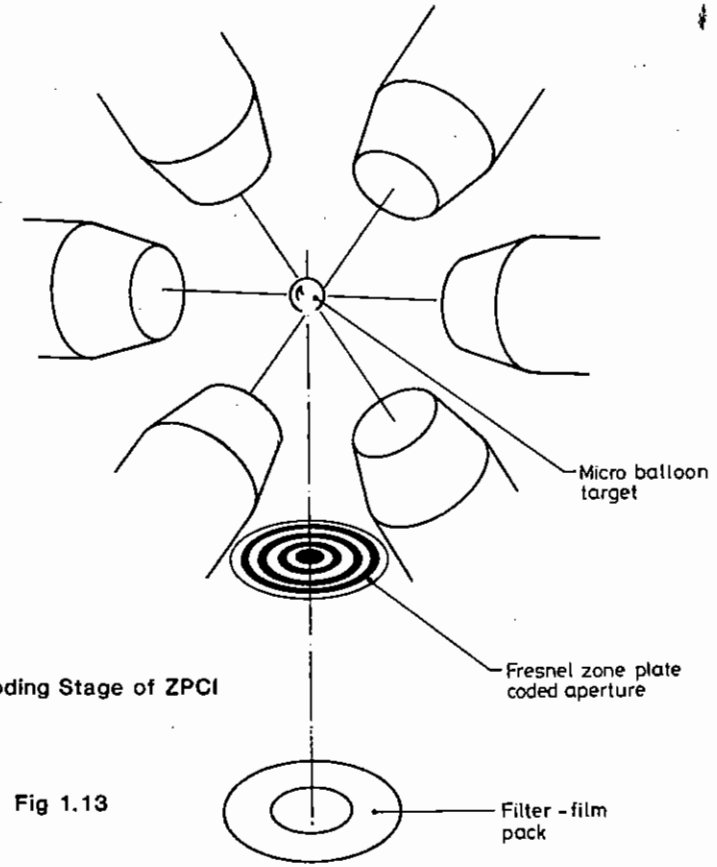

Encoding Stage of ZPCI

Fig 1.13

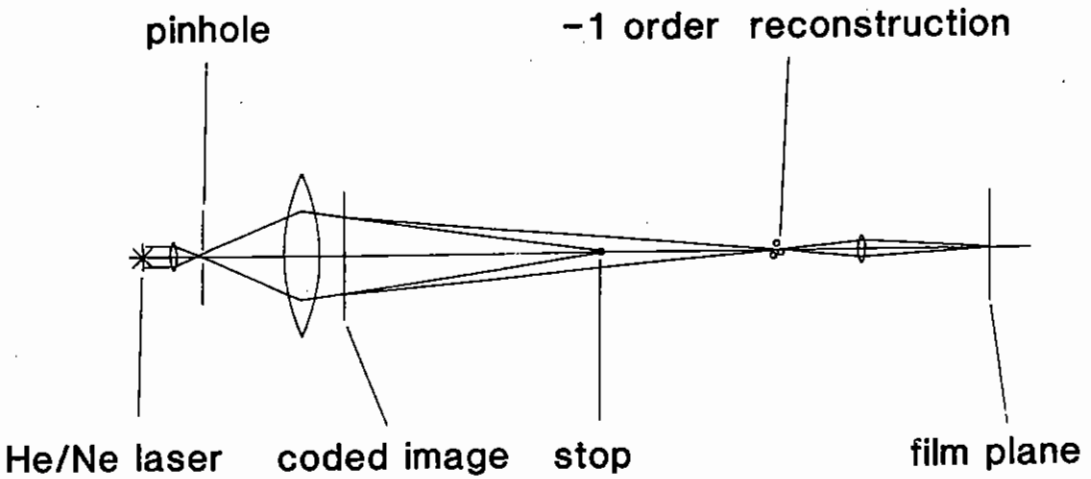

Fig 1.14 Reconstruction Stage of ZPCI

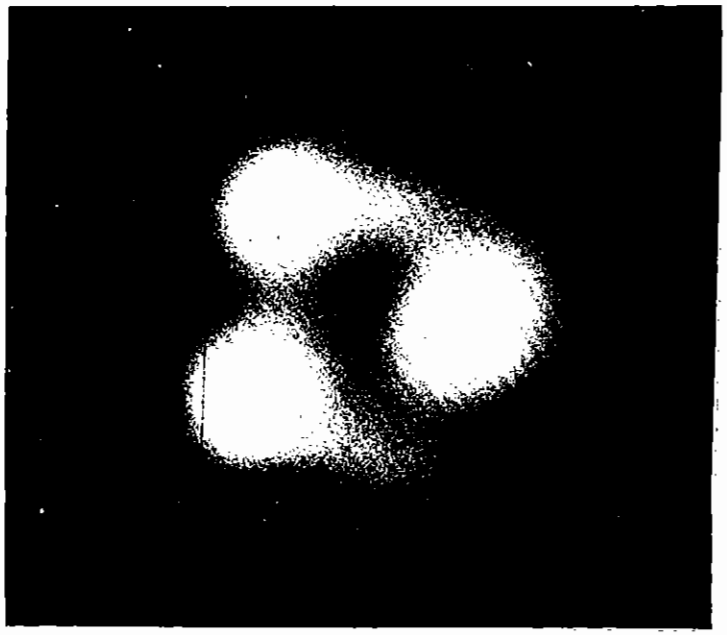

Fig 1.15 ZPCI-Target Irradiated With Six Beams

spatially filtered He/Ne laser to illuminate the coded image. One problem in reconstruction is the reduction in the signal to noise ratio of the image due to undiffracted light. This is overcome by using a lens in front of the zone plate which will bring the first diverging diffraction order to a real focus. The undiffracted light is brought to a focus in the Fourier plane of the lens and is removed with a small stop. This results in a great improvement in the signal to noise ratio of the image and reduces interference effects between the desired image and the undiffracted light.

The imaging system was first used in late November 1979 to image the self emission from targets irradiated with varying focusing conditions. Fig. 1.15 shows a target irradiated with six beams focused on its surface. The three bright spots are the south and upper and lower east beams and in between them can be seen fainter spots from the north and west beams.

In February 1980, the first experiments in Zone Plate Coded Radiography (ZPCR) were carried out successfully and the results from this are presented in more detail in the Ablative Compression Studies (section 5).

Higher resolution zone plates with more zones and a finer minimum zone width are being produced at present for future experiments. These zone plates will be made in gold to improve their opacity at higher X-ray energies which will give better image contrast.

C. Duncan, A. Raven and P.T. Rumsby.

1.6.2(d) Hard X-ray Pinhole Cameras

Recent improvements in X-ray pinhole imaging techniques have led to recording of the implosion process with increased sensitivity and resolution over that previously available. The improvements stem from the use of hard X-ray pinholes kindly supplied by J. Rizzo and B. Boni of LLE, Rochester.

The 5 μm diameter pinholes are microdrilled in 12 μm thick platinum substrates giving reduced substrate transmission of hard X-rays over the copper substrates previously used. Improved image signal to noise ratio allows closer working distances between plasma and pinhole giving a consequent increase in collection efficiency.

The attainable spatial resolution, as determined by the well known Rayleigh criterion is proportional to the recording energy. Spatial resolutions attained mainly in two beam compression experiments have been ∿ 15 μm, with recorded X-ray energy limited by instrumental sensitivity to ∿ 1.5 keV. Improved implosion symmetry and increased laser energy in six beam compression experiments have resulted in higher X-ray yields from the implosion core. Higher yields and increased pinhole camera sensitivity have facilitated the raising of the X-ray cut off energy to ∿ 4 keV with a consequent increase in spatial resolution.

For optimum resolution in a pinhole camera an ideal image distance exists where ℓ is a function of wavelength, pinhole diameter and magnification (1.04). The new pinholes have allowed the use of an ideal image distance ∿ half the normal viewing distance of 2.5 cm. With the optimization of all parameters the theoretical spatial resolution for the ideal case is ∿ 2 μm at 4 keV. A resolution ∿ 6 μm has been achieved at this energy.

Fig.1.16 shows a sequence of pinhole images of exploding pusher implosions with six beam target irradiation. The on target power was between ∿ 0.5 and 1 TW for each shot. The axis of observation of the pinhole camera was inclined at 55° to three of the beams. Fig.1.16(a) shows the implosion of a 10 bar DT filled microballoon. The 2.5 keV image is overexposed and shows three of the laser deposition zones and a 40 μm diameter implosion core. The neutron yield was 8×10^6. The images of Fig.1.16(b) and (c) were taken with 3.0 keV and 4.0 keV filtering respectively. In each case the emission from a symmetrical implosion core dominates the corona emission. The neutron yield from the 10 bar DT filled microballoon of Fig.-1.16(b) was 3×10^6. The image of Fig.1.16(c) from the implosion of a 0.4 bar Ar filled target shows a highly compressed core. A densitometer trace

through the core is shown in Fig.1.17(a). The half width of the core intensity peak is 10 μm. Fig.1.17(b) shows the implosion of a D rich DT filled microballoon which had a 17.5 nm Au surface coating. The X-ray cut-off energy was 4.0 keV. A tripartite structure is evident in the core indicating emission from the Au at centre convergence of the irradiated portions of the shell. The width at half intensity of each of the core emitting zones is ∿ 6 μm. The overall core diameter is 25 μm; 2×10^6 neutrons were detected.

In conclusion, the pinhole camera has been shown to have a useful resolution over a wide energy range and continues to be a convenient and valuable diagnostic. Thanks are due to T.A. Hall for help in obtaining the pinholes.

A. Moore.

1.6.3 X-ray Detectors

1.6.3(a) X-ray Continuum Measurements - X-ray Diodes

The measurement of the X-ray continuum emission from laser produced plasmas can be used to infer both the hot and cold electron temperatures. The cold component represents the bulk of the emission whereas the hot component is a smaller contribution and is in fact a second perturbative Maxwellian distribution on the former. These temperatures can be related to many interesting interaction processes both with the laser beam and the plasma and the fast electrons interacting with the target.

The detector signal is the resultant integral over a selected energy region (in our case from 1 keV to 100 keV) of the X-ray transmission through an energy selecting foil, the detector response and continuum distribution in this region and hence requires some computing support to unravel these temperatures and the percentage contribution of the fast and thermal component to this distribution. An 8 channel diode array utilizing six 125 μm P.I.N. diodes and two 500 μm diodes (Quantrail) has been constructed to measure emission at various regions to 30 keV.

Electron deflecting magnets and good collimation have been incorporated in the design to minimize the effects of foil flourescence. The signals are fed into Lecroy 2249 W A/D units and then integrated by the GEC 4080 computer system. Most of the 1979 experimental period has been occupied with the interpretation of signals recorded on oscilloscopes.

The results are compared with the channel ratios evaluated with the aid of a computer program which permits each channel to be characterized by a single foil or a sandwich of two foils and a particular diode sensitivity. Filter materials can be chosen from a set of 14 elements ranging from beryllium to gold and two plastic foils (mylar and PVC). The program can be run on the Rutherford IBM 360/195 system producing graphical output via the GINO package or in an interactive mode on the University of Essex DEC-10 system. In Fig.1.18 we show the evaluated transmission of eight channels normalized to the first channel (15μm Be). The temperature has been set to 5 keV and no hot electron component is included. It can be seen that some channels have a broad energy transmission window while others have a notch response below the K-edge transmission of the foil. In some cases this may be followed by a second broad hump. The foils and their thicknesses are chosen prior to an experiment to minimize this effect and to produce good accuracy in the expected temperature regime.

The diode signals normalized to the low energy channel are shown versus foil cut off energies in Fig.1.19 and can be used to optimize the foil combination for a particular temperature. Proposed improvements of the system in 1980 are based on incorporating the 2 temperature, 2 percentage fit of hot and cold temperatures and possible expansion of the diode array to provide analysis of plasmas in both target areas.

A.A. Pugatschew

1.6.3(b) X-ray Continuum Measurements - Scintillator Arrays

Scintillator-photomultiplier detectors are used to measure the continuum emission at energies greater than 30 keV which is a very low response region for P-I-N diodes or in experiments where low X-ray fluxes are encountered.

The four channel array is based on NE102A scintillator material of various thicknesses coupled to Mullard XP2008 photomultiplier tubes. Gain calibration of the tubes is performed with a Bi 207 radioactive source and a Lecroy 'qvt' multichannel analyzer and it is hoped to be able to perform this whilst the array is located at the target chamber. The computation of the channel response is performed with the previously described program but the diode response is replaced by the scintillator response functions (calibrated at AWRE Aldermaston).

A.A. Pugatschew

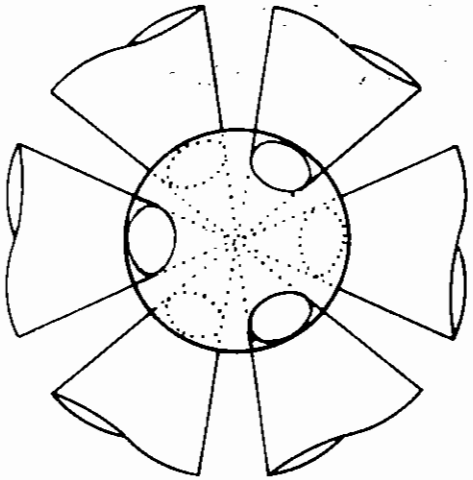

0·5 TW on target

8 J per beam in

100 ps

X-RAY PINHOLE IMAGES

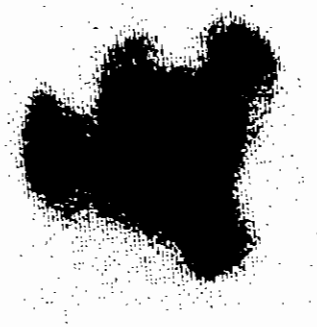

shell diameter

⟵ 83 μm ⟶

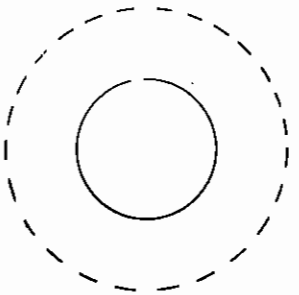

⟵ 40 μm ⟶

diameter implosion core

(a)

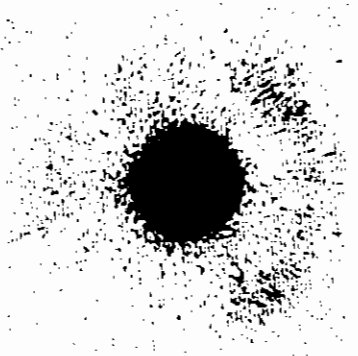

shell diameter

⟵ 84 μm ⟶

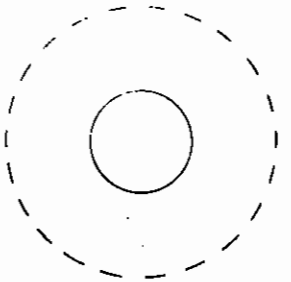

⟵ 30 μm ⟶

diameter implosion core

(b)

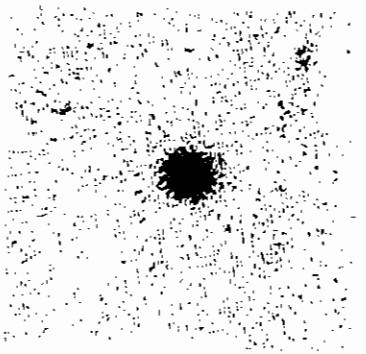

shell diameter

⟵ 77 μm ⟶

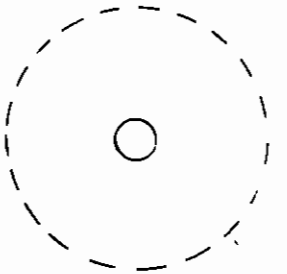

⟵ 10 μm ⟶

diameter implosion core

(c)

Fig 1.16

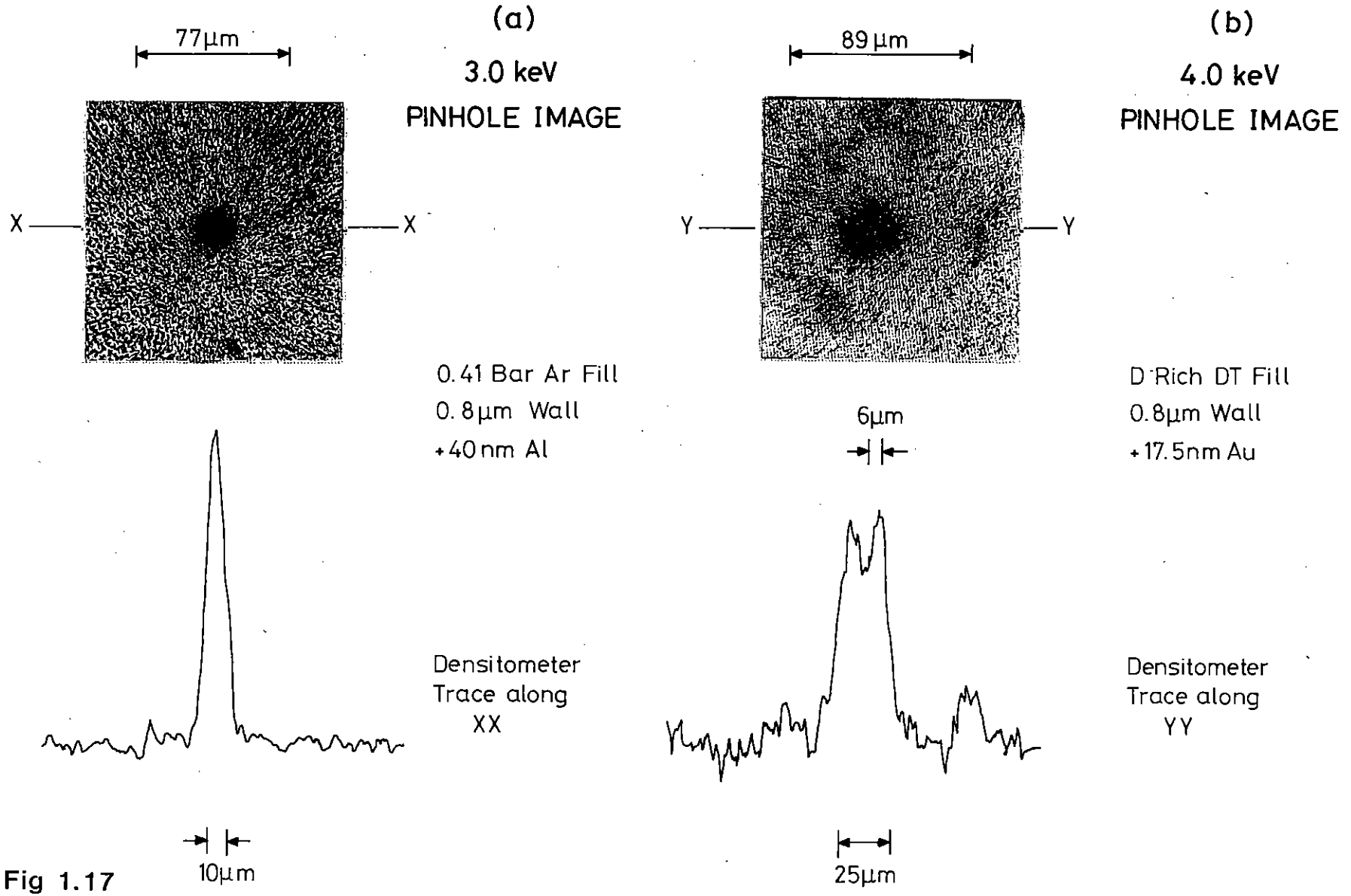
(a)
3.0 keV
PINHOLE IMAGE
77μm
X
X
0.41 Bar Ar Fill
0.8μm Wall
+40nm Al
Densitometer
Trace along
XX
10μm
(b)
4.0 keV
PINHOLE IMAGE
89μm
Y
Y
D Rich DT Fill
0.8μm Wall
+17.5nm Au
6μm
Densitometer
Trace along
YY
25μm

Fig 1.17

1.6.4 X-ray Calibration Source

The configuration and performance of an X-ray calibration source was governed by the need for an apparatus compatible with the range of instrumentation attached to or associated with laser plasma experiments. Whilst meeting the specification for a general illuminating source, the system was also required for specialised ancilliary measurements, such as microballoon topography, Fresnel zone plate coded imaging, etc. With due regard for these requirements, the X-ray generator was developed according to principles usually related to X-ray and electron microscopy (1.05, 1.06). This approach resulted in the construction of a demountable electron beam generated X-ray source, which is incorporated in a mobile vacuum system with integral power supplies, Fig.1.20. The test chamber has four instrument mounting limbs with flange and length dimensions equal to the target chamber. Any two limbs can be used to install the electron gun and X-ray production target wheel, Fig.1.21. The unit as a whole is free standing on wheels but can be made a fixture with the aid of jackable supports. The vacuum valving is pneumatically operated with failure protection system triggered by vacuum monitoring instruments and water cooling interlocks, Fig.1.22.

The electron gun has a voltage rating of 0 to 50 kV with an autobiased stabilised beam current in the range of 0 to 3 mA. It is of triode construction and features a hot cathode tungsten hairpin filament, a Wehnelt cylinder with re-entrant aperture and an anode disc with transmission aperture. The high voltage vacuum bushing is moulded from high thermal conductivity resin and has a re-entrant profile to provide adequate tracking length with compact design, Fig.1.23 and Ref.(1.07).

To ensure efficient usage of the intrinsic high brightness available from the electron gun, it was essential to design an optical system of high demagnification and low aberration thus optimising the electron beam loading of the X-ray production target. The optical requirement, coupled with the need to have apparatus in close proximity to the X-ray source spot, was resolved by adopting an electromagnetic lens with an unusual form of pole geometry, (1.08). A practical lens design was developed

using computer codes, with one pole in the form of a cone protruding through the much enlarged aperture of the other pole, Fig.1.24. This configuration produces a focus outside of the lens body with good optical qualities and easy spatial access. A detailed analysis of the optical properties of the lens was compiled by evaluating the magnetic flux throughout the iron circuit and surrounding space, for various excitations and computing the paraxial electron trajectories from the axial field along the core (1.09). The results of this study are presented as a function of ampere-turns NI and beam voltage V_r, in terms of the excitation parameter $NI/\sqrt{V_r}$, in Figs.1.25, 1.26 and 1.27.

For high resolution applications the performance of the X-ray source is to be judged solely on the amount of flux generated by the smallest possible focal spot. For the type of electron source used and the level of demagnification provided by the present lens, the X-ray spot diameter can be shown to depend on the spherical aberration created by the electron optical system. In the presence of spherical aberration a point source will be imaged as a disc of confusion of diameter D_s proportional to the third power of the angular aperture of the lens α_2 and to a factor C_s which depends on the optical properties of the lens so that

$$D_s = \tfrac{1}{2} C_s \alpha_2^3$$

For brightness invariance, α_2 is related to the source semi-angle α_1 by the magnification M, according to

$$\sin\alpha_2 = \sin\alpha_1$$

Consequently, selecting a value of α_1 by virtue of inserting an aperture stop in the lens bore will define a particular value for α_2 and hence D_s, for given excitation parameter, Fig.1.28. Such an exercise indicates that, to a good approximation, a simple relationship exists between focal spot size D_s and lens aperture stop diameter D_a, for practical working distances defined by the image distance Z_I, namely

$$D_s = 0.002375 D_a^3 (12 - Z_I) \text{ for } 3 < Z_I < 7 \quad (\text{mm})$$

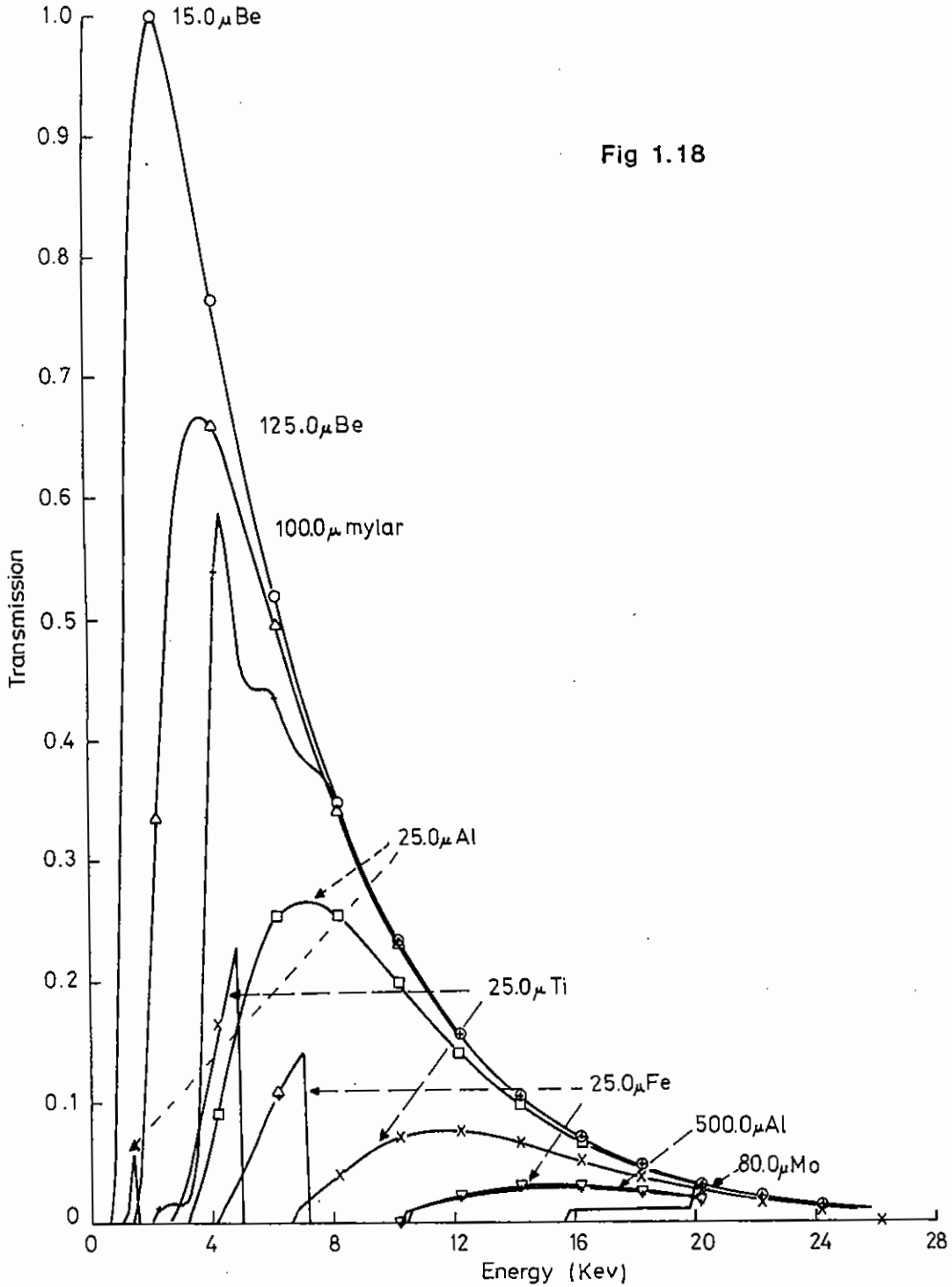

Fig 1.18

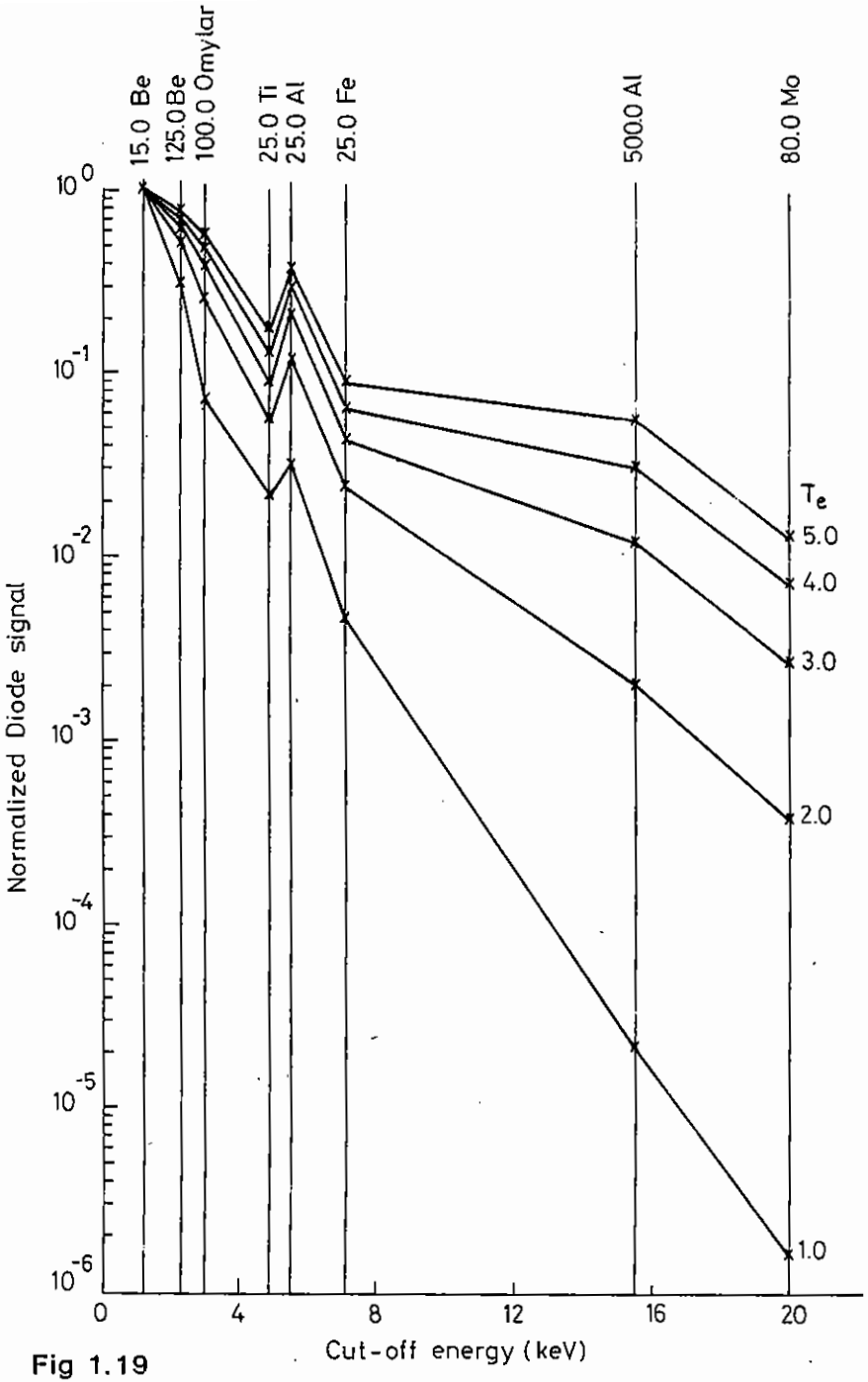

Fig 1.19

Some preliminary measurements have qualitatively endorsed the estimated performance of the X-ray source. In particular, simple polaroid film exposures have confirmed the resolution of a 1000 mesh grid (12 μm spacing) with a 1.5 mm lens aperture and of a 3000 mesh grid (4 μm spacing) with a 0.8 mm lens aperture. Without attempting to optimise the system, the beam current focused on the target was roughly 900 μA and 400 μA for the 1.5 mm and 0.8 mm apertures respectively. These figures represent a target loading well above other known reported systems of this type (1.10). To avoid surface melting and eventual rupture of the water jacket, the observed power inputs could be tolerated for short durations of time only (1.11). Provision has been made, however, to accommodate a pulsed application of the electron beam which should permit a higher input to the target material. It is possible to speculate that the present system would be capable of target loadings of $\sim$ 1000 kW/mm^2. This could only be supported by a high speed rotating target (1.12).

The existing arrangement of targets comprise a series of water cooled spindles, of differing metals, azimuthly located on a common wheel hub. Each spindle can be selected in turn and accurately positioned at the electron beam focal point. The metals, Al, Ti, Cu, Mo, Ag were chosen to cover the X-ray energy region 1.55 - 25.52 kV. The X-ray photon yield will depend on the target material and corresponding permissible power loading which is reflected in the choice of focal spot size. However, in general the levels of photon flux will not be too dissimilar from that derived for Cu, Fig.1.29.

P. Rockett, C.L. Brundin.

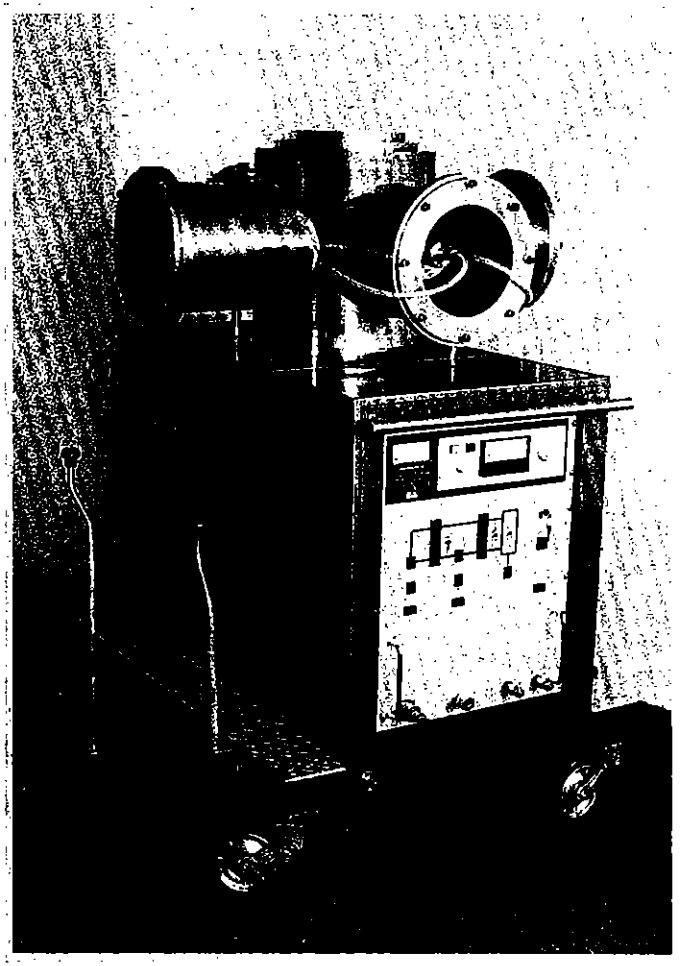

Fig 1.20

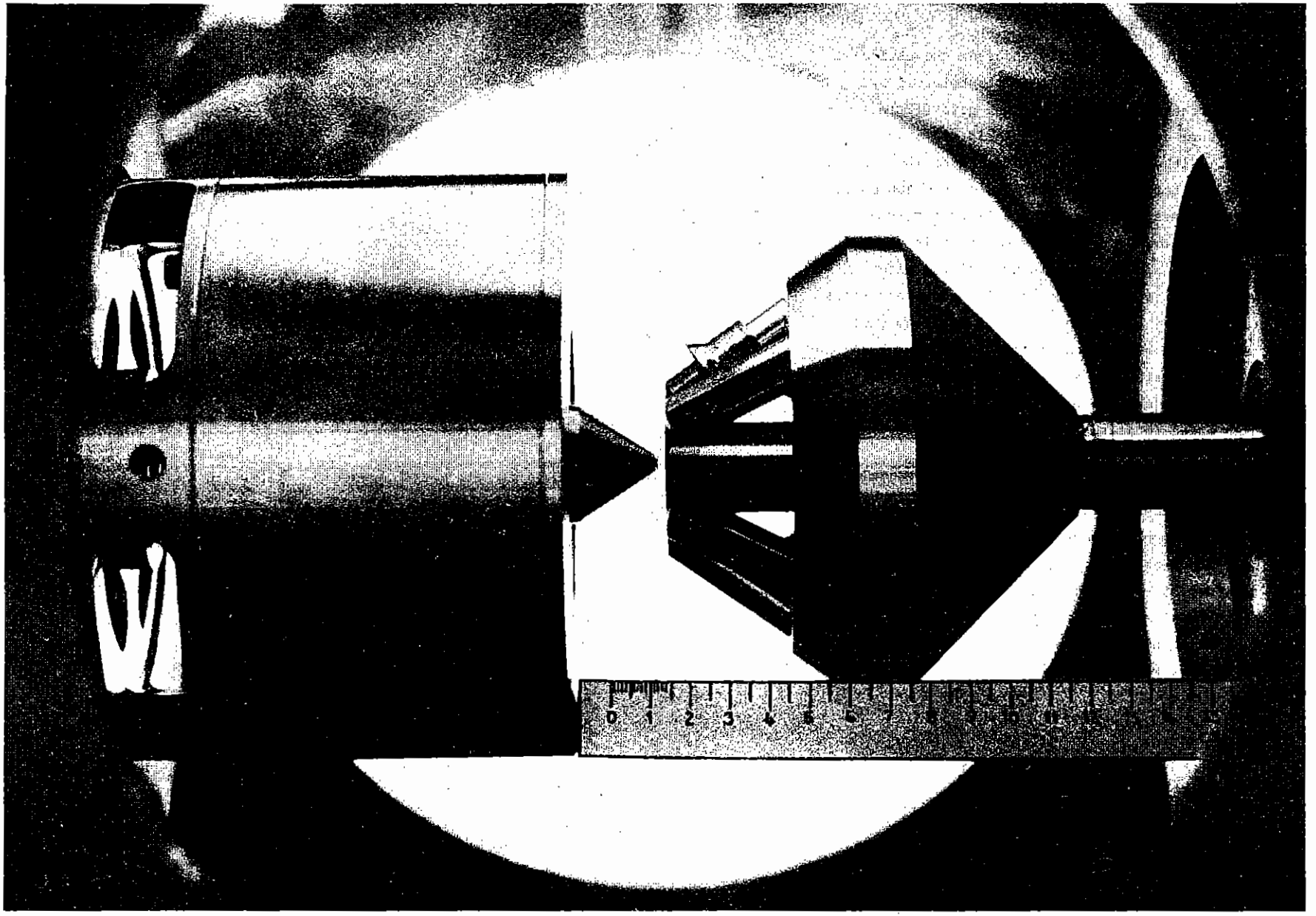

Fig 1.21

Fig 1.22 Schematic of X-Ray Calibration Sourse

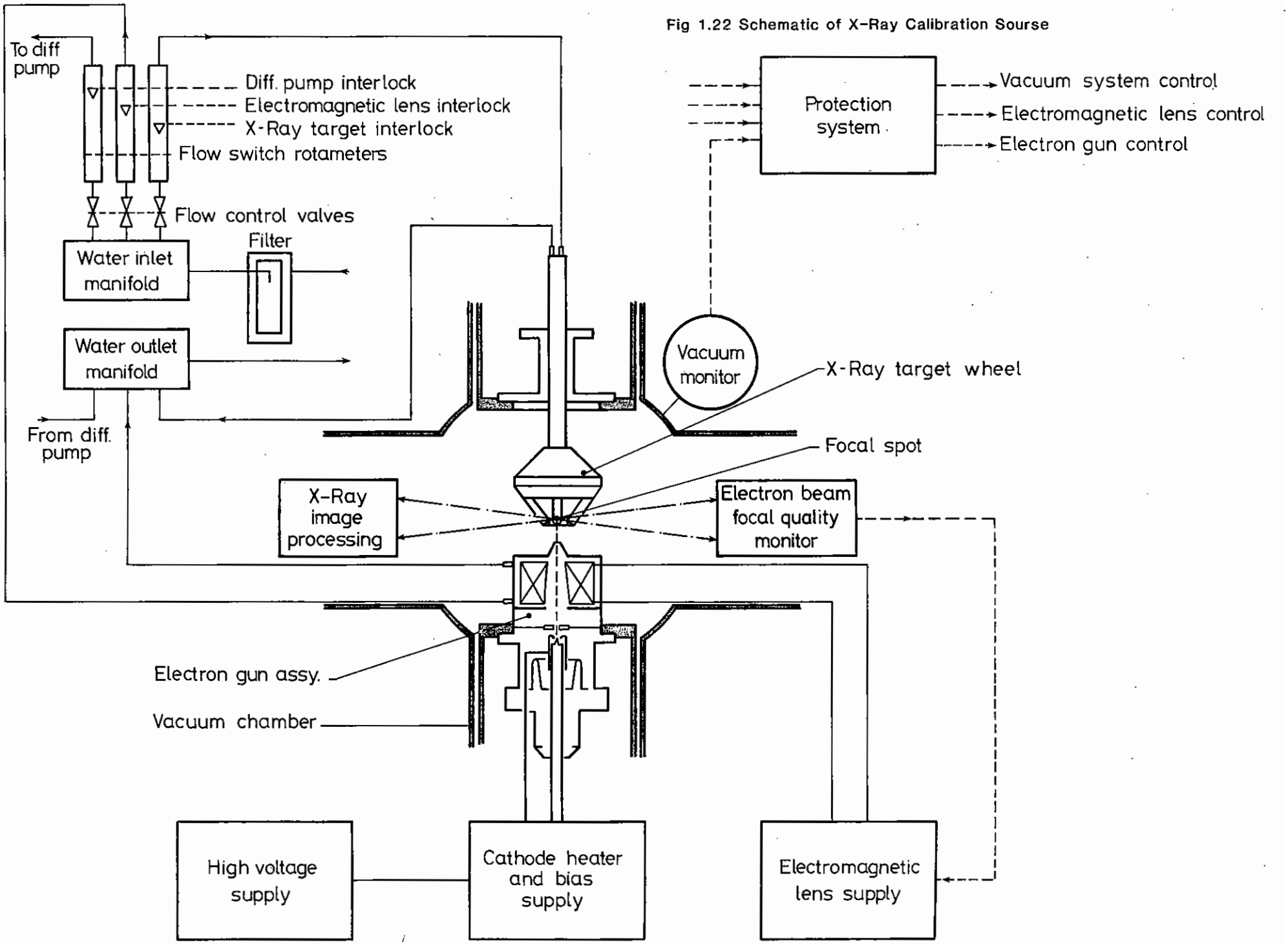

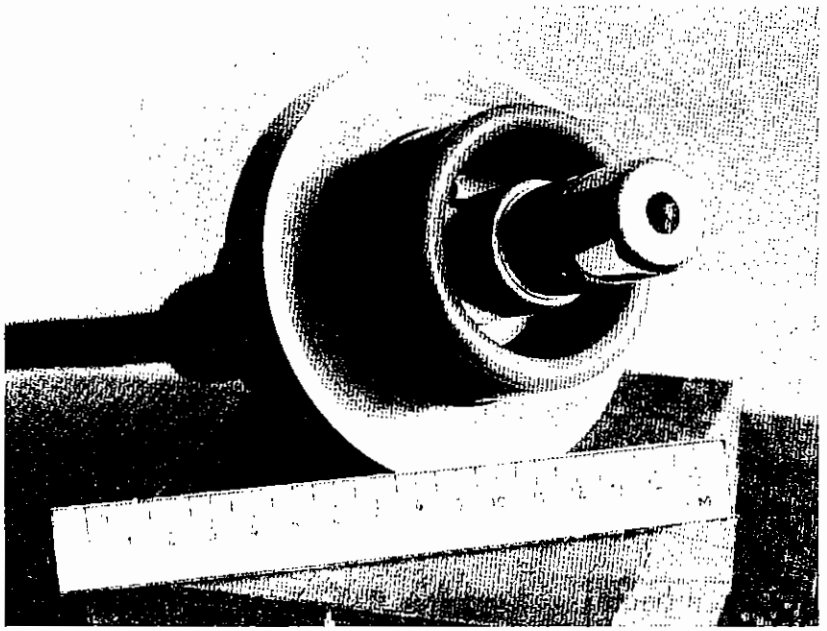

Fig 1.23

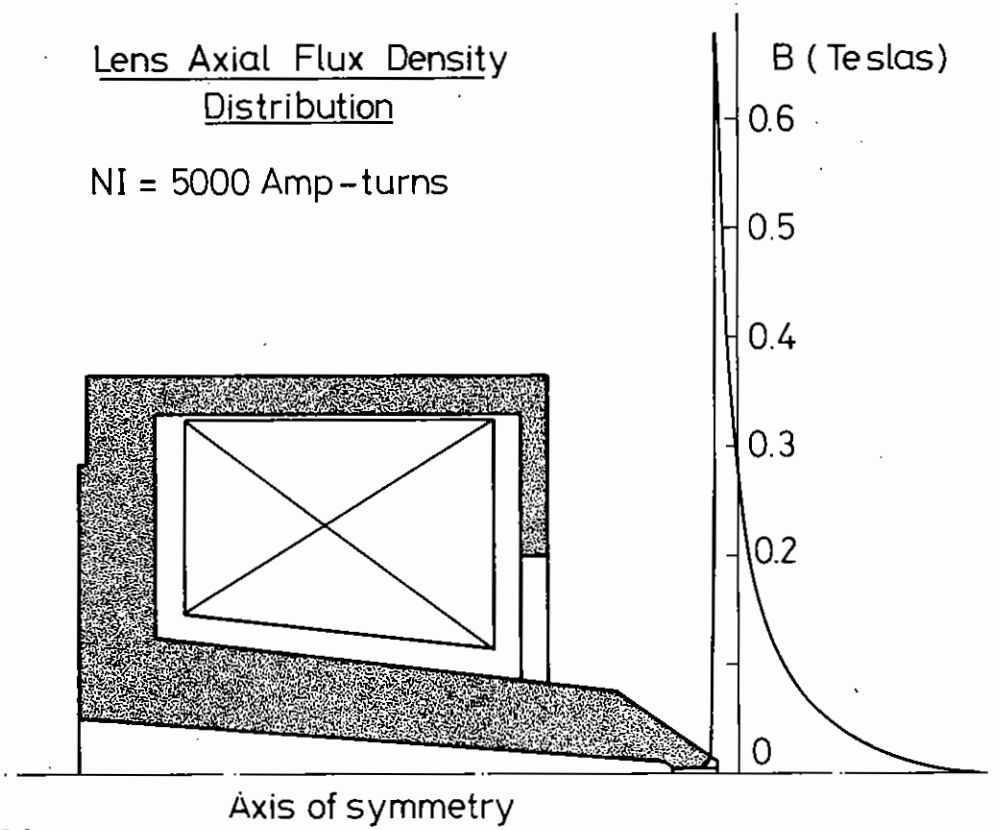

Fig 1.24

Fig 1.25

Spherical Aberration Cs

$NI/\sqrt{Vr}$ = Excitation parameter

NI = Lens ampere turns

Sym	NI
+	3500
×	5000
•	7000

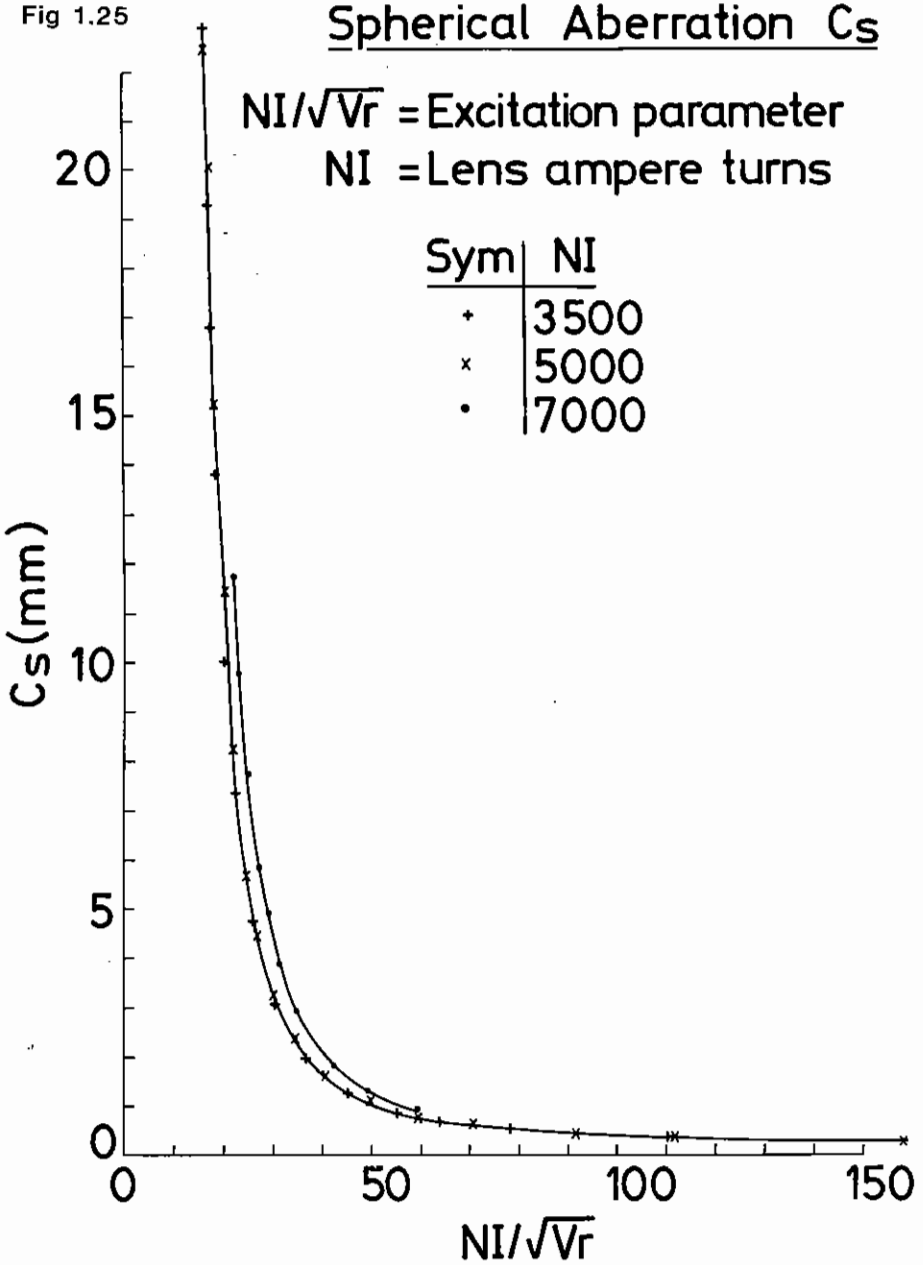

Fig 1.26

Magnification M

$NI/\sqrt{Vr}$ = Excitation parameter

NI = Lens ampere turns

Sym	NI
+	3500
×	5000
•	7000

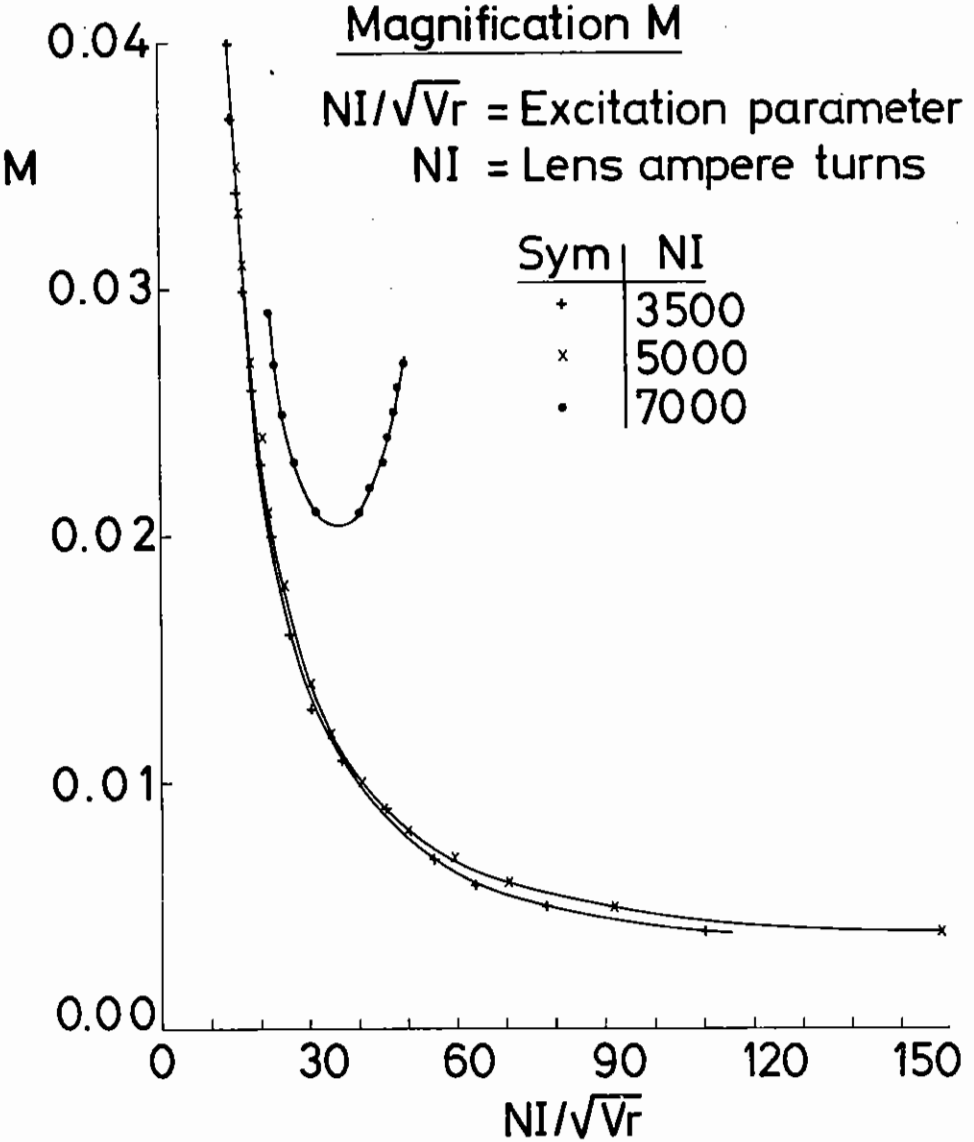

Fig 1.27

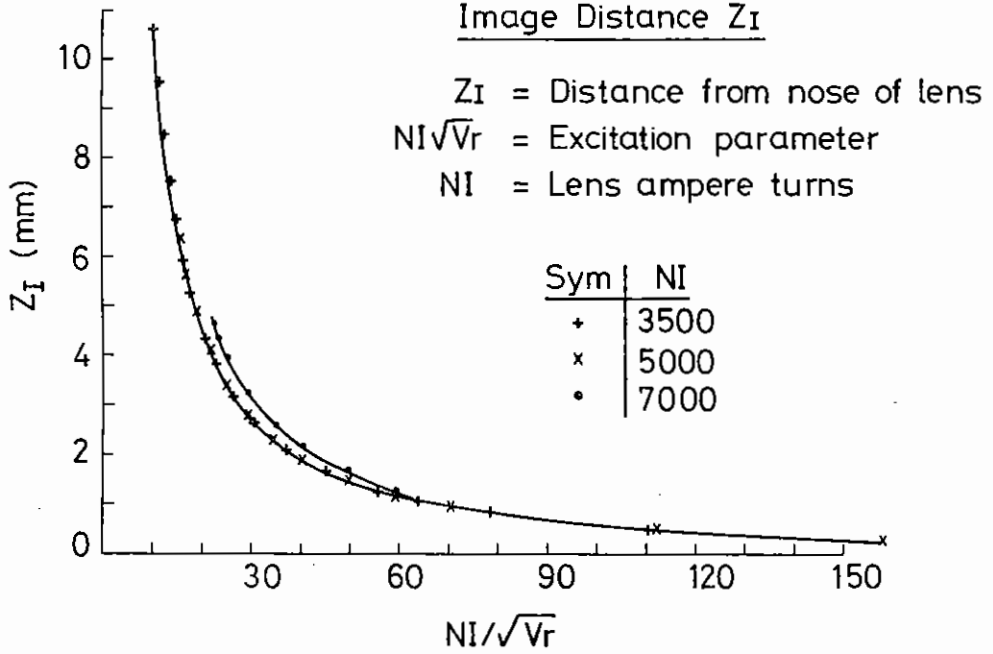

Fig 1.28

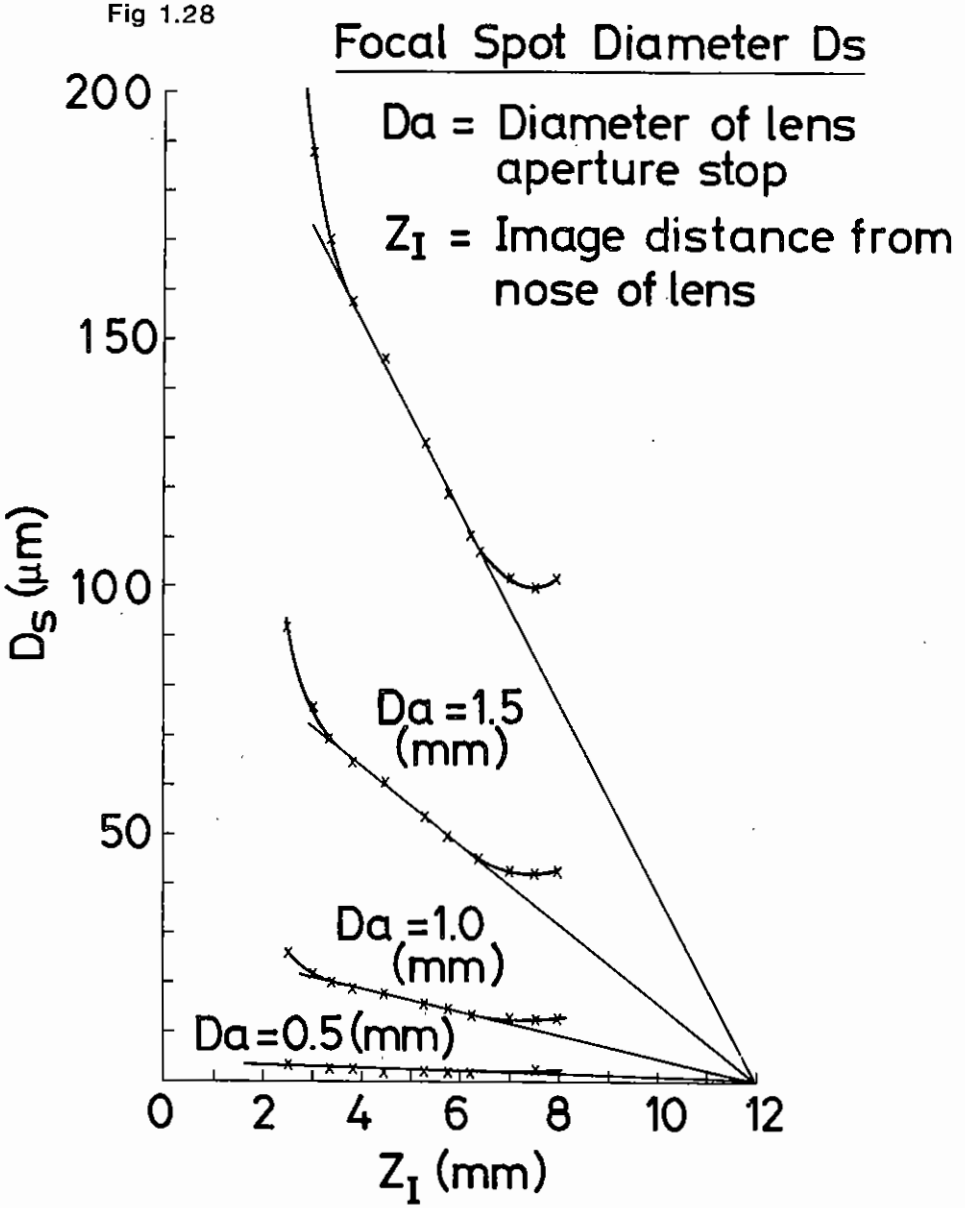

Fig 1.29

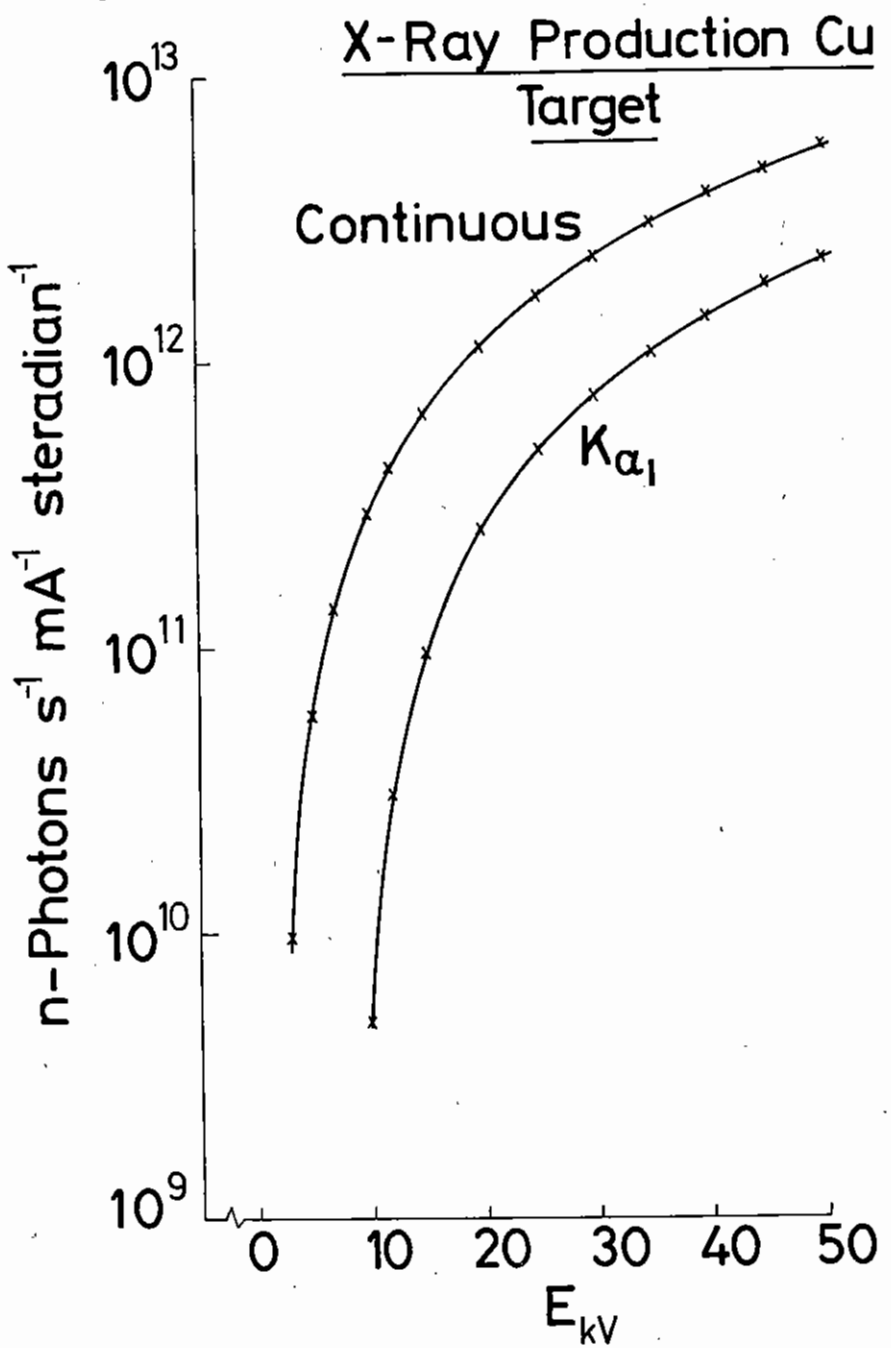

1.6.5 Plasma and Light Calorimetry

For accurate computer simulation of experiments it is essential to have information about the fraction of laser energy absorbed by the target. Up to now absorbed energies have not been measured routinely and have been deduced from Faraday cup signals for some exploding pusher experiments and from scattered and reflected light measurements using diodes for some plane target experiments. To overcome this limitation thermocouple type plasma and X-ray calorimeters have been built and installed in both target chambers.

The calorimeters are similar to those originally developed by Los Alamos Lab and contain two thin tantalum discs (5 μm thick, 4 mm diameter) in each head. Constantan-Chromel thermocouple leads are spot welded to the rear of each disc and connected inside the head so that only the difference signal between the two detectors is recorded. A glass plate is placed in front of one tantalum disc to stop plasma and X-rays up to several 10's of keV reaching it and so it only reponds to scattered laser light. The other disc is unobscured and so responds to plasma, X-ray and scattered light energy. The difference signal is thus that due to plasma and X-ray energy only.

Many of these detectors have been built and tested and the possible sources of error identified. Up to 10 of them are used routinely on both plane target and implosion experiments. In such cases the major source of error in calculating the total asorbed energy is that due to errors in the spatial integration. For six beam implosion experiments where the plasma expansion is very symmetric these detectors allow measurement of total absorbed energy to better than 5% error whereas for plane target experiments where plasma expansion is very asymmetric errors up to 10% are incurred.

With target to detector distances of 20 cm output signals typically lie in the range 0.05 to 1 mv amplitude and have less than 1 ms rise and slow

fall time of several seconds. Two methods of recording are used. For experiments where non uniform plasma expansion occurs chart recorders are used and the signals generally analysed by hand. For routine measurements of absorbed energy during implosion experiments the detector signals are amplified by high gain (x 700) DC amplifiers and read at peak value approximately one second after the laser shot by the experimental data acquisition computer via a sampling digital voltmeter. A polar plot of the signals (to show the symmetry of plasma expansion), and the integrated total absorbed energy value are then printed out at the computer terminal (section 1.6.6(b)).

In order to understand how the absorbed laser energy is partitioned between X-rays and particles, X-ray calorimeters have been built. These devices are very similar to the differential plasma calorimeters discussed above except that they have a thin ($\sim$0.2 μm) foil of plastic obscurring one tantalum disc and a glass plate over the other. The thin plastic foil transmits all X-rays down to about 100 eV energy and yet stops all plasma ions with velocities below about 10^8 cm.sec^{-1}, while the glass plate stops both ions and X-rays. Consequently, the difference signal from the calorimeter is that due solely to the X-ray energy collected. To reduce the sensitivity of both discs to scattered laser light they are coated with a 20 nm layer of gold to increase their λ = 1.05 μm reflectivity from 80% to greater than 95%.

Faraday cup detectors with 0.2 μm thick plastic foils obscuring the collector have been used to determine the minimum foil thickness that will stop all particles. For ablative type implosions where target irradiances less than 10^{14} W.cm^{-2} are used and ion velocities are generally less than 10^8 cm sec^{-1} these X-ray calorimeters can effectively collect most low energy X-rays and reject the ions. For exploding pusher experiments however with high values of target irradiance (I > 10^{15} W cm^{-2}), ions with velocities up to many times 10^8 cm sec^{-1} are produced which are readily transmitted by plastic foils of a fraction of a μm thick. Consequently this type of X-ray calorimeter is not suitable for measurements on these experiments.

Preliminary results from these X-ray calorimeters indicate that at laser intensities of about 10^{14} W cm^{-2} on spherical targets about 10% of the absorbed energy appears as X-rays for plastic targets whereas for glass targets at the same intensity this rises to about 20%.

D. Miller and P.T. Rumsby

1.6.6 Automated Data Processing

1.6.6(a) OMA and Streak Cameras

The two EPL streak cameras and the Imacon 675 were in regular use throughout the year. Timing jitter problems have been cured by the installation of the Hadland hard valve sweep circuits in both EPL cameras.

Work has proceeded on interfacing the Princeton Applied Research Optical Multichannel Analyzer (OMA) to the GEC 4080 computer. The OMA which was originally intended for 1-D operation has now been modified by PAR for 2-D and includes a dry ice cooled housing and Vidicon tube incorporating light shielding between the cathode heater and the target.

The OMA is linked to the computer via an auxiliary control unit using CAMAC. The CAMAC unit provides control, reads status and enables the computer to acquire the OMA data using an autonomous memory channel (AMC) which is part of the CAMAC system. It also contains line drivers/receivers to allow the auxiliary control unit to be situated some distance from the CAMAC crate close to the OMA and experimental equipment. The auxiliary control unit contains line drivers/receivers and multiplexing/demultiplexing circuits in addition to a 32 word FIFO to act as a buffer between the OMA data output and the computer. The data is generated in the OMA using a PC board, similar to the PAR option 06, which counts pulses equivalent in number to the analogue signal detected at the Vidicon. The Vidicon target is scanned in frames consisting of a pre-selected number of horizontal tracks with each track divided into 500 vertical lines. The sweep circuits allow up to 256 tracks to be selected.

During a frame scan data is output at 1 word/64 μs with a 0.7 ms gap at the end of each track to allow for flyback. Once a scan has been started it cannot be stopped until the end of the frame. The FIFO buffer increases the time for which the data stream is interrupted at the end of a track from 0.7 ms to a maximum of 2.7 ms. This, in principle, allows the AMC to be re-triggered without losing data.

The Vidicon tube used in the OMA is a Silicon diode array type which when cooled will retain data for up to 45 minutes. In operation, scanning of the initially fully erased target is stopped by cutting off the electron beam but keeping the sweep circuits running. The event to be recorded illuminates the target and scanning is recommenced in synchronism with the start of a frame.

The fraction of incident signal recovered from the Vidicon is a function of the recorded intensity so that to preserve linearity it appears necessary to recover all the signal by integrating over a number of frame scans. Each track is scanned in 32 ms making about 8 secs to scan a frame of 256 tracks. Under these conditions one frame scan is sufficient to recover the signal but since the scanning electron beam carries charge to the target at a limited rate, a frame of a few tracks needs many scans to recover the signal. Present indications suggest that operating in 256 track mode even when only one track is required, is in any case advantageous since it allows small area saturation of the Vidicon to be detected which could otherwise give rise to misleading data. Translation from 256 tracks to one track can be accomplished in the computer if required.

Due to the logical organization of the computer the AMC requires re-triggering after at most 16 tracks have been read. The existing interface allows a maximum of 2.7 ns in which re-triggering must occur. Unfortunately it has been found that this precision is unattainable in the operational environment of the computer and data is occasionally lost. While timing could be made less critical by extending the FIFO it now seems there would always be a chance of losing data and it has been decided to provide the OMA with dedicated memory to obviate this problem.

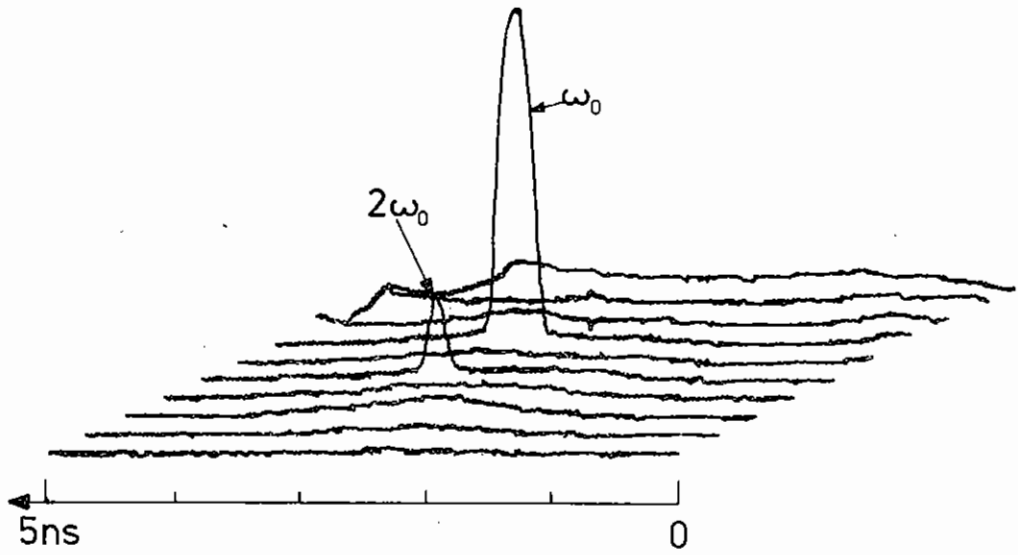

Fig 1.30

To make use of the 256 track capability of the OMA, 128k of 10 bit words are required.

The OMA has been in use with an EPL streak camera and Fig.1.30 shows the graphics output from a $2\omega_0$ irradiation shot displaying the shapes of ω_0 and $2\omega_0$ pulses recorded simultaneously. The output was reproduced from a single, 10 track, scan. The sensitivity of the OMA is roughly equivalent to fast film.

P Gottfeldt, J G Watson, C J Reason, W T Toner and D A Pepler.

1.6.6(b) Computer System Development

Additions have been made to the online computer system during the past year and the current configuration of the computer hardware and CAMAC systems are shown in Figs.1.31 and 1.32. The computer hardware consists of a GEC4080 Central Processor Unit (C.P.U.); 128 Kbytes of store; 19.2 Mbytes of disc on two spindles (each spindle having a fixed and a cartridge disc); a heat printer; a dot matrix printer; fast paper tape input and output; an asynchronous communications interface to the laboratory mainframe computer (an IBM 360/195) and a CAMAC interface. The CAMAC system consists of a GEC systems crate and, on a single branch, five user crates located in the control room, Target Area I (TAI), Target Area II (TAII), the laser area and the densitometer room. This gives the computer system access to, amongst other things, three visual display units, two graphics terminals with hard copy, a Tektronix graphics input tablet and a scanning microdensitometer. The computer operating system is configured to support these facilities and is at present being updated under the manufacturers instructions to rectify some errors and provide improved facilities. It is also being changed to simplify the Initial Program Load (I.P.L.) sequence by reading a real-time clock to determine the date and the time.

The suite of programs to control the laser and acquire the online data have been extended and improved during the year but the overall concept remaims the same. Changes may be necessary in the near future to rationalise the structure of the program when six active beams are operational. The laser control program has been changed to allow alternate shots into the two target areas more frequently than before.

Further checks are being made on interlocks and shutters as they are made available to the computer and the probe beam amplifier has been incorporated into the end of charge sequence. Online data acquisition now includes programs to monitor the total plasma energy in the TA2 target chamber and plot its distribution in polar co-ordinates; to acquire the image from a streak camera via the OMA operating in 2-D mode (section 1.6.6(a)); as well as programs for the 12 channel LeCroy ADCs (type 2249W); Tektronix waveform analysers (type R7912); the CCD digitiser etc. All these programs store their data on the 4080 disc from where it can be sent to the IBM 360/195 for further analysis or archiving on magnetic tape. The laser program has been improved to warn the operator when the 4080 disc is reaching its maximum capacity so that action can be taken to archive the data.

The offline analysis of data from film via the scanning microdensitometer (section 1.6.6(c)) has been an important development during the year. This can be controlled by a raster scanning program or an interpreter (GRACES) and the data is produced in the same form as that from the OMA. A suite of programs has been written to cross-section, contour, smooth, invert, integrate and plot (in '3-D' with hidden line suppression) the data which can also be sent (via the IBM 360/195) to a Prime 400 computer which is part of the Interactive Computing Facility (ICF) where a colour contour plot can be generated and copied. The other offline analysis programs, including ones that control the graphics input tablet (which has now been moved to the densitometer room) have been improved and continue to be in use.

C.J. Reason, P. Gottfeldt, J.C. Watson and M. Forster

1.6.6(c) Automated Densitometer

The Loyce-Loebl 2-D scanning micro-densitometer has been interfaced to the Laser GEC 4080 computer.

The densitometer incorporates a platform which carries the film to be analysed. This platform is driven in x and y directions by stepper motors

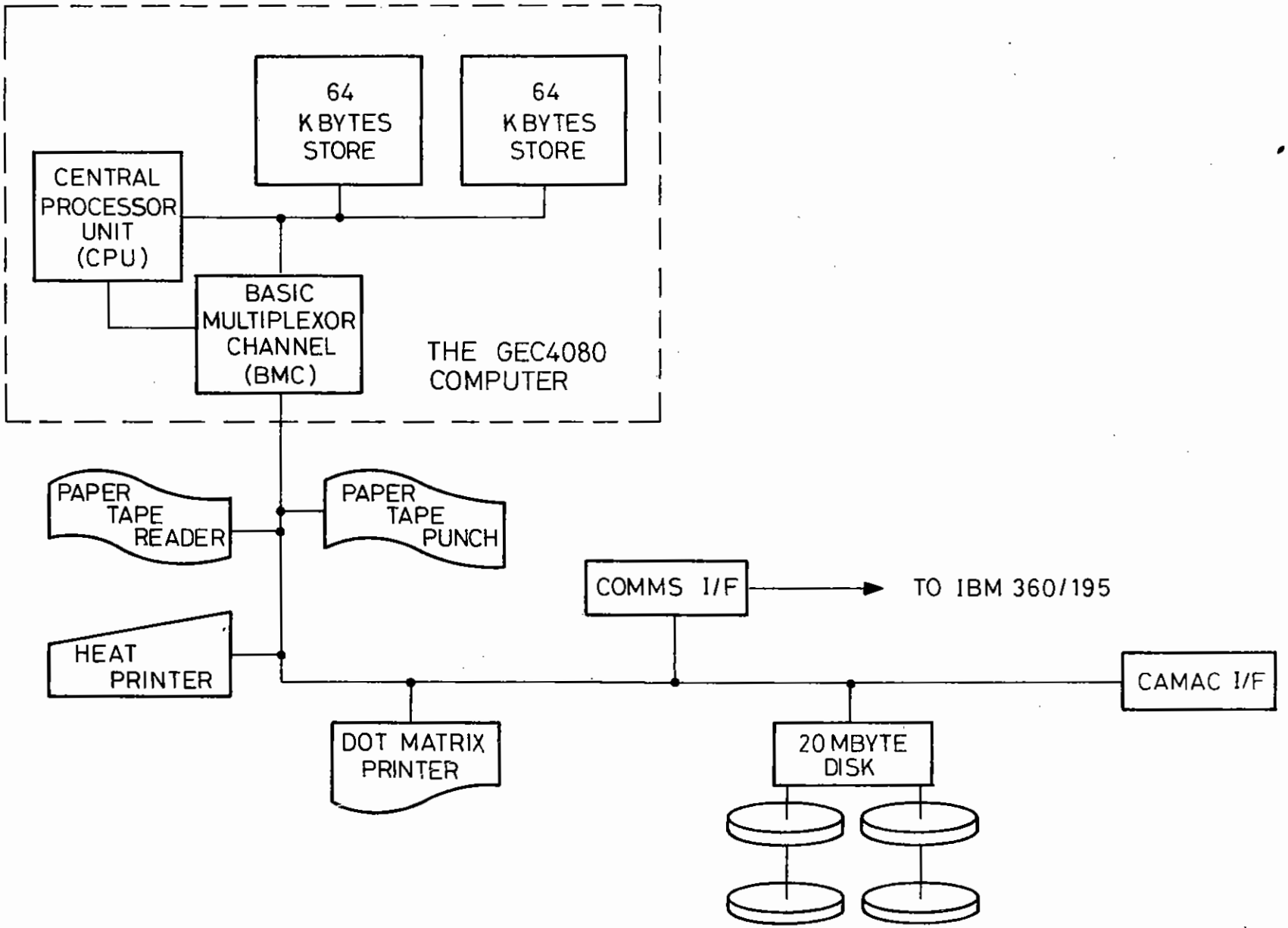

Fig 1.31 THE GEC 4080 COMPUTER HARDWARE

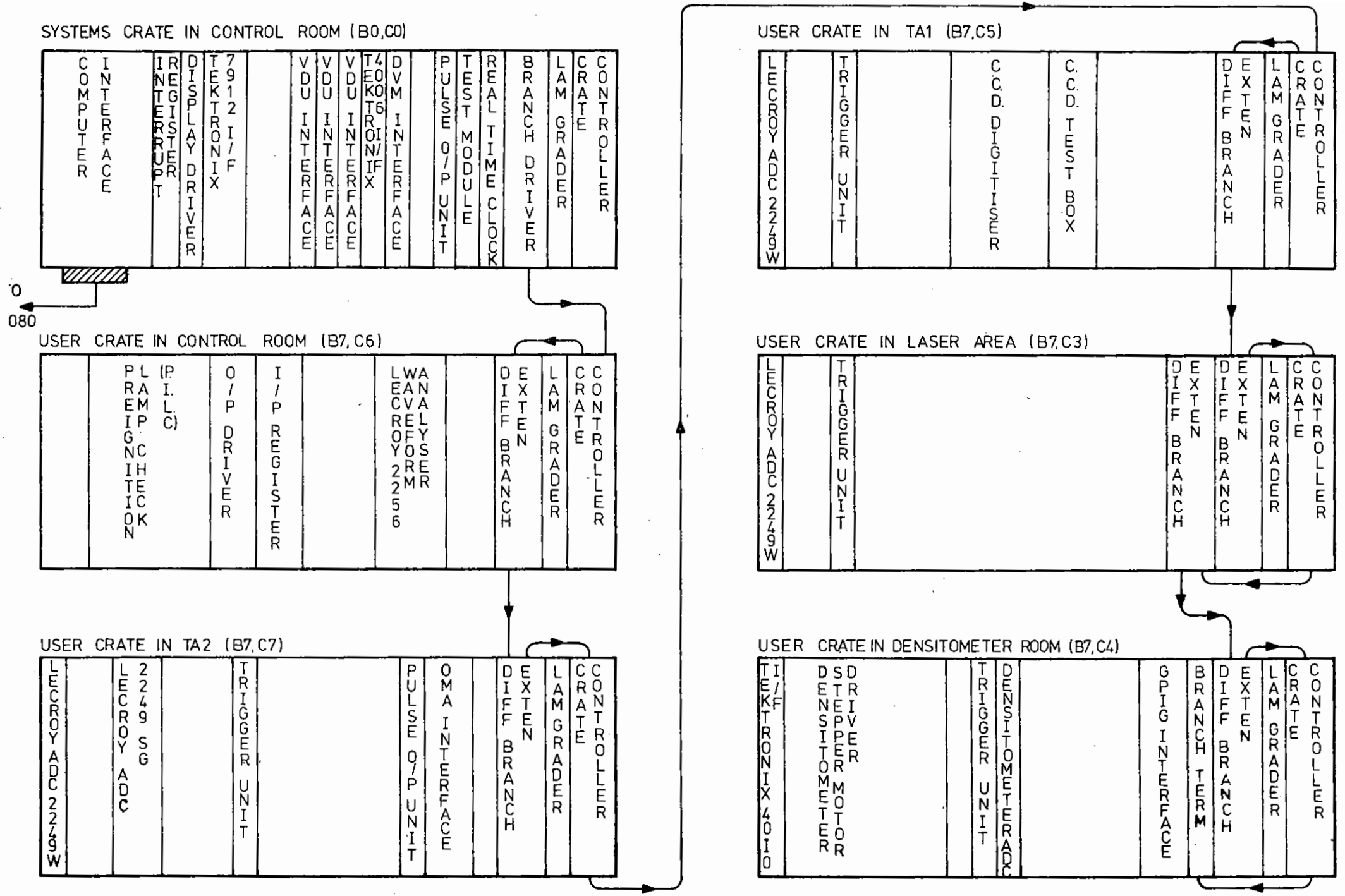

FIG.1.32 THE CAMAC SYSTEM

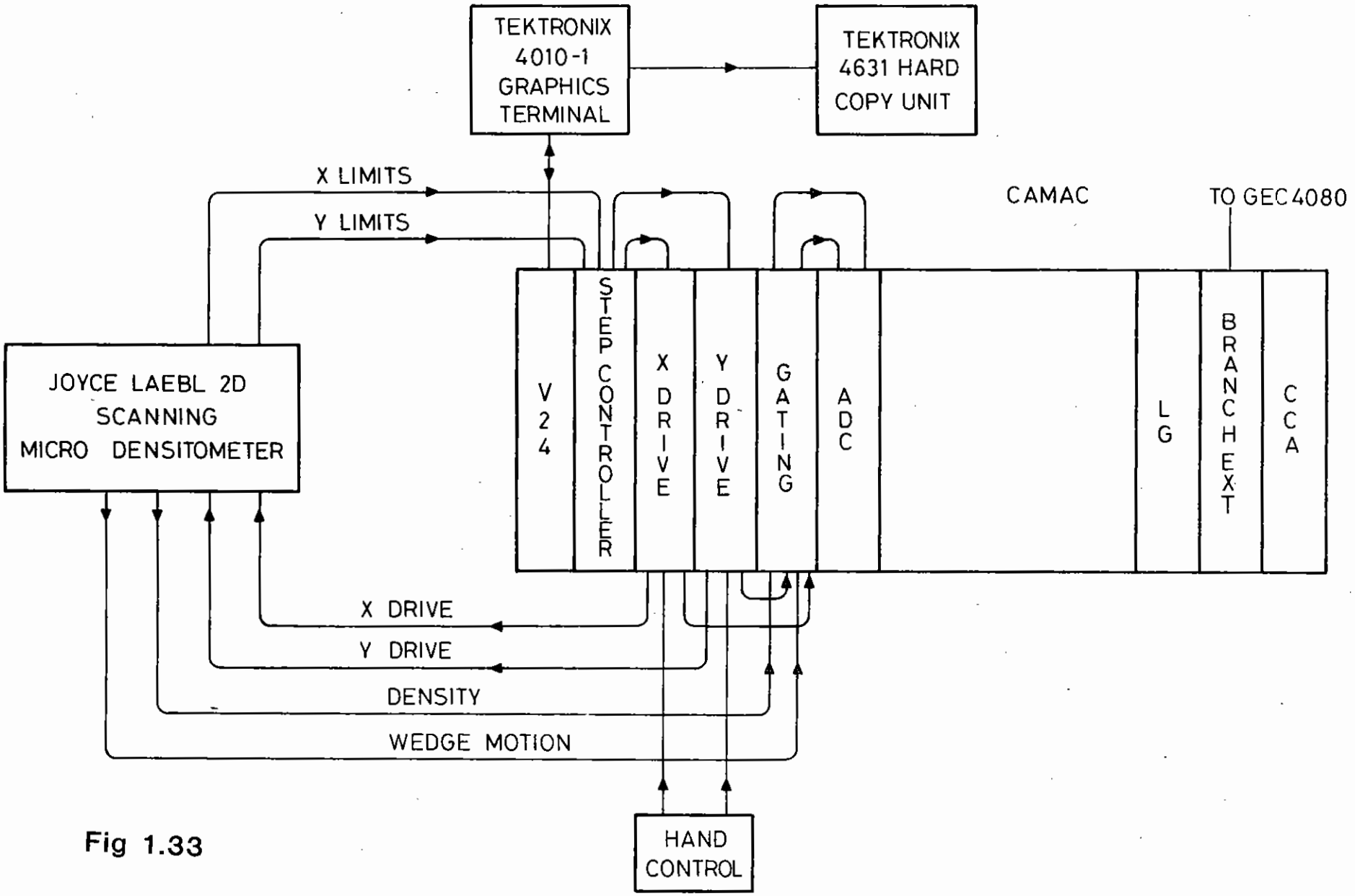
TEKTRONIX
4010-1
GRAPHICS
TERMINAL
TEKTRONIX
4631 HARD
COPY UNIT
X LIMITS
Y LIMITS
CAMAC
TO GEC4080
JOYCE LAEBL 2D
SCANNING
MICRO DENSITOMETER
V24
STEP CONTROLLER
X DRIVE
Y DRIVE
GATING
ADC
LG
BRANCH EXT
CCA
X DRIVE
Y DRIVE
DENSITY
WEDGE MOTION
HAND
CONTROL

Fig 1.33

giving minimum increments in x and y of 5 μm. At each point to be measured a servo-controlled optical wedge moves until the light transmitted by the wedge is equal to that passing through the film. The wedge is geared to a potentiometer which produces a voltage proportional to the position of the wedge and the voltage is thus a measure of film density. The interface to the computer uses CAMAC as shown in the block diagram Fig.1.33. The stepper motor controller is a Kinematic Systems dual pulse train generator Model 3360 which provides a programmable number of output pulses to each motor drive with a maximum count of 32768. Clockwise and anticlockwise outputs for each motor are available and there is provision for limit switch signals. The ADC used to digitize the density signal is a Harwell Module 7055-1 with 10 bit resolution. The motor drive units were constructed to provide the phase sequences and power amplification for the stepper motors. The ADC is triggered when the x and y stepper motors are at rest and when the optical wedge drive servo is stationary at the termination of a step sequence. A unit was constructed to detect this condition. While these additional units do not require the CAMAC dataway they were nevertheless built to plug into the CAMAC crate and use the CAMAC power supply. The motor drive units incorporate up/down counters with visual read-out so that the area to be scanned can be established in terms of step counts using a hand held manual control unit. These numbers can then be used in determining the parameters for the computer scanning programmes. Computer control of the densitometer is via a local Tektronix 4010-1 graphics terminal and the COP command process. Hard copy graphics may be obtained using the Tektronix 4631 Hard Copy Unit.

A scanning program as well as a number of analysis programes for producing contour plots and 3-dimensional representations are available. The GRACES interpretive language will also be available to operators to meet individual programming requirements. Data can be transmitted to the RL central computing facilities if more sophisticated analysis is required. This also gives the possibility of using the FR80 for producing high quality contour plots or the colour graphics of the Interactive Computing Facility for colour scale intensity representation.

M. Forster, P. Gottfeldt and C. Reason

CHAPTER 1 REFERENCES

1.01 G Mourou and W Knox, Appl Phys Letts 35 No 7 492 (1979).

1.02 M H White and R W Wyatt, Rutherford Report RL-79-099.

1.03 Annual Report to the Laser Facility Committee RL-79-036.

1.04 Los Alamos Scientific Laboratory Report LA-5919-PR (1975).

1.05 V E Cosslett and W C Nixon, 'X-ray Microscopy', Camb Univ Press (1960).

1.06 M E Haines and V E Cosslett, 'The Electron Microscope', E and F N Spon Ltd (1961).

1.07 P Grivet, 'Electron Optics', Pergamon Press, 484 (1965).

1.08 F Z Marai and T Mulvey, Eigth International Congress on Electron Microscopy, 130 (1974).

1.09 P W Hawkes, 'Image Processing and Computor Aided Design in Electron Optics', Academic Press, 284 (1973).

1.10 D J Pugh and P D West, Inst. Phys. Conf. Series No 36, Chapter 1 (1977).

1.11 W J Vosterkamp, Philips Res. Rep. 3, 303 (1948).

1.12 W J Vosterkamp, Philips Res. Rep. 3, 49 (1948).

CHAPTER 2 GAS LASER DEVELOPMENT

INDEX

CHAPTER EDITOR: F O'Neill

CHAPTER 2 GAS LASER DEVELOPMENT

2.1 Introduction

During the reporting year the work of the gas laser development group became more directed towards experiments with rare gas halide lasers. This concentration of effort occurred for two reasons. Firstly, it became apparent that other high power laser candidates (e.g. selenium and CdHg) would not operate at high enough efficiency to make them useful for application to laser-plasma interaction studies. Secondly, preliminary experiments in our laboratory on e-beam-excited rare-gas halide (RGH) lasers at high pump rate, showed that these lasers could achieve an overall operating efficiency of a few percent. These high efficiencies coupled with their short operating wavelengths (193 nm - 351 nm) makes the RGH lasers most attractive for plasma physics applications.

In this chapter we describe a number of experiments which were carried out to measure the efficiency of RGH lasers. This data has been used to design an e-beam-pumped, 200 J, 60 ns KrF laser, code-named SPRITE, which is at present under construction. SPRITE is considered as a test system for a future high energy ($\sim$ 1 kJ), short pulse ($<$ 5 ns) KrF laser and as such it has been designed to achieve a high overall electrical efficiency, hopefully in the region of 1 - 2%.

While the RGH lasers can operate efficiently at pulse-lengths of 60 ns, these long pulses are not suitable for laser-plasma interaction experiments where pulses of duration $<$ 5 ns will be required. Short pulse, high power e-beams would be prohibitively expensive to construct so some form of temporal pulse compression using optical means will have to be devised. Various schemes have been proposed in the literature and to date those receiving most attention are based on optical multiplexing and/or backward-wave Raman pulse compression. A considerably simpler approach would involve the use of a storage laser medium, preferably gaseous, pumped by an efficient RGH laser. Modest storage times would be required, say $>$ 100 ns, since optical pumping could be achieved using short pulse RGH lasers. It would however be desirable to have a high

conversion efficiency from pump light to storage laser output so that the overall system efficiency could be kept high. We have recently started experiments in this area and the first system investigated was the 342 nm molecular iodine laser pumped by the 193 nm ArF laser. High I_2 laser efficiency was achieved ($\sim$ 30%) but the storage lifetime of the excited I_2 state was found to be too short to make this system useful.

The above experiments are discussed in more detail below. In addition we also describe experiments related to the selenium laser and on metal vapor excimers.

F. O'Neill

2.2 Rare-Gas Halide Lasers

2.2.1 Rare-Gas Halide Laser Efficiency Measurements

The use of gas laser media with short excited state lifetimes (< 20 ns) for laser-plasma interaction studies is currently of interest due to the recent development of efficient schemes for optical pulse compression (2.01, 2.02). The short wavelength rare-gas halide lasers are particularly attractive for these applications because the coupling of laser radiation into plasmas is expected to be very efficient for lasers of wavelength < 500 nm (2.03). In addition it is believed that high power rare-gas halide lasers can be constructed with an overall operating efficiency (laser output energy/electrical input energy) of a few percent. This belief is based on recent work with e-beam-pumped KrF lasers (2.04, 2.05) where output energies $\sim$ 100 J have been obtained at intrinsic laser efficiencies (laser output energy/e-beam energy deposited in the laser volume) of approximately 10%. The experiments described in Ref (2.05) were particularly important because they demonstrated for the first time, that e-beam-pumped KrF lasers could operate at > 10% efficiency using short (50 ns), high excitation rate (2 - 7 MW/cm^3), pumping pulses. These results are important for two reasons. Firstly, by operating the KrF laser in a short pulse it is possible to reduce the complexity of a high energy, optical pulse compression system and secondly the use of high laser pump rates (> 1 MW/cm^3) will help to reduce the overall total volume of a high power KrF laser system.

We have carried out experiments which were designed to extend these efficiency measurements at high pump rate to other rare-gas halide lasers. We have measured the efficiency of ArF, KrF, XeCl and XeF lasers using 60 ns e-beam pumping at an excitation rate of 1.5 MW/cm^3 (averaged over the pump pulse). A cross-sectional view of the laser apparatus used for these experiments is shown in Fig.2.01. The electron-beam machine was operated at a voltage of 1 MV and a current of 50 KA (average) with a 60 ns (FWHM) output pulse. The beam has dimensions 5 cm x 35 cm. The high voltage electrons enter the aluminium laser cell through a dual titanium foil structure (50 μm prefoil, 25 μm main foil) and produce an

average power deposition of 1.5 MW/cm^3 in the laser gas. The walls of the laser cell were lined with a 1 mm thick tantalum sheet to reflect some electrons back into the laser gas. This produced an increase in e-beam deposition rate and also improved the uniformity of deposition in the gas.

The amount and distribution of e-beam energy deposited in the laser gas was obtained using pressure-jump measurements and cellophane dye dosimetry (2.06). A high speed transducer recorded the transient over-pressure in the laser cell due to the heating of the gas by the deposited e-beam energy and from this, using the ideal gas laws, the energy deposited could be calculated. Measurements were first carried out using pure argon (the main constituent in the KrF laser mix) and pure neon (used with ArF, XeCl, XeF) gas fills of equivalent e-beam stopping power. The measured deposition in argon was 20% less than in neon. In order to understand this result the e-beam energy deposition was measured in fills of pure N_2 and pure CO_2. The fill pressures were chosen, using standard tables of electron energy loss in gases (2.07), to give the same e-beam stopping power as the rare-gas fills. Results with these molecular gases agreed with the neon measurements. It was suspected that the low reading with argon was due to the loss of energy from the cell in the form of Ar_2^* emission. Previous experiments (2.08) have shown that e-beam energy is converted to Ar_2^* excimer radiation with very high efficiency. A small amount of Xe (1%) and O_2 (10%) was therefore added to the argon fill to quench fluorescence and when this was done the argon measurements agreed with the other gases. These results were used, with appropriate scaling, to calculate the energy deposited in the laser mixtures for the experiments described below.

The laser resonator for the present experiments was formed by 3.6 cm diameter internal plane reflectors centred 10.5 cm from the e-beam foil (dashed circle in the laser cell in Fig.2.01). Pressure-jump and blue cellophane measurements indicated that 33 J (estimated uncertainty, $\pm$ 10%) of e-beam energy was deposited in the laser volume defined by these mirrors. The inside surfaces of the laser cell were coated with black paint (3M Company, Nextel Black) to suppress parasitic oscillation off the

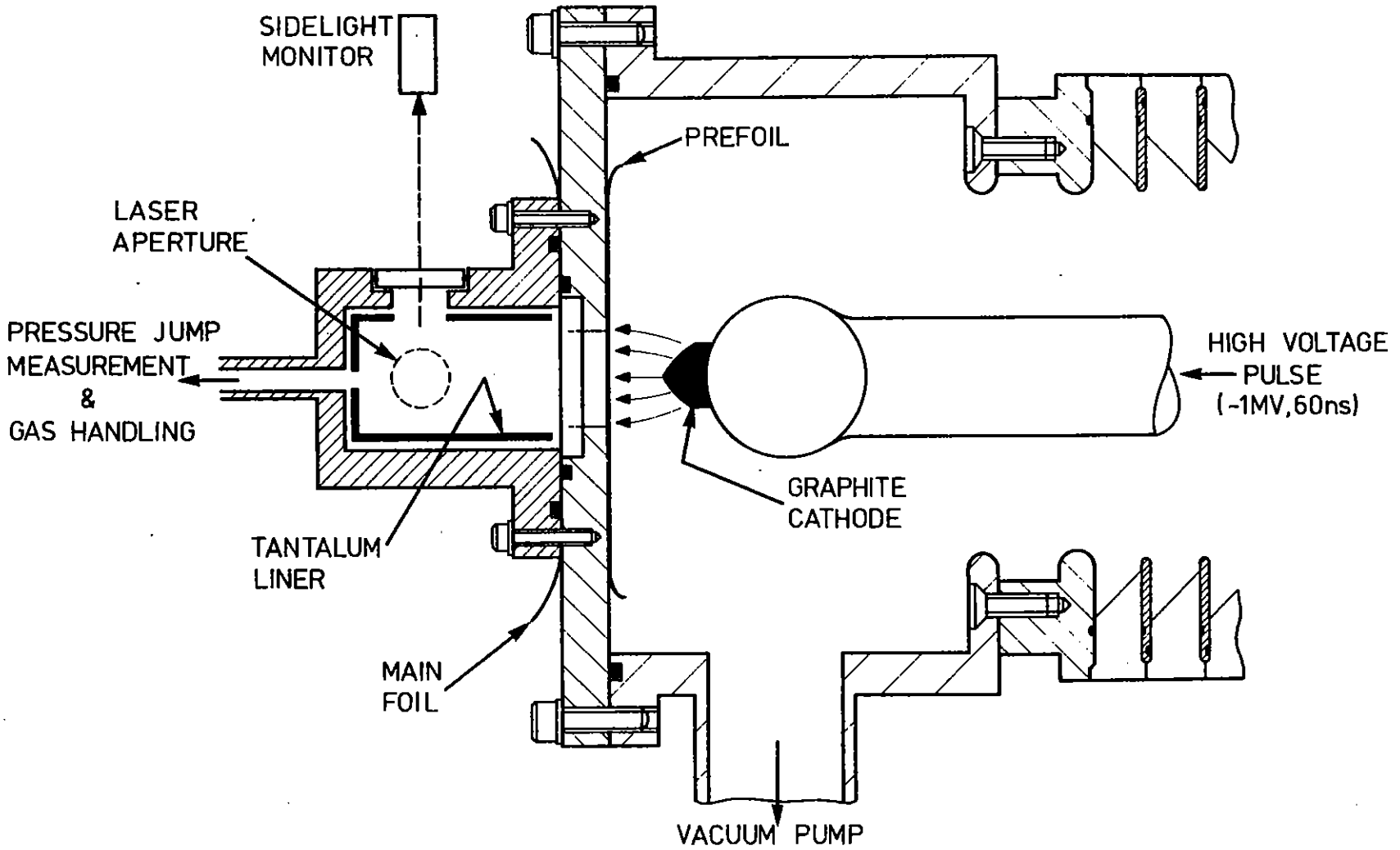

Fig.2.01

Cross-sectional diagram of the e-beam-pumped rare-gas halide laser apparatus.

cell walls. The laser output energy was measured by reflecting 8% of the beam off an uncoated quartz flat into a calibrated (2.09) calorimeter (Gen Tec, Ed-500). The temporal characteristics of the laser pulse and sidelight emission from the cell were monitored using vacuum photodiodes and a Tektronix type 7844 dual beam oscilloscope. The laser gases were mixed in the laser cell and were fed in from a stainless steel gas handling manifold. When changing from one rare-gas halide laser to another, the cell was thoroughly re-passivated with the new halogen donor gas. The effectiveness of our passivation procedure was verifed in the case of fluorine by measuring the F_2 concentration by UV absorption. These measurements showed that after proper passivation the F_2 partial pressure in the laser gas did not change from the value set using pressure gauges, in the filling procedure. A new gas fill was used for each laser shot to overcome problems due to halogen donor depletion and evolution of impurities from the cell walls as a result of electron-beam bombardment.

Experiments were performed with each rare-gas halide laser to optimise gas mixtures and the best mixtures are shown in Table 2.01. For each laser the total gas pressure was adjusted to keep the energy deposition the same. The total pressure of neon-buffered gas mixtures was the maximum that could be used in the present apparatus and was chosen to give the maximum possible pump rate in these experiments. For KrF the argon buffer pressure was chosen to give the same pump rate as for the lasers using the neon buffer. Experiments were then performed with the KrF and XeCl lasers to optimise the cavity output coupling using dielectric coated mirrors. Mirror transmissions in the range 20% to 92% were used and it was found that the optimum output coupling (%T) was $\sim$ 90% for KrF and $\sim$ 80% for XeCl. For comparing the efficiency of the rare-gas halide lasers of different wavelengths (Table 2.01) it was convenient to use a resonator comprising an aluminium coated rear reflctor (R $\sim$ 90%) and quartz etalon output couplers. For the KrF laser a single etalon was used and for the other lasers (ArF, XeCl, XeF) two etalons gave optimum output.

The output energy and intrinsic laser efficiency for each rare-gas halide laser is shown in Table 2.01. The laser efficiencies range from 3% to 11% the most efficient laser being KrF. Our measured KrF efficiency agrees

with Ref.(2.05). The output pulse shape for each laser was also measured and a typical record, in this case for the KrF laser, is shown in Fig. 2.02(a). For each rare-gas halide laser it was found that the onset of lasing was delayed relative to the start of the fluorescence pulse but the peaks of both pulses coincided. This delay was due to the time required to build up laser oscillation in the cavity. In a separate experiment with KrF this build-up time problem was overcome by initiating oscillation in the e-beam pumped laser by injecting a signal (1 MW/cm^2, 20 ns FWHM pulse) from an external, discharge-excited laser (Oxford Lasers, KX2) at the beginning of the pump pulse. Fig.2.02(b), which is a display of the laser output in this case, shows that the laser pulse duration is now equal to the pump pulse duration. This implies that for each rare-gas halide laser, higher pulse efficiency than that quoted in Table 2.01 would be achieved if laser oscillation could be started sooner. For these particular results, when the free running laser was operating slightly below optimum, the extracted laser energy was increased by 80% by injection initiation.

From the laser pulse profiles we have deduced the peak power efficiency which is important in relation to the use of rare-gas halide systems as amplifiers. This efficiency is defined as the peak laser output power divided by the peak pump power (625 MW in our case). These values are shown in the final column of Table 2.01 and indicate that the KrF laser power efficiency is 15%. The other lasers have lower power efficiency and in particular the XeCl efficiency is 7% and the XeF efficiency is 5%.

C B Edwards, F O'Neill and M J Shaw.

2.2.2 KrF Laser Experiments

The experiments described in the previous section clearly showed that under the present operating conditions the KrF laser is the most efficient of the rare-gas halide lasers. The maximum KrF laser output energy in these experiments was 3.6 J. A laser suitable for laser-plasma interactions experiments will have to produce an energy $\sim$ 1000 J in a pulse of $<$ 5 ns. This high energy laser will most likely be constructed from a

TABLE 2.01

Characteristics of rare-gas halide lasers. The total pressure of each gas mix was chosen to give the same e-beam energy deposition (33 J into an excited laser volume of 0.36 ℓ) in each case.

LASER	OUTPUT WAVELENGTH (nm)	GAS MIX (torr)	OUTPUT ENERGY (J)	PULSE EFFICIENCY (%)	PULSEWIDTH AT FWHM (ns)	PEAK POWER EFFICIENCY (%)
ArF	193	F_2 (4) He (76) Ar (200) Ne (2470)	2.0	6	28	11
KrF	248	F_2 (4) Kr (125) Ar (1371)	3.6	11	37	15
XeCl	308	HCl (4) Xe (100) Ne (2296)	1.4	4	30	7
XeF	351	NF_3 (7) Xe (30) Ne (2663)	1.0	3	30	5

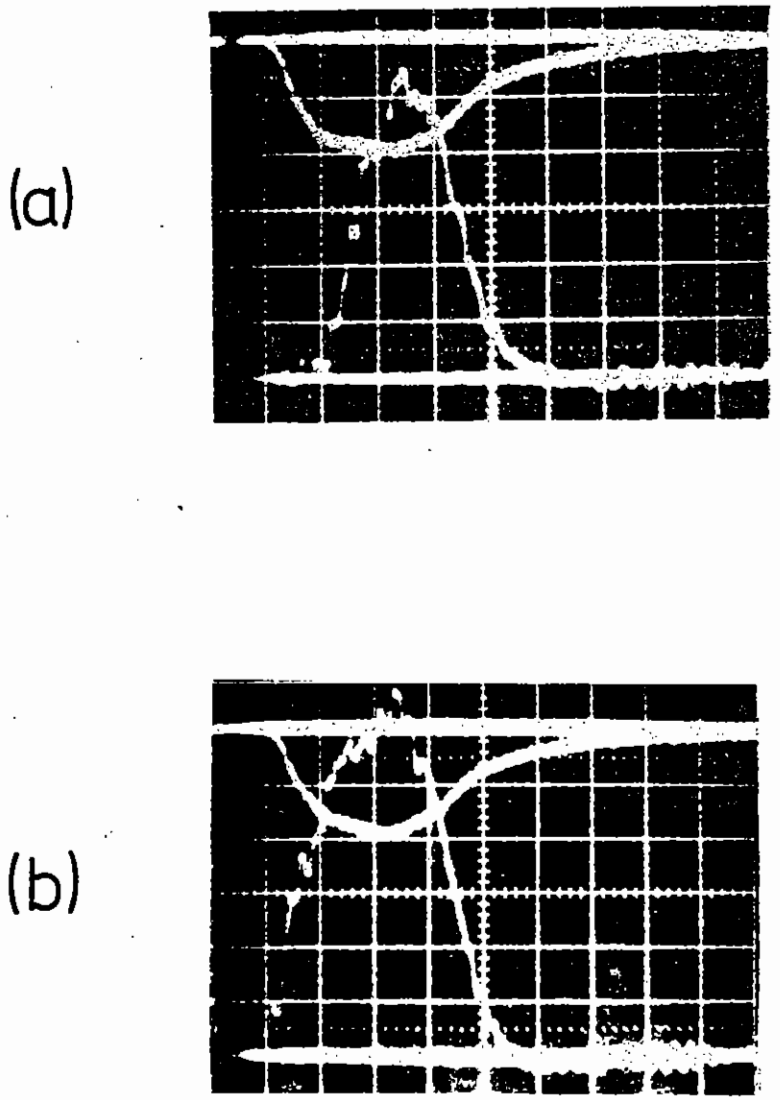

Fig.2.02

(a) Sidelight emission (upper trace) and free-running KrF laser output

(b) Sidelight emission (upper trace) and output of injection initiated KrF laser.

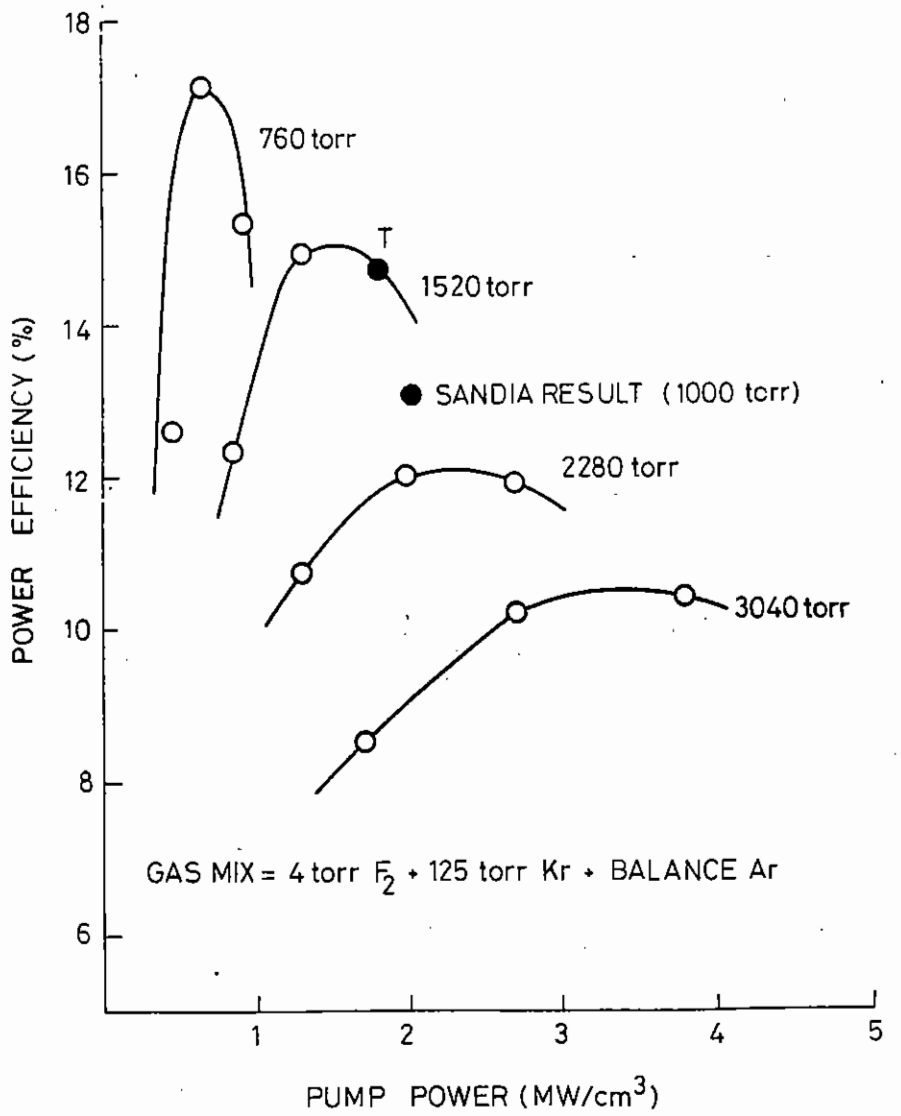

Fig.2.03

Peak power intrinsic efficiency of 60 ns e-beam-excited KrF laser as a function of pump power and gas pressure.

number of modules each producing an output energy ∿ 200 J from an aperture ∿ 20 - 50 cm^2 and we are presently planning to build such a module. Some details of this device are given in later sections.

In order to provide information for the design of a high energy (∿ 200 J) short pulse (∿ 50 ns) KrF laser module we have used the apparatus described in the previous section (Fig.2.01) to measure the KrF laser power efficiency as a function of e-beam pump power and gas pressure. The results of these experiments are in Fig.2.03 and show that for each gas pressure there is a clear optimum in the efficiency versus pump power curve. The initial increase of efficiency with pump power is most likely due to the increase in gain to loss ratio with a resultant improvement in extraction efficiency. The efficiencies measured at low pressure (760 torr) are somewhat higher than would be expected theoretically and this could be due to laser Q-switching resulting in a higher laser intensity than would be obtained at these pump levels in steady state. The fall off of efficiency at high pump rate could be due to electron quenching of KrF^* and this effect is presently being investigated further. Fig.2.03 also shows that the maximum achievable efficiency decreases with increasing argon pressure and this is due to quenching of KrF^* by the buffer gas.

The above results indicate that the KrF laser operates with best efficiency at low pressures (< 1500 torr) and low pump rates (< 1MW/cm^3). For a transversely pumped 200 J laser system this would require a low e-beam voltage and a large laser aperture to provide efficient stopping of the e-beam energy. Both of these requirements are undesirable - a low e-beam voltage would result in high foil losses, and the large laser aperture would necessitate the use of large diameter (and therefore costly) fused quartz windows. Fig.2.03 also shows that high pressures (> 3000 torr) and high pump rates (> 3MW/cm^3) are also undesirable because of the reduced laser efficiency due to KrF^* quenching. The optimum region of operation for high overall efficiency appears to be at a pressure of approximately 2000 torr and a pump rate of 1.5 - 2MW/cm^3.

C B Edwards, F O'Neill and M J Shaw.

2.2.3 SPRITE - A 200 J KrF Laser

In this section some of the considerations leading to the design of a high power KrF laser are set down. This system (which has since acquired the name "Sprite") is envisaged as a prototype for a laser which may replace the existing CLF glass laser in the mid 1980's. In energy terms Sprite will produce about a factor 10 more than the existing e-beam pumped laser ELF and about a factor 10 less than the final requirement. The desirability of short wavelength (250 - 350 nm) and high overall efficiency, dictated that this new laser should be basd on the most efficient rare gas halide laser viz KrF. Since such lasers have no storage capability the laser pulse duration is set by the length of the pumping pulse and since this is inevitably much longer than the required pulse duration for plasma interaction work, some form of laser pulse compression is desired. Techniques for efficient optical pulse compression are under development both in this laboratory (section 2.4.1) and elsewhere (2.01), and will not be addressed in this section other than to say that in order to minimize the complexity of the pulse compression system, the KrF laser pulse duration should be as short as possible (< 100 ns).

2.2.3(a) Choice of Pump Rate

This is determined mainly by the ratio of the gain, g_o to the non saturable loss, α. For an ideal amplifier the maximum extraction efficiency is given by:

$$\eta_{max} = 1 - 2\left(\frac{\alpha}{g_o}\right)^{\frac{1}{2}} + \frac{\alpha}{g_o} \qquad (1)$$

from which it can be seen that in order to extract > 50% of the available power g_o/α should be larger than 10. This effects the pump rate since the gain is proportional to pump rate ($g_o = R\sigma\tau$ where R is pump rate into upper laser level, σ the gain cross section and τ the level lifetime) whereas, for the e-beam-pumped KrF laser, the losses are either independent of pump rate (F_2 absorption) or proportional to $\sqrt{R}$ (F^-, Ar_2^+ absorption). A crude estimate of the desired pump rate may be obtained by

assuming a constant loss of about 0.01 - 0.02 cm^{-1}. Thus the desired g_o is > 0.2 cm^{-1}. Using the expression for saturation intensity $I_S = h\nu/\sigma\tau$ the power per unit volume deposited into the upper laser level is $Rh\nu = g_o I_S$ and if the fluorescence efficiency is η_f then the required specific power deposition rate is $W = g_o I_S/\eta_f$. At 1500 Torr $I_S \sim$ 2 MW/cm^3 and η_f = 0.25 thus W is $\sim$ 1.6 MW/cm^3 for a g_o of 0.2 cm^{-1}. As the buffer gas pressure increases, I_S increases (due to the decrease in τ by quenching) and the required pump rate also increases in broad agreement with the measured efficiency curves shown in Fig.2.03.

2.2.3(b) Choice of Pulse Duration

Once the pump rate is fixed, as described above, the maximum pulse duration is determined by the effects of fluorine consumption. For each KrF* formed, one fluorine molecule is dissociated. If the fluorine number density is $[F_2]$ and the maximum fractional reduction is ε then the pulse length is given by

$$\frac{W}{h\nu}\,\eta_f\,t_p < \varepsilon[F_2] \qquad (2)$$

$[F_2]$ max is about 2 x 10^{17} cm^{-3} and setting the maximum reduction at 20% the pulse duration should be less than 80 ns at a pump rate of 1.6 MW cm^{-3}. A choice of 60 ns was finally adopted.

2.2.3(c) Choice of Laser Dimensions and E-Beam Voltage

The choice of laser dimensions is determined firstly by the type of e-beam pumping. Whilst axial pumping has a number of advantages for high power applications, it was decided at an early stage to avoid the complexity of the high B-guide fields needed with this system and to go for transverse pumping. If the e-beam energy is to be utilized efficiently, it is required to deposit the majority of its energy in a length equal to the laser aperture. In order to avoid significant foil losses the e-beam voltage should be greater than 400 kV and thus the laser aperture is determined by the e-beam voltage and the buffer gas pressure. It turns out that the optimum aperture is larger than the maximum diameter single

piece fused silica windows which are routinely available and it is this commercial consideration which sets the laser aperture at 25 cm diameter. An e-beam voltage of 450 kV was chosen which implies an optimum buffer gas pressure (argon) of about 2000 Torr. At this pressure approximately 60% of the e-beam energy will be deposited in the extracted volume and the intrinsic laser efficiency will be about 10%. The gain length is determined by need for a short cavity build-up time when operating as an oscillator. In terms of the mirror reflectivities R_1R_2 and the initial fluorescence intensity I_f, the cavity build-up time is given by:-

$$A = \frac{\ell n\,(I_s/I_f)}{\frac{C}{2L}\,(2g_oL + \ell n\,R_1R_2)} \qquad (3)$$

In our case $\ell n(I_s/I_f)$ is about 13 and for a cavity build-up time of about 5 ns, g_oL needs to be between 12 and 15. Since g_o is likely to be in the 0.15 to 0.2 cm^{-1} region, the required gain length will be about 75 cm. For these large values of g_oL amplified spontaneous emission will be a problem and operation as either an injection locked oscillator or a saturated amplifier is envisaged.

Laser Parameters

The design criteria outlined above define the laser parameters which are summarized as follows:-

Laser diameter	25 cm
Pumped length	75 cm
Active volume	37 litres
Pulse duration	60 ns
Specific deposition rate	1.5 MW cm^{-3}
Total energy in laser gas	3.3 k J
Intrinsic efficiency	8 %
Output energy	250 J
Output power	4 GW

E-Beam Parameters

E-Beam voltage	450 kV
Foil and support transmission	55 %
Fraction deposited in laser volume	60 %
E-beam diode to gas efficiency	33 %
E-beam energy required	10 kJ
Overall diode impedance	1.2 Ω

In order to achieve this low impedance, four sided pumping is envisaged from four magnetically isolated 5 Ω diodes. Each cathode will be 75 cm long x 15 cm high and the current density will be 80 A cm^{-2}. The design of the pulsed power system is described below in section 2.5.2.

M.J. Shaw

2.3 Selenium Laser Experiments

2.3.1 Photolysis of OCSe Using 172 nm Radiation

Metastable (S_0) states of S and Se can be produced with ∿ unit quantum efficiencies by photolysis of OCS and OCSe respectively with Kr_2^* and Xe_2^* radiation (2.10). Laser action has recently been demonstrated in atomic selenium and sulphur by Powell et al (2.11, 2.12) using such an excitation scheme.

Stored energy in the laser upper level may be reduced by quenching by the parent triatomic molecule:

$$Se(^1S) + OCSe \rightarrow Se_2^* + CO \qquad (1)$$

and by photoionization by the photolysing radiation:

$$Se(^1S) + h\nu(172\ nm) \rightarrow Se^+ + e \qquad (2)$$

Quenching reaction (1) may be reduced by bleaching the absorption of OCSe by high laser fluences. Quenching by superelastic collisions with electrons produced in reaction (2) causes electron heating and subsequent multiplication which drastically reduces laser efficiency. Electron heating may be reduced by the addition of molecular gases (CO, N_2) but kinetic modelling requires a knowledge of the photoionization cross section (σ_i) and photodissociation cross section (σ_d).

These parameters have been measured using a high repetition rate tunable xenon laser, capable of a maximum output in excess of 25 mJ (2.13). The technique includes the use of a simple ionization chamber, shown in Fig. 2.04, in which the photoionization electrons are collected from a defined volume by a cylindrical anode in the photolysis region and detected with an electrometer. By operating at low pressures of OCSe (∿ 10^{-2} mbar), the densities of electrons (∿ 10^{11} cm^{-3}) and $Se^*(^1S)$ (∿ 10^{15} cm^{-3}) are

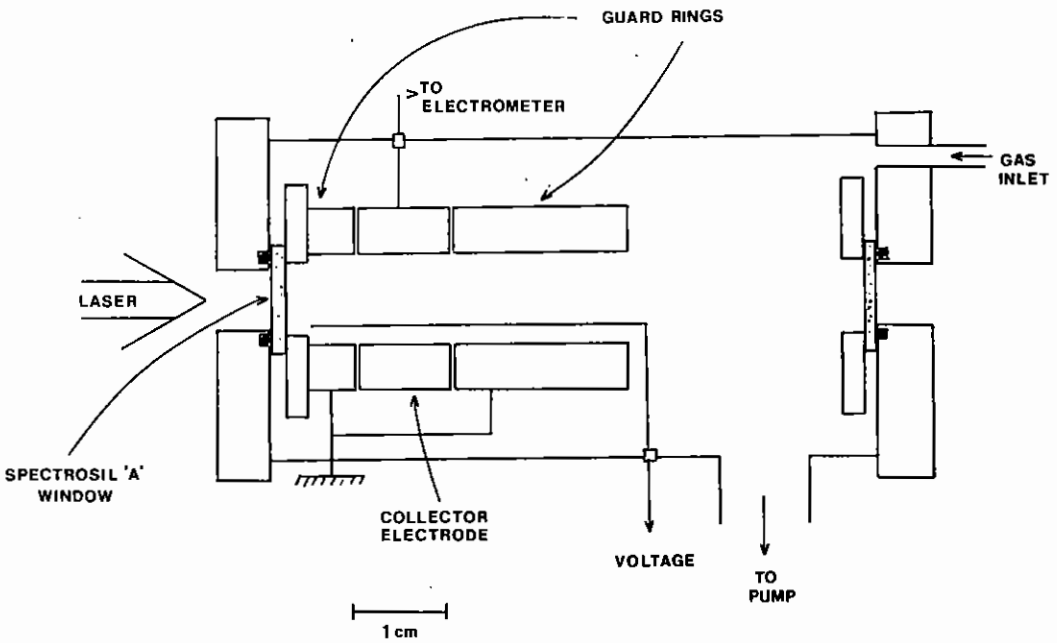

Fig 2.04 Ionization chamber.

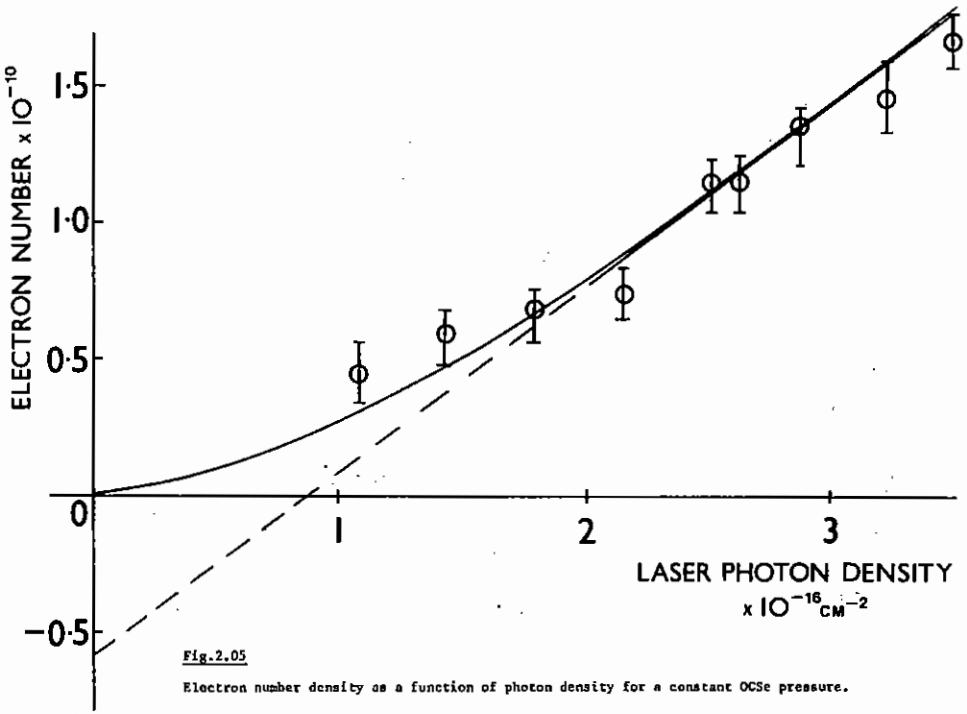

Fig.2.05

Electron number density as a function of photon density for a constant OCSe pressure.

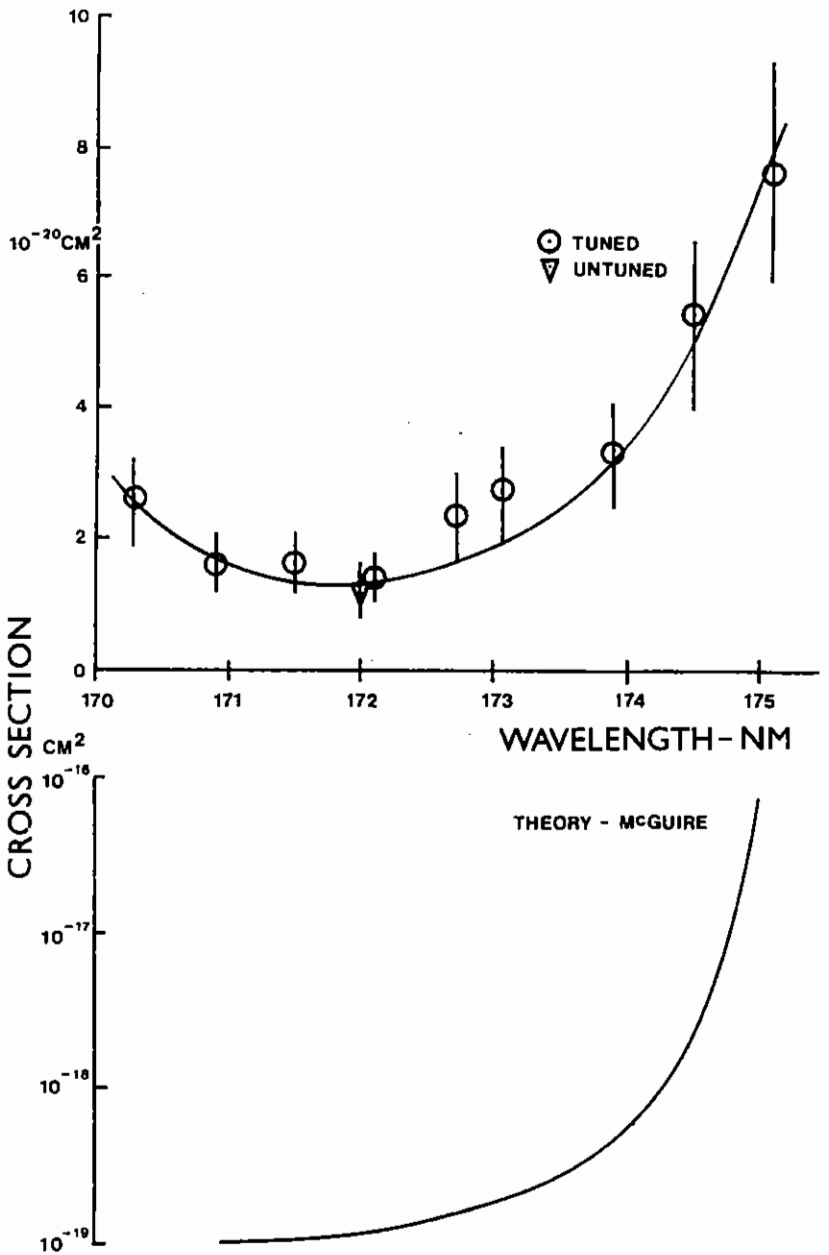

Fig.2.06

Experimentally observed variation of σ_i with wavelength (top) and theoretical calculation if σ_i over the same wavelength region (bottom) by McGuire (2.15).

sufficiently low for electron quenching and recombination to be insignificant.

When a sample of OCSe is photolysed by 172 nm radiation to yield Se(S) atoms, the photoionization rate of the product is given by:

$$\frac{\sigma n_e\ (x_1 t)}{t} = \sigma i \frac{I\ (x_1 t)}{h\nu}\ \rho^*_{h}\ (x_1 t) - [\text{Loss}] \qquad (3)$$

where $n_e(x,t)$ is the electron number density and $\rho^*(x,t)$ is the Se(S) number density given by:

$$\rho^*(x_1 t) = \phi[\rho_o(x) - (x_1 t)] \qquad (4)$$

where $\rho_o(x)$ and $\rho(x,t)$ are the initial and time varying OCSe densities and ϕ is the (^{1}S) quantum yield. I(x,t) is the input laser pulse intensity. The solution is given by (2,14):

$$N_e = \frac{AL\ \sigma_i\ \rho_o}{\sigma_d}\ [\ell nV + V^{-1} - 1] \qquad (5)$$

where N_e is the total number of electrons collected, A is the area of the laser beam, L is the collector length, E is the laser fluence (photons /cm^2) and V is given by:

$$V = \exp(\sigma_d E) + \exp(\sigma_d\ \rho_o x) - 1 \qquad (6)$$

Using the laser untuned (λ = 172 nm, $\Delta\lambda$ = 1 nm) plots of N_e v E are obtained (Fig.2.05) from which σ_d and σ_i are respectively determined to be 0.8 x 10^{-16} (± 25%) cm^2 and 1.2 x 10^{-20}(± 25%) cm^2 assuming unit quantum yield, ϕ (2.10). This measured value for σ_i is considerably smaller than a recently calculated value by McGuire (2.15) of $\sim 10^{-19}$ cm^2. However, recent measurements (2.14) of σ_i for S(^{1}S) at 157 nm also indicate values approximately one order of magnitude less than that

calculated (2.14). Also, the photoionization cross section of Cs vapour, determined by a similar technique, is in good agreement with recent theoretical work (2.16). The value of σ_d integrated over the untuned laser bandwidth ($\Delta\lambda$ = 1 nm) is in good agreement with that previously measured.

By tuning the laser over the range 170 - 175 nm ($\Delta\lambda$ = 0.2 nm), the variation in σ_i as a function of wavelength has been determined. This is shown in Fig.2.06 and confirms the theoretically predicted increase in σ_i with increasing wavelength (2.15), but is much less dramatic and suggests that a modification to the theoretical model may be necessary.

Thus, the maximum value of ϕ and a minimum value of σ_i both lie at 172 nm, the wavelength of the xenon laser, and confirm that Xe_2^* excimer radiation is a suitable choice of excitation for the Se photoiodissociation laser.

K T V Grattan and M H R Hutchinson.

2.3.2 Bleaching of OCSe Using the 193 nm ArF Laser

Experiments have been performed that measure the bleaching effects of high intensity short duration laser pulses propagating in highly absorbing media. Such phenomena are of importance in photolytically pumped high-energy storage lasers for fusion applications (2.17). Because the leading edge of the laser pulse experiences a much larger absorption than the tail, the pulse appears to sharpen and slow down. Evidence of this slowing down is shown in Fig.2.07 for an ArF 193 nm laser pulse propagating through Se_2 vapour (2.18).

The laser pulse reshaping, as applied to a bleached dissociative medium, has been modelled using a modified analysis of the propagation of a pulse through a saturable amplifier (2.19). Fig.2.08 shows the results of calculations of the change in laser pulse shape for different positions into the medium. The peak power of the pulse transmitted through the medium, P_{out}, and the input power, P_{in}, are related in this

analysis by:

$$\ell n \left[\frac{P_{in}}{P_{out}}\right] - 1 = - \frac{E_L}{E_b} + \ell n \left[e^{\alpha_o L} - 1\right] \qquad (1)$$

Thus a plot of the L.H.S. versus the input energy fluence, E_L, gives a direct measurement of the bleaching fluence $E_b = \frac{h\nu}{\sigma_d}$ of the medium (from the slope), as well as the small signal absorption coefficient α_o (from the intercept). Such an experimental plot is shown in Fig.2.09 for ArF 193 nm photolysis of OCSe. As can be seen the value of E_b from the slope is 15 mJ/cm^2 whereas that obtained (more indirectly) from the intercept using $E_b = \frac{h\nu}{\sigma_a}$ is 74 mJ/cm^2 (the absorption cross-section $\sigma_a = N_o/\alpha_o$). We beleive the reasons for this discrepancy are that either (i) not all OCSe molecules are accessible for dissociation by the photons i.e. $N_o \neq$ the total OCSe density or (ii) the OCSe dissociation cross-section $\sigma_d \neq \sigma_a$. We believe, however, that this direct method of measuring bleaching fluence is more reliable than inferring a value from small-signal absorption coefficient measurements. Because of the importance of the value of E_b for ArF pumped Se laser operation, we are currently performing further experiments to more accurately determine its value.

M.C. Gower, S.Rolt and M.J. Shaw

2.3.3 Photolysis of Se_2 at 193 nm

Because of the importance of the quenching reaction:

$$Se(^1S_o) + OCSe \rightarrow Se_2^* + CO \qquad (1)$$

to the operation of the photolytically pumped selenium laser (2.11), we have performed experiments on the pumping of Se_2 vapour by various U.V. lasers (2.18). A tubular oven was used to heat metallic selenium which was then irradiated by light at a variety of wavelengths from discharge excited rare gas halide and N_2 lasers. The fluorescence from the excited vapour was monitored through side viewing windows. Fig.2.10 shows

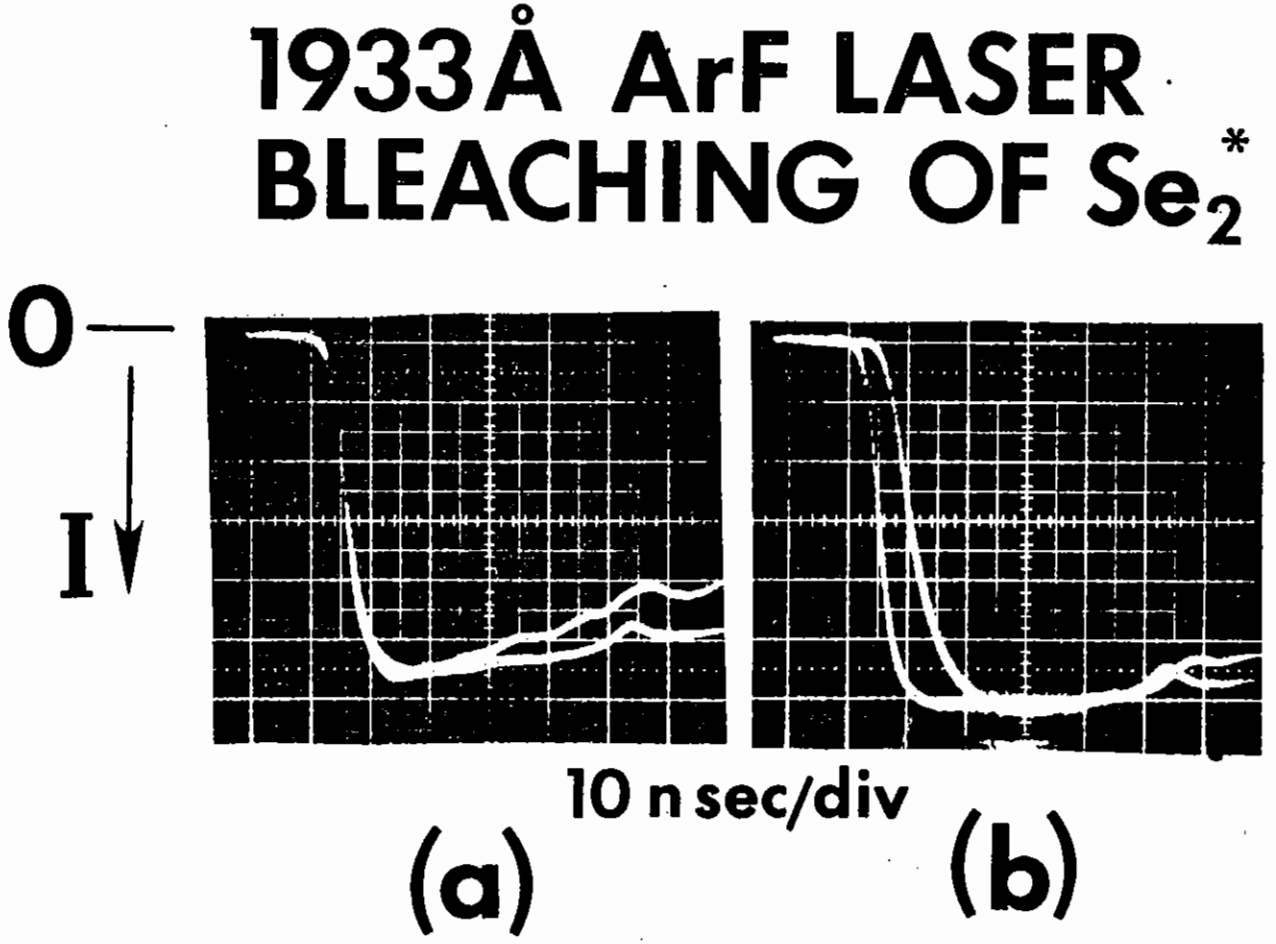

Fig.2.07

Se_2 B $^3\Sigma_u^-$ → X $^3\Sigma_g^-$ emission excited by an ArF laser. The two traces in both (a) and (b) were taken from side viewing windows separated by 10.5 cm along the selenium oven. In (a) $P_{se} \sim 0.6$ torr with no measurable delay in the signals (b) $P_{se} \sim 4$ torr with a delay of 3 nsec corresponding to a bleaching wave velocity of 3×10^9 cm/sec. A 100 torr He buffer gas pressure and $E_{laser} \sim 150$ mJ were used in both cases.

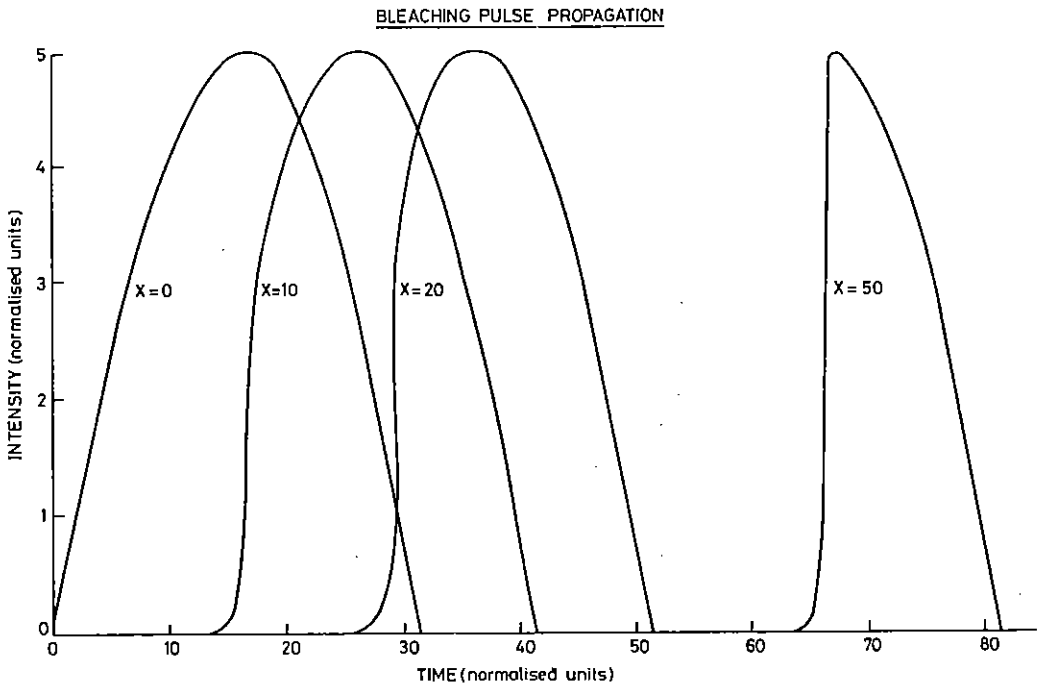

Fig.2.08

Numerical calculations of laser pulse reshaping as a function of time and distance into the medium using a Frantz-Nodvik analysis.

approximate experimental Se_2 potential curves and the various pump laser wavelengths. The results which we obtained can be summarised as follows:

(a) By pumping Se_2 with a 3371 Å N_2 laser the radiative lifetime of the Se ($B^3\Sigma_u^-$) was found to be 40 nsec. Quenching rates for a variety of buffer gases were measured for this state.

(b) As shown in Fig.2.11, pumping at 1933 Å with an ArF laser gave a broadband Se_2 emission between 3500 - 6000 Å as well as the atomic Se resonance lines between 1960 - 2500 Å. The broadband emission was found to be due to a combination of the Se ($B^3\Sigma_u^- \rightarrow X^3\Sigma_g^-$) transition and Se_2^* emission from an unidentified state which has a radiative lifetime of 1.7 μsec. We believe this unidentified state of Se_2^* to be the same as that produced in reaction (1) and so is not the B state as proposed by other workers (2.10). Quenching rates by different buffer gases of this Se_2^* state have also been measured.

(c) When CO gas was added to the ArF-pumped Se_2 vapour several dramatic observations were made. The broadband emission was now dominated by the Se($^1S_0 \rightarrow {}^3P_1$) transauroral transition as shown in Fig.2.12 while its decay time (in Fig.2.13) lengthened considerably.

The Se($^1S_0$) densities were estimated to be $\sim 10^{15}$ cm^{-3}. We have further investigated the production mechanism of the Se($^1S_0$) state in this experiment. By monitoring the increase in absorption through the cell at 1900 Å upon the addition of CO, and assumming that this increase is due to absorption by spontaneously generated OCSe, we measured OCSe densities of the same order as the Se($^1S_0$) density (10^{15} cm^{-3}). Furthermore, when the hot Se + CO cell was allowed to cool to 100° C, a temperature at which the selenium vapour pressure was negligible, the long decays were still evident and only disappeared upon evacuating the oven. Thus we believe that the substantial Se($^1S_0$) population is produced by the photodissociation of OCSe at 1933 Å, and that this OCSe is spontaneously produced when CO gas is added to the hot selenium oven.

M.C. Gower and S Rolt

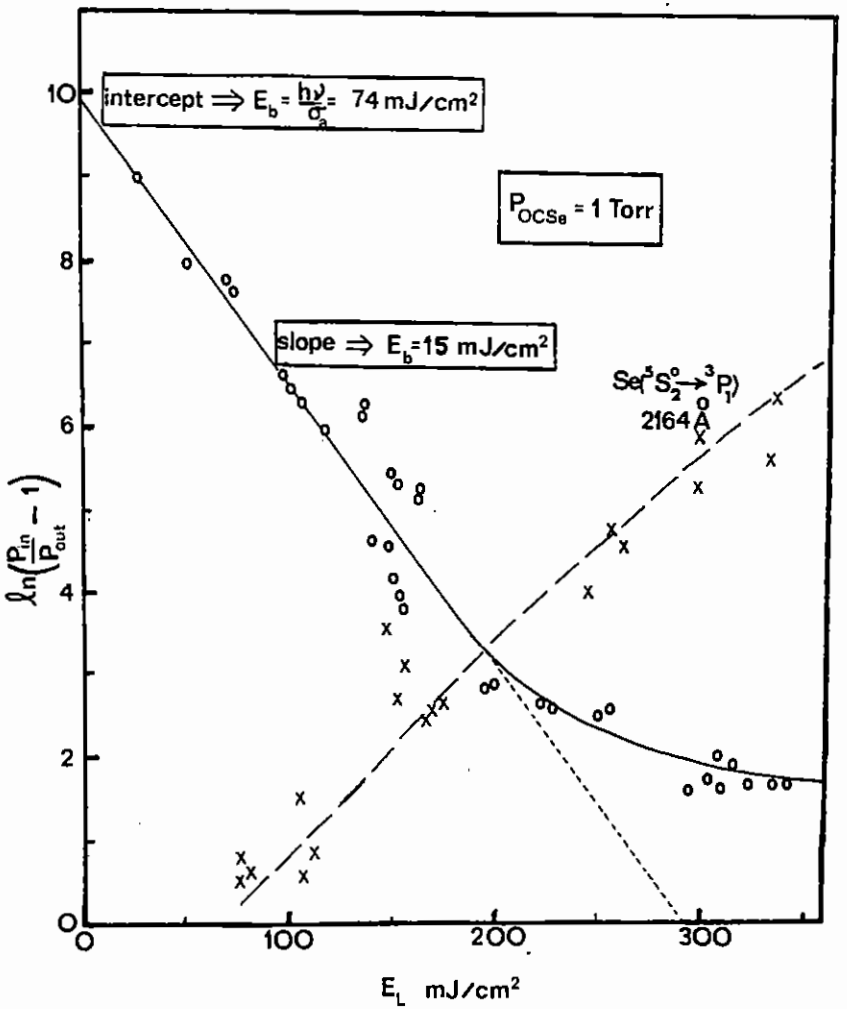

Fig.2.09

The data (o) were taken using matched photodiodes to measure the peak incident and transmitted power of the same ArF laser pulse through a cell containing 1 torr of OCSe. The data (x) measures on a linear scale the relative values of the Se ($^5S_2^o$) population created by two photons per step processes. Such processes at high laser fluences (> 230 mJ/cm²) are believed to be responsible for the departure from linearity of the $\ln\left(\frac{P_{in}-1}{P_{out}}\right)$ plot in this region.

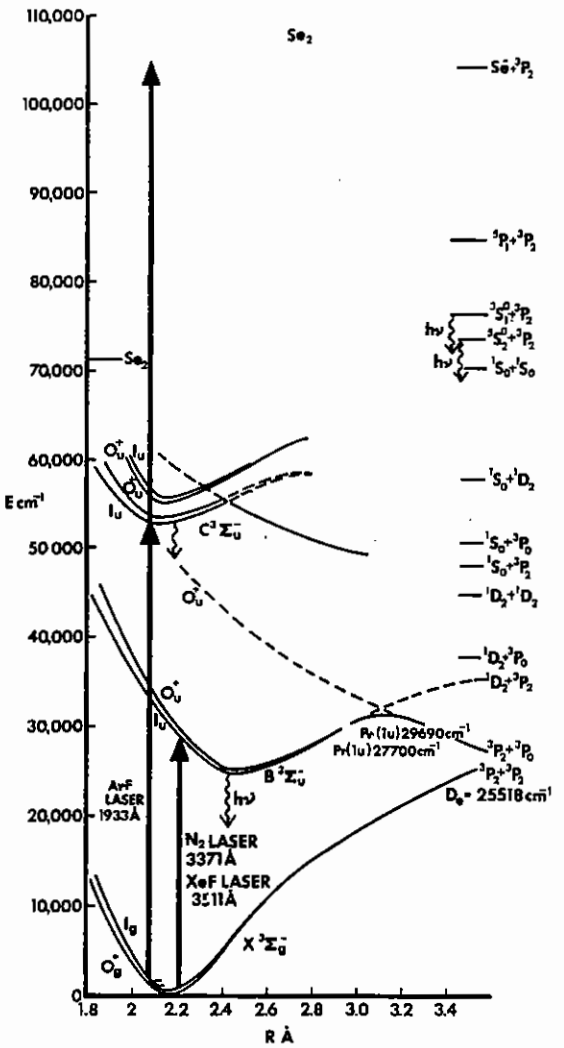

Fig.2.10

Approximate experimentally derived potential energy curves of Se_2 obtained from the data of ref (2.20) and (2.21). The pump laser wavelengths and some of the atomic and molecular selenium transitions observed are also indicated.

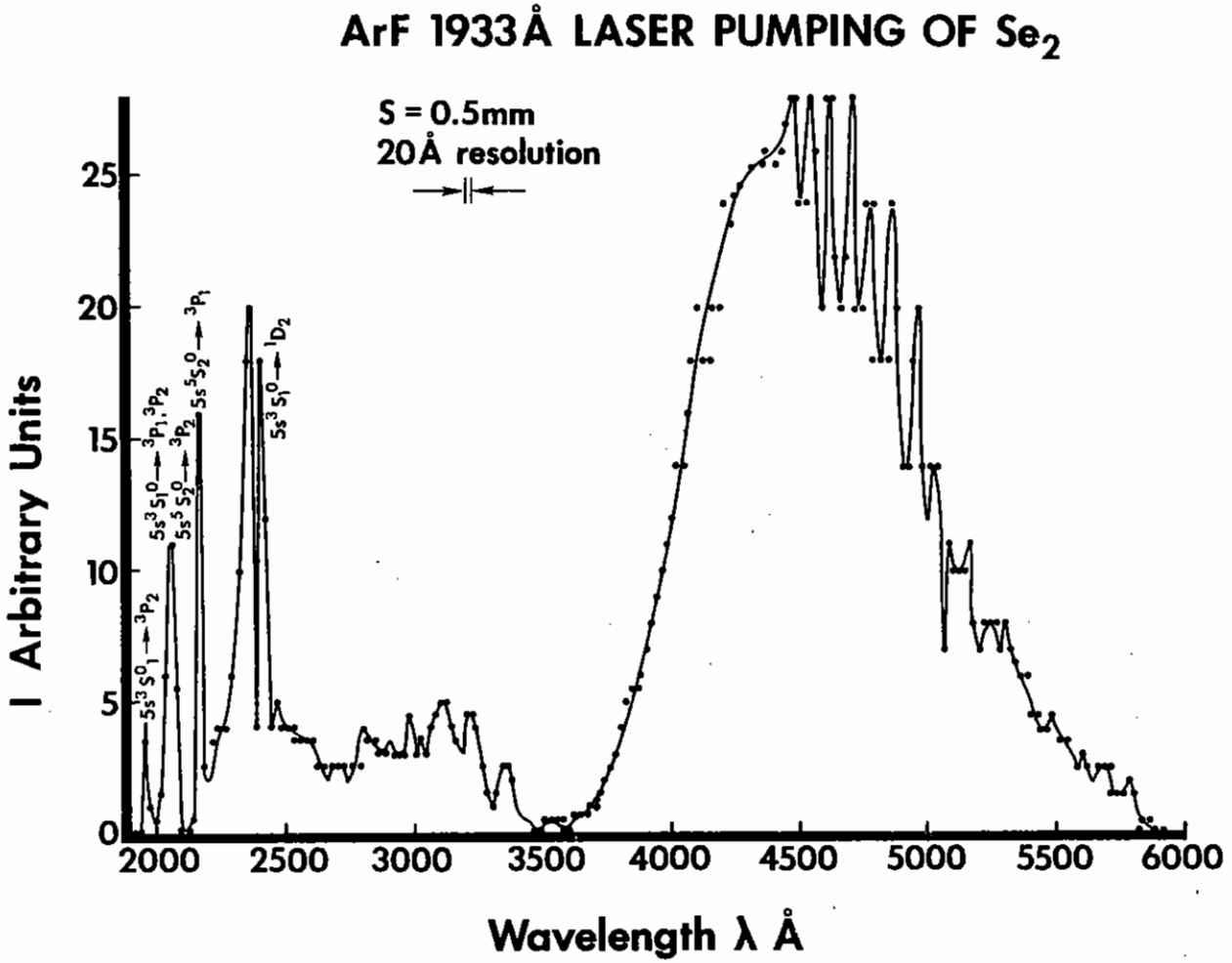

Fig.2.11

Sidelight spontaneous emission spectrum from Se_2 pumped by $\sim$ 1.5 J/cm^2 ArF laser radiation.

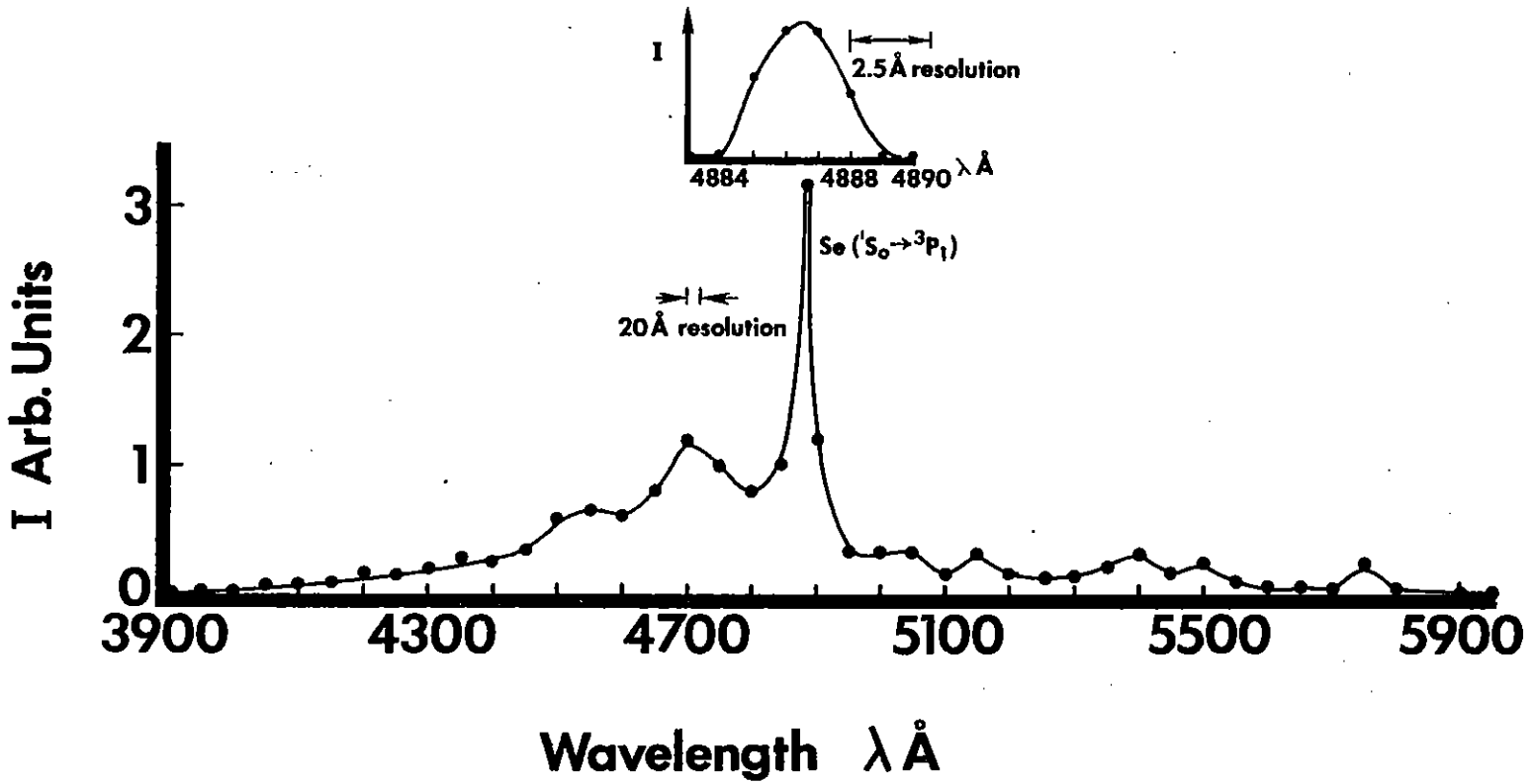

Fig. 2.12

Sidelight spontaneous emission spectrum from Se_2 buffered by 50 torr CO pumped by ∿ 1.5 J/cm^2 ArF laser.

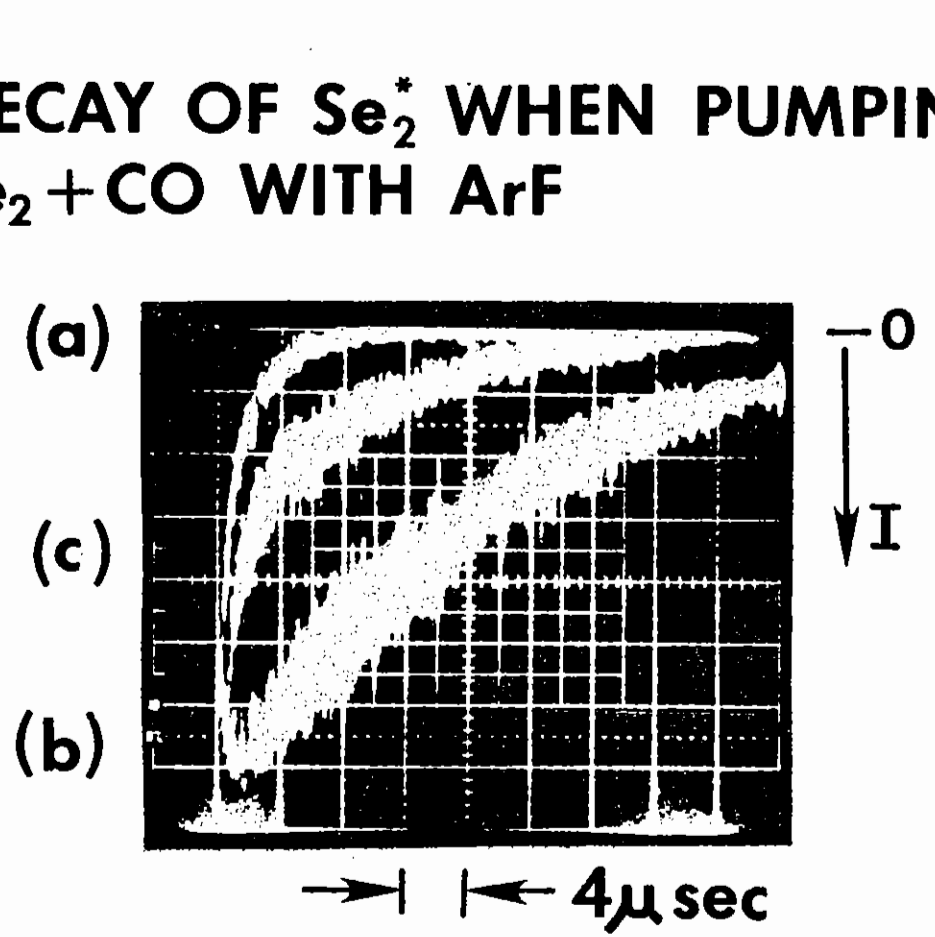

Fig.2.13

Oscilloscope traces of broad-band Se_2^* sidelight fluorescence with (a) no buffer gas, (b) 10 torr CO, (c) 10 torr CO + 10 torr He.

2.4 New Laser Concepts

2.4.1 Optically Pumped Lasers

The original goal for optically pumped lasers for fusion applications was for long lifetime ($\tau \sim 1$ μs) systems pumped by rare gas excimer radiation (e.g. Se (^1S) pumped by Xe_2^*). More recently the use of RGH lasers (e.g. KrF) followed by some pulse compression scheme has been shown to be potentially more efficient and to offer UV wavelengths. The two main contenders for KrF pulse compressers at present are backward Raman systems and optical multiplexers. In this section a third alternative viz short term energy storage media will be described.

Such a system would be pumped by a short pulse ($\sim$ 50 ns) RGH laser and would have a storage lifetime somewhat greater than this. A short T_2 time would allow extraction of the stored energy in $\sim$ 1 ns pulses. The desireable characteristics of such lasers are as follows:-

Level Lifetime (T_1)	50 - 200 ns
Homogeneous lifetime (T_2)	< 1 ns
Pumping wavelengths	193 nm ArF, 248 nm KrF
Lasing wavelengths	250 - 350 nm
Stimulated emission cross section	10^{-18} - 10^{-17} cm^2
Saturation energy	0.1 - 1.0 J cm^{-2}
Fluorescence efficiency	> 30 %

A prototype for such a system is ArF-pumped I_2 which has recently been operated for the first time at this laboratory. Although the lifetime T_1 is too short for energy storage purposes it does possess a number of the above requirements and is a promising laser system in its own right. Laser action on the 342 nm band of molecular iodine was originally obtained some years ago using electron beam excitation (2.22, 2.23, 2.24). The efficiency of the system was found however to be rather low and interest in it rapidly diminished particularly with the discovery, soon after, of the much more efficient rare gas halide lasers. On the other hand the fluorescence of optically excited I_2 in the presence of buffer

gases has long been recongized as efficient and the possibility of an optically pumped I_2 laser has been discussed by a number of authors (2.25, 2.26, 2.27). Indeed such lasers have been recently reported, pumped initially using light from exploding wires (2.28) and more recently employing conventional flash-lamps (2.29). The efficiency of these systems however has also proved to be very low, due to the poor coupling of the spectrally broad flash band to the narrow absorption band in the molecule.

Initial fluorescence experiments were carried out using a discharge excited ArF laser. Spectra were analysed using a PAR OMA II optical multichannel analyser system. The laser excites the D state of I_2 around v' = 133. The absorption cross section was measured to be $6 \pm 2 \times 10^{-18}$ cm^2. In the absence of a buffer gas, fluorescence occurs on an extensive series of bands (the McLennan bands) extending from the exciting wavelength through to the visible spectral region (Fig.2.14(a)) with peaks at 320 nm (D-X resonance fluorescence)(2.30) and at 420 nm (E-B bands) (2.31). Very little fluorescence is observed at 340 nm. The lifetime of both bands (measured using a fast photomultiplier and oscilloscope) at low I_2 pressures ($\sim$ 0.03 torr) was found to be 17 ± 3 ns in agreement with previous measurements for the D state lifetime (2.32).

With the addition of an inert buffer gas such as Ar or SF_6 the McLennan bands are rapidly attenuated and fluorescence at 340 nm becomes very strong (Fig.2.14(b)). Tellinghuisen (2.33) attributes this band to a $^3\pi_{2g} \rightarrow {}^3\pi_{2u}$ transition although some contribution from v' = 0 of the D-X system may also be expected in this region (2.31). As pressures are increased the band narrows and shifts to the red. Above one atmosphere of SF_6 the bandwidth and peak wavelength become constant at 1.5 nm (FWHM) centered at 342.0 nm. Under these conditions the lifetime of the transition is too short (< 10 ns) to be measured reliably by our apparatus due to the comparable decay time of the ArF laser. Sauer et al (2.34) give a value of 6.7 ns for the radiative lifetime and found it to be relatively independent of Ar pressure up to one atmosphere. SF_6 on the other hand appears to quench the 342 nm band with an apparent rate coefficient (2.27) in the region of 3×10^{-12} cm^3 s^{-1}. The actual lifetime at 3 atmospheres

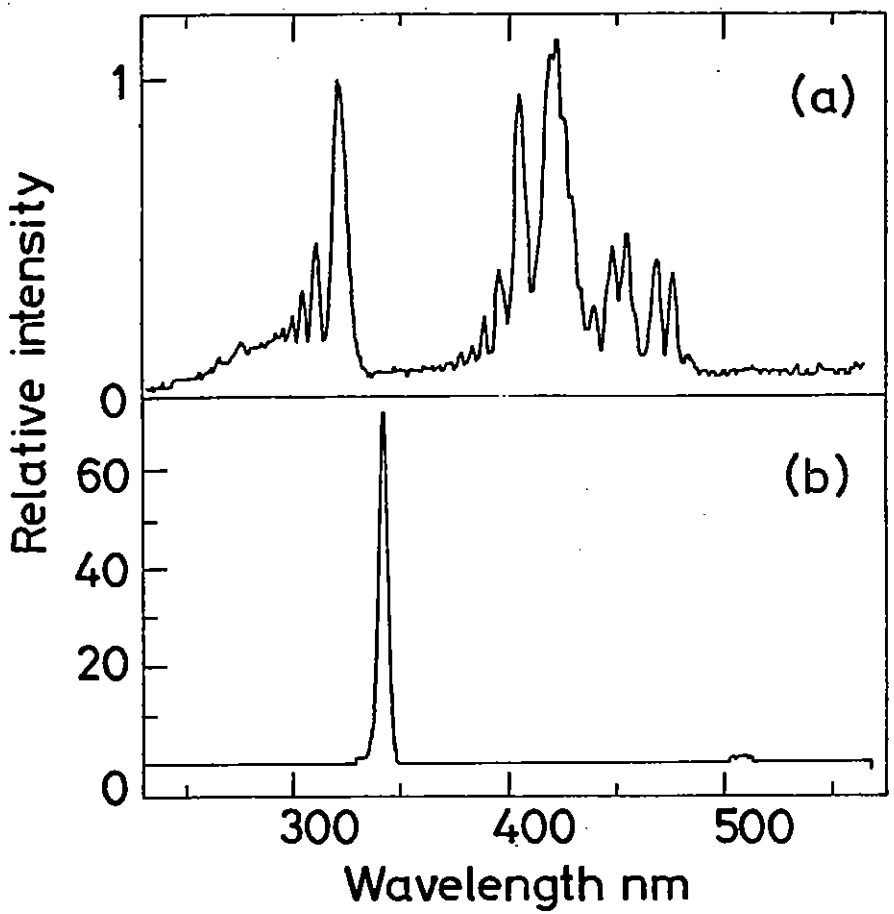

Fig.2.14

Low resolution OMA spectra of ArF-pumped I_2

(a) 0.2 torr I_2 showing D-X (320 nm) and E-B (420 nm) bands.

(b) 0.2 torr I_2 + 800 torr Ar showing 340 nm band. Note change of intensity scale.

SF_6 pressure would thus be approximately 2 ns.

With a knowledge of the radiative lifetime and the fluorescence bandwidth the stimulated emission cross section can be estimated to be approximately 2×10^{-15} cm^2. With a cross section of this magnitude, oscillation should be possible using short gain lengths at modest inversion densities. A transverse excitation scheme was thus devised, the essential features of which are shown in Fig.2.15.

The ArF laser used is a large volume e-beam excited device (2.35) which produces approximately 3.5 J in 30 ns in an 8 cm dia beam. A rectangular section of the beam 7 x 4 cm is focused by a cylindrical lens into the I_2 laser cell through a 10 cm dia fused silica window. The total energy entering the cell was measured by a joulemeter in place of the cell rear window and found to be approximately 1.5 J. The position of the focus was found from a polaroid burn pattern and is shown in Fig.2.15. The entire cell, windows and tubulation are heated to around 350°K to prevent condensation of I_2 on windows. The pressure of I_2 is controlled by varying the temperature of a heat bath surrounding a side arm which contains a few grams of reagent grade I_2 crystals. The laser aperture is 3.0 cm and is sealed by two fused silica etalons which are aligned perpendicular to the laser axis. External dielectric coated mirrors are used having reflectivities of 75% and 85% at 342 nm. The total output energy through both mirrors is measured by calibrated pyroelectric joulemeters (2.36).

Fig.2.16 shows the essential results. The optimum I_2 pressure was found to be 3 torr which agrees with the pressure calculated to maximise the pump energy in the laser volume. Both Ar and SF_6 buffer gases were used, the highest output occurring at the maximum working pressure of SF_6. This fact is initially somewhat surprising since SF_6 quenches the upper laser level. Its major role however is probably as a vibrational relaxer and these high pressures are needed to populate the upper laser level (v' = 0) and depopulate the lower level at rates comparable to the stimulated emission rate. The highest total output energy obtained was 230 mJ which when compared with the pump energy absorbed in the laser volume of 800 mJ gives an intrinsic energy conversion efficiency of 0.30 $\pm$ 0.05.

The fluorescence and laser pulse shapes were measured using vacuum photodiodes. The fluorescence was found to follow the 30 ns FWHM ArF pump pulse almost exactly. The laser pulse duration was also 30 ns but was delayed relative to the pump pulse by 5 ns due to the effects of cavity build-up and decay times.

The laser output spectrum was measured on the OMA II with a resolution of 0.4 nm. A single line with an apparent FWHM of 1.0 nm centered at 341.8 nm was obtained. This is at variance with previously reported laser spectra which show lasing on two main lines at 341.8 and 342.5 nm (2.24, 2.28). According to Tellinghuisen (2.30) the 341.8 nm line is a 0 → 12 (v' → v") transition and 342.5 nm a 1 → 14 transition in the $^3\pi_{2g} \rightarrow {}^3\pi_{2u}$ system. The predominence of v' = 0 in our laser compared with e-beam pumped systems could well be due to the absence of electron excitation and the effect of very rapid vibrational relaxation due to the high pressure SF_6 buffer gas.

One interesting feature of the laser output was obtained from polaroid burn patterns which showed that the strongest lasing region (shown shaded in Fig.2.15) was away from the focus of the cylindrical lens. Production of copious amounts of ionization in ArF-pumped I_2 has previously been observed (2.37) and with pump intensities of around 10^7 W cm^{-2} at the focus it seems plausible that photoionization is causing the problem. Direct de-pumping of the upper levels is probably not involved, however, since for reasonable estimates of the cross-sections involved, photoionization of the D state would not compete with relaxation to the $^3\pi_{2g}$ state and photoionization from there would be a small loss compared to stimulated emission. On the other hand simple estimates show that an ionization density of around $10^{13} - 10^{14}$ cm^{-3} may be produced which could cause problems due to ionic absorption features at the laser wavelength or population of the lower laser level by electron excitation from ground state I_2 molecules. In fact it may well be that the low efficiency of e-beam pumped I_2 lasers (where ionization is unavoidable) is due to these effects. The laser was found to operate well (at somewhat reduced energy) when the cylindrical lens was removed. The efficiency was found to be the same (∿ 30%) as for the focused case.

M J Shaw, R J Donovan, C Fotakis, C B Edwards and F O'Neill.

2.4.2 Population Inversion by Laser Switched Collisions

It has recently been suggested (2.38) that 'laser-switched' collisions, and in particular 'pair-absorption' could be used to optically pump and invert media to produce new lasers. Pair absorption, which forms a particular class of the more general phenomena of laser switched collisions (2.39, 2.40) can be described as occurring between atoms (or molecules) A and B such that

$$A + B + h\nu \rightarrow A^* + B^* \qquad \text{(i)}$$

where A^* and B^* represent excited states of A and B. One way of envisaging this process is to regard the photon as being absorbed in the quasi-molecule AB formed during a collision of A and B. Subsequent separation or dissociation of $(AB)^*$ leads to the formation of A^* and B^*. This reaction, which becomes resonant when E = hν is equal to the sum of energies of A^* and B^*, has recently been observed in absorption for ground state Ba atoms, (A = B = Ba) as well as for the A = Ba and B = Tl system (2.41). It has been pointed out by Falcone (2.38) that it should be possible to invert A^* with respect to the ground state provided that the concentration of B exceeds that of A and that the laser pumping fluence E exceeds the saturation fluence $\frac{h\nu}{\sigma_a}$ for the process (σ_a is the absorption cross-section for (i)).

Our interest in such a process is stimulated by the need for the development of a high energy storage laser operating in the visible/u.v. spectral region for laser fusion applications (2.17). One of the selection rules of pair-absorption is that atom A^* is a metastable state and B^* forms the upper state of an allowed transition to the ground state. We envisage such a storage laser operating on the inverted electric dipole forbidden transition $A^* \rightarrow A$. Because of their inherent high power and high efficiency in the u.v. spectral region, rare gas-halide lasers would then be the natural choice of optical drivers for such a process.

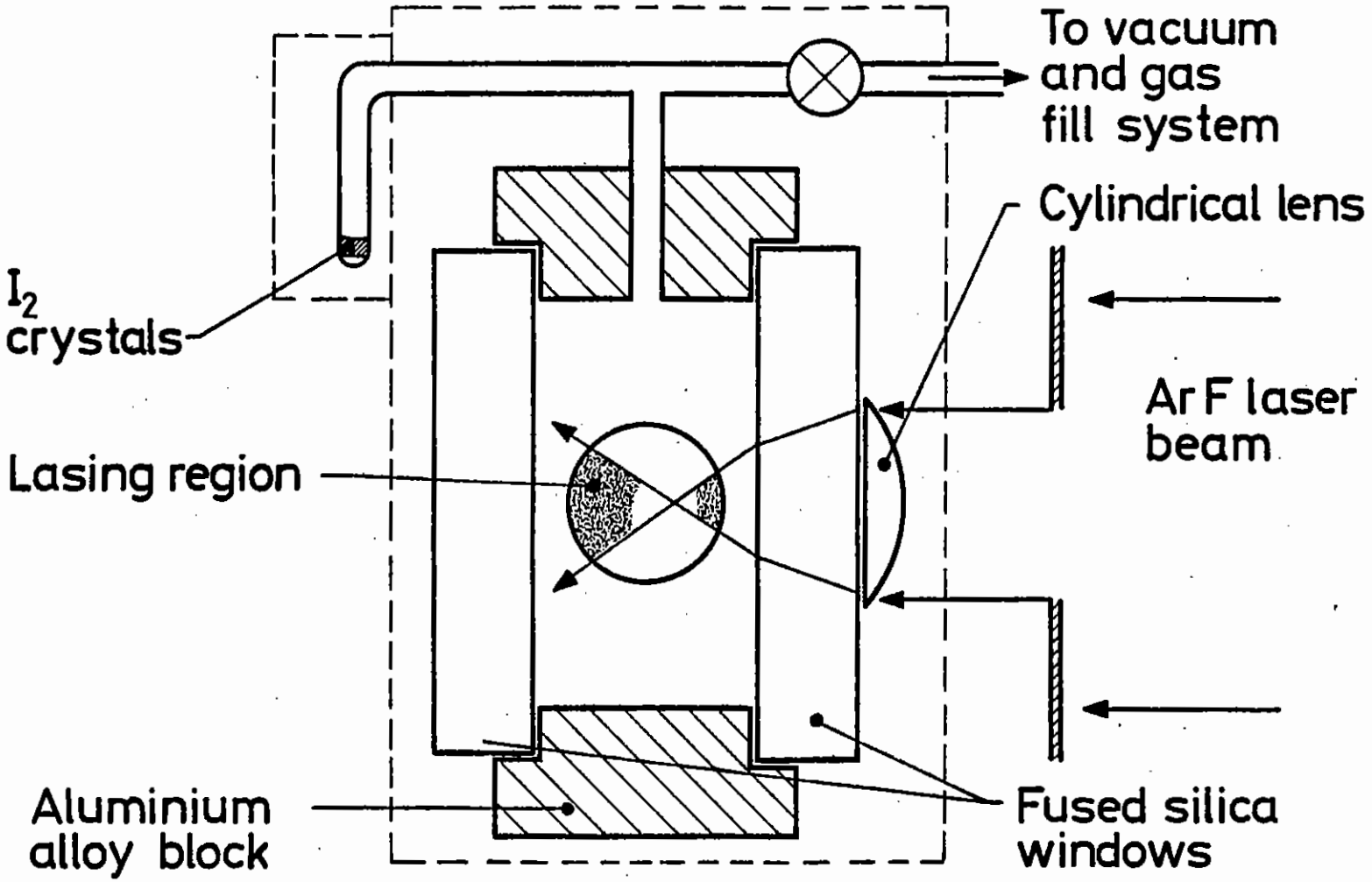

Fig.2.15

Schematic diagram of ArF-pumped I_2 laser. The large region within dashed outline is maintained at 350 ^{o}K.

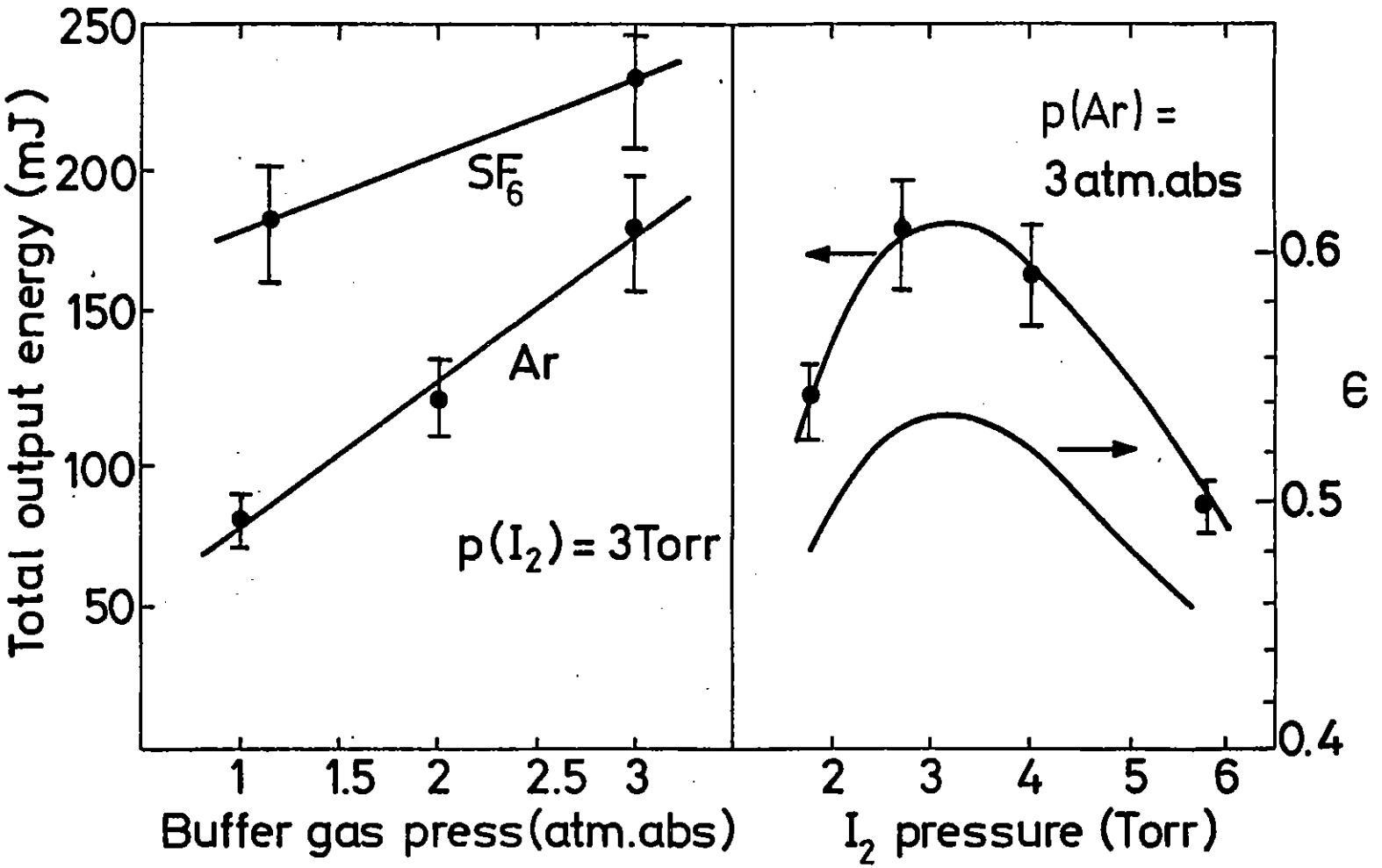

Fig.2.16

Variation of laser output energy as a function of Ar and SF_6 buffer gas pressure (left) and as a function of I_2 pressure (right). Also shown as a function of I_2 pressure (lower right hand curve) is the fraction, ϵ, of the pump energy entering the cell which is deposited in the laser volume.

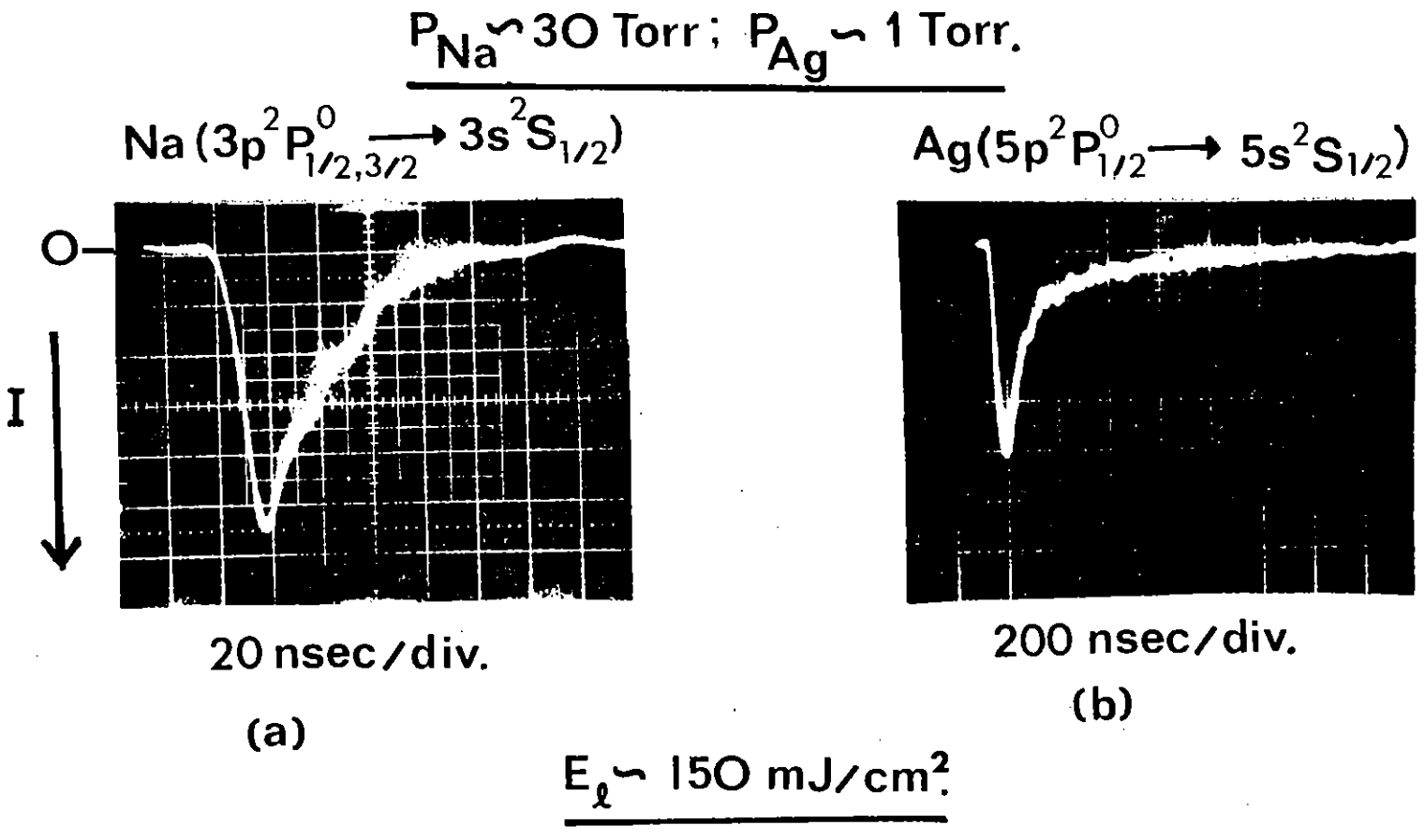

Fig.2.17

ArF laser-induced (20 nS FWHM pulse) fluorescence of (a) Na D lines and (b) Ag resonance line. Note that in (a) for P_{Na} = 30 torr the emission appears to be untrapped. There may however be a long tail to this emission which is buried in the noise of the PMT detector. In (b) the Ag emission is trapped.

We are performing experiments on the system

$$Ag(5s^2S_{\frac{1}{2}}) + Na(3s^2S_{\frac{1}{2}}) + 1935\ \mathring{A} \rightarrow Ag(5s^2D_{3_2}) + Na(3p\ P_{\frac{1}{2},\ 3/2})$$

pumped by an ArF laser. The $Ag(5s^2D_{3/2})$ state is metastable with respect to the ground state, while the resonance transition in Na possesses a large oscillator strength which should make the overall absorption cross-section for pair absorption relatively large. If it is possible to invert the $Ag(5s^2D_{3/2})$ state, then the transition to the ground state is at 2881 A - a wavelength that would be of great interest to laser fusion experimenters.

Because of the vastly different vapour pressures of Ag and Na, a special Na heat pipe oven has been constructed in the middle of which a high temperature (1500° C) resistively heated boat is situated to evaporate the Ag. Preliminary measurements of the fluorescence from above the boat induced by an ArF laser are shown in Fig.2.17. The emission from the $Na(^2P_{\frac{1}{2},\ 3/2})$ state increases by about an order of magnitude when the boat is turned on indicating that the above switched collision may be occurring. However, higher states in Na (up to $5d^2D_{5/2,\ 3/2}$) were also observed to increase by a similar magnitude in the presence of Ag (without Ag in the boat there was no increase in the Na emission when the boat was switched on). Further experiments are underway to confirm the occurance of this switched collision and to measure the pair-absorption cross-section at 193 nm for this system.

M.C. Gower

2.4.3 Metal Vapour Excimers

2.4.3(a) CdHg Excimer Kinetics

Further measurements have been made on the density and temperature dependence of the CdHg fluorescence following pulsed excitation at 266 nm. In previous work (2.42) the cadmium concentration n_c had been greater than the mercury concentration n_H, and the system kinetics was dominated by Cd_2 and Cd_3 with a decay via CdHg(b). In the present work with $n_H >> n_c$ the main species was the 2.4 μsec CdHg(a) state. The fluorescence data could only be modelled by proposing a new bound triatomic species Cd_2Hg lying 0.78 eV below CdHg(a). As the cadmium density increased, this non-radiating state held an increasing fraction of the system excitation and caused an increase in the system fluorescence lifetime. When the transmission of excited Cd/Hg mixtures was measured (for more detail see below) the trimer reservoir hypothesis was strikingly confirmed, and indeed the most accurate determination of the equilibrium constant between CdHg(a) and Cd_2Hg came from the transmission work. For $[CdHg(a)] = n_a$, $[Cd_2Hg] = n_r$, we find (2.43)

$$\frac{n_a}{n_r} = \frac{8 \times 10^{21}}{n_c(cm^{-3})} \exp\left(-\frac{0.78(eV)}{kt}\right)$$

The relative energies of CdHg(a) and $Cd(^3P_1)$ were also determined and the overall system is depicted in Fig.2.18.

2.4.3(b) CdHg(a) Transmission

Up to 20 mJ of TEM_{oo} light at 266 nm was employed to provide a relatively uniform excited state density of CdHg(a) over a 15 cm path length and in a 2 - 3 mm diameter. This was probed with argon laser lines and also with a Garton-type continuum lamp recorded on an Optical Multichanel Analyser. The temperature and density dependence of the observed absorption pointed clearly to the presence of two absorbing species which correlated precisely with the CdHg(a) and Cd_2Hg populations deduced from the fluorescence work. The Cd_2Hg absorption was much stronger than the

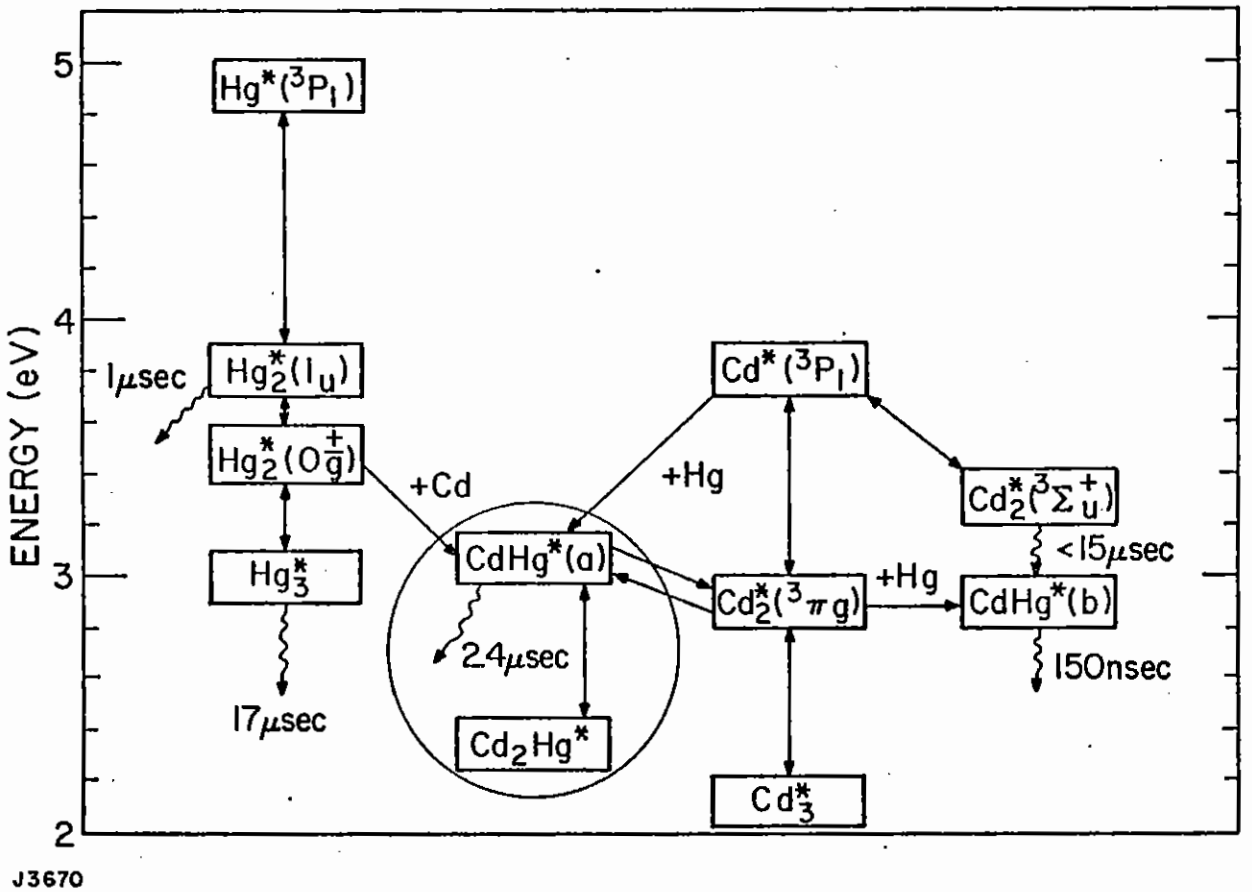

Fig.2.18

Energy relationships in the Cd-Hg system. Observed energy transfer processes are indicated by connecting lines. The CdHg(a) - Cd_2Hg subsystem is circled.

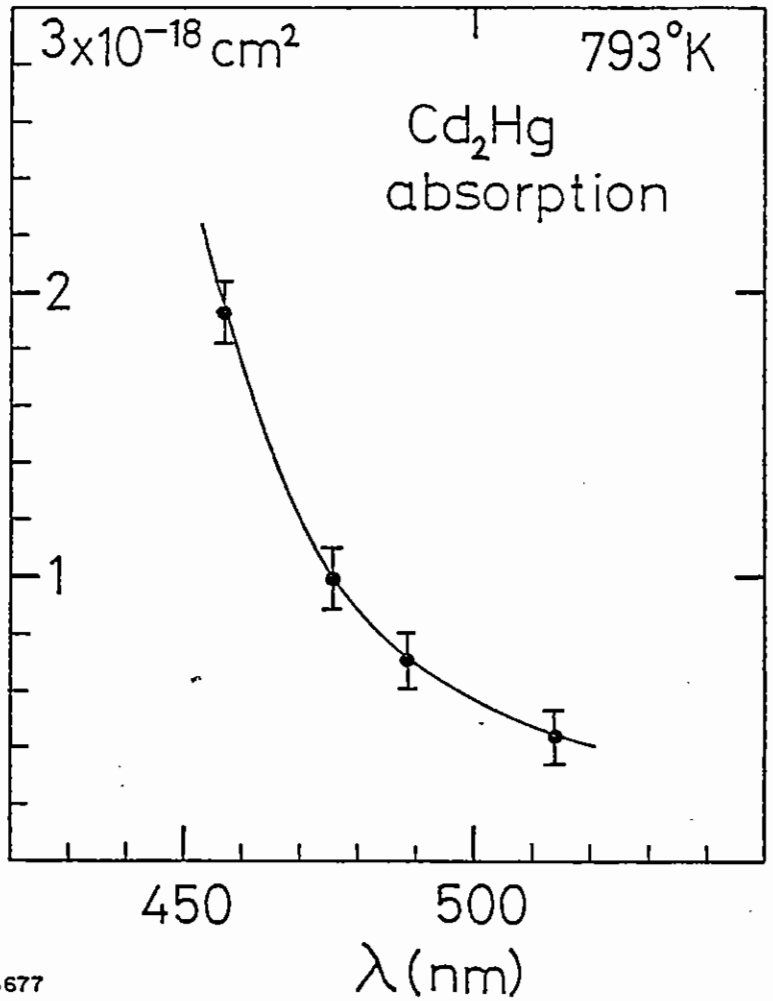

Fig.2.19

Absorption cross-section of Cd_2Hg. The error bars show the relative error due to the resolution of the absorption experiment. The scaling of the cross-section axis has an estimated error of ± 50%.

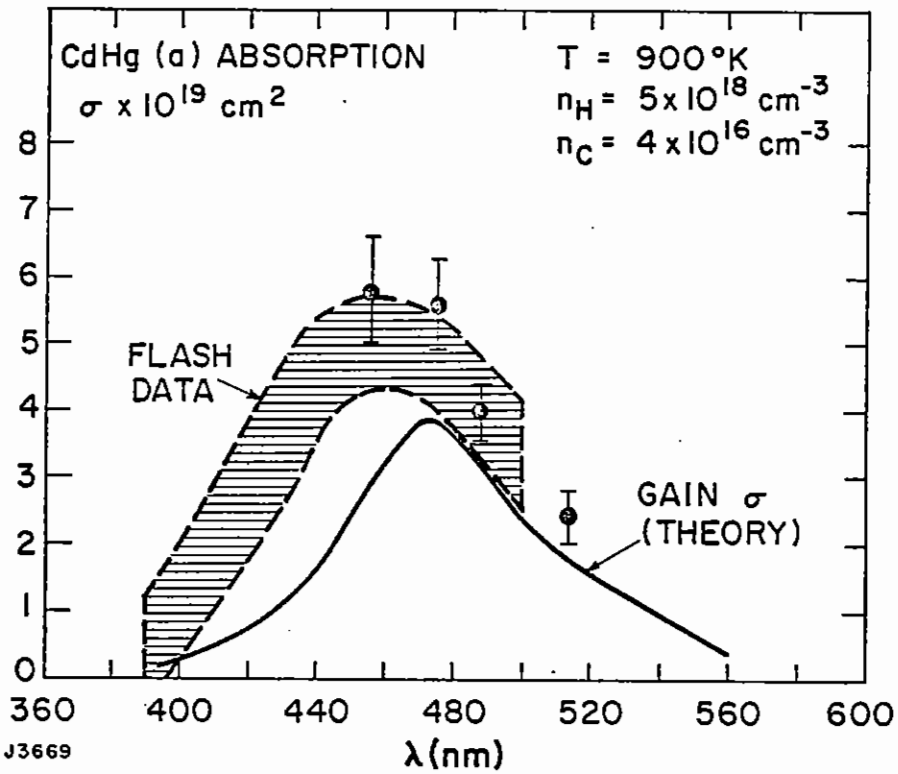

Fig.2.20

Absorption cross-section of CdHg(a). The measured absorption has been added to the theoretical stimulated emission cross-section. Points refer to the Ar^+ laser lines; shaded area refers to the continuum transmission data.

CdHg(a) absorption and both absorptions increased steadily between 514 nm and 457 nm. The absorptions are shown in Figs.2.19 and 2.20. A previous experiment (2.44) using excitation at 326.1 nm had shown net absorption in the CdHg system under conditions where the Cd_2Hg absorption dominated (according to the present interpretation). Both the flash spectroscopy and the laser absorption measurements showed a finite absorption at low n_c which was intrinsic to CdHg(a). This absorption peaked at 450 nm with a cross-section of $5 \pm 1 \times 10^{-19}$ cm^2 and was 90 nm wide at half maximum.

2.4.3(c) Conclusion and Prospect for ZnHg

The intrinsic CdHg(a) absorption is not very strong, but is positioned almost precisely on top of the expected gain band, so that the possibility of an efficient CdHg(a) laser is now looking remote. However, it is quite possible that cooling the vibrational temperature could shift the gain and absorption bands sufficiently to allow net gain, and that this could explain a previous measurement of gain (2.45) in which the metals expanded from a cool wall into a partial vacuum.

A cell was prepared with Zn and Hg, and pumped at 266 nm in the same transmission experiment as CdHg. An analogous energy transfer was observed from $Hg_2(0_g^{\pm})$ to ZnHg, which radiated with the 6.1 μsec lifetime that had previously been observed (2.46). When ZnHg transmission was probed at Ar^+ laser wavelengths, no absorption was observed at the $\pm$ 1% level at 457 nm. In analogous density conditions there was a loss of 10% at 457 nm in CdHg. This is encouraging preliminary evidence that the ZnHg intrinsic absorption does not completely overlap the ZnHg gain band.

The fluorescence efficiency of CdHg(a) in a discharge has been measured (2.47) to be 50%. The same efficiency is expected in ZnHg, so that further investigation of this system would be interesting.

M.W. McGeoch

2.5 E-Beam Technology

2.5.1 Performance of the ELF E-Beam Machine

During the past year, the high power electron beam generator, ELF, has operated reliably, providing some 1,600 excitation pulses during the year for the gas laser development programme. An important requirement for the experimental studies of rare gas halide laser efficiency (sections 2.2.1 and 2.2.2) was good pulse to pulse reproducibility of the excitation source, and ELF has proven to be most satisfactory in this respect.

The most recent experiments have involved synchronisation of the laser excitation with a probe signal and with a detection gate of approximately 100 ns. It has been possible to trigger the detection channel from the Blumlein monitor output with a jitter of < 10 nsec enabling transient absorptions to be measured in the e-beam-pumped laser with a time resolution of better than 5 ns.

Since only one spark gap in the ELF marx is triggered, due to the large trigger gap capacitance, the overall machine jitter is large ($\sim$ 1 μs) when operated in the usual way. For the purposes of the above experiments this has been reduced to 100 ns by operating the gaps close to the self-break curve (see Fig.2.07, Annual Report, 1979).

During the year, ELF was out of operation for a total of three weeks due to malfunctions. On one occasion, high voltage breakdown occurred between the Blumlein conductors at the Marx end of the lines. Once the cause was identified the fault was remedied by a simple modification to the field shaper support at the Marx output aperture. The other major fault was due to oil leaking into the Marx spark gap column through a seal around a trigger electrode. This caused a marked deterioration in the performance of the Marx, in particular the self-fire characteristic. The column was dismantled for cleaning, and the trigger electrodes were replaced as some erosion had occurred.

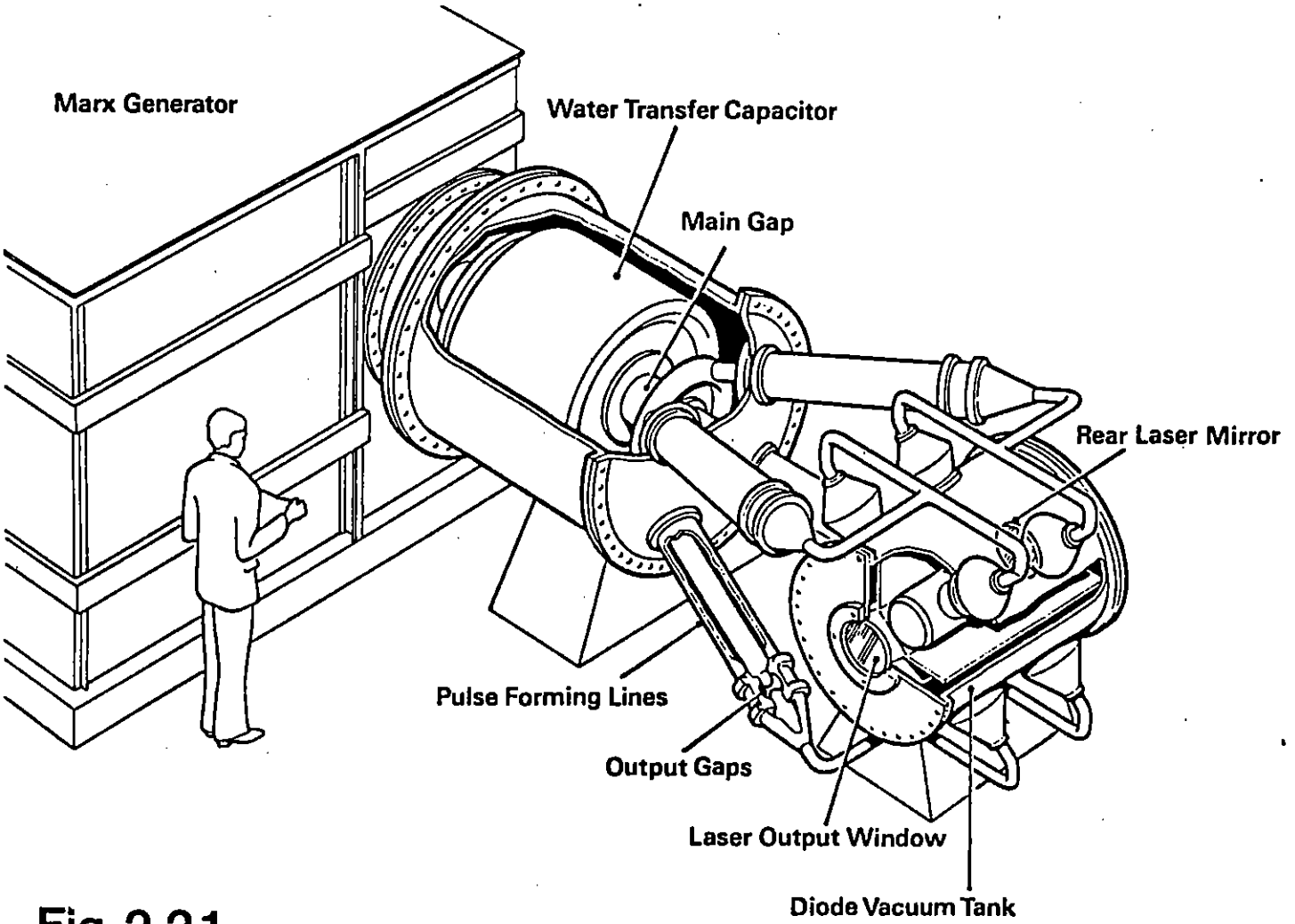

Fig 2.21

Artist's Impression of "SPRITE"

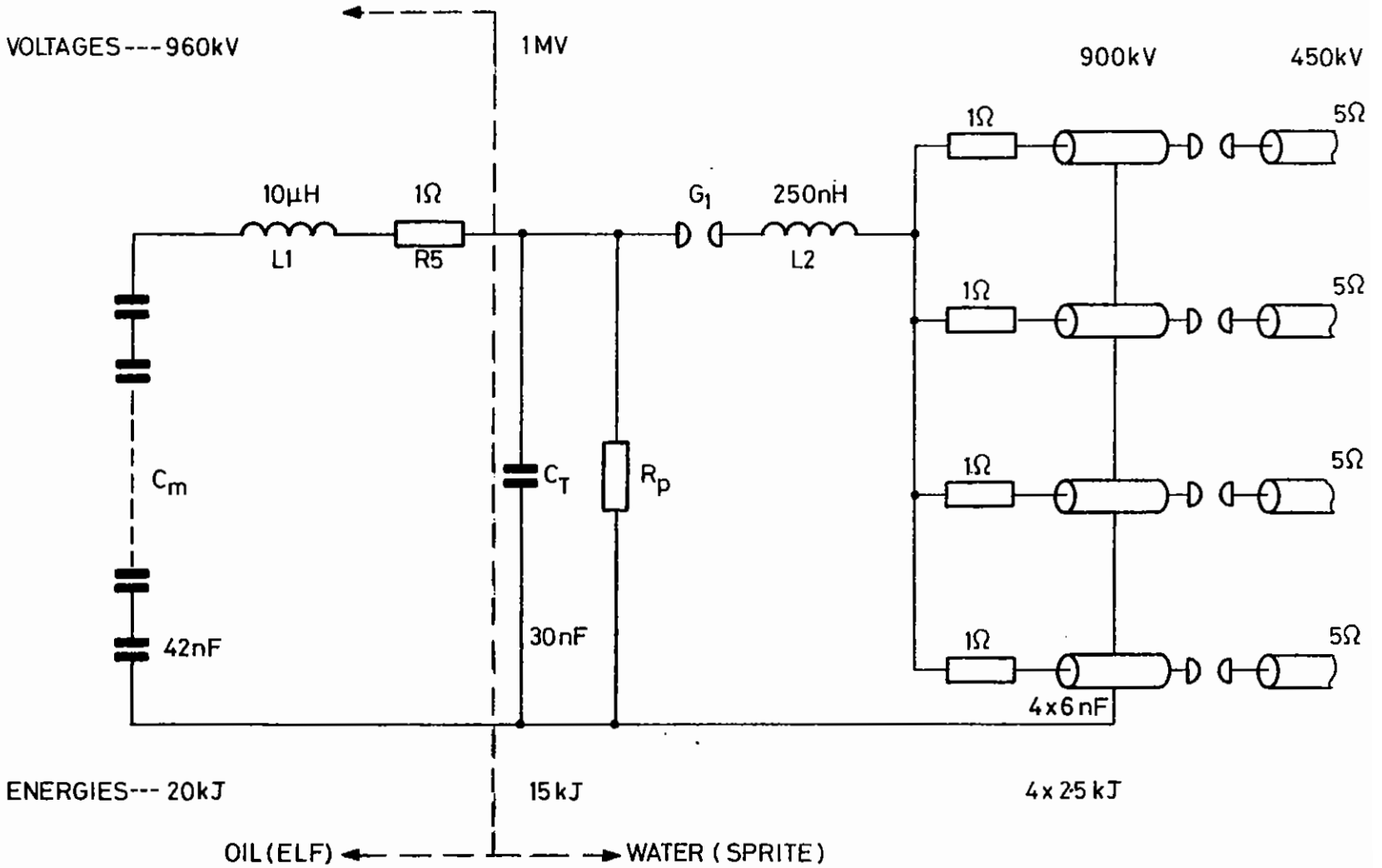

Fig 2.22 SPRITE Equivalent Circuit

Due to breakdown of oil in the main Blumlein spark gap, and to a lesser extent the prepulse gaps, the condition of the insulating oil in the generator has slowly deteriorated due to the build-up of suspended carbon particles. The electrical pumping of these conducting particles onto the main Marx components would eventually cause surface tracking in the Marx bank, and so a thorough cleaning of the machine components is scheduled, along with the installation of a more sophisticated oil filtration and circulation system, which is expected to extend the useful life of the oil indefinitely.

2.5.2 SPRITE Pulse Power

As described in section 2.2.3 the development of a 4 GW KrF laser implies a pulse power requirement of 10 kJ in 60 ns at 450 kV. The machine impedance is thus 1.25 Ω. The overall concept of the machine is shown in Fig.2.21. The laser is pumped from 4 sides by 5 Ω cold cathode diodes. Each diode is fed from two 10 Ω water filled distribution lines which in turn are fed in pairs from four 5 Ω pulse forming lines via SF_6 spark gaps. The pulse forming lines are rapidly charged through a single SF_6 spark gap from a large 30 nF cylindrical water capacitor. The energy stored on this capacitor is provided by the existing ELF Marx generator. In the remainder of this section some of the main design considerations for this system are described. The detail of this design were worked out in collaboration with J C Martin and D W Forster of AWRE, Aldermaston.

2.5.2(a) Water Capacitor

With reference to Fig.2.22 the inductance L_1 between ELF and SPRITE is taken to be 10 H since this is the same as the inductance between the ELF Marx and the existing oil Blumlein. Using this value the dynamic impedance of the transfer capacitor charging circuit is $Z_d = \sqrt{L_1/C_S} = 24\ \Omega$ where C_S is the capacitance of C_M and C_T in series. The peak voltage on C_T is then given by:-

$$V_{peak} = V_{MARX} \frac{C_M}{C_M + C_T} \left\{ e^{-\frac{\pi R_s}{2 Z_d}} + e^{-\frac{\pi Z_d}{2 R_p}} \right\} \qquad (1)$$

where R_S is the series resistance of the Marx (say 1 Ω) and R_P, the parallel resistance across C_T due to water conductance, is ∿ 300 Ω. Using the above formula then V_{peak} = 1.0 MV. The time to peak = $\pi\sqrt{L_1 C_S}$ = 1.3 μs. The energy stored = 15 kJ.

The inter-electrode separation will be determined by the breakdown at the +ve electrode and the breakdown field in MV cm^{-1} is given by:-

$$F = \frac{0.23\ A^{-0.058}}{(t_{eff})^{1/3}} \qquad (2)$$

where A is the electrode area in cm^2 (∿ 4×10^4 cm^2) and t_{eff} is the equivalent duration of the applied voltage (∿ 0.5 μs). Hence F = 0.15 MV cm^{-1}. Thus a plate separation of 10 cm will operate at 66% of self breakdown, an acceptable operating condition. A cylindrical capacitor was chosen with ϕ inner = 100 cm, ϕ outer 120 cm and the length given by:-

$$C = \frac{5.55\ \varepsilon \ell}{\ell n\ b/a}\ nF \qquad (3)$$

from which ℓ = 120 cm.

2.5.2(b) Charging the Lines

The main spark gap G_1 will fire at 1MV charging the four 6 nF pulse forming lines through an inductance calculated to be 300 nH and four 1 Ω $CuSO_4$ protection resistors. Using the same formula as for the charging of the the water transfer capacitor we can calculate the charging rates for the lines from the following parameters:

C_T = 30 nF
C_L = 24 nF
R_S = 0.25 Ω
R_P = 200 Ω
L_2 = 250 nH

Hence:

Z_d	=	4.3 Ω
Time to peak	=	180 ns
Peak volts	=	1.0 MV
Firing Point	=	900 kV
Rate at firing	=	5 kV/ns
Voltage Jitter	∿	2%
Timing Jitter	∿	4 ns

For convenience the lines should be constructed from standard stainless stell tubing. The outer line will be 10 inch stainless steel pipe (266 mm i/d x 3.4 mm wall). The inner will be from 127 mm o/d S/S tube. The ratio of these diameters gives an exact 5.0 Ω impedance. The worst case field is on the +ve (outer electrode) and is ∿ 100 kV cm^{-1}. The breakdown field is calculated to be 230 kV cm^{-1}. Thus as far as bulk breakdown is concerned, the lines are operated in a very safe region. However, the most likely breakdown mode will be across the dielectric/water interface at the diaphragm output gaps. Experiments are underway to ascertain the likely breakdown fields and how they may be elevated by appropriate field shaping.

The output gaps will run in high pressure SF_6 (10 atms) and will initially operate untriggered and an inevitable jitter of 5 ns will have to be tolerated. At a later state it is envisaged that the four gaps will be simultaneously laser triggered when the jitter will be reduced to < 1 ns. The rise-time of the pulse from the gaps comprises of two parts. Firstly, the resistive phase:-

$$\tau_+ = \frac{88}{Z\,/\,E\,/} \left(\frac{\rho_-}{\rho_o}\right)^{1/2} \text{ns} \qquad (4)$$

where (ρ/ρ_o) is the ratio of the gas to air density, Z is the line impedance and E the gap field in units of 10 kV cm^{-1}. The field is estimated to be about 450 kV cm^{-1} and the resistive phase rise-time turns out to be in the order of 1 ns. Secondly the inductive rise-time, $\tau = L/R$ where L

is the inductance of the gap (chiefly spark inductance given by $L = 2\ell(\ell n \frac{4\ell}{a} - 1)$nH where ℓ is the spark length, a is the spark radius ∿ 2 x 10^{-3} cm) and R is the impedance of line and load in series, i.e. 2 x 5 Ω. The gap inductance is estimated to be 40 nH and thus the inductive rise time will be ∿ 4 ns. The overall risetime including jitter will thus be about 10 ns for self breaking gaps and about 5 ns with laser triggering.

2.5.2(c) Distribution Lines

The output from the four 5 Ω pulse forming lines is divided into 8 x 10 Ω distribution lines connecting the 8 vacuum feed throughs into the diode tank. The line outers are most conveniently made from 3 inch dia copper tube (for ease of bending). The peak field inside the lines will be about 500 kV cm^{-1} and the breakdown field for the 60 ns pulse, ∿ 1 MV cm^{-1}. Experiments have already been conducted on the effects on pulse risetime of the discontinuity at the "Tee" junction between the 10 Ω and 5 Ω lines. The results obtained, using standard "Yorkshire" pipe fittings for Tees showed that the degradation of risetime amounted to 2 - 3 ns at worst. The skin effect resistance of the output lines was investigated. It was found that this could be a problem if low conductivity or high μ materials are used. Thus copper is specified for these lines.

2.5.2(d) Diodes

The 15 x 75 cm cathodes (most probably multi-bladed) will be mounted on 25 cm dia x 90 cm long cathode holders with coaxial current returns. In this way the inductance feeding current along the length and around the perimeter of the holder can be made quite small (∿ 5 nH and 15 nH per feed respectively). On the other hand, the inductance of the vacuum feed through stalk is quite large (∿ 35 nH). Thus two feedthroughs per cathode are required. The overall inductance per diode is estimated to be 35 nH and thus the L/R risetime for a matched load will be 3.5 ns.

In order to achieve high overall efficiency for Sprite a good diode design is essential. In order to investigate as many critical design areas as possible experimentally a mock-up Sprite diode has been built. This is

the same diameter but half the length of the final diode and is fed from a single stalk using the existing ELF diode chamber. Experiments using this test diode are underway and it is hoped to investigate such effects as cathode holder emission, beam pinching, cathode switch-on time, hibachi and foil transmission and e-beam deposition distribution at voltages and currents applicable to the final Sprite diodes.

M.J. Shaw, F Gilbert.

CHAPTER 2 REFERENCES

2.01 J J Ewing, R A Haas, J C Swingle, E V George and W F Krupke, IEEE J. Quantum Electron. QE-15, 368 (1979).

2.02 R P Sandoval, J. Appl. Phys. 49, 5745 (1978)

2.03 K A Brueckner and R S Janda, Nucl. Fusion 17, 305 (1977).

2.04 M Rokni, J A Mangano, J H Jacob and J C Hsia, IEEE J. Quantum Electron. QE-14, 464 (1978).

2.05 G C Tisone, E L Patterson and J K Rice, Appl. Phys. Lett. 35, 437 (1979).

2.06 E J Henley, Nucleonics 12, 62 (1954).

2.07 M J Berger and S M Seltzer, "Tables of Energy Losses and Ranges of Electrons and Positions", National Aeronautics and Space Administration, Washington D.C., report No. NASA SP-3012 (1964).

2.08 C E Turner, P W Hoff and J Taska, Proc. Int. Topical Conf. of Electron Beam Research and Technology, Albuquerque (1975). Sandia Laboratories Report No. SAND76-5122, p.224.

2.09 The calorimeter was calibrated by the National Physical Laboratory, Teddington, Middlesex, England.

2.10 G Black, R L Sharpless and T G Slanger, J. Chem. Phys. 64, 3985 (1976).

2.11 H T Powell and J J Ewing, Appl. Phys. Lett. 33, 165 (1978).

2.12 H T Powell, D Prosnitz and B R Schleicher, Appl. Phys. Lett. 34, 571 (1979).

2.13 C B Edwards, M H R Hutchinson, D J Bradley and M D Hutchinson, Rev. Sci. Instrum. 50, 1201 (1979).

2.14 J K Rice and J R Woodworth, "Laser Development for Laser Fusion Applications", Research Progress Report, Sandia Labs., Dec. 1978.

2.15 E J McGuire, in reference 2.14.

2.16 K T V Grattan, M H R Hutchinson and E S Theocharous, submitted to J. Phys. B. (1980).

2.17 J R Murray and C K Rhodes, J. Appl. Phys. 47, 5041 (1976).

2.18 M C Gower, A J Kearsley and C E Webb, J. Appl. Phys. 50, 5988 (1979).

2.19 L M Frantz and J S Nodvik, J. Appl. Phys. 34, 2346 (1963).

2.20 R F Barrow, G G Chandler and C B Meyer, Phil. Trans. R. Soc. A260 395 (1966).

2.21 R F Barrow, W G Burton and J H Callomon, Trans. Far. Soc., 66, 2685 (1970).

2.22 J J Ewing and C A Brau, Appl. Phys. Lett. 27, 557 (1975).

2.23 R S Bradford, E R Ault and M L Bhaumik, Appl. Phys. Lett. 27, 546 (1975).

2.24 A K Hays, J M Hoffman and G C Tisone, Chem. Phys. Lett. 39, 353 (1976).

2.25 P Venkateswarlu and D R Rao, Pro. Incian Acad. Sci. 64A, 9 (1966)

2.26 A B Callear and M P Metcalf, Chem. Phys. Lett. 43, 197 (1976).

2.27 Y Y Stoilov, Sov. J. Quantum Electron. 8, 223 (1978).

2.28 L D Mikheev, A P Shirokikh, A B startsev and V S Zuev, Optics. Commun. 26, 237 (1978).

2.29 V S Zuev, L D Mikheev, A V Startsev and A P Shirokikh, Sov. J. Quantum Electron. 9, 1195 (1979).

2.30 J Tellinghuisen, Chem. Phys. Lett. 29 359 (1974).

2.31 R S Mulliken, J. Chem. Phys. 55, 288 (1971).

2.32 A B Callear, P Erman and J Kurepa, Chem. Phys. Lett. 44, 599 (1976).

2.33 J Tellinghuisen, Chem. Phys. Lett. 49, 485 (1977).

2.34 M C Sauer, W A Mulac, R Cooper and F Grieser, J. Chem. Phys. 64, 4587 (1976).

2.35 C B Edwards, F O'Neill and M J Shaw, Appl. Phys. Lett. 36, 617 (1980).

2.36 The input energy was measured with a Gen Tec ED1000 (100 mm dia) joulemeter and the output with an ED500 (50 mm square). The calibrations of the joulemeters were checked one to the other and independently against a third, volume absorbing disc calorimeter (Sciented 38-0403).

2.37 R J Donovan, C Fotakis, M Martin and A G A Rae, "Proceedings of the Fourth National Quantum Electronics Conference" Edinburgh 1979; to be published by J Wiley & Sons Ltd.

2.38 R W Falcone, Appl. Phys. Letts. 34, 150 (1979).

2.39 S E Harris and J C White, IEEE J. Quantum Electron. QE-13, 972 (1977).

2.40 L I Gudzenko and S I Yakovlenko, Phys. Letts. 46A, 475 (1974).

2.41 J C White, G A Zdasink, J F Young and S E Harris, Opt. Letts 4, 137 (1979).

2.42 M W McGeoch, J. Chem. Phys. 72, 140 (1980).

2.43 M W McGeoch, to be published.

2.44 J B West, H Komine, E A Stapparts, J. Appl. Phys. 50, 7929 (1979).

2.45 M W McGeoch and G R Fournier, J. Appl. Phys. 49, 2659 (1978).

2.46 J G Eden, Opt. Commun. 25, 201 (1978).

2.47 A Mandl, D E Klimek, J H Jacob, B N Srivastava and M A Kovacs, to be published.

CHAPTER 3 LASER PLASMA INTERACTION

INDEX

CHAPTER EDITOR: D J Nicholas

CHAPTER 3 LASER PLASMA INTERACTION

3.1 Introduction

The bulk of the work on laser plasma interaction has been devoted to the study of harmonic emission from plane targets using long (∿ 1 ns) pulses, at both 1.05 μm and 0.52 μm wavelengths. However, towards the end of this period, density profile studies were carried out using ablatively driven targets: data from these experiments are still in the analysis stage.

Attempts to test the hypothesis that the second harmonic emission is generated by more than one process have been made by comparing the back-scattered and specular reflected radiation at $2\omega_o$, section 3.2.1.

Recent experiments with long pulses have yielded time resolved $3\omega_o/2$ spectra, section 3.2.2. The experiments fall into two catagories: for high irradiances $\sim 10^{15}$ W cm^{-2} the $3\omega_o/2$ spectra exhibits the doubled peak structure observed in previous short pulse experiments. At laser intensities $\sim 10^{14}$ W cm^{-2} the spectra is considerably modified and may be accounted for by the interaction of a photon with a plasmon generated by the Raman scattering instability.

Brillouin backscatter at 0.52 μm is considerably reduced from that at 1.05 μm as the calorimetry experiments, section 3.2.3 show. Time resolved spectra carried out at normal incidence and at 45° exhibited spectral shifts which have been noted previously at 1.06 μm by other workers. Comparison of data at these two angles enables an estimate of T_e to be made.

A study of $\omega_o/2$ backscattered radiation from near $n_c/4$, section 3.2.4, due to stimulated Raman scattering produced conversion factors $\sim 10^{-7}$ in good agreement with previous numerical simulations.

Section 3.3.2 compares some experimental density profile with those obtained by numerical simulations using MEDUSA in which the effects of the ponderomotive force had been included and good agreement is obtained with

experiment. This work is further discussed in section 7.2.4.

D.J. Nicholas

3.2 Harmonic Emission

3.2.1 The $2\omega_o$ Emission

3.2.1(a) Introduction

To test the hypothesis that $2\omega_o$ is generated by more than one process, scattered radiation has been analysed in the backwards and specular directions. The target has been tilted at various angles from 0 to 45° to the optical axis so that the scattered radiation may be collected, as shown in Fig.3.01, both through the laser focussing lens and by a paraboloid reflector. Laser pulses of 1.7 nanosecond duration, 1.0525 μm wavelength and energies up to 100 Joules were focused by an f/5 lens to a spot of 100 μm diameter. The targets consisted of 1 mm diameter steel pins, with one end ground and polished at the requisite angle. Gold or aluminium were evaporated onto this surface.

3.2.1(b) The Spectra

An example of the spectra recorded in the two directions is shown in Fig. 3.02. The specular spectrum consists of a line which is slightly displaced towards longer wavelengths from the precise value (526.25 nm) of $2\omega_b$ and is asymmetrically broadened. The backward spectrum is rich in spectral structure. A strong red shifted satellite occurs in nearly two thirds of the shots recorded, with fine structure in about half the shots; as many as twelve components being seen. The paraboloid collected light over a half angle of 62°, whereas that of the focusing lens was 5.7°. The bright lines and shadows which occur at right angles to the length of the slit are caused by imperfections in the paraboloid.

3.2.1(c) The Red Shift

The displacement of the peak of the $2\omega_o$ line is plotted in Fig.3.03 and is seen to be almost constant over the range of irradiance 5.10^{14} to 5.10^{15} W cm^{-2}. No appreciable change in this displacement was found if gold coated targets were replaced by aluminium coated ones, a result that suggests that burn through to the iron substrate may occur at an early stage. The smaller shift in the backscattered spectrum is equivalent to a Doppler blue shift of about 1 A, resulting from the critically dense surface expanding at 10^6 cm sec^{-1}.

Krokhin et al (3.01) quote a theory by Silin which attributes the displacement of the $2\omega_o$ spectrum to the coalescence in the plasma of a longitudinal wave with a light wave. From the Silin (3.02) expression for the red shift, a temperature of 10 keV is estimated which compares well with the rsults of Gitomer and Henderson (3.03) for an irradiance of 10^{15} W cm^{-2}.

3.2.1(d) The Fine Structure

The average spacing of the fine structure in Fig.3.02 is 0.9 A. A possible explanation of this close spacing is that there are discrete regions of the plasma where the frequency and wave number matching conditions for a parametric process are satisfied. The spectral structure is about ten times finer than that predicted by Cairns (3.04).

3.2.1(e) Angular Dependence of the Red Shift

In Fig.3.04 the displacement of $2\omega_o$ towards the red is plotted against the mean angle of incidence of the laser radiation on the target. It is seen that the backscattered radiation is almost unaffected by the target angle, whereas the specular component suffers a displacement which decreases with angle. The latter displacement was measured at a position in the spectrum which corresponds to twice the angle of incidence and is corrected for the curvature which occurs in the spectrometer. Each line is a 'least squares' fit to the experimental results. The varying

displacement with angle is attributed to the second term in the Silin expression which depends on the penetration of the beam into the plasma.

A different type of angular dependence is obtained for one specular spectrum. The red shift was measured as a function of angular position. Then from the wavelength shift and the angular displacement it is possible to determine the frequency shift $\Delta\omega$

$$\Delta\omega = \frac{2\omega_o}{\lambda_o}\,\Delta\lambda$$

and a wavenumber $k = k_o \cos\theta_o$. These values are plotted as a dispersion relation in Fig.3.05. The diffuse nature of this radiation indicates the existence of a process which is not accounted for by the classical theory of resonance.

3.2.1(f) Conclusions

Both backscattered and specularly reflected spectra display a red shift which may be attributed to the same interaction with an ion acoustic wave, the slight difference in their wavelengths being due to the former suffering a Doppler shift. The existence of radiation with a frequency $2\omega_o$ and a displacement which is approximately equal to kc_s supports the view that the harmonic is produced by coalescence of a photon $T(\omega_o)$ and a plasmon $L(\omega_L)$

$$T(2\omega_o) \rightarrow T(\omega_o) + L(\omega_L)$$

The plasmon could be produced by an ion decay process

$$T(\omega_o) \rightarrow L(\omega_{ia}) + L(\omega_L)$$

$$\omega_{ia} = kc_s$$

It has also been confirmed that other radiative processes occur, one generating fine structure on the harmonic and the other causing diffuse scattering. These process have still to be explained.

J. Elazar, N. Sayed and E.R. Wooding

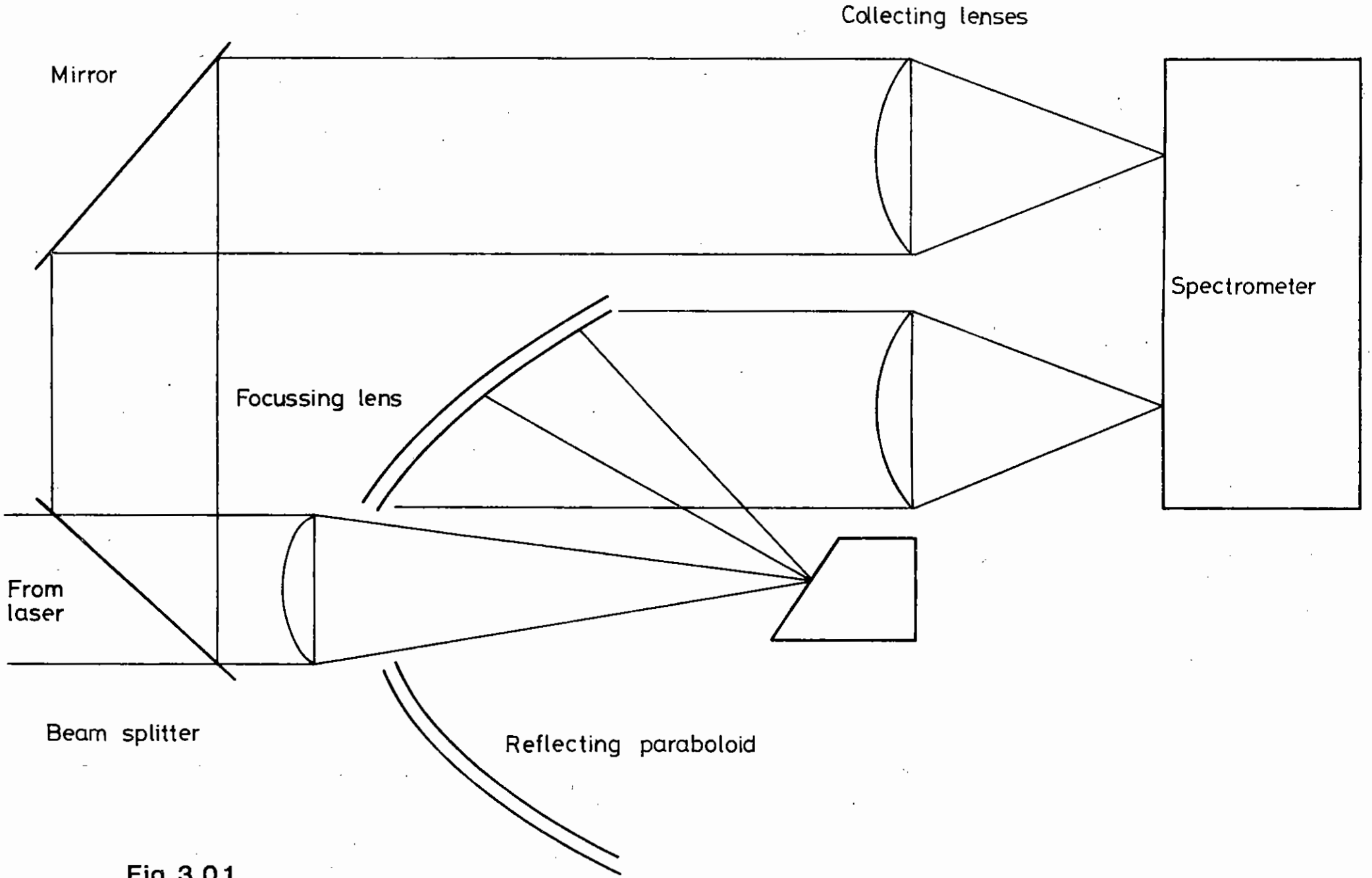
Collecting lenses
Mirror
Spectrometer
Focussing lens
From
laser
Beam splitter
Reflecting paraboloid

Fig 3.01

3.2.2 Time Resolved $3\omega_o/2$ Harmonic Emission

At the quarter critical density surface two processes - stimulated Raman scattering (3.05) and the two-plasmon decay (3.06) - produce $\omega_o/2$ plasmons, and so both can give rise to $3\omega_o/2$ emission. Two generation mechanisms are thought to exist: interaction of an incident photon with a plasmon, or three plasmons coalescing to give $3\omega_o/2$ emission:

$$\omega_b + \omega_o/2 \rightarrow 3\omega_o/2$$

$$\omega_b/2 + \omega_o/2 + \omega_o/2 \rightarrow 3\omega_o/2$$

Earlier work performed by the group (3.07, 3.08) on time resolved $3\omega_o/2$ emission has concentrated on short ($\sim$ 100 ps) high irradiance laser pulses. The results obtained show that the spectra consist of two peaks symmetrically shifted to the red and blue of the nominal $3\omega_o/2$ wavelength. These peaks occur simultaneously and their separation varies in time. The emission was also observed to come in bursts.

The theories put forward to explain this phenomena, by Avrov (3.09) and by Barr (3.10) consider that the main mechanism for producing $\omega_o/2$ plasmons is that of two-plasmon decay of the incident photon since the Raman scattering instability generally has a much higher threshold (3.11). However, for long scale lengths the threshold for Raman scattering is lowered and may fall below that of the two plasmon decay (3.12).

In recent experiments on time resolved $3\omega_o/2$ emission, the emission from plane targets with long pulses ($\sim$ 1.8 ns) has been observed. Fig.3.06 shows the experimental layout. The laser provided energies of $\gtrsim$ 100 J in 1.8 ns, onto plane targets of tungsten, iron and aluminium on glass. The irradiance was varied from $\sim 10^{13}$ W cm^{-2} to $\sim 5 \times 10^{15}$ W cm^{-2} by defocusing the beam on target. The backscattered emisssion was collected by the f/1 aspheric doublet lens optically coupled to the entrance slit of the 0.5 m, 600 lines mm^{-1} spectrograph, which was operated in second order. The output from the spectrograph was then imaged onto the Imacon streak

camera, which has an S - 1 photocathode and was operated at a streak speed of 1.75 ns cm^{-1}.

Photographic recordings of the streak data were made on Kodak 2485 film. Spectral calibrations were obtained by separate exposures of the He-Ne laser line (λ = 6328 A). The streak velocity and sweep linearity were calibrated in an earlier experiment (3.07). The present experimental arrangement gave a spectral resolution of $\sim$ 10 A determined by the 400 μm slit width of the spectograph and a temporal resolution of $\sim$ 175 ps determined by the streak camera slit width of 100 μm.

The results appeared to fall into two main categories determined by the irradiance on target. Fig.3.07(a) shows a typical example of the data obtained for high irradiances ($\sim 10^{15}$W cm^{-2}) when a small focal spot size ($\sim$ 30 μm) was used. The $3\omega_o/2$ harmonic spectrum is broad ($\sim$ 250 A FWHM) and exhibits a double peak structure with a separation of $\lesssim$ 70 A. Periodic modulations of the intensity are observed in time. These data are very similar to the results obtained for short pulses (3.08) where the separation of the peaks was interpreted by the Barr theory to be proportional to the electron temperature T_e at the quarter critical density surface. The pulsed nature of the $3\omega_o/2$ emission was attributed to density fluctuations originating from the unstable plasma flow across a steepened density profile (3.13). The timescale for these bursts is then given by $\tau \approx L/v_{ia}$, where L is the density scale length and v_{ia} the ion sound speed. If we assume L $\sim$ 60 μm and $v_{ia} \sim 3 \times 10^7$ cm s^{-1}, then $\tau \sim$ 200 ps, which agrees approximately with the observations.

Fig.3.07(b) shows an example of the data obtained for irradiances below 5×10^{14} W cm^{-2} where the focal spot size $\gtrsim$ 125 μm. The spectra are much narrower $\lesssim$ 100 A, single-peaked and all show a blue shift. The $3\omega_o/2$ harmonic emission in this case is thought to be due to the interaction of a photon with a plasmon generated by the stimulated Raman scattering instability. The Raman scattered photon is red shifted (3.12), hence the plasmon will be blue shifted. If this plasmon now recombines with a photon at ω_o, then the resulting $3\omega_o/2$ photon will be blue shifted. Evidence for the stimulated Raman scattering instability is provided by

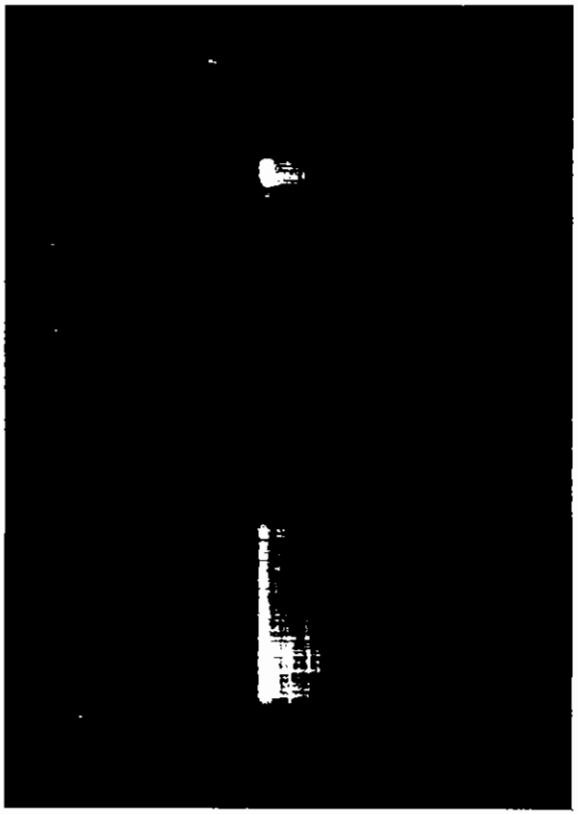

Fig 3.02

simultaneous observations of $\omega_o/2$ emission during this experiment by Elazar et al (section 3.2.4 of this report) for irradiances $\gtrsim$ 5 x 10 W cm^{-2}.

Hence, these experimental observations indicate that the mechanisms for generating $3\omega_o/2$ harmonic emission are both varied and complex, resulting in very different types of spectra depending on whether the two plasmon decay or the stimulated Raman scattering process is dominant. Further analysis of the data is still being carried out.

E. McGoldrick, S.M.L. Sim.

3.2.3 Brillouin Scattering at 0.52 μm

The presence of the Stimulated Brillouin Instability in laser produced plasmas is potentially very detrimental to the prospects of laser fusion. Many workers have made measurements of Stimulated Brillouin Scattering (SBS) at 10.6 μm and 1.06 μm (3.14). However, due to the favourable wavelength scaling of such parameters as ablation pressure and preheat much interest is currently centred on the use of a short wavelength laser driver.

The experimental arrangement to study SBS at a laser wavelength of 0.52 μm is shown in Fig.3.08. The main laser, capable of producing up to 150 J in 1.3 ns at λ = 1.05 μm, was frequency doubled using a full beam diameter KDP crystal. The damage threshold of this component limited the maximum laser energy to $\lesssim$ 70 J. The typical conversion efficiency at these intensities was 40% giving a maximum energy of 25 J at λ = 0.52 μm. The laser beam was focused onto plane solid targets by an aspheric doublet f/1 lens. The focal spot size was measured to be about 30 μm. The backscattered light was diverted into a 0.5 m Spex grating spectrograph, together with a fraction of the incident pulse. The output of the spectrograph was then optically coupled to a Hadland Imacon streak camera with an S20 streak tube. The wavelength and time resolutions were approximately 1 A and 300 ps respectively. The incident and reflected energies at 0.52 μm were monitored by calorimeters.

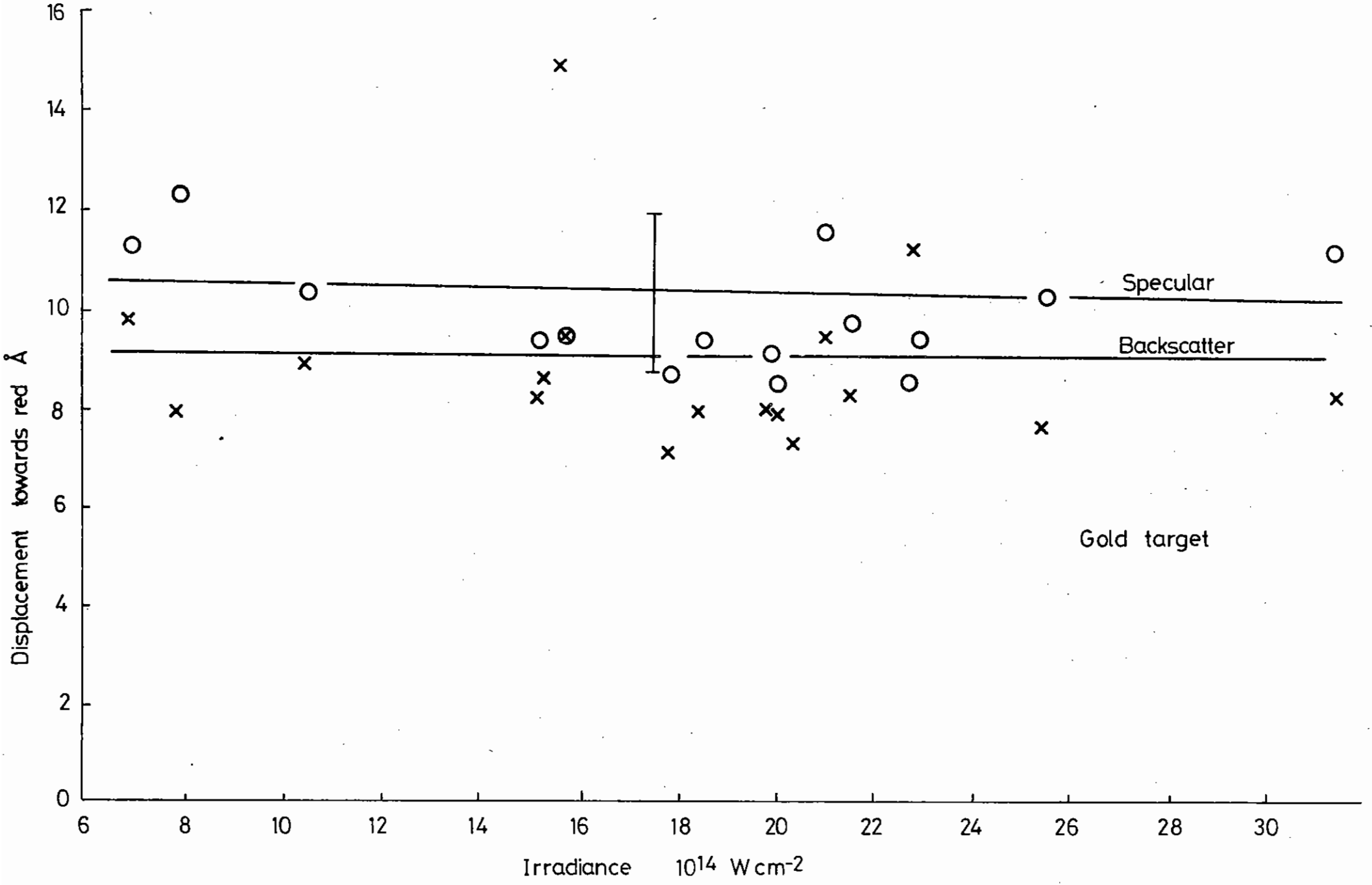

Fig.3.03

Displacement of $2\omega_o$ with increasing irradiance • specular component x backscatter gold targets

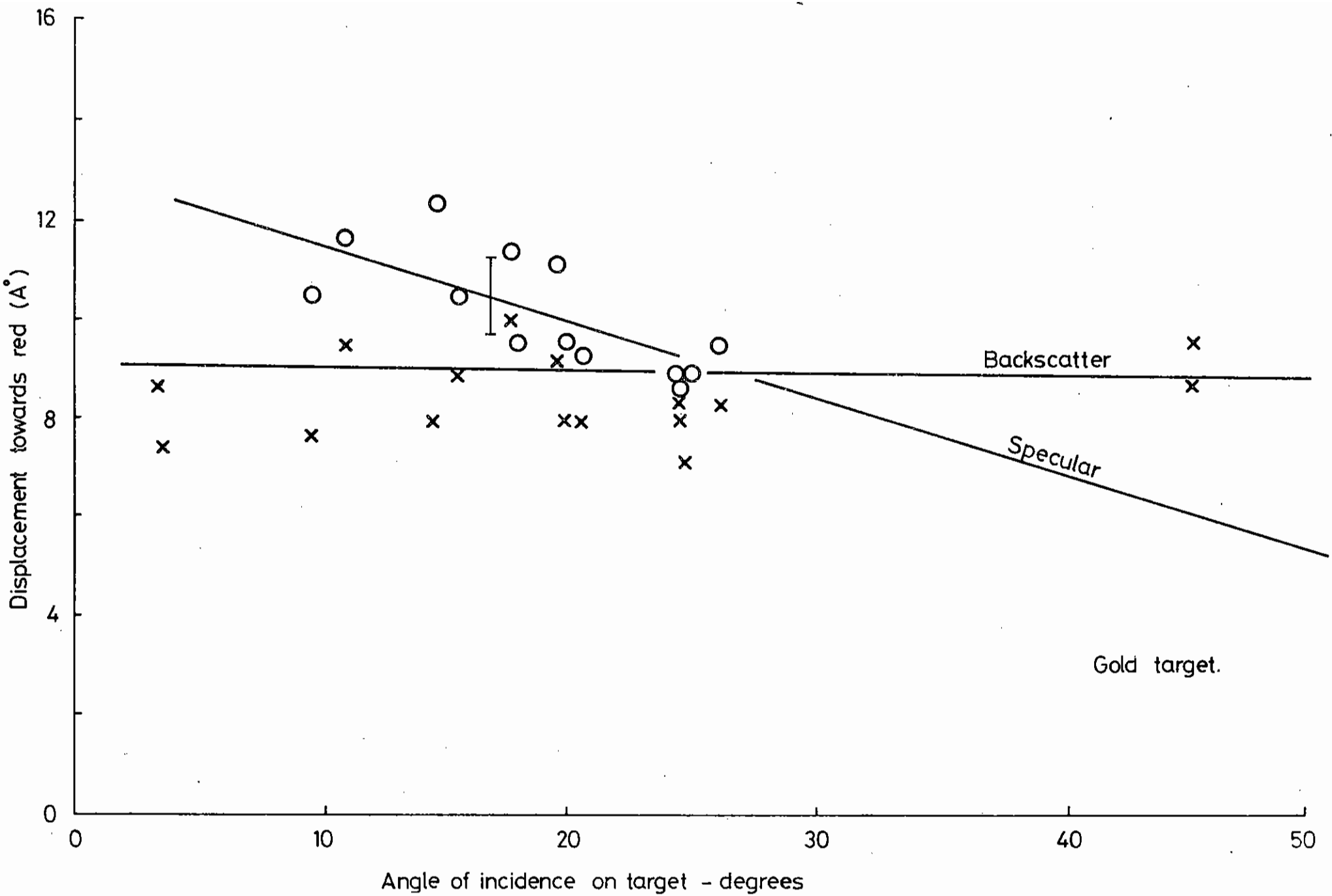

Fig.3.04

Variation of displacement of $2\omega_o$ with angle of incidence on target · specular component x backscatter

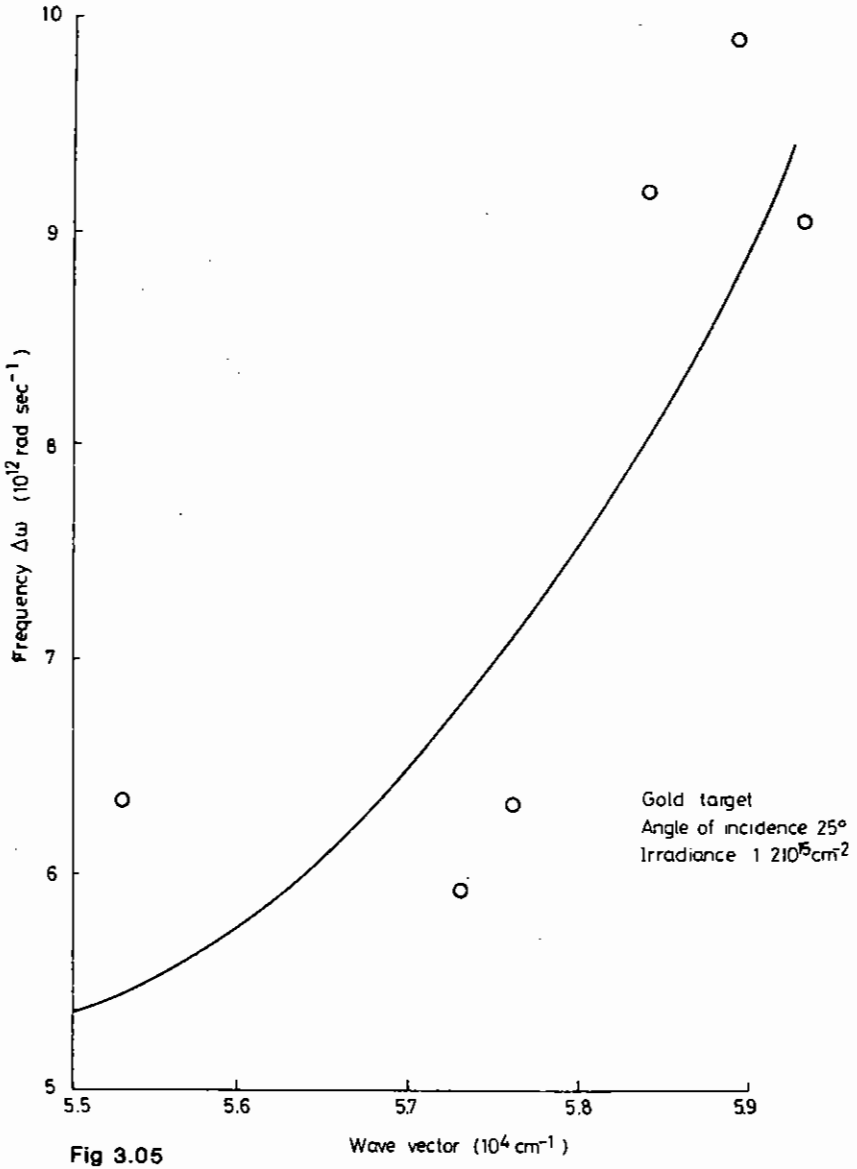

Fig 3.05

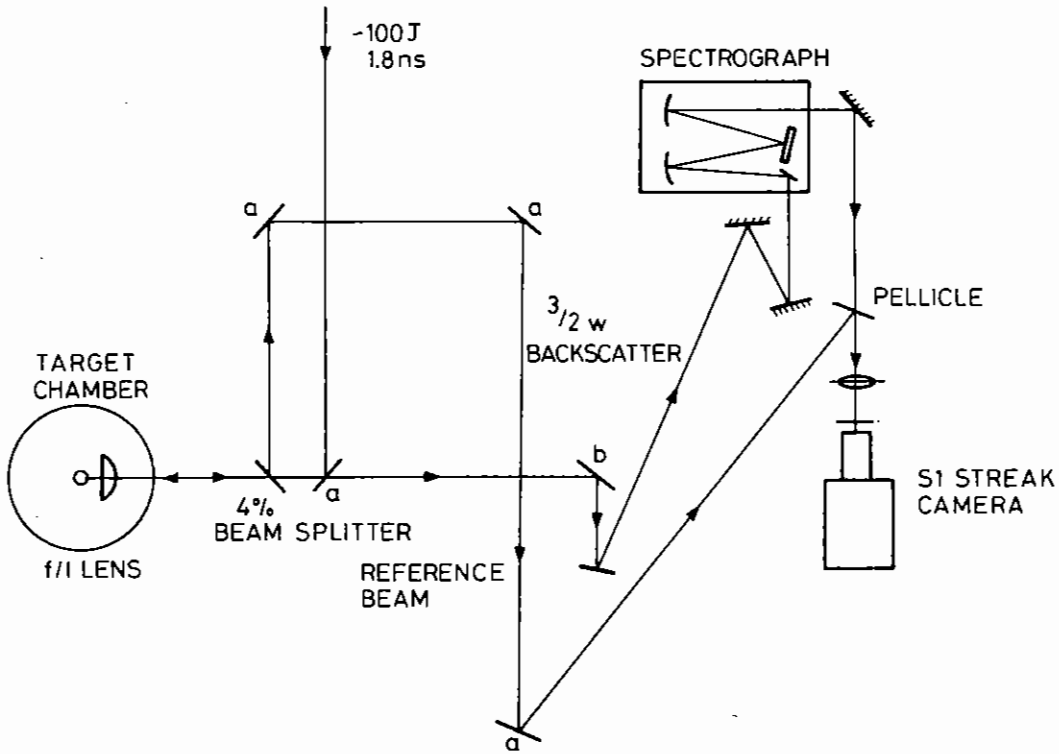

Fig.3.06

Experimental layout for time resolved spectroscopy of 3/2 ω_o emission

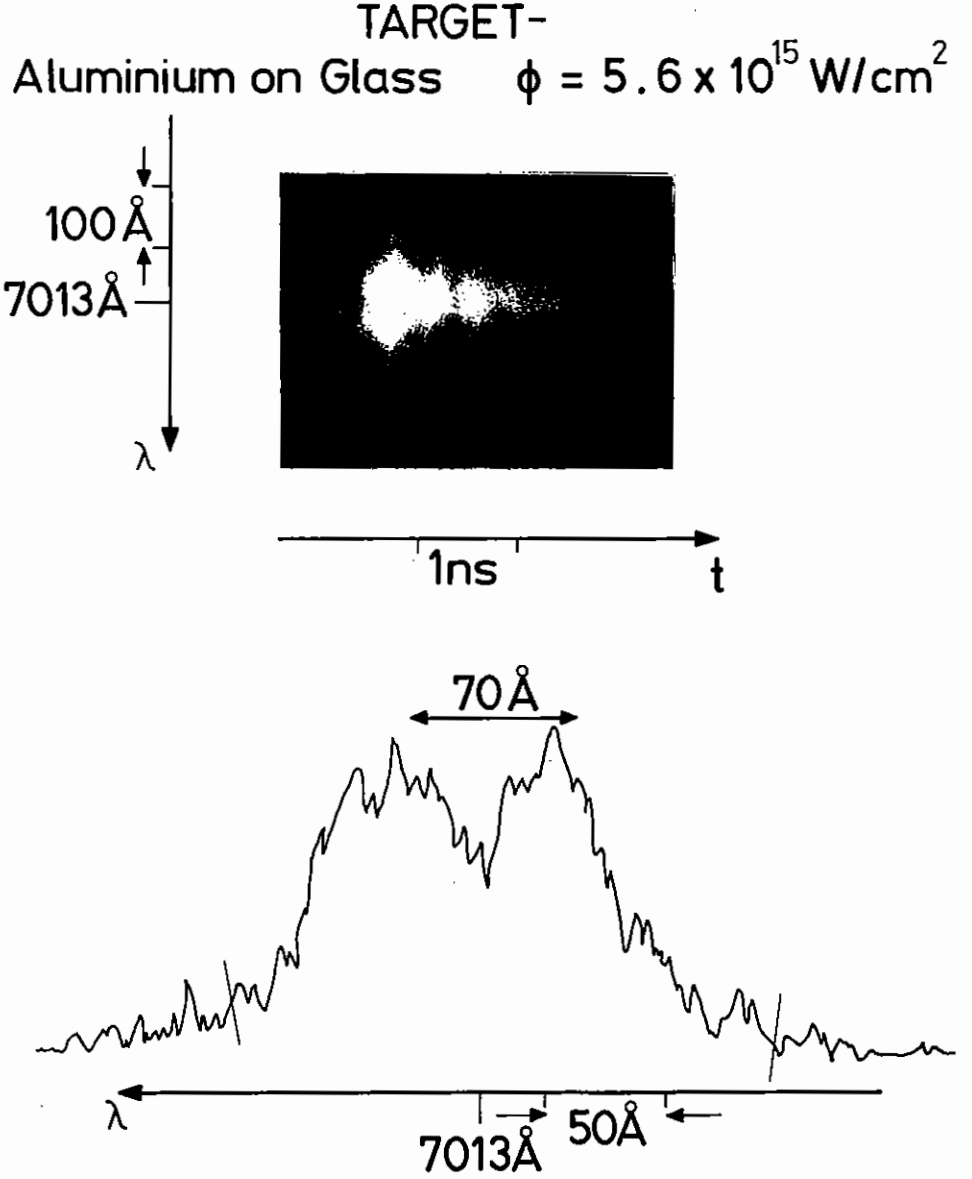

Fig.3.07

(a) Time resolved spectrum of $3/2\omega_o$ emission for irradiances $\sim 10^{15}$ W cm^{-2}

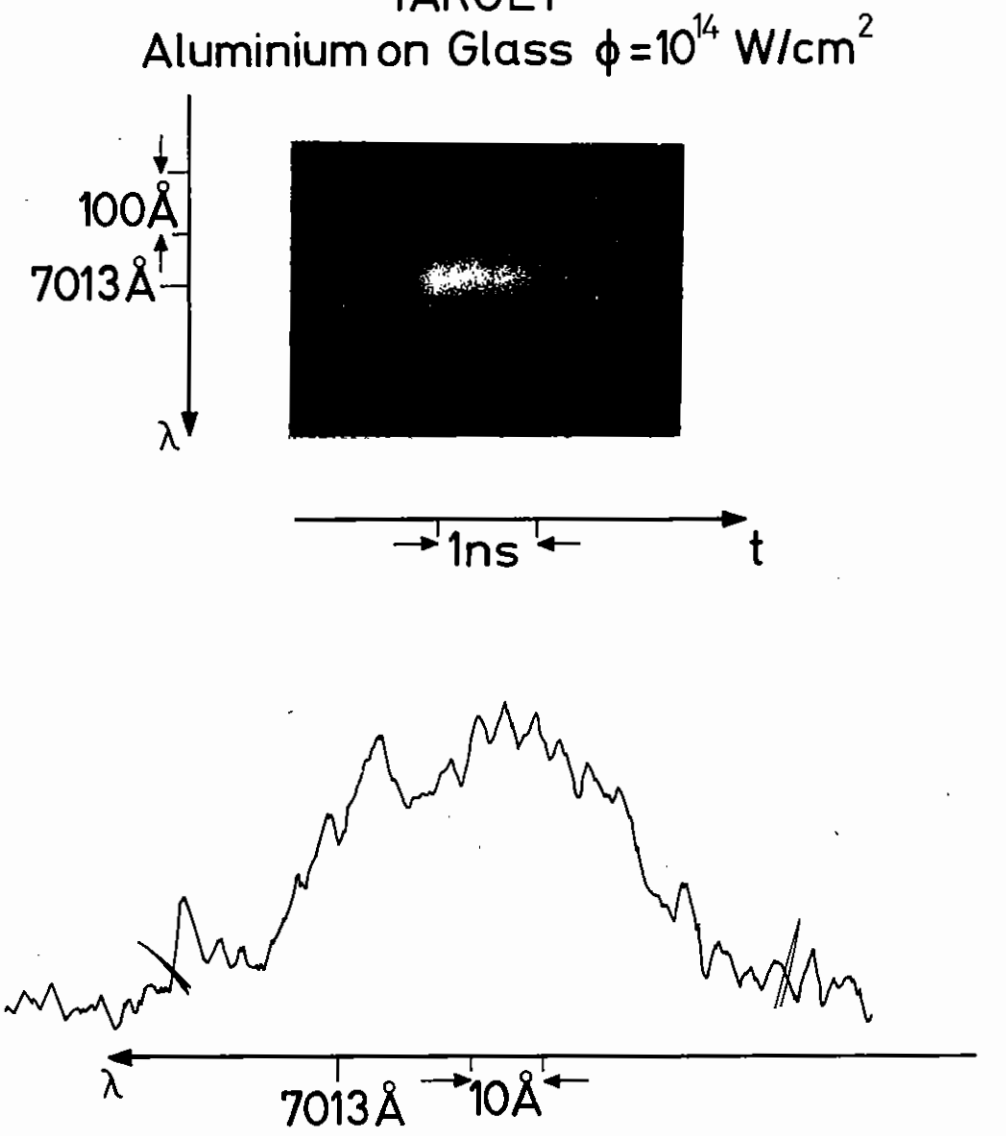

Fig.3.07

(b) Time resolved spectrum of $3/2\omega_o$ emission for lower irradiances $\sim 5 \times 10^{14}$ W cm^{-2}

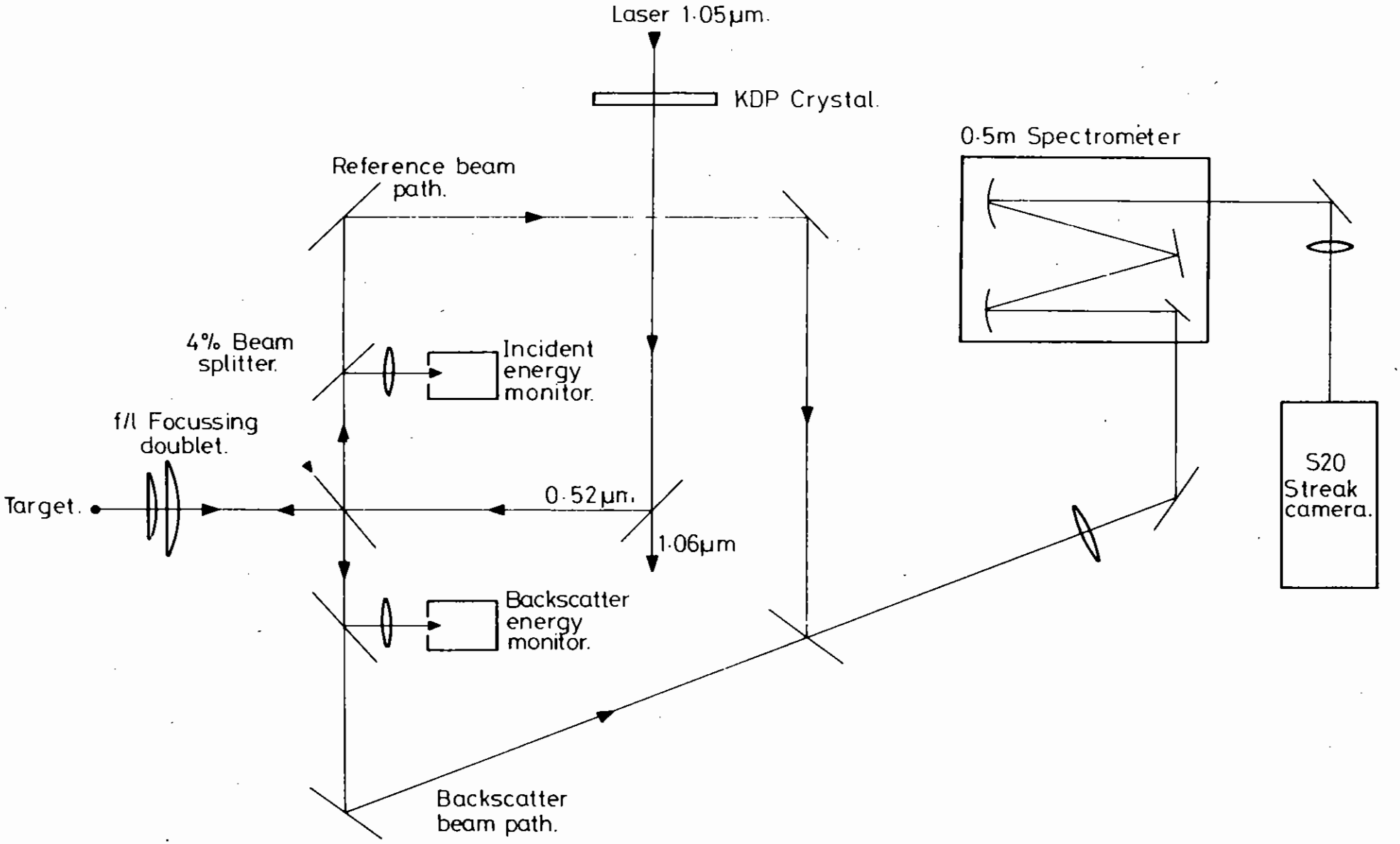

Fig 3.08 EXPERIMENTAL ARRANGEMENT FOR TIME RESOLVED SPECTROSCOPY AT 0·52μm.

Calorimetry

The results of the calorimetry are shown in Fig.3.09. The levels of backscatter observed from targets irradiated at normal incidence were as follows:

i) aluminium, the percentage of the incident energy backscattered into the main focusing lens varied between 1% and 7%, the mode value being about 2%;

ii) tungsten, the percentage backscatter varied in this case between 4% and 8%;

iii) plastic, only one result was obtained in this configuration, the percentage backscatter being 4%.

For targets at 45° to the laser axis, very little variation in the amount of backscatter was observed between the different target materials. The percentage backscatter was fairly constant at about 1%, slowly increasing with increasing irradiance.

The difference between the results at normal incidence and at 45° is probably due to a sizeable proportion of the backscatter at normal incidence being specular. The backscattered fraction at 45° is small compared with similar irradiances and pulse lengths at $\lambda = 1.06\mu m$ (3.15) suggesting that SBS has been substantially reduced by the change to shorter wavelengths.

Time resolved spectra

Some examples of time resolved backscatter spectra are shown in Fig.3.10 - 3.13. Comparing Fig.3.10 and Fig.3.11 (tungsten targets at normal incidence and 45°) it is noticeable that at normal incidence there is essentially no wavelength shift of the backscatter relative to the incident pulse while at 45° the backscatter is shifted to the red by about 5 A. Similar results were noted by Rosen et al (3.16) in the irradiation of gold disks at $\lambda = 1.06\mu m$ and the interpretation is due to the varying degrees of cancellation of the Doppler (blue) shift and Brillouin (red) shift as the angle of incidence is varied.

At normal incidence the wavelength shift $\Delta\lambda$ is

$$\frac{\Delta\lambda}{\lambda} = \frac{2c_s}{c}(1 - M)$$

where c_s is the sound speed in the plasma, $c_s = \left(\frac{ZkT_e}{Mm_p}\right)^{\frac{1}{2}}$, c is the speed of light and M is the Mach number of the plasma expansion flow $M = v_a/c_s$. At 45° the effect of the expansion is reduced and

$$\frac{\Delta\lambda}{\lambda} = \frac{2c_s}{c}\left(1 - \frac{M}{\sqrt{2}}\right)$$

For the particular values of $\Delta\lambda$ measured here we have: $M \simeq 1$

$$\sqrt{2}\, c_s/c \simeq 5/5200$$

$$v_a \simeq c_s \simeq 2 \times 10^7 \text{ cm s}^{-1}$$

$$\frac{ZT_e}{M} = 420 \text{ eV}$$

In the high Z plasma the tungsten will be far from fully ionised and we estimate $\langle Z \rangle \sim 30$ giving

$$T_e \simeq 2.5 \text{ keV}$$

Comparing Fig.3.11 and Fig.3.12 (tungsten and aluminium targets at 45°) we note that the backscatter from Al begins early-on in the incident pulse and may be cutting off towards the end of the incident pulse whereas the backscatter from tungsten is slower to begin but persists until later in the incident pulse.

The delay in the onset of backscatter from the high Z material is due to the reduced sound speed and expansion velocity of the cooler, partially ionised material, and the longer time needed to establish a region of underdense plasma. The apparent cut off of the backscatter from the Al

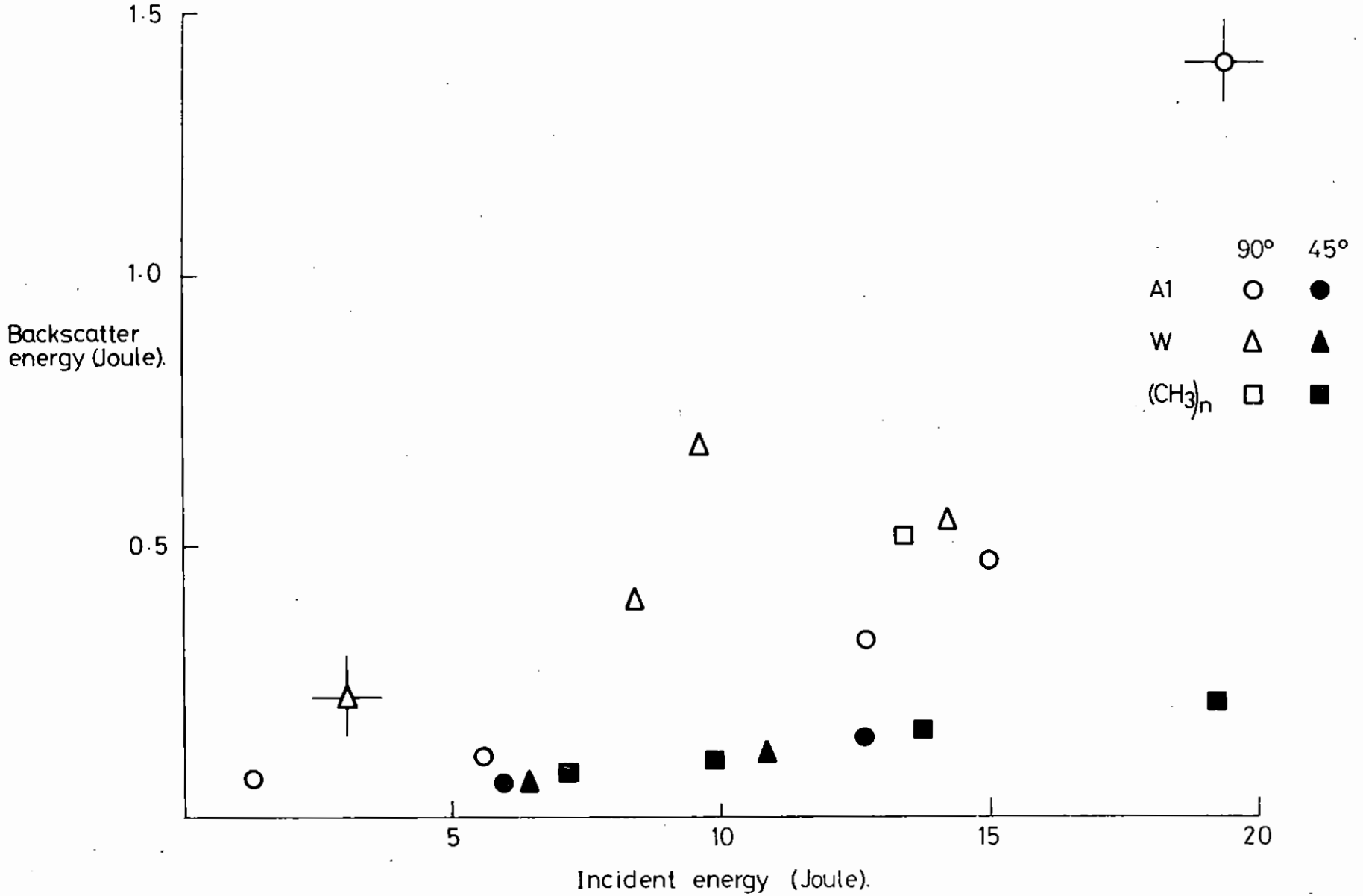

Fig 3.09 BACKSCATTER ENERGY AS A FUNCTION OF INCIDENT LASER ENERGY.

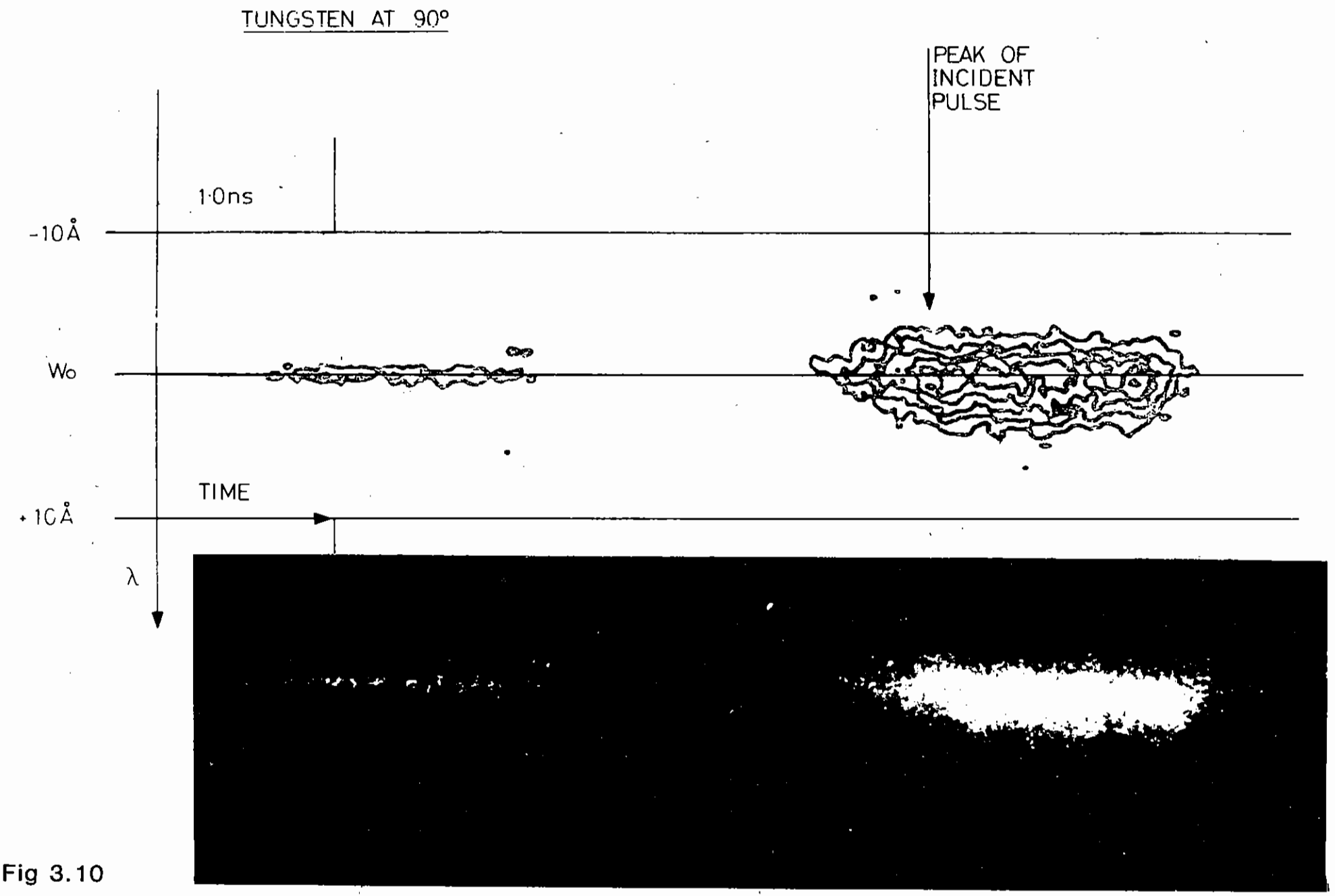

Fig 3.10

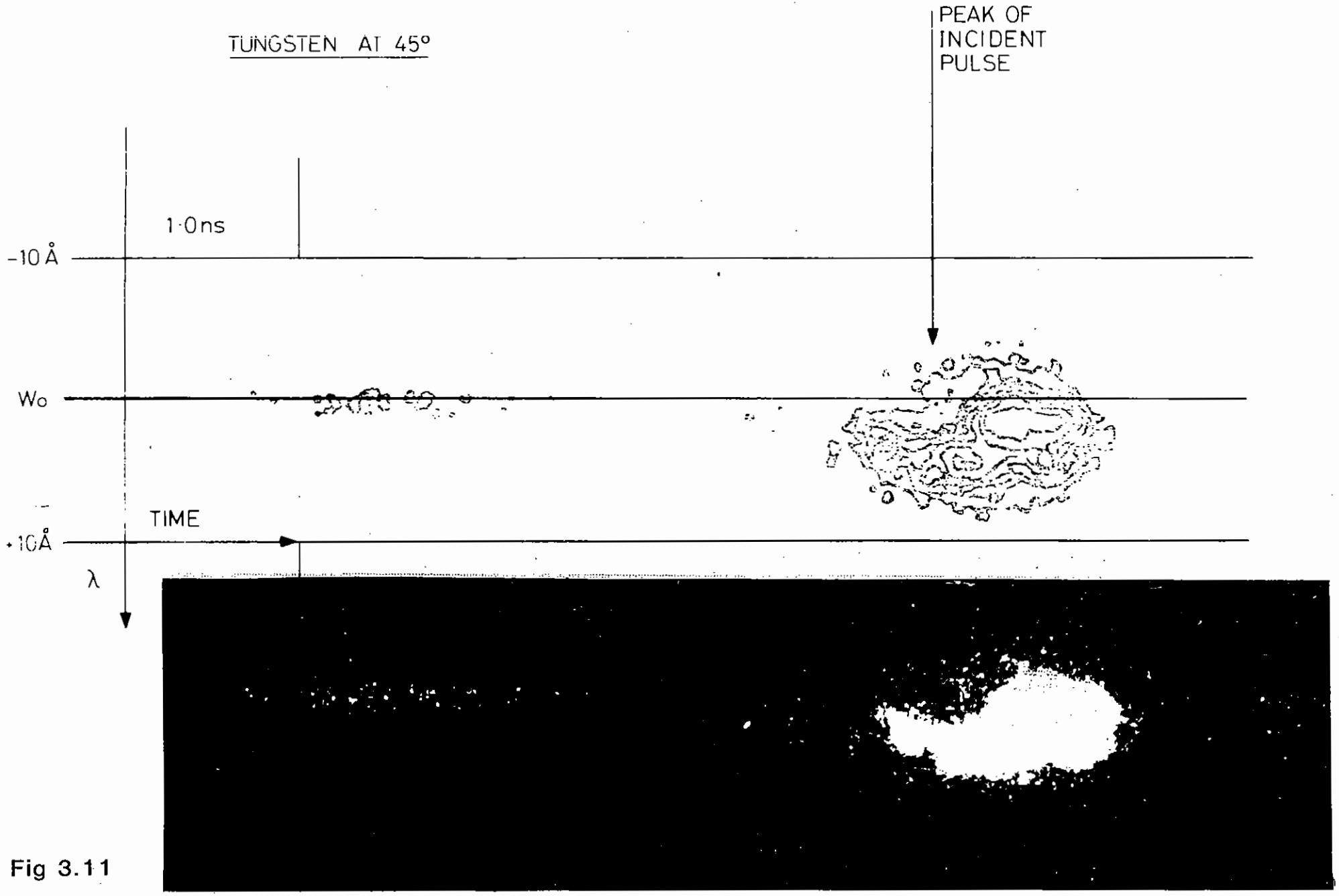

Fig 3.11

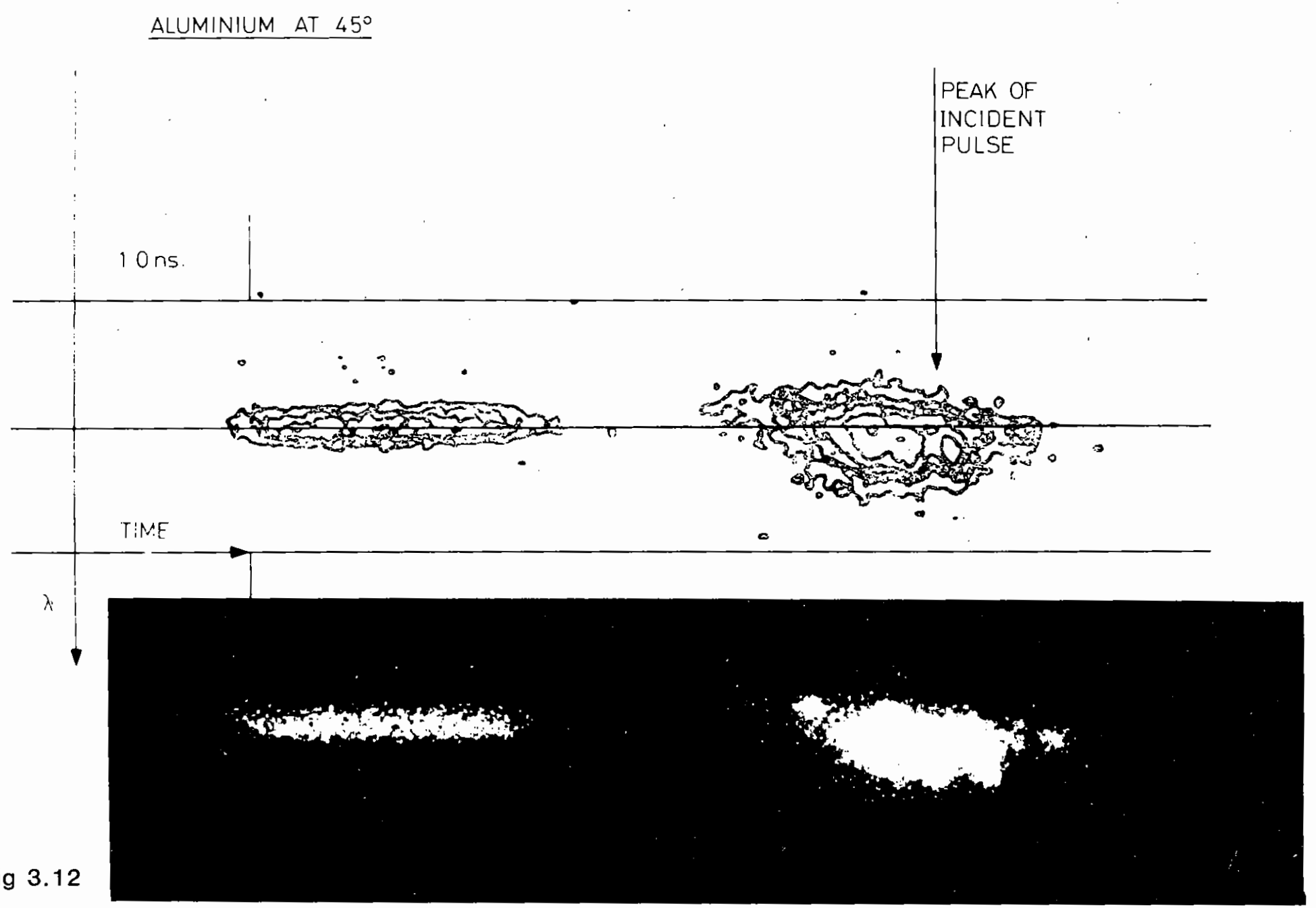

Fig 3.12

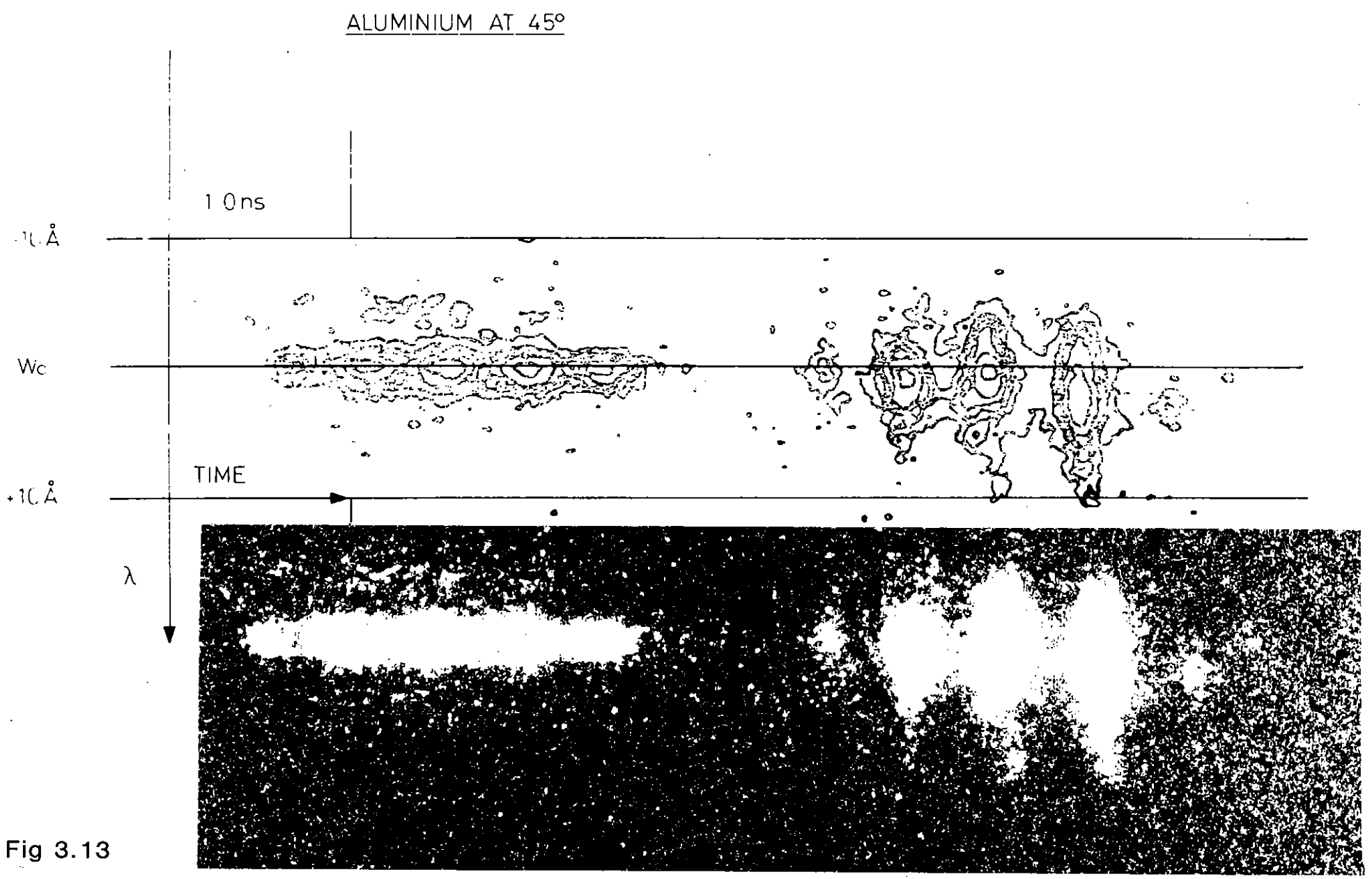

Fig 3.13

targets is less easy to understand but may be due to ponderomotive effects reducing the scale length of the underdense plasma.

Fig.3.13 shows the backscatter spectrum in the presence of strong mode beating of the incident laser pulse. The backscatter is modulated in sympathy and becomes broader and more red-shifted as the pulse train progresses.

A.J. Cole, J. Murdoch, S.M.L. Sim, R.G. Evans.

3.2.4 Backscattered Radiation at $\omega_o/2$ from Neodymium Laser Plasma Interactions

When intense laser radiation interacts with an inhomogeneous plasma, parametric proceses may occur in the region where the electron density is a quarter of the critical value n_c (3.17). Stimulated Raman scattering (SRS) causes radiation of half the laser frequency ω_o to be scattered backwards whilst two plasmon decay (TPD) is absorptive with consequent plasma heating. In the experiment now described, the intensity of $\omega_o/2$ radiation has been measured with a range of laser energies and target materials.

Ping Lee et al (3.18) looked for $\omega_o/2$ radiation but found none, possibly because the laser pulse duration was only 25 ps, although a cooled InAs detector was used. A unique measurement of 2.12 μm radiation was carried out by Bobin et al (3.19) with a 50 CVP photomultiplier (S1 photocathode) and a grating spectrometer diffracting 2 μm radiation into the first order. The neodymium laser pulse consisted of 45 lines spaced 0.95 A apart. The breadth of the scattered spectrum was about 50 A. Baldis et al (3.20) showed by Thomson scattering that the two plasmon decay generated an enhanced level of plasma waves where the density was about $n_c/4$. Simulations carried out by Kruer (3.21) and Biskamp and Welter (3.22) have predicted large conversion ratios in the vicinity of $n_c/4$.

It appears that there may be competition between SRS and TPD in the $n_c/4$ region. The threshold irradiances I_{th} for the two processes are;

SRS $(v_o/c)^{3/2} k_o L > 1$ - absolute backscatter instability (1)

(see Liu et al (3.23)).

TPD $\frac{1}{3}(\frac{v_o}{v_{th}})^2 k_o L > 1$ (2)

(see Rosenbluth (3.24)).

The relationships between the threshold irradiance (through v_o^2) and the density scale length L are plotted in Fig.3.14. The growth rates γ of the two processes are given by

SRS $\gamma = \frac{k_p v_o}{2}$

(Liu et al (3.23))

TPD $\gamma = k_o v_o$

suggesting that TPD grows faster than SRS, if the temperature is below about 10 keV. However, for Landau damping to be negligible near $n_c/4$, the temperature should be less than about 30 keV. The effect of TPD is to steepen the density gradient and hence reduce L (Chen and Liu (3.25)).

Experiments have been carried out with the neodymium phosphate glass laser at the Rutherford Laboratory Central Laser Facility using the optical system shown in Fig.3.15. The operating wavelength was 1.053 μm, the incident beam being focussed onto the target with an f/1 lens. The oscillator was operated in the Q switched mode, which allowed pulses of 1 or 2 nanosecond duration to be switched out. The pulse duration was measured by means of a streak camera and an optical multichannel analyser. Plane targets consisted of solid brass, aluminium on glass or multilayers, the material being specified for other experiments carried out simultaneously with the $\omega_o/2$ measurements. The focal spot diameter was estimated from X-ray pinhole images.

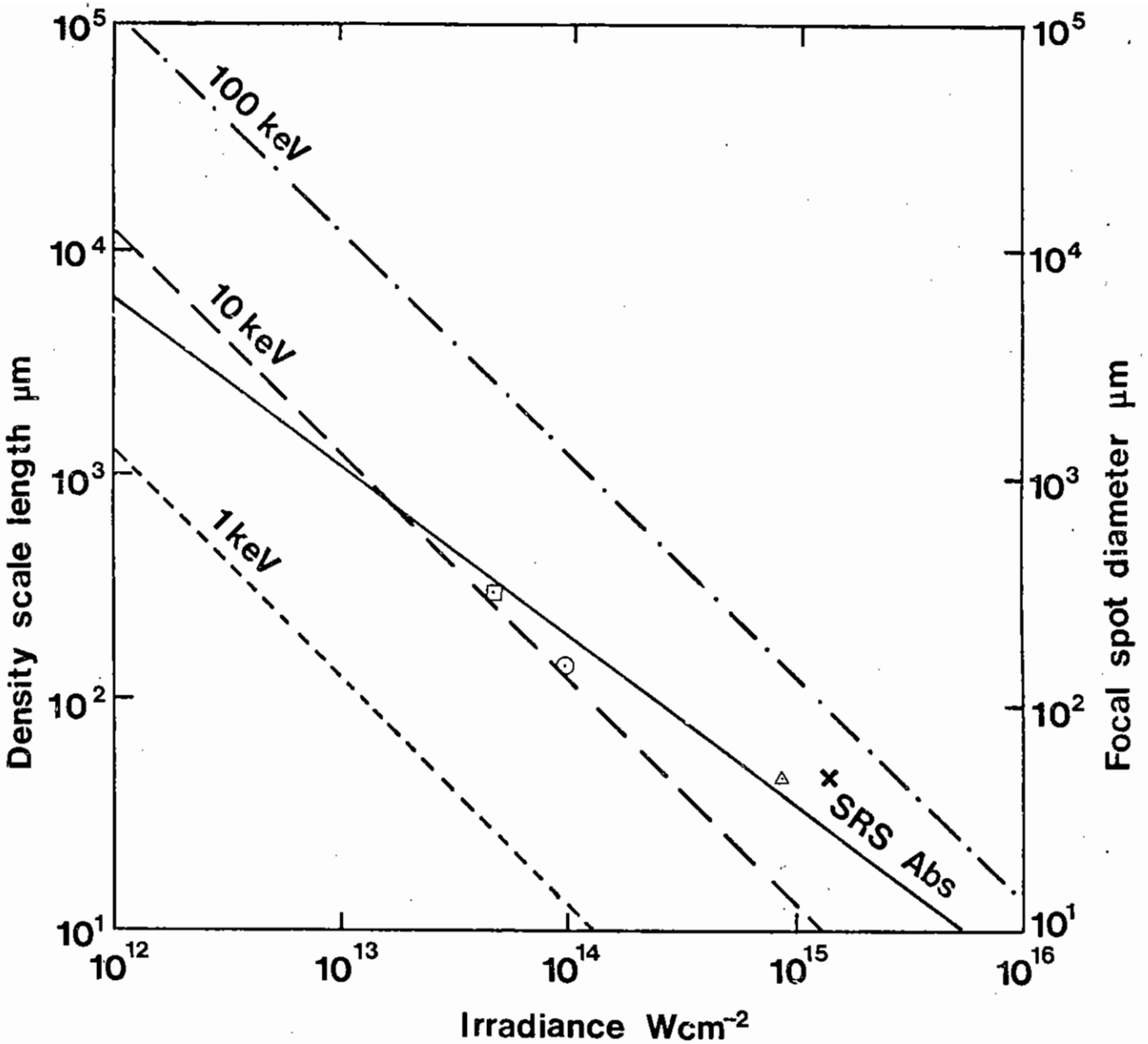

Fig.3.14

Density scale length and focal spot diameters against threshold irradiance

△ Brass target
× KCl on Ti
⊙ Aluminium on glass
⊡ Gold film

——— Stimulated Raman Scattering (Absolute)
·-·-·-·- Two Plasmon Decay 100 keV
— — — Two Plasmon Decay 10 keV
- - - - Two Plasmon Decay 1 keV

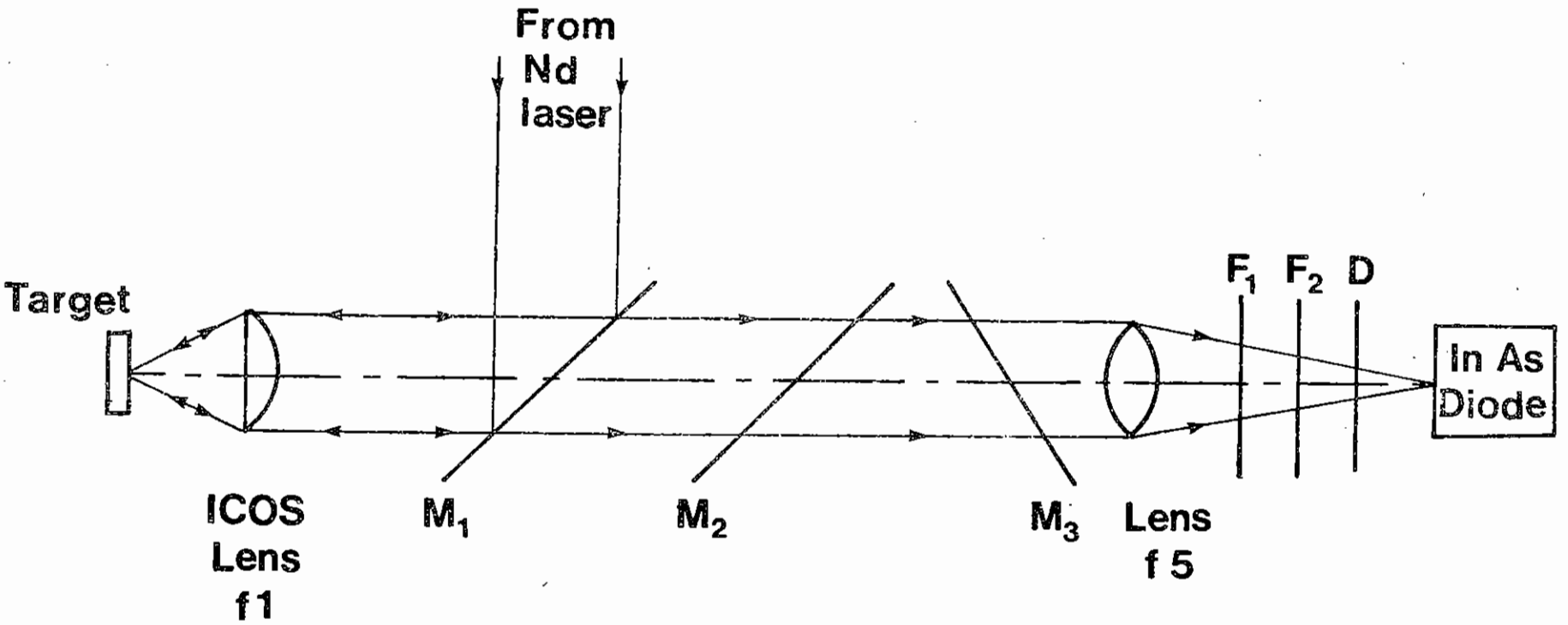

Fig.3.15

The irradiation and detection system

M1 and M2, Mirror 98% reflectivity at 1.06 μm
32% transmittance at 2.12 μm
M3 80% reflectivity at 0.707 μm
40% transmittance at 2.12 μm

F1 Narrow band filter, peak transmission 56% centred on 2.12 μm with 5% bandwidth
F2 Cut-on filter transmitting 98% at wavelengths greater than 1.7 μm but 10^{12} at 1.06 μm
D Diffuser

Radiation at $\omega_o/2$ backscattered into the angle of the lens (half angle 26.6°) was detected with an indium antimonide photovoltaic detector (Barnes A 100), operating at room temperature. Radiation at frequencies other than $\omega_o/2$ was rejected by a 5% bandwidth filter F1 which had a peak transmission of 56% centred on 2.12 μm. There was also a cut-on filter F2 with a transmission of 98% above 1.7 μm. These two filters were protected from backscattered radiation at ω_o by two dielectric mirrors M_2 and M_3. The overall rejection of backscattered radiation at 1.05 μm relative to 2.10 μm was of the order of 1 to 10^{16}. The sensitivity of the detector was 100 mV/ J, at 2.1 μm, a value derived from the manufacturer's spectral response curve after calibration against varying intensities of 1.053 μm wavelength. The irradiance was varied by changing the laser energy and by displacing the target from the focus of the lens. The laser line width was of the order of 0.1 A. The noise level was well below 1 mV whilst signal levels were 2 to 40 mV.

The conversion ratio of incident ω_o to backscattered $\omega_o/2$ energies is shown as a function of irradiance in Fig.3.16. It is seen that each group of results shows a threshold irradiance which is related to a particular target and pulse duration. The conversion factor initially increases with irradiance at a rate of the order of 10^{-21} cm^2 W^{-1}on each curve.

The focal spot size affects the plasma flow and the density scale length, the latter determining the threshold irradiance. The estimated focal spot radii are plotted against experimental values of threshold irradiance in Fig.3.14. These thresholds were determined from the linear plots of the conversion ratio for each target against irradiance. In Fig.3.16, these plots are combined by using a logarithmic scale. It should be noted that a threshold value of SRS derived by Drake and Lee (3.26) includes a collisional term ν_c resulting in an increased value of irradiance

i.e. $$\frac{v_o}{c} = \frac{1}{\sqrt{3}} \frac{\nu_c}{\omega} + 0.52\,(k_o L)^{-2/3}$$

At a temperature of the order of 10 keV, the collisional term causes an increase in I_{th} of 20%.

To test the hypothesis that the measured radiation comes from a line near to $\omega_o/2$, the narrow band filter F1 was removed for two of a series of nine consecutive shots with the same focusing conditions and target type. The signal level increased by a factor of $2.4 \pm .3$ whereas a line at the centre of the filter characteristic would have shown an increase of a factor of 1.8. This confirms that the signal was predominantly line radiation at a frequency close to $\omega_o/2$. If the small discrepancy is attributed to a temperature dependent downshift we can use the expression derived by Kruer et al (3.27) for the frequency shift $\Delta\omega$ of the $\omega_o/2$ feature,

$$\frac{\Delta\omega}{\omega_o} = \frac{9}{8} \frac{v_{th}^2}{c^2}$$

together with the filter transmission characteristic to estimate a coronal temperature of $3.7 \pm \frac{0.7}{2.5}$ keV for the present experiment. The flux limited temperature (Gitomer and Henderson (3.28) would be between 1 and 10 keV for this range of irradiances.

Although the target materials cover the range of atomic weights from 16 to 197, there is no obvious relationship between the conversion factor and atomic weight.

This study has shown that backscattering due to stimulated Raman scattering occurs at $\omega_o/2$ when the experimental conditions are adjusted to produce large density scale lengths. The conversion factor is of the order of 10^{-7}, increasing with irradiance.

An independent measurement of $\omega_o/2$ was made when the incident beam was green, (λ_o = 530 nm) produced by doubling the laser frequency in a crystal. This procedure had the advantage that $\omega_o/2$ was near to 1 μm and was relatively easy to detect with a silicon pin diode. However, an appreciable and variable amount (∿ 1 μJ) of Nd laser light leaked through the system making a quantitative assessment difficult. The $\omega_o/2$ conversion efficiency was near to 10^{-7}.

J. Elazar, W. Toner and E.R. Wooding

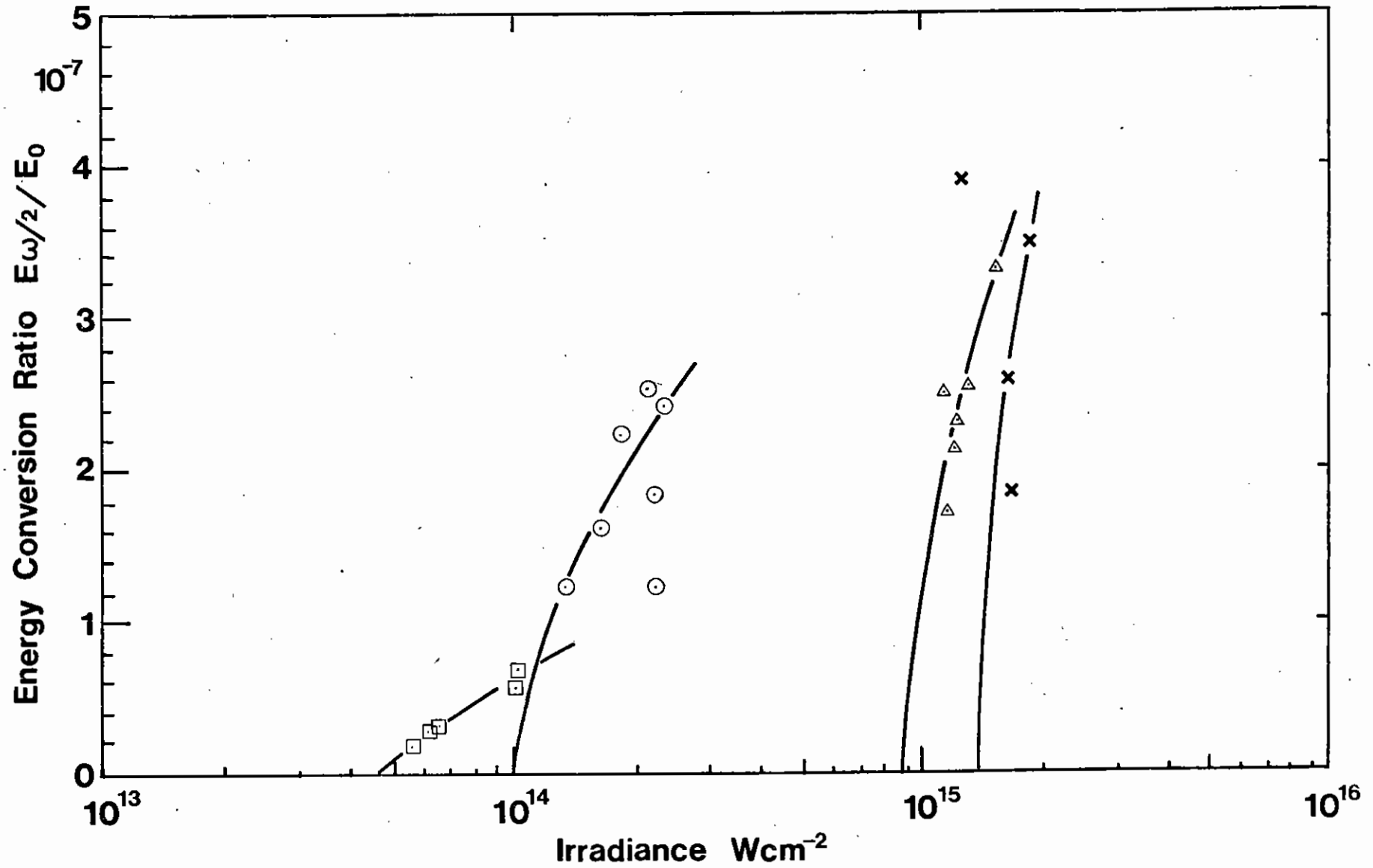

Fig.3.16

Energy conversion ratio for $\omega_o/2$

△ 50 μm focal spot diameter brass target 2 ns pulse
x 50 μm focal spot diameter 0.5 μm KCl layer on Ti 2 ns pulse
⊙ 150 μm focal spot diameter Al on glass 2 ns pulse
⊡ 300 μm focal spot diameter gold film 1 ns pulse

3.3 Density Profile Studies

3.3.1 Experimental Measurements

Experiments have been carried out to study density profiles and self generated magnetic fields on ablatively driven targets using a stracked heating pulse (1.2 ns) and a short probe pulse (50 ps). The probe beam arrangement is discussed in section 1.6.1. Toroidal magnetic fields have been observed on plane targets as well as on non uniformly illuminated microspheres at irradiances in the region of 10^{13} to 10^{14} W cm^{-2}. However, the final data analysis is still in progress.

O. Willi

3.3.2 Numerical Simulations

Recent measurements (3.29, 3.30) have confirmed that the radiation pressure modifies the electron density profiles of laser produced plasmas. To predict these experimental results, the ponderomotive force term was included into the 1-D Lagrangian hydrodynamic code MEDUSA (3.31)

To include the effects of the ponderomotive force in the code fine zoning of the mesh in the critical density region is required. Therefore the glass shell of 0.6 μm is divided into 70 zones of equal initial thickness and the interior deuterium-tritium mixture into only 10 zones. To obtain the local laser field amplitude the wave equation is solved on an auxilary mesh, created by subdividing each fluid zone into a number of smaller zones each of about 50 nm. The electron density at each of these cells is calculated using a linear interpolation. The initial density profile at the target surface is assumed to be an exponential tail with a scale length of one micron.

For the high irradiances and short density scale length of our simulations, the inverse bremsstrahlung absorption of the laser light is almost negligible and most of the absorption occurs via collective processes at the critical density. In solving the wave equation for the

the electric field of the laser we neglect the absorption effects i.e. we assume ε and hence E to be real.

We solve the wave equation for plane waves $\partial^2 E/\partial r^2 + k^2 \varepsilon E = 0$ since the use of the spherical ∇^2 operator $\partial^2 E/\partial r^2 + \frac{2}{r} \partial E/\partial r$ hinders the use of a fully centered difference scheme. This approximation requires that the target radius be many times the density scale length which is always true. The wave equation is integrated starting on the high density side of critical and going out far enough on the low density side that the solution may be matched to the vacuum field of the laser. To include the spherical convergence the electric field E is multiplied by $\frac{r_o}{r}$ where r_o and r are the initial and local radii respectively. The ponderomotive force F_p in each cell of the spatial mesh is then calculated as

$$F_p = - \frac{1}{8\pi} \frac{n_e}{n_c} \nabla \langle E^2 \rangle$$

where n_e is the electron density, n_c the critical electron density (10^{21} cm^{-3} for 1 μm light) and E the local laser field amplitude. F_p is added to the normal kinetic pressure gradient of the plasma $F_{th} = - \nabla(n_i k T_i + n_e k T_e)$ where n_i and n_e are the ion and electron densities, T_i and T_e the ion and the electron temperatures and k is the Boltzmann constant.

The MEDUSA code has adjustable parameters for energy absorption, fast electron generation and inhibition of the electron thermal transport but we emphasize in what follows that these parameters have not been adjusted from the empirical values determined from comparison with experiments on X-ray emission and implosion of microballoons (3.32). The values used were:

anomalous absorption fraction at critical = 10%;
fraction of above into superthrmal electrons = 0.9
flux limiter = 0.03 x classical free streaming limit.

All of our simulations have been performed at a laser wavelength of 1.06 μm, a Gaussian laser pulse of 50 ps full width half maximum irradiating microballoons 40 μm in diameter with a shell thickness of 0.6 μm.

Fig.3.17 depicts the results of the MEDUSA simulation at $\phi = 10^{16}$ W cm^{-2} compared with the measurements of (3.30) at the same irradiance, shortly after the peak of the laser pulse, where a) is the measured profile and b) the calculated one. Agreement of the shape of the profiles is excellent with the height of the density step and the appearance of a small super-critical density bump being reproduced by the code. In order to obtain agreement at very low electron densities we have to add to the MEDUSA fluid densities the effect of the superthermal electrons. We calculate the density of hot electrons n_h by requiring that the energy input into hot electrons E_{abs} is carried away in the free streaming limit $E_{abs} = n_h T_h v_h$. At an irradiance of 10^{16} W cm^{-2} and $T_h = 15$ keV we find that $n_h = 0.05 \times n_c$ and this additional electron density is also shown in Fig.3.17. Thus the height of the lower density shelf is governed by the hot electron density. The velocity of the calculated plasma expansion is larger than the measured one. This is probably due to the two dimensional plasma expansion in the experiment.

Further simulations have been performed for irradiances in the range of 2.5×10^{14} W cm^{-2} up to 2×10^{16} W cm^{-2} to obtain scaling laws for the critical density scale length and the step height. The code predictions are compared with the measurements of (3.29) and (3.30). The plotting of the measured density scale length as a function of the laser irradiance has to be done with caution because the measurements might have been limited by the resolution of the optical systems as well as of the plasma motion. Fig.3.18 shows the critical density scale length obtained from the experimental data (circles) of (3.29) and (3.30) in comparison with the code predictions (squares). The dotted line represents the theoretical prediction given by Estabrook and Kruer (3.33) for steepening due to resonance absorption.

A comparison between the measured step heights with those predicted by the code is not subject to the experimental uncertainties noted above and is depicted in Fig.3.19. Once more data from (3.29) and (3.30) have been used.

This excellent agreement in the shape, the critical density scale length and the density step height encouraged us to examine the code results for

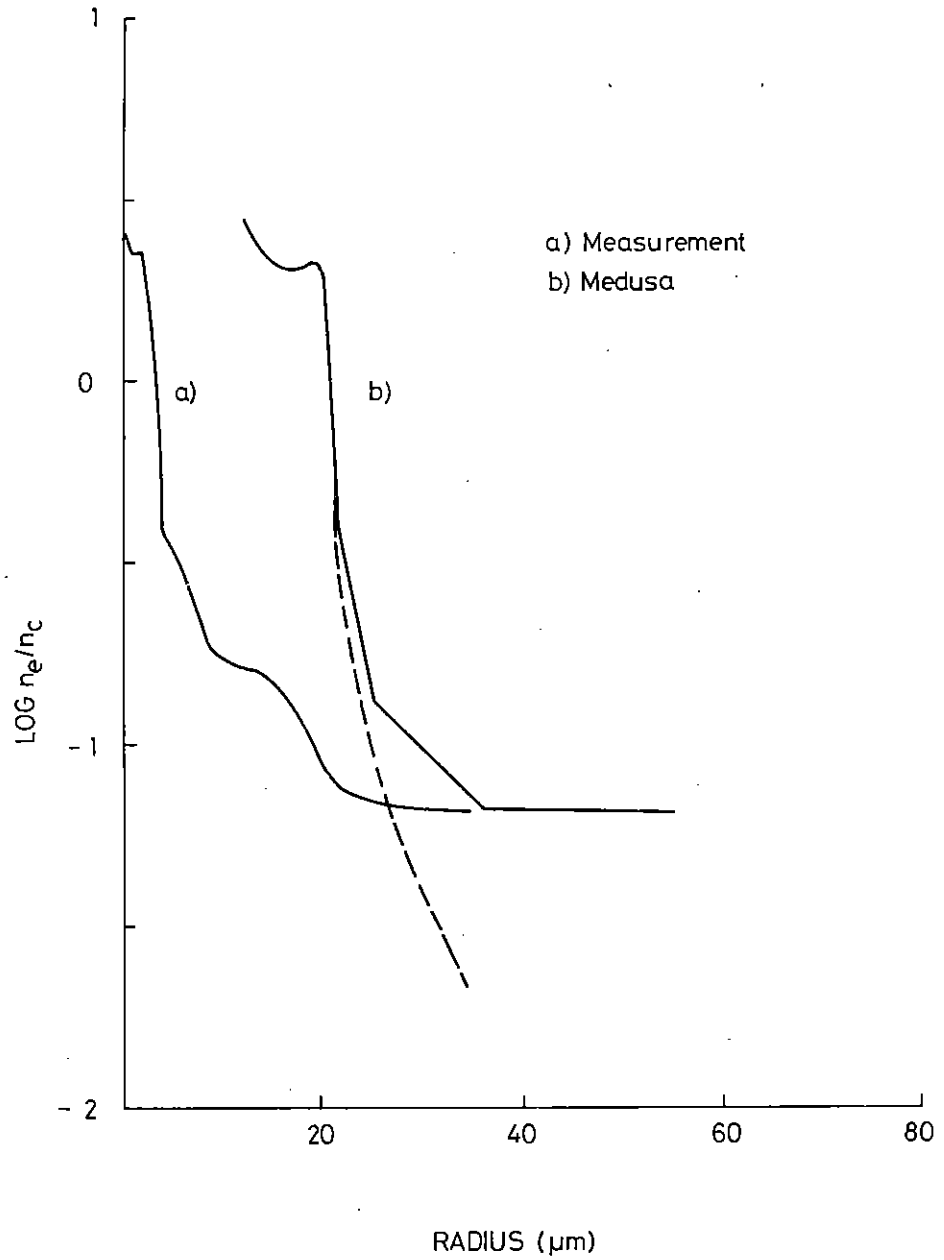

Fig.3.17

Comparison of a measured electron density profile a) and a predicted one b) at the peak of the laser pulse for an irradiance of 10^{16} W cm^{-2}. The dotted curve of b) represents the electron density profile without superthermal electrons whereas the solid line is obtained by adding $0.05 \times n_c$ of hot electrons.

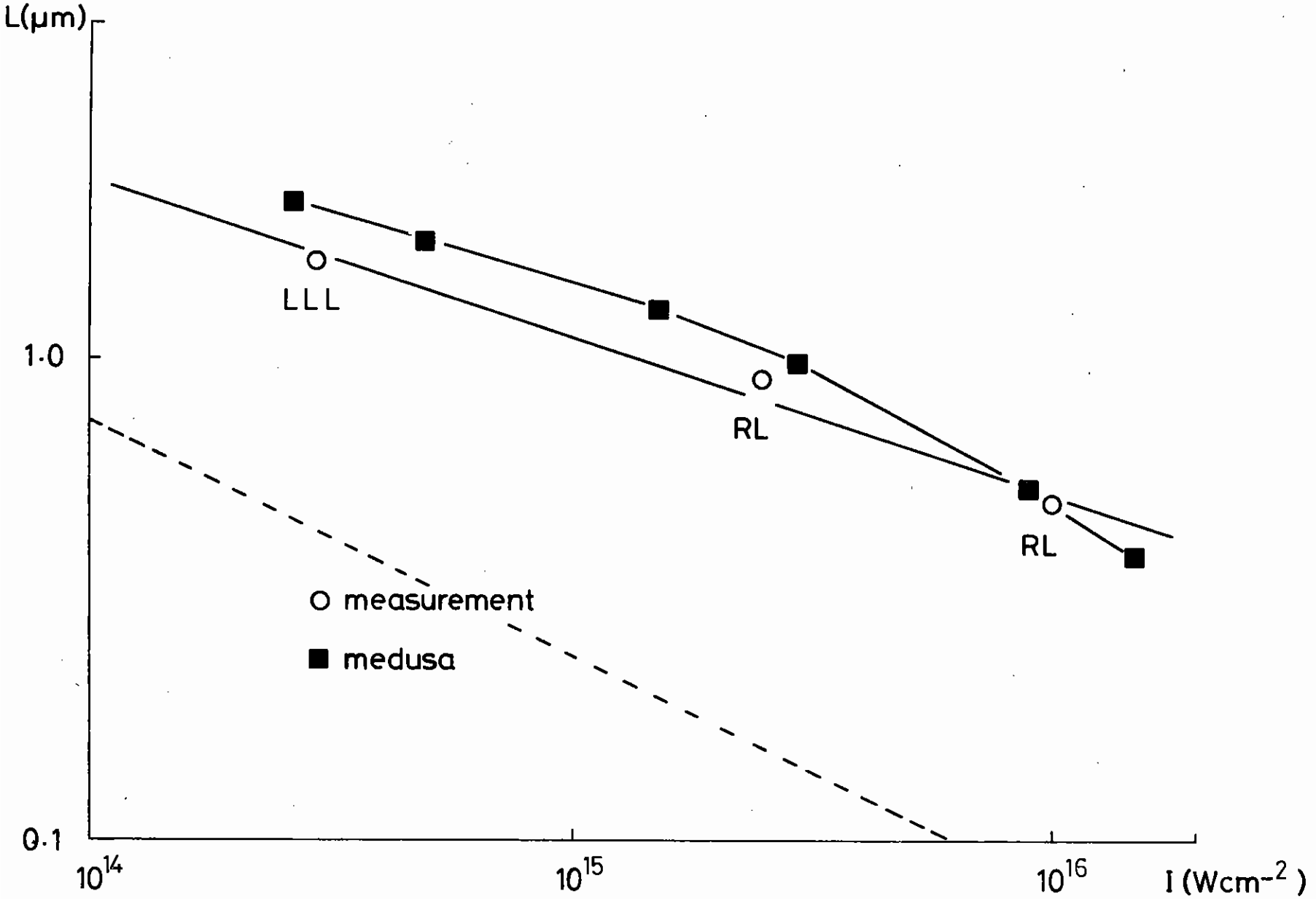

Fig.3.18

Predicted (squares) and measured (circles) scale elngths of the critical density region as a function of laser irradiance. The dotted line shows the theoretical prediction for steepening due to resonance absorption of Ref. (3.32).

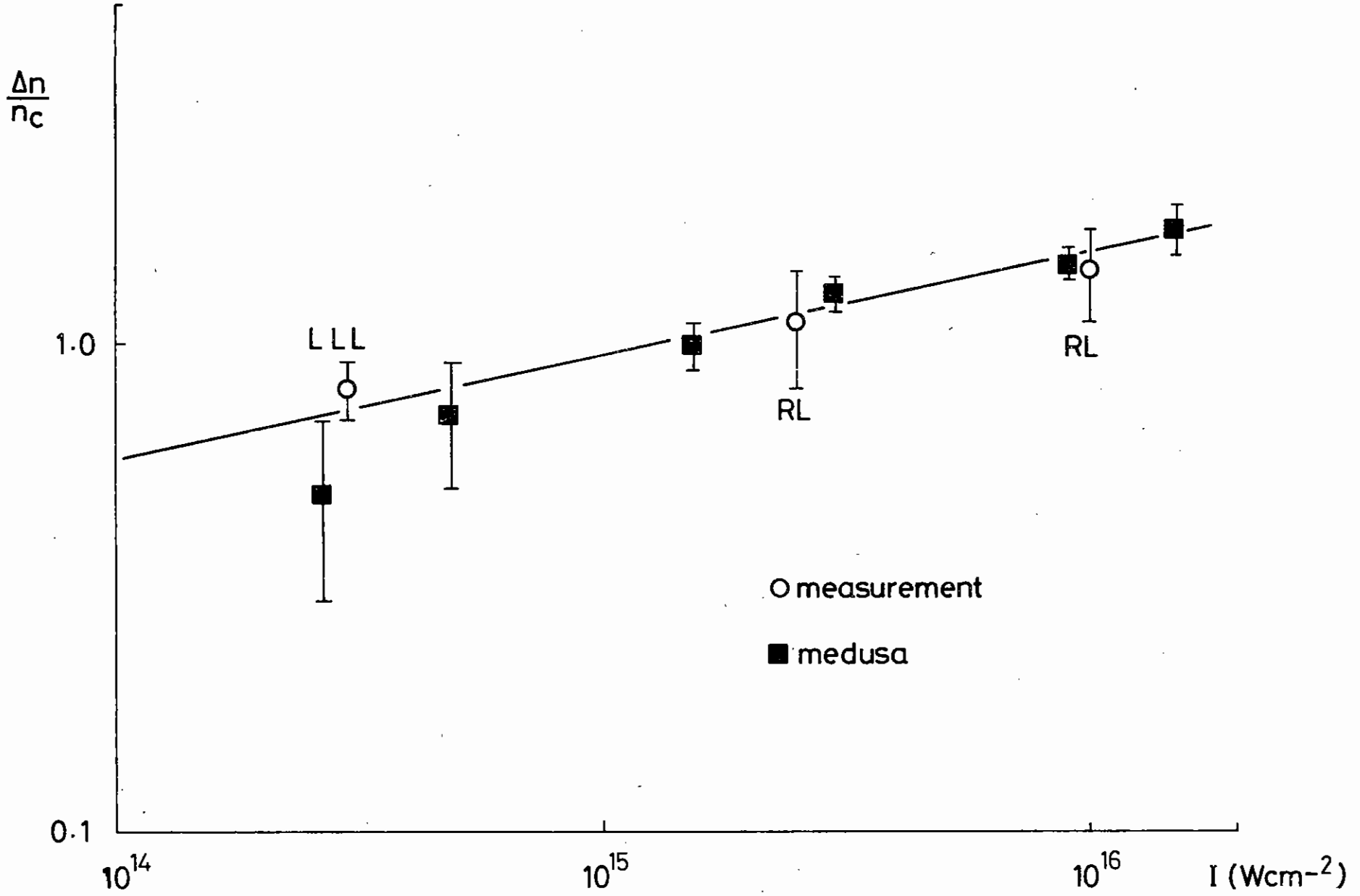

Fig.3.19

Computed and measured step heights as a function of laser irradiance.

irradiances of 10^{16} W cm^{-2} in more detail. A closer look at the time evolution of the plasma flow revealed four different regions.

1) At about 30 ps before the peak of the heating pulse, the first signs of steepening in the expanding plasma are visible. Fig.3.20 depicts a density profile at about 10 ps before the peak of the laser pulse. The flow velocity in the density region beyond critical is subsonic in a frame where the critical surface is stationary. This type of profile is called a D-front in the steady state case.

2) Although the input Mach number is still subsonic the formation of an overdense bump (Fig.3.21) appears a few ps after the peak of the pulse. Max and McKee (3.34) showed that in the steady state a similar behaviour is only possible with a supersonic input flow into the critical region. But in the non-steady state case the plasma accumulates at the light pressure wall even if the input flow velocity is a fraction of the sound velocity.

Introducing a characteristic time τ which we assume to be the duration of the laser pulse at full width half maximum (50 ps) and a characteristic distance δ, the distance from the ablation surface to the point where the radiation pressure of the laser light is largest, a characteristic velocity $\frac{\delta}{\tau}$ can be calculated. If $v = c_s - v_f$ is the information velocity, i.e. the velocity which transfers the information about the existence of the light pressure upstream, then constraints are placed on v for the formation of a density step (D-front) as in (3.29) so that

$$v = (c_s - v_f) > \frac{\delta}{\tau}$$

where c_s is the sound speed
v_f is the fluid velocity.

However, where $v < \frac{\delta}{\tau}$ i.e. $v_f > c_s - \frac{\delta}{\tau}$ an overdense bump is formed because the information of the laser pressure cannot reach the ablation surface within the characteristic time. For the simulation

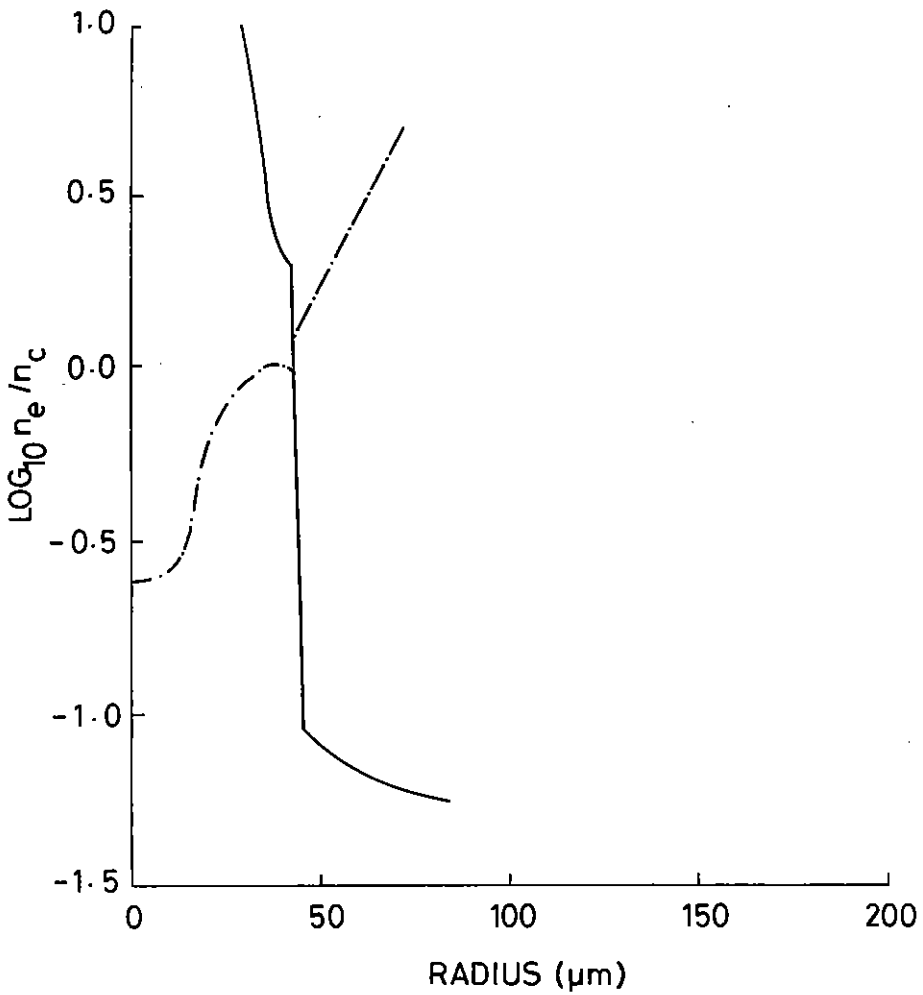

Fig.3.20

Typical D-front (solid curve) of electron density profile predicted by the code. The time is 10 ps before the peak of the heating pulse.
The dotted curve is the Mach number in a frame where the critical surface is stationary.

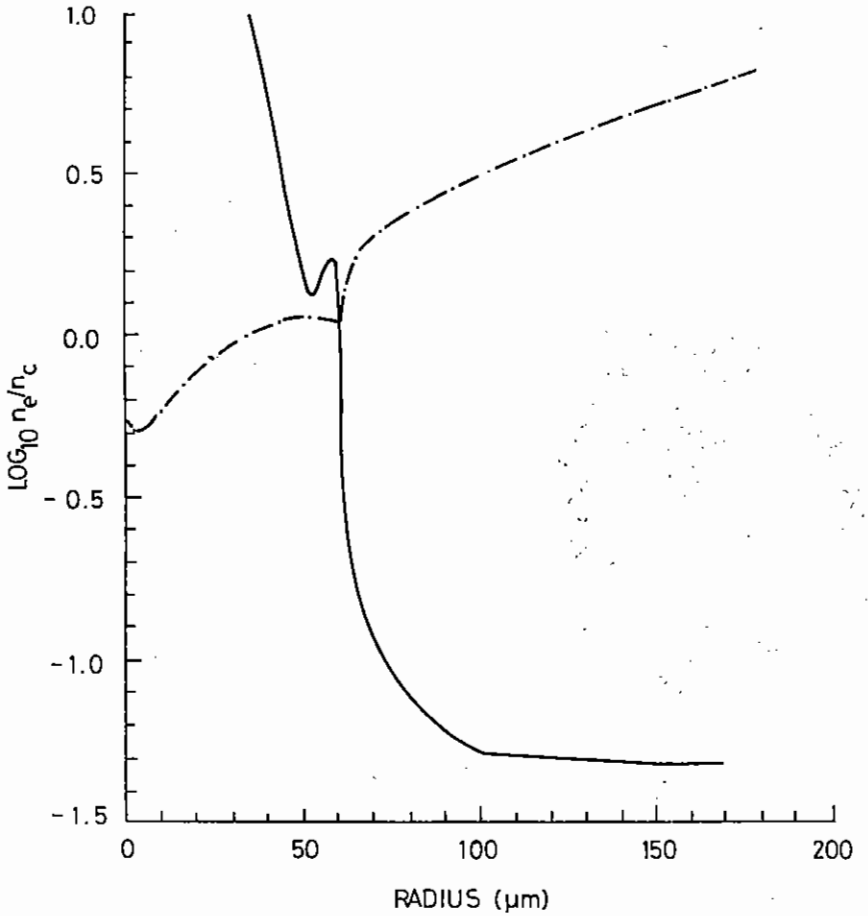

Fig.3.21

A supercritical density structure is observed in the expanding plasma flow 18 ps after the maximum of the laser pulse although the input flow is still subsonic.

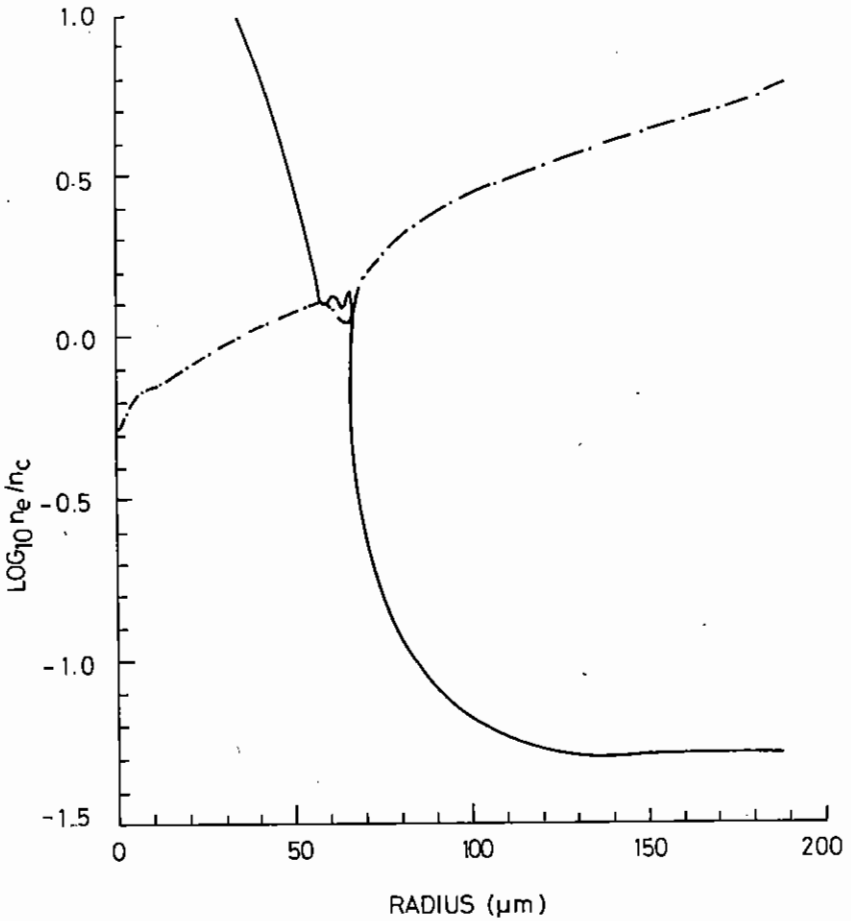

Fig.3.22

An instability in the overdense bump is seen when the flow velocity in the high density region reaches the sonic point (30 ps after the peak of the laser pulse).

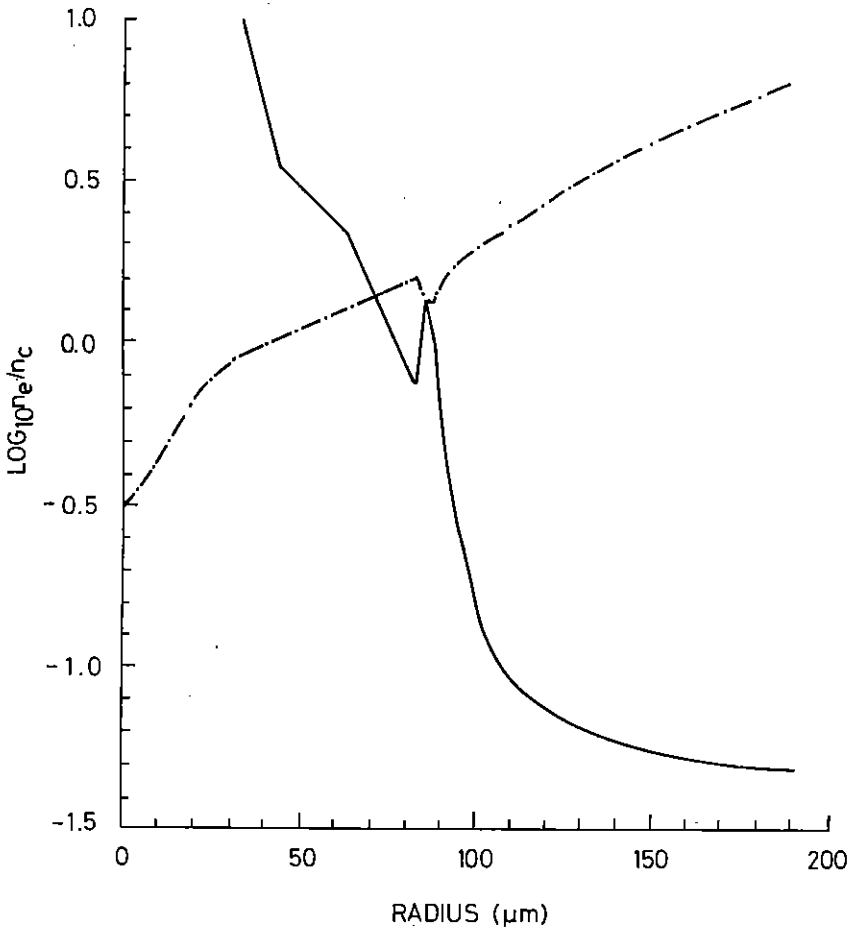

Fig.3.23

60 ps after the peak of the laser pulse an electron density profile with a clear overdense bump is observed. The input flow Mach number is larger than unity.

conditions we estimate this transition flow velocity to be Mach 0.5. In the steady state ($\tau = \infty$) the subsonic overdense bump cannot exist since the transition flow velocity becomes the sound speed.

3) Oscillations in the shape of the overdense bump occur while the laser is still on. These are related to the sonic point in the flow moving to the density minimum just upstream of the bump, i.e. $v_f \sim c_s$ or $v \sim 0$. At this point a weak shock may be formed which propagates outwards and reflects as a rarefaction from the top of the density step. This cycle then repeats a small number of times. This is probably part of the region of unstable solutions proposed by Max and McKee when the input Mach number is close to unity. In Fig.3.22 the instability of the overdense bump can be seen.

4) In the region where $v < 0$, i.e. $v_f > c_s$ or $M > 1$ an overdense bump arises again (Fig.3.23). This is the condition required in the model of (3.34) for the formation of a shock to form and whereas Max and McKee suggest that a collisionless shock will occur producing ion turbulence, we note that in MEDUSA the von Neumann artificial viscosity serves the same purpose. As the bump propagates outwards in the supersonic flow, the trailing edge steepens which is the correct behaviour of a supersonic density perturbation.

We also observe oscillations in the magnitude of the laser electric field at the critical density. The electric field is enhanced by the reduction in group velocity and the amount of the swelling is dependent on the shape of the profile. The peak values of E_c^2 and the vacuum field E_o^2, i.e. the laser pulse, as a function of time are shown in Fig.3.24. It does not appear that these oscillations are related to the oscillations in the supercritical density bump since the field oscillations begin before the supercritical bump is formed. Mayer et al (3.35) have considered the possibility of resonant under dense plasma profiles which result in large Fresnel reflection of the incident laser pulse. The oscillations observed here are probably due to the under dense plasma profiles moving through several "resonances" as the plasma expands. The appearance of the peak of E_c^2 earlier in time than the maximum of the vacuum laser electric field is due to the expansion of the critical surface.

These oscillations in the electric field at the critical surface may be responsible for the oscillations in the emission of the second harmonic of the laser light (3.36). In our simulations the period of oscillation varies from about 20 ps down to about 5 ps, whereas the observed periodicity of the harmonic emission in (3.36) was about 20 ps. Furthermore, this may be an explanation of the rapid time variation of the tenth and eleventh harmonic emissions of a CO_2 irradiated plasma observed by Jaanimagi et al (3.37).

Excellent agreement between the predicted density profiles and the experimental results is obtained even if the resonance absorption effects are not included in the code. Resonance absorption, however, is the most favourable absorption mechanism for critical density scalelengths which are short compared to the laser wavelength. To understand this good agreement, the code was modified for oblique incident light and the results are described in section 7.2.4.

O.Willi

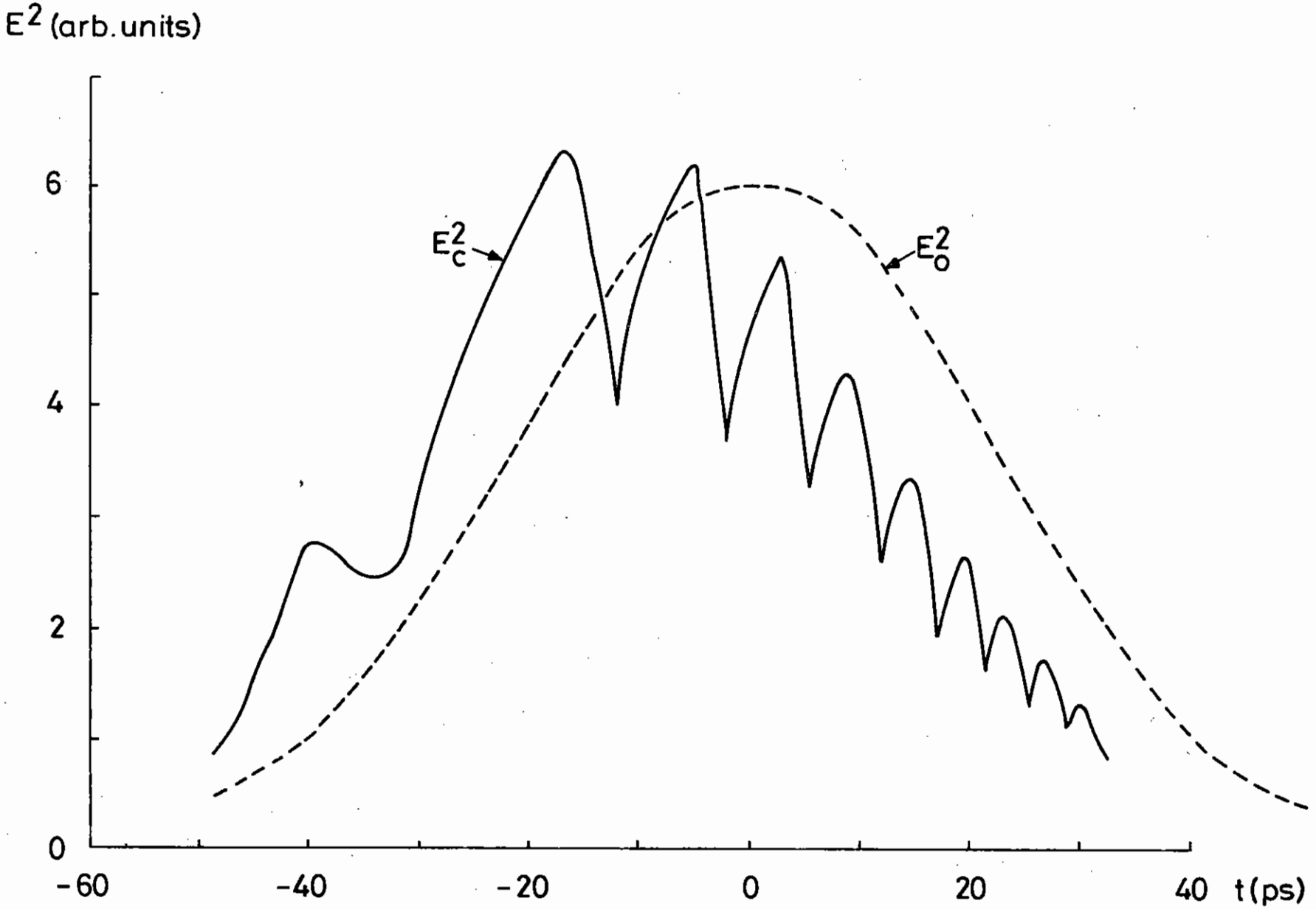

Fig.3.24

The solid curve represents the oscillations of the peak electric field E_c^2 at the critical surface whereas the dotted curve is the vacuum laser electric field E_o^2

3.4 Limitations on Brillouin Scattering

3.4.1 Competition Between Inverse Bremstrahlung and Brillouin Scattering

In the quest for higher densities and ρR products in laser driven compression it is expected that laser pulse durations τ and target radii R_T will increase, beyond these being used for target experiments at the present time.

As the scale length of underdense plasma increases the plasma is more susceptible to Stimulated Brillouin Scattering (SBS) and to Stimulated Raman Scattering (SRS). SBS is a particularly serious problem for absorption of laser light since a very large fraction of the incident power may be reflected. The threshold and linear growth rates for SBS have been known for some time (3.38) but of greater interest is the non-linear phase of SBS when the ion wave amplitude has been limited by ion heating or trapping. This problem has been tackled by Kruer (3.39) and by Evans (3.40) and has also been the subject of numerical simulations with particle-in-cell (PIC) codes (3.41).

The PIC codes are essentially collisionless and thus do not include the effects of collisional absorption of the laser light (inverse bremsstrahlung). This collisional absorption is beneficial firstly because it heats the plasma electrons without forming unwanted 'hot' electrons and secondly because it reduces the laser intensity available to drive SBS. In this section we calculate under what conditions the inverse bremstrahlung can be large enough to significantly affect the SBS and even to quench it completely.

The cross-section for inverse bremsstrahlung is well known and is given in a convenient numerical form in the book by Hughes (3.42) valid for electron temperatures above about 10 eV

$$a_\lambda = \frac{3 \times 10^5 \, Z \, (n_e/n_c)^2}{\lambda^2 \, T^{3/2}} \quad \text{cm}^{-1}$$

a_λ = absorption coefficient (cm^{-1})
Z = nuclear charge

(n_e/n_c) = ratio of electron density to critical density
λ = laser wavelength (μ)
T = electron temperature (eV)

In this equation we have neglected the so-called Cillie Factor which expresses the reduction in phase velocity as $n_e \to n_c$ since the simulations (3.41) show that SBS is strongest at electron densities $n_e \simeq 0.3\, n_c$. In the steady state the plasma density profile is assumed to be set by the spherical divergent flow from the pellet

$$n_e/n_c = \left(\frac{R_c}{r}\right)^2$$

where R_c is the radius of the critical density surface, we assume $R_c \sim R_T$, the initial target radius. The absorption of the incident laser light up to a radius $R > R_c$ is given by

$$\tau_R = \int_\infty^R a_\lambda \, dr$$

$$= \frac{3 \times 10^5 \, Z}{\lambda^2 \, T^{3/2}} \int_\infty^R (n_e/n_c)^2 \, dr$$

$$= \frac{3 \times 10^5 \, Z}{\lambda^2 \, T^{3/2}} \, \frac{R_c^4}{3R^3}$$

where we have assumed that Z and T are constant throughout the under dense plasma.

If instead of R we use the ratio of density at radius R to critical density, $\beta = n_e/n_c$

$$\tau_\beta = \frac{3 \times 10^5 \, Z}{\lambda^2 \, T^{3/2}} \times \frac{R_c \beta^{3/2}}{3}$$

In order to significantly reduce the SBS at densities greater than βR_c we require $\tau_\beta \gtrsim 1$ or

$$R_c \gtrsim \frac{\lambda^2 T^{3/2}}{10^5 Z \beta^{3/2}} \qquad (1)$$

Assuming $\beta \simeq 0.3$

$$R_c > \frac{\lambda^2 T^{3/2}}{1.6 \times 10^4 Z} \quad \text{cm}$$

This can conveniently be expressed as

$$Z R_c = \frac{\lambda^2 T^{3/2}}{1.6 \times 10^4} \qquad (2)$$

and the lines of constant ZR_c are shown in Fig.3.25. This graph shows for instance that with a 1 μ laser and an electron temperature of 1000 eV a ZR_c product of about 20 mm is required for inverse bremsstrahlung to reduce Brillouin Scattering. On the other hand with a 0.25 μ laser and an electron temperature of 1000 eV a ZR_c product of just over 2 mm would be effective. If $Z \sim 20$ for a high Z absorber then targets with radius greater than 100 μ would be able to reduce Brillouin Scattering.

It is more convenient to express these results in terms of laser irradiance ϕ rather than electron temperature and using a simple steady state ablation model of Ahlborn (3.43) we have

$$T_e \simeq 10^{-3} (\phi\lambda)^{4/9} \qquad (3)$$

with T_e in eV, λ in μ and ϕ in W cm^{-2}, thus

$$ZR_c = 2.0 \times 10^{-9} \phi^{2/3} \lambda^{8/3} \qquad (4)$$

and the contours of ZR_c as a function of ϕ and λ are shown in Fig.3.26 These contours and also those of Fig.3.25 indicate the circumstances in which SBS will be reduced (but not eliminated) by the action of inverse bremsstrahlung.

If the inverse bremsstrahlung is sufficiently strong it forces the SBS to occur at lower and lower densities and consequently larger radii. At larger radii the scale length of the plasma increases but the irradiance of the converging laser beam decreases. The possibility arises that inverse bremsstrahlung will force the SBS to such low densities that the irradiance falls below the SBS threshold.

The inhomogeneous plasma threshold for SBS is normally given as

$$1/8 \, (v_o/v_e)^2 \, (\omega_p/\omega_o)^2 \, k_o L > 1 \qquad (5)$$

where v_o is the oscillatory velocity of the electrons in the electric field of the laser,
v_e is the electron thermal velocity
ω_p, ω_o are the local plasma frequency and laser frequency respectively,
k_o is the wavenumber of the pump laser,
L is the density scale length.

This may be converted into the more convenient form

$$\frac{\phi\lambda^2}{T} \beta\left(\frac{L}{\lambda}\right) > 10^{13} \qquad (6)$$

since $\beta = n_e/n_c = \omega_p^2/\omega_o^2$.

At the point in the underdense plasma where $n_e = \beta n_c$ the density scale length is given by

$$L^{-1} = \frac{1}{n_e} \frac{\partial n_e}{\partial r}$$

$$L = \frac{r}{2} = R_c/2\sqrt{\beta} \qquad (7)$$

and the local laser irradiance is

$$\phi = \beta \phi_c \qquad (8)$$

where ϕ_c is the irradiance at critical density.

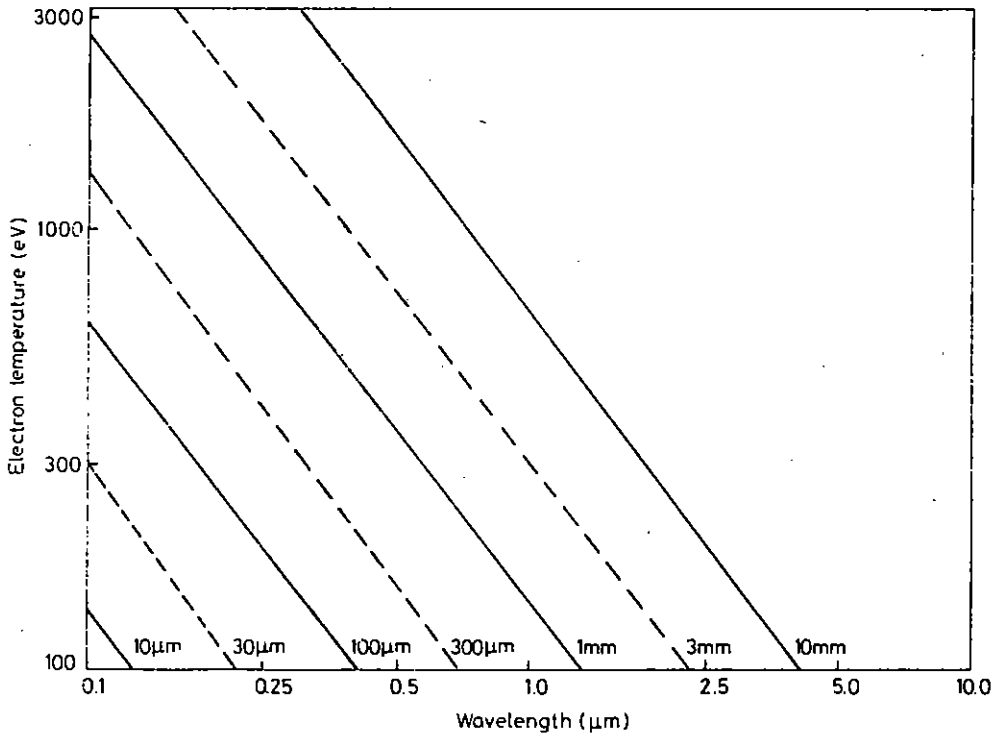

Fig.3.25

Contours of ZR_c for reduction of SBS by inverse bremstrahlung (λ vs T_e)

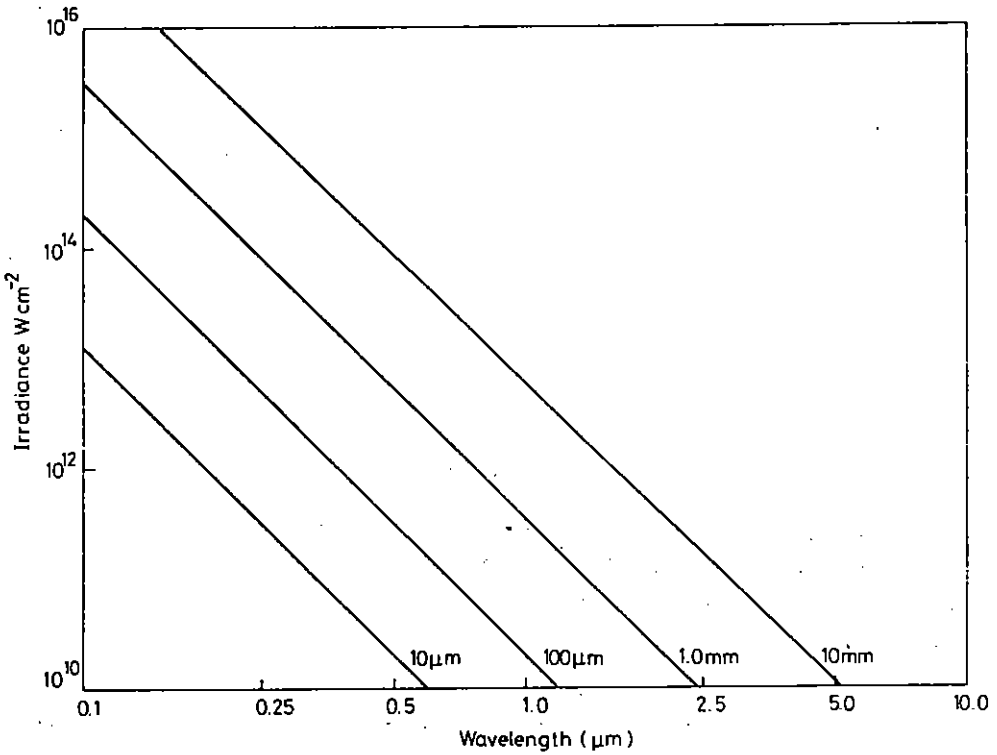

Fig.3.26

Contours of ZR_c for reduction of SBS by inverse bremstrahlung (λ vs ϕ)

If we take β to be defined by equation (1) as the point where the inverse bremsstrahlung has reduced the incident irradiance to $^1/_e$ of its initial value then by substitution of (7) and (8) in equation (6)

$$\beta \frac{\phi_c \lambda^2}{T} \beta \frac{R_c \times 10^4}{2\sqrt{\beta}\ \lambda} = 10^{13}$$

(the factor of 10^4 arises since the equation for β assumes that R_c is in cm and λ is in μm)

$$\text{i.e.} \quad \frac{\phi_c \lambda R_c \beta^{3/2}}{T} = 2 \times 10^9 \qquad (9)$$

We now substitute for β from equation (1) to obtain the "quenching" condition

$$\frac{\phi \lambda R_c}{T} \frac{\lambda^2 T^{3/2}}{Z R_c \times 10} = 2 \times 10^9$$

$$\text{i.e.} \quad \frac{\phi \lambda^3 T^{1/2}}{Z} = 2 \times 10^{14} \qquad (10)$$

or on substituting the approximate expression for T from equation (3)

$$\frac{\phi \lambda^{29/11}}{Z^{9/11}} = 1.75 \times 10^{12} \qquad (11)$$

This equation does not allow for the fact that β given by equation (1) may be larger than the "preferred" value $\beta = 0.3$. It is also necessary to calculate the threshold condition directly from equation (9) with $\beta = 0.3$

$$\frac{\phi_c \lambda R_c}{T} > 1.2 \times 10^{10} \qquad (12)$$

or again substituting for T from (3)

$$\phi_c \lambda = \frac{6.3 \times 10^{11}}{R_c^{9/5}} \qquad (13)$$

It is the larger value of ϕ obtained from equations (10) and (12) (or from (11) and (13)) which sets the effective threshold for stimulated Brillouin scattering.

In Fig.3.27 the threshold condition for various targets and laser wavelengths is shown. The advantages of short wavelengths and high Z target materials are obvious.

Conclusion

The foregoing arguments attempt to make a quantitative estimate of the effects of inverse bremstrahlung in reducing or eliminating Stimulated Brillouin Scattering in laser fusion pellets. Not surprisingly high Z target materials and short laser wavelengths are beneficial and in favourable cases target irradiances of 10^{15} W cm^{-2} may be usable without severe Brillouin reflection.

The theory presented here contains a rather gross approximation in the use of equation (3) for the electron temperature but the equations (2), (10) and (12) are much more reliable, if independent estimates of the electron temperature are available.

R.G. Evans

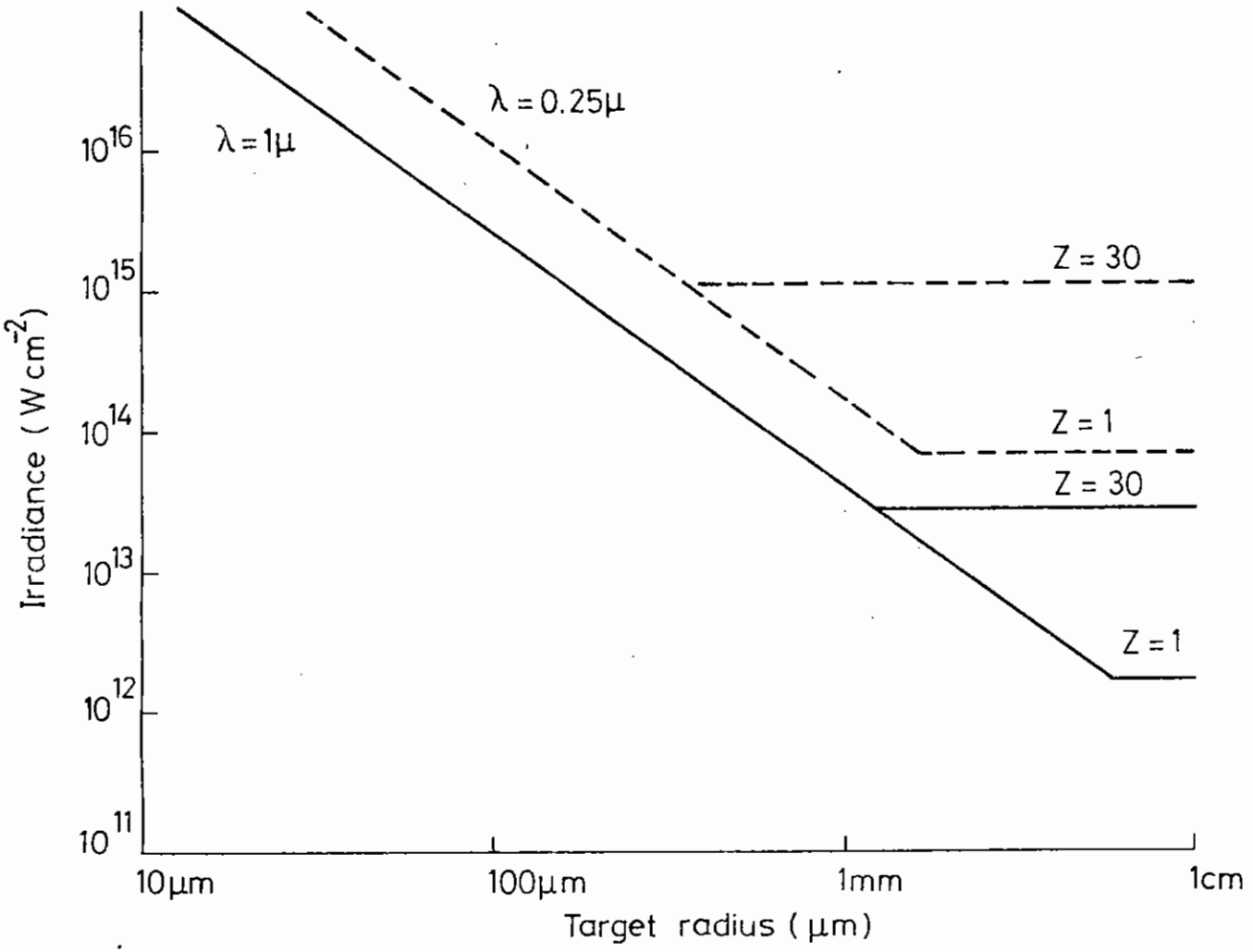

Fig.3.27

Locus of threshold of SBS as set by inverse bremstrahlung (ϕ vs R_c)

3.4.2 Saturation of Brillouin Scattering

As laser driven implosion experiments move to longer pulse durations and consequently to larger amounts of underdense plasma the problem of Stimulated Brillouin Scattering (SBS) becomes more severs. SBS has been the subject of much theoretical and experimental work (3.41) - (3.44) and in particular it is important to know the saturated level of Brillouin scattering (3.39, 3.45, 3.46).

The ion wave generated by SBS may saturate either by particle trapping or by ion Landau damping. Generally the wave will first saturate by ion trapping and will then heat the ions (also producing a nonthermal tail to the ion distribution) eventually causing ion Landau damping. It is the purpose of this note to show that in the presence of ablation at approximately the ion sound speed, the equilibrium ion temperature may be too low to produce significant ion Landau damping. The SBS is then limited only by ion trapping and may lead to extremely high reflectivities, with a consequent serious drop in the energy absorbed by the plasma.

3.4.2(a) Saturation by Ion Trapping

This case has been treated by Kruer (3.39); he considers a slab of uniform underdense plasma of length L and electron density n_p, with the laser intensity well above threshold. If the saturated amplitude of the ion wave is δn then the reflectivity r is given by

$$r = \left(\frac{1-\beta^2}{1+\beta^2}\right)^2 \quad \text{where } \beta = \exp\left(-(\alpha L \frac{\delta n}{n_p})\right) \tag{1}$$

and

$$\alpha = \frac{\frac{\pi}{2} \, n_p/n_{cr} \, 1/\lambda_o}{\sqrt{1 - n_p/n_{cr}}}$$

n_{cr} is the critical density for absorption of laser light of wavelength λ_o.

The amplitude of the ion wave as limited by ion trapping is given by Kruer

$$\delta n/n_p = \tfrac{1}{2}(\sqrt{1 + T_i/ZT_e} - \sqrt{3T_i/ZT_e})^2 \quad , \tag{2}$$

where T_e, T_i are the electron and ion temperatures and Z is the average ion charge.

When the amplitude of the ion wave has reached a steady state all the energy pumped into the ion wave by the Brillouin scattering process will appear as ion heating. For low density plasmas, of low atomic number Z, the ion thermal equilibration time τ_i will be long compared to the characteristic time for ion heating and a nonMaxwellian tail to the ion distribution will be formed. For the sake of simplicity we neglect this effect and describe the ions by a single temperature T_i. We also neglect the effects of ion thermal conduction which is a good approximation in a plasma ablating at the ion sound speed.

For very short wavelength lasers, $\lambda_o \sim 0.1\ \mu$ and Z = 1 we note that ion-electron thermal relaxation, producing $T_i \simeq T_e$, is important in determining the saturated level of SBS. For the remainder of this note we neglect this effect which occurs only for the shortest wavelengths of interest.

3.4.2(b) Saturation by Ion Heating

Suppose a fraction r of the incident laser flux ϕ is backscattered from a length L_B of plasma at an electron density $n_p = B\, n_{cr}$. The rate at which the ions will be heated is

$$k \frac{\partial T_i}{\partial t} = \frac{r \, \phi \times 10^7 \, \omega_{ia}/\omega_o}{L_B \, (B \, n_{cr}/Z)} \tag{3}$$

where k is Boltzmann's constant, ω_{ia}, ω_o are the frequencies of the ion accoustic wave and the laser respectively and the factor of 10^7 arises because we consider ϕ to be in W cm^{-2} and all the other quantities to be c.g.s.

The cooling of the ions may be calculated by either of two methods which yield essentially the same result.

(i) If we consider adiabatic expansion of the ions at a velocity v across a density scale length of L_D then in the steady state the cooling rate is

$$\frac{1}{T_i}\frac{\partial T_i}{\partial t} = -\frac{(\gamma-1)v}{L_D} \qquad (4)$$

where γ is the adiabatic index of the ions, we take $\gamma = 5/3$.

(ii) If we consider the ions within the length of plasma L_B (which contains the ion wave) to be heated to a temperature T_i much larger than the temperature at which ions enter this region through the ablation flow, then the rate at which energy is advected away by the flow is

$$k\frac{\partial T_i}{\partial t} = -(kT_i)\cdot\frac{v}{L_B} \qquad (5)$$

Within the approximation that

$$L_B \sim L_D/(\gamma-1)$$

these two formulations lead to identical results. We take the more convenient form

$$\frac{1}{T_i}\frac{\partial T_i}{\partial t} = -\frac{v}{L_B}\ .$$

Here v is the ablation velocity relative to the frame in which the plasma density profile is stationary. Experimental evidence (3.47) and also general fluid dynamic arguments would suggest that $v \simeq v_{ia}$, i.e. the ablation is approximately sonic near critical density.

Equating the heating and cooling rates we obtain the equilibrium ion temperature

$$T_i = \frac{Z\, r\, \phi \times 10^7\, \omega_{ia}/\omega_o}{k\, v_{ia}\, B\, n_{cr}}$$

and using $\omega_{ia}/v_{ia} = k_{ia} \simeq 2k_o$ we obtain

$$T_i = \frac{2 \times 10^7\, Zr\, \phi}{c\, B\, n_{cr}} \qquad (6)$$

using more usual units with T_i in eV and the laser wavelength λ_o in μm we have numerically

$$T_i = 4.16 \times 10^{13}\ \frac{Z\, r(\phi\lambda^2)}{B}\ \text{eV}.$$

3.4.2(c) Saturated Level of Brillouin Scattering

In the general case we may calculate the saturated level of SBS as follows. Taking the equations (1) and (2) we calculate r, assuming T_i/T_e to be small. Using (6) we calculate T_i and at this point we need to have an independent estimate of T_e in order to close the set of equations and iterate to a solution. If the first estimate of T_i yields $T_i \gtrsim \frac{ZT_e}{2}$ then the ion wave is saturated by ion Landau damping rather than particle trapping and we may obtain the reflectivity directly from equation (6), in which case the result is independent of the size of the underdense plasma

$$\text{i.e.} \qquad \frac{2 \times 10^7\, Z\, r\, \phi}{c\, B\, n_{cr}} = \frac{ZT_e}{2}$$

and

$$r = \frac{T_e\, c\, B\, n_{cr}}{4 \times 10^7\, \phi} \qquad (7)$$

or in the same convenient units as used previously

$$r = 2.4 \times 10^{12}\ \frac{BT_e}{(\phi\lambda^2)} \qquad (7a)$$

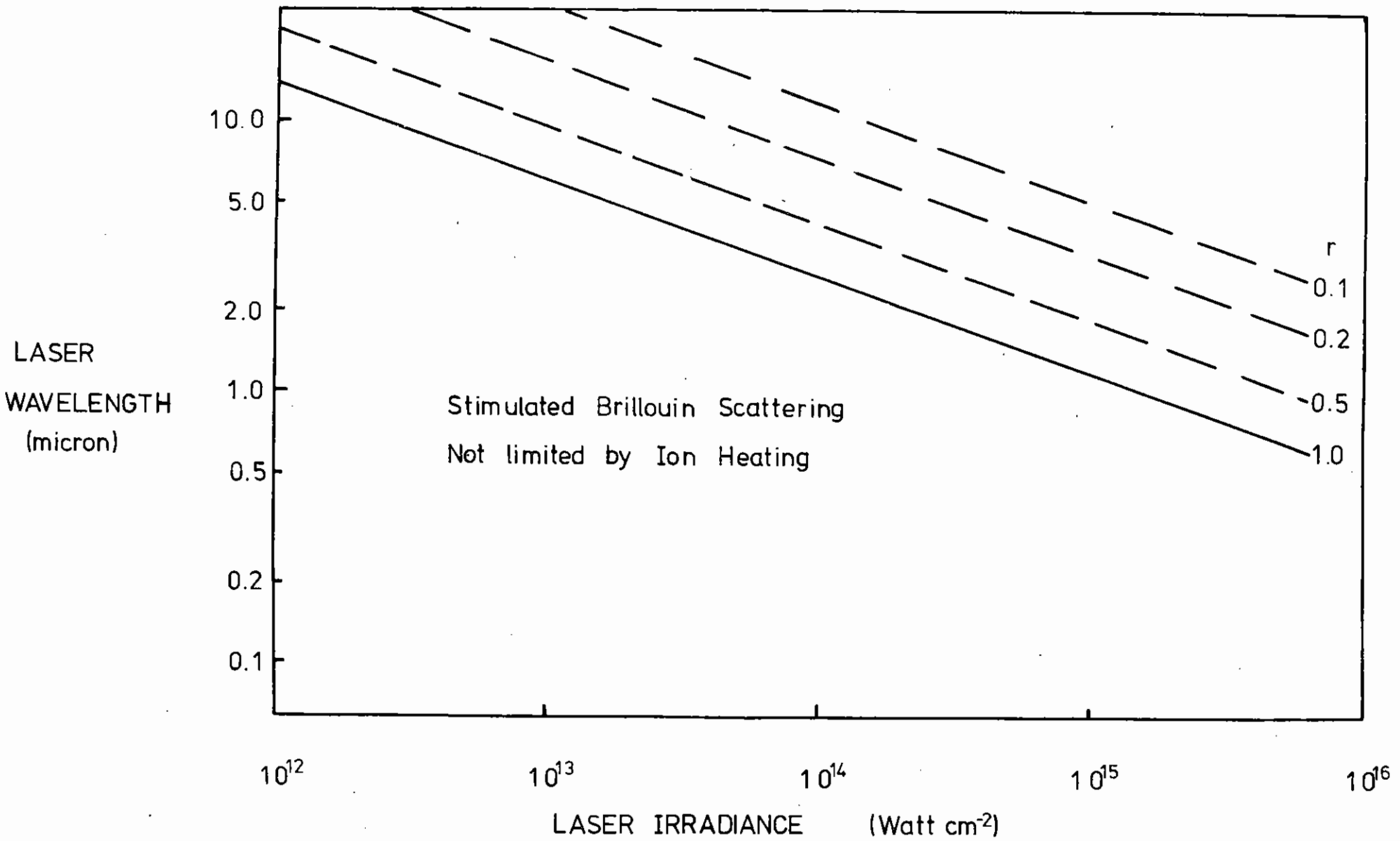

Fig 3.28 Saturation of Brillouin Scattering by Ion Heating

3.4.2(d) Discussion

Equation (7a) shows immediately that given a large amount of underdense plasma, short wavelength lasers may be subject to large amounts of SBS because of their large critical density. Long wavelength lasers are less subject to SBS because of the smaller heat capacity of the underdense plasma. If we take the case $\phi = 10^{15}$ W cm^{-2}, $\lambda = 1$ μ and take $T_e \simeq 5$ keV (the value of T_e at subcritical densities is rather uncertain (3.47) and $B = 0.1$ as suggested by plasma simulations (3.41)), then $r = 1.2$, i.e. the ions cannot reach $T_i = ZT_e/2$, even with 100% backscatter.

In order to obtain a general indication of the values of ϕ and λ for which large values of SBS may be expected we take $B = 0.1$ and a simple formula for T_e based on a steady state ablation model of Ahlborn (3.43)

$$T_e \simeq 10^3 \ (\phi\lambda)^{4/9} \ \text{eV},$$

thus

$$r = \frac{2.4 \times 10^6}{\phi^{5/9} \ \lambda^{14/9}} \qquad (8)$$

Fig.3.28 shows r for various values of ϕ and λ and also the region where ion heating does not cause saturation of the Brillouin scattering. In this region an iterative solution to equations (1), (2) and (6) will yield the reflectivity.

From Fig.3.28 we see that a CO_2 laser at a target irradiance of $\phi = 10^{14}$ W cm^{-2} could never produce more than about 10% Brillouin scatter because of ion heating, at $\phi = 10^{13}$ W cm^{-2} the same laser could produce about 50% SBS. We note that despite the simplicity of the model these results agree rather well with data obtained with the HELIOS laser LASL (3.48) and by Offenberger's group at Alberta (3.46). In the same range of irradiances a 1.06 μ laser could produce 100% backscatter given a large enough volume of underdense plasma.

R.G. Evans

CHAPTER 3 REFERENCES

3.01 O N Krokhin, V V Pustovalov, A A Rupasov, V P Silin, G V Sklizhov, A N Starodub, V P Tikhonchuck and A S Shikanov, JETP Lett 22, 21 (1975).

3.02 VP Silin, Parametricheskoevozdeistvie izlucheniya bolshoi moschchnosti na plazmu, Nauka Moscow (1973).

3.03 S J Gitomer and D B Henderson, Phys Fluids 22, 364 (1979).

3.04 R A Cairns, J Plasma Phys 22, 149 (1979).

3.05 C S Liu, M N Rosenbluth and R B White, Physics of Fluids 17, 1211 (1974).

3.06 C S Liu and M N Rosenbluth, Physics of Fluids 19, 967 (1976).

3.07 1979 Rutherford Annual Report, RL-79-036.

3.08 P D Carter, S M L Sim, H C Barr and R G Evans, to be published in Phys Rev Letts.

3.09 A I Avrov et al, Societ Physics JETP 45, 507 (1977).

3.10 H C Barr, private communication

3.11 T P Hughes, 20th SUSSP, St Andrews 1979.

3.12 W L Kruer et al, Lawrence Livermore Laboratory Report UCRL-82394.

3.13 C E Max and C F McKee, Phys Rev Lett 39, 1336 (1977).

3.14 A Ng, L Pitt, D Salzmann and A A Offenberger, Phys Rev Lett 42, 5 (1979).

3.15 Rutherford Lab Report RL-79-036 (1979) section 3.4.

3.16 M Rosen et al, UCRL Preprint 82146, submitted to Phys Fluids.

3.17 M N Rosenbluth and A A Sagdeev, Comments on Plasma Physics and Fusion 1, 129-136 (1972).

3.18 Ping Lee, D V Giovanelli, R P Godwin and G H McCall, Appl Phys Lett 24, 406-408 (1974).

3.19 J L Bobin, M Decroisett, B Meyer and Y Vitel, Phys Rev Lett 30, 594-597 (1973).

3.20 H A Baldis, J C Samson and P B Corkum, Phys Rev Lett 41, 1719 (1978).

3.21 W L Kruer, K G Estabrook and K H Sinz, Nucl Fusion 13, 952 (1973).

3.22 D Biskamp and H Welter, Phys Rev Lett 34, 313 (1975).

3.23 C S Liu, M N Rosenbluth and R B White, Phys Fluids 17, 1211 (1974).

3.24 M N Rosenbluth, Phys Rev Lett 29, 565 (1972).

3.25 H H Chen and C S liu, Phys Rev Lett 39, 881 (1977).

3.26 J F Drake and Y C Lee, Phys Rev Lett 31, 1197 (1973).

3.27 W L Kruer, K Estabrook, B F Lasinski and A B Langdon, Lawrence Livermore Lab Report UCRL-82394.

3.28 S J Gitomer and D B Henderson, Phys Fluids 22, 364 (1979).

3.29 D T Attwood, D W Sweeney, J M Auerbach and P H Y Lee, Phys Rev Lett 40, 184 (1978).

3.30 A Raven and O Willi, Phys Rev Lett 43, 278 (1979).

3.31 J P Christiansen, D E T F Ashby and K V Roberts, Comp Phys Com 7, 271 (1974).

3.32 M H Key et al, Rutherford Lab Rep RI-79-014 (1979) (unpublished).

3.33 K Estabrook and W L Kruer, Phys Rev Lett 40, 42 (1978).

3.34 C E Max and C F McKee, Phys Rev Lett 39, 1336 (1977).

3.35 F J Mayer, R K Osborn, D W Daniels and J F McGrath, Phys Rev Lett 40, 30 (1978).

3.36 Rutherford Lab Annual Report, RL-79-036
P D Carter, S M L Sim and T P Hughes, Opt Comm 27, 423 (1978).

3.37 P A Jaanimagi, G D Enright and M C Richardson, IEEE Trans Plasma Sci, PS-7, 166 (1979).

3.38 C S Liu, M N Rosenbluth and R B White, Phys. Fluids 17, 1211 (1974).

3.39 W L Kruer, Lawrence Livermore Laboratory preprint UCRL 82701 (1979). Submitted to Phys. Fluids.

3.40 R G Evans, Rutherford Laboratory Report RL-79-061 (1979). Submitted to Plasma Physics.

3.41 D W Forslund, J M Kindell and E L Lindman, Phys. Fluids 18, 1017 (1975).

3.42 T P Hughes, "Plasmas and Laser Light", published by Adams Hilger, p.45.

3.43 B Ahlborn, Rutherford Laboratory Report RL-79-047 (1979).

3.44 B H Ripin, J M McMahon, E A McLean, W M Manheimer and J A Stamper Phys. Rev. Lett. 33, 634 (1974).

3.45 W L Kruer, E J Valeo and K G Estabrook, Phys. Rev. Lett. 35, 16 (1975).

3.46 A Ng, D Salzmann and A A Offenberger, Phys. Rev. Letts. 42, 307 (1979).

3.47 M D Rosen, D W Phillion, V C Rupert, W C Mead, W L Kruer, J J Thompson, H N Kornblum, V W Slivinsky, D J Caporaso, M J Boyle and K G Tinsell, Lawrence Livermore Laboratory preprint UCRL 82146 (1978). Submitted to Phys. Fluids.

3.48 D W Forslund, paper presented at the 9th annual conference on Anomalous Absorption of Electromagnetic Waves, May 15 - 18, 1979, University of Rochester, NY (1979) (unpublished).

CHAPTER 4 TRANSPORT AND PARTICLE EMISSION

INDEX

CHAPTER EDITOR: W T Toner

CHAPTER 4 TRANSPORT AND PARTICLE EMISSION

4.1 Introduction

The work of this group in the past year has centered around the avoidance of fast electron preheat whether by resistive inhibition (sec.4.2) or the use of shorter wavelengths (sec.4.3). Substantial preheat reduction was found to be produced by the use of small amounts of gold deposited on targets at one percent of solid density. Experiments are planned for the coming year to see if this can be exploited in implosions. Long pulse green irradiations showed very significant increases in ablation pressure above the values obtained with 1.06 μm and have led to the plan to use six green beams for implosion physics later this year.

A small number of exploding pusher targets were irradiated during the commissioning of the six beam target area (sec.4.4). The more uniform irradiation led to implosions which were much more symmetrical in appearence when viewed with the X-ray pinhole camera. Neutron yields of well over 10^7 per shot were recorded but this increased yield was principally due to better matching of the laser pulse length and energy to the target parameters, and no effect depending on illumination symmetry was found in a rather brief trial.

W T Toner

4.2 Resistive Inhibition of Preheat

It is now well established that when high intensity light is incident on solid targets a considerable fraction of the laser energy is converted into suprathermal electrons with a temperature T_H much greater than that of the thermal plasma (4.01, 4.02, 4.03). Some of the energy of these electrons heats the target to comparatively large depths. Experiments using 1.06 μm lasers on layered targets containing K fluors (4.04) have measured the range of these suprathermal electrons and found that the range was consistent with the hard X-ray measurement of temperature and the Bethe-Bloch formula (4.05) for energy loss with scattering included.

Preheat would have to be minimised for an ablative compression, and the use of a vacuum gap (4.06) might be one way of optimising a target to prevent preheat. In this report we demonstrate an alternative target design for reducing the preheat range by including a high resistivity, low volume density material within the target. The effect is explained simply; it is confirmed by a numerical simulation and by direct experimental measurements.

Consider a laser beam incident on a semi-infinite plane target. A fraction of the absorbed laser power is converted into suprathermal electrons flowing into the target carrying a current density j_H, which is typically 10^{10} A cm^{-2} at an intensity of 10^{15} W cm^{-2} (4.04). The very high energy deposition rapidly ionises the target which becomes a high electron density ($N_e \sim 10^{23}$ cm^{-3}), low electron temperature ($T_e \sim 200$ eV) plasma of resistivity η. As such a plasma has a very small skin depth for the time-scale of the laser pulse, a return curent j_c must flow so that:

$$j_H + j_c = 0$$

The resistive electric field $E = \eta j_c = -\eta j_H$, decelerates the suprathermal electrons, converting a part of their energy into Ohmic heating; ηj_c^2. If the collisional range of the suprathermal electrons is r_a(gm cm^{-2}) and the target density is ρ then in the absence of electric field inhibition the suprathermal electrons will go a distance r_a/ρ, and the electrostatic potential a distance r_a/ρ into the target will be $\eta j_H r_a/\rho$. However if $\eta j_H r_a/\rho \gtrsim kT_H/e$ the resistive electric field will appreciably impede the suprathermal electrons. The potential within the target is estimated in Table 1 for solid density gold and for gold at 1% of its solid density (0.2 gm cm^{-3}), with $j_H = 10^{10}$ A cm^{-2} for 100 ps as suggested by experiment (4.04). The resistivity is calculated using LTE (4.07) and Spitzer resistivity (4.08). It is clear that in normal density gold the target potential is negligible compared with the electron energy whereas in low density gold the target potential will be large and thus the suprathermal electrons will be inhibited by the resistive electric field. The three factors in low density gold which enhance

this inhibition are (i) the large stopping distance r_a/ρ at low density, (ii) the high state of ionisation ($\sim$ 30) achieved for small temperature rises in gold, (iii) the LTE state of ionisation being larger at lower electron density for a given T_e.

DENSITY	SOLID	1% SOLID
Target thickness (X)	0.5 μm	50 μm
Current density (j_H)	10^{10} A cm^{-2}	10^{10} A cm^{-2}
Resistivity (η) (LTE and SPITZER)	$8 \times 10^{-5}\Omega$ cm	$4 \times 10^{-4}\Omega$ cm
POTENTIAL j_H η X	40 V	2×10^{4} V

TABLE 4.01

To predict the effect of the resistive electric field we have used a Monte Carlo calculation with a self consistent electric field. Hydrodynamics and thermal and radiation transport are neglected. The transport of the fast electrons at any one time is solved iteratively by a time independent Monte Carlo transport calculation in slab geometry. The scattering is represented by random Rutherford scattering from Fermi screened nuclei and Debye shielded ions. In between the scattering events electrons follow parabolic trajectories representing the effect of the resistive electric field. A new electric field is determined from Ohm's law using a resistivity given by the equation of state for the local energy deposition

and Ohmic heating up to that time, and $j_c = -j_H$ determined from the transport calculation. The electron transport is then iterated to find a consistent E and j_H. The collisional energy deposition is calculated using the continuous slowing down approximation accounting for bound electrons (4.05) and plasma electrons (4.09).

The calculation was used to simulate typical experimental parameters. Experiments at $I = 3 \times 10^{15}$ W cm^{-2} indicate (4.10) that the fast electron energy spectrum is of the form $f(u) = u^{3/2} \exp(-u/kT_H)$ with $T_H \approx$ 14 keV and with 8% of the incident energy in this distribution. Fig. 4.01 shows model results for this distribution. It is clear that in the solid density gold targets the resistive field has a negligible effect, whereas for low density gold the range is reduced because of the resistive electric field.

To confirm the effect an experiment was performed using tracer layers to detect fast electrons by the K_α radiation they produced (4.04). Targets were normally irradiated with 10 J, 90 ps, 1.05 μm laser pulses focused with a f/1 lens to a 70 μm diameter spot, at an intensity of 2.8×10^{15} W cm^{-2}. The targets consisted of 0.1 μm Al; 2.5 μm mylar; 3 μm KCl; Gold; 2 μm CaF_2, and were fabricated by evaporating the various layers onto the mylar substrate. A very thin (0.01 μm) layer of CaF_2 was deposited on top of the aluminium on some shots to provide marker lines in the region of CaK_α. The gold layer was deposited at various densities. Solid gold layers were made by vacuum evaporation; low density layers ($\sim$ 1% solid density) were made by slowly evaporating the gold in an atmosphere of 800 mTorr of argon thus creating voids in the gold. The targets were constructed in pairs of equal area mass density but with solid and $\sim$ 0.6% solid density gold. The area density of the low density targets was determined by weighing and measuring their depth with a scanning electron microscope. The structure of the low density gold is on a submicron scale length. Expansion velocities are sufficiently high that it becomes uniform before the peak of the laser pulse.

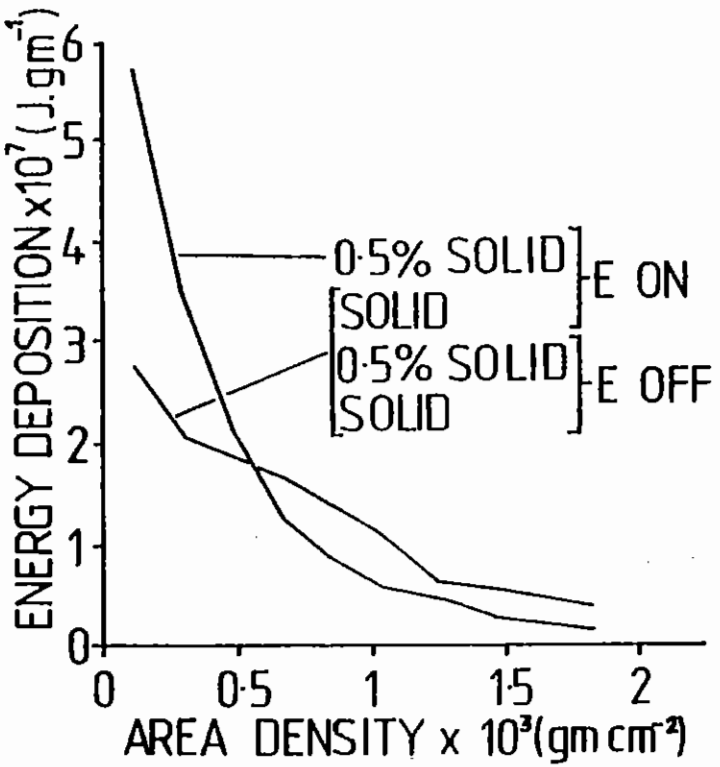

Fig.4.01

Computational results for solid and low density targets. At the rear of the low density target ∿ 50% of the deposition is due to J.E.

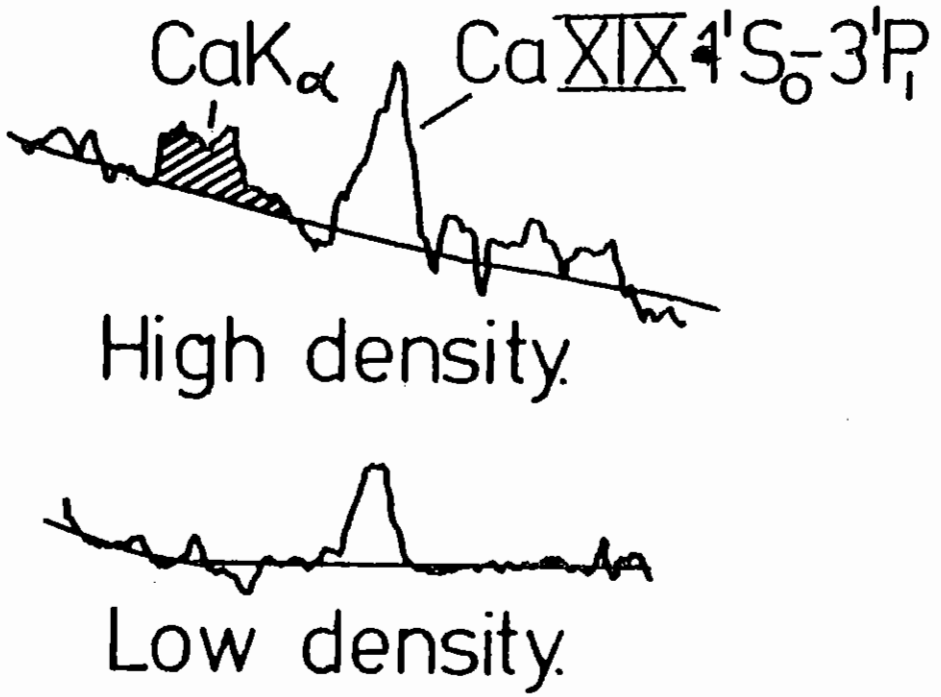

Fig.4.02

Microdensitometer tracings in the region of the CaKα line for a typical pair of targets containing equal area mass densities but different volume densities of gold. For these particular shots the area mass density of gold was 0.72 mg cm ^{2}. The density of the low density layer was 0.62% solid.

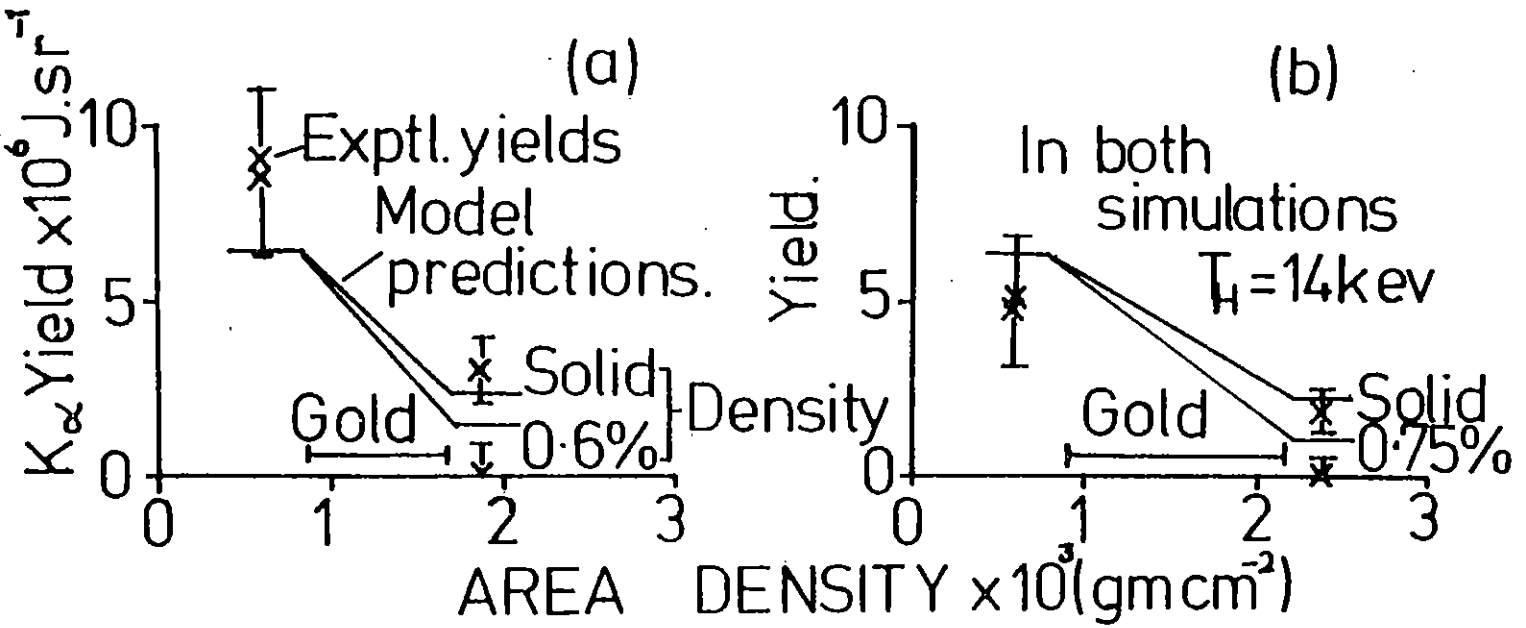

Fig.4.03

Experimental and predicted Kα yields for two pairs of high and low density targets. In both cases the predicted inhibition is less than that observed.

The laser was incident on the aluminium which provided a flat and well characterised ablation plasma. The Ca in CaF_2 and K in KCl acted as fast electron detectors by the K_α emission that was induced in them (4.04). The gold acted as a variable density electron filter. However, as shown below, the depth within the target of the gold reduced the resistive inhibition effects.

The K_α emission was recorded by two miniature, flat, P.E.T. crystal spectrometers, absolutely calibrated in sensitivity (4.04). One spectrometer was placed at the front of the target and recorded the K K_α emission and the Al plasma radiation. The other, at the rear, recorded the Ca K_α emission.

A typical tracing of the Ca K_α line for low and high density gold of the same area density is shown in Fig. 4.02 . With low density gold there is no observable K_α line. The yields either side of the gold are shown in Fig. 4.03 . The large error bar on the zero value with low density gold is due to consideration of spatial spreading of the fast electrons as they pass through the gold. Nevertheless it is clear that low density gold reduces the K_α yield, and therefore the energy deposition by fast electrons, by at least a factor of 3 over the same area density of high density gold.

The K_α yields predicted by the Monte Carlo calculation are also shown in Fig. 4.03. The inhibition predicted for low density gold is small compared with the case in Fig. 4.01 because of the large amount of material that electrons have to pass through before they reach the gold. The predicted inhibition in Fig. 4.03 is also much less than observed experimentally. This is probably due to defects in the model, the most important being the application of the Spitzer formula to a low log Λ (~ 2) partially stipped plasma where the minimum impact parameter is $\lesssim$ the size of the atoms. The modelling was repeated with increased coefficients of resistivity. A factor of three increase in resistivity brought the low-density Ca K_α yields just inside the experimental error bars.

In conclusion we have shown both theoretically and experimentally that

fast electron specific energy deposition can be greatly increased by the use of a suitable low density target material. This effect could be advantageous in ablative type compressions. For targets with high and low density layers of similar area mass density a larger irradiance may be used with the low density target before preheat becomes important.

D J Bond, J D Hares and J D Kilkenny.

4.3 Time Resolved Measurements of X-ray Emission and Ablation Pressure

A series of experiments was undertaken to examine the wavelength dependence of the ablation pressure. At the beginning of the run an unexpected time dependence in hard x-ray emission was discovered as discussed in 4.3.1. This led to the series of measurements of ablation rates using time resolved spectroscopy described in 4.3.2.

4.3.1 Streaked X-ray Imaging and Pulsing Hard X-ray Targets

Thin Al foils were irradiated near an edge by 600 ps 0.53 μm laser pulses. The 2 keV X-ray emission from the front of the targets was imaged with a 10 μm Cu slit onto the photocathode of an X-ray streak camera as shown in Fig.4.04 together with a typical streak. The lines on the streak are the shadow of a fiducial grid on the front of the photocathode with a spacing corresponding to 25 μm in the object plane. It had been hoped to observe motion of the X-ray emitting region due to acceleration of the Al foil by the ablation pressure. However, as seen in Fig.4.04, no such motion was observed although the expansion of the plasma plume back towards the incident laser at a velocity of 2×10^7 cm s^{-1} is clearly visible. With hindsight the absence of observable motion is consistent with the pulse length which was unknown at the start of this run.

Experiments were also performed with layered targets consisting of thick Al, 1.8 μm of plastic and 20 nm of Pt. The resulting streak is shown in Fig.4.05. It had been hoped to observe pulsing in the X-ray emission through the slit, corresponding to the ablation front being in various average Z plasmas at different times during the pulse. A microdensi-

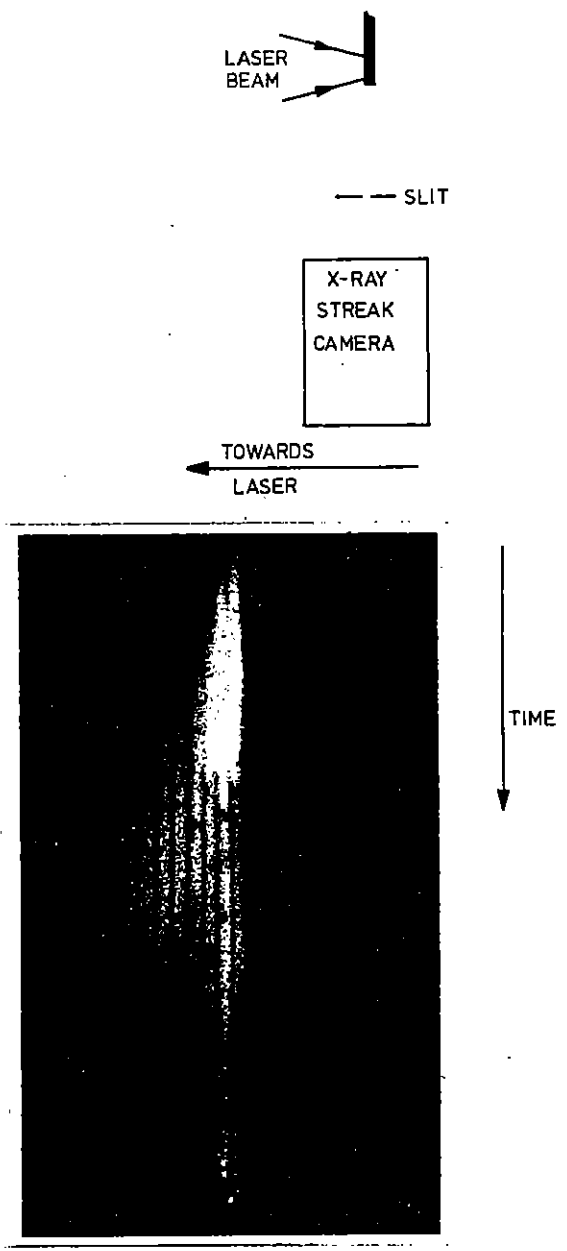

Fig.4.04

Diagram of target, slit and streak camera arrangement and resulting streak record.

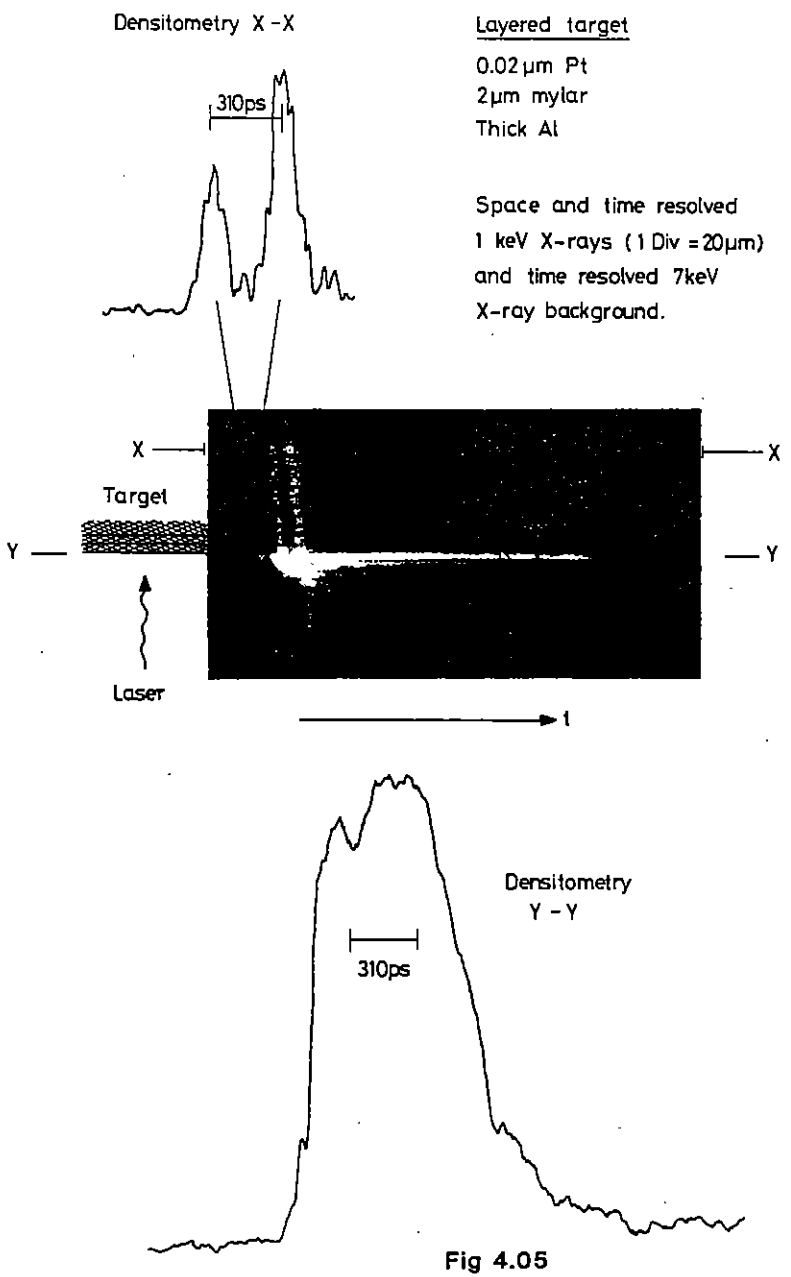

Fig 4.05

tometer tracing along the soft X-ray image is shown on Fig.4.05 and indicates a double pulse in the soft X-ray emission but with little contrast. However, there is clearly pulsing on the photocathode on both sides of the image. This is due to transmission of hard X-rays at $h\nu$ = 8 keV through the 'K window' of the Cu slit. The hypothesis is that when the absorption region of the plasma is in a high Z (i.e. Al or Pt) plasma the hard X-ray emission is substantially higher than if the absorption region is in a low Z (CH) plasma.

Further experiments were then performed deliberately observing hard X-ray emission. The imaging slit in front of the streak camera was replaced by three K edge filters: 12.5 μm Ti (4.5 keV), 10 μm Cu (8 keV) and 25 μm Fe (6.5 keV). The laser pulse length was also increased to 1.3 ns. Fig.4.06 shows the streak record for a target with a 2 μm mylar layer between 20 nm of Pt and an Al backing. The streak clearly shows two pulses of hard X-rays within the 1.3 ns f.w.h.m. laser pulse. Note that although the Fe filter is softer than the Cu filter the streak record is fainter as the peak transmission is 0.3 compared with 0.75 for the Cu filter. When densitometered and converted to X-ray intensity using the H-D curve of the film (H-P 6) the X-ray emission is found to reduce in intensity by a factor of 20 in the centre of the laser pulse, due to the mylar in the centre of the target.

To corroborate this observation a similar target, except that the mylar thickness was increased to 3.5 μm, was irradiated. The streak record in Fig.4.07 clearly shows only the first pulse of hard X-rays. Presumably the laser did not burn through the thicker plastic during the laser pulse.

This appears to be a way in which a short pulse of hard X-rays can be produced from a long laser pulse. Fig.4.06 shows that a 220 ps f.w.h.m. hard X-ray pulse can be produced from the 1.3 ns laser pulse. This corresponds to burning through the 20 nm of Pt: if a thinner layer of Pt were used, the hard X-ray pulse might be shorter. This type of target is potentially useful in providing a short pulse backlighting source for radiography of a target imploded by a long laser pulse.

Experiments were repeated at λ = 1.06 μm. However, no pulsing was observed, the hard X-ray pulse being of similar length to the laser pulse.

4.3.2 Measurement of the Mass Ablation Rates and Ablation Pressures for 1.05 μm and 0.53 μm Laser Pulses by Time Resolved Spectroscopy

The generation of high pressure by a laser interacting with a solid results from absorbed laser energy penetrating to a density greater than the critical density and causing an ablative flow of material towards the incident beam. Measurement and understanding of the ablation rate and pressure are crucial for laser compression.

Several measurements of ablation pressure P_a have been made at low intensities I $\sim 10^{13}$ W cm^{-2} with 1.06 μm light(4.11, 4.12, 4.13). At higher intensities, $\sim 10^{14}$ W cm^{-2}, measurements of P_a have been either by shock wave propagation(4.14, 4.15), or by torsion balance measurements (4.16), or spectroscopically (4.17). The drawback of the first two methods is that it is not easy to distinguish between momentum imparted to the target (or shock wave) over a time considerably longer than the laser pulse by relaxation of a layer of target preheated by fast electrons (4.18). It is in the high intensity regime that electron preheat becomes dominant.

In this section we describe the use of time resolved X-ray spectroscopy to obtain instantaneous mass ablation rates, $\dot{M}$, over a wide range of intensities at 1.05 μm with 1.5 ns pulses, and over a narrower range of intensities with 0.53 μm laser pulses. Values of P_a are also deduced from $\dot{M}$ and ion measurements. The results show a clear advantage in using 0.53 μm pulses.

A 1.05 μm single laser beam giving about 130 J in 1.5 ns was used for these experiments. About 60 J of this wavelength could be delivered onto a target with an f/1 doublet. The prepulse energy was 10^{-7} of the incident energy. Alternatively, the beam was frequency doubled, the 1.05 μm energy was rejected and 15 J in 1.3 ns was delivered on target by the same doublet but set for minimum aberration at 0.53 μm (4.19). The targets

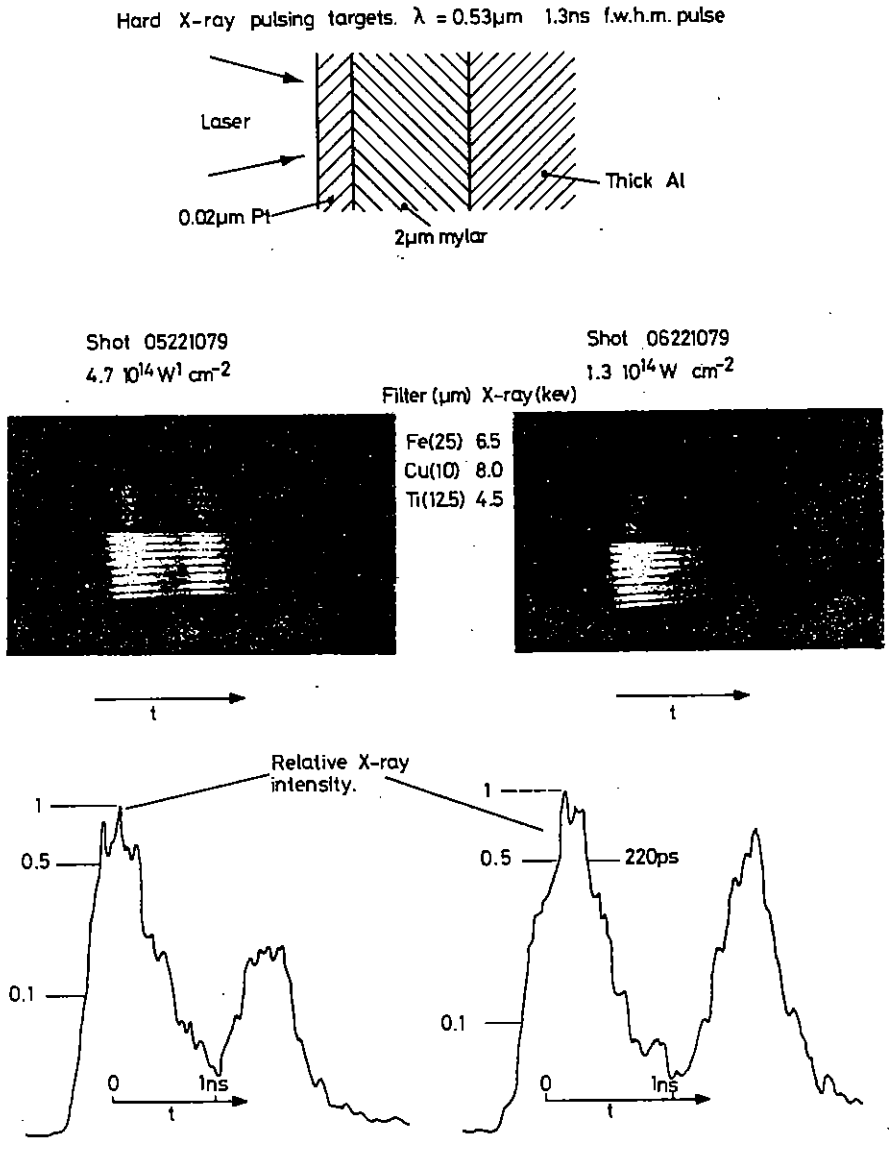

Fig 4.06

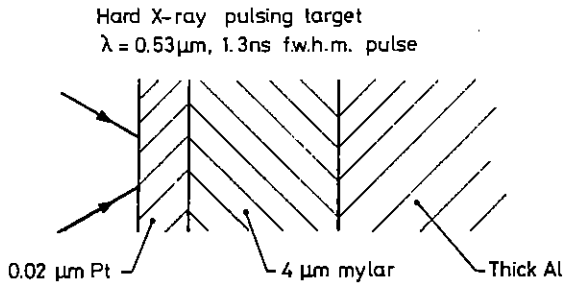

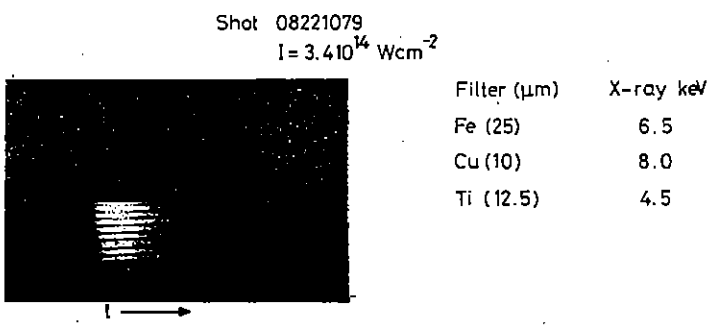

Filter (μm)	X-ray keV
Fe (25)	6.5
Cu (10)	8.0
Ti (12.5)	4.5

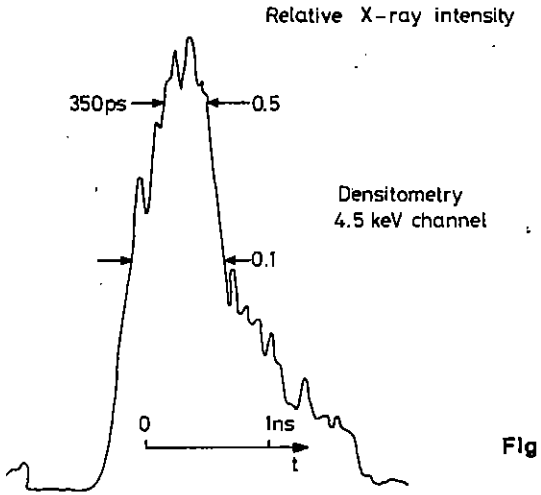

Fig 4.07

for the 1.05 μm experiments had various thicknesses of Al in the range 0.25 μm to 1 μm coated on glass microscope slides. The surface roughness was about 0.1 μm and it was established that the Al coating was not damaged by prepulses from the laser. Targets were inclined with their normal 15° from the axis of the laser beam and the intensity on target was varied by defocusing by known amounts. The intensity was calculated from the measured energy and pulse shape and the size of the X-ray image of the focal spot, which generally agreed with spot size calculated from the known defocusing.

X-ray spectral emission was measured with a time resolving crystal spectrometer. This consisted of a P.E.T. crystal, a low density CsI X-ray photocathode (4.20) and a streak camera with temporal resolution of 100 ps. A typical streaked spectrum is shown in Fig.4.08. There is a clear delay of $t_1 = 0.92 \pm 0.1$ ns between the Al line emission and the Si emission from the underlying glass. If t_1 is the time taken for the Al layer of initial thickness x to ablate, the mass ablation rate $\dot{M}$ is simply

$$\dot{M} = \rho x / t_1 \qquad (1)$$

For the experiments at 0.53 μm the targets were either Cr on Ti or CaF_2 on Ti and the spectral region about $\lambda = 2.7$ Å was examined.

On most shots a time integrated spectrum was also recorded with a P.E.T. crystal spectrometer. For the 1.05 μm laser shots the X-ray temperature could be deduced from the slope of the hydrogen and helium like Al recombination continuum. For the 0.53μm laser shots simple Al targets were used for this time integrated measurement. Ion emission at 15° to the target normal was measured by Faraday cups. The ion velocity v_i was deduced from the time of the peak of the signal and the distance.

Results are shown in Fig.4.09 for the three basic observables $\dot{M}$, T_e and v_i. Measurements were made up to a laser intensity of 3×10^{15} W cm^{-2} at 1.05 μm by using a tight focus with a measured X-ray spot of 30 μm

f.w.h.m., and down to 2 x 10^{13} W cm $^{-2}$. In this range, T_e and v_I are insensitive to both the intensity and the wavelength as shown in Fig.4.09. However, $\dot{M}$ scaled as $I^{0.3\pm.1}$ and in the range 2 - 6 x 10^{14} W cm^{-2}, $\dot{M}$ was 3 to 4 times larger at 0.53 μm than at 1.05 μm.

There are at least two possible experimental errors in deducing $\dot{M}$ as in Fig.4.09(c) from eqn.(1). Firstly, t_i is the delay in heating underlying material to a temperature at which it will emit appreciable helium- and hydrogen- like spectral lines. The heat wave will penetrate ahead of the critical density region. Stark broadening measurements (4.17) show that the density of the X-ray emitting region is 10^{22} cm^{-3}. For a simple estimate, if the heat flow in ($\tilde{=} \kappa T_e/L$) is equated to the enthalpy flux out, then for a perfect gas equation of state the area density of the penetration of the heat front is

$$t_H = 2nm_H L = \frac{4}{5}\frac{\kappa T_e m_H}{kT_e V}$$

For classical thermal conductivity κ, t_H is typically 10 μg cm^{-2} equivalent to 0.05 μm of Al. Typically 0.5 μm coatings of Al were used, so this emission from the underlying material is due mainly to ablation rather than conduction. Secondly, for the smallest focal spots used of 30 μm f.w.h.m., two dimensional effects (i.e. cratering) may make the measured $\dot{M}$ higher than it would be in the absence of edges. Finally, an improved value of $\dot{M}$ can be obtained by taking account of the intensity variation during the laser pulse. The laser pulse had a fast rise (0.3 ns) and a slow fall and can be represented by

$$I(t) = I_o(1 - t/t_o) \text{ with } t_o = 3 \text{ ns.}$$

Taking $\dot{M} = K\, I^{0.3}$ from Fig.4.09(c), K can be determined from

$$\rho x = \int_o^{t_1} K\, I^{0.3}\, dt$$

These corrected values of $\dot{M}$ evaluated at peak intensities are shown in Fig.4.10.

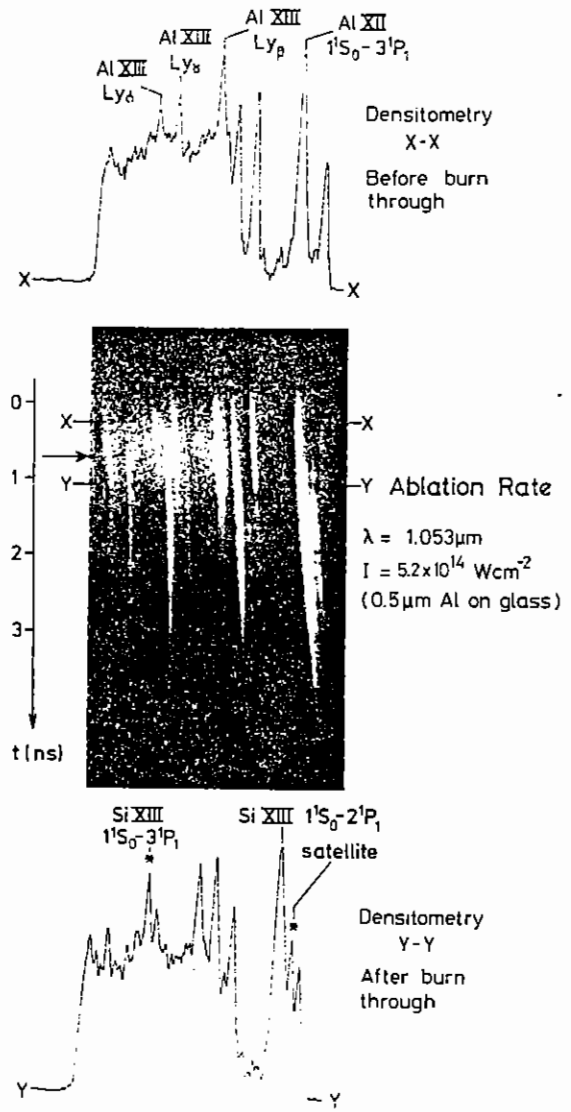

Fig.4.08

Typical streak from a target with a 0.5 μm coating of Al on glass at 5.2 10^{14} W/cm^2 showing aluminium and silicon hydrogen-and helium-like lines with a time delay of t_i = 0.92 ± .2 ns.

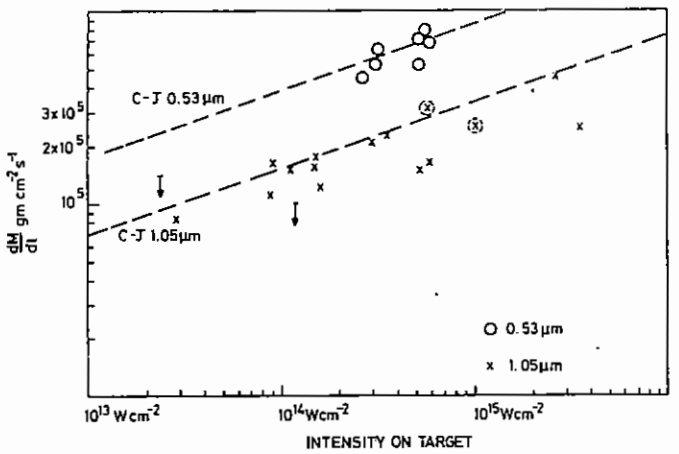

Fig 4.09(a) MASS ABLATION RATES FOR 1.5ns, 1.05μm PULSES AND 0.53μm PULSES

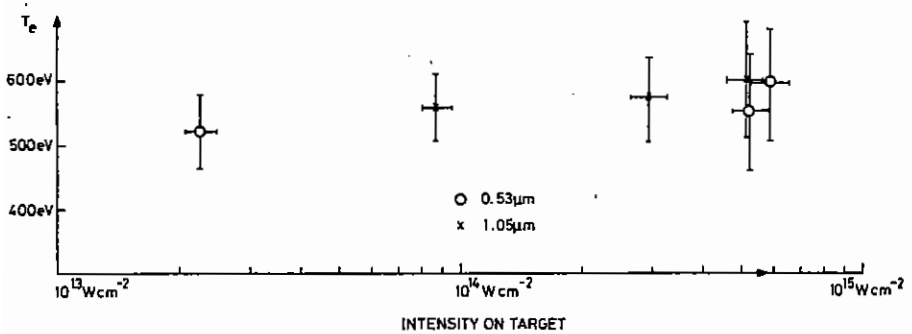

Fig 4.09(b)ELECTRON TEMPERATURE FROM RECOMBINATION CONTINUUM SLOPE

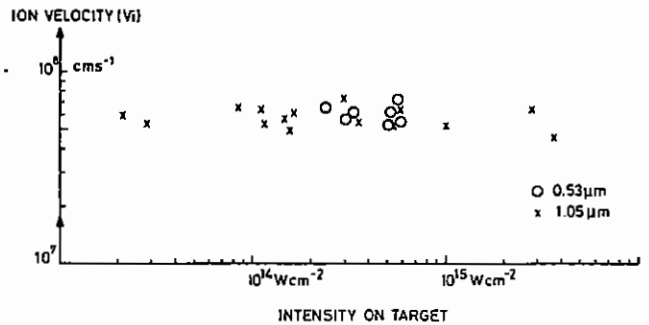

Fig 4.09(c)

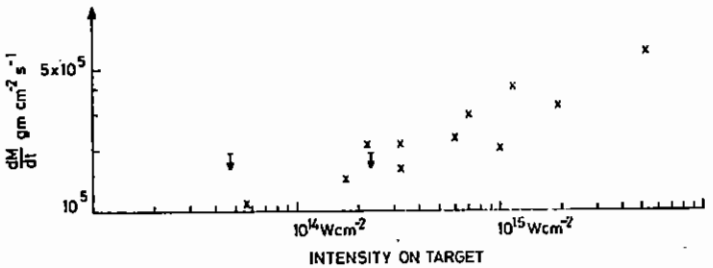

Fig 4.10 CORRECTED MASS ABLATION RATES FOR 1.5ns, 1.05 μm PULSES

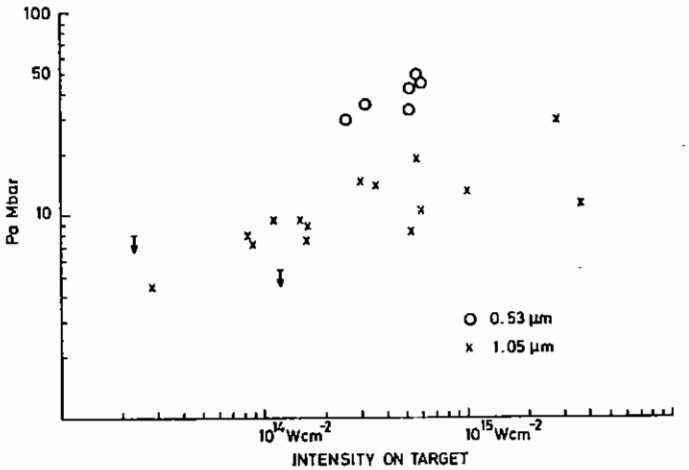

Fig 4.11 ABLATION PRESSURES FOR 1.5ns, 1.05 μm PULSES AND 1.3ns, 0.53 μm PULSES

Values for the ablation pressure P_a can be obtained simply from

$$P_a = \dot{M} v_i .$$

This is the ablation pressure that instantaneously imparts momentum to the expanding plasma plume. Note that this is a time resolved measurement in the sense that $\dot{M}$ is time resolved. Mass ablation at a later time due to relaxation of a deep lying layer heated by fast electrons would not be measured in this way. Values of P_a are shown in Fig.4.11.

A detailed comparison of these results with hydrodynamic simulations has not yet been made. However, comparison with the simple Chapman-Jouguet deflagration model (4.21) which gives

$$\begin{aligned} \dot{M} &\propto I^{1/3} \lambda^{-4/3} \\ v_i &\propto I^{1/3} \lambda^{2/3} \\ P_a &\propto I^{2/3} \lambda^{-2/3} \end{aligned}$$

is shown on Fig.4.09.

As can be seen, the mass ablation rate agrees quite well with the simple model for both wavelengths. However, this is presumably fortuitous as the ion velocity and therefore the ablation pressure are in disagreement with the simple model. It is interesting that the shape of the ion cup signal with time, and therefore the ion velocity distribution appeared to be independent of intensity.

Some of the factors omitted from this comparison are:

1) The comparison should be against absorbed laser intensity, not incident intensity. This is one reason why $\dot{M}$ is observed to be larger for 0.53 μm than 1.05 μm.
2) The transport of energy to higher density than critical should be considered. The fact that the measured $\dot{M}$ scales with I and λ, whereas v_i is essentially constant implies that the density in the ablation region is changing.

3) Two dimensional effects are probably important for small spot sizes, thus leading to an artificially high mass ablation rate at high intensity. One could speculate that in the absence of edge effects $\dot{M}$ might be independent of I for $I \gg 10^{14}$ W cm^{-2} as more energy is being absorbed into fast electrons in this regime and so is not contributing to prompt mass ablation.

In conclusion, we have used a new technique to measure the instantaneous mass ablation rate and shown that it scales as $I^{0.3}$ and is 3 to 4 times larger for 0.53 μm than for 1.06 μm laser pulses. This clearly demonstrates a significant advantage in using 0.53 μm rather than 1.06 μm light for compression.

M H Key, J D Kilkenny, C L S Lewis and S A Veats.

4.4 Experiments with Exploding Pusher Targets

4.4.1 Introduction

No systematic exploding pusher work was carried out in the past year but a few exploding pusher targets were irradiated during the commissioning of the six-beam target area. A marked improvement in the spatial symmetry of the implosion resulting from the use of six beam illumination is evident from the high resolution pinhole pictures discussed in section 1.6 (Figs. 1.15, 1.16 and 1.17). Some evidence for pusher-fuel mixing in the core was obtained from spectroscopic analysis of a shot on an argon filled target (4.4.2). The shorter pulse length and improved beam quality of the reconfigured laser led to enhanced neutron yields from D-T filled targets (4.4.3) but the yields did not seem to depend on the number of beams used. However, no attempt was made to optimise the focusing for maximum yield. Results from the Thomson parabola detector in two shots on plastic coated targets suggest that Si and O ions from the implosion core can be detected (4.4.4).

W T Toner

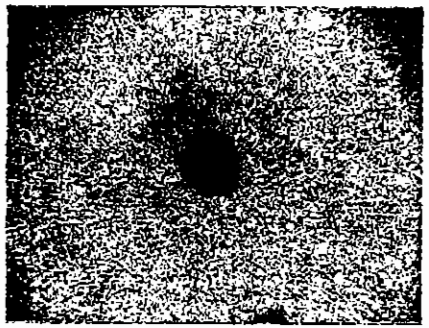

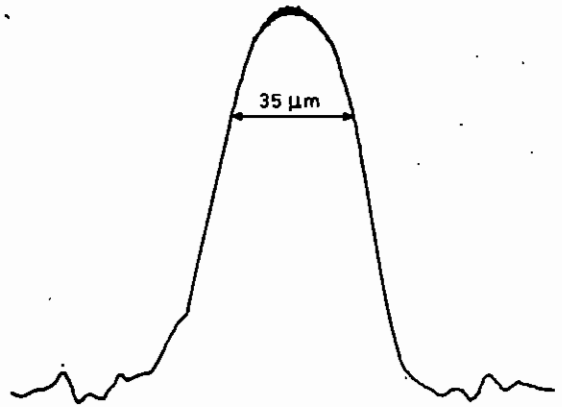

FIG. 4.12. PINHOLE PHOTOGRAPH AND DENSITOMETER TRACE OF THE IMPLODED ARGON AND GLASS CORE

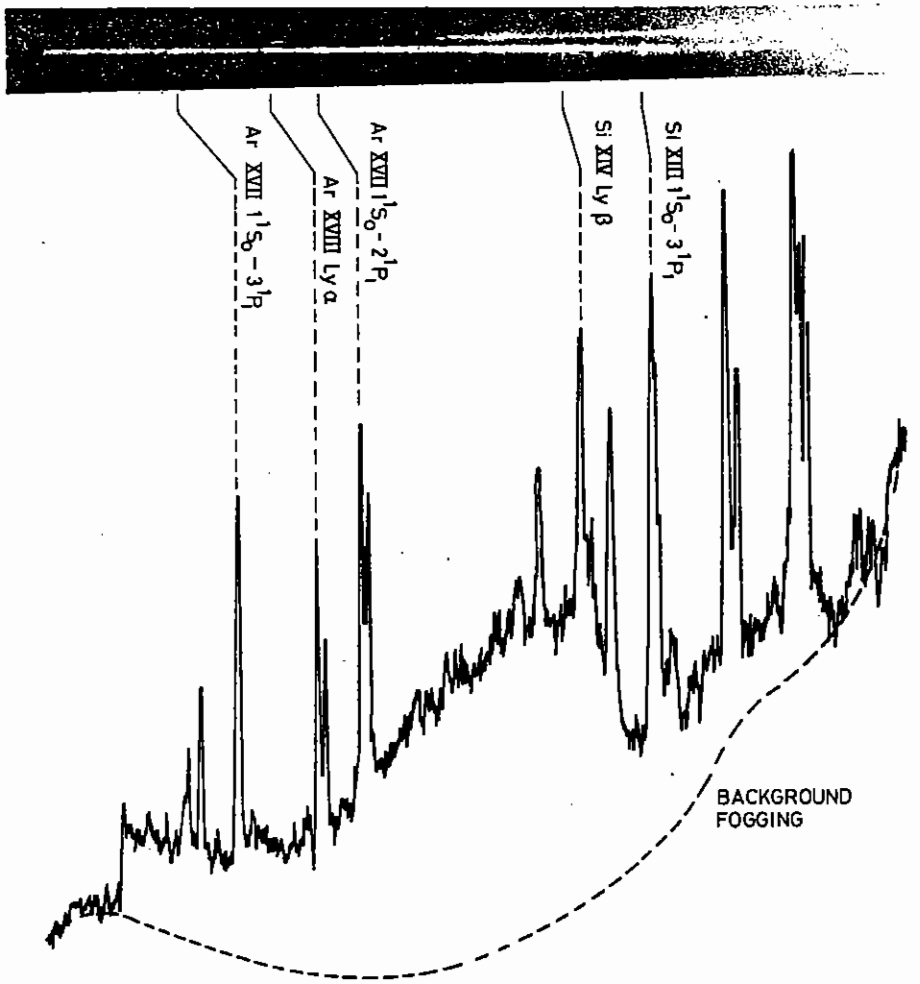

Fig 4.13 Space resolved spectra showing Si and Argon lines and Si recombination continuum

4.4.2 Spectroscopic Analysis of an Argon-filled Exploding Pusher Target

A glass microballoon 70 μm in diameter with a 1 μm wall, filled with 0.4 bar argon, was imploded by a 100 ps pulse at 1.05 μm in six beam irradiation geometry. The total energy on target was 60 Joules and the focused intensity at the target surface was about 10^{15} W cm^{-2}.

Diagnostic instruments consisted of two X-ray crystal spectrometers and an X-ray pinhole camera. The pinhole camera had a 5μm pinhole with a 25μm Be filter in front which transmitted 1.3 keV X-rays. The magnification was x4. Both crystal spectrometers had PET crystals. One of them had a 10 μm slit to give spatial resolution and had a spectral range of 3 A to 7 A. The other was space integrating and had a smaller spectral range.

The pinhole camera gave directly the size of the emitting core as 35 $\pm$ 1μm (Fig.4.12). This also includes the emission from the imploded shell. Measurements from the space resolved spectrum also gave the silicon emitting region as 35 $\pm$ 1μm but the source size for the argon emission was only 26 $\pm$ 1μm. A sphere of this diameter containing all the argon originally in the target would have a nuclear density of 2.1 x 10^{20} cm^{-3}.

An electron temperature of 540 $\pm$ 50 eV was obtained from the recombination continuum recorded on the spectrometers (Fig.4.13). In a coronal model this gives the fraction of the argon in a helium-like state as about 80% with an electron density 16 times greater. Thus, the electron density (n_e) for a pure argon core should be about 3.4 x 10^{21} cm^{-3} with a helium like ground state density of about 1.7 x 10^{20} cm^{-3}. Since the nearly optically thin silicon L_β and L_γ show an electron density of about 10^{23}cm^{-3} it is obvious that the luminous core is predominantly composed of glass plasma.

The densities can also be obtained by fitting theoretical line profiles to the experimental ones (4.10). The main influences on the width of the line are n_e and n_1. The width of a line is not a unique function of these variables but it is single valued so by fitting two or more spectral

lines from a sequence the intersection on a plot of n_e against n_1 gives the actual value of these variables.

A typical fit on the argon $1s^2$ - 1s3p line is shown in Fig.4.14 and a plot of the lines of best fit for the Ar $1s^2$ - 1s3p and Ar $1s^2$ - 1s4p transitions is shown in Fig.4.15. Taking n_1 = 1.7 x 10^{20} cm^{-3} gives n_e = 2 $\pm$ 0.5 x 10^{23} cm^{-3}. A similar fit on the silicon Ly_α and Ly_β lines gives n_e as (1.2 $\pm$ .4) x 10^{23} and n_1 as (1.2 $\pm$ 2) x 10^{21}. The argon figures are enough at variance with the numbers worked out from the source size and the total number of atoms to indicate some mixing of the glass and argon in the core.

4.4.3 Thermonuclear Neutron Yields

A number of D-T filled microballoons were imploded in the new target chamber with 2, 4 and 6-beam irradiation geometry. The neutron yields and shot parameters are summarised in Table 4.02. The table also gives an ion temperature deduced assuming a uniform core temperature and density. The ion temperature is insensitive to the compression ratio used and since core sizes were not available for all shots, a value of x75 was used throughout. The last column gives ion temperatures predicted by the Storm model, (4.22). The predicted compressions in this model vary from 65 to 100.

The yields are an order of magnitude greater than those reported in last year's annual report (4.10). Empirical and model ion temperatures are plotted in Fig.4.16 where the numbers in circles denote the number of beams used and points refer to our earlier two beam data. It can be seen that there is no significant change from our early data in the relationship between data and model which implies that the differences in shot parameters, particularly energy and pulse length, are sufficient to account for the enhanced yields. No effect due to implosion symmetry can be seen.

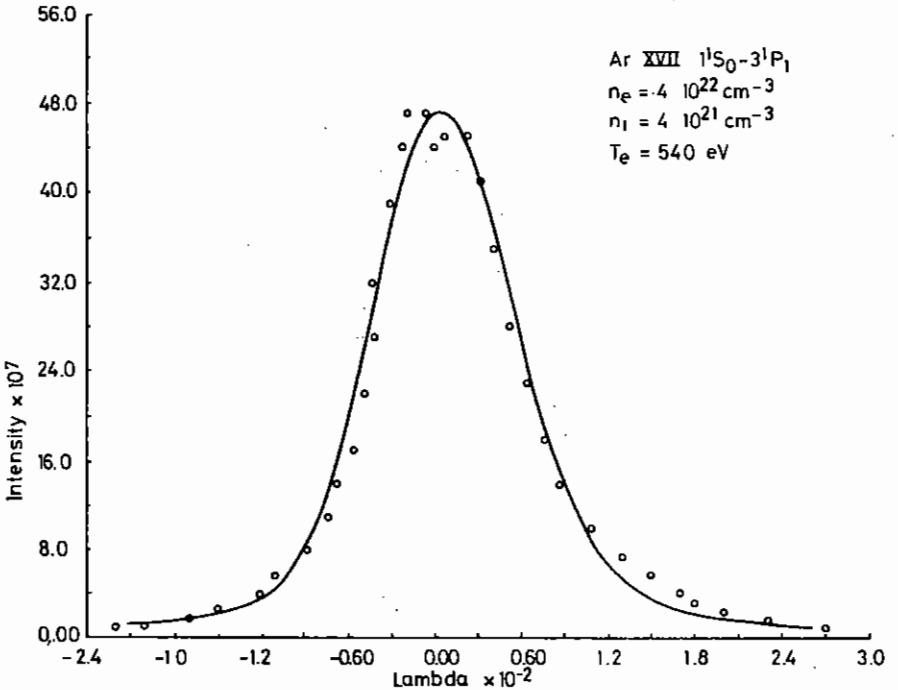

FIG 4.14 A typical best fit for the Ar XVII $1^1S_0-3^1P_1$ transition

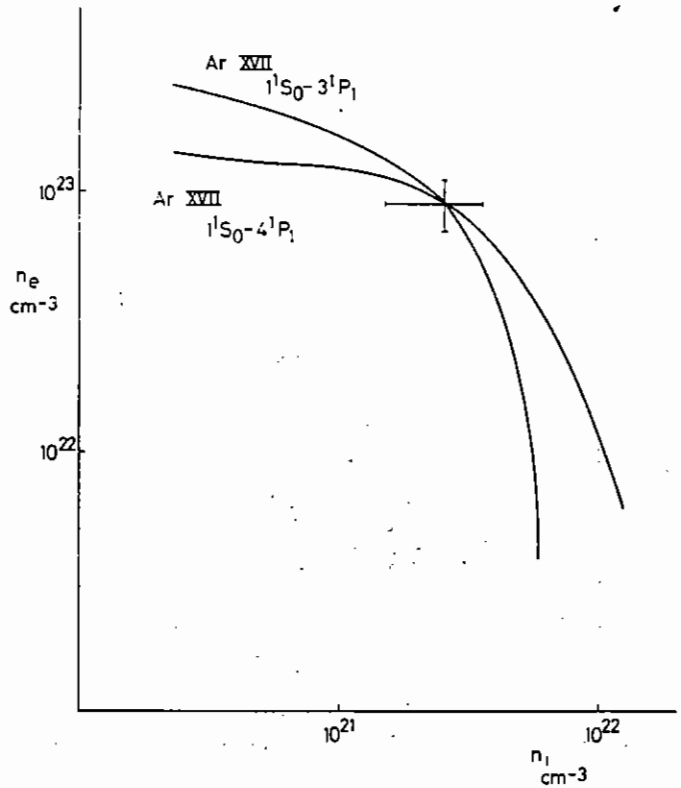

FIG 4.15 Lines of best fit in n_e, n_i parameter space for Ar XVII $1^1S_0-3^1P_1$ AND Ar XVII $1^1S_0-4^1P_1$ transitions

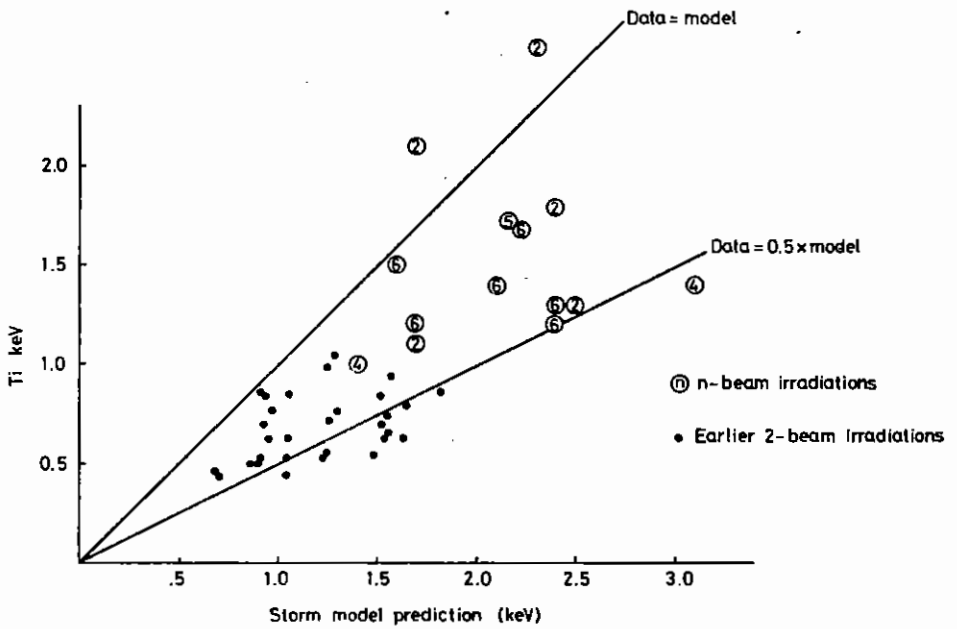

Fig 4.16 Ion temperatures from neutron yields compared with Storm.

TABLE 4.02

Shot Number	No of Beams	Target		P_{inc}* (TW)	Neutron Yield (x 10^6)	Ti(η=75) (kev)	Model Ti** (kev)
		2R(μm)	ΔR(μm)				
31057904	2	69	0.58	0.37	0.65	1.1	1.7
31057905	2	73	0.66	0.83	1.60	1.3	2.5
01067906	2	56	0.61	0.61	9.60	2.6	2.3
01067907	2	94	0.88	0.75	35.00	2.1	1.7
01067908	2	93	0.82	1.15	18.00 +	1.8	2.4
21067913	4	86	0.77	0.45	1.0 +	1.0	1.4
21067914	4	71	0.66	1.22	2.3	1.4	3.1
25097920	5	69	0.8	0.72	4.6	1.7	2.2
25097921	6	83	0.8	0.86	9.8	1.7	2.2
25097922	6	84	0.74	0.92	3.0	1.3	2.4
25097923	6	87	0.8	0.84	4.8	1.4	2.1
25097924	6	72	0.66	0.81	0.9 +	1.2	2.4
26097926	6	88	0.66	0.55	1.8 +	1.2	1.7
26097927	6	89	0.82	0.61	7.0	1.5	1.6

* Power on target. Pulse length was 70 pSec

** Absorbed energy assumed to be 25%

\+ Yield corrected to equimolar DT equivalent from D-rich

4.4.4 The Thomson Parabola

As reported briefly in the 1979 annual report, a Thomson Parabola ion analyser is in use to obtain information upon both fast (using cellulose nitrate film) and slower ions (using an active detector). A schematic of the system is shown in Fig.4.17.

The colinear E and B fields ensure (4.23) that ions of a given M/Z ratio lie upon a single parabola. The track-density (number of tracks per unit length) can give the velocity spectrum.

In the past year interest has shifted towards the study of the slower ions produced in ablative-compression experiments. This has necessitated a change in the ion detector since the cellulose nitrate film used hitherto (4.24) is not sensitive to ions below approximately 100 keV/nucleon. The detector now used is a micro-channel plate - see Table 4.03 and Fig.4.18. Ions striking the front of the channel-plate generate secondary electrons which are accelerated by the applied bias voltages - first to the back of the plate held at between 450 and 1000 volts, and then to the phosphor at 4.5 to 5 kV. The phosphor is deposited upon a fibre-optic window which has photographic film placed in contact with its other end. A second, smaller, Thomson Parabola has been made which uses cellulose nitrate film and can be placed relatively close to the target.

TABLE 4.03

MICRO CHANNEL PLATE SPECIFICATION

Plate type	:	Varian VUW 8900Y
Plate dia.	:	25 mm
Plate thickness:		4.7 mm
Channel dia.	:	12.1 μm
Channel sep.	:	14.9 μm
Bias	:	5°
Effective Area	:	61%

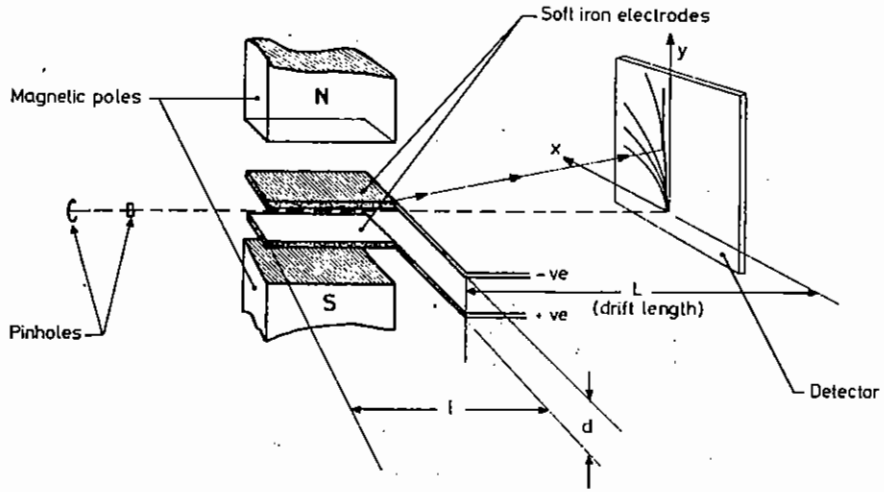

Fig 4.17 Diagram of deflection system of Thomson parabola

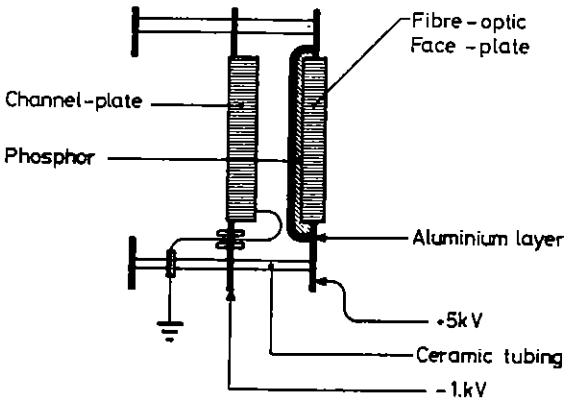

Diagram of ion detector using a micro-channel plate as an electron multiplier

Fig 4.18

Data-analysis

a) Cellulose-nitrate

When cellulose-nitrate film is used as the detector (4.25) data analysis is easy, if tedious. The film is etched in 10% NaOH solution at 60°C for approximately 5 minutes. Tracks of individual ions can then be counted under the optical microscope and their position measured. Typical data is shown in Fig.4.19. This shows the parabolae obtained from a 159 μm diameter balloon, coated with 2.6 μm of plastic $(CH_2)n$ irradiated by 50 J in 100 ps. The output of a computer program used to identify these parabolae and obtain the velocities of the ions is shown in Fig.4.20. Note that although parabolae of C^{+} to C^{6+} are visible, the parabolae of C^{5+} and C^{4+} are the most intense. This will be discussed later. Other, fainter, parabolae can be seen - they correspond to Si(10+) and O(6+). The plastic coating of the micro-balloon should have been sufficient to prevent the laser pulse burning through the plastic to the glass and it is therefore possible that these ions came from the imploded core, not from the corona. Confirmation of this hypothesis came from the following shot where the target was a solid glass sphere coated in plastic and no Si or O parabolae were seen.

b) Active-detector

When the micro-channel plate is used, however, it is extremely difficult to obtain velocity spectra for several reasons which will be discussed below. Charge-states can of course still be obtained, and typical data are shown in Fig.4.21 and 4.22.

Fig.4.21 shows the parabolae of Si and O obtained from a 60 μm diameter glass microballoon irradiated by 3 Joules of 1.05 μm light with a stacked pulse (eight 100 ps pulses of roughly equal intensity in approximately 1ns) in a single beam. The parabolae end abruptly at the right at the aperture of the system.

Fig.4.22 shows the parabolae for a plastic coated microballoon hit by a similar laser pulse. It can be seen that the parabolae have been distorted by extraneous fields within the chamber, though the nature of these fields has yet to be identified.

Response of the Active Detector to Charged Particles

The gain of the active detector is determined by:

a) the number of electrons emitted by an incident ion,
b) the gain of the MCP,
c) the quantum efficiency of the phosphor, and
d) the film response.

a) Secondary emission. The number of secondary electrons emitted by an ion when it hits the front surface of the plate depends on the mass and energy of the ion, its charge, and the angle of incidence.

There are two processes which cause ejection of electrons by ion bombardment: potential and kinetic emission. Potential emission occurs if the potential of the ion is greater than twice the work function of the solid. The yield, δ, of secondaries is thus strongly dependent upon the charge of the ion but only weakly dependent upon its velocity (because the probability of Auger emission is dependent upon the time that the ion is near to an atom). Kinetic emission, however, occurs when some of the kinetic energy of the ion is transferred to the electron. Consequently it is to be expected that in this case δ will be strongly dependent upon the ion energy, and independent of the charge on the ion. For energetic ions (corresponding to velocities of interest here) kinetic emission is dominant.

A further influence upon δ is the cleanliness of the front surface of the plate. Dirty surfaces produce up to 5 times more secondaries than do atomically clean ones.

b) Inherent Gain of the MCP. If we assume that δ is constant and

Deflection voltage	±2·15KV
Field	$1{\cdot}39\times10^{5}$ Vm^{-1}
Magnetic field	0·12 Tesla
Magnification	×7·5

Fig.4.19

Photograph of cellulose nitrate record of ions from plastic coated microballoon.

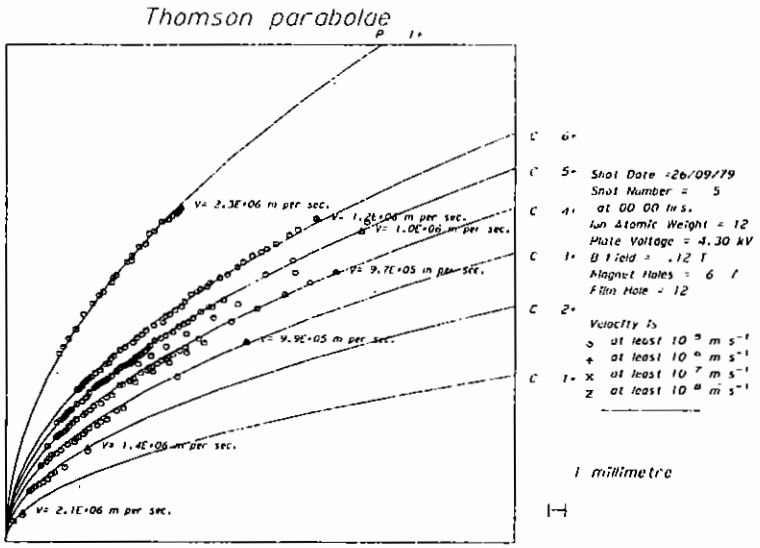

Fig.4.20

Computer analysis of data from Fig.4.19

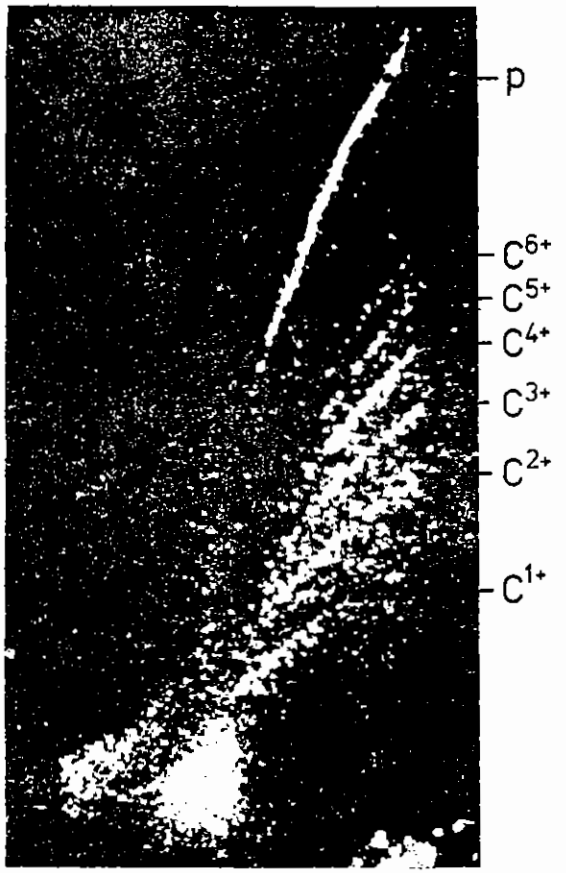

THOMSON PARABOLAE	
Deflection voltage	200V
Field	3.3×10^4 Vm^{-1}
Applied field	0.045 Tesla
DETECTOR VOLTAGES	
Channel - plate	-550V
Phosphor	4.5KV

Fig.4.21

Active detector record of ions from glass microballoon.

THOMSON PARABOLAE

Deflection voltage	-30V
Magnetic field	0·045T

ACTIVE DETECTOR VOLTAGES

Channel - plate	600V
Phosphor	4·5KV

Fig.4.22
Active detector record of ions from plastic coated microballoon.

proportional to $\sqrt{V_c}$ where V_c is the electron collision energy in eV then the gain of the plate is, according to Schagen (4.26):

$$G = \left(\frac{AV}{Z\alpha V_o}\right)^{\frac{4V_o\alpha^2}{V}}$$

where: V = channel voltage; V_o = initial energy of a secondary electron ($\sim$ 1 eV); α = length to diameter ratio of the holes in the plate, and A is given by

$$\delta = AV_o^{\frac{1}{2}} \qquad (A \sim 0.2)$$

As V increases, so does V_o, but the number of collisions within the channel decreases, and there is thus a maximum in the gain-voltage curve. In practice (4.27) it is found that the curve cuts off at large V. This is due to secondary emission that is not normal to the channel walls. The gain of the plate used in this Thomson parabola could be varied between 10 and 10,000 by changing the applied voltage.

c) Phosphor Quantum Efficiency. As all the electrons striking the phosphor in any one shot have been accelerated by the same voltage the quantum efficiency will not vary significantly over the area of the detector and can be allowed for.

d) Film Response. This too can be allowed for.

To try to calibrate the active detector a long, thin Faraday cup is being made. This will be placed just in front of the MCP and will record the sequential arrival of each M/Z species. Relating this signal to the film density will, it is hoped, allow the detector to be calibrated (4.28).

Further Problems

The beam of plasma defined by the pinhole undergoes radial space change

expansion (4.29) when the electrons have been removed by the magnetic field. This expansion is strongly dependent on the density and can cause the beam to expand sufficiently for the parabolae to overlap. It is therefore necessary to reduce the density of ions at the detector to some suitable level. This can be done in two ways - either by i) moving the detector further from the target, or ii) placing further pinholes in the beam.

The problem with moving the detector further from the target is that residual gas in the chamber may cause the high charge-states to recombine to some extent (this is why in Fig.4.19 it was the lower charge-states that were the most intense - not C^{6+}); a background pressure of 2×10^{-6} or less has been shown (4.30) to be necessary to avoid this effect. If we use supplementary pinholes instead then we distort the velocity spectra. This is because the pinhole removes electrons from the plasma and as the plasma passing through the hole has a nett charge it will suffer expansion and the density will decrease. This is precisely why we would use such a pinhole. Unfortunately it obviously preferentially removes the lower energy ions.

Instead of a pinhole it is possible to use a fine mesh - removing by obscuration rather than by expansion. This has been tried and seems to work, although there is as yet little data.

T J Goldsack, J D Kilkenny, S Sartang, W T Toner and S Veats.

CHAPTER 4 REFERENCES

4.01 D W Forslund, J M Kindel and R Lee, Phys. Rev. Lett. 39, 284 (1977).

4.02 P M Campbell et al, in Proceedings of the Sixth International Conference on Plasma Physics and Controlled Nuclear Fusion Research, Bertchesgaden, West Germany, 1976 (International Atomic Energy Agency, Viena, 1977), Vol.1.

4.03 E K Storm et al, University of California Radiation Laboratory Report No. UCRL 50021-76, 1977 (unpublished), pp. 5.85 - 5.126.

4.04 J D Hares, J D Kilkenny, M H Key and J G Lunney, Phys. Rev. Lett. 42, 1216 (1979).

4.05 H A Bethe, Ann. Phys. Leipzig, 5 325 (1930).

4.06 K Lee, D W Forslund, J M Kindel and L E Lindman, Nuclear Fusion 19, 1447 (1979).

4.07 Ya B Zel'dovich and Yu P Raiser, Physics of Shock Waves and High Temperature Hydrodynamic Phenomena, p.201, Academic Press (1966).

4.08 L Spitzer and R Harm, Phys. Rev. 89, 977 (1953).

4.09 D Pines and D Bohm, Phys. Rev. 85, 338 (1952).

4.10 Rutherford Laboratory Central Laser Facility Annual Report 1979, RL79-036, Chapter 4 (1979)(unpublished).

4.11 P T Rumsby, M Michaelis, M Burgess, Opt. Comm 15, 422 (1975).

4.12 B H Ripin et al, Phys. Rev. Lett. 43, 350 (1979).

4.13 M Galanti and N J Peacock, J. Phys. B, 8, 2427 (1975).

4.14 R J Trainor, J W Shaner, J M Auerbach and N C Holmes, Phys. Rev. Lett. 42, 1154 (1979).

4.15 CGM Van Kessel and R Sigel, Phys. Rev. Lett. 33, 1020 (1974).

4.16 S Zweigenbaum, V Gazit and Y Komet, Plasma Phys. 19, 1035 (1977).

4.17 Reference 4.10, section 4.5.

4.18 J D Kilkenny, M H Key and J G Lunney, Phys. Rev. Lett. 42, 1216 (1979)

4.19 D J Nicholas, C Pataky and W T Welford, App. Optics 17, 3368 (1978).

4.20 Reference 4.10, p.1.43.

4.21 C Faquinon and F Floux, Phys. Fluids, 13, 386 (1970).

4.22 E K Storm, J T Larsen, J M Nuckols, M G Ahlstrom and K R Manes, UCRL preprint 79788, Nov. 1977.

4.23 J J Thomson, Phil. Mag. 6(20), 752 (1910).

4.24 Reference 4.10, p.1.47.

4.25 R L Fleischer, P B Price and R M Walker, "Nuclear Tracks in Solids", University of California press (1975).

4.26 P Schagen, "Advences in Image Pick-up and display", Vol. 1, Acedemic Press (1974) p.1.

4.27 Nuclear Instruments and Methods, 162 (1979), 587.

4.28 G L Payne et al, J. Appl. Phys. 49(9), 4688 (1978).

4.29 S J Gitomer and H Brysk: Appl. Phys. Lett. 32(10), 616

4.30 "A t^{-2} energy spectrometer for ion studies of laser produced plasmas", Clement, Miles et al, Swansea (unpublished).

CHAPTER 5 ABLATIVE COMPRESSION STUDIES

INDEX

CHAPTER EDITOR: P T Rumsby

CHAPTER 5 ABLATIVE COMPRESSION STUDIES

5.1 Introduction

The commissioning of the new six beam target chamber during 1979 has meant that ablative compression experiments can now be conducted with greatly improved illumination uniformity compared to the two beam system used previously.

Initial experiments were aimed at finding the optimum lens focusing conditions in order to achieve most symmetric ablation pressure on the target surface and to determine the fraction of incident laser energy absorbed by the target.

The dynamics and hydrodynamic stability of ablatively imploded hollow shell targets have been studied using both X-ray emission and absorption techniques and the data used to check plane target measurements of ablation pressure scaling with intensity. In addition these experiments have demonstrated for the first time that implosion stability deteriorates rapidly as target aspect ratio is increased. Plane target layer mixing experiments, aimed at indirectly observing hydrodynamic instability in accelerating foils, have not however shown evidence for dramatic target breakup.

Implosion core density measurements by streaked X-radiography have been performed at 1.7 keV X-ray energy using pure polymer shell targets and initial experiments aimed at developing zone plate coded radiography techniques for obtaining two-dimensional data have been carried out at 4 to 5 keV. These latter experiments have demonstrated the potential of zone plates for the necessary extension of radiography methods to X-ray energies above 10 keV.

P T Rumsby

5.2 Spherical Target Illumination Uniformity

Due to lens supply problems all six beam implosion experiments during the period of this report have been conducted using a combination of two f/1 doublet lenses on one chamber axis and four f/1.5 singlet lenses on the other two. This situation will be corrected in early 1980 when additional supplies of f/1 lens become available but has led to complications in the attainment of good target illumination uniformity.

A series of six beam implosions were carried out using various hollow and solid sphere targets to determine empirically the optimum lens focusing conditions. Symmetry of ablation plasma properties were determined by X-ray pinhole camera imaging and arrays of plasma and X-ray calorimeters were used to determine target energy absorption. The pulse length used was 1.5 ns which with energies on target up to 100 J in all six beams giving target irradiances up to 10^{14} W cm^{-2}.

Computations of target illumination uniformity indicated that a good starting point for these experiments would be to use a focusing condition of d/R = 2 for the f/1 lenses and 3 for the f/1.5 lenses, where d is the distance beyond the target centre at which the beams focus and R is the target radius. For these conditions the computations indicated an irradiance uniformity of $\pm$ 30%. Pinhole camera images of targets illuminated in this manner however showed the presence of significantly more intense X-ray emitting regions associated with each of the six beams suggesting that the beams should be defocused more.

A lens focusing condition of d/R = 3 and 4.5 for the f/1 and f/1.5 lens respectively was found to give good uniformity as demonstrated by the pinhole camera photograph shown in Fig.5.01. At this lens condition one would expect significant ammounts of laser energy to miss the target and the absorption fraction to decrease. This was not demonstrated in the experiments however as calorimeter array measurements indicated that absorption remained constant at 50 - 60% up to this condition. For lens focusing with d/R values greater than 3 and 4.5 the pinhole camera images showed good uniformity but absorbed energy fraction decreased.

These results can be explained if expansion of the coronal plasma surrounding the target is considered. At the intensities used in these experiments (10^{12} - 10^{14} W cm^{-2}) laser light absorption takes place predominantly in plasma of density somewhat less than critical. Computations show that for shell targets this region of plasma initially moves outwards from the target surface to distances of a few tens of microns before moving inwards again as the shell implodes.

Comparison of absorption measurements on solid spheres and thin wall hollow shells of the same diameter show absorption dropping to less than 40% for the latter targets confirming the late time inward movement of the absorption region for shells where the implosion time is significantly less than the laser pulse.

C.J. Hooker, S.J. Knight, D. Miller, P.T. Rumsby

Fig.5.01

Pinhole camera photograph of 250 μm diameter glass shell target irradiated with 6 laser beams at an intensity of 2.10^{13} W cm^{-2} in a 1.5 ns pulse, showing uniformity of ablation plasma.

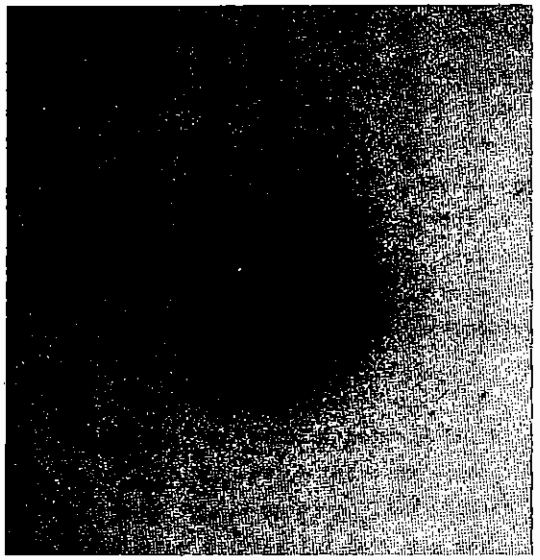

SHOT 55. 070180

Target diameter 196 µm

Coated with 2.2 µm plastic

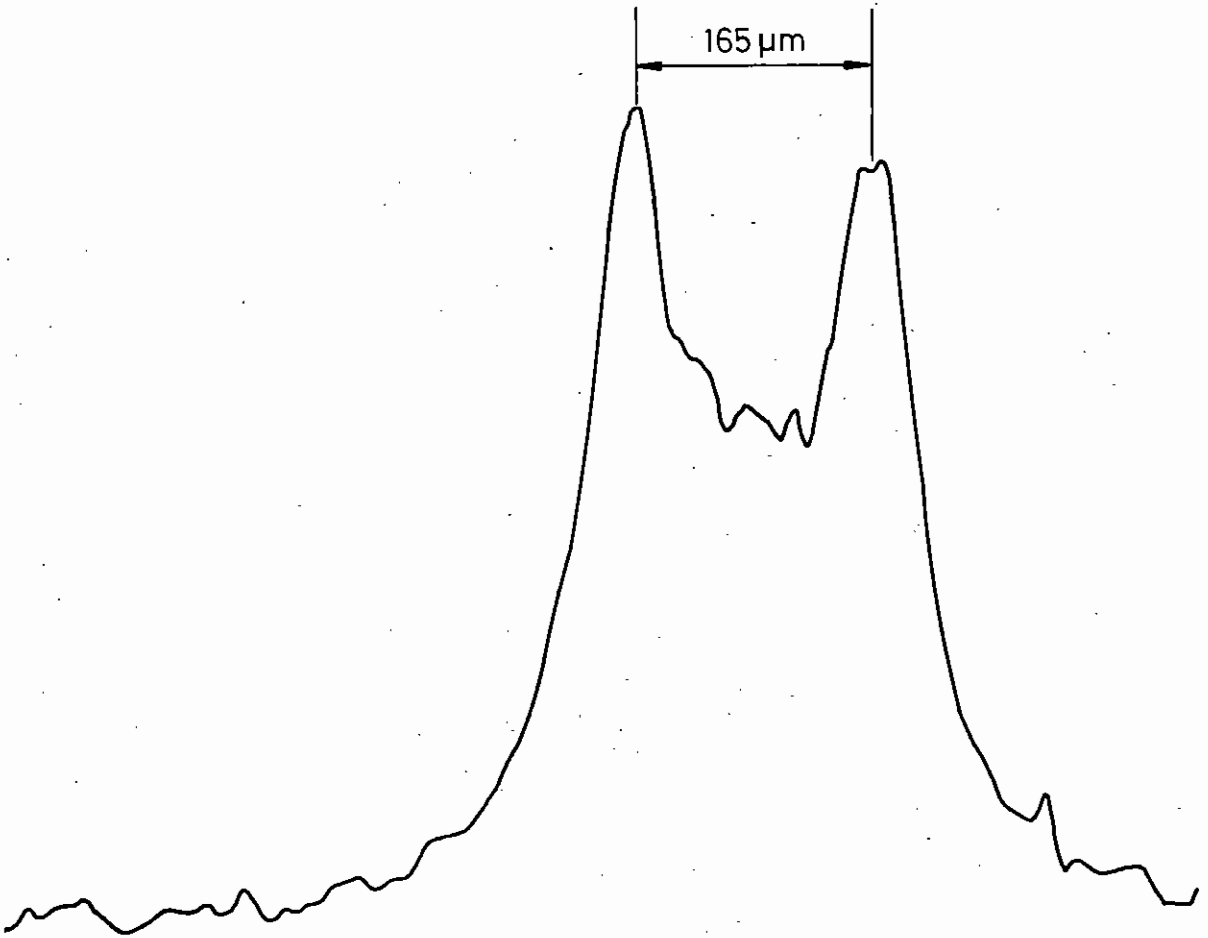

Fig.5.02

Pinhole cameral photograph of ablatively imploded glass shell target coated with 2.2 µm of plastic. Original target diameter 196 µm. Intensity 2.10^{13} W cm^{-2}.

5.3 Layered Spherical Target Experiments

Experiments to detect the motion of the X-ray emitting region of accelerated flat foil targets have been carried out and are described in section 4.3.1. Similar experiments but with spherical geometry have been conducted in the 6 beam target chamber using glass targets coated with plastic to delay the intense emission from the glass. A pinhole camera, filtered with 25 μm of Be, imaged the emission from both plastic coated shell targets and plastic coated solid glass spheres. Filter transmission was primarily above 2 keV and so the camera was sensitive to Si XIII and Si XIV emission.

The thickness of plastic coating on solid spheres needed to reduce the intensity of the pinhole image significantly below that for on uncoated target was found to be approximately 3 μm. Thus emission with a 2 μm coating of plastic would occur towards the end of the 1.5 ns laser pulse, at which time the X-ray emitting region would have moved due to the ablative compression. A mass ablation rate of 3 μm of plastic in 1.5 ns at an intensity of 2.5×10^{13} W cm^{-2} is a factor of 2 to 3 higher than the measurements made on plane targets (section 4.3). This discrepancy has yet to be resolved.

Pinhole camera images of coated and uncoated solid glass spheres showed that the diameter of the peak emmission region was greater than the initial balloon diameter by about 10%. On the other hand, pinhole images from imploding plastic coated shell targets show considerably smaller diameter emission regions due to the inward movement of the target walls as shown in Fig.5.02. In this case the diameter of the emission region has decreased by 30 μm. The amount of shell motion that would be expected based on measured ablation pressures (sections 4.3.2 and 5.4) and the length of the laser pulse is in reasonable agreement with the experimental observations.

S. Veats, J. Kilkenny, P.T. Rumsby.

5.4 Streaked X-ray Shadowgraphy Experiments

X-ray shadowgraphy as a technique to diagnose cold dense plasmas has been discussed previously (5.01). Recent application of the method has provided data on the ablative implosion of shell targets using six beam irradiation and long pulses ($\gtrsim$ 1 ns) at 1.05 μm. The main objectives of the experiments were to study the dynamics and hydrodynamic stability of ablatively imploded shells and to measure compressed core densities by X-radiography.

The apparatus is illustrated in Fig.5.03. A single channel Kirkpatrick-Baez X-ray microscope was used to image a microballoon with x15 magnification onto the cathode (CsI on 25 μm Be) of an X-ray streak camera. A slit at the object plane was used to select a portion of the image corresponding to a 30 μm wide strip in the target equatorial plane. A seventh beam, which could be advanced or retarded in time with respect to the six main beams was used to irradiate the backlighting target. This target was a 50μm thick foil tilted 10° down from the target equatorial plane and the backlighting plasma was positioned 500μm from the main target. An X-ray film cassette and a phospher coated (2.5 mg/cm^2,P11) fibre optic plate with 50/40 image intensifier could be located in the streak camera cathode plane as alternative image detectors. The streak camera was differentially pumped and typical working pressures in the tube of $\sim 10^{-6}$ torr appear to extend the useful lifetime of the CsI cathodes. All streaks in the investigation were at a sweep speed of 200 ps/mm on film and with a temporal resolution of $\sim$ 100 ps.

Optimum focusing conditions for the six main beams was determined from the uniformity of microballoon self-emission detected with a pinhole camera and from the coupling of energy into the target as estimated from ion calorimetry. Typically 50 - 60% of the incident energy was usefully coupled to the target (see section 5.2).

The phosphor screen was used for coarse alignment of backlighting target, balloon, microscope and sampling slit. Using the tip of a 100 μm diameter

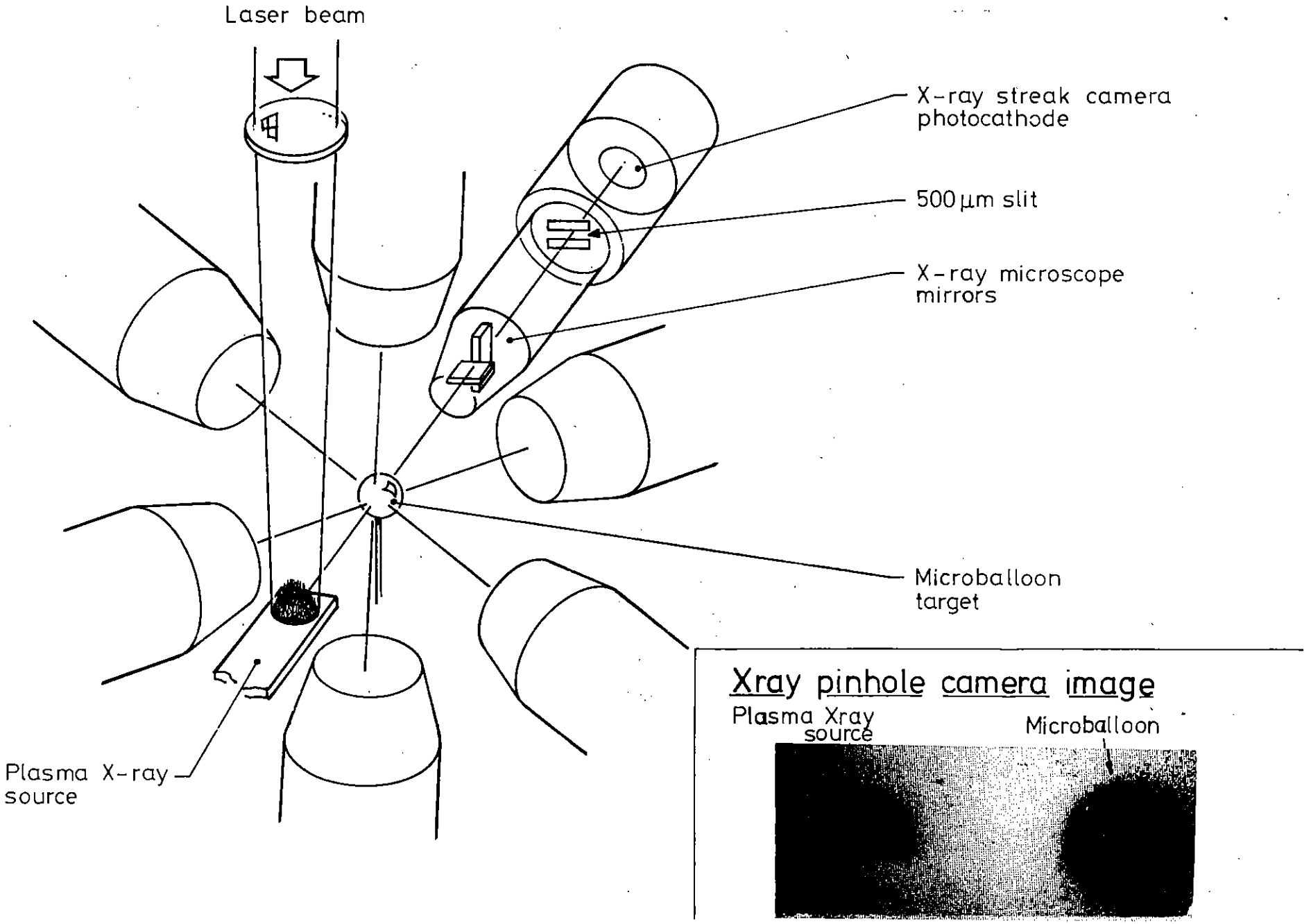

Fig.5.03

Apparatus for 6 beam irradiation of microballoon targets and streaked X-ray shadowgraphy.

KB MICROSCOPE STATIC X-RAY SHADOWGRAPH
OF A GLASS MICROBALLOON

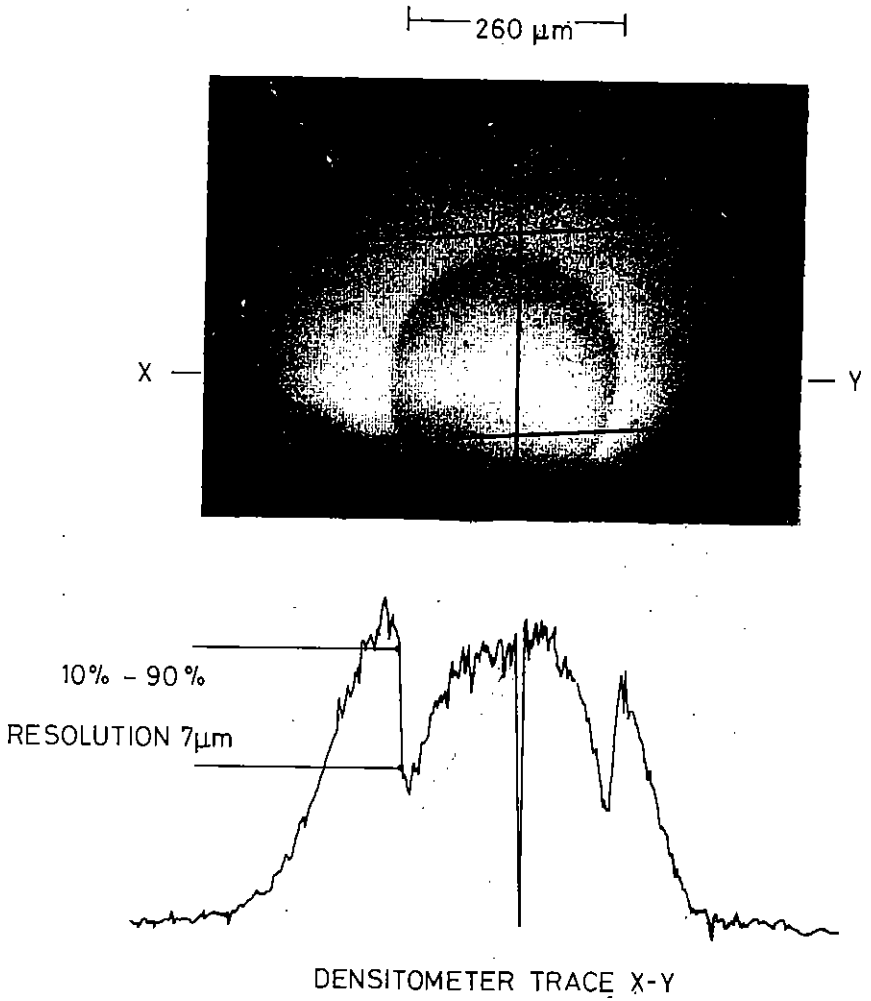

Fig.5.04

X-ray shadowgraph of an unirradiated glass microballoon showing the resolution of the KB microscope.

wire to simulate the balloon position and a massive backlighting target high repetition rate, low energy (∿ 5 J) seventh beam shots were sufficient to record static images. The microscope resolution was checked with the X-ray film cassette. Fig.5.04 shows an image of a backlit (∿ 2 keV) microballoon and a spatial resolution of 7μm in the balloon plane was measured. The measured resolution through the microscope and streak camera system was 17 μm.

Aluminium foils were chosen as the backlighting targets. The emission was filtered at the microscope with 40μm Be and a 4.5μm thick SiO layer on 2μm mylar. The backlighting spectrum was recorded with a space resolving spectrometer using a PET crystal and the above filters and the spectrum absolutely calculated for experimental analysis (see later). As illustrated in Fig.5.05 the backlight source was quasi-monochromatic with the bulk of the spectral intensity in the hydrogen and helium like resonance lines, below the Si K-edge. A high energy spectral cut-off was provided by the gold mirrors in the microscope at ∿ 2.2 keV. This choice of backlighting source had several advantages. The quasi monochromatic nature of the spectrum simplified the spectral integration proceedure used later in calculating opacity profiles, self-emission from glass in the balloon targets was discriminated against by the SiO filter, improving image contrast, and the spectrum was readily excited at irradiances of ∿ 10^{13}W cm^{-2} making large backlighting source areas (500μm diameter) possible.

About twenty streak records were obtained suitable for analysis. These records spanned target irradiance from 5 x 10^{12} - 10^{14} W cm^{-2} and balloon aspect ratio ($r/\Delta r$) from 10 - 100. Balloon targets were empty glass shells (Δr = 1μm) with diameters from 100 - 300 μm. Low aspect ratios were obtained by coating balloons with up to 7μm plastic. A few pure polymer balloons and two 10 Bar neon filled glass balloons were also imploded. The inset to Fig.5.03 shows a SiO filtered pinhole picture of the backlight and balloon plasmas from which the self emission contribution in the streak record can be estimated.

Fig.5.06 illustrates the results obtained by results obtained by varying

the target aspect ratio. Here the backlighting pulse is delayed by 0.9 ns to display the final implosion core size. Shot 5/2/80/05 shows an implosion with initial aspect ratio 12. The target had a 6.6 μm polymer coating on a 1.1 μm glass shell and the overall diameter shown to scale in the diagram above the streak was 186 μm. The irradiation intensity was 2.5 x 10^{13} W cm^{-2}. There is no discernable self emission from the target prior to the backlighting due to the low X-ray emission from polymer coated targets. There is also no discernable transmission through the centre of the target due to its rather thick polymer coating. The boundary of the opaque region is quite sharply definedthroughout the implosion.

The central streak in Fig.5.06 is for aspect ratio 43 (shot 25/1/80/05) with a 2.0 μm polymer coating on a 1.0 μm glass shell with an overall target diameter of 268 μm irradiated at 10^{13} W cm^{-2}. Here the streak shows just discernable self emission of the target prior to the backlighting. There is also pronounced transmission through the centre of the target with the wall absorption feature prominent in the early stages of the implosion. The boundary of the opaque region is quite sharp and as the implosion develops the total opacity becomes sufficient to cut off measurable transmission through the centre of the target.

The right hand streak in Fig.5.06 (shot 24/1/80/08) shows an example of maximum aspect ratio where an uncoated glass microballoon 1.3 μm thick and 284 μm in diameter was irradiated at 5 x 10^{12} W cm^{-2}. Here the self-emission of the target is clearly seen before the backlighting starts but it is significantly lower in intensity than the backlighting. It is interesting to note that the limb brightening of the self emission defines the implosion trajectory quite well in the early stages and it includes an absorption feature due to the wall. The backlighting in this case shows strong transmission through the centre of the target but the wall absorption feature is poorly defined by comparison with the adjacent shot 25/1/80/05. The boundary of the absorbing region is not sharp and shows some evidence of gross fluctuations particularly at the left hand side of the streak. The minimum diameter of the absorption core is large and the core absorption profile has a diffuse boundary. Transmission through the

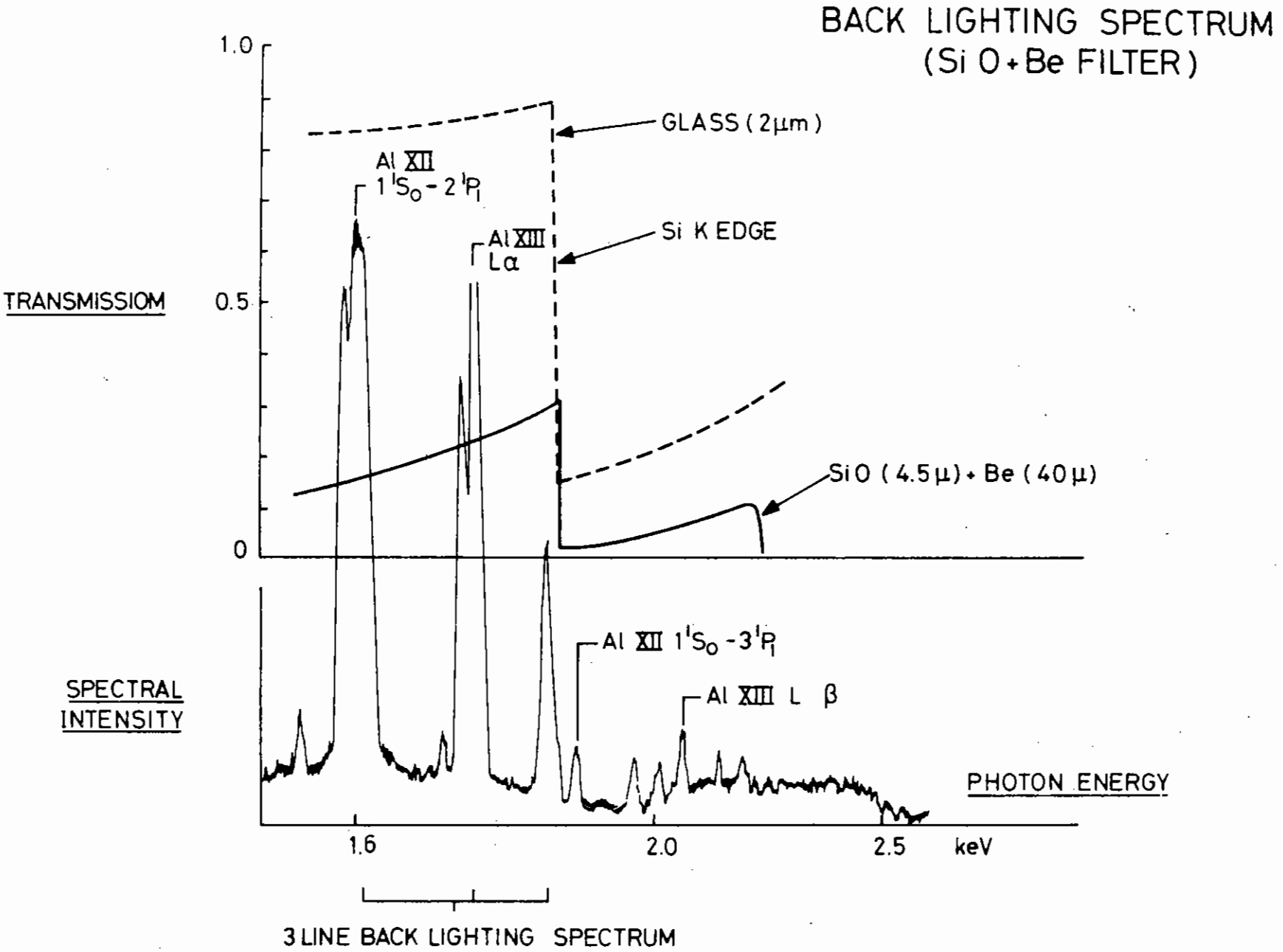

Fig.5.05

A densitometer tracing of the X-ray spectrum of the Al plasma backlighting source after filtering through 4.5 μm SiO + Be filter and of 2 μm of glass are also shown.

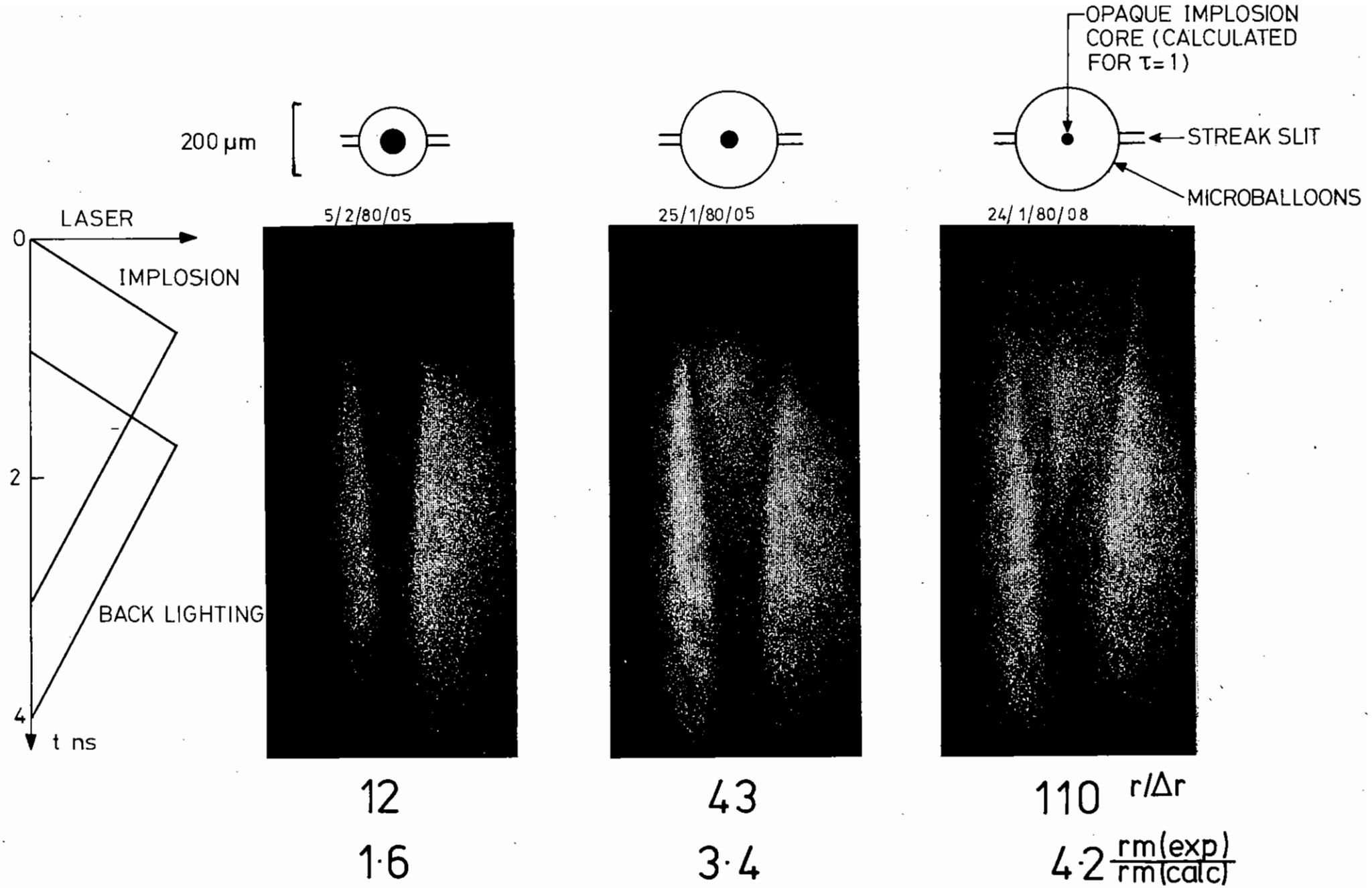

Fig.5.06

3 examples of streaked X-ray shadowgraphy of implosions with aspect ratios 12 43 and 110. The diagrams above each streak photograph are drawn to scale and show their initial target diameter, the calculated size of the opaque core at peak compression and the streak slit width.

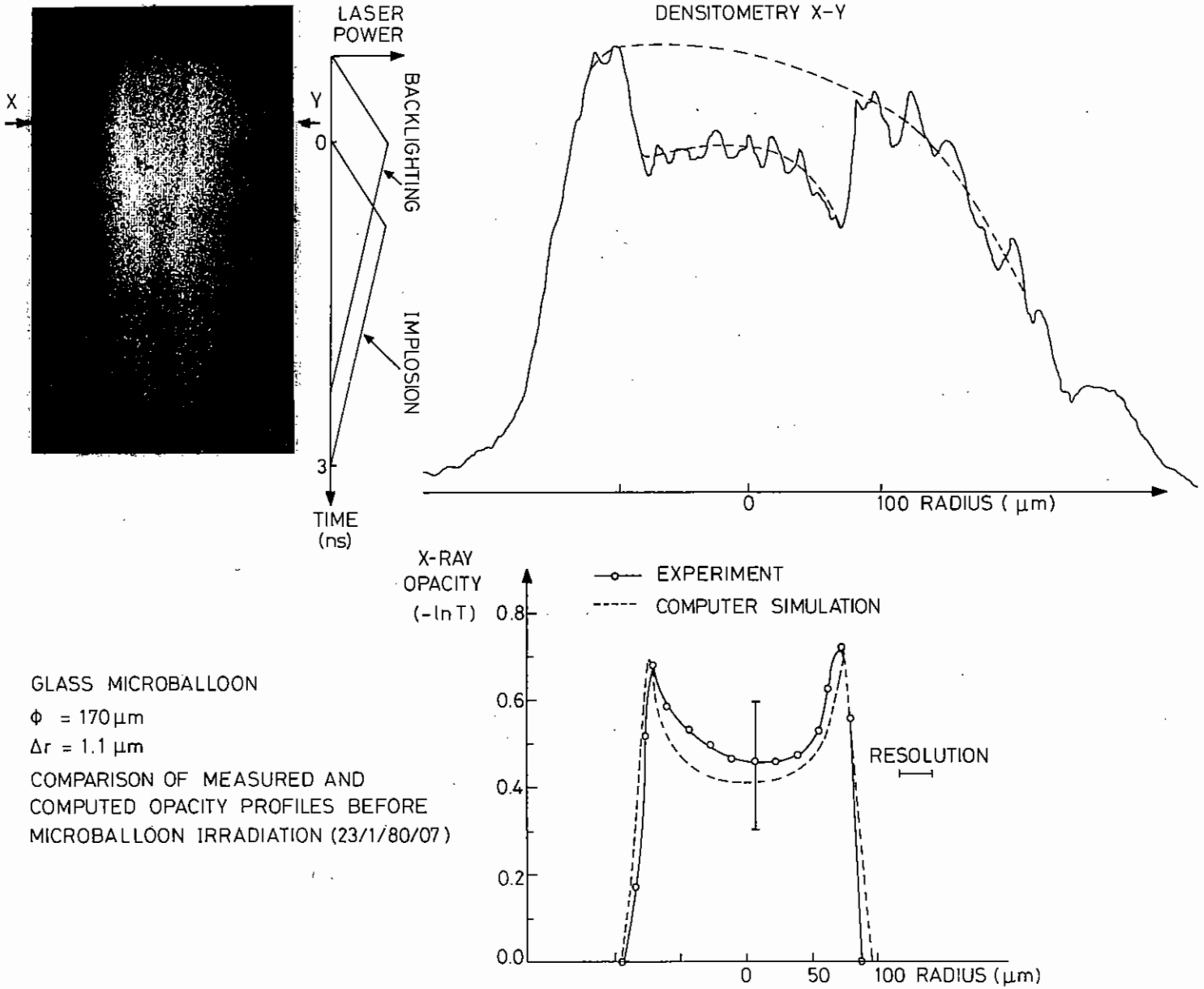

Fig.5.07

Analysis of a streaked X-ray shadowgraph at a time prior to the start of irradiation showing computed and measured opacity profiles.

centre is seen almost up to the time of minimum core diameter suggesting a low peak opacity. The wall boundary was arbitrarily defined as the opacity (τ) = 1 position i.e. where the backlight intensity was reduced to 37%. Experimental r-t plots for particular shots were compared to simulation predictions.

MEDUSA was run for each set of balloon parameters. Laser power and absorbed energy was matched to experimental measurements (see section 5.2) and a trangular pulse profile as measured by an S-1 streak camera was used. The pulse had a FWHM duration of 1.5 ns rising to peak intensity in 0.8 nsec. MEDUSA output (on disc files) included a line of sight integration of opacity along chords of the target in the equatorial plane. Opacities were calculated at each time step at fixed frequencies above and below the Si K edge. Using a post-processing routine the absolute backlighting spectrum was spectrally integrated using a ν^3 dependence and opacity profiles $\tau(r)$ obtained. These curves were finally convolved with the measured instrumental resolution, 17μ in the object plane. Checks on the opacity calculations were possible both in static shots where the balloon was not irradiated and in streaks where the backlighting arrived before the main beams. Fig.5.07 shows good agreement between measured and calculated profiles for a "cold" balloon backlit at early time.

Opacity profiles at different times were used to plot $r(\tau = 1)$ against t and comparison with experiment is shown in Figs.5.08, 5.09 and 5.10 for the streaks shown in Fig.5.06. It is clear that agreement is good in the early stages of the implosion but that experimentally the implosion appears to stagnate earlier than predicted. Since the inward shell velocity (dr/dt) is in agreement up to the time of discrepancy it is proposed that experimentally the shell motion is not directed completely radially thereby producing a "diffuse" core.

A compilation of data showing the ratio of measured to calculated core diameters is shown in Fig.5.11 where the cube of the ratio giving the volume ratio is also plotted. There is a clear trend to greater disparity ratio with increasing shell aspect ratio which suggests that the effect may be due to degradation of the radial implosion by fluid instabilities

originating either in shell surface perturbations or illumination non-uniformity.

Other possible explanations for the observations were considered. Experimental error in locating the slit centrally in the image of the microballoon can lead only to a reduction in the observed diameter of the opaque region together with a loss of sharpness in the boundary increasing with decreasing core size. In the limit it would also lead to apparent transmission through the core. The streaks in Fig.5.06 cannot therefore underestimate the disparity ratio due to any alignment error and moreover do not show the characteristics described above.

Preheating of the imploding shell by hot electrons, shocks and radiation if sufficiently intense would increase the final size of the opaque core. The code simulations include the effect of shock heating and hot electron preheating. The latter was modelled with a hot electron temperature scaling with $I\lambda^2$ as

$$T_H \propto (I\lambda^2)^{0.25} \text{ for intensities above } 10^{15} \text{ W cm}^{-2}$$

and

$$T_H \propto (I\lambda^2)^{0.67} \text{for lower intensities.}$$

However, at the low irradiance of these implosions the simulated hot electron effects were negligible. Since radiative preheat was not included in the modelling and since it might be argued that the hot electron preheat modelling was in error, calculations were run in which a variable fraction of the absorbed energy was uniformly distributed in the shell mass. The ratio of final diameter with preheating to that of the basic simulation was typically 1.5 for 3% and 2.0 for 10% preheat. This shows that quite unrealistic levels of preheat for the low irradiance used here would be needed to produce disparity ratios of the order shown in Fig.5.11.

These considerations and the increasing disparity ratios and the ragged

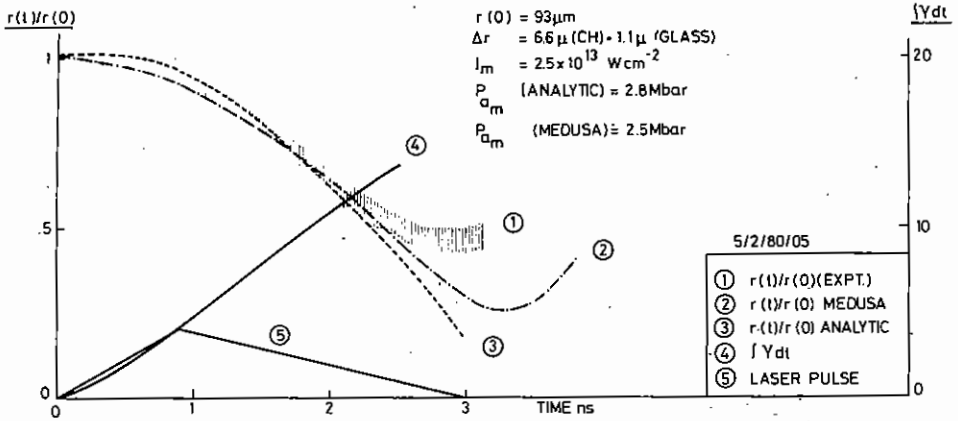

Fig 5.08

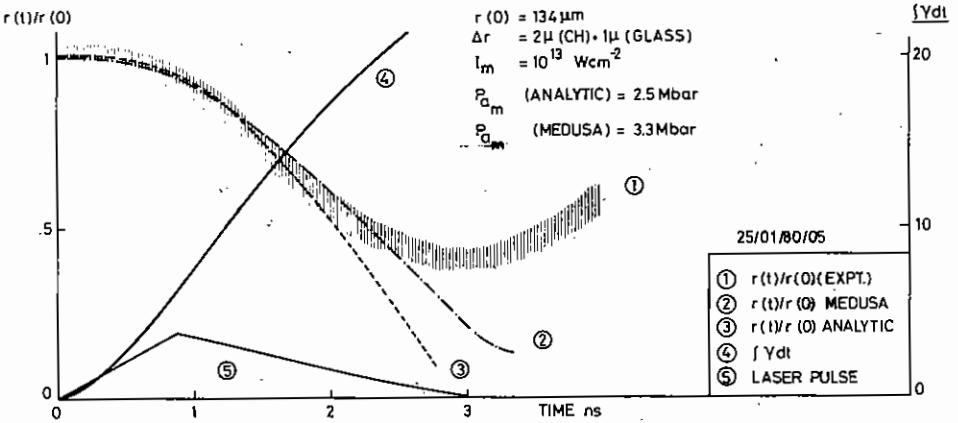

Fig 5.09

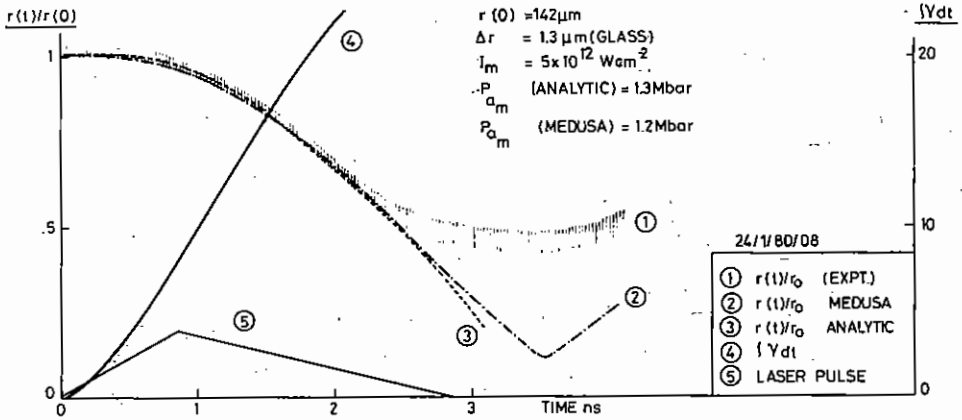

Fig 5.10

Figs.5.08, 5.09, 5.10

Analysis of the 3 implosions shown in figure 5.06 showing (1) the measured trajectory of the boundary of opacity $\tau = 1$, (2) the computer simulated trajectory, (3) the trajectory from the simple analytic model, (4) the growth exponent of the classical Rayleigh Taylor instability of wave length equal to the shell thickness from the simple analytic model, (5) the approximation to the experimental laser pulse shape used in the calculations.

Values of the ablation pressure P_{a_m} at the peak of the pulse derived from the computer simulation (2) and the analytic model (3) are also shown.

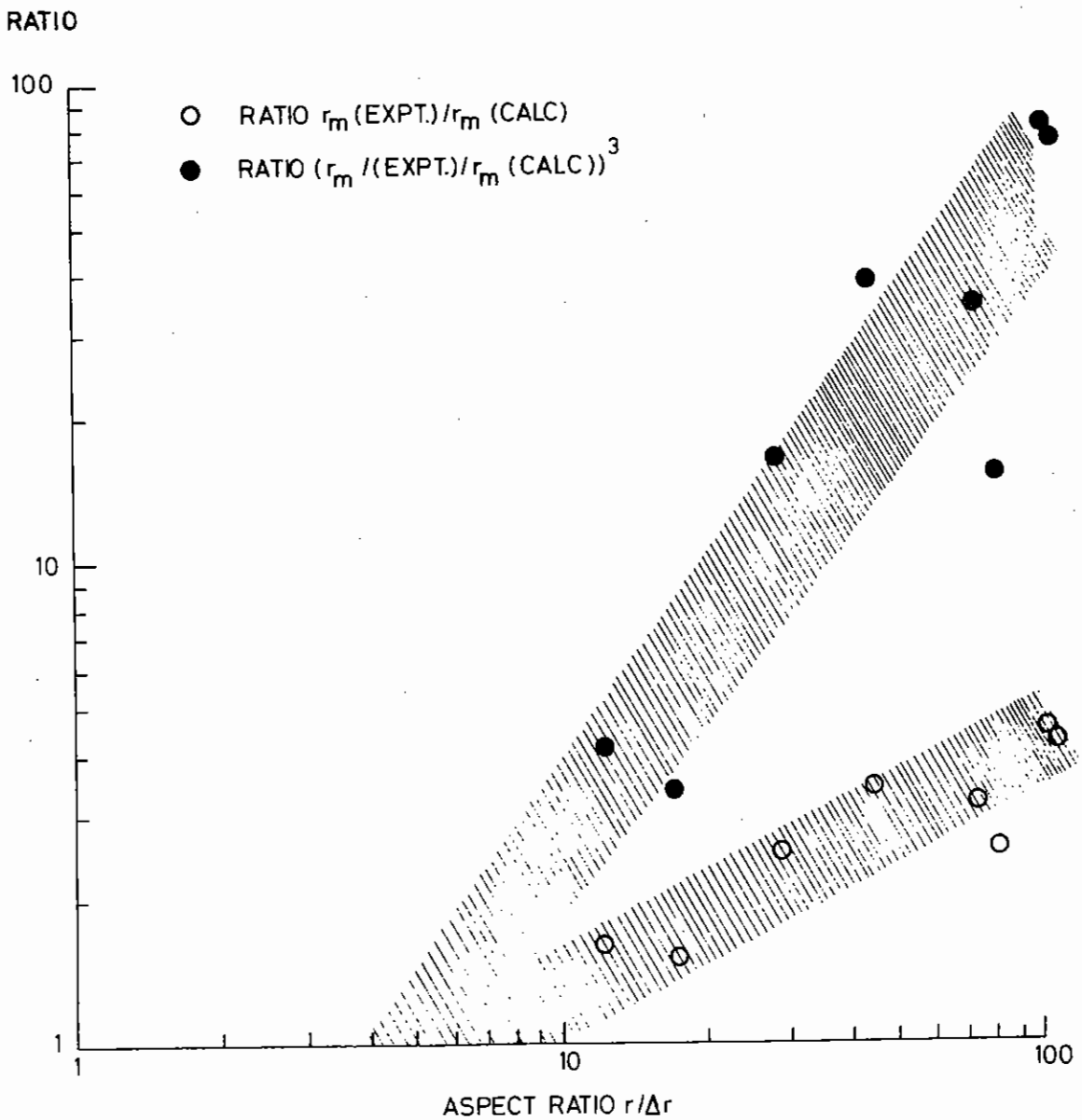

Fig.5.11

Ratios of the observed to calculated diameters of the opaque core at peak compression (open circles) and hence ratios of the volumes solid circles, as a function of shell aspect ratio r/Δr.

boundary of the absorbing region in the limit of high aspect ratio lead us to explain the observations as evidence of fluid instability during ablative acceleration. The fact that the r(t) characteristic retain the qualitative features of an ablative implosion suggest that the fluid instabilities are on a small scale and degrade the implosion core size by making the radial flow diffuse rather than purely radial.

A simple one dimensional analytic model was developed to generate r-t curves to fit to experimental data. Best fits were then used to estimate driving pressure generated in the ablation plasma. From the mass ablation rate data in section 4.3 the ablation pressure for $I \leq 10^{14}$ W cm^{-2} follows closely the Chapman-Jouguet predictions and may be expressed as $P_a = kI^{2/3}$. Assuming negligible mass loss from the shell the wall acceleration may be written as $d^2r/dt^2 = P_a/\rho\Delta r$ in a one dimensional approximation. Taking the laser pulse as triangular rising to a power I_o in time t_o and terminating at time t, the wall position may be expressed after integration as

$$r/r_o = 1 - A\, t^{8/3} \quad \text{for } 0 \leq t \leq t_o = 1$$

and

$$r/r_o = 1 - A\left(\frac{(3-t)^{8/3}}{2^{2/3}} + 8t - 11\right) \text{ for } 1 \leq t \leq t_1 = 3$$

where t is in nsec and

$$A = \frac{9\, kI_o^{2/3}\, 10^{-18}}{40\, \rho r_o\, \Delta r}$$

Particular shots were fitted using A as a parameter and the ablation pressure than estimated from A. Figs.5.08 - 5.10 also show the analytic fits (which make no allowance for stagnation) and Fig.5.12 shows the calculated pressures as a function of irradiance and compares them with results from plane target experiments. It is seen that although the ablation pressures measured from spherical targets lie within the experimental scatter of plane target measurements (section 4.3) the values are consistently lower.

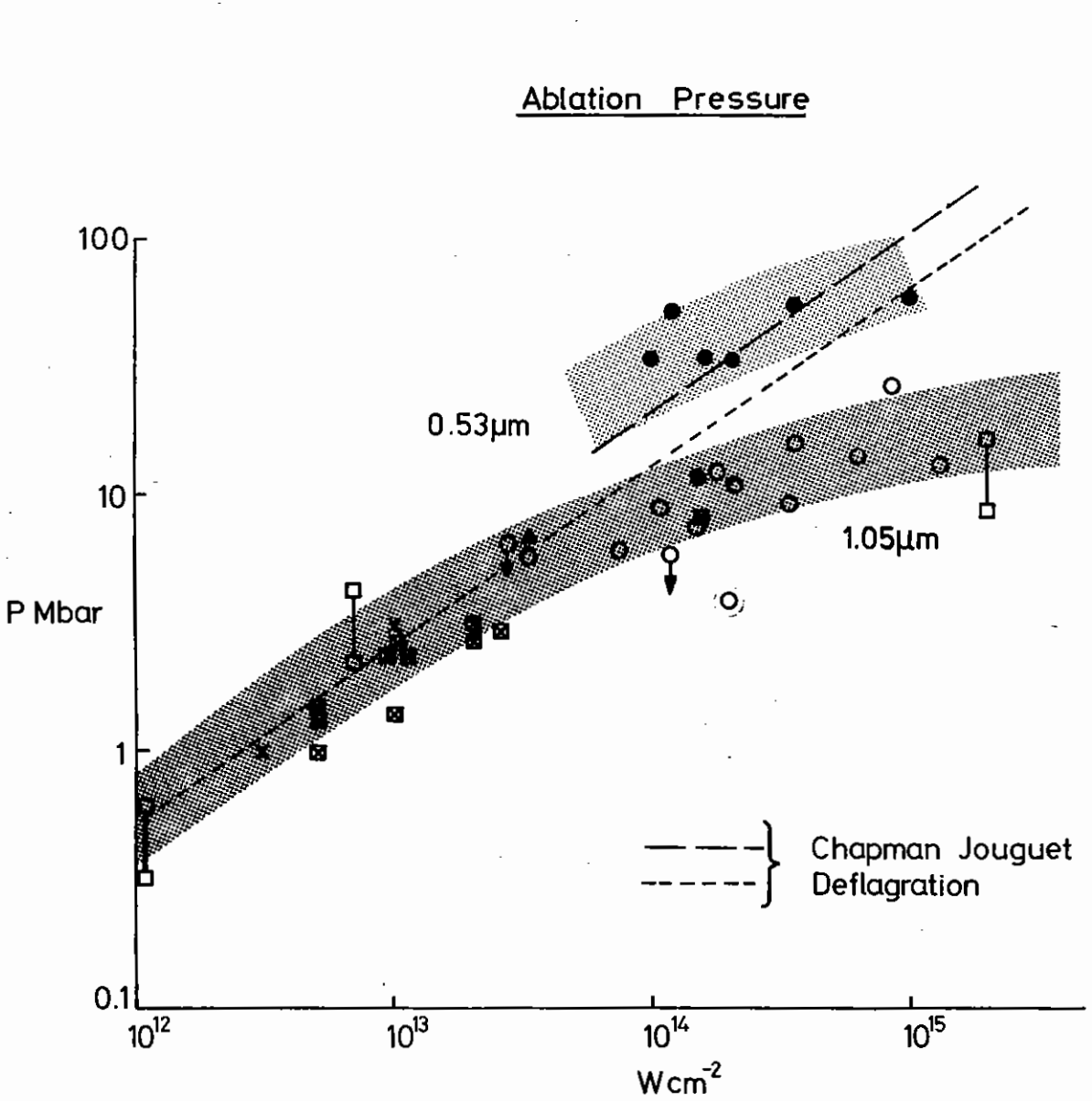

Fig.5.12

Ablation pressure as a function of irradiance with calculated values for λ = 0.53 and λ = 1.05 μm (dashed lines) above and below respectively) and experimental data including; results from ablation rate measurements (solid circles λ = 0.53 μm + open circles λ = 1.05 μm); results from ablatively driven acceleration of shells measured by streaked X-ray shadowgraphy for 1.06 μm irradiation (squares with diagonal crosses); Additional data for λ = 1.06 μm from other sources comprising; crosses (ion measurements of Decoste et al (13)); open squares (spectroscopic $n_e kT_e$ with cross bore allowing for flow up to Mach 1. Galanti et al Proc Int Conf on Plasma Phys and Controlled Fusion. Paper CM33/13-4 Publ IAEA Vienna and Key et al J Phys B 12 L213 1979) solid triangle (shock wave measurements Trainer et al Phys Rev Letts 42 1154 1979); double (shock wave measurements Van Kessel and Sigel Phys Rev Letts 41 243).

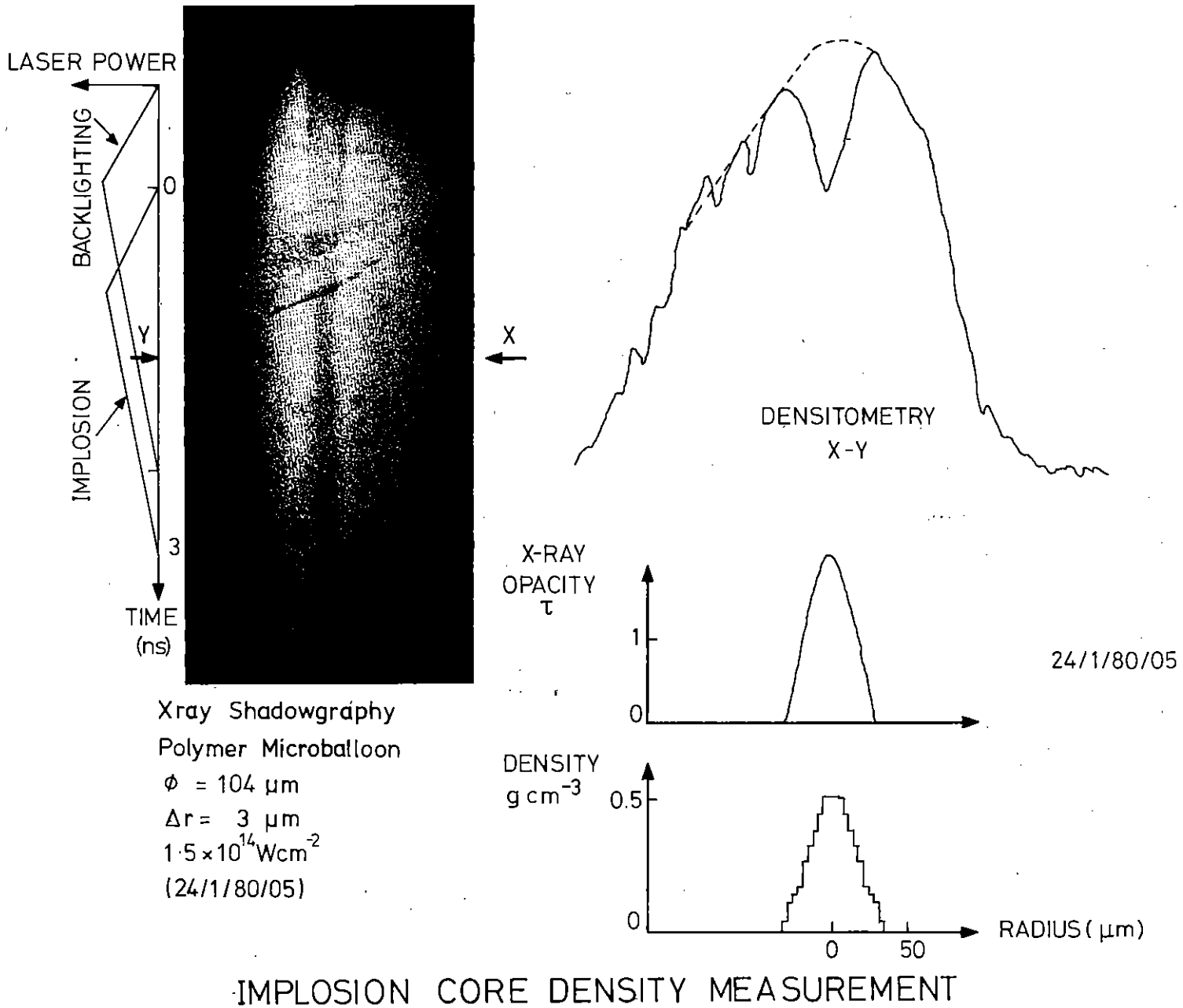

Fig.5.13

A streaked X-ray shadowgraph of the implosion of a polymer shell with analysis of the opacity profile at peak compression.

The analytic model may also be used to estimate the magnitude of Rayleigh Taylor growth exponents by calculating

$$G = \int \gamma \, dt = \int \left(\frac{2\pi}{\Delta r} \frac{d^2 r}{dt^2} \right)^{\frac{1}{2}} dt$$

This leads to

$$G = 4(r_o/\Delta r)^{\frac{1}{2}} A^{\frac{1}{2}} t^{4/3} \text{ ns} \qquad 0 \leq t \leq 1$$

and

$$G = 4(r_o/\Delta r)^{\frac{1}{2}} A^{\frac{1}{2}} \left(1 + \frac{2^{4/3} - (3 - t)^{4/3}}{2^{1/3}}\right), \quad 1 \leq t \leq 3$$

where A is the same parameter defined above. The growth exponent is also plotted in Figs.5.08 - 5.10. An exponent of 4 is sufficient to drive $\simeq$ 200 A perturbations to $\simeq$ 1μm amplitude and this condition would be satisfied at early times in the implosion of a plastic coated balloon.

The hydrodynamic efficiency of an implosion may be estimated as

$$(1 - f)\frac{2\pi r^2 \Delta r \rho}{E_{abs}} \left(\frac{dr}{dt}\right)^2$$

where f is the fractional mass loss and E_{abs} is the absorbed energy. Typical shots indicate the efficiency to be as low as $\simeq$ 5%.

In addition to measuring implosion r(t) characteristics and seeking evidence of fluid instability a further objective of these experiments was to directly diagnose implosion core opacity profiles and hence density profiles. Simulations have shown that pure polymer shells are optimum for such measurements because of their low X-ray opacity and that if filled with high Z gases absorbing above their K edge direct determination of the gas density may also be possible.

A preliminary investigation of this possibility was made in the present experiment. Fig.5.13 shows the implosion of a pure polymer shell 3 μm thick and 104μ m in diameter. There is obvious strong transmission of the

backlighting X-rays throughout the implosion. The initial wall absorption features quickly disappear as a rather diffuse implosion core forms (presumably due to fluid instability as in the other cases which might here be exacerbated by the poorer thickness uniformity of this target). The densitometer profile shows the absorption feature at peak compression which is displayed below as an opacity profile. Abel inversion of the opacity profile assuming spherical symmetry gave a radial profile of absorption coefficient which is shown in the diagram as a density profile (neglecting any loss of opacity by ionization since this unstable behaviour could not be simulated). Direct density determination in this way is in pricipal possible for any implosion with an appropriate backlighting X-ray energy.

The densities in the implosions shown in Fig.5.06 could not be estimated in this way since there was insufficient transmission at the implosion peak. However, average densities assuming that the residual mass after ablation loss is contained within the opaque region could be estimated giving values of 5.0, 1.0 and 0.3 g cm^{-3} for the 3 cores from left to right. The one dimensional simulation densities were considerably higher by factors of the order of the volume disparity ratios shown in Fig.5.11.

Two shots with high aspect ratio shells filled with 10 Bar of neon showed more stable implosions (i.e. smaller cores) compared to empty similar shells. Although a tentative observation this suggests a line for future experiments.

In conclusion we have observed evidence for instability in high aspect ratio shell targets which may be a result of combinations of shell uniformity, irradiance uniformity and Rayleigh Taylor instability. We have also measured ablation pressure in spherical geometry and found it to be slightly lower than in planar geometry.

L. Cooke, R. Evans, C. Hooker, M. Key, C. Lewis, P. Rumsby and M. Ward

5.5 Layered Planar Target Stability Experiments

There are two main problems recognised in laser compression; preheat and Rayleigh Taylor instabilities. Several experiments have investigated the preheat level (5.02, 5.03), but the only experimental work reported on the Rayleigh Taylor instability is on the inner surface instability of electron beam compressed targets (5.04). The classical treatment of the Rayleigh Taylor instability of an accelerating interface of high and low density inviscid incompressible fluid gives the well known growth rate

$$\gamma = (ka)^{\frac{1}{2}} A$$

where k is the wavenumber of the perturbation, a is the acceleration and A is the Attwood number, equal to 1 for a vacuum-fluid interface. When viscosity is included (5.05) the maximum growth rate corresponds to the maximum wavenumber

$$k_{max} = 0.49 \ (a/\nu^2)^{1/3}$$

where ν, the kinetic viscosity, determines the maximum γ. However, in an ablative acceleration there is some theoretical evidence that flow through the narrow unstable region where ∇p and $\nabla \ell$ are antiparallel stabilise (5.06), the Rayleigh Taylor mode. In constrast recent theoretical work (5.07, 5.08) suggests that the simple formulas for γ are good approximations for the ablation surface.

We have carried out an experiment designed to detect mixing in the surface layers of an accelerating foil target. The concept of the experiment is shown in Fig.5.14. Under a steady acceleration of a foil the unstable surface layer should deform resulting in tongues of high density fluid protruding into the vacuum. If the surface of the target is layered the stretching of the topmost layer would spread it and bring the underlying layer close to the ablation front, across the protuberance. When the underlying material moves into the hot ablation front it will start to emit X-rays. The topmost layer will be ablating off during the instability growth time thus evidence of instability would be that X-ray

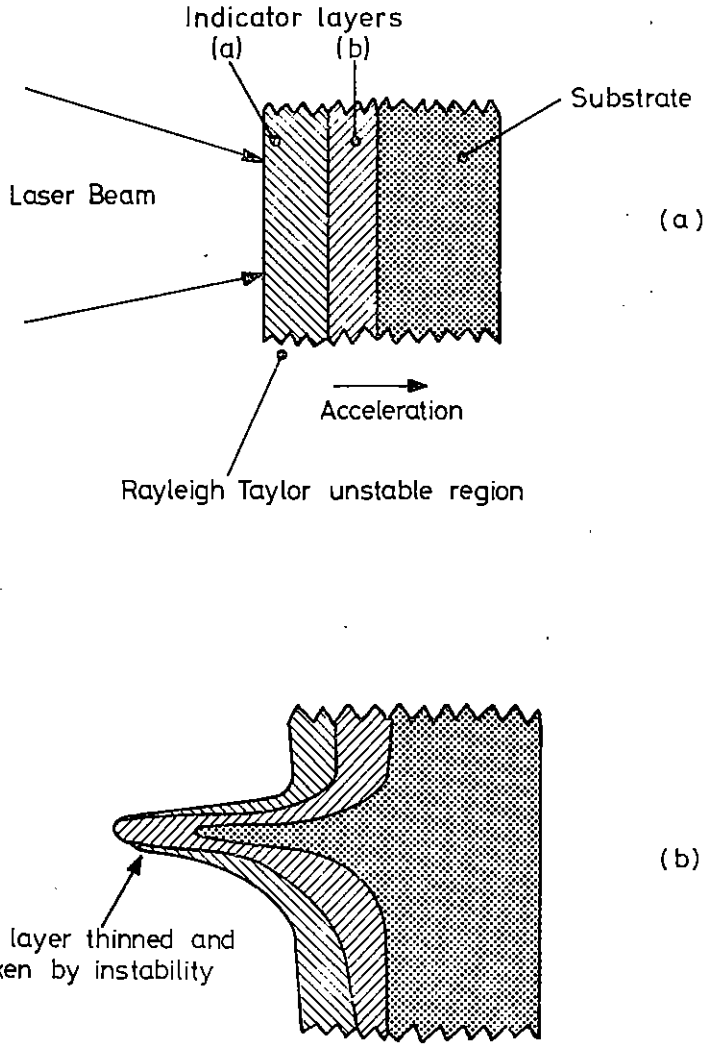

Fig.5.14

Break through of underlying layer because of stretching of topmost layer across the Rayleigh Taylor protuberances. Layer a is Al and layer b is SiO.

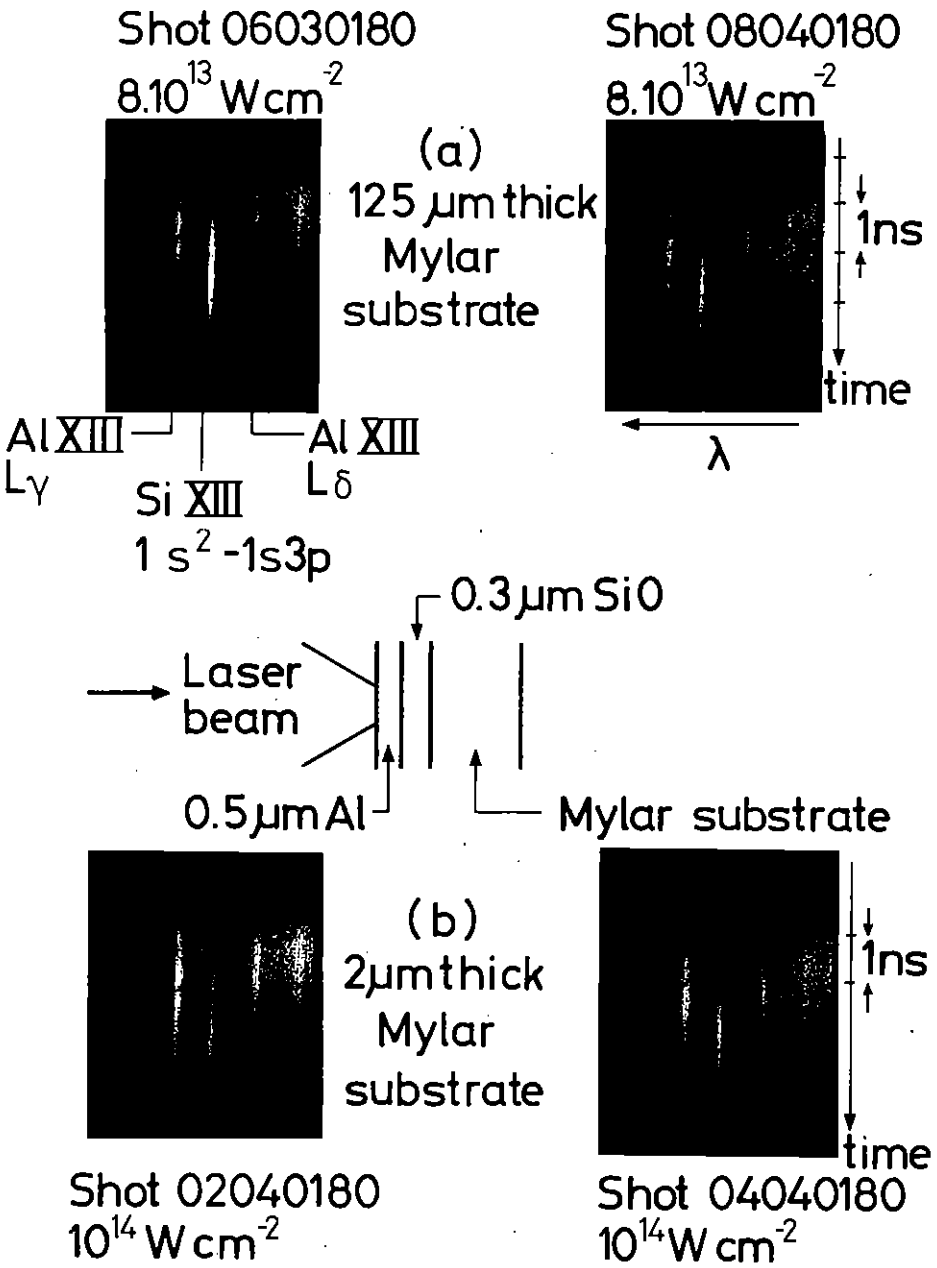

Fig.5.15

X-ray streaks showing the Ae XIII L_γ and L_δ lines and delayed emission on the Si XIII $1s^2 - 1s3p$ after the Al has been ablated off. Streaks are shown for effectively massive targets (125 μm myler) and thin targets for which calculated $\int\gamma dt \gtrsim 15$. Instability mixing would manifest itself by shorter delays for 2 μm myler targets.

emission from the underlying material would appear more rapidly in an unstable accelerating target than in a massive target, which would be stable because the ablation surface would be moving at a constant velocity behind the laser driven shock.

Experiments were first performed with a 0.5 μm layer of Al on 0.3 μm of SiO supported by a thick substrate, 125 μm of mylar. This thickness can be considered semi infinite as the shock transit time at $v_s \sim 5\ 10^6$ cm s^{-1} is 2 nsec. The targets were irradiated at a peak intensity of 8×10^{13} W cm^{-2} over a 200 μm laser spot, with a 1.5 ns fwhm laser pulse at 1.05 μm. The X-ray emission around 5.7 A was observed with a TLAP X-ray crystal and an X-ray streak camera. Typical streak spectra are shown in Fig.5.15(a); showing Al XIII L_γ and L_σ lines starting promptly and then after a delay of 0.9 ± 0.1 ns the Si XIII $1s^3 - 1s^3p$ line from the underlying SiO appears. The average mass ablation rate M is then the area density of the Al divided by the delay time i.e. $1.5\ 10^5$ gm cm^{-2} s^{-1}. The ion velocity v_i was measured by Faraday cups to be $5\ 10^7$ cm s^{-1} and thus the ablation pressure is $M v_i = 7.5$ Mbar.

Experiments were then performed with identical targets except that the substrate was thin enough that there should have been steady acceleration during the laser pulse. Targets with 0.5 μm Al on 0.3 μm of SiO supported by 2 μm thick mylar substrate were irradiated at approximately the same intensity, and typical streaks are shown in Fig.5.15(b). The Si line is delayed by the same time, 0.9 ± 1 ns as in the case of a massive target.

For these thinner targets the shock transit time is $\sim 0.5\ 10^{-10}$ s, after which there will be a constant acceleration $a = P/M = 2\ 10^{16}$ cm s^{-2} using the measured pressure P = 7.5 Mbar. Putting numerical values in for k with Z = 10, $n_e = 10^{22}$ cm^{-3} and $T_e = 500$ eV (as suggested by X-ray spectroscopy) then $k_{max} = 6 \times 10^3$ cm^{-1} and $\gamma = 1.0 \times 10^{10}$ s^{-1}, so that during the 1.5 ns pulse $\int\gamma dt \approx 15$. That is, on these simplistic arguments the ablation surface of the target should be highly unstable. The fact that experimentally no such instability is observed could be taken as evidence that either the ablation flow or heat conduction or some other effect

omitted from the classical treatment is stabilising the Rayliegh Taylor instability. On the other hand there is no definite evidence that this method of testing for instability works. It could be that protuberances do not effect the underlying material enough, or that the unstable region where ∇p is antiparallel to $\nabla \ell$ moves to too low a density to affect underlying material, in which case Rayleigh Taylor instability is unimportant. Further corroborative experiments using radiography are planned.

J. Kilkenny

5.6 Zone Plate Coded Radiography of Ablative Implosions

The current interest in laser driven ablative compression makes it desirable to develop new methods for diagnosing the dense but cool implosion cores that are generated. Such cores do not emit X-rays strongly like the hot but tenuous cores produced by exploding pusher compressions, and consequently the spectroscopic methods that have been developed in the past cannot be used.

Recently however X-radiography or shadowgraphy techniques using a subsidiary laser produced plasma as a backlighting source have been developed at the Rutherford Lab. Up to now such experiments have used pinhole cameras or Kirkpatrick-Baez microscopes as the X-ray imaging devices and consequently have been limited in collection solid angle to less than about 2×10^{-6} sr and in X-ray probing energy to less than about 3 keV. In order to probe the dense implosion cores anticipated in future ablative experiments it is vital to develop these techniques in the X-ray region around and above 10 keV. In this high energy region zone plates used in the coded aperture mode make ideal X-ray imaging devices with resolution of a few microns readily attainable and having the necessary high collection solid angle of up to 10^{-1} sr.

Zone plate coded imaging of the X-rays emitted from hot exploding pusher implosions has been developed extensively by Ceglio at Lawrence Livermore Laboratory (5.09) using X-ray energies up to about 40 keV. Preliminary static backlighting tests of unirradiated targets have also been carried out at LLL using zone plate techniques at an X-ray energy of about 4 keV.

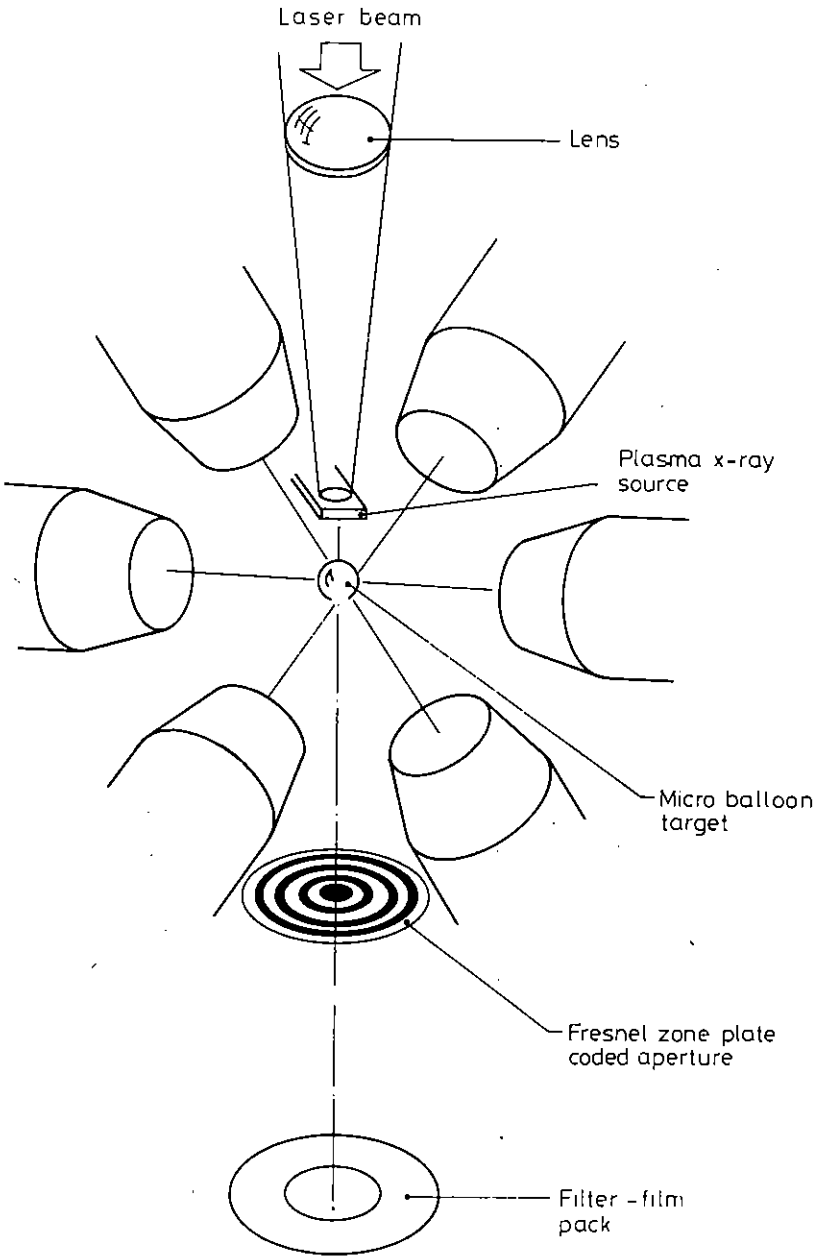

Fig.5.16

Experimental arrangement for zone plate coded radiography of 6 beam ablatively imploded targets.

We have extended this work and used zone plate coded radiography (ZPCR) techniques for the first time to obtain two dimensional X-ray shadowgrams of laser driven ablatively imploded targets.

Fig.5.16 shows a schematic diagram of the experimental arrangement used for ZPCR of imploding targets. The laser output (200 J in 1.5 ns) is split into 7 beams, 6 of which are used to irradiate and implode various hollow shell targets, while the 7th beam is delayed and arranged to irradiate (via an f/2.5 lens) a subsidiary target to act as a backlighting X-ray source. Precise alignment of the backlighting source, target, zone plate and film pack is essential and this was achieved easily and reliably by irradiating the backlighting target from the rear as shown. With this straight line geometry it was possible to first align the backlighting laser beam on the main target, which was then displaced. The film pack and zone plate were then inserted on this beam axis and the main target replaced. Finally, the backlighting target was inserted on the same axis 1.5 mm above the main target and the backlighting lens refocused to give the correct spot size.

With this rear irradiation system the X-ray flux recorded by the zone plate camera was only that which penetrated the backlighting target and consequently these targets were fabricated from strips of mylar 125 μm thick and about 1 mm wide coated on the top face with thinlayers (∿ 2 μm) of various materials. To optimize these targets in terms of high energy X-ray flux a range of materials was irradiated at an intensity of 4×10^{13} W cm^{-2} (400 μm diameter spot size) in a pulse of half width 1.5 ns. The time resolved X-ray emission was recorded in various energy bands from 2 to 10 keV using an X-ray streak camera with filter pack in front of the photo cathode. Potassium chloride (KCl) was found to be the most efficient emitter of X-rays in the 4 - 5 keV band and consequently for all implosion experiments mylar targets coated with 2 μm of KCl were used. The temporal half width of the X-ray emission recorded in the 4 - 5 keV channel was found to be shorter (0.8 ns) than that for lower X-ray energies (1.5 2.0 ns), an effect which improved the temporal resolution of the radiogaphy results.

The zone plates used were made of copper (10 μm thick) and had a diameter of 7.3 mm. Placed at distance of 5 cm from the target they then had a collection solid angle of ∿ 10^{-1} sr. Minimum zone width was 15 μm giving a resolution limit of about 20 μm. Coded images were recorded on Kodak Kodirex film behind filters of 25 μm of Al and 125 μ Be in a film pack placed at 175 μm from the main target. Fig.5.17 shows the relative reconstruction intensity of the experimental system over the spectral range of interest. This is obtained by combining the X-ray filter transmission and the Kodirex sensitivity with the relative reconstruction intensity due to the X-ray transmission of the zone plate material (5.10). This curve together with the X-ray source spectrum which indicated negligible intensity above 5 keV demonstrates that the dominant X-ray probing energy was that in the 4 - 5 keV band.

The exposed coded images were contact printed onto Kodak High Resolution Plates and reconstructed using a He/Ne laser. More details of the zone plate fabrication and reconstruction proceedures are given in section 1.6.2(c) of this report.

Static radiography was performed on various unirradiated thick walled shells to test the system. Experimental opacity profiles were consistent with those calculated on the basis of the X-ray probe energy and 20 μm system resolution. It was also noted that the diameter of the X-ray backlighting source was only about 200 μm, much smaller than the focal spot diameter of 400 μm, showing that as the X-ray probe energy was increased, so the region of plasma hot enough to emit was reduced.

For radiography of ablative implosions, large targets (∿ 250 μm dia) coated with layers of polymer were irradiated with the six main laser beams at an intensity of 10^{13} W cm^{-2}. These parameters were chosen to give a long implosion time so that the 0.8 ns resolution time of the backlighting pulse would not smear the radiographs too severely. Data from similar implosions obtained from streaked shadowgraphy experiments (section 5.4) using a Kirkpatrick-Baez microscope system in the 1.6 - 1.9 keV X-ray region showed that such targets imploded to a diameter of about 120 μm at a time about 2 ns after the peak of the main pulse. The core

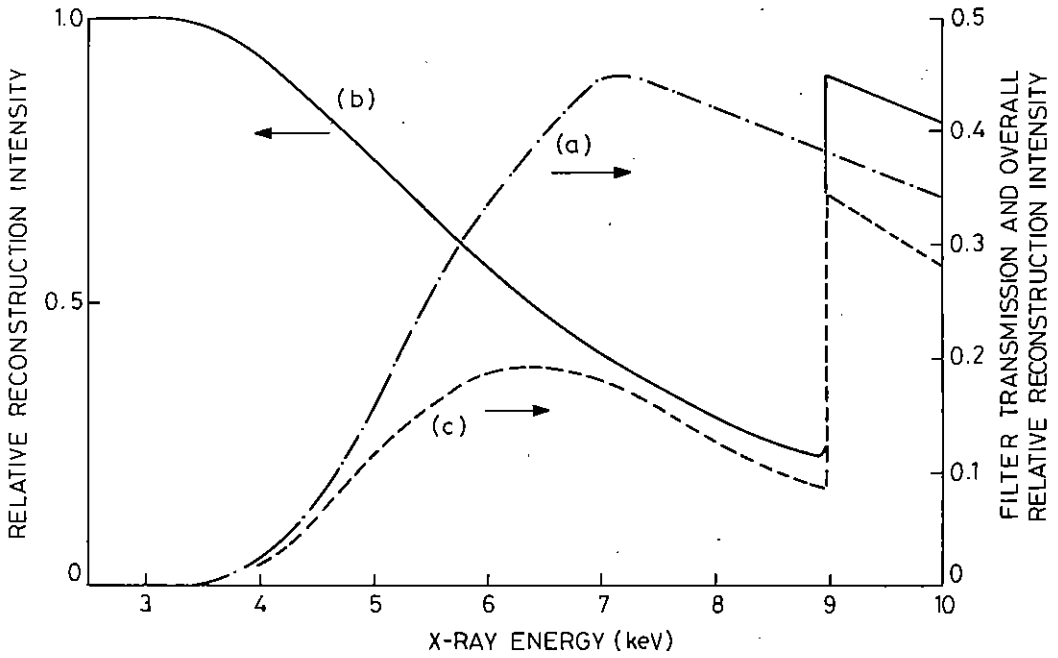

Fig.5.17

Recording system response against X-ray energy. Curve a) Filter transmission with film sensitivity. Curve b) Relative reconstruction intensity due to zone plate transmission. Curve c) Overall system response obtained by combining a) and b).

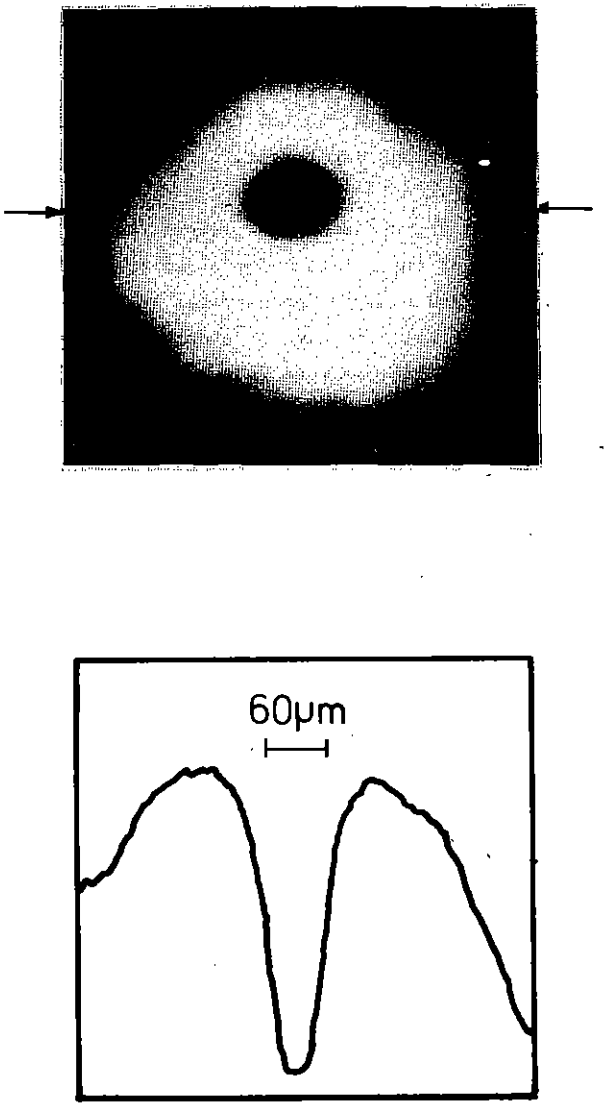

Fig.5.18

Radiograph and microdensitometer trace at peak compression of ablatively imploded 250 μm dia, 1 μm thick glass shell target coated with 2 μm of polymer.

diameter did not change greatly over a period of about 1 ns and consequently the backlighting beam was set to irradiate the KCl target at this time. Data obtained from an identical zone plate camera viewing the target from the side showed that for targets with polymer coatings the self X-ray emission in the 4 - 5 keV region was negligible compared to that from the KCl backlighting target.

Fig.5.18 shows a two-dimensional reconstructed ZPCR image and microdensitometer trace of the ablative implosion of a 250 μm diameter polymer coated target and clearly demonstrates the presence at peak compression of a small opaque implosion core of about 60 μm diameter. This result is consistent with that obtained from streaked radiography where with about 1.7 keV X-rays a minimum core size of about 120 μm was observed. By assuming a gaussian core density profile and scaling this diameter with X-ray energy we calculate the diameter of the material with similar opacity at 5 keV to be about 70 μm. A peak core density of a few gm.cm^{-3} is implied.

Such core radiographs clearly demonstrate the potential of ZPCR for probing the dense plasmas that will be generated in future ablative compression experiments.

C. Duncan, C. Lewis, A. Raven and P.T. Rumsby.

CHAPTER 5 REFERENCES

5.01 M H Key, C L S Lewis, J G Lunney, A Moore, T A Hall and R G Evans, Phys. Rev. Letts. 41, 1467 (1978), and Rutherford Lab Report No. RL-79-036.

5.02 K B Mitchell and R P Godwin, J. Appl. Phys. 49, 3851 (1978).

5.03 J D Hares, J D Kilkenny, M H Key and J G Lunney, Phys. Rev. Lett. 42, 1216 (1979).

5.04 F C Perry, L P Mix, L Baker, A J Toepler, Bull. Am. Phys. Soc. 23, 854, (1978).

5.05 I Chandrasekhar, "Hydrodynamic and Hydromagnetic Stability" OUP, London (1961).

5.06 K A Bruekner, S Jorna and R Jarda, Phys. Fluids 17, 1554 (1974).

5.07 K A Bruekner, S Jorna and R Jarda, Phys. Fluids 22, 1841 (1979).

5.08 R L Morse, Bull. Am. Soc. 24, 946 (1979).

5.09 N M Ceglio and J T Larsen, Phys. Rev. Lett. 44, 599 (1980).

5.10 N M Ceglio and H I Smith, Rev. Sci. Inst. 49, 15 (1978).

CHAPTER 6 X-RAY SPECTROSCOPY AND XUV LASERS

INDEX

CHAPTER EDITOR: R G Evans

CHAPTER 6 X-RAY SPECTROSCOPY AND XUV LASERS

6.1 Time Resolved X-ray Emission Spectra

Time resolved X-ray spectroscopy as a diagnostic technique has been described briefly in previous annual reports (6.1) when used with short ($\tilde{}$ 100 ps) laser pulses. Plane targets were used to study the time dependence of resonance to satellite line intensity ratios for aluminium, and neon filled glass microballoons were used to measure implosion times and time resolved Stark widths of neon line emission (Ly_β) from the core (6.2). More recently the technique has been applied to long pulse (1.5 ns) irradiation of layered targets at 1.05 μ and 0.52 μ to measure mass ablation rates as a function of irradiance (see section 4.3). The experimental configuration will be described in some detail here.

The apparatus is shown schematically in Fig.6.01, with the target to streak camera photocathode distance L = 18 cm. The useful spectral range is limited by the acceptance length $\ell \approx$ 15 mm on the cathode. The cathode is made by depositing ≈ 100μm of CsI at ≈ 5% solid density on 25μm beryllium substrates. Some useful formulae related to the apparatus can be expressed from the notation in Fig.6.01. The displacement of the crystal x from a line joining the source and the cathode centre to record a wavelength λ at the cathode centre is given by

$$x = \frac{L\lambda}{4d}\left(1 - (\lambda/2d)^2\right)^{-\frac{1}{2}} \qquad (1)$$

where d is the interatomic crystal spacing. The spectral range covered under the above conditions for a useful length of cathode ℓ is given by

$$\Delta\ell = \frac{2d}{L}\left(1 - (\lambda/2d)^2\right)^{3/2} \qquad (2)$$

However, due to the finite length, D, of crystal used the spectral range will be further restricted by the crystal at sufficiently low Bragg angles. In the present case this criterion is given by $\theta_B = \tan^{-1}\left(\frac{\ell}{2D}\right)$ or with ℓ = 15mm and D = 38 mm by $\lambda \approx 2d/5$ Å.

The spectral resolution available can be estimated by replacing "ℓ" in equation (2) by a value $\Delta\ell$ representing a length of cathode typical of a source limited spectral line width convolved with a spatial resolution element of the streak camera imaging system. Typically $\Delta\ell \tilde{}$100μm and $\ell \approx$15 mm. Fig.6.02 illustrates the dependence of x and $\Delta\lambda$ for on λ for a range of useful crystals, PET, Ge, RAP and ADP.

Temporal resolution is attained with a vertical slit of width w placed between source and crystal. For a source of width s the projected spectral strip has a width W ≈ 2s + 3w which is independent of wavelength or crystal. Typically for s ≈ w ≈ 100μm a temporal resolution of ≈ 40 ps is achieved on the fastest sweep speed.

Some typical streaked spectra are shown in Figs.6.03 and 6.04. These records were obtained during mass ablation rate investigations and are discussed fully in section 4.3. In all cases $\tilde{}$ 1.5 ns pulses were used to irradiate layered targets and temporal resolution is ≈ 100 ps. Fig.6.03 shows Al and Si emission in the range 5.3 - 6.7 Å using a TlAP crystal. Fig.6.04 shows Ti and Cr helium-like resonance lines and satellites using a PET crystal.

C.L.S. Lewis, M.J. Lamb, J.D. Kilkenny, S.Veats, M.H. Key

6.2 Dielectronic Satellite Lines of Lyman α in Hydrogen-like Al and Si

The dielectronic satellites close to the L_α lines of H-like Al and Si were recorded in microballoon and plane target experiments. While these satellite lines were not used for diagnostic purposes, it was observed that their relative intensities showed the predicted density dependence. Fig.6.05 shows the Al XIII L_α line and dielectronic satellites emitted

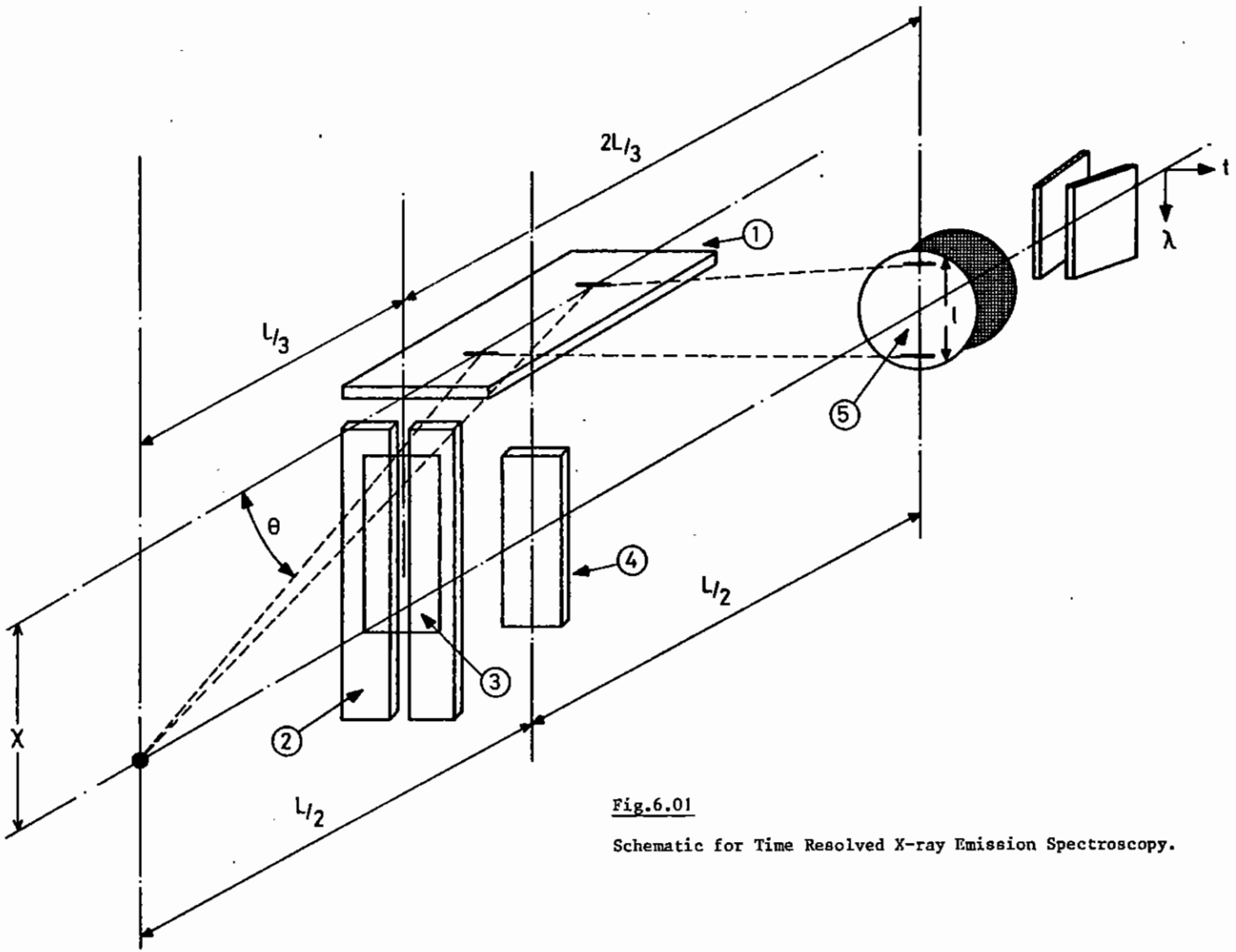

Fig.6.01

Schematic for Time Resolved X-ray Emission Spectroscopy.

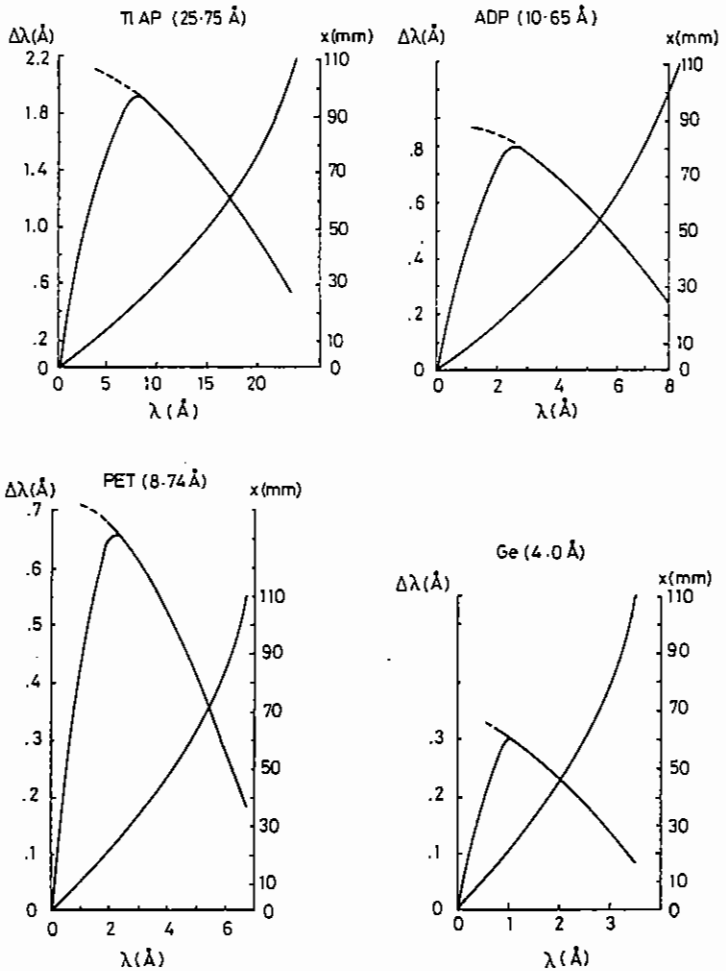

Fig.6.02

Design parameters for crystal spectrometer.

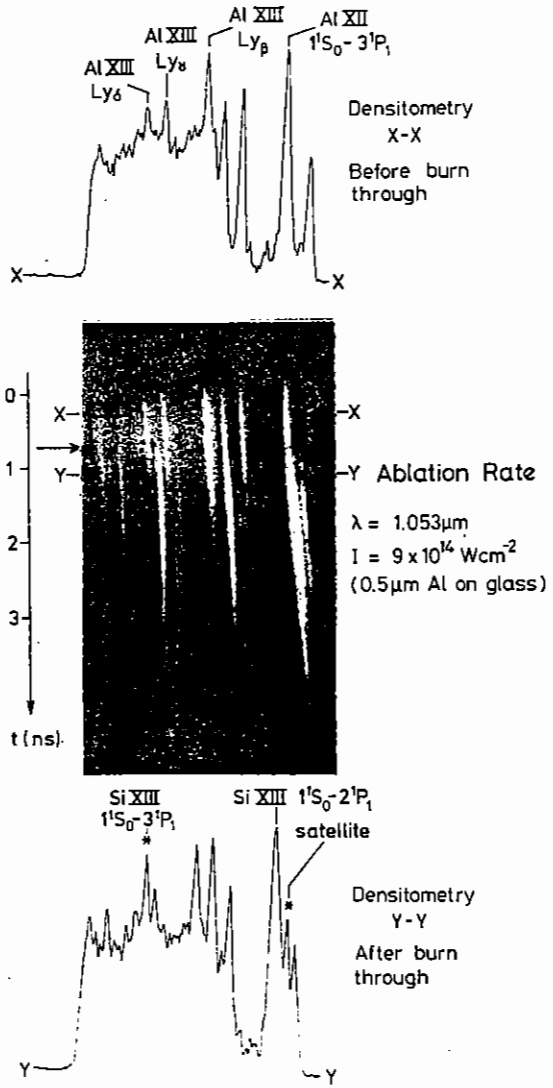

Fig.6.03

Time Resolved X-ray emission spectrum - 0.5 μm Al on glass substrate.

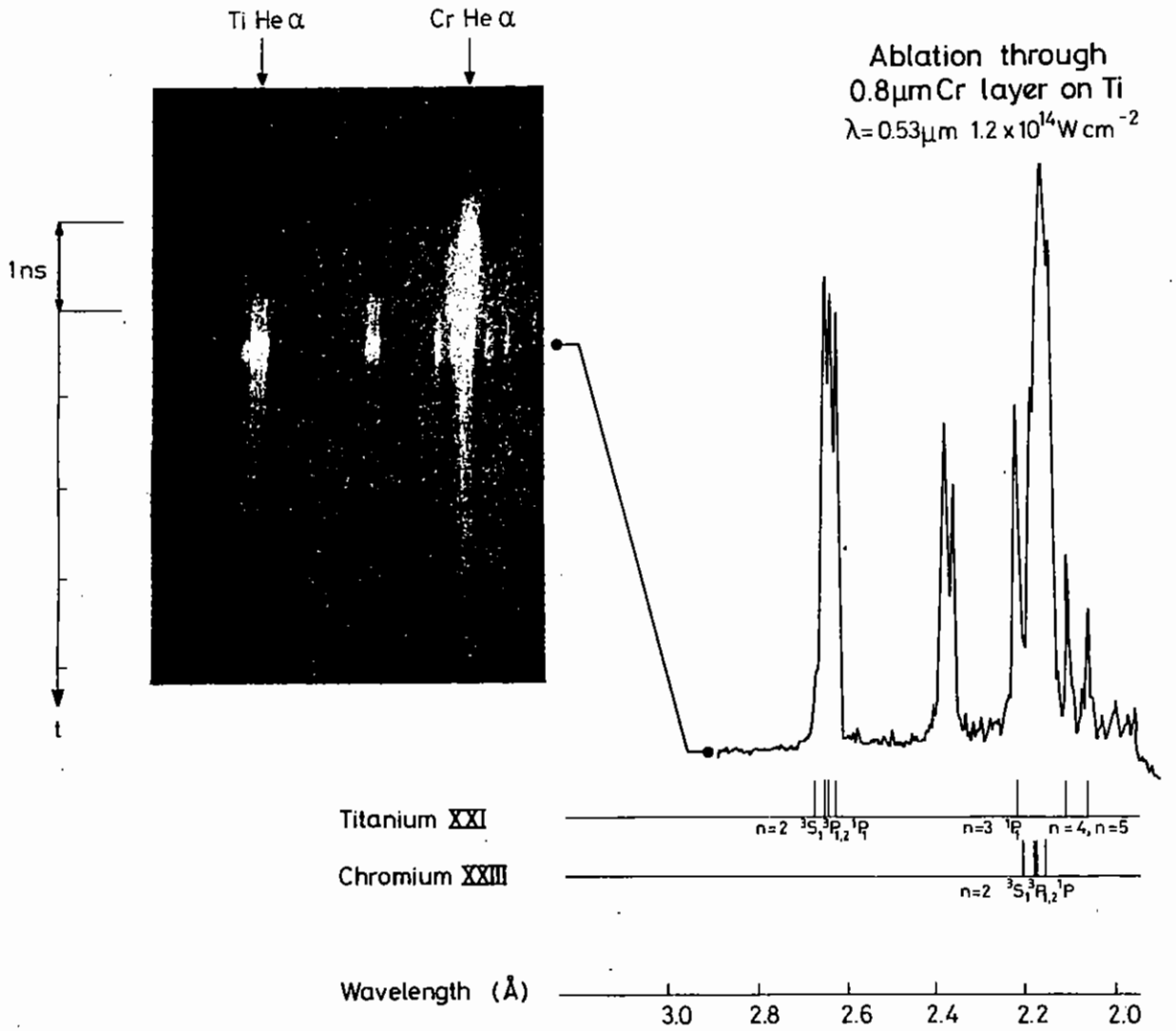

Fig.6.04

Time Resolved X-ray emission spectrum - Cr on Ti substrate.

from the ablation plasma of an aluminium coated microballoon target (shot 209). The satellite lines were identified using references (6.03), (6.04) and (6.05).

In plasmas of low electron densities the doubly excited '2121' levels are primarily populated by dielectronic recombination, and are depopulated by auto-ionisation and radiative decay. The satellite line intensities are then proportional to

$$q_{ij} = \frac{g_i \, r_i \, A_{ij}}{\lambda_{ij} \, (\Gamma_i + \sum_k A_{ik})}$$

where Γ_i is the autoionisation rate and A_{ij} is the radiative rate. As the electron density in the plasma increases, the doubly excited levels are mixed by electron collisional transitions (6.06 - 6.09). It has been shown (6.06, 6.08, 6.09) that for $n_e \gtrsim 10^{21}$ cm^{-3} electron collisions transfer excitation from the $2s2p\ ^3P$ levels to the $2P^2\ ^3P$ levels, making the intensity ratio (β) of the $1s2p\ ^3P - 2p^2\ ^3P$ (B) and $1s2s\ ^3S - 2s2p\ ^3P$ (A) lines density dependent as shown in Fig.6.06. At even higher electron densities ($\gtrsim 10^{22}$ cm^{-3}) excitation is transferred from the singlet to the triplet levels, and then the intensity of the sum of the triplet lines $1s2p\ ^3P - 2p^2\ ^3P$ and $1s2p\ ^3S - 2s2p\ ^3P$ relative to the singlet line $1s2p\ ^1P_1 - 2p^2\ ^1D_2$ is density dependent (6.07) as shown in Fig.6.07.

It can be seen in Fig.6.05 that lines A and B are of approximately equal intensity, which indicates, from Fig.6.06, that the electron density is $\sim 10^{22}$ cm^{-3}. It has been shown (6.01) that the ablation plasma electron density as measured by line broadening is also 10^{22} cm^{-3}. Fig.6.07 does not contain a curve for the intensity ratio $\sigma = \frac{I_A + I_B}{I_C}$ as a function of n_e for Al, but that curve will be between the curves for Mg and Si. In any case, the observed ratio of $\sigma = 1.3$ implies an electron density that is much higher than is expected for the ablation plasma. In another experiment where the Si XIV L_α line and its satellites were recorded from a plane layered target with 0.4 μm Al on SiO, the triplet-singlet ratio

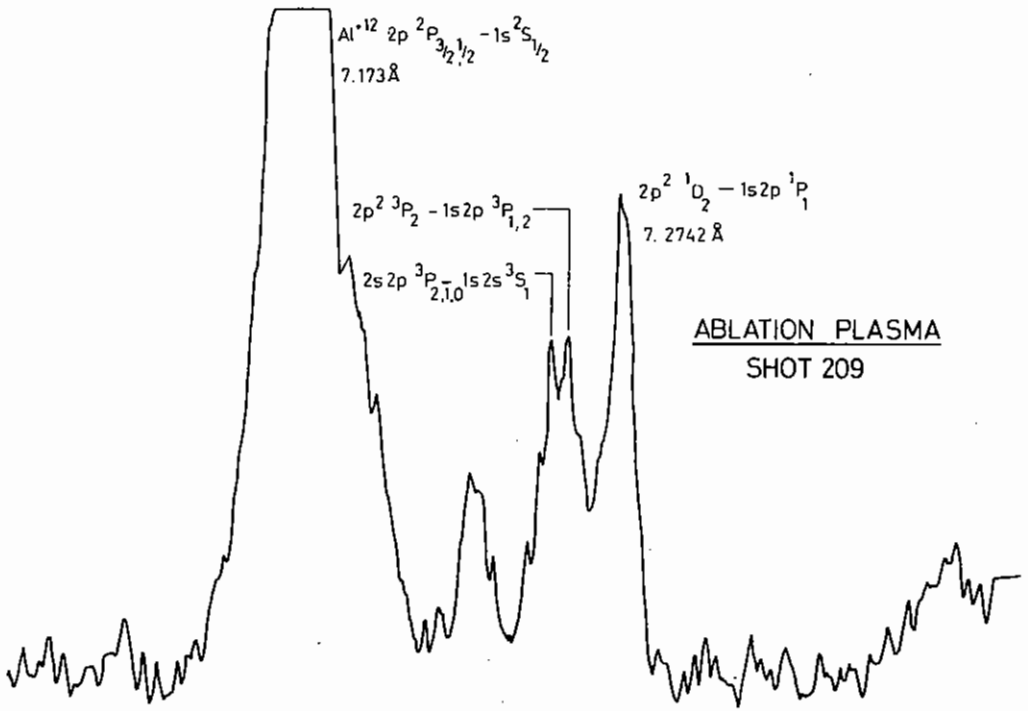

Fig 6.05 DIELECTRONIC SATELLITES OF Al+12 LYMAN α

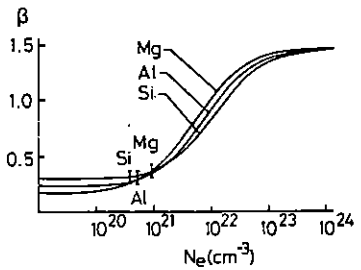

Fig.6.06

Dielectronic satellite line ratios from Reference 6.8.

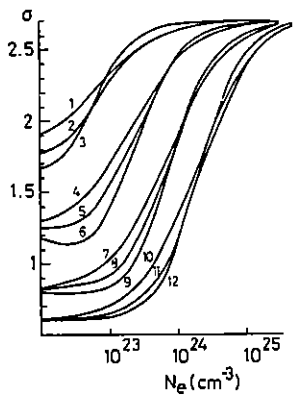

Fig.6.07

Dielectronic satellite line ratios from Reference 6.7.

was $\sigma = 0.87$. Using Fig.6.07 this ratio implies that $n_e = 6 \times 10^{23}$ cm^{-3} against the measured ablation plasma density of 1×10^{22} cm^{-3}.

It has been pointed out (6.09) that the calculation of σ in reference (6.07) does not include three-body recombination from the excited hydrogenic levels whose populations are enhanced by the reabsorption of the optically thick L_α line.

In the space resolved spectrum from the implosion of an argon filled microballoon, it was noted that triplet-singlet ratio σ for the Si lines was greater in the core plasma than in the ablation plasma as shown in Fig.6.08. These satellite spectra were analysed by J.F. Seely (6.10) at the Naval Research Laboratory. His analysis showed that the value of σ in the ablation plasma implied an electron density of less than 5×10^{22} cm^{-3} while in the core the value of σ showed the electron density to be 1.1×10^{23} cm^{-3}, which agrees with the Stark broadening measurement. Fig.6.08 shows a comparison of the theoretical satellite spectrum with microdensitometer tracings of the ablation plasma and implosion core spectra; the response of the recording film is proportional to exposure for the range of neutral density spanned by the satellite lines.

Seely's (6.10) calculation shows that for Si the singlet-triplet ratio is strongly density dependent for $n_e > 5 \times 10^{22}$ cm^{-3}, while reference (6.07) shows that σ is density dependent only for $n_e > 2 \times 10^{23}$ and that the measured value of $\sigma = 1$ in the core plasma indicates that $n_e \approx 9 \times 10^{23}$ cm^{-3}. The experimental results seem to favour the more comprehensive calculation due to Seely (6.09). Work is in progress to analyse the Si L_α satellite spectra from a range of laser implosions where the measured imploded core electron densities lie in the range $3 \times 10^{23} < n_e < 2 \times 10^{23}$ cm^{-3}, and to compare these spectra with theoretical predictions.

J.G. Lunney

6.3 Observation of Population Inversion Between the n = 3 and n = 4 Levels of Si XIII and Al XII

In experiments to investigate the transport of energy in laser irradiated plane layered targets the X-ray emission spectrum of the ablation plasma was space resolved in the direction along the laser axis. The front layer heated by the laser was usually either silicon monoxide or aluminium. In either case, the resonance line emission of He-like Si and Al were recorded at distances up to 200 μm from the target surface. It was noted that for distances greater than 150 μm from the target surface the $1^1S_0 - 4^1P_1$ line showed stronger emission than the $1^1S_0 - 3^1P_1$ line for both Si XIII and Al XII. Fig.6.10 shows a space resolved spectrum for a laser irradiated target where the front layer was SiO.

A similar observation of population inversion has been reported elsewhere (6.11). In that experiment a 10 J, 200 ps laser pulse was focussed on a plane Al target, and a magnesium foil at 100 μm from the target surface was used to cool the expanding plasma. At distances greater than 300 μm the Al XII $1^1S_0 - 4^1P_1$ line was found to be stronger than the Al XII $1^1S_0 - 3^1P_1$ line. The observed spectrum was used to derive the temperature and density as a function of distance from the target surface. It was concluded that in the region where the intensity ratio is anomalous, the lines in question are optically thin, and the observed intensity ratio is direct evidence of population inversion between the n = 3 and n = 4 levels. It was also concluded that the inversion was mainly due to the enhanced cooling provided by the magnesium foil. The transverse dimension of the plasma was measured to be 200 μm, and the gain coefficient on the $3^3D - 4^3F$ manifold at 129.7 Å was estimated to be ~ 10 cm^{-1}.

The spectrum shown in Fig.6.09 was recorded when a 10 J, 100 ps, 1.06 μm laser pulse was focussed to a spot diameter of ~ 100 μm on a plane layered target where the front layer was SiO. The slit size was 25 μm and the Bragg crystal was PET. At 160 μm from the target surface the Si XII $1^1S_0 - 4^1P_1$ and Si XIII $1^1S_0 - 3^1P_1$ lines are optically thin, and the intensity ratio implies that the population density ratio of the inverted levels is:

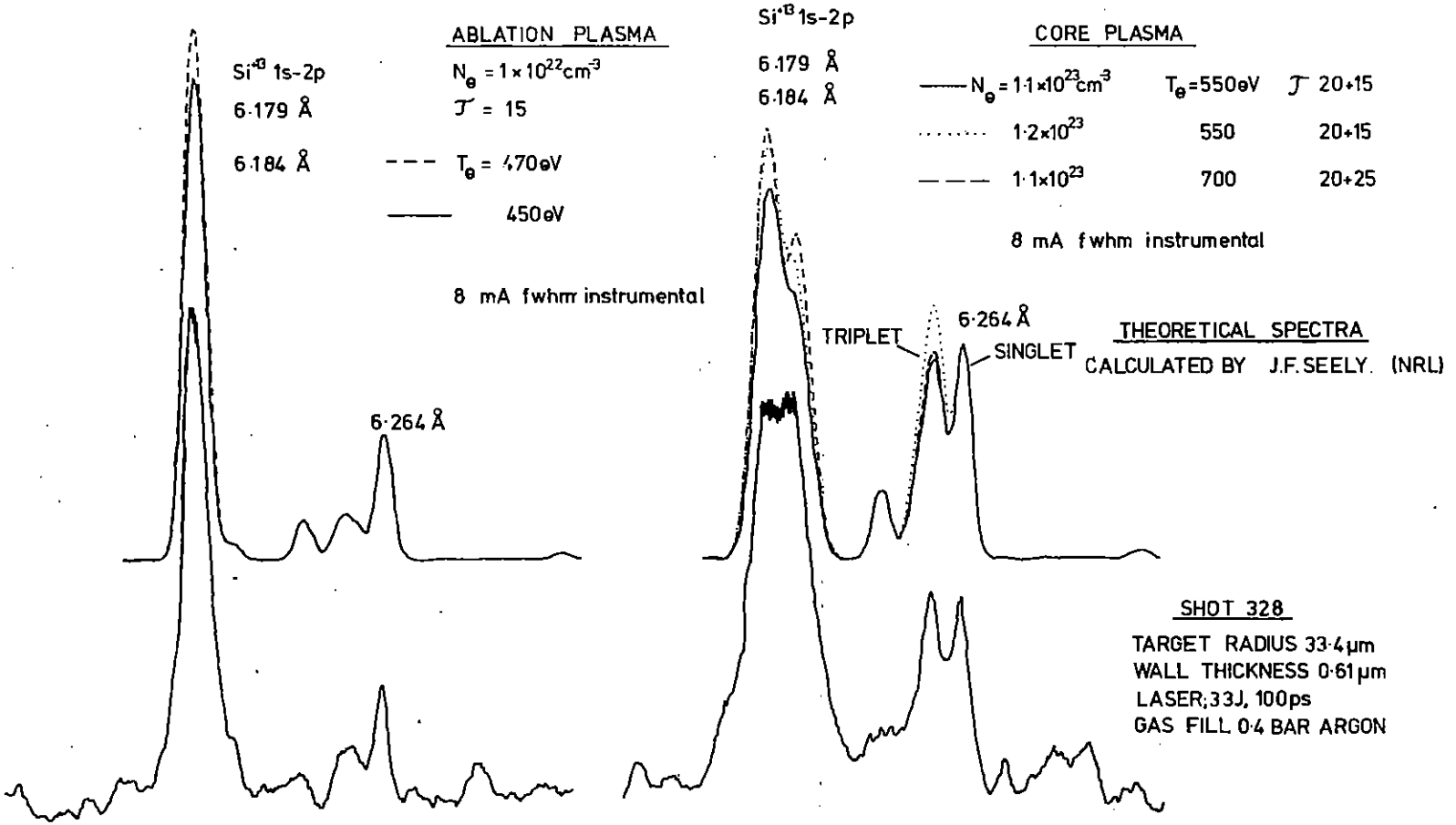

Fig 6.08 DENSITY DEPENDENT DIELECTRONIC SATELLITES OF Si^{+13} LYMAN α

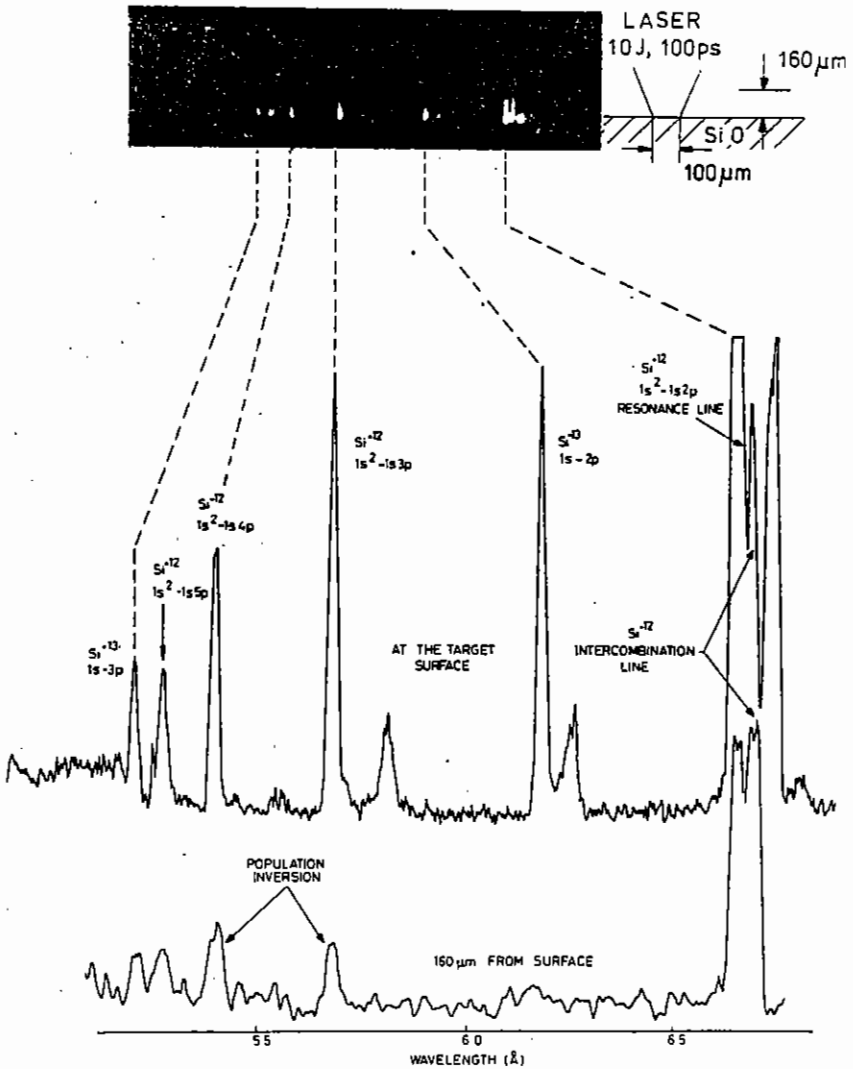

Fig 6.09 POPULATION INVERSION OF Si^{+12} LEVELS IN A LASER PRODUCED PLASMA

$$\frac{n(1s4p\,^1P)}{n(1s3p\,^1P)} = 3.7$$

A similar population inversion was derived in reference (6.11), but at a distance of ~ 300 μm from the target surface. Thus it would seem that adiabatic cooling in the expanding plume is sufficient to establish population inversion without the addition of an extra cooling channel.

It was also noted that at distances greater than 160 μm from the target, the intercombination line ($1^1S_0 - 2^3P_1$) was more intense than the resonance line ($1^1S_0 - 2^1P_1$). It has been shown by Boiko et al (6.12) that this is expected in a "supercooled" plasma, where radiative recombination makes a significant contribution to the population of the 2^3P_1 and 2^1P_1 states. This evidence of supercooling is consistent with observation of population inversion.

J.G. Lunney

6.4 X-ray Emission Spectra for Plasma Diagnosis

6.4.1 Ion Acoustic Features in High-z Emitters

The possibility that ion acoustic mode enhancement occurs in high-z plasmas has been studied recently to determine the effects on the line profiles emitted in the compressed cores of the laser imploded targets (6.13). The profiles of greatest interest are the hydrogen-like Lyman γ (i.e. level 1 to level 4) transition for a number of reasons:

(a) The Lyman γ profile has a unshifted central component.
(b) The ion acoustic feature will appear at very small frequency separation from line centre, roughly at frequencies less than ω_{pi}, the ion plasma frequency.
(c) The optical depth of Lyman γ is small, so that the line centre is observable in experiments.

The fact that the charge state of the plasma affects the ion acoustic enhancement leads to the possibility that the Lyman γ line will be a possible diagnostics of the plasma charge state. This of course would compromise any use of Lyman γ as a plasma electron density diagnostic.

To illustrate the effects of the widely differing ion species in the plasma on the profile, we choose the Ar XVIII Lyman γ transition emitted from a plasma at a temperature of 5.2×10^6 K and an electron density of 3.10^{23} cm^{-3}. The conditions have already been attained and represent realistic parameters. Five different cases were studied: first, no ion dynamics, a calculation that would reproduce the "standard" form of line shape theory; second, a case with z = 1 representing an argon seed in a hydrogen fill (note this will be comparable to a D-T fill in terms of the line profile); third, an average $\overline{z}$ of 9.3 representing a mean ion approximation to a plasma with 40% z = 15 and 60% z = 1; fourth, the full calculation with the z = 15 and z = 1 species; and, finally the case of pure argon with an average $\overline{z}$ of 15. For the case in which only electrons are included in the collisional broadening, the peak is a factor of 1.4 higher than the peak for the z = 1 perturbers, for simplicity, it has been excluded from Fig.6.10. The method of comparing the various cases was to use equal area normalization and the abscissa is measured in frequency separation from the line centre. The effect of differing ion plasma charges does significantly alter the central region of the profile. The trend is also as expected with the higher z plasma showing greater damping in the line core. However, the use of an average $\overline{z}$ is <u>not</u> valid for the details of the profile, but may still suffice as long as this core is obliterated by experimental limitations.

To prove that the effect does arise from the dynamics alone, the microfield is shown for three cases in Fig.6.11. Here the microfield probability is plotted against microfield strength measured in mean field units $E_o = 2.61\ e\ N_e^{2/3}$. It is apparent that the microfield, although varying slightly, does not change sufficiently to provide observable changes in the line profile. This result has been verified by detailed calculation. Further, we note that, in the standard formulations, where perturber charge enters only in the microfield, the width of the profile

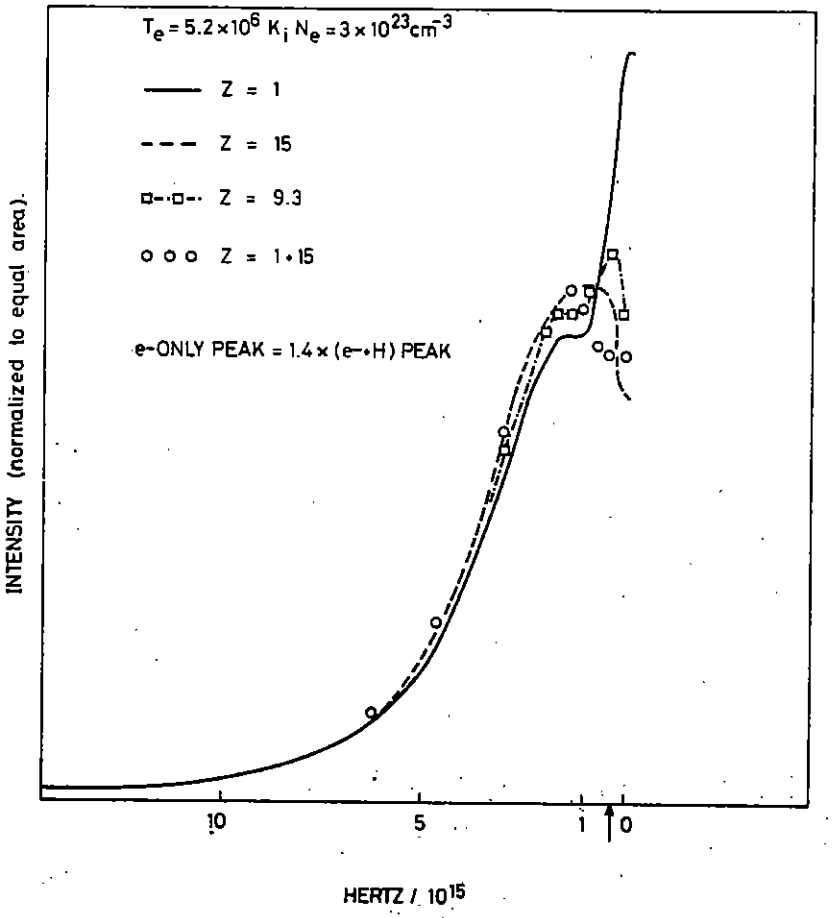

Fig.6.10

Argon XVIII Lyman γ line profiles for different perturbers.

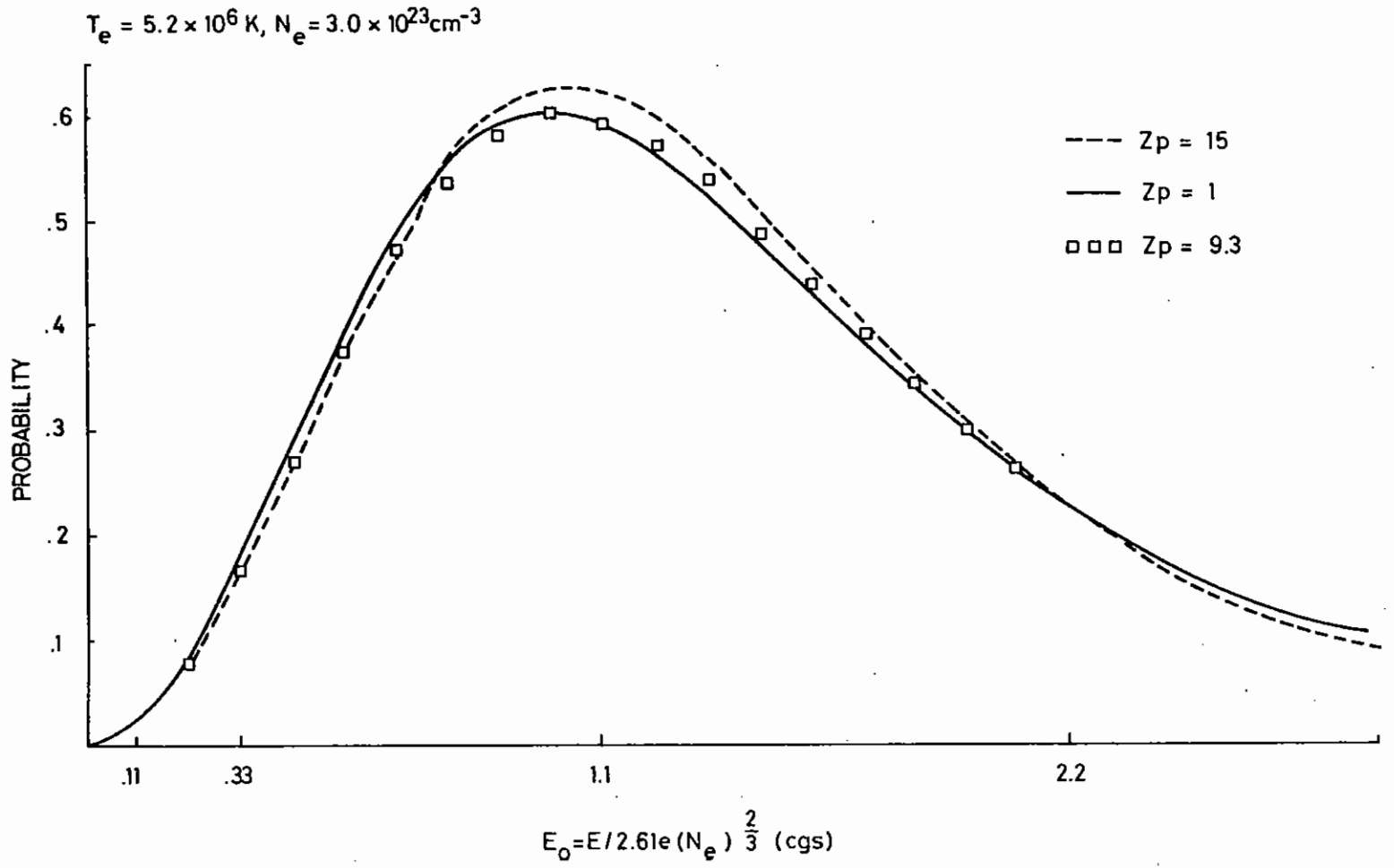

Fig.6.11

Microfield distribution function.

is independent of perturber ion charge. This result indicates that the statement in Yaakobi et al (6.15) that the width varies as $z_p^{1/3}$ is incorrect.

The results of the present calculations indicate that the charge state of the plasma should affect the central region of the hydrogenic Lyman γ transition from high z emitters. On the one hand, our finding will compromise the use of this transition as a diagnostic for electron density since its width will be a function of ion species concentration. On the other hand, this transition can possibly provide a diagnostic for the charge state of the plasma which is, in itself, of considerable interest. Further, there is the possibility of performing experiments to measure the substantial differences in line shape in the two extreme cases, i.e. a hydrogen plasma and a pure Argon plasma.

Finally, we note that the same effect will occur in the Lyman α transitions but, due to the large optical depth, the effect will provide no new diagnostic material but must be included to obtain appropriate estimates of the hydrogenic species ground state number densities (6.16)

D. Burgess, D. Everett, R. Lee

6.4.2 Possible Appearance of Plasmon Satellites on Spectral Lines

In previous experiments, Aluminium which was coated on the outer layer of the microballoons, was diagnosed to be present in the compression core (6.17). The method used to determine the presence of the Al in the core was the width of the Al hydrogenic lines emitted. These lines however show a fascinating feature which until now has remained unexplored. On the wings of these lines sit emission features which correspond to a plasma frequency separation from line centre. The possibility that these features are "plasma satellites" is novel and interesting.

The appearance of plasma satellites on Hydrogenic and Helium-like line profiles has been theoretically studied in the context of laser compression experiments previously only for non-thermal but equilibrium

conditions (6.17). This study illustrated the weakness of the features due to the large Landau damping rate at the high densities of interest. The experiments which illustrate the hydrodynamically unstable mixing of the Aluminium into the core on the other hand indicates the possibility of a highly non-equilibrium plasma (at least for the period of Al XIII Ly α emission). The study of these features under the assumption they are plasma satellites will yield information on the state of a plasma which could produce these resonances.

In Fig. 6.12 we illustrate the Al XIII Ly α line and a fit to it indicating an electron density, n_e. Note the satellite features on the two wings are separated by the plasma frequency. Further note that the features are asymmetric with the red feature being more intense, and the Ly α line itself is "leaning" towards the red. To model the plasmon we use two facts:

(a) The collective enhancement of the electron feature will not be present in the wave-vector integrated structure factor $S(\omega)$,

$$S(\omega) = \int d\vec{R}\ S(\vec{R},\omega)$$

at frequencies less than ω_{pe}, the electron plasma frequency.

(b) The Landau damping will be overwhelming at frequencies greater than $\omega > 1.18\ \omega_{pe}$.

Thus the spectrum of the plasma collective mode can be modelled using an equilibrium non-thermal $S(\omega)$ and then enhancing the collective feature. This then allows us to find a $S(\omega)$ spectrum and use it in the dispersion relation to find the "shift" part of the line function due to the plasma (see R.W. Lee (6.17) for details of the equilibrium cases).

The enhancement factor is essentially a measure of the non-equilibrium nature of the plasma. The area under the "plasma bump" in the $S(\omega)$ is also a measure of the energy in the collective mode (6.18). The fact that the satellites are asymmetric and the line leans toward the more intense feature is consistent with the observations made for equilibrium plasmas

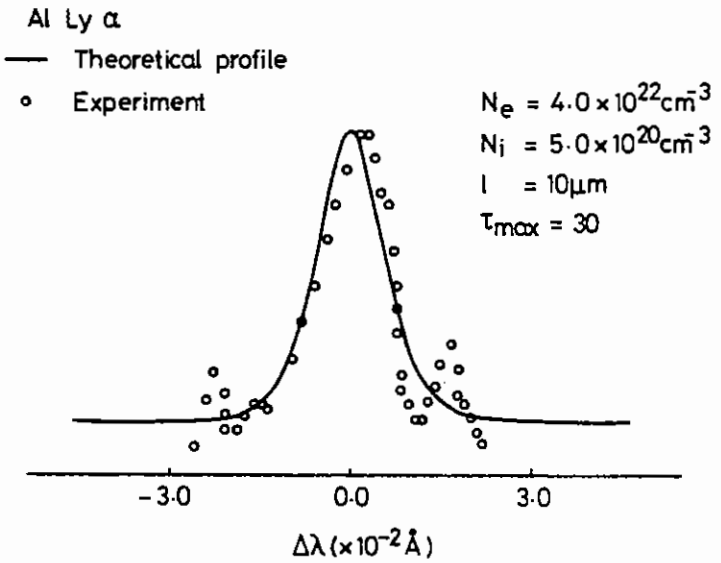

Fig.6.12

Al XIII Lyman α profile showing plasma satellite.

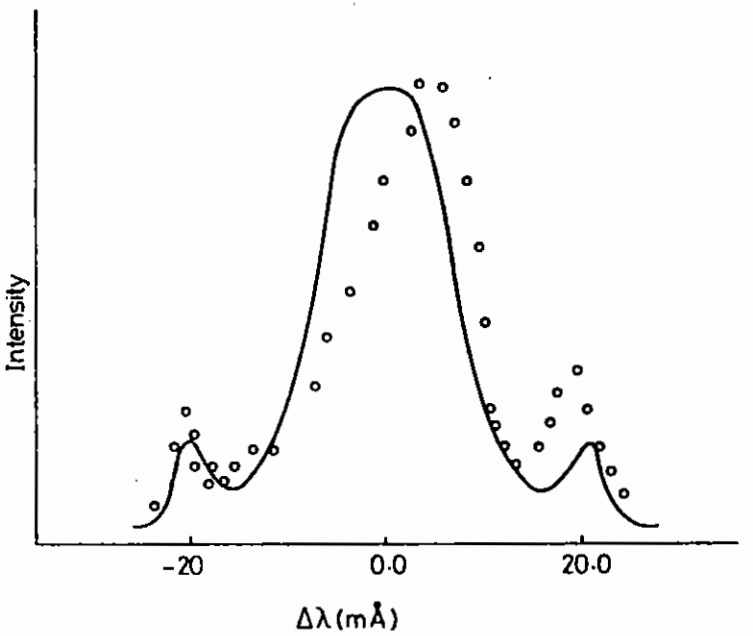

Fig.6.13

Theoretical line profile with plasma satellites.

in which a velocity drift exists between the plasmon producing component and the bulk plasma. In this instance the evidence would support the case for a "drift" inward of the Aluminium with the bulk of the plasma at rest. (Note: Inward is away from the observer.)

To illustrate the first of these suppositions we show in Fig.6.13 the theoretical profile with a 1000 times enhancement of the plasmon feature. Note that the resonances are appropriately placed with approximately the correct integrated intensity in each. This represents a ratio of collective to thermal energies of .08, which is extremely large. The source of the energy must be assumed to arise from some form of instability which has a frequency higher than (or equal to) the plasma frequency. This would seem to negate ion mass related instabilities. Further, the modifications of the higher series members, due to enhancements of this size, are drastic - virtually no line profile is observable, one only observes plasma resonances associated with the numerous Stark splittings.

Finally, work is now proceeding to estimate the relative "drift" velocity of the plasma components.

D. Burgess, E. Everett, R. Lee

6.4.3 Studies of Radiation Transport in the Compressed Core

The radiative transfer in the compressed core of the microballoon is being studied in two separate ways. First the detailed radiation transport is required to analyze the accuracy of the analytic model we use for fast diagnostics on line shapes. In this way the assumptions such as spatial uniformity and the single transition LTE transfer can be analyzed in the light of a more accurate simulation. Also the assumptions of temporal uniformity and a static plasma can be scrutinized. Second, the more fundamental aspects of the formation of the spectrum can be investigated. In this latter role the work of the simulation is to provide a base from which one can determine the importance, and ultimately the observability of processes as they affect the spectral character of the plasmas.

As a simple example of the former use of the radiation transport model we show in Fig.6.14 a comparison of the emitted intensity from two microspheres with the same mean plasma conditions. In one case the plasma has a complex density and temperature structure of the type predicted by computer simulation of a collapsed core, while in the second case a spatially uniform plasma is studied. In Fig.6.14 we see that the line spectra for the two cases is similar and indeed the widths of the various features are comparable. This gives an indication that the simpler diagnostic procedures now in use may be valid for a variety of plasma conditions. Further studies of a more detaled nature are planned.

The role of the radiation transport simulation as a tool to search for more fundamental aspects in the plasma of interest is illustrated in Fig.6.15. Here we have included the helium-like and hydrogenic emitters of Neon and the coresponding continuum edges. In addition the intercombination lines from the Ne IX ($1s^2\ ^1S$ - $1s2p$, $2s\ ^3P$, ^3S) transition and the dielectronic satellite lines arising from the doubly excited states of the helium-like features are present. The importance of this simulation is in the number of interactive effects which are present and how they affect the final emitted spectrum. Note, for example, that in the spectrum the ionization potential depression of the helium-like resonance series and the resonance line of the hydrogenic species will depend closely on each other. Further, this figure shows in a unified manner all the spectral features which can be sued for diagnostics in the frequency range.

We plan to study in detail the interaction of the various processes which lead to the complex spectrum shown in Fig.6.15.

D. Burgess, D. Everett, R. Lee

6.4.4 Implementation of the Kernal Approximation for Determining the Non LTE Effects in the Two Level Atom Approximation

The previous work performed on diagnostics using emission spectra employed a fast interactive procedure to determine the regions of best fit between theory and experiment. One interesting aspect of these comparisons was

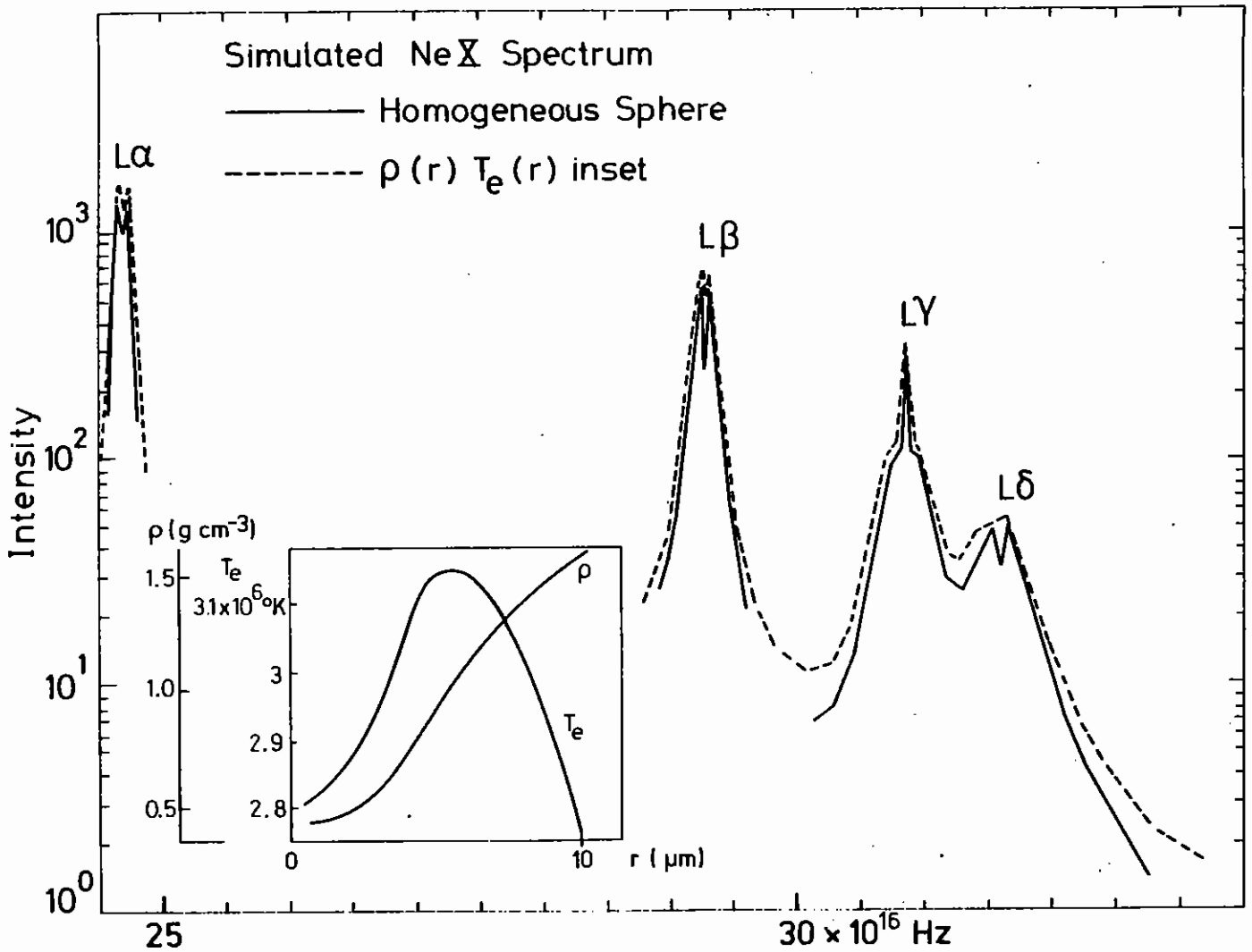

Fig.6.14

Simulated Ne X spectra for homogeneous core and in homogeneous cor (g, Te shown inset).

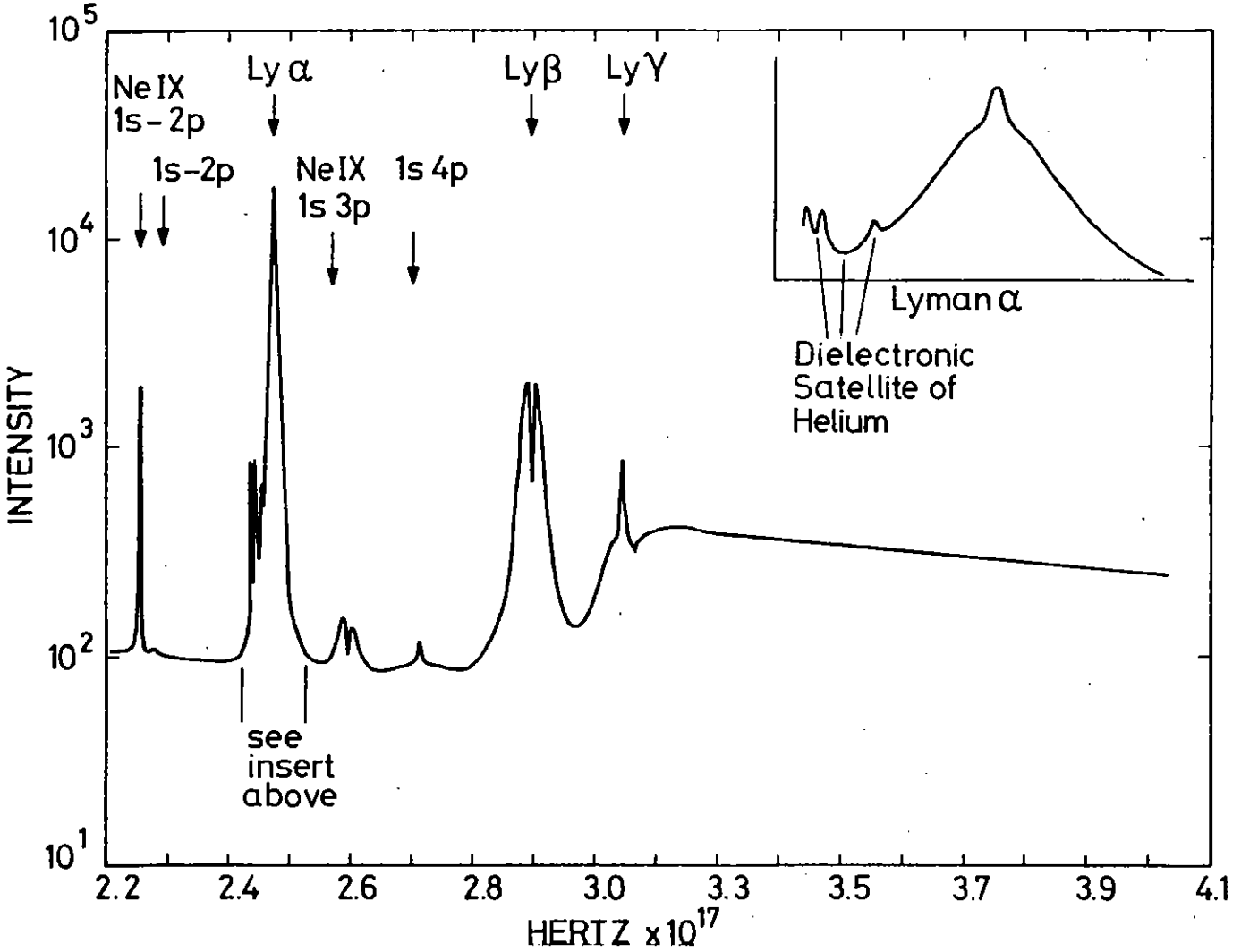

Fig.6.15

Ne IX and Ne X spectrum from simulations of a sphere with temperature and density that varies as shown in inset on Fig.6.14. The region of the Ne X Lyman α line is shown inset to indicate the dielectronic satellite.

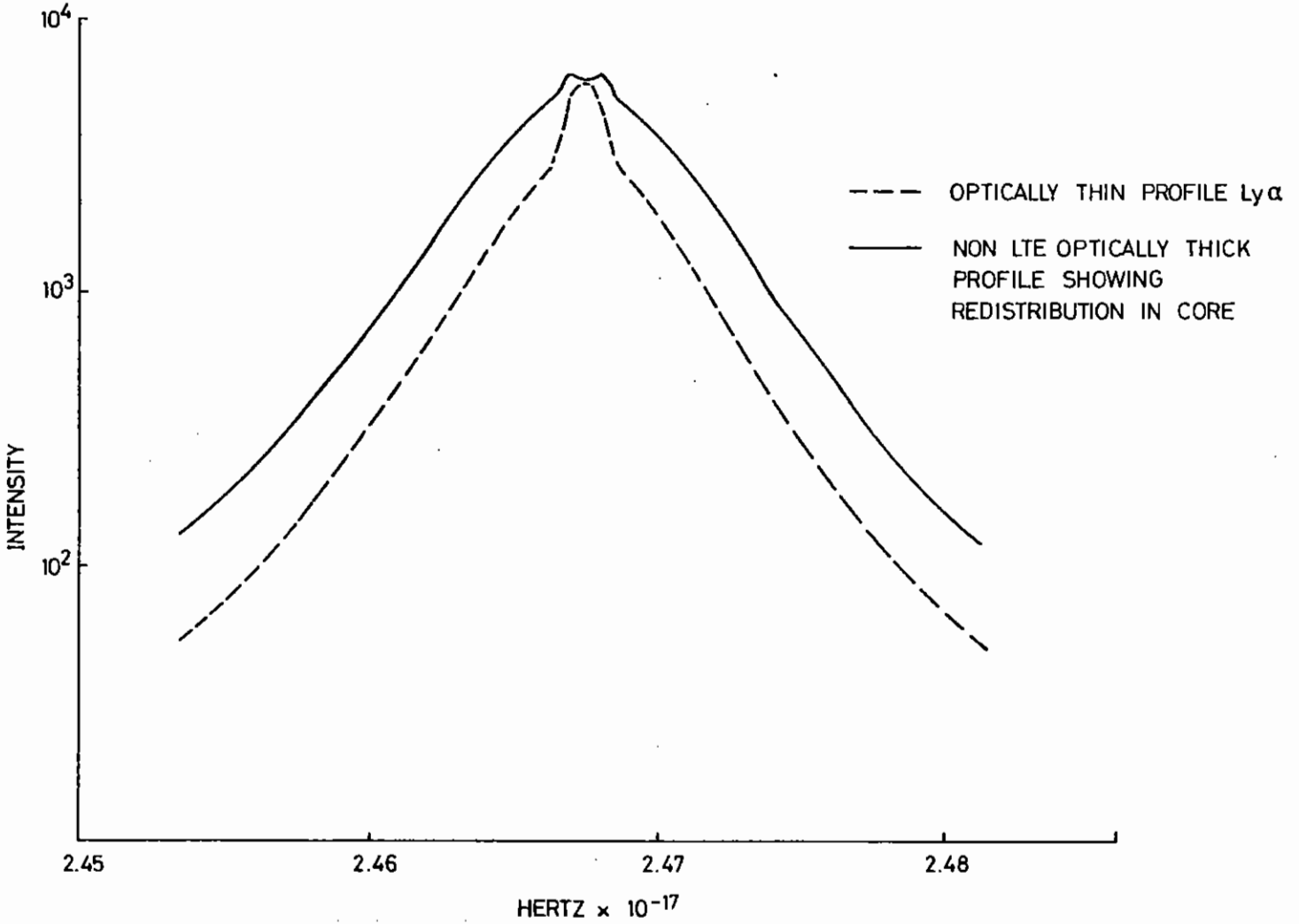

Fig.6.16

Non LTE simulation of Ne X Lyman α line profile

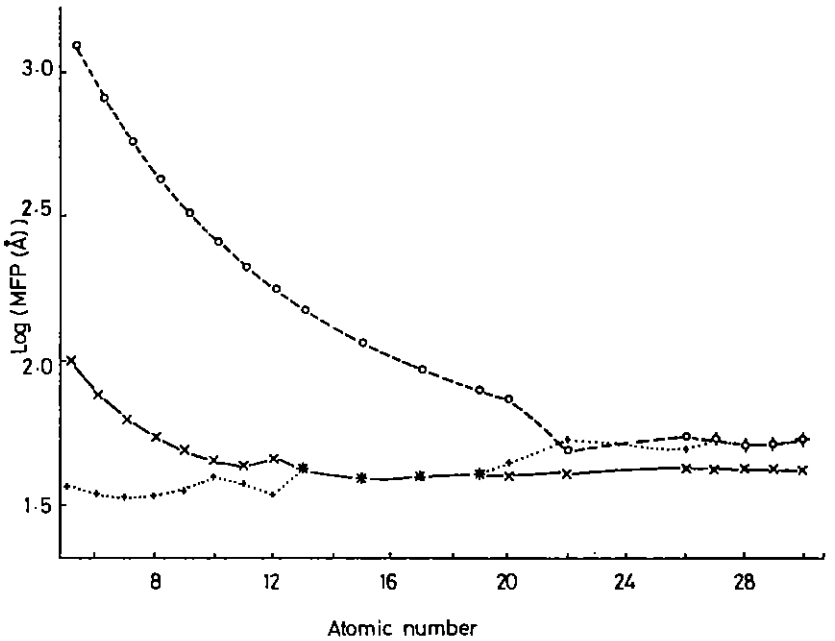

Fig.6.17

Emitter mean free path versus atomic number.

the fact that Non LTE effects in the radiation transport of the two level system produced improved fits. To estimate these effects we use a simple analytic formulation (6.19) which is only valid in the Eddington approximation. To improve on the analytic formulation we have reformulated the method of the Kernal approximation (6.20, 6.21) for the case where the line function ϕ is not analytically known. This case arises since we are interested in profiles which are a combination of quasi-static, collisional and Doppler shapes. The method which relies heavily on the method of Avrett and Loeser (6.21) to determine the Kernal approximation is used to produce the intensity emitted from a uniform sphere.

As an example of this method Fig.6.16 shows a Lyman α line for Neon X. Note the redistribution of intensity out of the central core of the line even though there is no temperature gradient.

This method is now being implemented in the interactive procedure to facilitate more accurate estimates of the radiation transport in the compressed cores.

D. Burgess, D. Everett, R. Lee

6.4.5 Suppression of Doppler-Broadening for XUV Emission from Laser Plasmas

In order to establish the temperature and density of a laser-produced or laser-compressed plasma from spectral line shapes, it is necessary to know what part of the line-broadening is attributable to thermal Doppler broadening.

It has recently been shown (6.22, 6.23) that when the ion-ion mean free paths become very short, as must happen in a dense plasma containing highly charged ions, the usual line-broadening process becomes modified by collisions. Principally this affects Doppler broadening, but it should be noted that the ion-dynamic contribution to Stark broadening is also modified by collisions (6.22) and that Doppler and Stark broadening cease

to be statistically independent processes in a collision-dominated plasma (6.24).

Calculations performed by the authors show that, for elements of atomic number greater than twenty, Doppler broadening is the dominant process for typical laser-plasma conditions of density and temperature ($10^{20} < n_e < 10^{23}$, 100 eV < T_e < 1000 eV) for resonance lines, and for all elements it controls the line width of $\Delta n = 0$ transition spectral lines. This appears to restrict the use of line-shapes for diagnostics to low-z elements, and preferably higher transitions. It is of course difficult to obtain good signal-to-noise beyond the first few transitions of a resonance series, since the weaker lines are more optically thick.

Doppler broadening is also of importance in XUV laser schemes, since the optical depth of the depopulating transition for the lower state would be Doppler-width determined, from the discussion above.

Dicke (6.25) showed that the usual (Gaussian) Doppler-profile does not develop under conditions in which the emitter mean free path λ_{90} becomes short compared with the wavelength of interest. Calculations carried out at Imperial College (see Fig.6.17) show that λ_{90} may be as short as 30 Å for an electron density of 2×10^{23} cm^{-3}.

6.4.5(a) Summary of Development

The usual Gaussian line profile is obtained so long as the Doppler width as usually defined, i.e.

$$\Delta\omega_D = \frac{\omega_0 \langle V \rangle}{C}$$

exceeds the reciprocal of the collisional mean free time of the ions i.e.

$$t^{-1} = \frac{\lambda_{90}}{\langle V \rangle}$$

It can be shown that for a suitable collision probability distribution $P(D,\lambda_{90})$ which satisfies the Fickian diffusion law

$$\frac{\partial P}{\partial t} = D \nabla^2 P$$

where the diffusion coefficient is a function of $\bar{v}\lambda_{90}$, then the lineshape for short λ_{90} is a Lorentzian,

$$I(\omega - \omega_0) = \frac{2D/\lambda_0^2}{(\omega - \omega_0)^2 + D^2/\lambda^4}$$

with a halfwidth of

$$\Delta\omega = \frac{4\pi D}{\lambda_0^2} = 2.8 \frac{\lambda_{90}\, \Delta\omega_D}{\lambda_0}$$

The dependence on the mean free path λ_{90}, or equivalently, on the collision frequency ν, represents the division of the XUV radiation from each emitter into a sequence of incoherent wave-trains, each of duration ν^{-1}. Within these the frequency is displaced by $\langle v \rangle/\lambda$. But these individual trains cannot be considered incoherent if they are shorter than one wavelength, so that all emission within $\langle v \rangle \lambda$ must interfere. Interference between successive trains can only be neglected when they are longer than one cycle.

Therefore in a collision-dominated dense plasma, any emission which has been Doppler-shifted away from the central frequency will interfere destructively, and the normal Doppler profile will not be observed.

6.4.5(b) Plasma Model

We have approximated the ion-ion collision cross sections by

$$\bar{q}_{sr} = 2\pi \; b_{sr}^2 \; \ell n \; (\Lambda^2 + 1)$$

$$\simeq 2\pi \; b_{sr}^2 \; (2\ell n\Lambda)$$

where Λ is typically 3, and the impact parameter b_{sr} is approximately,

$$b_{sr} \simeq \frac{1}{3} \; \lambda_{ii}$$

$$= \frac{z_s \; z_r \; e^2}{3k \; T_i}$$

The ion-ion correlation length, λ_{ii}, is the ion separation at which the electrostatic interaction is comparable to the thermal energy of the ions. We assume that

$$T_{i,s} = T_{,t} \simeq T_e$$

(In practice, $T_i < T_e$ over most regions of a laser plasma.)

Then without taking account of Debye shielding (which is included in our complete model), we obtain for several ion species k,

$$\lambda_{90} = \frac{(k \; T_i)^2}{z^2 \; \ell n \; \Lambda \; \Sigma_k n_k \; z_k^2 \; e^4}$$

This is just a generalization of the result derived in Spitzer (6.26). This quantity is shown in Fig. 617 for varying target atomic numbers, and for different plasma temperatures, taking $T_i = 0.5 \; T_e$.

6.4.5(c) Practical Considerations

Unfortunately, consideration of the black-body source function shows that at long wavelengths very few photons are available. In order to study an effect which is localised to the densest regions of the laser-plasma, we require spatial resolution of the spectral lines. Therefore the solid angle of the spectrograph aperture is very small, which restricts the flux even more. Trials with the GML5M spectrograph have shown that even averaging over three shots, very few lines can be detected at above 50 Å even without a spatially resolving slit. (We are presently carrying out a detailed numerical study of instrumental/luminosity limitations on such lineshape experiments in general.)

D. Burgess, D. Everett, R. Lee

6.5 XUV Laser Studies

The development of a working laser in the XUV spectral region would represent a significant advance towards the ultimate goal of an X-ray laser. To this end a collaborative programme involving the University of Hull, Queen's University, Belfast and the Rutherford Laboratory has been under way for the past three years. Over this time progress has been slow as a variety of technological problems have appeared, and other more urgent experiments have prevented any laser time being available in the current year.

Two distinct approaches to the problem are being considered: collisional excitation and recombination in a rapidly expanding plasma; the latter scheme has been considered more promising, and has therefore had most attention. In contrast, work has only just been initiated on the second approach.

Recombination Laser

The development of a population inversion in expanding laser heated carbon fibres has been demonstrated experimentally (6.27, 6.28) and the

scaling of such systems to a working laser investigated theoretically (6.29). The measurement of gain by a direct backlighting experiment described in the previous annual report (6.01) has, however, not yet been carried out due to delays occasioned by problems arising from the preliminary experiments also described previously.

In the earliest experiments (6.27) in which inversion was observed the fibre was irradiated with a simple spherically focusing lens. The excellent agreement of the intensities of the emitted spectra with numerical computation indicated good coupling of the laser to the fibre with ~ 20% energy absorption.

In contrast interferometric measurements of cylindrically irradiated targets showed a cold core, indicative of poor coupling (6.01). At the same time spectrographic measurements at Hull also showed weak spectra of markedly different intensity structure with cylindrical focusing - again indicative of a hot blow-off plasma with a cold core.

Detailed two-dimensional computer modelling with the Lagrangian code LAG2 revealed the essential role of the pre-pulse providing a background plasma generated at the irradiated front surface, which rapidly flowed around the fibre enveloping it in a plasma "blanket". As a result of this behaviour the Lagrangian cells become severely distorted, and the code unsatisfactory. The addition of an expanding grid to the Eulerian code MAGT has allowed us to follow the development of this "blanket" by the main laser pulse. These studies show clearly that good coupling is achieved provided the "blanket" plasma is well formed, and the laser flux is not excessively high to cause strong flux limitation, and fast electron generation. The estimated optimum heating configuration fortunately fall below this latter limit.

Experiments at Hull have now resolved this issue. By repeating the earlier "spherical" focusing experiments it was found that the spectrograph response had fallen off. Taking this into account, improvements in focusing have now lead to spectra from line plasmas which are consistent with the earlier work.

Alternative target geometries have also been proposed to improve the laser-fibre coupling. These include the use of thin ribbons rather than fibres, whose cross sectional area to the beam is significantly larger than that of the fibre. Calculations indicate a comparable performance to fibres. However, such targets are likely to be much less robust than fibres. A second alternative which has been suggested (6.30) involves the exploding pusher mode collapse of thin cylindrical shells. Estimates show that these require about twice as much energy as the equivalent fibre.

Observations have also been made of population inversion in Al XI formed in the expansion of laser heated solid aluminium targets. Further study of these is planned in the coming year.

Electron Collisional Pumping

Electron collisional pumping offers considerable promise as a means of generating laser action in the VUV range (300 - 1000 Å). In this spectral region many of the problems associated with X-ray laser action can be relaxed, and resonant cavities constructed. As a result considerable attention has been paid to the analogues of visible ion lasers, which may operate in a quasi- CW mode. Most attention (6.31, 6.32) has concentrated on the 3s - 3p transition of ions with a $2p^n$ shell. In this case pumping occurs as a result of the large collisional excitation rate of the forbidden transition 2p - 3p.

Detailed calculations of this system are hampered by an absence of accurate atomic data at high degrees of ionisation. However, calculations for carbon-like and neon-like ions clearly indicate the potential of the scheme. The gain is strongly temperature and density dependent. One dimension of the plasma must be restricted to allow the line 3s - 2p to be optically thin.

Estimates of the gain for the transition 3p - 3s in Ca XI give values as large as 100 cm^{-1} (6.33). Experiments involving the irradiation of a calcium sandwich by a 30 J Nd laser pulse of duration 2.5 - 5 nsec, using

a line focus have been reported, showing plasma conditions near the predicted values for generating inversion. It is proposed to extend the experiment in the coming year by a detailed spectroscopic analysis of the plasma using both normal and grazing incidence vacuum spectrographs in an effort to detect and measure the inversion thus formed. If gains of the calculated values are indeed produced it should be relatively straight-forward to construct a suitable cavity to demonstrate laser action.

G Pert

CHAPTER 6 REFERENCES

6.01 Rutherford Laboratory Annual Reports RL-78-036 and RL-79-039.

6.02 M H Key , C L S Lewis, J G Lunney, A Moore, J M Ward and R K Thareja, "Time-resolved X-ray Spectroscopy of Laser Produced Plasmas." Submitted to Phys. Rev. Lett.

6.03 V A Boiko, A Ya Faenov and S A Pikuz, J. Quant. Spect. Rad. Trans. 19, 11 (1978).

6.04 V A Boiko, S A Pikuz, U I Safronova and A Ya Faenov, Sov. J. Quantum Electron., Vol.7, No.3, 333 (1977).

6.05 U Feldman, G A Doschek, D J Nagel, R D Cowan and R R Whitlock, Astrophys. J. Vol. 192, 213 (1974).

6.06 A V Vinogradov, I Ya Skobelev and E A Yukov, Sov. Phys. JETP, Vol. 45, 925 (1977).

6.07 A V Vinogradov and I Yu Skobelev, JETP Letts., 27, 88 (1978).

6.08 V A Boiko, S A PIkuz and A Ya Faenov, J. Phys. B., 12, 1889 (1979).

6.09 J F Seely, Phys. Rev. Letts., 42, 1606 (1979).

6.10 J F Sely, private communication.

6.11 V A Ghagavatula and B Yaakovi, Optics Comm., 24, 331 (1978).

6.12 V A Boiko, A Yu Chugunov, A Ya Faenov, S A Pikuz, I Yu Shobelev, and E A Yujov, J. Phys. B., 12, 213 (1979).

6.13 (a) R W Lee, J. Phys. B. 11, 1112 (1979).
(b) R W Lee, J. Phys. B. 11, 1129 (1979).

6.14 H R Griem, M Blaha and P C Kepple, Phys. Rev. A 19, 2421 (1979).

6.15 B Yaakobi, D Steel, E Thorsos, A Hauer, B Perry, S Skupsky, J Geiger, C M Lee, S Letzrong, J Rizzo, T Mukaiyama, E Lazarus, G Halpern, H Deckman, J Delettrez, J Soures and R McCrory, Phys. Rev. A 19, 1247 (1979).

6.16 J Kilkenny, R W Lee, M H Key and J Luney, submitted to Phys. Rev. A (1979).

6.17 R W Lee, J. Phys. B 11, 1145 (1979).

6.18 G Bekefi, "Radiation Processes in Plasmas", J Wiley, New York (1966).

6.19 J D Kilkenny, R W Lee, M H Key and J Lunney, submitted to Phys. Rev. A (1980).

6.20 E H Averett and R Hummer, MNRAS, 130, 295 (1965).

6.21 E H Averett and R Loeser, Smithsonian Institution Astrophysical Observatory Special Report 203 (1966).

6.22 D D Burgess, "Physics of Ionzed Gases", published by Institute of Physics, Belgrade, pp. 501-542.
Culham Laboratory Report CLM-P567 (1979).

6.23 D D Burgess, D Everett and R W Lee, J. Phys. B 12, 23 L755 (1979).

6.24 S G Rautian and S I Sobel'man, Sov. Phys. Usp. 9, 701 (1967).

6.25 R H Dicke, Phys. Rev. 89, 472 (1953).

6.26 L Spitzer, "Physics of Fully Ionized Gases", London (Interscience) (1956).

6.27 R J Dewhurst, D Jacoby, G J Pert and S A Ramsden, Phys. Rev. Lett. 37, 1265 (1976).

6.28 M H Key, C L S Lewis and M J Lamb, Optics Comm. 28, 311 (1979).

6.29 G J Pert, J Phys. B 12, 2067 (1979).

6.30 G J Pert, paper presented at National Quantum Electronics Conf. (1979).

6.31 L J Palumbo and R C Elton, JOSA 67, 480 (1977).

6.32 L A Vainshtein et al, Sov. J. Quant. Elec. 8, 239 (1978).

6.33 A A Ilyukin et al, JETP Lett. 25, 535 (1978).

CHAPTER 7 THEORY AND COMPUTATION

INDEX

CHAPTER EDITOR: C J Webb

CHAPTER 7 THEORY AND COMPUTATION

7.1 Introduction

The work of this group is divided between theoretical studies and the development of fluid and particle codes and their application to problems in laser-plasma interactions.

Most of the developments involving fluid codes are reported in 7.2 on laser compression studies. The one-dimensional code MEDUSA is still the only general purpose fluid code available in the Facility programme. It has been widely used throughout the past year and the results of research at Glasgow University on radiative preheat effects in laser-compression suggest that radiative preheat may degrade substantially the final target compression.

There are both Eulerian and Lagrangian 2D-codes at various stages of development though neither is yet available for general use. The Lagrangian code LAG2 was written at Hull University and is now implemented at the Rutherford Laboratory. The developments carried out in the past year are reported in 7.2.5. Throughout this period the Eulerian code CASTOR has suffered from a series of setbacks which are still unresolved. In view of these difficulties it has not yet proved possible to use the code in the research programme.

A time-dependent hydrodynamic code incorporating Monte-Carlo or multi-group diffusion has been developed at Imperial College and its application to fast electron transport problems is reported in 7.2.6.

The development of particle codes has continued during the period under review. A 2D version of the code EMPIRE has now been written and tested at the University College of North Wales before being transferred to the CRAY. The 2½-D code developed jointly at Bangor and the Rutherford Laboratory is at present undergoing tests and progress is reported in 7.3.4.

At the University of St. Andrews work on interpreting the second harmonic emission observed in experiments has continued. The model developed last year to explain the fine structure has been extended to give the intensity and angular distribution to be expected from various density profiles. A simple numerical model has been used at UCNW Bangor to examine the morphology of the self-generated magnetic fields seen in the experiments at the Rutherford Laboratory and reported on last year. This model has produced satisfactory agreement with the measured magnetic field structure and density profiles (7.3.1).

During the period under review work on transport physics has been extended. At Oxford University the study of ion emission from plasmas containing multiple ion species has continued. The role of electrostatic micro-instabilities and in particular the temperature-gradient driven ion acoustic instability, has been examined at St. Andrews in a general analysis of an infinite Vlasov plasma in a uniform magnetic field. At UCNW Bangor a nonlinear theory of ion turbulence has been extended to show that the levels of turbulence excited in many experiments are likely to be too low to explain the heat flux inhibition that has been reported widely.

7.2 Laser Compression Studies

7.2.1 Scaling Laws for Ablative Implosions

Introduction

Simplified models of implosions which lead to scaling laws relating the initial target parameters to those in the compressed core are a useful adjunct to modelling with hydrodynamic computer codes. In earlier work models for implosions of the exploding pusher type have been developed (7.01, 7.02, 7.03). This mode of implosion occurs when the scale length of energy deposition by hot electrons λ_h is greater than the wall thickness Δr of a spherical shell target. Conversely if $\lambda_h \ll \Delta r$ the bulk of the shell and the gas fill are not exposed to preheating and the implosion develops through inward acceleration of the shell by the pressure resulting from surface ablation.

Ablative implosions are potentially important since they permit isentropic compression (without preheating) and thus lead to maximum compressed density for a given final pressure. Isentropic compression is however obtained only in the absence of shock heating and elimination of shock heating requires shaping of the laser pulse driving the implosion and/or multi-shell target design. The initial experiments in this field are being conducted with unshaped laser pulses and simple gas filled single shell targets. It is therefore interesting to consider a scaling law model for ablative implosions driven by a constant applied pressure such as would be generated by an idealised 'square' laser pulse.

A Model of Implosions with Small Mass Loss

Fig.7.01 shows schematically the space time diagram of the implosion (7.04). The surface of the target shell is ablated by a subsonic deflagration wave in which the exhaust density is much lower than the intake density and a shock wave is driven ahead of the ablation front. The pressure driving the shock is P_a, the ablation pressure, and therefore the flow velocity u_a behind the shock is given by the strong shock Rankine Huguniot equations and,

$$u_a^2 = \frac{2}{\gamma+1} \frac{P_a}{\rho_p} \tag{1}$$

where γ is the specific heat ratio in the shocked pusher medium and ρ_p the unperturbed pusher density.

When the shock reaches the contact surface and the pressure P_1 in the fill gas is small relative to P_a the shell material will unload with about the thermal speed u_a and the contact surface velocity u_c which is the sum of this unloading velocity and the flow velocity can be shown to be approximately (7.05)

$$u_c \simeq 2u_a \tag{2}$$

The contact surface velocity drives a shock in the fill gas and the shock pressure P_2 is

$$P_2 = \frac{\gamma+1}{2} \rho_1 u_c^2 \tag{3}$$

where ρ_1 is the initial fill gas density and from equations (1) to (3)

$$P_2 = 4 \rho_1/\rho_2 P_a \tag{4}$$

The strong shock in the gas raises its density to

$$\rho_2 = \frac{\gamma+1}{\gamma-1} \rho_1 \tag{5}$$

Shock reflection at the centre can be adequately treated in the plane shock approximation for most of the mass of the gas fill (located at radii not much smaller than the initial contact surface radius). In this limit the double shocked pressure P_4 is

$$P_4 = \frac{3\gamma-1}{\gamma-1} P_2 \tag{6}$$

and the double shocked density is

$$\rho_4 = \frac{\rho_2(\gamma+1)\frac{P_2}{P_4} + (\gamma-1)}{(\gamma-1)\frac{P_4}{P_2} + (\gamma+1)} \tag{7}$$

Further shock reflections when this shock meets the contact surface again (see Fig.7.01) are weak and may be treated as a final phase of adiabatic compression.

An estimate of the final pressure P_f can be obtained by considering the acceleration of the shell in the limit of small fractional mass loss (extension to larger mass loss via the rocket equation is straight forward). The shell of thickness Δr is accelerated over a distance of the order r and neglecting spherical convergence its velocity reaches u_p where

$$u_p^2 = 2 \frac{P_a}{\rho_p} \left(\frac{r}{\Delta r}\right) \tag{8}$$

Stagnation of the implosion converting the kinetic energy to pressure gives a ram pressure P_f where

$$P_f = \rho_p u_p^2 = 2 P_a \left(\frac{r}{\Delta r}\right) \tag{9}$$

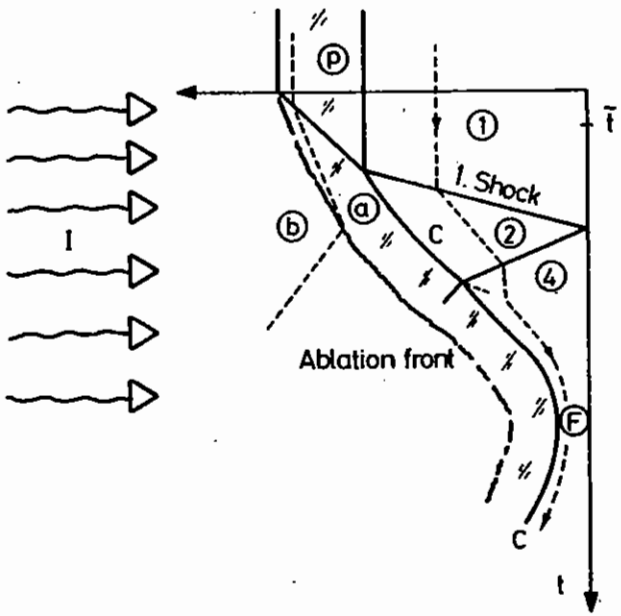

Fig.7.01

Space time trace of ablative pusher. Dashed lines show the path of particles regions:
- 1 undisturbed fill gas
- 2 shock heated fill gas
- 4 heated by first and reflected shock
- F maximum compression state
- p unperturbed pusher
- a shock compression pusher
- b ablated pusher

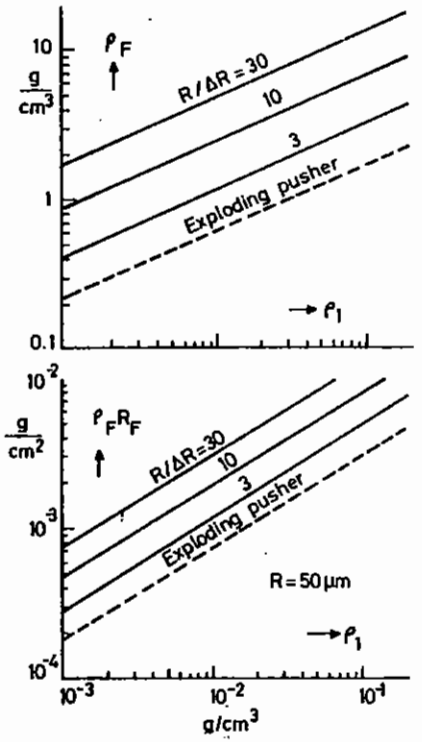

Fig.7.02

(a) Maximum density ρ_F as function of fill gas density ρ_1 for exploding pusher (——) and ablative pusher (solid lines)

(b) Line density $\rho_F R_F$ as a function of fill gas density for exploding (——) and ablative pushers (solid line)

Assuming that the compression from P_4 to P_f is isentropic it follows that the final density ρ_f is,

$$\rho_f = \rho_1 \left(\frac{\rho_2}{\rho_1}\right) \left(\frac{\rho_4}{\rho_2}\right) \left(\frac{P_f}{P_4}\right)^{1/\gamma} \qquad (10)$$

1st shock ↗ 2nd shock ↑ isentropic ↖

which for $\gamma = 5/3$ reduces to

$$\rho_f = 2.1\ \rho_1^{2/5}\ \rho_p'^{3/5} \left(\frac{r}{\Delta r}\right)^{3/5} \qquad (11)$$

where $\rho_p' \simeq \rho_p$ is the density of the imploding shell at peak velocity u_p.

The line density $\rho_f r_f$ is given by,

$$\rho_f r_f = 2r \left(\frac{r}{\Delta r}\right)^{2/5} \rho_p'^{2/5} \rho_1^{3/5} \qquad (12)$$

and the temperature T_f by

$$(kT_f/1\ \text{keV}) = 1.4 \times 10^{-3}\ (P_a/1\ \text{Mbar}) \left(\frac{r}{\Delta r}\right)^{2/5} \rho_1^{-2/5} \rho_p'^{-3/5} \qquad (13)$$

Discussion

Figs.7.02(a) and (b) show plots of ρ_f and $\rho_f r_f$ from equations (11) and (12) which include the exploding pusher limit (from earlier work (7.03)). There is an additional compression factor $(r/\Delta r)^{3/5}$ relative to the exploding pusher limit obtained in this ablative mode of implosion.

The final density in this model is independent of the ablation pressure P_a because the preheating by shocks is proportional to P_a. The final temperature and pressure increases linearly with P_a in this limit (eqn.13).

The model calculations have been compared with simulations using the MEDUSA code for 'square' pulse irradiation of glass shells of 50 μm radius and 3 μm wall thickness with $\rho_1 = 10^{-2}$ gcm^{-3}. Fig.7.03 shows the radial profiles of parameters at a stage where the initial shock has propagated through the shell and through half of the gas. The simulation

is for 10^{15}W cm^{-2} irradiance at wavelength $\lambda = 0.25$ μm for which low value of $I\lambda^2$ there is negligible hot electron preheating and the shock structure discussed in the model is clearly seen in the simulation.

There is also agreement in computer simulated and model predicted final density ρ_f as shown in Fig.7.04. The agreement is good where the mass ablation fraction is small and hot electron preheating is negligible as assumed in the model, i.e. for $\lambda = 1$μm and 0.25 μm at irradiances $\leq 10^{13}$ W cm^{-2}. In the limit of dominant hot electron preheating with $\lambda_h > \Delta r$ exploding pusher behaviour occurs as seen for the 1 μm and 10 μm simulations with $I\lambda^2 > 10^{15}$W cm^{-2} m^1. The 0.25 μm simulations with $I \sim 10^{13}$ W cm^{-2} exhibit greater compression resulting from ablation of a significant fraction of the shell mass and the results therefore lie above the simple model predictions.

Ablative Acceleration with Significant Mass Loss

It is well known (see eg (7.05)) that integration of the equation of motion of a 'rocket' driven by a mass loss rate $\dot{M}$ at velocity v_b yields a velocity v(t) given by

$$\frac{v(t)}{v_o} = \ln\left|\frac{M(0)}{M(t)}\right| + \frac{\Delta M(t)}{M(0)} \qquad \text{Lim } \Delta M \to 0 \qquad (14)$$

M(t) is the time varying mass and $\Delta M(t)$ is the total mass lost at time t.

Also the efficiency of converting the energy input into the rocket system into 'payload' kinetic energy is

$$\varepsilon = 4\left(\frac{\gamma-1}{\gamma+1}\right) \frac{(v(t)/v_b)^2}{(\exp \frac{v(t)}{v_b} - 1)} + \frac{\Delta M(t)}{M_o} \qquad \text{Lim } \Delta M \to 0 \qquad (15)$$

The optimum efficiency of ablative acceleration requires ablation of about 80% of the initial mass at which point v(t) reaches about $3v_b$.

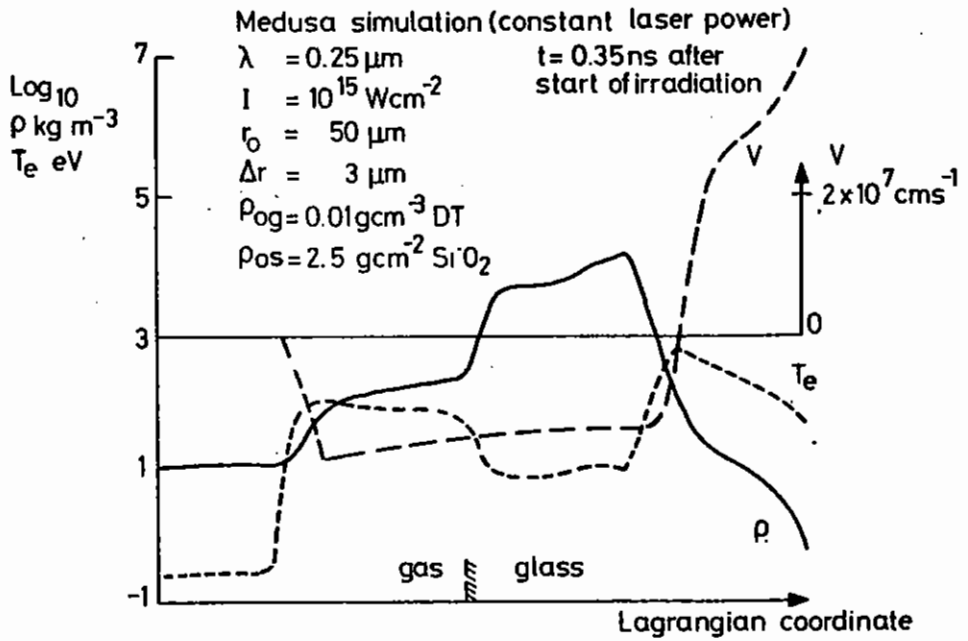

Fig.7.03

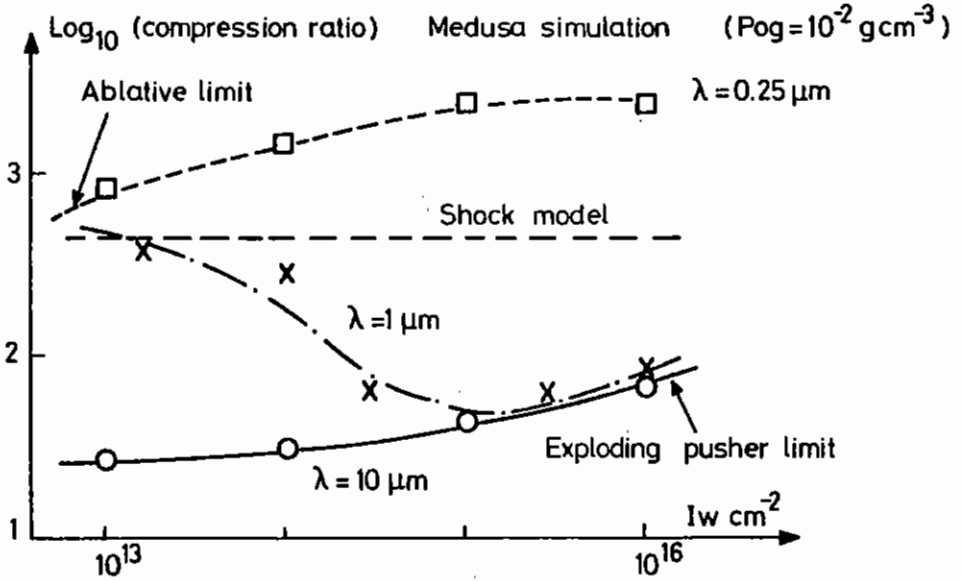

Fig.7.04

Implosions with Constant $\Delta M/M(0)$

If the constraint of constant efficiency ε is imposed in the limit of small mass loss $\Delta M/M(0)$ then it follows that acceleration of a shell of thickness Δr over a distance r leads to the relationship

$$r/\Delta r = \varepsilon^2 \frac{\rho_P}{\rho_b} \qquad (16)$$

which shows that if $\rho_b << \rho_P$ (as is typically true when ρ_b is close to the critical density) then high values of the aspect ratio $r/\Delta r$ are imperative for high hydrodynamic efficiency.

Ablative Implosions and Laser Wavelength

The ablative mode of implosion with $\lambda_h << \Delta r$ is obtained for $I\lambda^2$ less than a limiting value related to the shell thickness Δr. The mass ablation rate $\dot{M}$ and ablation pressure P_a can be estimated (see section 4.3 ibid) using the critical density Chapman-Jouguet deflagration model which suggests $\dot{M} \propto \lambda^{-4/3} I^{1/3}$ and $P_a \propto \lambda^{-2/3} I^{2/3}$.

For constant Δr and therefore constant $I\lambda^2$ the CJ model implies ablation pressure scaling as λ^{-2}, ablation front flow density $\rho_b \propto \lambda^{-2}$ and ablation velocity v_b constant. It follows then from equation (16) that constant hydrodynamic efficiency and thus implosion velocity v(t) and final pressure P_f are obtainable by scaling $r/\Delta r \propto \lambda^2$. However for constant Δr this requires an increase of target surface area $A \propto \lambda^4$ and thus laser power $P_L \propto \lambda^2$, implosion times $\tau \propto \lambda^2$ and laser energy $E_L \propto \lambda^4$. These aspect ratio, power and energy requirements strongly favour short wavelengths for ablative implosions. Alternatively if as seems probable the aspect ratio is constrained to a constant value by fluid instabilities, than for a constant shell thickness Δr, r is constant and the laser power $P_L \propto \lambda^{-2}$ the implosion time $\tau \propto \lambda$, the energy $E_L \propto \lambda^{-1}$ the final pressure $P_f \propto \lambda^{-2}$ and the hydrodynamic efficiency $\varepsilon \propto \lambda^{-2}$.

In this case also short wavelength laser radiation maximises ε and P_f. Fuller discussion of these scaling concepts is given in (7.04) and (7.05).

7.2.2 The Equation of State in MEDUSA

Three new options for the equation of state have been included in MEDUSA, each based on the Thomas-Fermi equations. The equation of state must be adequate over a large range in temperature, density and pressure. The pressure range extends up to the order of 10^6 Mbar, the temperature ranges up to tens of keV and the density ranges from gaseous density up to the order of 10^4 times solid density. In this very large regime, electron degeneracy, ionization by pressure and temperature, and the binding forces of solids and liquids all play an important part. The aim of the present work has been to improve the equation of state to take into account as many of these effects as possible. Although in many ways approximate, the resulting equation of state represents a considerable improvement over the previously available equations which included degeneracy but not ionization or binding forces.

There were two equations of state available before the present time. These were firstly the perfect gas equation and secondly the Fermi-Dirac equation of state which included the degeneracy pressure of free electrons in the absence of space charge associated with positive ions. Neither of these equations models changes in ionization and hence the number of free particles remains constant. This means that, if the degree of ionization is chosen to be that appropriate for a hot compressed gas, there are too many free particles at normal temperatures and densities. This is particularly serious in the case of the Fermi-Dirac equation of state since the degeneracy pressure of the large number of free electrons is very high and material at solid density and room temperature is accorded a pressure of the order of 10 Mbar. The problem can be seen clearly in Fig.7.05 which plots pressure against density for different temperatures as given by the Fermi-Dirac equation of state for aluminium. The dotted lines represent data compiled at Los Alamos from experimental data (7.06) and for our purposes can be taken as a standard for comparison. The upper part of the diagram is the fully ionized perfect gas regime. The Fermi-Dirac zero temperature degeneracy curve is a power law. The Fermi-Dirac model is adequate at high temperatures and densities but in the lower part of the diagram, where the number of free electrons should diminish, the FermiDirac model gives very high pressures while the

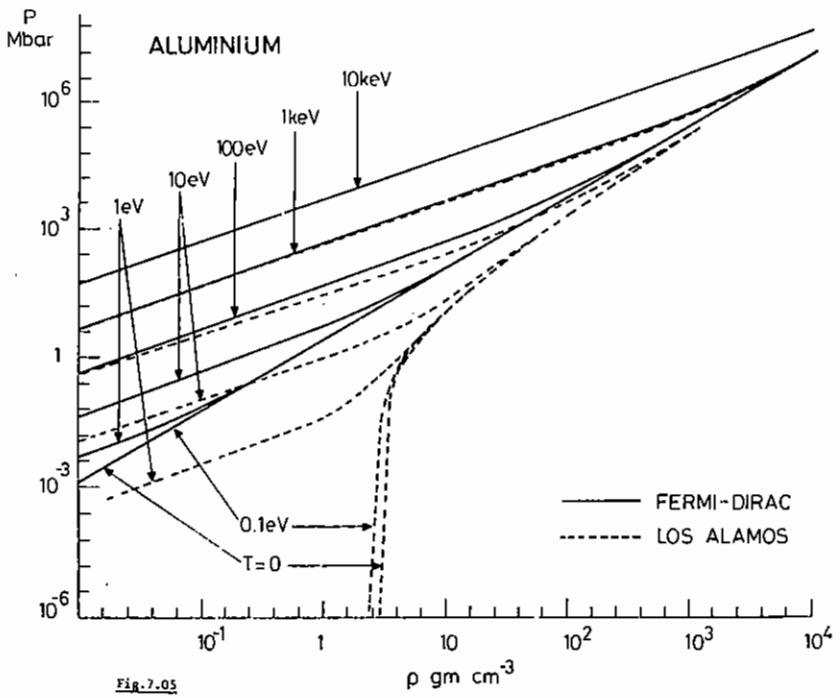

Fig.7.05

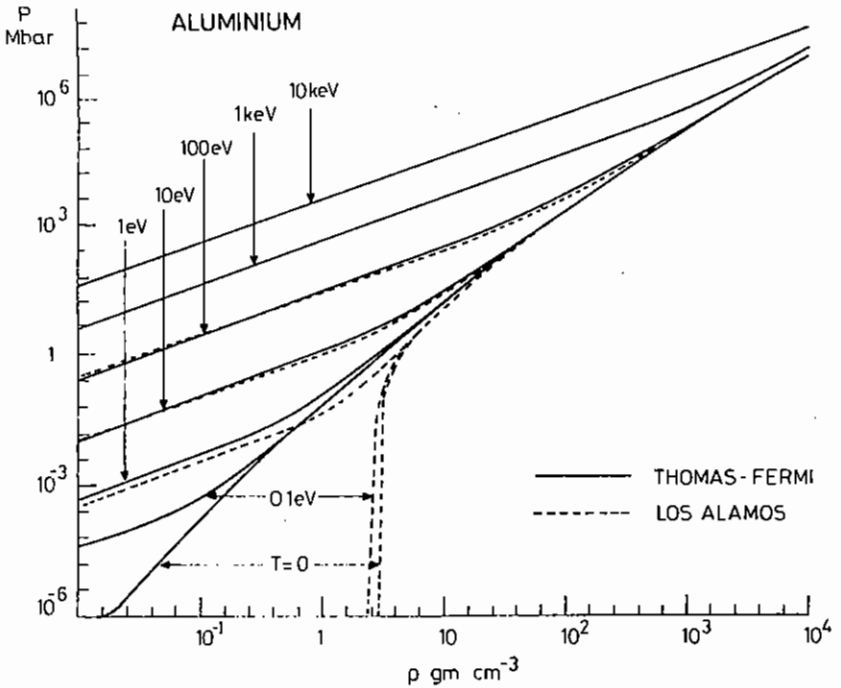

Fig.7.06

Los Alamos data gives much lower pressures going to zero at the solid density of 2.7 gm cm^{-3}.

Thus, althought the Fermi-Dirac equation does include degeneracy effects it is only adequate when pressures in excess of 10 Mbar are involved. In the case of laser heated targets the pressures are initially a few Mbar rising to thousands of Mbar only when the material is highly compressed. For this reason some improvement ot the Fermi-Dirac model is needed.

The Thomas-Fermi equation of state is an improved form of the Fermi-Dirac equation. Whereas the Fermi-Dirac equation assumes that the electrons sit in a uniform potential, the Thomas-Fermi equation takes account of the potential wells around the bare nuclei. At low temperatures the electrons fall into these potential wells to give a crude form of atom. At high temperatures or densities the energy of the electrons is larger than the depth of the potential wells around the nuclei and they escape to become free electrons. The distribution of electrons around each nucleus is given by Fermi-Dirac statistics. This results in a poor model for the internal structure of an atom but it is sufficient to give a much improved equation of state.

Fig.7.06 plots pressure against density as given by the Thomas-Fermi equation of state. The degeneracy curve on the log-log plot is no longer a straight line but curves downwards at low density as the electrons fall into the nuclear potential well. Comparison with the Fermi-Dirac plot of P against ρ shows that the non-degenerate pressure at low temperature is also decreased because of a reduction in the number of free particles due to recombination. The Thomas-Fermi equation is most accurate when the majority of electrons are nearly free and the crude model of atomic structure is not so important. It is also more accurate for high Z materials when the large number of electrons per nucleus makes the statistical approach a better approximation.

Although the Thomas-Fermi model reduces the pressure at solid densities by an order of magnitude compared with the Fermi-Dirac model the pressure is still of the order of 1 Mbar, and the model cannot deal with the solid or liquid phases because it does not include binding forces. The Thomas-Fermi

equation can be further improved by the inclusion of exchange and quantum corrections to obtain the 'corrected-Thomas-Fermi' equation. These corrections introduce binding forces and were derived by Kirzhnits (7.07) from the quantum-mechanical equations by neglecting all high order quantum effects. The lowest order quantum effect is the Pauli exclusion principle which is included in the Thomas-Fermi model. Keeping the next order terms introduces the quantum corrections of the corrected-Thomas-Fermi model. This model is similar to the Thomas-Fermi-Dirac model which includes exchange forces but omits other quantum corrections of comparable magnitude.

The quantum corrections to the pressure are negative representing a binding force and at low temperature and a density of around 1 gm cm^{-3} they dominate the uncorrected positive term and the overall pressure becomes negative. This represents the solid or liquid phase with the solid density given by the density at which the two terms cancel to give zero pressure. Fig.7.07 is the pressure against density plot for aluminium according to the corrected-Thomas-Fermi model. The degeneracy curve passes through zero pressure at a density of 3.3 gm cm^{-3} which is slightly higher than the measured solid density of 2.7 gm cm^{-3}. The main difference between the corrected-Thomas-Fermi curves and the Los Alamos data is the temperature at which aluminium vaporises. According to the corrected-Thomas-Fermi model aluminium is a solid at a temperature of 1 eV. Experimentally it is known to vapourise at about 1/4 eV.

The corrected-Thomas-Fermi model gives the solid density as a function of nuclear charge. The volume occupied by one atom of the solid is a smooth function of Z and is plotted in Fig.7.08 in units of 10^{-30} m^3. For comparison the measured atomic volumes of the elements are given. The theoretical atomic volume smooths through the peaks and troughs given by the shell structure of elements in different parts of the periodic table. It is possible to improve the fit to the solid density for a particular material by adjusting the corrected-Thomas-Fermi Equation. The quantum corrections can be added in to a greater or lesser extent as required. This is not justified theoretically but it can give a better equation of state.

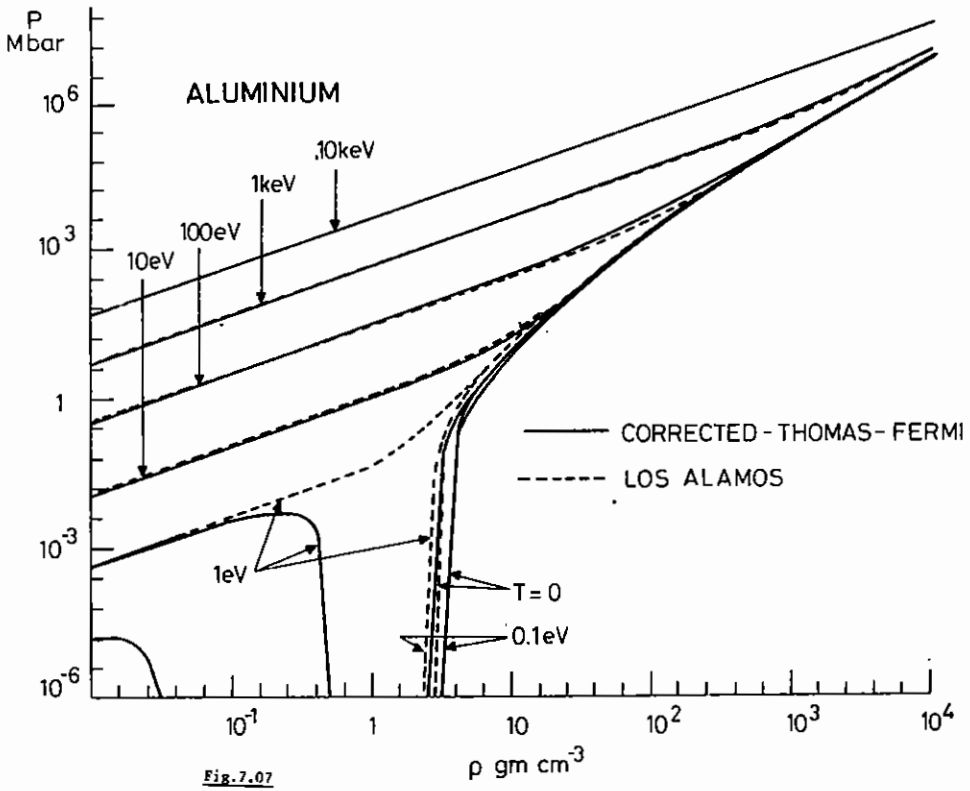

Fig.7.07

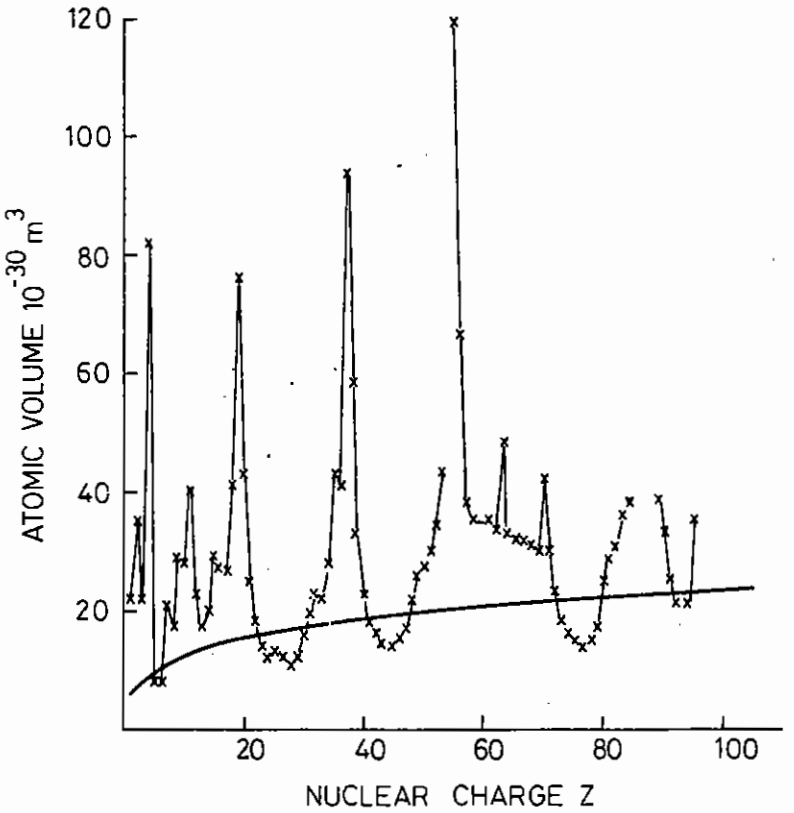

Fig.7.08

Three new options for the equation of state have been included in MEDUSA: 1) the Thomas-Fermi equation, 2) the corrected-Thomas-Fermi equation, 3) the corrected-Thomas-Fermi equation with the quantum correction scaled to give an accurate solid density. Self-consistent analytic approximations to internal energy and pressure as a function of temperature and density were constructed from data given by Latter (7.08) and McCarthy (7.09). These approximations are generally accurate to about 10% over the range of interest. It was then possible to examine the effect of different equations of state on laser compression simulation. The program was run for a standard case of a hollow micro-balloon of inner radius 50 μ and thickness 10 μ containing a deuterium-tritium mixture at an initial density of 0.1 gm cm^{-3}. The shell material was defined to have an atomic mass of 20, a nuclear charge of 10, and an initial density of 2.5 gm cm^{-3}, the solid density given by the corrected-Thomas-Fermi equation of state. The laser wavelength was taken to be 0.25 μ so that fast electron generation did not make the shell an exploding pusher except possibly at the highest laser power considered.

The initial investigation was performed with unshaped constant power laser pulses as a means of identifying the regimes in which each equation of state can be relied upon. The results are presented in Table 7.01 which shows as a function of laser power the maximum mean density of the filler gas, the time t_o taken for completion of the implosion, and the maximum pressure in the shell at $\frac{1}{2}t_o$. The pressure in the shell is included to indicate the magnitude of the pressure which is driving the shell inwards. The final column in the pressure table gives the starting pressure in the shell before the laser is switched on, and this depends on the equation of state. In the simulations the laser is focused on the centre of the target and a constant laser power therefore implies a constant power per unit solid angle throughout the implosion. In the table it is given as an irradiance in Watt cm^{-2} at a radius of 50μ, the initial radius of the micro-balloon. Table 7.01 shows that at an irradiance of 10^{16} W cm^{-2} all equations of state give very similar answers. This is because the laser immediately ionizes the target and pushes it above the regime where the equations of state differ. As the laser pwoer is reduced the ionization becomes partial and the inability of the Fermi-Dirac equation to model ionization makes it unreliable. At an irradiance of 10^{15} watts cm^{-2} a difference in the density attained is beginning to show between the Fermi-Dirac and the other two equations of state, and at lower irradiances the

VOLUME COMPRESSION

	Irradiance				
EOS	10^{13}	10^{14}	10^{15}	10^{16}	W cm^{-2}
FD	6.04	29.0	107	156	
TF	25.9	91.5	145	153	
TFC	41.9	107	152	155	

TIME FOR IMPLOSION (ns)

	Irradiance				
EOS	10^{13}	10^{14}	10^{15}	10^{16}	W cm^{-2}
FD	1.51	2.47	1.02	0.45	
TF	5.17	2.26	1.00	0.46	
TFC	4.38	2.21	1.00	0.45	

MAX PRESSURE IN SHELL AT $\frac{1}{2}t_o$ (Mbar)

	Irradiance				Initial shell pressure
EOS	10^{13}	10^{14}	10^{15}	10^{16}	
FD	1.3	7.9	28.8	145	15.5
TF	1.1	4.3	25.7	141	1.29
TFC	2.1	6.2	30.9	141	0

TABLE 7.01 Volume compression, implosion time and maximum pressure in the shell at half the implosion time for unshaped Laser pulses with irradiances of 10^{13}, 10^{14}, 10^{15} and 10^{16} W cm^{-2}. The equations of state are Fermi-Dirac (FD), Thomas-Fermi (TF) and corrected-Thomas-Fermi (TFC).

difference becomes large. The reason for this can be seen in the column giving initial shell pressures. It is only at an irradiance above 10^{15} W cm^{-2} that the laser generates greater pressure than the fictitiuos initial pressure in teh case of the Fermi-Dirac equation. At low irradiances the fictitious pressure is dominant and drives the implosion itself without any aid from the laser giving a shorter implosion time than the other equations of state and also less compression because the shell then acts as an exploding pusher resulting in inefficient compression. In comparison, the Thomas-Fermi model gives a fictitious initial pressure which is smaller and is dominated by the laser generated pressure at irradiances above 10^{14} W cm^{-2}. Consequently the Thomas-Fermi model is adequate for such irradiances and the results agree well with the more sophisticated corrected-Thomas-Fermi model. It is only at 10^{13} W cm^{-2} that the Thomas-Fermi model gives greatly misleading pressures and the resulting compression differs significantly from that given by the corrected-Thomas-Fermi equation of state.

A Bell

7.2.3 Results from CASTOR

Work on CASTOR has continued during the year and a modification to the code now allows for simulation of turbulent diffusion via the introduction of an anamalous collision frequency.

Apart from basic testing and checking of the code which is still in progress and about which we shall comment later, most of our numerical simulations have been concerned with studies of self generated magnetic fields and their concomitant effects. Motivation for this work has continued to be the experimental work of Raven et al (7.10) at the Laboratory.

In last year's report (section 8.2.2, page 8.5) we compared CASTOR's predictions with the experimental measurements now published in Ref.(7.10), but a serious shortcoming has been our inability to obtain dynamically a good match with the measured density profile in the coronal region. This serious discrepancy has now been overcome and Fig.7.09 shows the best estimate from CASTOR for the parameters of the experimental data displayed

in Fig.3 of Ref.(7.10). Fig.7.10 shows an isometric plot from which the data in Fig.7.09 has been extracted.

We note the discrepancy in spatial distribution of B_{max}. In our many simulations we have observed large fields just in front of the critical density region. For times relevant for comparison, the fields predicted by CASTOR do not die away as we approach the critical density surface from towards the corona as suggested by experimental measurements in Ref.7.10. These fields have high growth rate (under our typical conditions they rise to megagauss level in about 40 pico seconds) and are created rapidly in time during the laser pulse. Collision rates in the subcritical plasma being insufficient for the fields to diffuse, the main loss mechanism occurs with the ablative motion on hydrodynamic timescale. Our current conclusions from our studies are that either the critical density region has not been sampled properly in experimental measurements or other sources and mechanisms must be operative. This matter is of course crucial to settle because of its implications for thermal transport. If large fields occur in the coronal plasma only, then the effect on thermal conduction towards the super critical region are unimportant, wheras if they exist in the vicinity of the critical region then the situation is entirely different.

Returning now to the performance of the code it is disappointing to have to report that certain anomalies and certain shortcomings in the numerics have continued to be sources of trouble. One source of problems in the numerics seems to be associated with an inadequate treatment of thermal magnetic waves that arise from non-linear couplings between T_e and B (7.11). Inadequate treatment of these can give rise to spurious numerical waves and efforts to damp them by artificial diffusion can lead to corruption of the solution and poor energy conservation. CASTOR is being upgraded to run on a finer mesh and will eventually be shifted on to the CRAY computer at Daresbury. It is also hoped, in the near future, to do some comparison and cross checking with the 2-D Eulerian Code developed by G. Pert at Hull University. The code at Hull uses a different difference scheme on the thermoelectric terms of the magnetic field equation which has given rise to numerical problems.

S.J. Abas

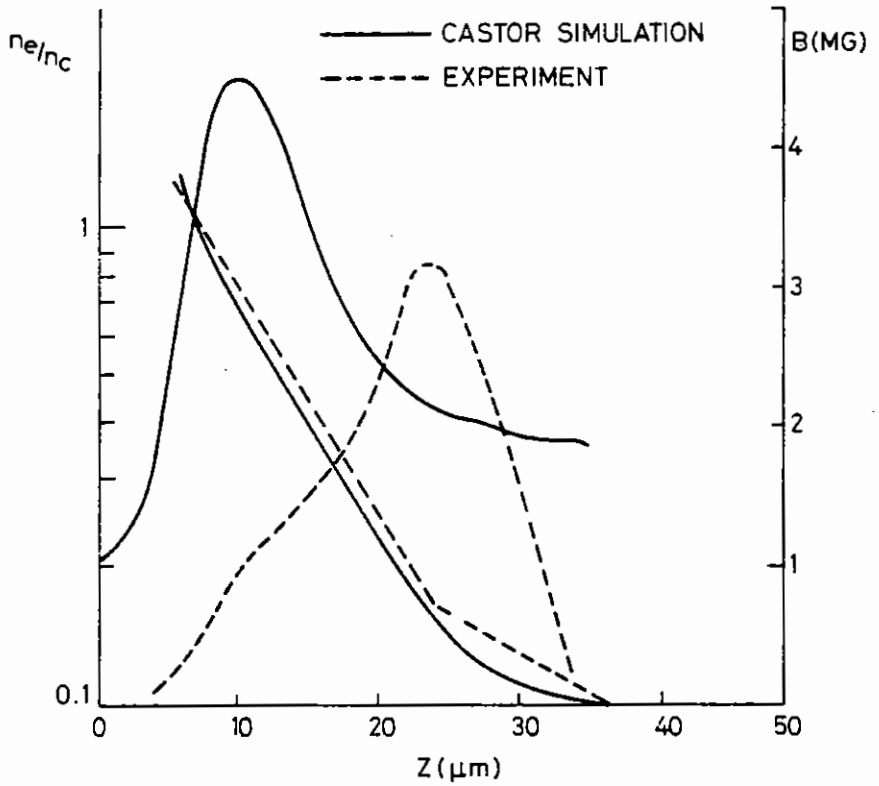

Fig.7.09

Comparison of magnetic field profiles at the edge of the focal spot, perpendicular to the target surface.

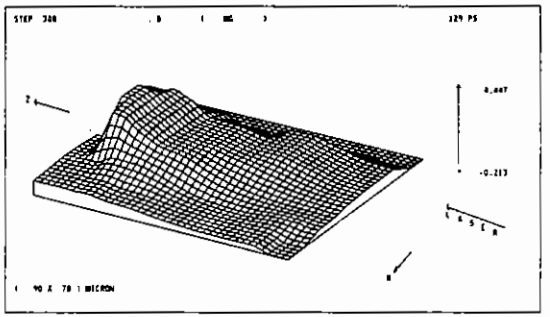

Fig.7.10

Isometric plot of B

7.2.4 Ponderomotive Force for Obliquely Incident Radiation

In this section, we investigate the effects of the ponderomotive force on the density profile of laser produced plasmas. This is done by means of an 1-D Lagrangian hydrodynamic code based on MEDUSA (7.12) where the ponderomotive force has been included in the momentum equation. We consider both normal and oblique incidence on spherically symmetric, radially expanding plasma.

In section 3.3.2, the effects of the ponderomotive force for normally incident light is described. The results show good agreement with experimenta results. However, at high intensities and short laser pulses, experiments (7.13) indicate that resonant absorption is an important absorption mechanism. Therefore, MEDUSA was extended to take into account the ponderomotive force due to the obliquely incident radiation.

The nonlinear ponderomotive force may be written as the divergence of the field's stress tensor (7.14), averaged over several laser periods

$$F_{PM} = -\nabla \cdot \langle \underline{\underline{\sigma}}_R \rangle \tag{1}$$

where

$$\underline{\underline{\sigma}}_R = -\frac{1}{8\pi}(E^2 + H^2)\underline{\underline{I}} + \frac{1}{4\pi}(\varepsilon' \underline{E}\,\underline{E} + \underline{H}\,\underline{H}) \tag{2}$$

$\underline{\underline{I}}$ is the unit tensor and ε' is the complex dielectric permitivity

$$\varepsilon' = 1 - \frac{\omega_p^2}{\omega_o^2}\left(1 + i\,\frac{\nu_{coll}}{\omega_o}\right) \tag{3}$$

with ω_p being the electron plasma frequency, ω_o the laser light frequency and ν_{coll} the electron-ion collision frequency, which is given by (7.15)

$$\frac{\nu_{coll}}{\omega_o} \simeq 0.265\,\frac{k_o \langle Z \rangle (N_e/N_{crit})}{(k_B T_c)^{3/2}}\,\ell n\Lambda \tag{4}$$

for k_o (the wavenumber of the laser light) in μm^{-1} and $k_B T_c$ (the cold electron temperature) in eV. <Z> is the averaged charge state of the

plasma, (N_e/N_{crit}) is the electron density normalised to the critical density and $\ell n\Lambda$ is the Coulomb logarithm.

In these calculations, the diameter of the simulated targets is much larger than the focal spot size, therefore little error will be introduced by solving the following wave equation for the electric field

$$\nabla^2 \underline{E} - \nabla(\nabla \cdot \underline{E}) + k_o^2\,\varepsilon' \underline{E} = 0 \tag{5}$$

in a plane-parallel geometry. In deriving this equation, we neglected "thermal effects", responsible for the generation of electron plasma waves, and assumed that all field quantities vary as $\exp(i\omega_o t)$ (7.16). Only p-polarized light, with the electric field in the x-y plane ($x = R - R_{crit}$), will be considered. x is the symmetry axis of the incident laser beam. The y dependence of the fields is assumed to be periodic and to be of the form $\exp(-ik_o y \sin\theta_o)$, where θ_o is the angle of incidence. Under these conditions, the radial or x-component of the ponderomotive force is

$$F_{PM} = \frac{d}{dx}\left[-\frac{1}{16\pi}(|\underline{E}|^2 + |\underline{H}|^2) + \frac{\varepsilon}{4\pi}|E_x|^2\right] \tag{6}$$

where $\varepsilon(R) = \varepsilon(x)$ is the real part of ε'. Using Faraday's law, $\nabla \times \underline{E} = -ik_o \underline{H}$, and eqn.(5), we can write (6) as

$$F_{PM} = -\frac{d}{dx}\left[\frac{1}{16\pi}(\cos^2\theta_o\,|E_x|^2 + |E_y|^2 + \frac{1}{k_o^2}\,|\frac{\partial E_y}{\partial x}|^2)\right] \tag{7}$$

The expression within the square brackets can be identified with a scalar pressure, P_{rad}, associated with the fields. It is this pressure which, when incorporated in MEDUSA via the momentum equation, will account for the ponderomotive force effects.

The fields that will be used in eqn.(7), are obtained from the numerical solution of the wave equation on an auxiliary mesh, created by subdividing the Lagrangian fluid cells into smaller cells of about 0.04 λ_o (λ_o is the laser light wavelength). The wave equation is integrated starting on the high density side of the critical surface and going out to the outer edge of the plasma where the solution is matched to the vacuum field

$$\underline{E} = \underline{E}_o \left(e^{\alpha_o} e^{-k_o x \cos\theta_o} + R\, e^{ik_o x \cos\theta_o}\right) \qquad (8)$$

The phase α_o and the complex reflectivity R are determined from the matching conditions. The normalization constant E_o is derived from the condition

$$\frac{1}{\lambda_o}\int_{\lambda_o} |\underline{E}|^2_{\text{numeric}}\, dx = E_o^2 (1 + |R|^2) \qquad (9)$$

at the edge of the plasma. The calculated values for the fields are then substituted into eqn.(7) given the radiation pressure associated with the auxiliary mesh. The radiation pressure, $\overline{P_{rad}}$, associated with a cell of the main Lagrangian mesh is obtained by numerically averaging P_{rad} over this cell. The radiation pressure in the outermost cell (vacuum) is

$$\overline{P_{rad}} = \frac{I_o}{c}\cos^2\theta_o (1 + |R|^2) \qquad (10)$$

where I_o is the irradiance of the incident light. The momentum equation in MEDUSA may then be written as

$$\rho \frac{du}{dt} = -\nabla(P_{th} + \overline{P_{rad}}) \qquad (11)$$

where ρ is the plasma mass density, u the plasma flow velocity and $P_{th}(= P_e + P_i)$ is the normal thermal pressure.

All our calculations have been performed at a laser wavelength of 1.06 μm and a Gaussian laser pulse of 50 psec (FWHM). Targets consisted of 40 μm diameter microballoons with a glass shell thickness of 0.6 μm, filled with a DT mixture. The peak laser power, P_{peak}, was varied to simulate different incident irradiances. The plasma is allowed to undergo free expansion until the laser power equals 0.2 P_{peak}. At this time the ponderomotive force is switched on and remains on for the rest of the pulse. During the initial stage of the pulse, a constant absorption (10%) is assumed. Afterwards, when the fields are on, the absorption is given by the larger of {10%, AB}, where AB(= $1 - |R|^2$) is the self-consistent absorption calculated from the solution of the wave equation. AB includes inverse

Bremsstrahlung and resonant absorption (for oblique incidence). Part of the absorbed energy is allocated to superthermal electrons characterized by a hot electron temperature $T_H = \alpha T_c$, where α is a parameter. This energy is carried away in the free-streaming limit. The remaining absorbed energy is allocated to thermal electrons. The thermal transport is assumed to be flux-limited, with a flux-inhibition coefficient equal to 0.03.

In our calculations we only consider angles of incidence up to 5°. We did not consider larger angles because, for realistic experimental conditions, we expect most of the incident energy to be concentrated near normal incidence. This might not be true if density ripples occur at the critical surface; however, no density rippling has been observed in any of the microballoon experiments so far (7.17, 7.18)

Fig.7.11 shows the calculated density profiles near the peak of the laser pulse. The total energy of the incident laser pulse is 0.05 J and the maximum irradiance is 3.0×10^{14} W cm^{-2}. As can be seen, the two density profiles are quite similar and our calculations show that there is no marked differences between the density profiles for normal and oblique (5°) incidence in the irradiance range $10^{14} - 10^{15}$ W cm^{-2}. This lack of sensitivity is explained by the fact that, for these intensities, collisions provide an effective saturation mechanism for the resonant electric field at the critical surface. Therefore, the amplitude of the electric field for small angles of incidence is not much larger than for normal incidence and, consequently, max $\overline{P_{rad}}$ (oblique) ∿ max. $\overline{P_{rad}}$ (normal). This is not the case for higher irradiances. Fig.7.12 shows the density profile near the peak of a 2.5 J laser pulse with maximum irradiance equal to 7.4×10^{15} W cm^{-2} for normal incidence and 8.0×10^{15} W cm^{-2} for 2° oblique incidence. The calculated values of max $\overline{P_{rad}}$ are quite different in the two cases and so are the density profiles. The reason for such a considerable discrepancy is that for irradiances above 10^{15} W cm^{-2}, the calculations show very large resonant field amplitudes at the critical surface even for very small angles of incidence. This is due to the inefficiency of collisions as the saturation mechanism at these high irradiances and cold electron temperatures. If a more efficient saturation mechanism, such as plasma wave convection, was used the electric field would be saturated at lower amplitudes, bringing its effects more in line with the conditions at

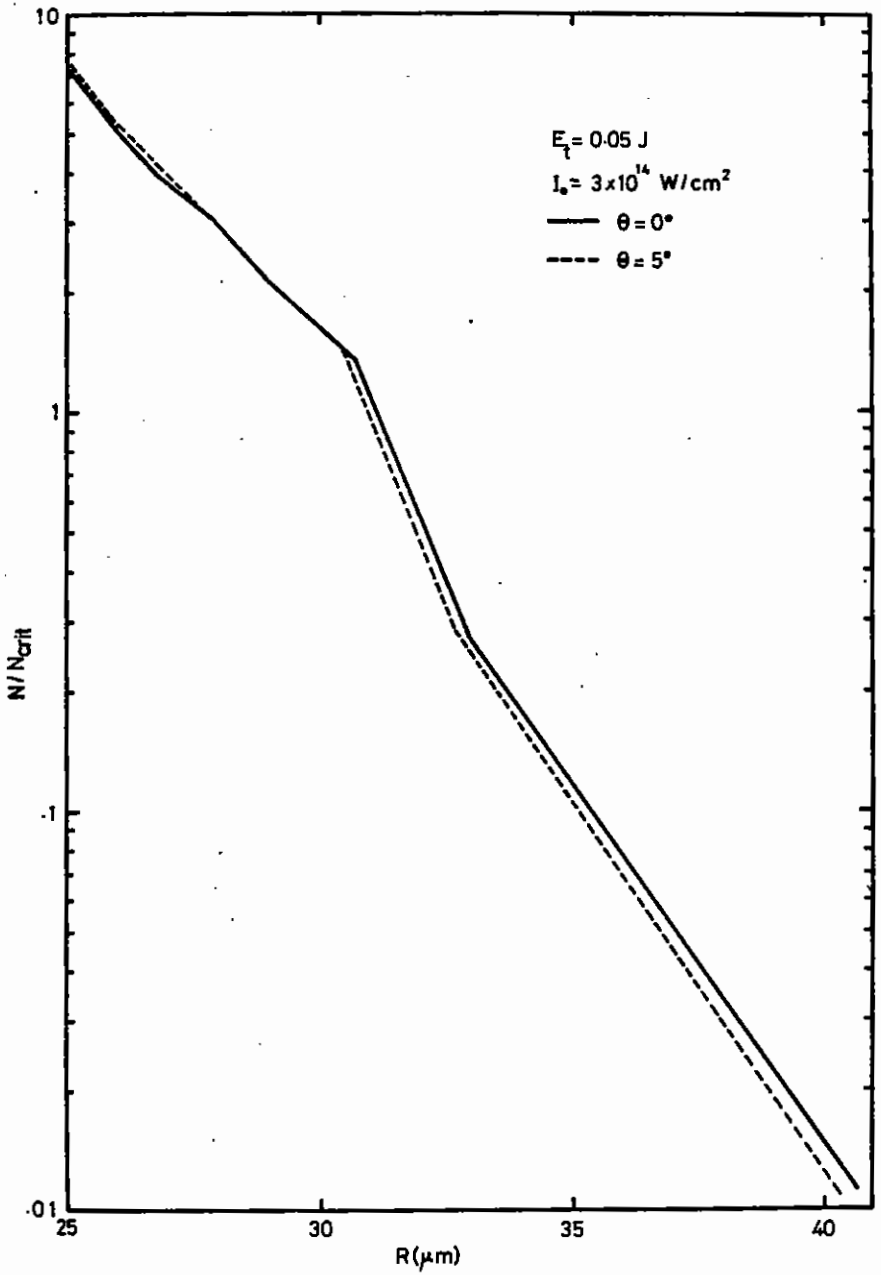

Fig.7.11

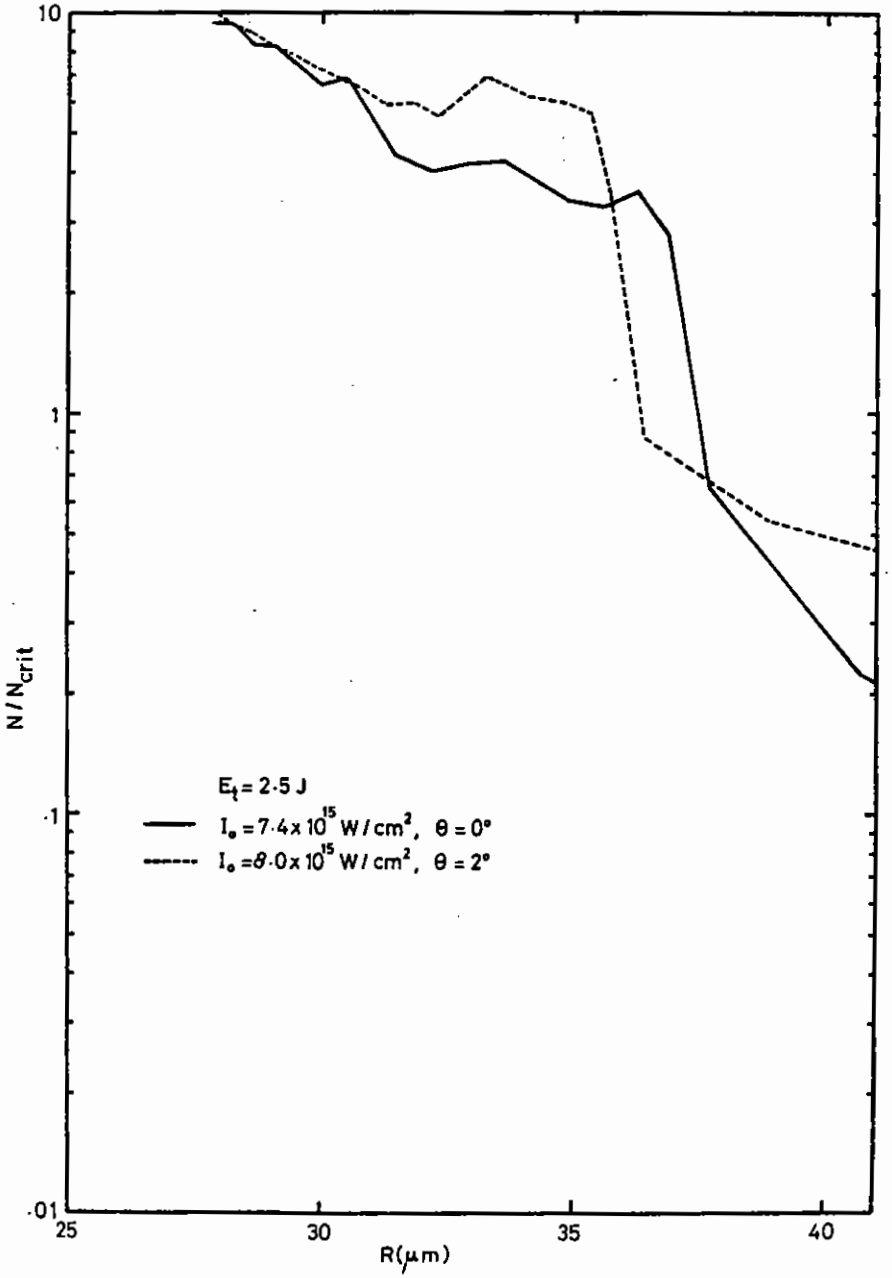

Fig.7.12

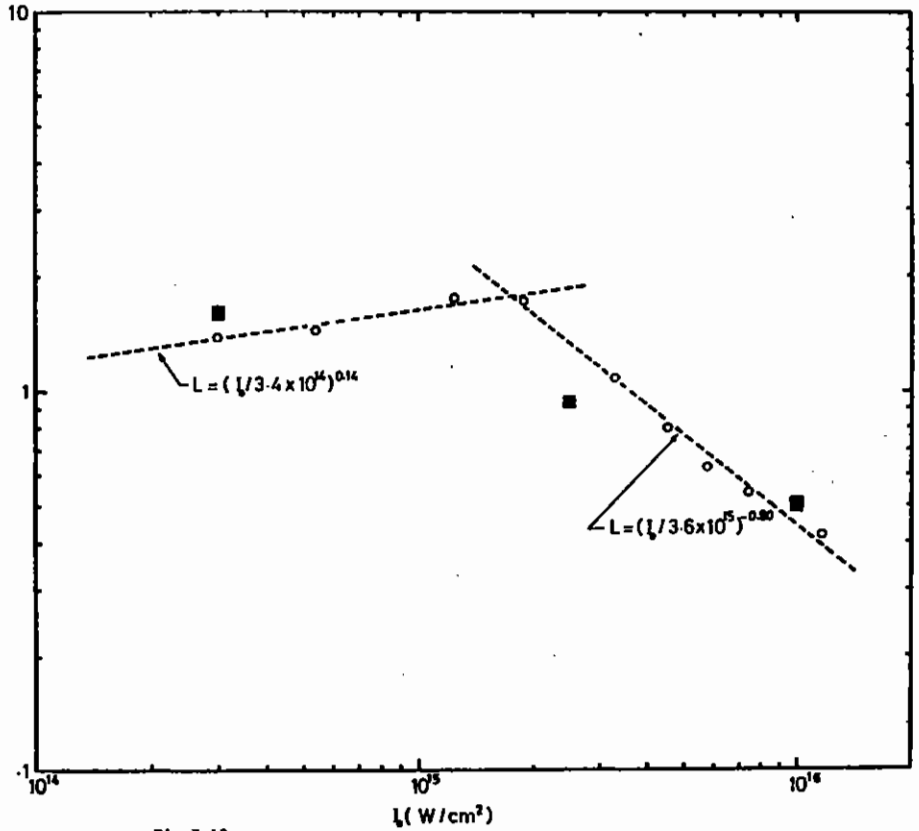

Fig.7.13

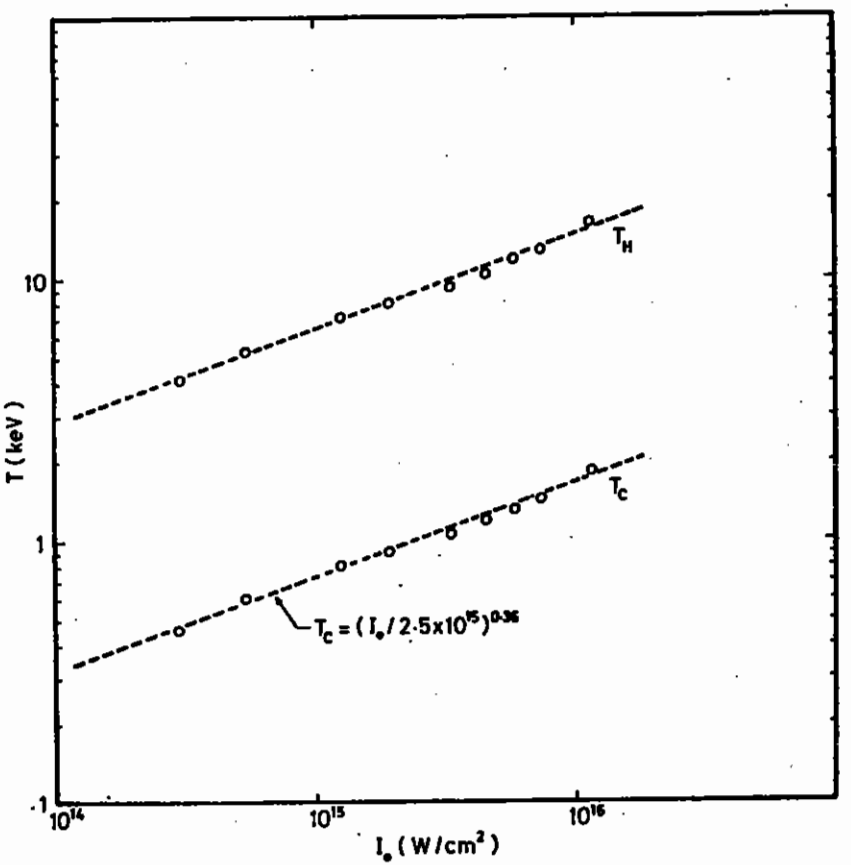

Fig.7.14

lower irradiances. Therefore, our results indicate that to simulate the hydrodynamic flow of laser-produced plasmas on microballoon targets, it is sufficient to consider only normally incident light. The fact that part of the focused laser light is obliquely incident will not change the overall density profile, though its presence can still be invoked to explain the production of hot electrons in these experiments (7.13).

For normal incidence, the main difference between the present calculations and those described in section 3.3.2 is in the absorption. In section 3.3.2, the absorption effects were neglected in solving the wave equation and a constant absorption was considered throughout the calculations. In the present approach, the self-consistent absorption (due to Inverse Bremsstrahlung) calculated in each time-step, from the solution of the wave equation, is substituted back into MEDUSA for the determination of the density and temperature profiles associated with the next time-step.

Fig.7.13 shows the variation with intensity of the critical density scale length, near the peak of the laser pulse, derived from the density profiles calculated by the code with the inclusion of the self-consistent absorption. The experimental data (squares), from (7.17) and (7.18), are shown for comparison. To explain the numerical results, we rewrite eqn.(11) as follows

$$\rho \frac{du}{dt} = - \nabla P_{th} + F_{PM} \qquad (12)$$

where $F_{PM} (= - \nabla \overline{P_{rad}})$ is the ponderomotive force. If $|F_{PM}/\nabla P_{th}| \ll 1$, F_{PM} can be neglected in eqn.(12) and we have the usual momentum equation for a freely expanding plasma. In this case, the scale length (L) increases with increasing incident irradiance (I_o) (7.19). For $|F_{PM}/\nabla P_{th}| < 1$, F_{PM} can not be neglected in eqn.(12); the expansion is still dominated by the hydrodynamic force but we expect there to be some profile modification due to the presence of a non-negligible ponderomotove force. In our calculation, the conditions described above occur for irradiances in the range $\sim 10^{14} - 10^{15}$ W cm^{-2}. In this range L increases with I_o, though very slowly ($L \propto I_o^{0.14}$). Above $\sim 2 \times 10^{15}$ W cm^{-2}, the expansion is strongly influenced by the presence of the ponderomotive force. The density profile adjusts itself so that, near the peak of the laser pulse, the hydrodynamic force above the critical surface reaches a regime of dynamic

equilibrium with the confining part of the ponderomotive force. Therefore, the scale length decreases with increasing incident irradiance. A power law fit gives $L \propto I_o^{-0.80}$. It is interesting to notice that the experimental values of the hot electron temperature also show a change, in their variation with irradiance, at $I_o \sim 10^{15}$ W cm^{-2} (7.20) this change was attributed to the transition from a regime of weak, to one of strong, profile modification.

The values of the hot electron temperature obtained in our calculations are displayed in Fig.(7.14). They do not show any change in behaviour, which is not surprising considering the crude model used in their calculations ($T_H = \alpha T_c$, α constant). The calculated T_H values are smaller than the experimental ones for similar conditions (short laser pulses, glass microballoon targets)(7.13), nonetheless, their scaling with irradiance ($T_H \alpha I_o^{0.36}$) is in good agreement with scaling derived from these experiments ($T_H \alpha I_o^{0.39}$).

A Montes, O Willi

7.2.5 2-D Lagrangian Code Development

The 2-D Lagrangian fluid code developed at the University of Hull has now been implemented and is in regular use at the Rutherford Laboratory. The code is a two temperature code with separate electron and ion temperatures and ion-electron equilibration by collisions. The diffusion of thermal energy on the quadrilateral mesh is handled by the 9 point difference scheme of Kershaw (7.21) with ICCG (7.22) to solve the resulting equations. The hydrodynamics use a Jacobian method with full tensor artificial viscisity. The acceleration term is the integral form FGI-q of Browne and Wallick (7.23). At present perfect gas equations of state are used but work is in hand to include the equations of state described in 7.2.2. The incident laser beam is traced in straight lines only (in the absence of refraction) up to critical density where a specified portion is reflected. Absorption of the laser energy is by inverse Bremsstrahlung together with the specified dump at critical density.

The code agrees well with "standard" 1-D lagrangian codes on spherically symmetric targets and also campares well with Schultz's (7.24) data on compression of spleroids under uniform applied pressure.

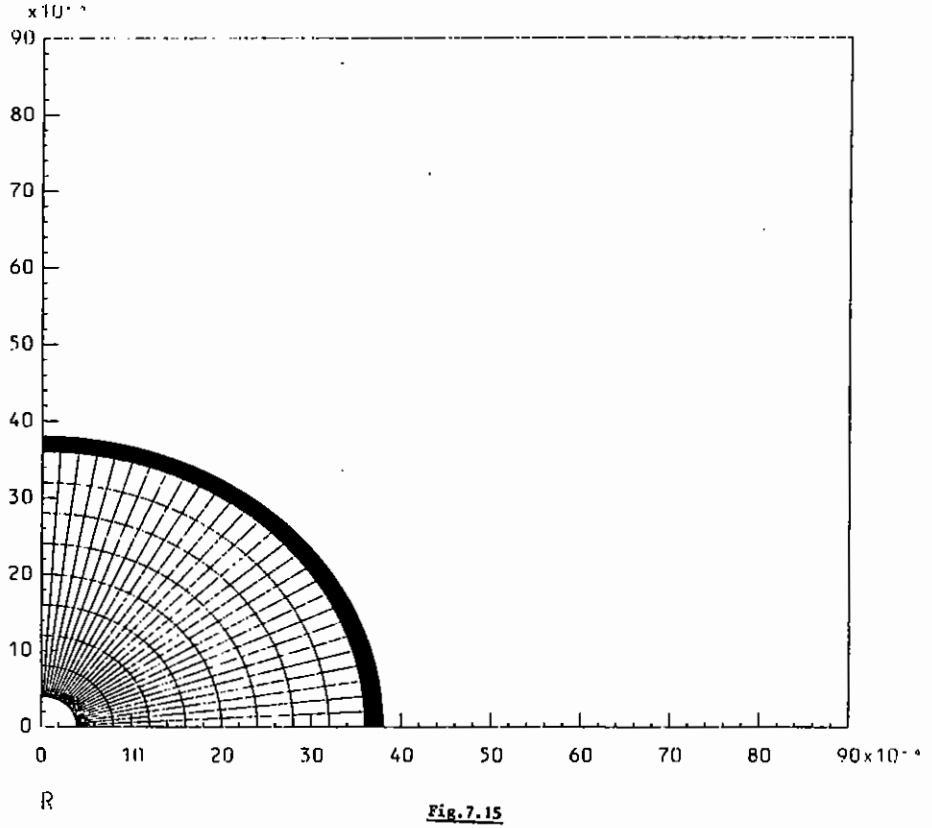

Fig.7.15

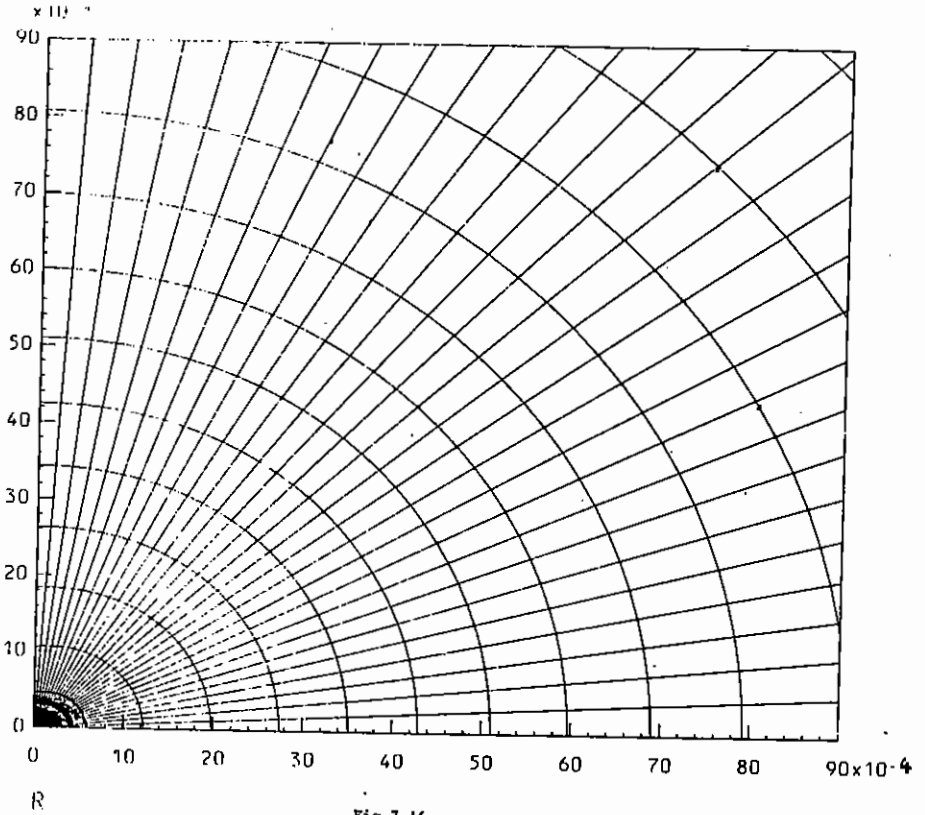

Fig.7.16

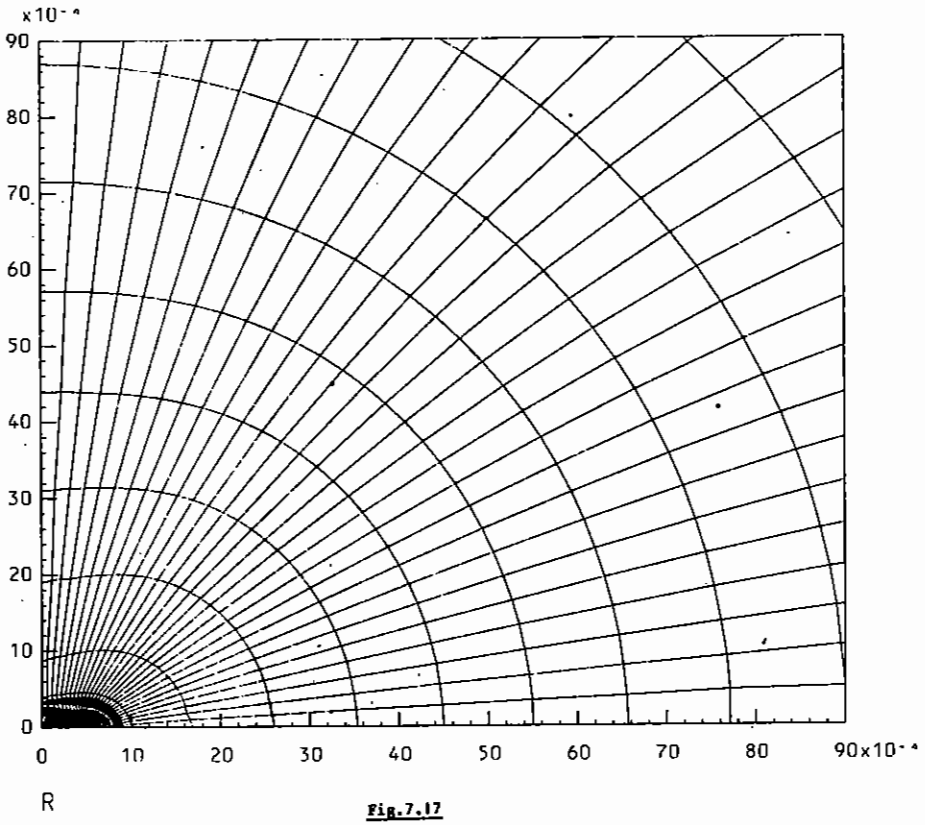

Fig.7.17

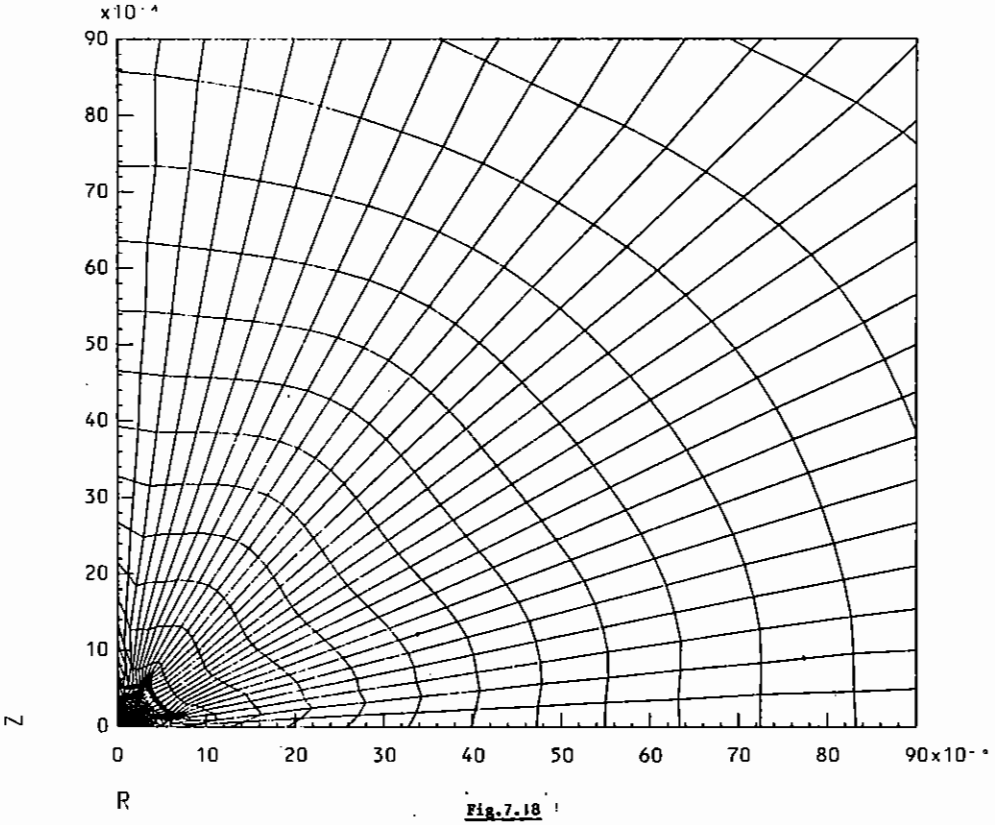

Fig.7.18

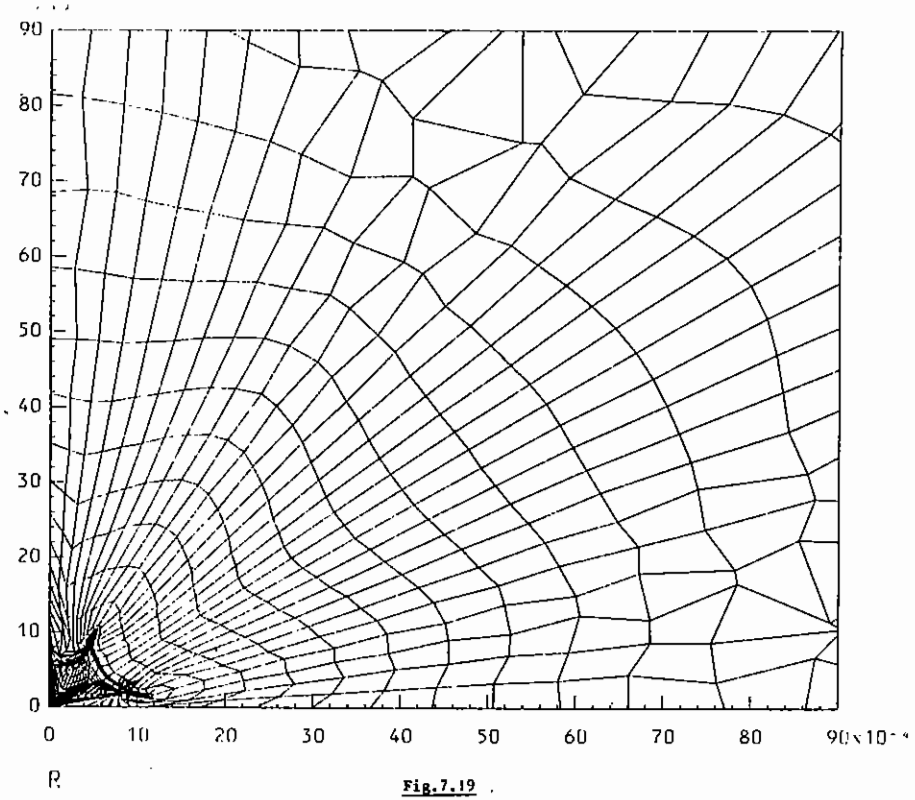

Fig.7.19

With the present limitations of the code it is not suitable for detailed comparison with experimental data but it has been used to study the effects of gross non sphericity in both targets and incident laser irradiance. At the University of Birmingham the code has been modified to handle heavy ion deposition and is being used to investigate effects of the geometry of heavy ion deposition with a finite number of beams.

The results presented here show implosion calculations of 40 μm radius, 2 μm thick shells irradiated at about 3.10^{15} W cm^{-2} with a 1.06 μm laser of various degrees of non-uniformity.

Fig.7.15 shows the initial position of the mesh in all cases while Fig.7.16 and Fig.7.17 show the mesh at maximum compression in the cases where there was a smooth variation of irradiance from pole (the Z axis) to equator (the R axis). In Fig.7.16 the ration of irradiances at the pole to the equator was 1:0.8 producing a very acceptable implosion with an ellipsoidal but well compressed core. In Fig.7.17 the ration of irradiances was rather more extreme at 1:0.25, a pronounced flattening of the implosion core and a marked degradation in volumetric compression are observed.

Fig.7.18 and Fig.7.19 show the cases where the irradiance was modulated as $I(\phi) = I_o(1 + \alpha \cos n\phi)$ where ϕ is the angle between the incident rays and the Z axis. The parameter n was set so as to give 1½ cycles of modulation (two peaks and two troughs) from pole to equator and Figs. 7.18 and 7.19 show the imploded configurations for $\alpha = 0.2$ and $\alpha = 0.5$. The case with $\alpha = 0.5$ should not be taken very seriously since severe tangling of the computational mesh has occurred. This serves mainly to indicate the degree of uniformity of illumination that is required and the results agree well with some simple calculations of Nicholas and Evans who suggested that a uniformity of about ±20% was needed to achieve radial convergence of 10:1. The 2-D lagrangian calculations show that ±20% modulation significantly degrades the compression (10:1 in radius) that is achieved with uniform illumination. Although only preliminary these calculations do show that uniformity of illumination may be a serious limitation of the 6 x f/1 lens illumination system.

G Pert, A J Bennett, R G Evans.

7.2.6 Numerical Simulation of Fast Electron Transport

Two approaches to fast electron transport simulation have been explored in the last year.

(A) Multi Total Energy Group Diffusion

The inclusion of E field effects greatly complicates the solution of the multi group diffusion equations. The fully implicit solution of the multi group equations is easier if total energy, $\varepsilon_T = \frac{1}{2}MV^2 - e\phi$, is used as a coordinate instead of kinetic energy. Transforming the Fokker-Plank equation so that, ε_T, x, t and μ are independent coordinates and then using the diffusion approximation gives multi group equations of the form:

$$\frac{\partial N_s}{\partial t} + \frac{\partial}{\partial x} \alpha \frac{\partial}{\partial x} \frac{N_s}{V} + \frac{\partial}{\partial \varepsilon_t} \left(P - e \frac{\partial \phi}{\partial t} \right) N_g = \text{source/sink} \quad (1)$$

This is differenced fully implicitly using Leleviers method (7.25) for the $\frac{\partial}{\partial \varepsilon_T}$ term. The coefficients are evaluated using the potential at the advanced time level. The potential is determined interatively from the condition J total = 0. At each iteration a quindiagonal ILUCG algorithm is used to solve the multi group equations.

(B) Monte-Carlo, PIC Model

Two methods for calculating the quasineutral, J total ≈ 0, E field in a time dependent simulation are being studied. Firstly the method of plasma period dilation used by Mason (7.26). The E field is calculated using:

$$\nabla . \varepsilon_m E = \rho \quad (2)$$

ε_m is chosen to dilate the plasma period to a few computational time steps. Secondly an interative method which uses:-

$$\Delta E_{eff_i} = \frac{-J_i}{\left(\frac{\partial J}{\partial E_{eff}} \right)_i} \quad \text{(i is a grid index)} \quad (3)$$

Where E_{eff} is related to E_{i-1}, E_i, E_{i+1} by the PIC weighting and interpolation which is used.

D J Bond.

7.2.7 Radiative Preheat Effects in Laser-Compression Simulations

7.2.7(a) Introduction

In this report we present a brief summary of hydrodynamic simulation work performed at Glasgow during the past year. Our main interest was to study radiative preheat effects in laser-compression simulations. These simulation results have been carried out using an updated version of a 1-D Lagrangian computer code MEDUSA (7.12) which has been extensively modified by the authors by inclusion of atomic and radiation physics effects and also by allowing handling of gas filled microballoons and layered targets (7.27)(7.28)(7.29). Previously (7.29)(7.30) we presented simulation results using a 10 μg solid carbon microsphere compressed by an ideal laser-fusion pulse with total energy 600 J/Steradian. These results show that typically the final density is reduced by a factor of 6 due to radiative preheat of the target. In our present calculations we consider a neon-filled thin glass microballoon irradiated by a Gaussian laser pulse with parameters within the capability of the Nd. glass laser at the Central Laser Facility, Rutherford Laboratory. These calculations show that the radiative preheat reduces the final gas density by up to a factor of 3 while the shell density drops from 10^5 kg/m^3 to 1.8×10^4 kg/m^3. In the following we discuss these results in detail.

7.2.7(b) Results

Target initial condition
Inner radius of microballoon: 35 μm
Wall thickness of microballoon: 0.9 μm
Neon density: 15 kg/m^3
Electron, Ion and radiation temperature: 5×10^4 K

A Gaussian laser pulse with total energy 70 J and FWHM 100 ps(τ) is used to compress this target. Experiments suggest that about 10% of the laser energy is absorbed under these conditions. This partial absorption is treated in our calculations by inclusion of a factor in the absorption subroutine of the computer code. For comparison we have simulated the compression with and without radiation effects. In the former case the

energy is transported by flux limited photon and electron thermal conduction while in the latter case the thermal electrons are the only means of energy transport. It is seen from Table 7.02 that the radiation temperature in the gas rises rapidly causing electron heating due to electron-radiation interaction. The electrons heat the ions and the total pressure increases before the target is compressed. This is because the photons created at the critical density have longer mean free path than the thermal electrons. As a result the photons transport energy more rapidly and cause preheat of the target. Excluding the radiation effects we achieve final neon density $\sim 2 \times 10^4$ kg/m^3 and maximum shell density $\sim 10^5$ kg/m^3. The radiative preheat reduces the gas density to 7×10^3 kg/m^3 and the shell density to 1.8×10^4 kg/m^3.

TABLE 7.02

Time	T_r	T_e	T_i	P
ps	10^5K	10^5K	10^5K	10^9J m^{-3}
40	4.75	0.60	0.50	0.72
60	10.0	0.79	0.60	1.45
80	11.4	1.23	0.87	2.90
100	12.0	1.86	1.38	5.75
125	13.0	2.50	2.00	10.00

where T_r, T_e and T_i denote radiation, electron and ion temperatures respectively while P is the total pressure (hydrodynamic + radiation).

We have also done calculations varying τ in the range 70-250 ps, keeping the total energy in the laser pulse constant. Results are given in Table 7.03. It is seen that in the range τ = 70-150 ps the final gas density with and without radiative transport increases steadily due to minimisation of shock heating. In the range τ = 150-250 ps, excluding the radiation effects the final density achieved does not change much, while inclusion of radiation effects increases the final gas density. This is due to *radiation cooling* of the target which takes place with longer laser pulses.

N A Tahir and E W Laing

TABLE 7.03

Total Energy Absorbed: 7 J

	Radiation off		Radiation on	
τ	ρ_m	T_e	ρ_m	T_e
ps	10^4kg m^{-3}	10^7K	10^4kg m^{-3}	10^7K
70	1.30	4.50	0.48	2.70
100	2.00	4.00	0.70	2.50
130	3.10	4.00	1.35	2.00
160	5.00	4.00	2.00	1.70
190	2.50	3.30	3.50	1.35
220	2.70	3.00	4.00	1.20
250	3.80	2.80	5.00	1.00

7.2.8 Code Development at Hull

During the past year both the two-dimensional codes, MAGT in Eulerian geometry and LAG2 in Lagrangian have been fully implemented on the ATLAS system, and a number of minor implementation difficulties resolved. In addition further improvements to the numerical analysis in the codes has been made and is described below.

Extremum Limited Diffusion

It is a classic property of diffusion that extrema decay in time, and is a direct consequence of the maximum principle. This simple result ensures the overall stability of diffusion. In view of this it is natural to seek to retain this property in a finite difference solution, for not only does it guarantee the overall stability of the numerical algorithm, but also maintains the correct physical form in the solution.

A slightly weaker form of the condition is expressed in the extremal condition; namely that the new value generated at any point, ε_i, should satisfy the condition:

$$\text{Min } (\varepsilon_j^o, \varepsilon_b) \leq \varepsilon_i \leq \text{Max } (\varepsilon_j^o, \varepsilon_b) \qquad (1)$$

with respect to the old set of values ε_j^o, and those on the spatial boundaries, ε_b.

It can be shown that an operator, G,

$$\varepsilon_i = G(\varepsilon_j^o) \qquad (2)$$

is extremal if and only if its differential (ie $\varepsilon_i = \varepsilon_i^o$ if $\varepsilon_i^o = \varepsilon_j^o$ for all i,j) and non-negativity maintaining (ie if $\varepsilon_j^o \geq 0$ for all i,j). Application of this theorem to finite difference representations of diffusion requires the spatial difference - the diffusion matrix - to be the negative of an M-matrix.

In cases of isotropic diffusion on an orthogonal mesh this condition is

readily established by a simple finite difference form. If, however, the mesh is non-orthogonal it follows from a theorem by Kershaw that a consistent form of the diffusion matrix cannot take an M-matrix form. To treat this case we have developed a new 9-point differencing form based on integral flux transport, which allows the non M-matrix terms to be directly identified as an "anti-diffusion" flux. In this form we may extremally difference both the residual M-matrix and the "anti-diffusion" terms to generate an algorithm which is overall extremal. This algorithm has been successfully implemented on LAG2 and has proved most satisfactory.

When a magnetic field is present, the cross product Righi-Leduc terms introduce difficulties unless care is taken to ensure they have an M-matrix form. This is easily achieved by noting their similarity in form to advection terms and differencing similarly in terms of upstream forward or backward differences. It is readily shown that such differencing ensures convergence to the correct physical limit. This form is used in MAGT.

In running large codes of this type, one endeavours to write as many operations as possible in forms which do not limit the time-step. Diffusion, which is convergent, should clearly be written in this stiff form. Extremal forms, which are convergent if positivity-maintaining, are particularly suitable. We have shown furthermore that the accuracy of a two-step stiff solution may be improved by the use of simple weights between the implicit and explicit parts, if the weight is chosen such as to just maintain positivity.

In practice the use of extremal diffusion algorithms allows three benefits: avoids generation of spurious negative energy; improves accuracy of stiff solutions; ensures stability under the most general conditions.

Expanding Grid Eulerian Hydrodynamics

The need to treat the expansion of laser heated fibres within an Eulerian framework has led to the development on an expanding grid re-zoning algorithm in MAGT. The convective hydrodynamics in MAGT use a simple

flux-corrected transport algorithm within which the grid expansion is easily accomplished by means of additional velocity representing the motion of the grid through the fluid. The pressure acceleration/work done terms, treated within the Lagrangian energy step, are only weakly conservative. Despite the loss in accuracy, this allows a simpler convection stage than a strict energy conservation.

The grid is expanded maintaining a uniform spacing, with the velocity of the boundaries determined by the velocity of cells whose density exceeds some prescribed value.

Instability of the Thermo-electric Magnetic Field Generation Term

The inclusion of the complete thermo-electric terms in the source of the magnetic field can lead to difficulties associated with the cross-product term. These terms take the form:

$$\frac{\partial B}{\partial t} = \frac{\partial}{\partial z}\left(\beta_\wedge \frac{\partial E}{\partial z}\right) + \frac{\partial}{\partial r}\left(\beta_\wedge \frac{\partial E}{\partial r}\right) \qquad (3)$$

where E is the electron internal energy. Noting that the coefficient:

$$\beta_\wedge = \gamma B \qquad (4)$$

we see that the source equation is equivalent to a convection equation in the magnetic field B with velocities $\gamma\ \partial E/\partial z$ and $\gamma\ \partial E/\partial r$.

In the past we have used a simple explicit centre difference form for $\beta_\wedge$, which on the basis of advection might be expected to be unstable. In fact the complete algorithm used can be shown to be stable, but does none-the-less have undesirable extremum generating behaviour.

The solution to this problem, once identified, is obvious. We have now differenced B implicitly with upstream differencing in the existing Newton-Raphson iteration in MAGT. Preliminary tests indicate that this source of error has now been eradicated in this manner.

G J Pert, A Bennett

7.3 Laser Plasma Interactions

7.3.1 Magnetic Field Structure

Some characteristics of the self-generated magnetic fields in laser-produced plasmas have been known from early studies using magnetic and current probes. However, until the work of Stamper, McLean and Ripin (7.31, 7.32) and of Raven, Willi, and Rumsby (7.33) it was not possible to extend the measurement of the field into the laser focal region. These measurements were made using Faraday rotation techniques and confirmed the presence of large (megagauss) fields in plasmas produced by the high intensity irradiation of solid targets. Fields of this magnitude are capable of affecting the transport of thermal energy into the target. There is evidence from a variety of experiments that points to significant inhibition of electron energy transport in laser-target plasmas to values much less than those from simple estimates based on flux-limited diffusion. Consequently a close study of their morphology is important.

The most detailed work undertaken so far is that of Raven and co-workers (7.10) who have studied the effect of target size and composition on the generation of thermoelectrically driven magnetic fields, using a single beam of the neodymium glass laser at the Rutherford Laboratory. This delivered up to 10 J in a 100 ps pulse and produced irradiances of several x 10^{16} W cm^{-2} over a focal spot of diameter 15 μm. A range of target plasmas was observed using Faraday rotation and interferometric techniques with either a Raman-shifted second harmonic probe beam at 0.639 μm or a UV fourth harmonic probe at 0.266 μm. The targets used were variously plane and spherical, structured and unstructured, hollow and solid (in the case of spherical targets, the diameters of which ranged from 40 - 250 μm). The observations showed a number of interesting effects both in spherical and plane geometry. With spherical targets it was found that magnetic fields were only present for targets the diameter of which exceeded 100 μm, and were independent of target wall thickness. Very strong fields (in the megagauss range) were seen from large plane targets though no field was measureable from small discs. Raven et al, have concluded from these observations that the size of the magnetic field generated is determined effectively by the electrical capacity of the target.

The experimental results (Fig.7.21) show that the thermoelectrically generated field at the edge of the focal spot rises from zero at the refractive cut-off to about 600 kG at the critical density, n_c and increases steadily to just above 3 MG at 0.2 n_c before dropping steeply to zero around 0.1 n_c. The main conclusion from the work on plane targets is the occurrence of the strongest fields in the low-density coronal plasma. The application of a large prepulse resulted in the fields being strongly structured in the radial direction.

The fact that the field peaks in the low-density corona rather than near the critical density is important in relation to the role often suggested for these self-generated fields in limiting electron thermal transport. Raven's observations confirmed earlier predictions by Colombant and Winsor (7.34) who showed on the basis of a numerical simulation that peak fields in the megagauss range were present in the corona. There is however no quantitative agreement with the observations. Their model of the evolution of the magnetic field shows after 62 picoseconds, a peak field of just over a megagauss about 70 μm in front of the critical surface and at a radius of approximately 100 μm. From Fig. 7.21 the peak field occurs at $z \sim 25$ μm at the edge of focal spot ($r = 7 - 15$ μm).

Given the complexity of the problem it is of some interest to see whether a simpler approach cannot provide some insight into the problem. We have chosen to ignore the hydrodynamics in view of the short pulse nature of the experiment and model the conditions of the Rutherford experiment explicitly albeit in a way that is not self-consistent. The general expression for the evolution of the magnetic field may be expressed as

$$\frac{\partial \underline{B}}{\partial t} = \underline{\nabla} \times (\underline{U} \times \underline{B}) - \frac{c^2}{4\pi} \underline{\nabla} \times \left[\underline{\underline{n}} \cdot (\underline{\nabla} \times \underline{B})\right]$$

$$- \frac{ck}{eN_e} (\underline{\nabla} N_e \times \underline{\nabla} T_e) + \frac{c}{4\pi e} \underline{\nabla} \times \left\{\frac{1}{N_e} \underline{\nabla} \left[\frac{\underline{B}}{2} - (\underline{B} \cdot \underline{\nabla})\underline{B}\right]\right\}$$

$$- \frac{c}{e} \underline{\nabla} \times \left[\underline{\underline{\beta}} \cdot \underline{\nabla} (kT_e) - \alpha \underline{\hat{b}} \times \underline{\nabla}(kT_e)\right]$$

$$+ \frac{c}{e} \underline{\nabla} \times \left[\frac{1}{N_e} \underline{\nabla} \cdot \underline{\underline{P}}_R\right] \qquad (1)$$

in which $\underline{U}$ is the fluid velocity, $\underline{\underline{\eta}}$ the resistivity tensor and N_e, T_e the electron density and temperature respectively. The quantities α and $\underline{\beta}$ are thermal transport coefficients which depend on $\Omega_e\tau_{ei}$ where Ω_e is the electron cyclotron frequency and τ_{ei} the electron-ion collision term. Finally, $\underline{\underline{P}}_R$ is the radiation pressure tensor. The various terms appearing on the right hand side of equation (1) are identified for completeness. The first two are the familiar hydromagnetic terms describing convection and diffusion. The third term is the basic source term which generates the magnetic field. The fourth term - the so-called Hall term - consists of two parts; the first is the magnetic pressure term while the other derives from the curvature of the field. The penultimate term has its origins in the imbalance of the frictional force on electrons in the prescence of a thermal gradient. This term does not of itself generate magnetic fields though it certainly contributes to their morphology. The final term involving the radiation pressure is a true source and an important one in general though we shall exclude it from our calculations for reasons given later.

We propose first to exclude the hydromagnetic terms from equation (1). To justify this for the special conditions of the Rutherford Laboratory experiment in which short (i.e. 100 ps) pulses were used we may estimate a field convection time

$$\tau_C \sim \frac{L_N}{c_S}$$

where L_N is a characteristic density scale-length and c_S a typical ion acoustic speed. Thus

$$\tau_C \sim L_N \left(\frac{m^+}{ZT_e}\right)^{\frac{1}{2}}$$

which for values typical of the experiments i.e. $L_N \sim 40$ μm, $T_e \sim 700$ eV, $Z_{AVE} \sim 6$ gives $\tau_C \sim 400$ ps. The second hydrodynamic term in equation (1) is characterized by a field diffusion time τ_D where

$$\tau_D \simeq \frac{4\pi L_N^2}{c^2 \eta_\perp}$$

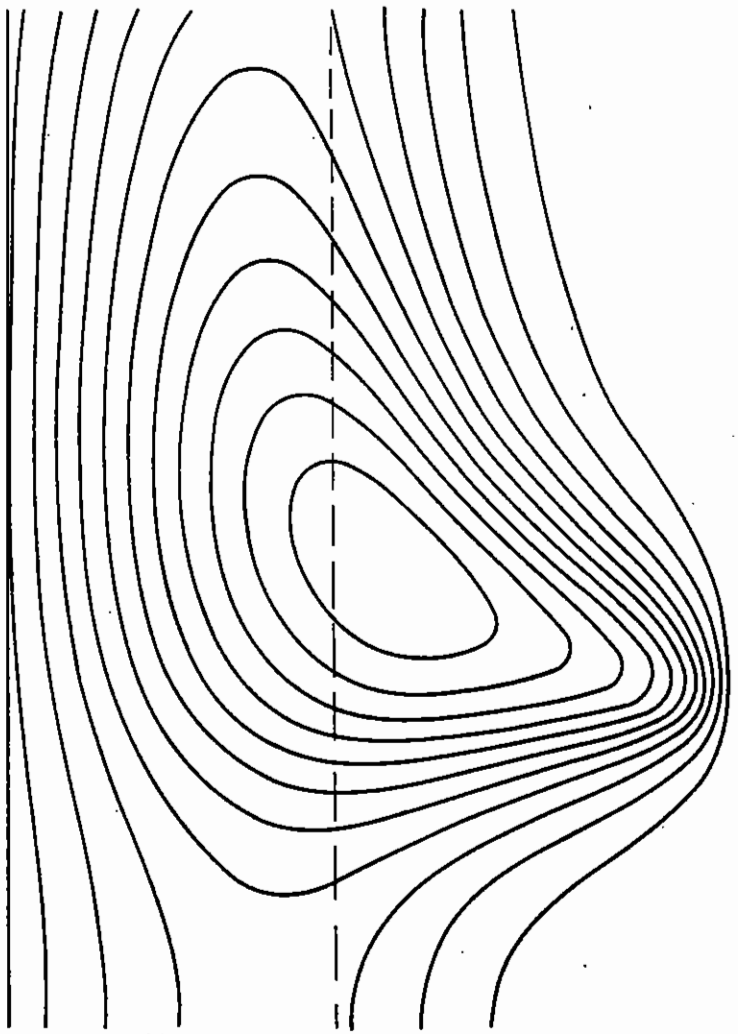

Fig.7.20

Dashed line denotes position of axial profile

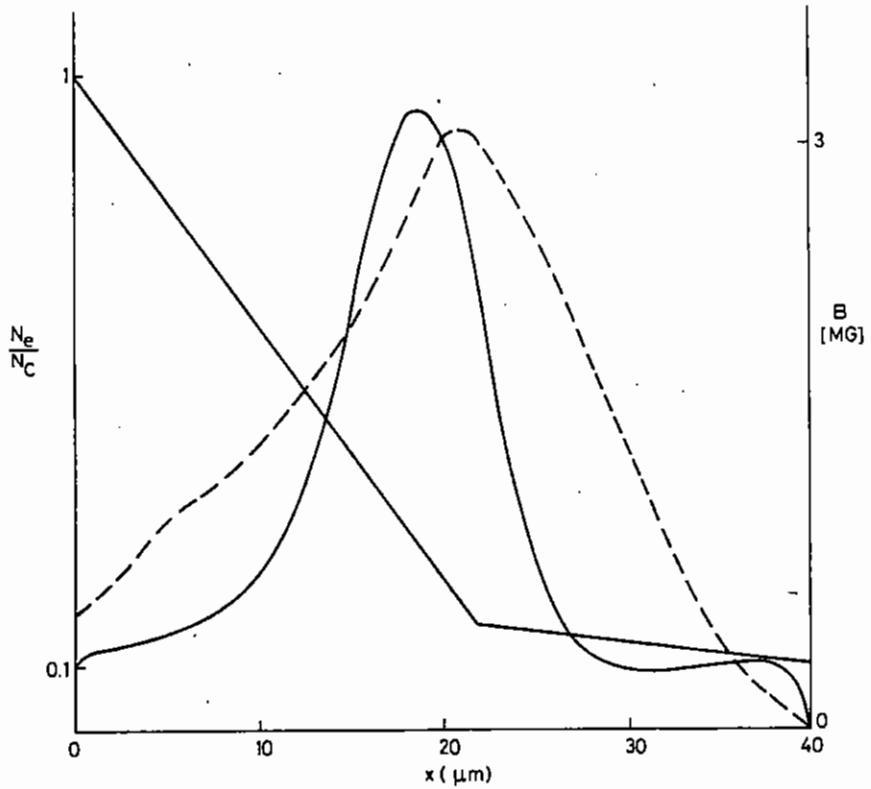

Fig.7.21

Magnetic field profile at edge of focal spot. The dashed curve is the measured profile (7.18); the continuous curve is the computed profile.

in which $\eta_\perp$ is the resistivity perpendicular to the field given by

$$\eta_\perp = 1.15 \times 10^{-14} T_e \ln \Lambda Z.$$

Inserting values appropriate to the experimental conditions gives $\tau_D \sim$ 8ns. In view of these estimates of τ_C and τ_D which are greater than the characteristic times involved we shall omit the hydromagnetic terms in equation (1) from consideration. We have also excluded the radiation pressure source term on the grounds that it effects will be localized to the critical density region whereas we shall be interested mainly in the field in the far corona. Thus for our purposes the right hand side of equation (1) reduced to terms 3, 4 and 5.

$$\frac{\partial \underline{B}}{\partial t} = -\frac{ck}{eN} \nabla N \times \nabla T - \frac{c}{8\pi e N^2} \underline{\nabla} N \times \underline{\nabla}(B^2)$$
$$- \frac{c}{e} \nabla \times \left[\underline{\underline{\beta}} \cdot \underline{\nabla}(kT) - \alpha \hat{\underline{b}} \times \underline{\nabla}(kT)\right] \qquad (2)$$

To study the evolution of the field on this basis we have carried out a numerical analysis of this reduced equation .

The model sets up first of all the initially prescribed, electron number density and temperature profiles. Equation (2) is then used to predict the magnetic field structure, the equation of motion is used to advance the electron velocities and continuity equation evaluates the new electron number density profile. Initially the electron velocity distribution is prescribed by the thermal velocity distribution associated with the prescribed initial temperature. It is also assumed that there are no magnetic fields present at the start of the run. The initial electron number density scale-lengths and temperature distributions were chosen so as to model the observed experimental profiles (7.10, 7.18) as closely as possible. The form of $\langle E_L^2 \rangle$ used in the ponderomotive force term in equation (2) was modelled axially from a pre-calculated Airy function solution and radially in accordance with the pulse above.

All the figures (7.20 to 7.22) come from the computer simulation and are taken at ≃ 100 ps into the run so as to facilitate comparison with the experimental results (7.10, 7.18) presented. Figure 7.20 shows the mag-

netic field contour plot with the magnetic pressure term included in the magnetic field evolution equation. The peak field contour corresponds to a magnetic field of approximately 3 MG and the contours are evenly spaced at 300 KG intervals. The effect of the magnetic pressure term is to drive a radial current in such a manner as to inhibit the magnetic field generation in the radial region between the beam axis and the position of the maximum field intensity, and to enhance the field generation at larger radii. The effect is strongest in the region of the maximum magnetic field. This is observed in the simulation results as a marked outward shift of the magnetic field contour lines.

Fig.7.21 comes from the same data as Fig.7.20, and is an axial magnetic field profile taken along the edge of the focal spot. This profile is taken so as to allow direct comparison with experimental result(7.10). The agreement as far as the magnitude and spatial position of the maximum magnetic field and the overall structure of the profiles is seen to be satisfactory. The slight enhancement of the field seen at very low densities in the computer simulation is non-physical and comes from the local density profile assumed to satisfy boundary conditions. The simulation also under-estimates the field at densities approaching the critical density. This is to be expected as in this region the condition for neglecting the radiation pressure term is violated and, thus, an incomplete picture of the field in this region results from the present simulation.

Figs. 7.22 and 7.23 show, respectively, the theoretical and experimental (7.18) electron number density profiles for densities less than 0.6 N_c. Within this region the theoretical density profile can be seen to agree well with the experimental profile, in that, at higher densities the typical ponderomotive force on-axis through can be seen. Whereas at lower densities $N = (0.2 - 0.4)N_c$ the on-axis density build-up due to the magnetic field pressure can be clearly seen both in the experimental results and in the computer simulation. In the lower density region the maximum radial magnetic fields lie in the off-axis density depression (7.33) and, as is predicted by Fig.7.20, both the radius at which this depression occurs, and the radial extent of the field, are greatest at the position of the maximum magnetic field, $N \simeq 0.3\ N_c$. This effect shows up

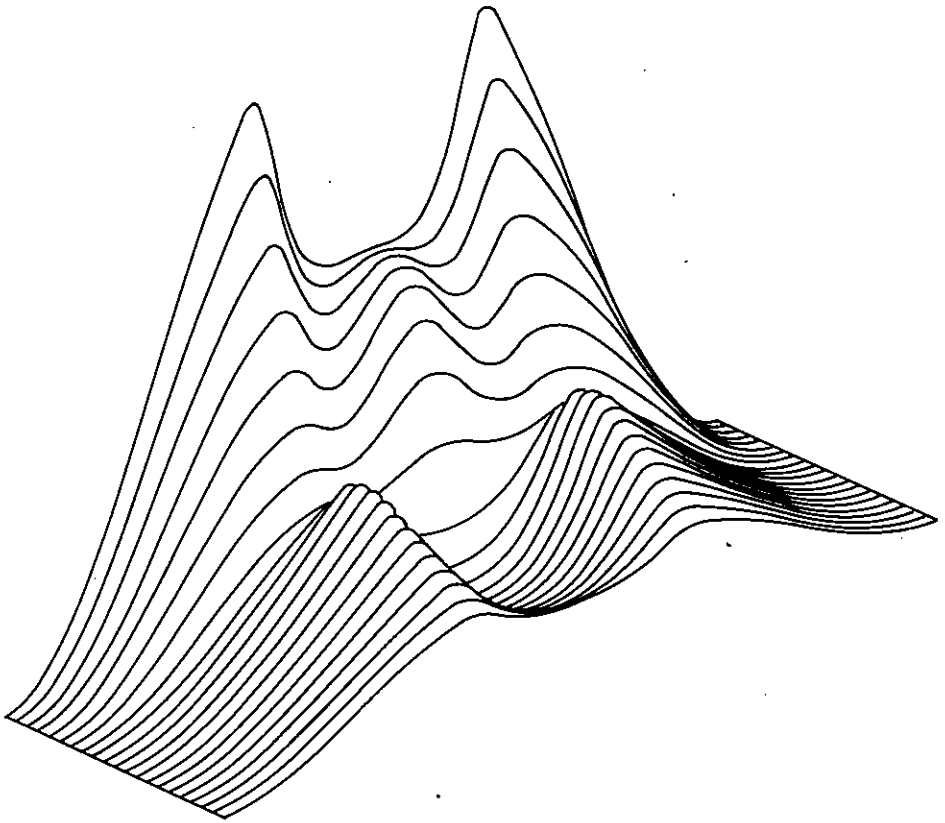

Fig.7.22

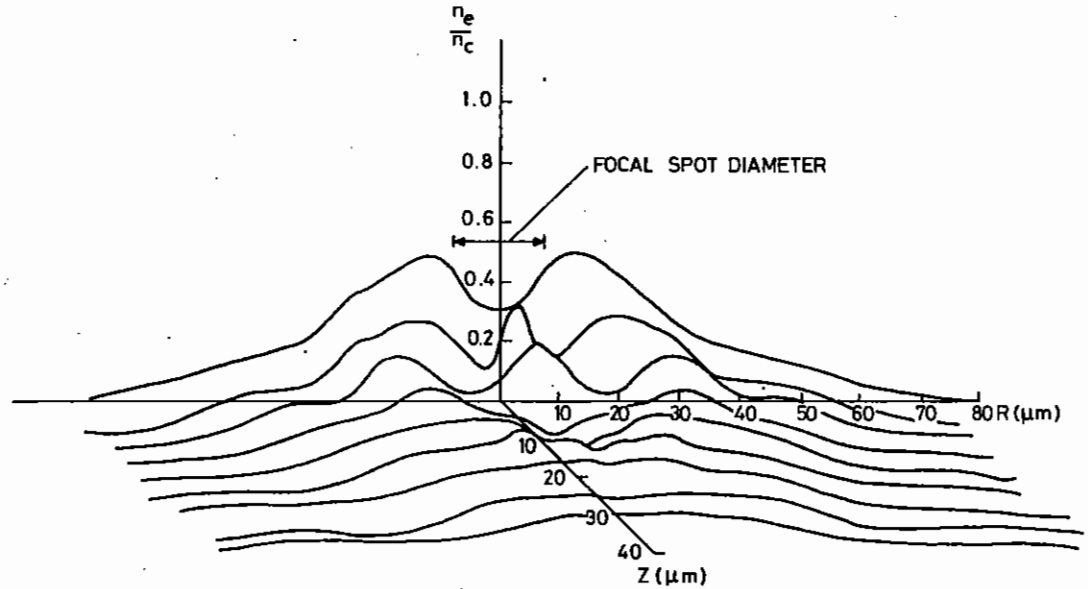

Fig.7.23

clearly in the experimental profile Fig.7.23 and is also present in the simulation results (Fig.7.22). However, in the latter case, the precise radial position of the density is not so easily identified.

T J M Boyd, G J Humphreys-Jones, D Cooke

7.3.2 Application of Simple PIC Codes

Two fairly simple particle-in-cell (PIC) codes have been developed over the past year. The motivation for this work has been partly to provide some experience of the use of PIC codes before the 2½ D code HERMES is operational, and partly to study some plasma physics which is amenable to a 1 D or 1½ D analysis. Two codes exist at present, a 1 D electrostatic code OMEGA and a 1½ D relativistic electromagnetic code RIGEL.

1 D Electrostatic Code OMEGA

The 1 D model considers only motion in the x direction and electric fields produced only by the electrostatic forces in the plasma i.e. by the solution to Poisson's equation. The boundary condition on Poisson's equation enables a time varying longitudinal field to be applied to the plasma, the so-called capacitor model. This field can be sinusoidal to simulate a single mode laser, or a sum of many sinusoids to simulate a multi line or finite bandwidth laser.

The code solves the following equations repetitively for a large number of electrons and ions

$$\frac{dx_i}{dt} = v_i$$

$$\frac{dv_i}{dt} = \frac{e}{m} E_i$$

$$\frac{\partial E}{\partial x} = \rho$$

The electric field E and charge density ρ are calculated only on an equispaced mesh of points and are then linearly interpolated onto the particle

positions x_I. Since the particles have an effective distance of closest approach which is equal to the mesh spacing, the code is essentially a simulation of collisionless plasmas (i.e. of the Vlasov equation) if the grid spacing dx is about equal to the Debye length λ_D. The use of rationalised cgs units eliminates the need for factors of 4π in Poisson's equation.

The OMEGA code initialises the system as a warm plasma with, if desired, an initial density gradient and drift velocities. A 'quiet start' procedure forces the iniital electron and ion currents to exactly equal the drift currents. The plasma then evolves under the influence of the applied electric field and its self consistent electric field.

To date the code has mainly been used to study the generation of Langmuir turbulence near a heat front (a possible heat conduction inhibitor) and to study the effects of finite bandwidth lasers on resonance absorption.

The heat conduction simulations have been carried out using an initially "cool" plasma which is heated at one end by the random addition of $\pm\Delta v$ to the particle velocities. By the central limit theorem this will produce a Gaussian heated distribution. The proceedure is very similar to that of Morse and Nielson (7.35) who attempted to study heat conduction in the presence of "hot" electrons.

Fig.7.24 shows the electron phase space of the initially cool plasma and indicates the region which is to be heated, and also the points at which the heat flux is subsequently measured. In Fig.7.25 the heating is evident and in Fig.7.26 the heated electrons in the lower half of the phase space are beginning to move into the cool plasma. The velocity distribution function near the heat front now becomes multi peaked and drives a form of two stream instability. Those electrostatic waves are beginning to be noticeable at this time and it is also apparent that the electric field at the heat front is accelerating the cool electrons back towards the heated region.

In Figs. 7.27 and 7.28 the Langmuir turbulence is more developed and the cold return current remains evident. During the calculation, the "heat

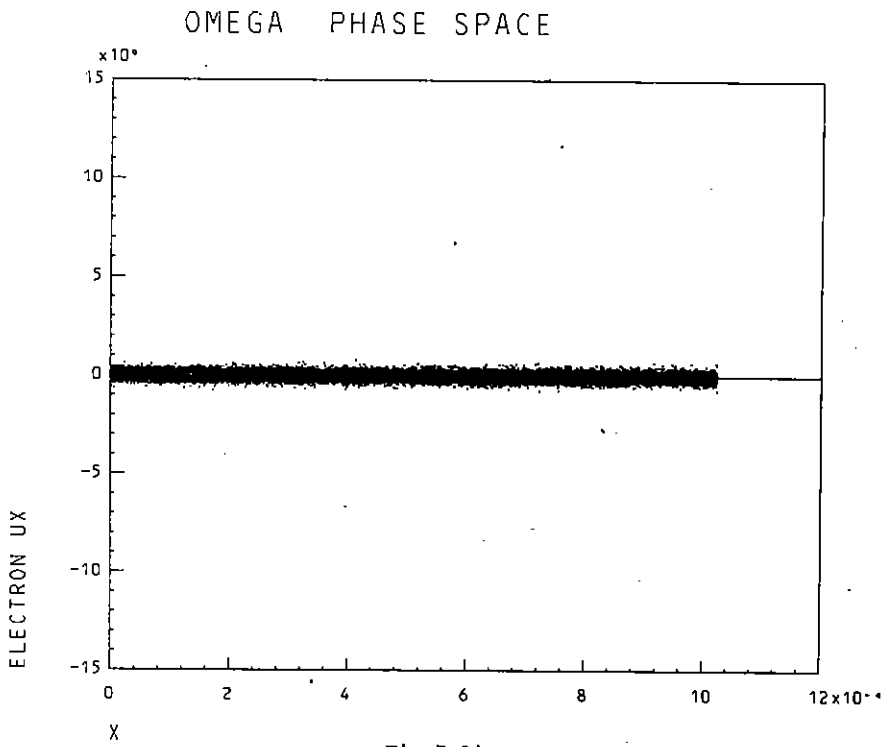

Fig.7.24

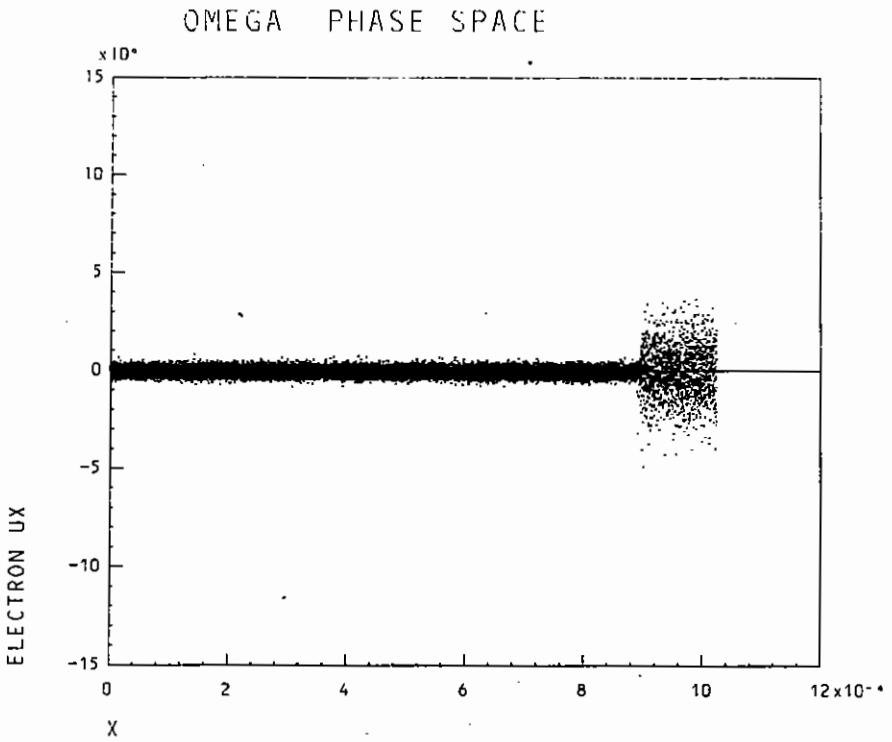

Fig.7.25

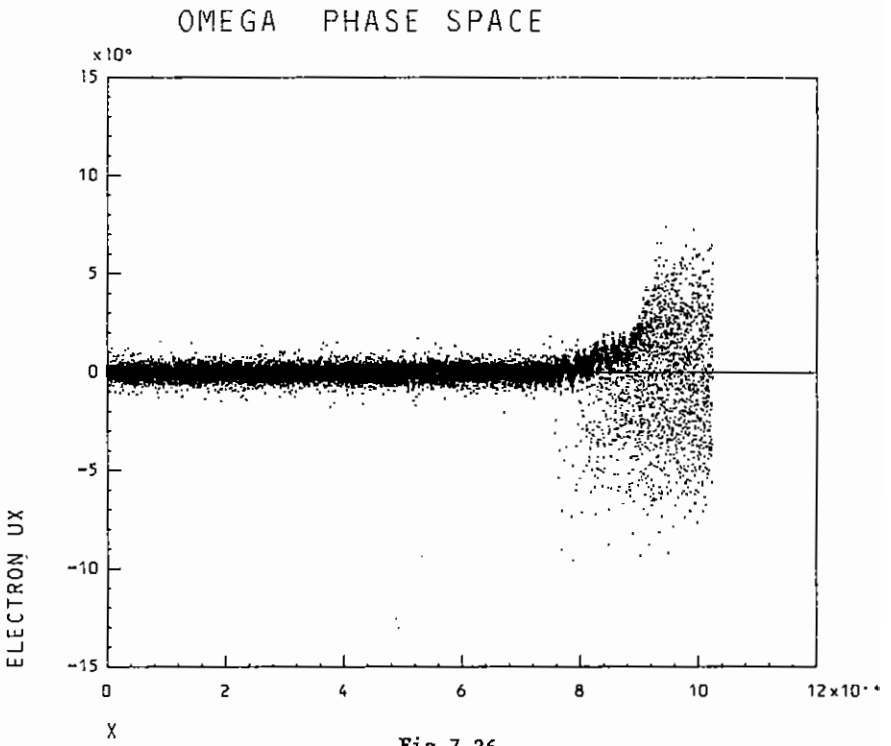

Fig.7.26

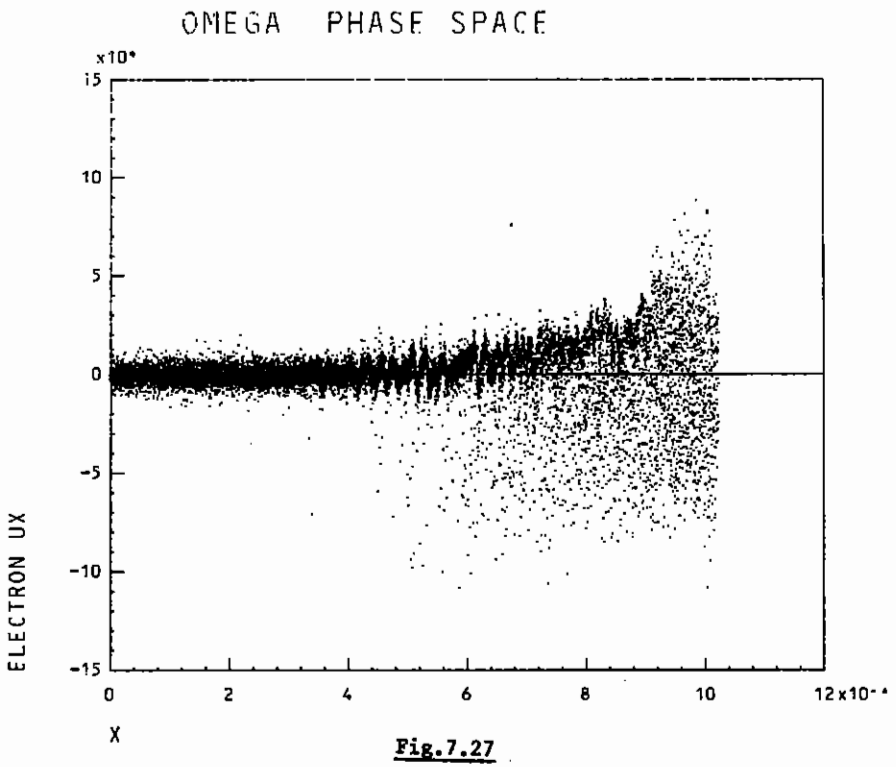

Fig.7.27

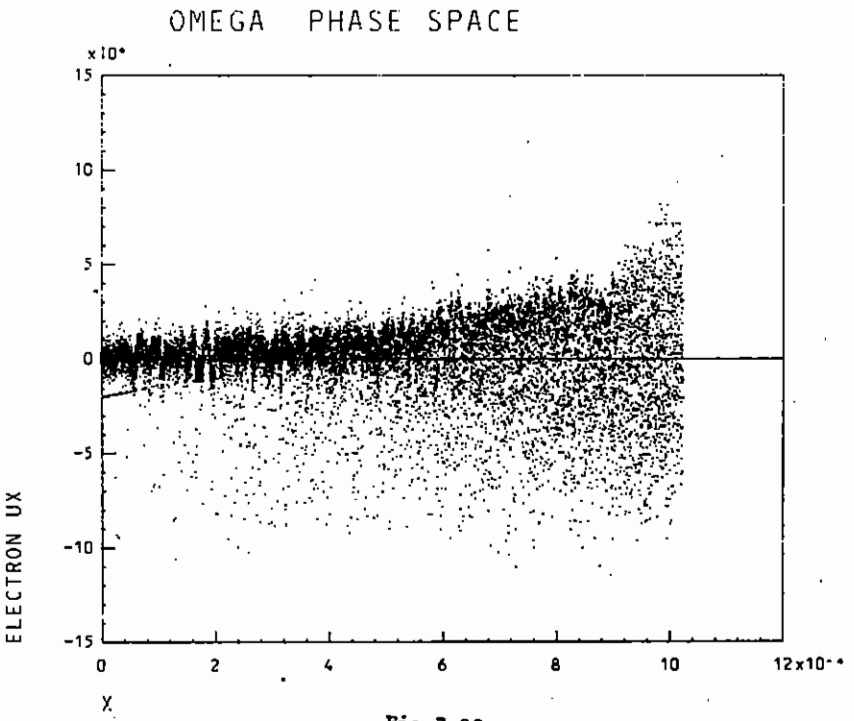

Fig.7.28

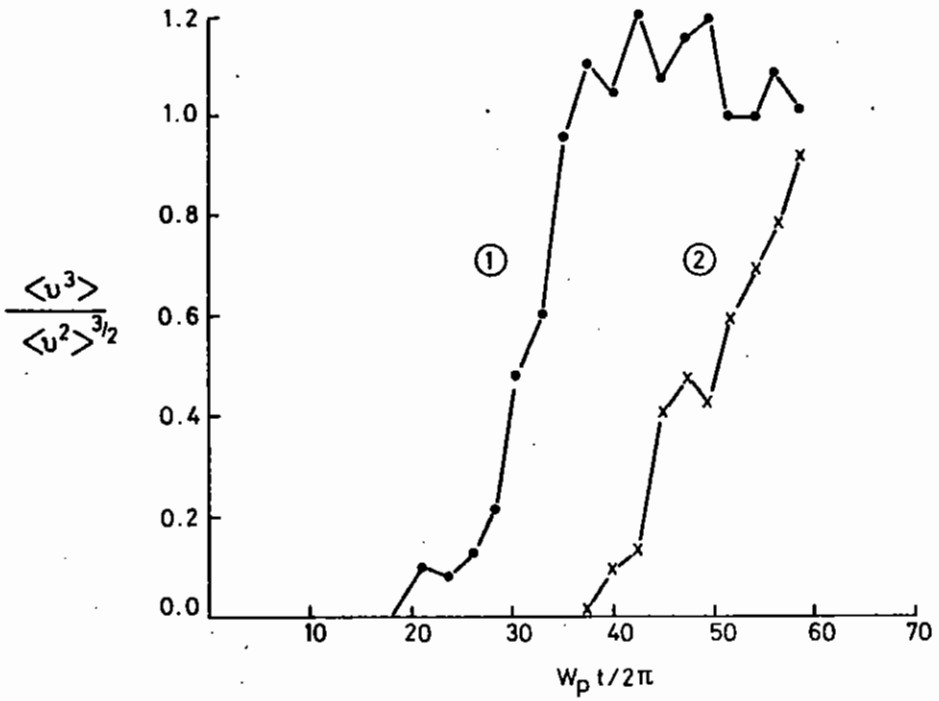

HEAT FLUX vs TIME IN A COLLISIONLESS PLASMA

Fig.7.29

flux" $\langle v^3 \rangle$ is calculated over regions of 128 cells ($\sim$ 150 Debye lengths) centred as shown in Fig.7.24. In Fig.7.29 the heat flux in the region relative to the mean thermal velocity $\langle v^2 \rangle$ in the heated region is shown as a function of time. The quantity $\langle v^3 \rangle / \langle v^2 \rangle^{3/2}$ has the form of the "flux limit" parameter f which is generally required to take the value $f \sim 0.03$ in order to explain experimental data on laser heated targets. In the 1 D collisionless case it is clear that $f \sim 1.0$ despite the large amounts of electrostatic plasma turbulence that are seen in the simulations. These simulations have a real ion-electron mass ratio and the simulation period is too short for ion acoustic waves to develop.

R.G. Evans

7.3.3 The Development of a 2 D Version of EMPIRE

In this Electro Magnetic Particle code with ions and Relativistic Electrons (EMPIRE) the problem domain is divided into cells and the charged particles, selected with a prescribed Maxwellian velocity distribution, are shared amongst them in such a way as to produce the number density profile required. The distributions of charge and currents so produced are used to calculate grid values appropriate to the numerical scheme used for the solution. A staggered finite difference mesh is used in which mesh values of charge density are associated with cell centres whereas values of current density are associated with cell walls, both distributions being set up using the area weighting techniques of the particle in cell method. For some problems quiet start techniques are invoked. In our code the magnetic field component is also associated with the cell centre and the electric field components with cell walls.

When the code is run, at each time step Maxwell's equations are solved directly to produce a distribution of electric and magnetic field components. The finite difference scheme used is time centred, second order accurate and time reversible. Steps are taken to ensure that self forces are eliminated and that the charge and field distributions are mutually consistent. In the second stage the particles are pushed and their new velocities and coordinates are computed. Particle velocities may become

very large so that relativistic effects have been allowed for the model. Multistepping is sometimes employed to speed up execution, but this may lead to numerical instabilities. By following the motion of the particles and the evolution of the state variables the processes that are excited in a plasma by an incident electromagnetic wave may be studied.

Our $1\frac{1}{2}$ D code has been running successfully for 2 years but only permits state quantities to vary in one space dimension thus limiting the physical processes that can be modelled. The code has now been upgraded to allow variation in 2 space dimensions permitting us to study more processes arising in laser/plasma interactions; for example 2 plasmon decay, Filamentation, Parametric decay, Oscillating two stream instability, Resonance Absorption and side scatter in addition to 1 D processes.

The 2 D code has been implemented on the DEC-10 UCNW, Bangor and on the CRAY-1 at SRC Laboratory Daresbury and test runs undertaken.

The major test problem studied so far has been a resonance absorption simulation in which a laser beam, p polarised, is obliquely incident at 24^{o} (the optimum angle for the geometry used) to a linear plasma ramp. This is a particularly stringent test of the code since strong fields are excited and hot electrons generated. The simulation parameters were as follows: mesh 32 x 128, 30 K electrons and 30 K ions, mass ratio 100, temperature ratio 10, and $k_o L = 5$. We have monitored number density profiles, velocity distribution functions and the field variables and all results point to the code being well behaved. As illustrations we show in Figs. 7.30 and 7.31 how the number density profiles have been modified by time 120 ($\frac{1}{\omega_o}$). In addition we have analysed the backscattered radiation. Its frequency spectrum is shown in Fig.7.32. From that diagram it can be seen that the ratio of the amplitude of the second/third and third/fourth harmonics are constant at about 5. The harmonic peaks are frequency down shifted and a periodic structure is observed on the harmonics.

G. A. Gardner

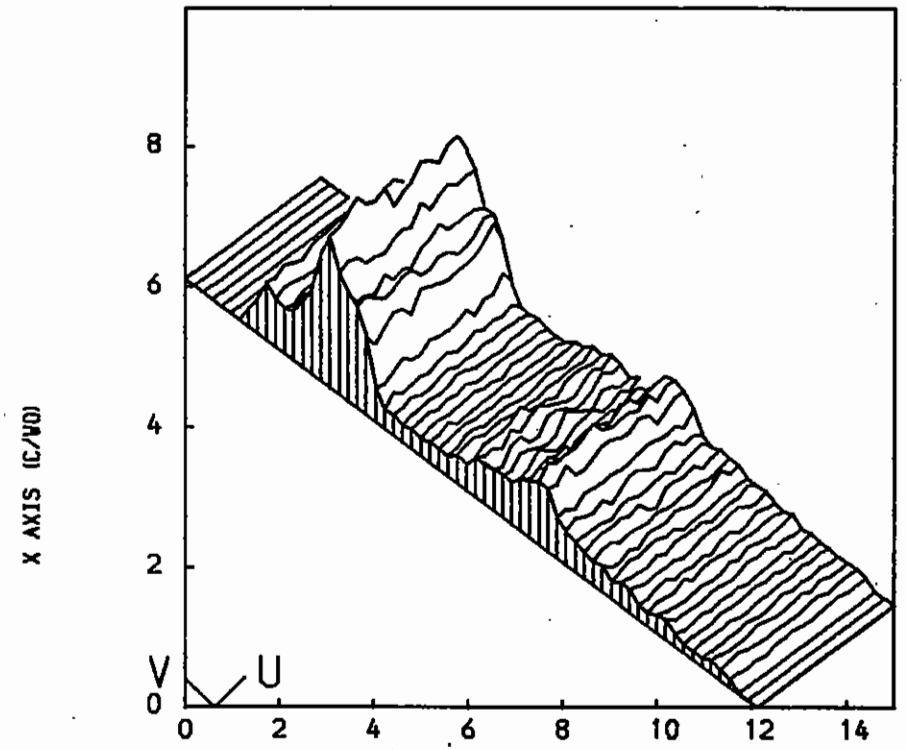

Fig. 7.30

Ion Number Density

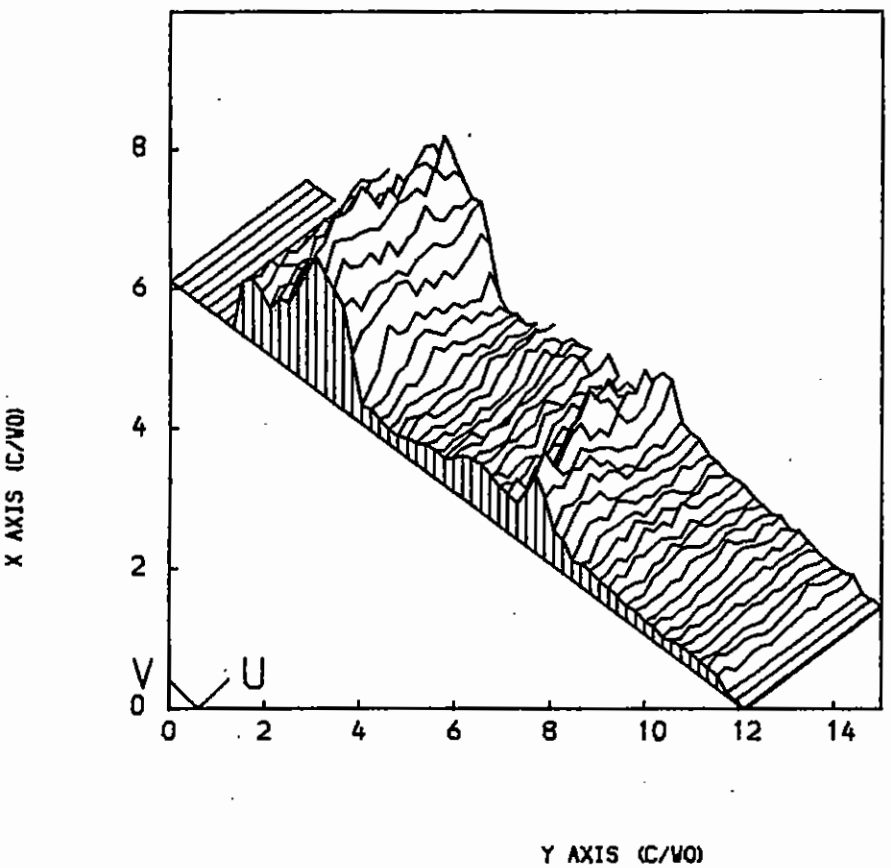

Fig.7.31
Electron Number Density

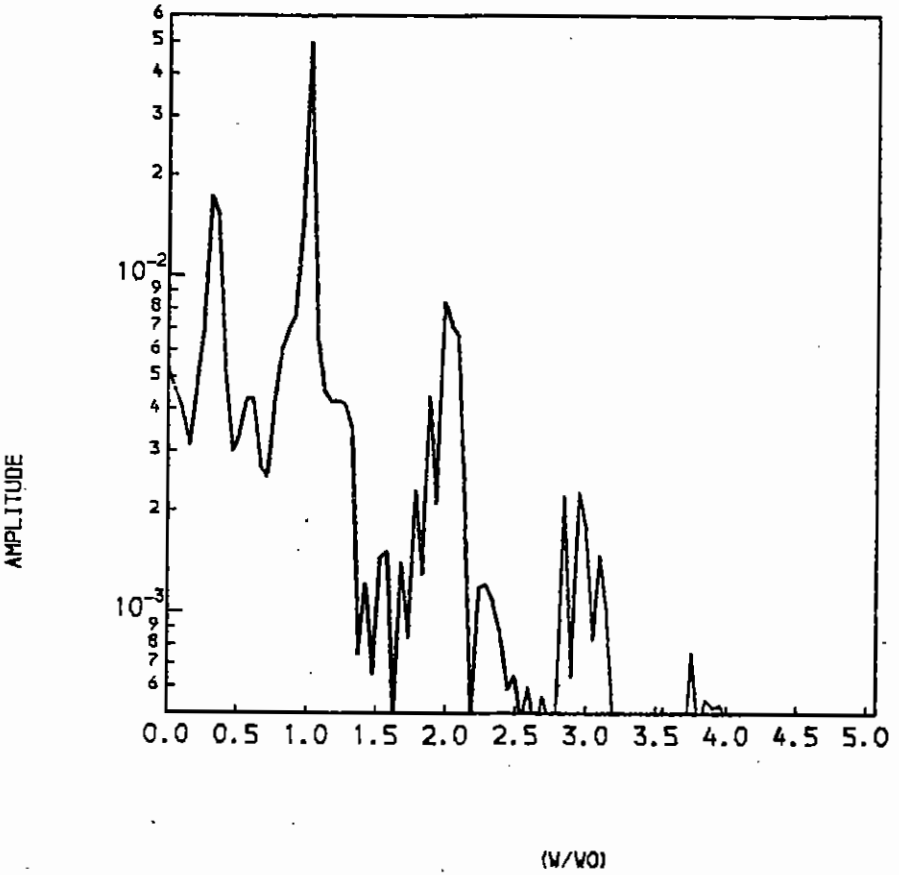

Fig.7.32

7.3.4 Development of a 2½ D PIC Code

HERMES (7.36) is a 2½ D particle in cell code currently being developed by the University College of North Wales (Bangor) and the Rutherford and Appleton Laboratories. The programme is relativistic and electromagnetic. The finite difference algorithms (7.37) are second order, time reversible and time centred.

Last year the code was in a very preliminary state, in particular it suffered some major restrictions:-

i) Only some 300 particles were available out of the design maximum of 10^5 to 10^6.
ii) The maximum mesh size was 33 x 33 (design maximum 129 x 129)
iii) No restart facility was available.
iv) The diagnostics consisted of a few ad hoc graphics routines.
v) The boundary conditions in the x direction were those of Lindman (7.38) and were periodic in y.
vi) The number of mesh points in the y direction was $2^n + 1$.

Most of these have been relaxed.

The particles are paged from a direct access dataset using DRIO (7.39). The maximum number of particles in a simulation is set by the CPU time required to process them and the real time to run the programme. It is currently being run with some 50000 particles.

The maximum mesh size is still small, 1628 mesh points in all. To increase this further would make the programme prohibitively large. Some design work has been performed on a paging system for the fields, but this will not be implemented until the current version has been in production for some time. This will make the particle paging much more complicated.

A working restart system is in use. Every few minutes of CPU time (usually 5 minutes) a dump is taken onto tape. A disk catalogue is updated which allows an automatic restart. It may also be restarted from any earlier dump if required.

Information is written to the diagnostic tape at regular intervals. A diagnostic programme, ATHENA, may be used to produce graphical output in the form of graphs, contour plots, arrow plots or scatter diagrams. Fig. 7.33 shows an arrow plot of the electric field. A laser is incident from the left at a small angle to the plasma density ramp. The electric field can be seen to swell at its turning point. At a later time (Fig. 7.34) the laser has turned round and been reflected out of the plasma. The interference of these two waves produces the "box" like pattern. A statistics and histograming package, HBOOK (7.40) is currently being implemented.

Increased flexibility in the mesh size in the y-direction has been made possible by the successful implementation of a new Fourier transform package. These routines are capable of processing vectors of the standard length of $2^n + 1$ and also $3 \times 2^n + 1$. A reduction routine exists for periodic boundary conditions in the x-direction, as well as the open boundary condition option. The main use for the double periodic system is for testing the programme.

Obliquely incident laser propagation across the mesh is now in operation, with good conduction properties at the open boundaries i.e. no reflection.

Research has been performed on difference schemes for field advancement, in the hope of relaxing the Courant stability condition on the size of the timestep.

Since the completion of the restart facilities, a successful, essentially 1 D, simulation of a normally incident laser on a density gradient has been completed. This involved some 30,000 macro electrons with a neutralising background on a long narrow mesh of 8 x 120 cells. The standard Airy function shape of the electric field at critical density was reproduced.

Some "mini" resonance absorption simulations are now in progress by way of testing problems.

The Problem Program Efficiency package (7.41) was used to obtain timing statistics on the code. Table 7.04 shows how heavily the programme is

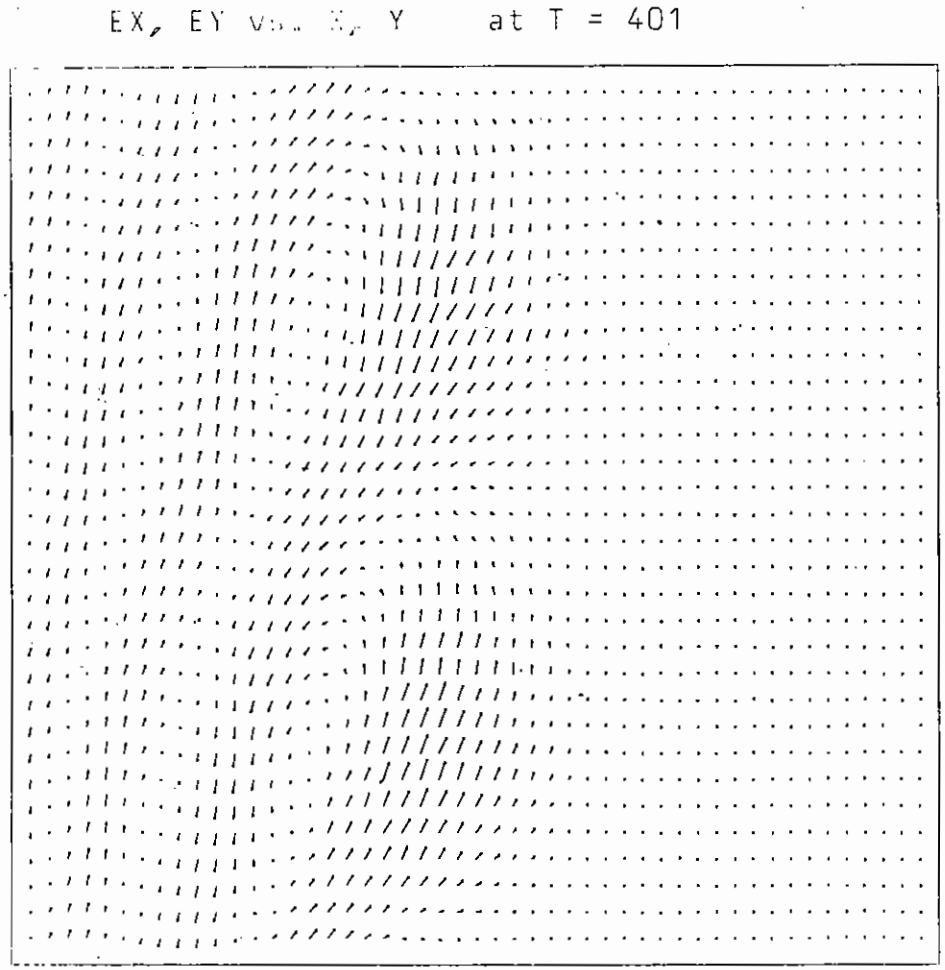

Fig.7.33

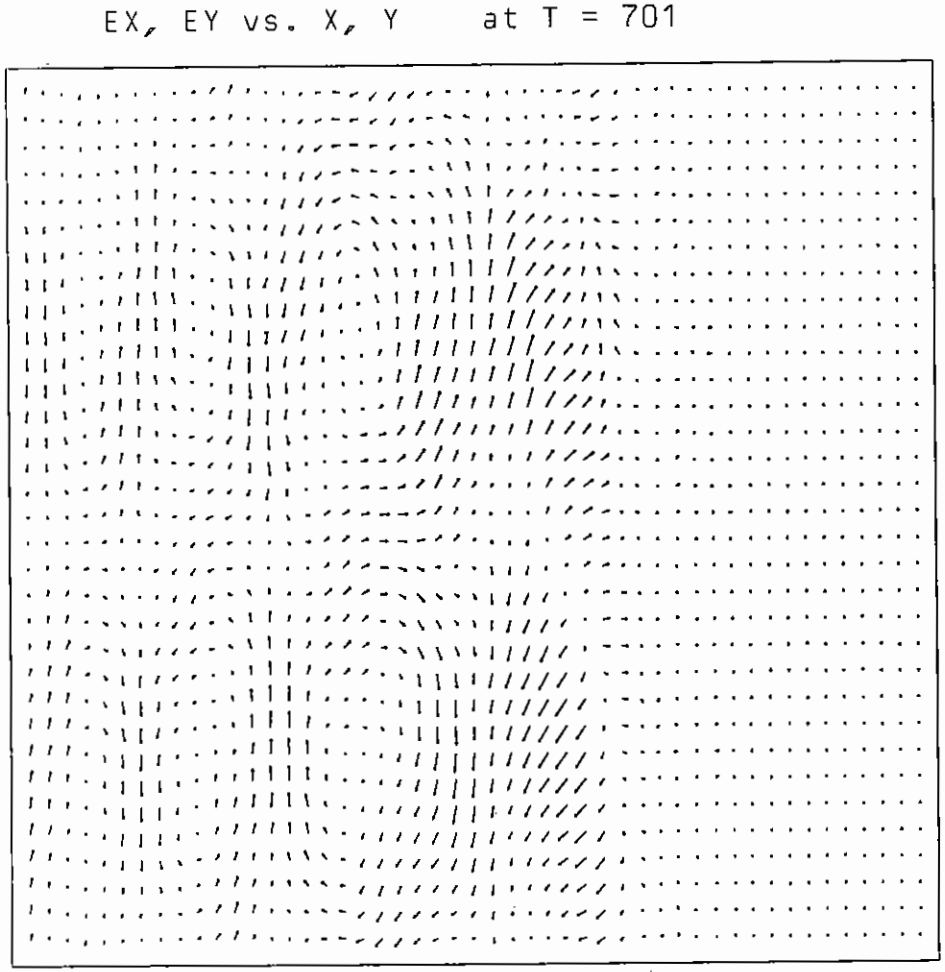

Fig.7.34

I/O bound. An asynchronous paging system has been developed which should reduce the problem. A second method that is also being worked on is to compress the data before writing it to disk. This would reduce the I/O by 30% but would increase the CPU time.

TABLE 7.04

Time Usage as a Percentage of Total Time

CPU time	13%
I/O wait time	84%
other	3%

TABLE 7.05

CPU Usage as a Percentage of CPU Time

Pushing particles	(particle pusher	52.1%
	(square root	7.5%
	(paging	25.6%
		85.2%
Tape positioning		8.1%
Everything else including fields		6.7%
		100 %

It can be seen from Table 7.05 that the field advancement routines account for a very small fraction of the CPU time. Optimization would clearly be advantageous in the particle pusher.

C J Webb and D Cooke

7.4 Transport Processes

7.4.1 Ion Emission from Multi-ion Species Two Electron Temperature Plasmas

In references (7.46) and (7.47) a self-similar theoretical model for the free expansion of a single ion species, two electron temperature plasma was developed. This model enabled theoretical ion emission velocity spectra to be derived and favourably compared with those obtained experimentally from fully stripped laser-produced SiO_2 source plasmas. Many laser produced plasmas, however, contain ions with more than one charge to mass ratio (7.42 - 7.45), resulting in different accelerations for each ion species. Under these circumstances of a source plasma containing ions with more than one charge to mass ratio a multi-ion fluid description is required. Here a fluid model for the free expansion of a multiple ion species, two electron temperature plasma is developed and relevant quantities such as the total momentum in each ion species computed.

The initial conditions at time $t = 0$ and for positions $x < 0$ are those of an undistrubed, cold ion, collision free, quasineutral plasma-slab consisting of electrons with temperatures and densities T_c, T_h and n_{co}, n_{ho} respectively and ions of charge $Z_1 e$, $Z_2 e$, mass M_1, M_2 and densities n_{10} and n_{20} such that $n_{eo} = n_{co} + n_{ho} = Z_1 n_{10} + Z_2 n_{20}$ i.e. a quasineutral source plasma with a total electron density of n_{eo}.

For $x > 0$ at $t = 0$ vacuum exists, and for times $t > 0$ this half space becomes occupied by quasineutral plasma freely expanding from the $x < 0$ half space. Each electron species follows its respective Boltzmann density distribution $n_c = n_{co} \exp(e\phi/KT_c)$ or $n_h = n_{ho} \exp(e\phi/KT_h)$ such that $n_e = n_c + n_h = Z_1 n_1 + Z_2 n_2$, where n_1 and n_2 are the number densities of ion species 1 and 2 respectively, n_e is the total electron density and the electrostatic potential, ϕ, is zero in the undisturbed source plasma. The cold-ion, collision-free fluid equations used to model the plasma expansion are those of momentum

$$\partial v_1/\partial t + v_1(\partial v_1/\partial x) = -(Z_1 e/M_1)(\partial\phi/\partial x) \qquad (1)$$

$$\partial v_2/\partial t + v_2(\partial v_2/\partial x) = -(Z_2 e/M_2)(\partial\phi/\partial x) \quad (2)$$

and continuity

$$\partial n_1/\partial t + \partial(n_1 v_1)/\partial x = 0 \quad (3)$$

$$\partial n_2/\partial t + \partial(n_2 v_2)/\partial x = 0 \quad (4)$$

where v_1 and v_2 are the velocities of species 1 and 2 ions respectively. Transforming the above equations to $\xi = x/t$ as the independent variable gives

$$\frac{dv_1}{d\xi} = -\frac{(Z_1 e/M_1)}{(v_1 - \xi)}\frac{d\phi}{d\xi} \quad (5)$$

$$\frac{dv_2}{d\xi} = -\frac{(Z_2 e/M_2)}{(v_2 - \xi)}\frac{d\phi}{d\xi} \quad (6)$$

$$\frac{dn_1}{d\xi} = \frac{(Z_1 e/M_1)n_1}{(v_1 - \xi)^2}\frac{d\phi}{d\xi} \quad (7)$$

$$\frac{dn_2}{d\xi} = \frac{(Z_2 e/M_2)\, n_2}{(v_2 - \xi)^2}\frac{d\phi}{d\xi} \quad (8)$$

and for non-zero derivatives the constituitive relation

$$\frac{Z_1^2\, en_1}{M_1(v_1 - \xi)^2} + \frac{Z_2^2\, en_2}{M_2(v_2 - \xi)^2} = \frac{dn_e}{d\phi} \quad (9)$$

Taking the derivative of (9) w.r.t. ξ closes the above set of ordinary differential equations with

$$\frac{d\phi}{d\xi} = -\left(\frac{2Z_1^2\, en_1}{M_1(v_1 - \xi)^3} + \frac{2Z_2^2 en_2}{M_2(v_2 - \xi)^3}\right) \Bigg/ \left(\frac{3Z_1^3 e^2}{M_1^2}\frac{n_1}{(v_1 - \xi)^4} + \frac{3Z_2^3 e^2}{M_2^2}\frac{n_2}{(v_2 - \xi)^4} - \frac{d^2 n_e}{d\phi^2}\right) \quad (10)$$

an algebraic relation for $d\phi/d\xi$ in terms of the dependent and independent variables.

Fig.7.35 shows computed ion charge-density profiles ($Z_1 n_1$ and $Z_2 n_2$), obtained by numerically integrating equations (5) - (10) for a freely expanding, fully ionized ($Z_1/Z_2 = 6$; $M_1/M_2 = 12$) CH_2 source-plasma ($n_{10}/n_{20} = 0.5$) with a hot to cold electron temperature ratio of $T_h/T_c = 9$ and a cold to hot source-plasma electron density ratio of $n_{co}/n_{ho} = 30$. The importance of the ion charge densities $Z_1 n_1$ and $Z_2 n_2$ (as opposed to the ion number densities n_1 and n_2) in determining the expansion hydrodynamics, via the electric field, follows because $(\partial\phi/\partial x) = (\partial[Z_1 n_1 + Z_2 n_2]/\partial x)/(dn_e/d\phi)$. An abrupt drop in plasma density where the cold electrons are reflected by this self-consistent electric field is evident in Fig.7.35. In the early stages of the expansion depicted in Fig.7.35 the C^{6+} (species 1) ions and cold electrons have the greater charge density and therfore determine the ion accelerating electric field, $d(e\phi/KT_c)/d(\xi/C_{c1}) \simeq -1$, where $C_{c1} = (Z_1 KT_c/M_1)^{\frac{1}{2}}$, the ion-acoustic speed in a cold-electron, ion-species-1 plasma. This field preferentially accelerates the higher charge to mass ratio H^+ (species 2) ions until at large distances ($\xi/C_{c1} > 5$), the H^+ ions charge density greatly exceeds that of the C^{6+} ions and the self-consistent electric field, $d(e\phi/KT_h)/d(\xi/C_{h2}) \simeq -1$, (where $C_{h2} = (Z_2 KT_h/M_2)^{\frac{1}{2}}$) is determined by the H^+ ions and the hot electrons alone. Substituting the above approximate values for the self-similar transformed electric fields into equations (5) - (8) and integrating gives the equations of the <u>slow</u> C^{6+} (species 1) and H^+ (species 2) asymptotes as

$$n_1 \simeq n_{10}\exp(-v_1/C_{c1}) \quad (11)$$

and

$$n_2 \simeq (n_{20}/\beta)\exp(-v_2/[\beta C_{c1}]) \quad (12)$$

respectively, while the equations for the <u>fast</u> C^{6+} (for large enough ξ) and H^+ asymptotes are

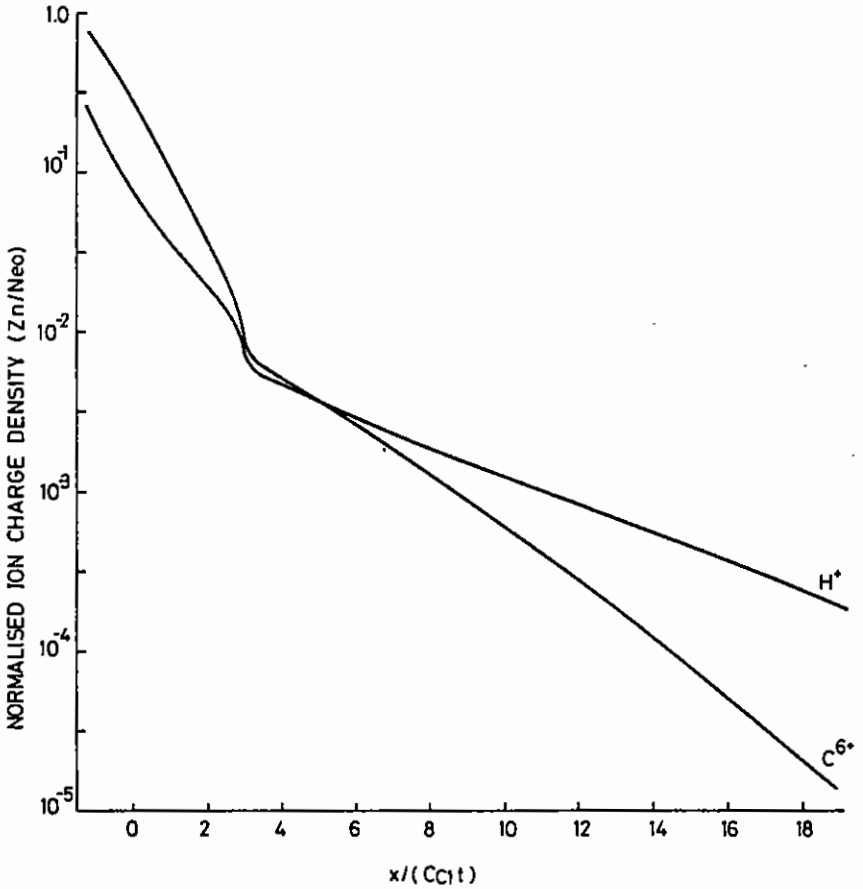

Fig.7.35

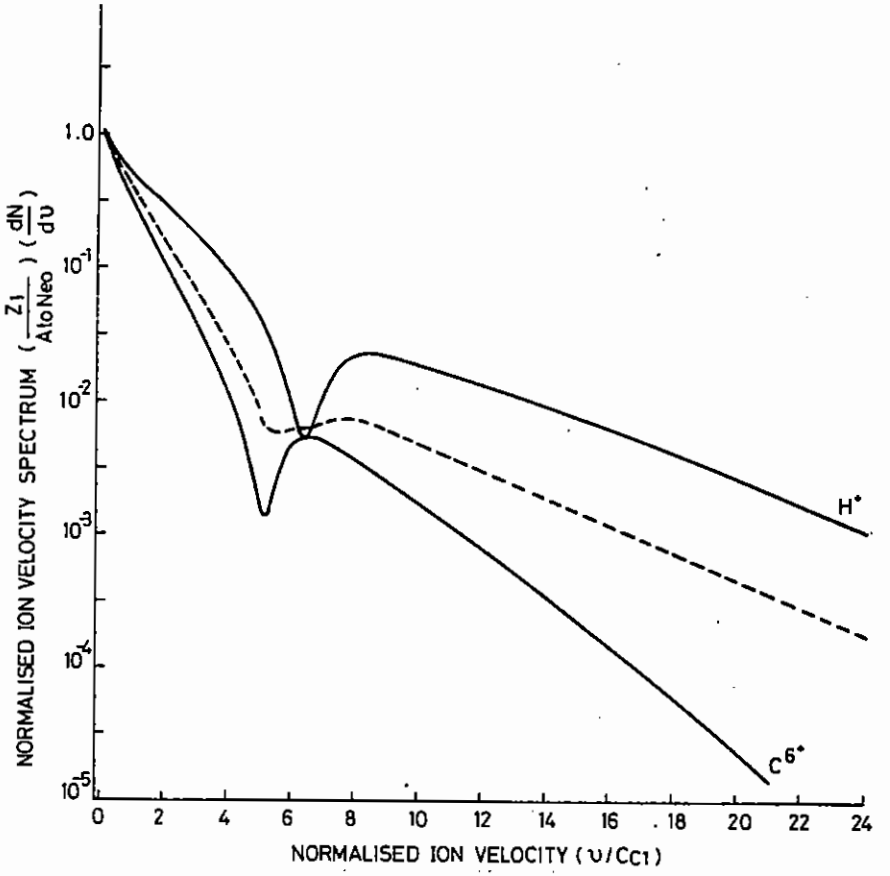

Fig.7.36

The dashed curve is the effective ion velocity spectrum calculated from the total ion current.

$$n_1 \alpha \exp(-\beta v_1/C_{h2}) \quad (13)$$

and

$$n_2 \alpha \exp(-v_2/C_{h2}) \quad (14)$$

where $\beta = (Z_2/M_2)/(Z_1/M_1)$. From Fig.7.35 the majority of the fast ions are H^+ ions in a fully ionised CH_2 source plasma expansion. Fig.7.36 shows the corresponding ion velocity spectra.. Note again that there are many more fast H^+ ions than C^{6+} ions, and that even in the slow portions of the spectra ($v/C_{cl} < 5$) there are more H^+ than C^{6+} ions. The slopes of the fast and slow asymptotes are the same as the corresponding portions of Fig.7.35 and obtainable from relations (11) - (14). Fig.7.37 shows the current traces that would be generated by each ion species at a Faraday cup. It can be seen that the C^{6+} ions contribute much of the slow ion current, while both C^{6+} and H^+ ions are important components of the fast ion current. When using Faraday cup currents to obtain ion velocity spectra for source plasmas containing ions with more than one charge to mass ratio some ambiguity is therefore involved. The dashed curve in Fig.7.36 shows the ion velocity spectra computed from the total current curve of Fig.7.37 by assuming that the current is composed mainly of C^{6+} ions. The resulting C^{6+} velocity spectrum clearly over-estimates the actual C^{6+} velocity spectrum. Note that separate C^{6+} and H^+ current peaks are not visible on the total current trace. Fig.7.38 shows the ion energy flux to a remote probe against arrival time, for fully ionised CH and CH_2 source plasmas. The area under the curves represent the energy given to each ion species. In both the CH and CH_2 source plasma expansions well over 50% of the total ion energy lies in the fast ion component, while the slow C^{6+} ions ($C_{cl}/v > 0.2$) carry much of the slow ion energy. Fig.7.39 shows fast ion energy spectra for fully ionised CH and CH_2 source plasmas. The area under the curves represent the total number of fast ions. It can be seen that the fast ion component contains relatively few of the total number of ions yet from Fig.7.38 it contains the majority of the ion energy. This means that the fast ion component imparts little recoil momentum to the target compression. Fig.7.40 shows plots of ion momentum

in the expansion against ion velocity, for fully ionised CH and CH_2 source plasmas. The majority of the ion momentum can be seen to lie in the slow C^{6+} ion component. In the CH source plasma expansion even the fast C^{6+} ions contain more momentum than the slow H^+ ions. Thus, in both CH and CH_2 coated glass microballoon implosions, it is essentially the ablation of the slow C^{6+} ions that drives the implosion.

Finally, Fig.7.41 shows the self-similar transformed electric field in an expanding, fully ionised, CH_2 source plasma. Note the abrupt increase in the electric field at the point in the expansion where most of the cold electrons are reflected, corresponding to the density drop in Fig.7.35. Further details are contained in (7.48).

L.M. Wickens and J.E. Allen

7.4.2 Free Expansion of a Magnetised Plasma

Measurements on planar target laser produced plasmas have shown that magnetic fields greater than 100 tesla and with a plasma to magnetic field pressure ratio (β) of order unity can be obtained (7.33). These magnetic fields can inhibit the ablation of plasma from the target. To help understand how a strongly magnetised, laser produced plasma can inhibit plasma ablation a planar, 1-D analytic model is derived.

The initial conditions are those of a quasi-neutral, collision free, cold ion plasma slab of ion density n_o strongly magnetised in the Z direction by a magnetic field B_o, free to expand in the x direction and uniform in the y direction (see Fig.7.42). The magnetic field source terms are assumed to be in the vicinity of the critical density surface, so they can be neglected in the underdense plasma regions of interest here. Neglecting electron inertia in the x direction (since $ZM_e/M_i \ll 1$ and $v_{ix} = v_{ex}$ as $(\underline{\nabla} \times \underline{B})_x = 0$), the x component of the ion momentum equation becomes (for $n_e = Zn_i = Zn$)

$$nM_i\left[(\partial v/\partial t) + v(\partial v/\partial x)\right] = (\underline{J} \times \underline{B})_x - \partial(ZnKT)/\partial x \quad (1)$$

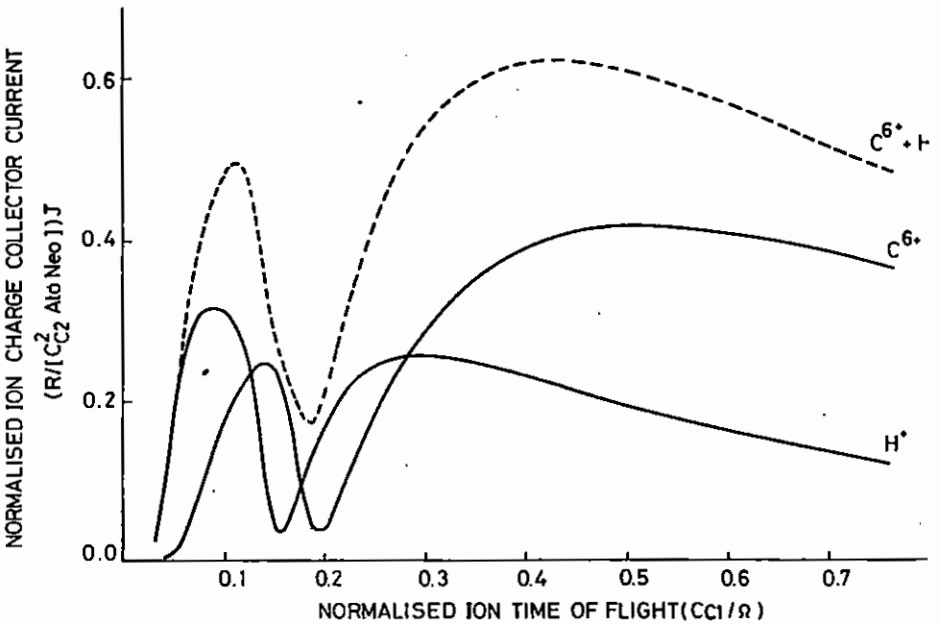

Fig.7.37

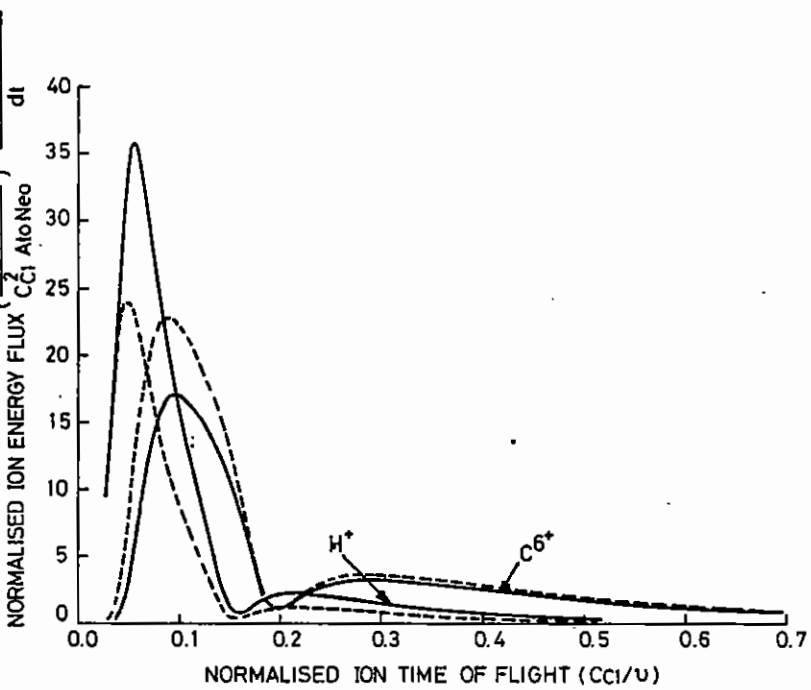

Fig.7.38

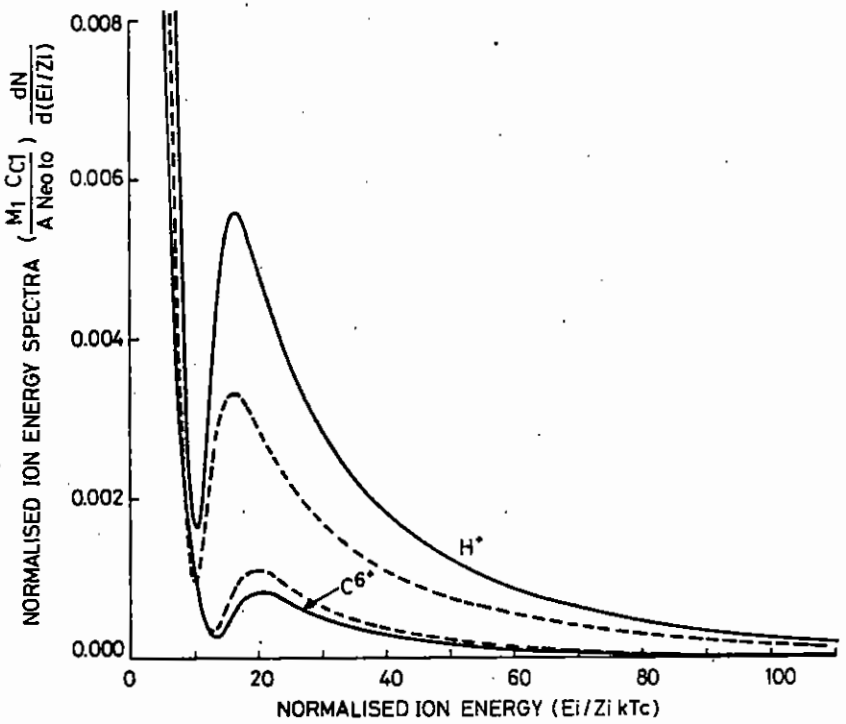

Fig.7.39

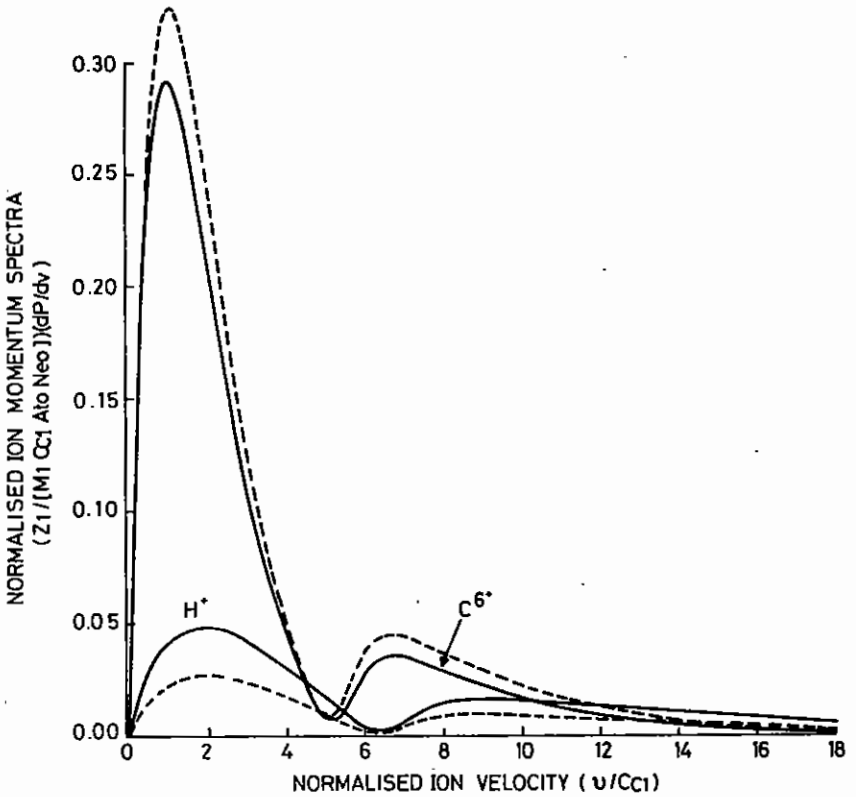

Fig.7.40

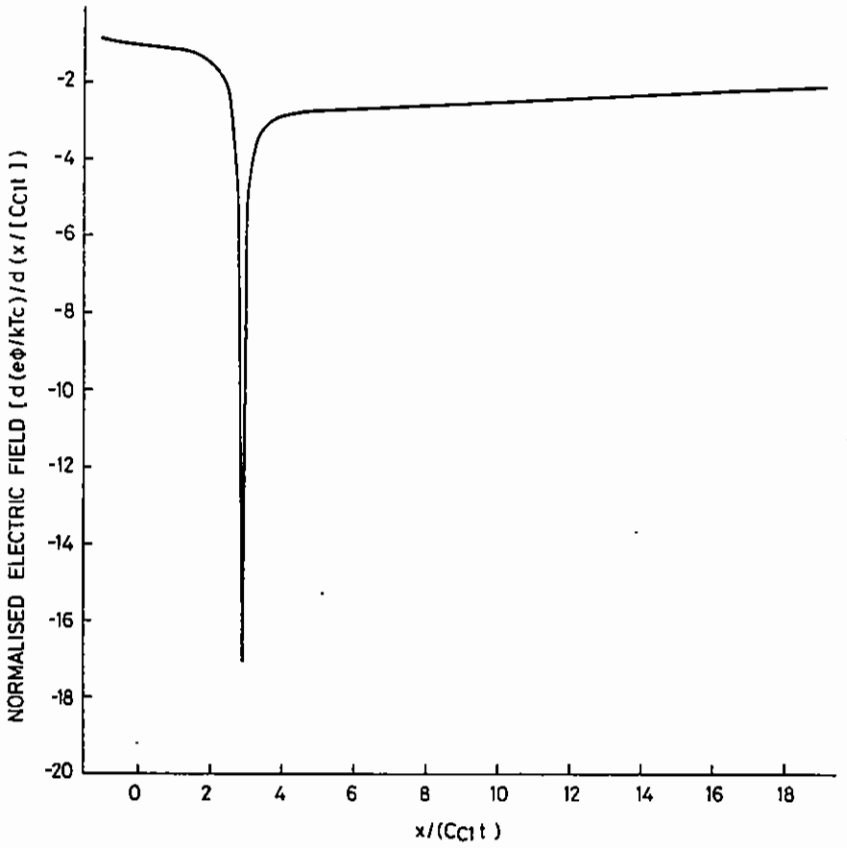

Fig.7.41

while the ion continuity equation is

$$\partial n/\partial t + \partial(nv)/\partial x = 0 \qquad (2)$$

where v is the ion velocity in the x direction, Ze, M and n the ion charge, mass and number density respectively, J the current density, K Boltzmann's constant, T the electron temperature, and all quantities are assumed to vary in the x-direction only. The pressure gradient and $\underline{J} \times \underline{B}$ force terms in equation (1) act so as to accelerate ions away from the source plasma. Using $\underline{\nabla} \times \underline{B} = \mu_o \underline{J}$ in equation (1) gives the more convenient form

$$\frac{\partial v}{\partial t} + v\frac{\partial v}{\partial x} = -\frac{1}{nM}\left[\frac{\partial}{\partial x}\left\{\frac{B^2}{2\mu_o} + ZnKT\right\}\right] \qquad (3)$$

For typical Nd:glass laser-produced source plasma parameters of $|B|$ = 250 Tesla, Z = 10, and $n_i = 0.2\, n_{ci}$ ($n_{ci} = 10^{26}$ m^{-3}) $\omega_{ce}\tau_{ei} \sim 20$, where ω_{ce} is the electron cyclotron frequency and τ_{ei} the electron-ion collision time. Also, $\omega_{ce}^{-1} << \tau$ where τ (the hydrodynamic time scale) $\sim$ 1 ps and $\omega_{ce}^{-1} \sim 0.02$ ps. The electron momentum equation can thus be approximated by $ne\left[\underline{E} + \underline{v}_e \times \underline{B}\right] = -\underline{\nabla}(ZnKT)$. Taking the curl of this equation and neglecting source terms in the underdense plasma gives

$$\frac{B}{n} = \text{const} = \frac{B_o}{n_o} \qquad (4)$$

at a fluid particle (i.e. frozen in field lines). Since the plasma electrons are tied to the field lines thermal conduction is inhibited and an adiabatic expansion may also be assumed, so that $p/n^{\gamma} = \text{const}$. The expansion has two degrees of freedom so $\gamma = 2$ and hence

$$\frac{KT}{n} = \text{const} = \frac{KT_o}{n_o} \qquad (5)$$

Substituting equations (4) and (5) into equation (3) then gives

$$\frac{\partial v}{\partial t} + v\frac{\partial v}{\partial x} = \frac{v_{Ho}^2}{n_o}\cdot\frac{\partial n}{\partial x} \qquad (6)$$

where $v_{Ho} = (v_{Ao}^2 + C_{so}^2)^{\frac{1}{2}}$ is the fast magneto-acoustic speed and $v_{Ao} = B_o/(\mu_o M N_o)^{\frac{1}{2}}$, $C_{so} = (2ZKT_o/M)^{\frac{1}{2}}$.

Equations (2) and (6) have the analytic solution (7.49)

$$v = (2/3)\, v_{Ho} \left[1 + x/(v_{Ho}t)\right] \qquad (7)$$

$$n = (4/9)\, n_o \left[1 - x/(2v_{Ho}t)\right] \qquad (8)$$

The important aspect of the solution (8) is the existence of a wavefront at $x = 2v_{Ho}t$, beyond which no ions exist. Fig.7.43(a) and (b) show normalised plots of ion density and ion velocity in the rarefaction expansion respectively, against $x/(v_{Ho}t)$, as obtained from equations (7) and (8).

At the wavefront, $x = 2v_{Ho}$, equation (7) gives the maximum ion emission velocity as $2v_{Ho}$. This is in marked contrast to the case of a freely expanding plasma with no magnetic field (dashed curves in Figs.7.43(a) and (b)) where no similar maximum ion emission velocity exists. In Ref.(7.50) similar features are obtained numerically. Note that the solution obtained is analogous to that found in collision dominated gas dynamics (7.51).

J.E. Allen and L.M. Wickens

7.4.3 Transport Theory of Electrostatic Micro-Instabilities

Applying a general second order perturbation theory for electrostatic micro-instabilities in an infinite, Vlasov plasma to the case of density and temperature gradients perpendicular to a uniform magnetic field, the momentum and energy exchange rates may be expressed in terms of integrals over wave vector space, each integrand being a product of the fluctuation energy density and another factor involving the contribution of the relevant species to the linear dielectric function. These exchange rates and the heat flux are then derived by a two-step process, namely, a perturbation expansion (ε = fluctuating field energy/mean kinetic energy) followed by a velocity integration of the ensemble-averaged second order Vlasov equation.

The results of this theory applied to the ion acoustic instability, driven by an electron temperature gradient, are

$$\underline{\text{momentum}}: \quad \nu_{pe} = \frac{\sqrt{2\pi}\, k_e^2}{m_e n_o V_{de}} \sum_{\underline{k}} \frac{E(k,t) k_y}{k^3 V_e} \left(k_y (V_{de} - \frac{3}{2} V_{Te}) - \omega_r \right)$$

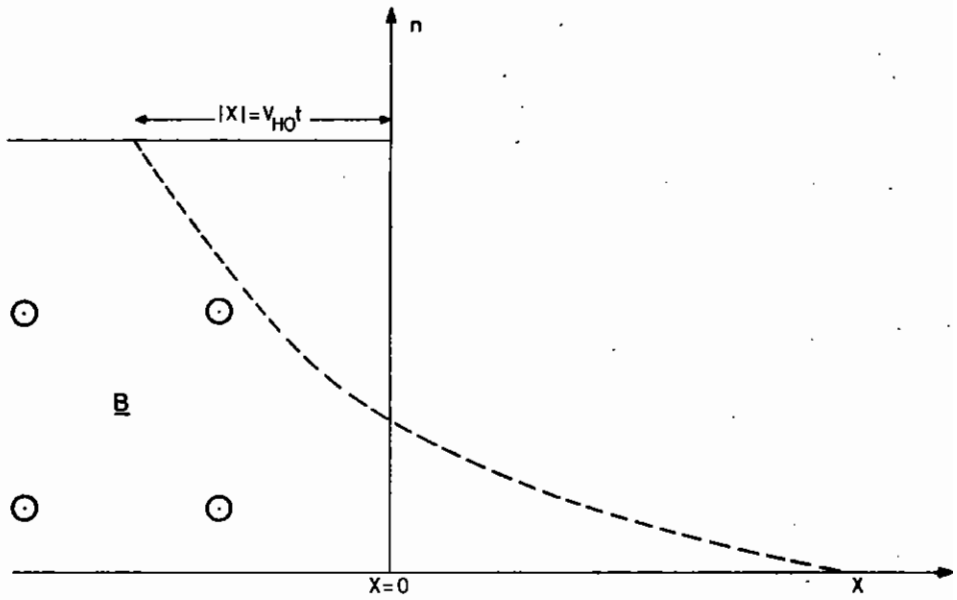

Fig.7.42

Schematic of initial conditions for a freely expanding magnetised plasma

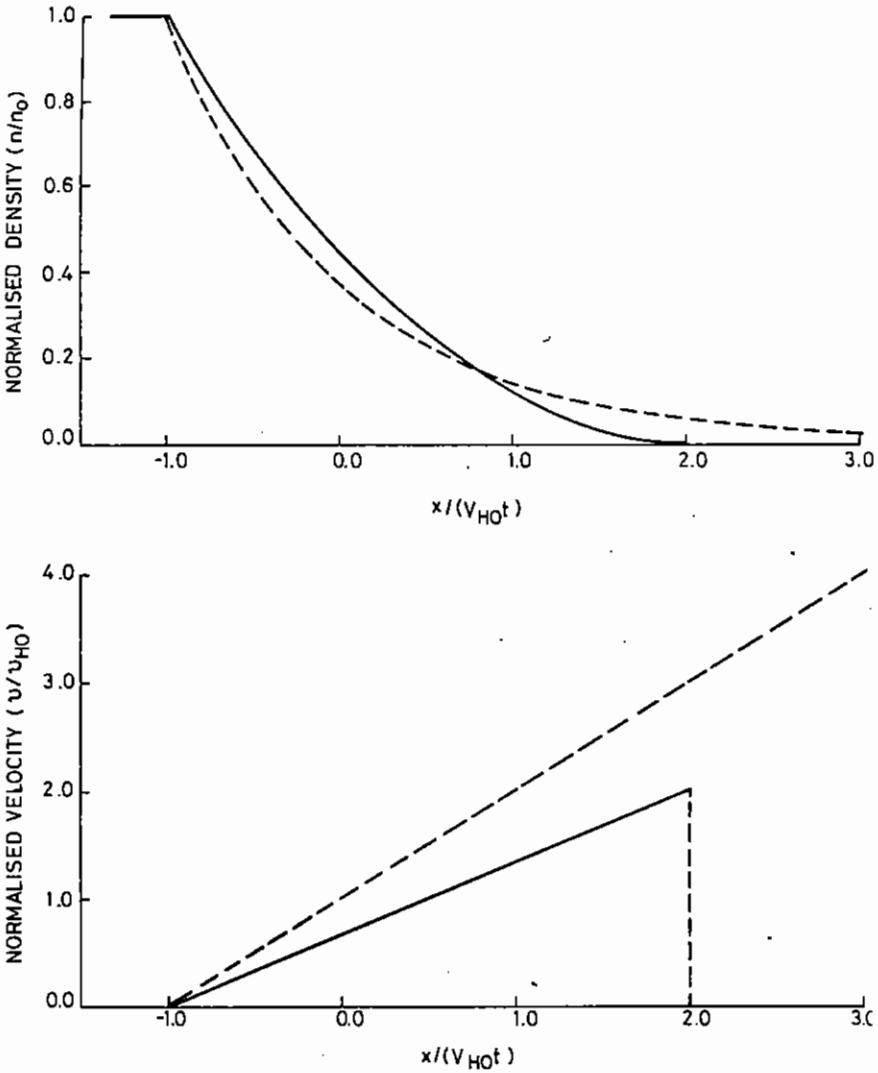

Fig.7.43

(a) Normalised ion density profile

(b) Ion velocity curves

<u>heating</u>: $$\nu_{Te} = \frac{-2\sqrt{2\pi}\, k_e^2}{3n_o T_e} \sum_{\underline{k}} \frac{E(\underline{k},t)}{k^3 V_e} (\omega_r - k_y V_{de}) \left(\omega_r - k_y (V_{de} - \tfrac{3}{2} V_{Te})\right)$$

<u>heat flux</u>: $$\nu_{Qe} = \frac{2\sqrt{2\pi}\, k_e^2}{5m_e n_o V_{Te}} \sum_{\underline{k}} \frac{E(\underline{k},t) k_y}{k^3 V_e} \left(k_y (V_{de} - \tfrac{1}{2} V_{Te}) - \omega_r\right)$$

where k_e, V_e are the electron Debye wave-number and thermal speed, $V_{de} = V_{ne} + V_{Te}$, and V_{ne} and V_{Te} are the electron diamagnetic drift speeds due to the density and temperature gradients. If these results are used with estimates of the maximum fluctuation level, $E(k,t)$, wave-particle transport coefficients may easily be determined.

For further details see (7.52) and references contained therein.

J. Sanderson

7.4.4 Computation of Radiative Transfer in Simulation of Microballoon Experiments

We have a twofold aim in computing radiative transfer in laser produced plasmas in microballoon experiments. One is the application for diagnostics where one should know the detailed dependence of the radiation field on frequency in a relevant part of the spectrum and calculate the emitted spectral lineshape for comparison with experiment. The radiative energy transfer may constitute a small part of the total energy balance of the process and if so the computation may be divided into two steps. In the first step hydrodynamic computation is carried out ignoring the effect of radiation, and in the second the radiation field is computed using at each timestep the given map of thermodynamic variables. This procedure has obvious shortcomings.

The second objective is analysis and design of experiments where the radiative energy transfer constituted a non-negligible part of the total energy balance, as in configurations in which significant cooling by radiative transfer takes place. Here one is interested only in the integral of the radiative transfer over the spectral region - both continuous and discrete.

In both of the above cases one has to solve for the photon distribution function $f(\vec{r}, \nu, \hat{\Omega}, t)$. Solution of the coupled radiative transfer and hydrodynamic equations requires prohibitively long computer-time. Different simplifying assumptions about the form of f are made by various authors. For example the dependence of f on the frequency ν is assumed to be that of a black body of radiation temperature T_R; another simplification is to obtain the dependence of f on the direction of motion of the photon $\hat{\Omega}$ from the diffusion model. Examination of typical parameters of plasmas obtained in both exploding-pusher and ablation type experiments performed in the Rutherford Laboratory, shows that the plasmas are not really optically thick in the relevant X-ray spectral region, and the black body approximation cannot be valid. The diffusion approximation is also not volid as the plasma dimensions are not large in comparison with the mean free path of photons in the spectral region concerned.

We are using a radiation code which calculates f at each timestep for a given map of thermodynamic variables. Dependence of f on $\hat{\Omega}$ is approximated by distributing the photons between two groups moving in opposing directions. Dependence on frequency ν is calculated in detail. Population of all levels relevant to hydrogen-like and helium-like lines is calculated by solving rate equations (since the assumption of local thermodynamic equilibrium is invalid). At present the radiation code is used as a post processor and is not incorporated into the plasma code, since this increases computer time by a large factor. Examining experimental data and observing that significant emission by the plasma takes place over a short time relative to the total implosion time, a possible solution is suggested. After running the radiation package as a post processor, the time-interval during which most of the emission (by the shell or the core) takes place is approximately found. It is planned to run the radiation code and MEDUSA coupled together for the relevant (short) time interval.

A. Shalom and R.W. Lee

7.4.5 Thermal Flux Inhibition

In hydrodynamic computer codes modelling inertial confinement, thermal conductivity is usually given by the classical theory (7.54) with an additional upper limit imposed on the heat flux of a numerical factor times a free-streaming limit $nkT\left(\frac{kT}{m}\right)^{\frac{1}{2}}$. Comparison with experiment indicates that the maximum heat flux is rediced from the free-streaming limit by between one and two orders of magnitude (e.g. (7.53)). Various mechanisms for this flux inhibition have been suggested but the explanation has yet to be generally agreed upon. Spitzer's theory is only valid for gentle thermal gradients and therefore one possible line of investigation is to examine the effect of classical collisions in thermal gradients with scale-lengths of only a few mean free paths. We have chosen to do this by writing a computer program to solve the electron fluid equations in phase space. The equations are solved in one spatial dimension and two velocity dimensions using the Balescu-Lenard collision terms. In dimensionless units the equations are (7.55)

$$\frac{\partial f}{\partial t} + v\cos\theta \frac{\partial f}{\partial x} + E \frac{\partial f}{\partial (v\cos\theta)} =$$

$$\frac{1}{v^2}\frac{\partial}{\partial v}\left[v^2\left(Cf + \tfrac{1}{2} D_1 \frac{\partial f}{\partial v}\right)\right] + \tfrac{1}{2}\frac{D_2}{v^2}\frac{1}{\sin\theta}\frac{\partial}{\partial\theta}\left(\sin\theta \frac{\partial f}{\partial\theta}\right)$$

$$D_2 = \frac{4}{3N_D}\frac{1}{v}\int_0^v \frac{u^2}{v^2} F(u)\, I(u)\, du$$

$$D = \frac{2}{3N_D}\frac{1}{v}\int_0^v \left(1 - \frac{u^2}{v^2}\right) F(u)\, I(u)\, du + Z\frac{I(0)}{3N_D v}$$

$$C = \frac{2}{3N_D}\frac{1}{v}\int_0^v u \frac{\partial F}{\partial u} I(u)\, du$$

$$F(v) = \pi\int_v^\infty\int_0^\pi u\, f(u, \theta)\sin\theta\, d\theta\, du \qquad v \geq 0$$

$$I(u) = \frac{\psi_r}{2|\psi_i|}\left[\tan^{-1}\left(\frac{3N_D - \psi_r}{\psi_i}\right) + \tan^{-1}\left(\frac{\psi_r}{\psi_i}\right)\right]$$

$$+\frac{1}{4}\ln\left[\frac{(3N_D - \psi_r)^2 + \psi_i^2}{\psi_r^2 + \psi_i^2}\right]$$

$$\psi_r(v) = P\int_{-\infty}^{\infty} \frac{du}{u - v} \frac{\partial F}{\partial u} \qquad \psi_i(v) = \pi \left|\frac{\partial F}{\partial v}\right|$$

$$\frac{\partial E}{\partial x} = A \int_0^{\infty}\int_0^{\pi} v^2 f(v, \theta) \sin\theta \, d\theta \, dv$$

These equations embody the following features:

1) The Balescu-Lenard collision term has been used because the electron distribution can be far from Maxwellian and consequently the scattering frequencies can be higher than those given by the more usual collision terms which neglect the wave contribution to scattering.

2) Ions are assumed to be immovable and contribute only to the angular scattering via the second term in D_2.

3) The electric field E is artificially reduced in magnitude to make the period of Langmuir oscillations longer than the timestep in the program. However, the weakened electric field is retained to ensure quasi-neutrality.

4) Velocity distribution instabilities and their effect on particle scattering have been neglected since a completely isotropic distribution is always stable and anisotropies are expected to be small if the flux is strongly inhibited. Similarly, only the isotropic part of $f(v, \theta)$ is used in the calculation of the coefficients C, D_1 and D_2, making them independent of θ.

5) The equations are only valid for a large number of electrons per Debye sphere. For a plasma at solid density this is only true for temperatures much greater than 10 eV.

Although the equations have been put in a dimensionless form, the simulated problem can be described as follows. A 12.2 μ thick slab of plasma consisting of electrons and triply ionised ions has an initial temperature of 75 eV and an electron density of 10^{23} cm^{-3}. A 1.5 μ thick region at one edge of the slab is heated quickly to a temperature of 1.25 keV and continuously heated so as to maintain that temperature thereafter. The heated

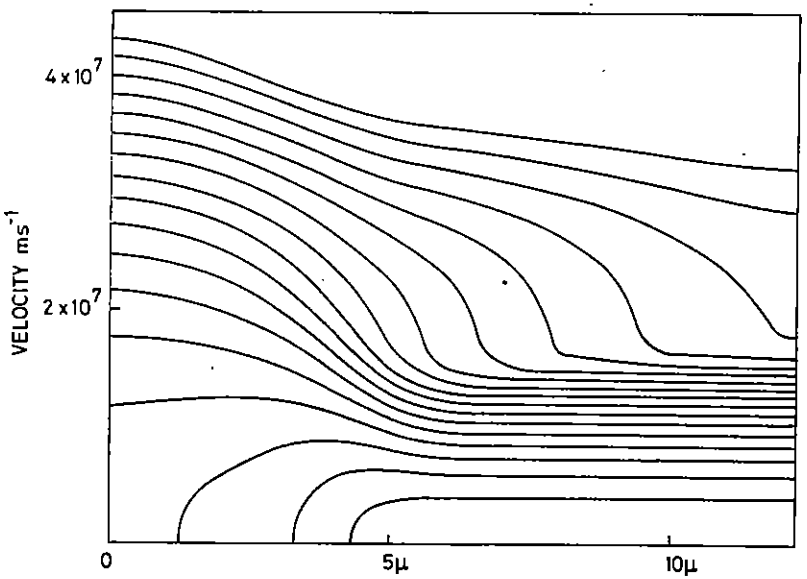

Fig.7.44
The electron density in phase space as a function of x and v (magnitude of velocity) after a time interval of 4.5 ps. The plasma is heated on the left hand side. The contour interval is logarithmic with successive contours in the ratio $10^{\frac{1}{4}}$.

electrons have a m.f.p. of about 0.4 μ. The simulation cannot accurately reflect the situation in a laser-plasma experiment where the density varies by many orders of magnitude across the conducting region, the initial laser target is solid and the plasma flows through the region of interest thus enabling steep thermal gradients to persist for longer times. However, the program does simulate a time-dependent situation in which there are steep thermal gradients, and the occurence of flux inhibition in the simulation should be directly relevant to the laser-plasma situation. An example of the computer output is shown in Fig.7.44.

When the simulated heat source is initially turned on steep temperature gradients exist on the scale of a mean free path. The tendency of the most energetic electrons to stream away from the heated region sets up non-Maxwellian distributions and the wave contribution to the collision term is active. The temperature gradients become progressively less steep and the wave contribution soon becomes negligible. Given sufficient time, the thermal gradient will relax to a point where the familiar classical theory is fully applicable. The analysis of the simulation results is still at an early stage but there seems to be evidence for a flux limit of about 1/40 the free-streaming limit when the temperature gradient is spread over a few mean free paths. The wave contribution to the collision term does not appear to be responsible for this. Instead, the dominant mechanism seems to rely on the high collision frequency of the cold electrons making it difficult for them to supply the return current. Further work is needed before firm conclusions can be reached.

A. Bell

7.4.6 Saturation Levels of Heat Flux and Fast Electron Driven Ion Acoustic Wave-Turbulence

There is now a substantial body of evidence pointing to the inhibition of electron energy transport in laser-target plasmas to values much less than those found from simple estimates based on flux-limited diffusion. The evidence, all of it indirect, comes from a range of experiments showing variously that

(a) the extent of the heated plasma is smaller than expected (7.56)
(b) an appreciable fraction of the energy absorbed may go towards the production of fast ions (7.57)
(c) there appears to be a much reduced burn-depth in structured microballoon targets and a slower spread of the burn-through in thin film experiments than expected from arguments based on classical transport (7.58)
(d) observations of the density profile show flattening in the outer zones of the corona that is consistent with strong flux inhibition (7.59).

The most recent evidence is that from the experiments at the Rutherford Laboratory by Kilkenny and others (7.58). In this work the thermal transport was inferred from studies of microballoon targets coated with varying thickness of Al and irradiated by two 1.06 μm, 100 ps beams at irradiances of 2×10^{15} W cm^{-2}. A variety of plasma parameters was measured. For example X-ray spectra yield the thermal electron temperature while the electron density is found from Stark broadening and from the intensity of the recombination continuum. A comparison of the relative intensities of the Al XII $1^1S_0 - 4^1P_1$ to the Si XIII $1^1S_0 - 3^1P_1$ line gives a direct measurement of the burn-depth. A best fit ot the results obtained in this work was found from a computer model with two free parameters, namely the fractional absorption of laser energy into the thermal ablation plasma, δ, and the flux inhibition factor, f, suitably chosen. A best fit was given by $\delta = 0.025$ and $f = 0.03$.

Other transport experiments (7.58) produced time and space resolved data from the irradiation of thin polystyrene films with 100 ps Nd glass laser

pulses ranging from 2 - 12 J. The radial extent of the underdense plasma was measured by backlighting the target with a ruby laser probe at 0.69 μm and imaging with a streak camera. The burn-through hole was seen to propagate radially at a rate which depended on the foil thickness and which was slower than that predicted from simulations using a 2-D hydrodynamic code.

On the basis of the evidence from these and other experiments various mechanisms for flux inhibition have been proposed by way of interpretation. It has been suggested, for example, that the self-generated magnetic fields present in some - but not all - target plasmas could be strong enough to limit thermal transport. However, we know that in microballoon targets this is not likely to be so. Indeed in plane target experiments, where megagauss fields have been measured, there is now compelling evidence (7.10) that the peak fields occur in the coronal plasma around 0.2 n_c where n_c is the critical density and are not likely in consequence to have any marked effect on transport phenomena in the region of peak absorption.

A widely canvassed alternative mechanism is one based on ion acoustic turbulence in the target plasma. The idea is that if by some means a spectrum of ion trubulence is excited then this turbulence could scatter electrons effectively and so reduce the heat flow. The role of turbulence in interpreting so-called anomalous behaviour in plasma physics is well established (7.60). Indeed direct evidence of its importance in laser-plasma interaction physics is to be found in work by Gray and others (7.61) who measured the thermal conductivity of an underdense plasma heated by a CO_2 laser pulse. They found that the thermal conductivity was limited to about 0.03 times the free streaming limit and from light scattering measurements concluded that fluctuation levels of 9% were present in the plasma, a level adequate to explain the inhibited heat flux. It has been suggested that comparable levels of turbulence are present in microballoon and slab target plasmas and lead to the reduction in heat flow inferred from the observations.

There is however som evidence from computer simulations suggesting that the levels of turbulence present are too low to explain the observed flux levels (7.45). Lindman has reported results from a 2-D particle-in-cell code which lead to anomalous collision frequencies much less than the

various analytic estimates in the literature. These in turn depend on predictions of saturation levels of the ion acoustic turbulence which are arrived at in the main from simple estimates based on ion trapping arguments (7.62). It is our contention that these levels are often substantial over-estimates and we present here values based on a more sophisticated model (7.60), which predicts turbulence levels much closer to those seen in the computer simulations and which, in some parameter ranges at least, would not result in any marked heat flux inhibition.

The evolution of ion turbulence from an instability may be pictured in the following model. Electrons are heated at the critical surface. As they move into the overdense plasma they draw a return current of cold electrons from the background plasma. Provided the electron drift velocity corresponding to this cold electron current is greater than the ion acoustic speed in the plasma the positive slope of the electron distribution function will result in electron Landau growth. Ion Landau damping on the other hand will be negligible provided $ZT_e/T_i \gg 1$ and under these conditions ion acoustic turbulence can develop. The growth of the ion wave is limited in turn by the nonlinear dynamics of the ions i.e. by "ion trapping." We derive a nonlinear dispersion relation from which the saturation levels of the ion turbulence are inferred from a marginal stability argument. In particular our model is applied to obtain results corresponding to parameters characteristic of those in experiments at the Rutherford Laboratory. Thus the thermal electron temperature is taken to be 500 eV and the mean energy of the hot electrons measured from K_α spectroscopy 10 keV which we shall partition between a genuine hot electron temperature T_h and a hot electron current with drift velocty v_h. The suprathermal electron density in these experiments was measured at several times 10^{19} cm^{-3}which corresponds to an $\varepsilon \sim 3\%$. We shall in fact let ε range from 1 to 10%. Finally we shall assume a mean Z = 10 and a cold electron to ion temperature ratio of 2.

The energy flux from critical density - where the bulk of laser energy is absorbed - into the overdense plasma core may be divided, rather artificially, into two parts: a heat flux due to temperature gradients and thermoelectric effects plus a particle flux of decoupled suprathermal electrons arising from anomalous absorption processes like resonance absorption. Charge neutrality means a return current of cold electrons which if they

are resistive implies the presence of an electric field. To model this simply, we adopt the following one dimensional (in the direction of the hot and cold drifts) electron distribution function:

$$F_e(v) = (1 - \varepsilon)\, F_c(v) + \varepsilon F_h(v)$$

$$F_c(v) = \frac{1}{\sqrt{2\pi}\, V_c} \exp\left[-\tfrac{1}{2}\left(\frac{v + v_c}{V_c}\right)^2\right]\left[1 + \frac{f}{6}\left\{\left(\frac{v + v_c}{V_c}\right)^3 - 3\left(\frac{v + v_c}{V_c}\right)\right\}\right]$$

$$F_h(v) = \frac{1}{\sqrt{2\pi}\, V_h} \exp\left[-\tfrac{1}{2}\left(\frac{v - v_h}{V_h}\right)^2\right]$$

where ε is the fraction of 'hot' electrons, $V_c(V_h) = \sqrt{T_c(T_h)/m}$, $T_c(T_h)$ is the cold (hot) electron temperature (in energy units), v_c, v_h are cold and hot electron drifts which are related through the zero current condition, $\varepsilon v_h = (1 - \varepsilon)v_c$ and the cold distribution carries a heat flux f x its free streaming vlaue $\frac{1}{2}\, nmV_c^3$.

This allows us the freedom of varying the return current and hence the strength of the ion acoustic instability. At one extreme, no net drift of hot electrons and hence no return current from them means that the return current is due solely to the cold electron heat flux. In the opposite limit we have the unrealistic case of a monoenergetic stream of hot electrons and hence the maximum return current. This gives us upper bounds on the return current and hence on the growth rate of the instability. A comment on this model is in order; the distribution function chosen is two humped and therefore beam unstable. This would be a serious problem in simulations but presents no problems in an analytical treatement. Moreover, $F_c(v)$ becomes negative for large enough negative values of $v(v + v_c < 0.5V_c)$. However, this region of velocity space plays a negligible role in the present analysis and the presence of $F_h(v)$ does improve this.

Assuming a stationary Maxwellian for the ions, the linear dispersion relation is

$$1 + K_i + K_c + K_h = 0$$

where

$$K_i = -\frac{1}{2k^2\lambda_h^2}\, Z'(\zeta_i) \qquad \zeta_i = \frac{\omega}{\sqrt{2}kV_i}$$

$$K_h = -\frac{1}{2k^2\lambda_h^2}\, Z'(\zeta_h) \qquad \zeta_h = \frac{\omega - kv_h}{\sqrt{2}kV_h}$$

$$K_c = -\frac{1}{2k^2\lambda_c^2}\left[Z'(\zeta_c)\{1 - \sqrt{2}\, f\, \zeta_c(1 - \zeta_c^2/2)\} - \frac{f}{\sqrt{2}} Z(\zeta_c) - \frac{\sqrt{2}\, f\, \zeta_c}{6}\right]$$

$$\zeta_c = \frac{\omega + kv_c}{\sqrt{2}kV_c}$$

and

$$Z(\zeta) = \frac{1}{\sqrt{\pi}} \int_c \frac{e^{-x^2}}{x - \zeta}\, dx$$

is the usual Fried-Conte function.

When $\zeta_c << 1$ and since $f << 1$, $ReK_c \simeq 1/k^2\lambda_c^2$. Also $|ReK_h| << |ReK_c|$ whenever $\lambda_h^2 >> \lambda_c^2$ i.e. $T_h/T_c >> \varepsilon/1 - \varepsilon$. Then, if $ZT_c/T_i >> 1$ we obtain the usual dispersion relation for ion acoustic waves dependent only on cold electron properties:

$$\omega = \alpha\, k\, c_{Sc} \qquad c_{Sc}^2 = ZT_c/m_i$$

$$\alpha^2 = \frac{1}{1 + k^2\lambda_c^2} + \frac{3T_i}{ZT_c} \quad .$$

Provided the mean hot electron energy is large enough i.e. $\frac{m}{2} v_h^2 + T_h >> T_c$ then $|ImK_h| << |ImK_c|$ and the Landau damping due to hot electrons is negligible. Then, the growth rate is

$$\frac{\gamma}{|\omega|} = \sqrt{\frac{\pi}{8}}\, \alpha^2 \left[\frac{v_D - \alpha c_{Sc}}{V_c} - \left(\frac{ZT_c}{T_i}\right)^{3/2} \exp -\left(\frac{\alpha^2 ZT_c}{2T_i}\right)\right]$$

where $v_D = v_c + \frac{f}{2} V_c$ is the effective return current of cold electrons due to the cold electron heat flux f and the suprathermal particle flux v_h.

We attempt next to determine the saturation level for this instability by employing perturbed orbit theory, developed originally by Dupree (7.63) and Weinstock (7.64). We derive a nonlinear dispersion relation which incorporates turbulently broadened resonance functions and from which we may deduce the energy in the spectrum by assuming marginal stability. The nonlinear dispersion relation takes the form:

$$1 + K_i(\underline{k},\omega) + K_e(\underline{k},\omega) = 0$$

$$K_\alpha(\underline{k},\omega) = -\frac{i\omega_{p\alpha}^2}{k^2}\int d\underline{v}\ \Gamma_\alpha(\underline{k},\underline{v},\omega)\underline{k}\cdot\frac{\partial}{\partial\underline{v}} f_{0\alpha}(\underline{v}) \qquad (\alpha = i,e)$$

$$\Gamma_\alpha(\underline{k},\underline{v},\omega) = \int_0^\infty dt\ \exp\left[i(\omega - \underline{k}\cdot\underline{v})t - i\frac{\partial}{\partial\underline{v}}\cdot\underline{\underline{D}}_\alpha(\underline{v})\cdot\underline{k}\frac{t^2}{2} - \underline{kk}:\underline{\underline{D}}_\alpha(\underline{v})\frac{t^3}{3}\right]$$

$$\underline{\underline{D}}_\alpha(\underline{v}) = \left(\frac{q_\alpha}{m_\alpha}\right)^2 \sum_{\underline{k}} \frac{\underline{kk}}{k^2} E_{\underline{k}}^2\ \Gamma_\alpha(\underline{k},\underline{v},\omega) \quad .$$

We see that the resonance function Γ is modified by the presence of diffusion and viscous-like terms which, if set equal to zero, gives the usual linear result. We now make the following assumptions:

(i) the electrons are assumed to behave linearly or quasi-linearly. The phase velocity is already deep in the main body of the electron distribution and so any electron resonance broadening can affect the growth rate only marginally. Moreover the three dimensional nature of the ion wave spectrum helps in validating this assumption.

(ii) the waves are assumed dispersionless which is approximately true, particularly when $k\lambda_c < 1$.

(iii) the spectrum is assumed narrow and peaked about the fastest growing mode, $k\lambda_c \sim \frac{1}{\sqrt{2}}$, and hence approximately one dimensional in the direction of the return current. This mode necessarily absorbs most of the energy as the spectrum grows out of noise-it is only after it is saturated that a significant proportion of energy is distributed to other modes.

(iv) on the time scale for saturation of this mode, we assume the ion distribution maintains its Maxwellian shape.

In fact, ion "trapping", i.e. the ion orbit perturbation by the waves,

causes ion acceleration and hence tail formation in the ion distribution. The present analysis therefore describes the phase prior to tail formation. Renormalizing the above equations with

$$\omega_b = \left[\frac{ZeE_k k}{M}\right]^{\frac{1}{2}} \qquad \text{(ion bounce frequency)}$$

$$u = (kv - \omega)/\omega_b$$

$$\tau = \omega_b t$$

$$d(u) = k^2 D(v)/\omega_b^3 = \omega_b \Gamma(k, v, \omega)$$

we get

$$d(u) = \int_0^\infty d\tau\ \exp\left[-d(u)\frac{\tau^3}{3}\right]\cos\left[u + d'(u)\frac{\tau^2}{2}\right]$$

This is plotted in Fig.(7.45). The width of this resonance corresponds almost exactly to those velocities for which an ion would be trapped by this single dominant mode. The extreme points $u \simeq \pm 2$ corresponds to velocities where the work done by viscous force on an ion is equal to the energy in the wave itself i.e. an ion cannot change its energy by more than is contained in the wave itself. For $|u| > 2$, $d(u) = 0$ i.e. at marginal stability the nonresonant contribution is zero. Then

$$\text{Im}\ K_i = \frac{1}{k^2\lambda_i^2}\left(\frac{\omega_b}{kV_i}\right)\frac{1}{\sqrt{2\pi}}\int du\ d(u)(u - u_p)\exp\left[-\tfrac{1}{2}\left(\frac{\omega_b}{kV_i}\right)^2(u - u_p)^2\right]$$

where $u_p = \omega/\omega_b$. Then $\text{Im}(K_e + K_i) = 0$ may be solved to give $E_k = -ik\phi$ as a function of ZT_c/T_i and v_D/V_c (or γ, the linear growth rate) at marginal stability. The results are shown in Figs.7.46 and 7.47. It is instructive to compare the results of this analysis with the widely quoted result derived from simple trapping arguments (7.62)

$$\frac{e\phi}{T_c} \simeq \frac{1}{4}\left[\frac{1}{(1 + k^2\lambda_c^2)^{\frac{1}{2}}} - \left(\frac{3T_i}{ZT_c}\right)^{\frac{1}{2}}\right]^2 .$$

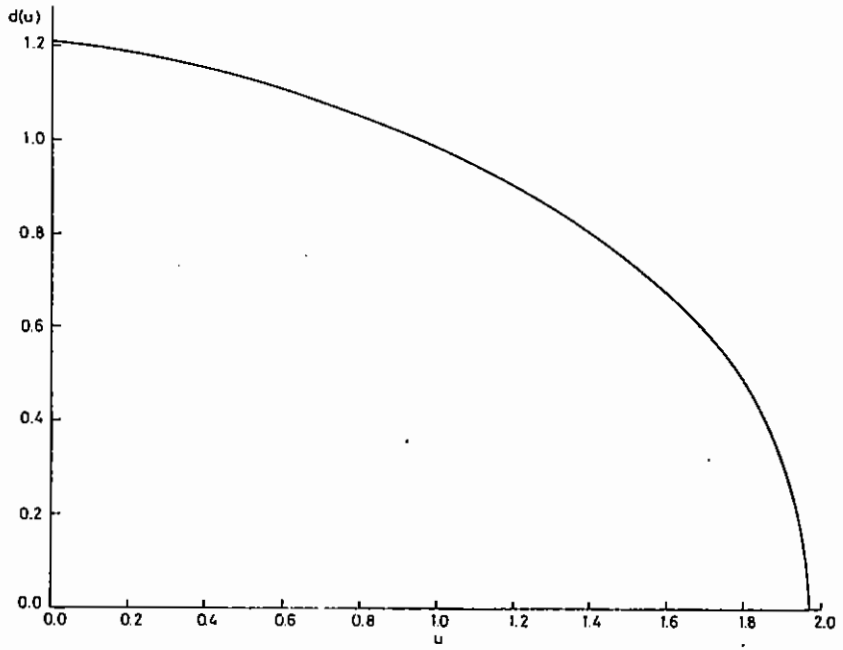

Fig. 7.45

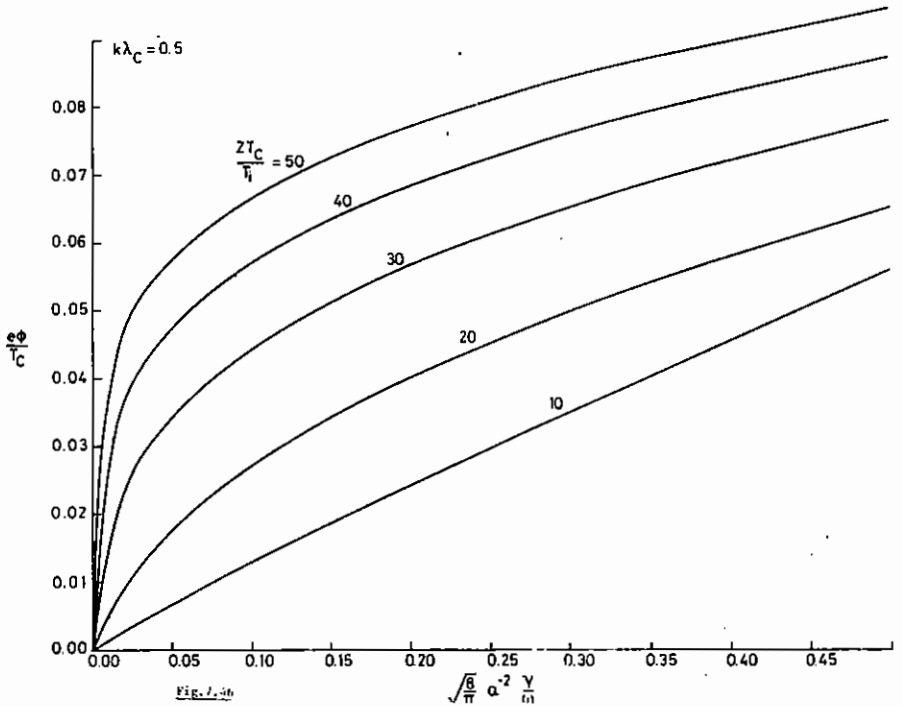

Fig. 7.46

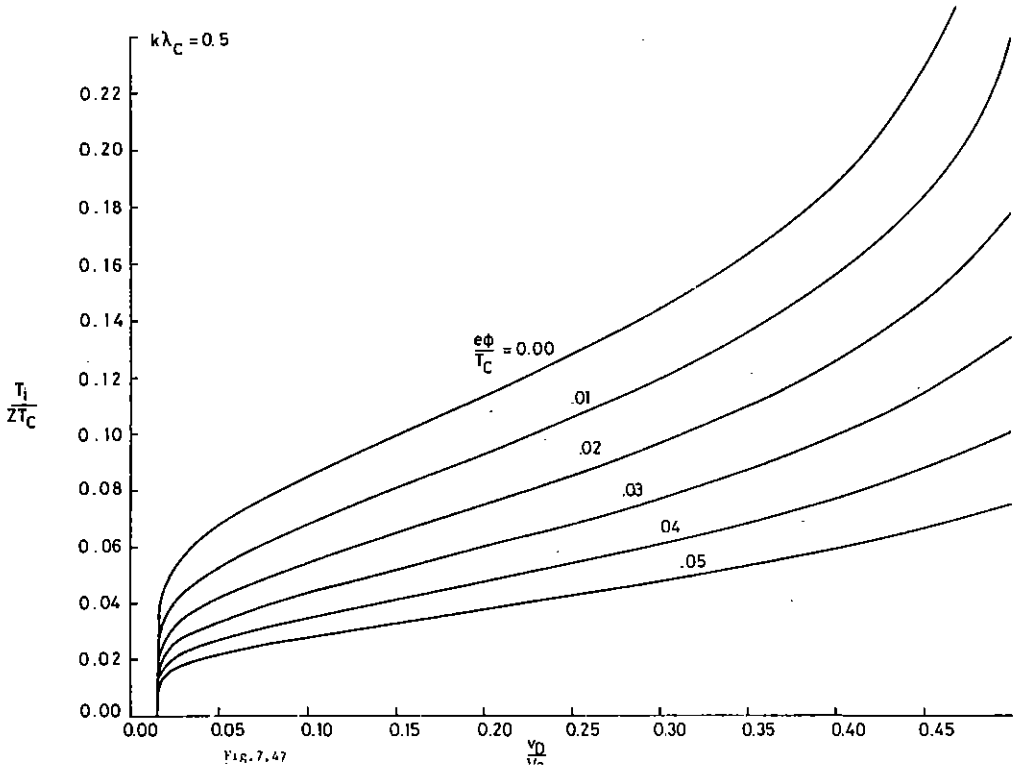

Fig.7.47

A similar expression to this may be derived from our analysis by using a model resonance function

$$d(u) = \frac{\pi}{4} \qquad |u| \leq 2$$

$$= 0 \qquad |u| > 2$$

Then

$$\frac{\exp(-x^2/2) - \exp\{-(2A - x)^2/2\}}{A - x} = 2\left\{\frac{T_i}{ZT_c}\right\}^{3/2} \frac{v_D - \alpha c_{Sc}}{v_c}$$

where $A = \alpha\sqrt{\frac{ZT_c}{T_i}}$ and

$$\frac{e\phi}{T_c} = \frac{1}{4}\left[\alpha - x\sqrt{\frac{T_i}{ZT_c}}\right]^2$$

$$\simeq \frac{1}{4}\left[\frac{1}{1 + k^2\lambda_c^2} - x\sqrt{\frac{T_i}{ZT_c}}\right]^2$$

To retrieve the expression based on simple trapping estimates would require setting $x \simeq \sqrt{3}$ when in fact it is a complex function of ϕ.

For values of the parameters appropriate to the experiments at the Rutherford Laboratory, we shall take $ZT_c/T_i \simeq 20$ and a total suprathermal electron energy ε of 10 keV i.e. $\varepsilon/T_c \simeq 20$. Then $v_D/v_c = \varepsilon\sqrt{(2 - T_h)/T_c}\ /\ (1 - \varepsilon) + 0.5f$ whence $.015 < v_D/v_c < .211$ $(\varepsilon > T_h > 0)$. When $T_h = 2\varepsilon$, the heat flux in the thermal electron distribution alone provides free energy to drive the instability. From Fig.7.47 we see that under such conditions ion waves are barely unstable. Hence for instability (for our parameters) an additional free energy source is needed and this is provided by the suprathermal electron current. An upper limit is given by $T_h = 0$ hence $e\phi/T_c = 3.5\%$. The corresponding trapping value is 8.6%. To achieve such values return currents very much higher than are ever likely in the Rutherford experiments are required. In theoretical modelling Manheimer (7.65) has deduced that given a turbulence level of about 10% one can get values for $f \sim 0.03$. These figures, however, apply when

the thermal flux is the dominant energy transport process (i.e. $v_c \ll fV_c/2$ whence $v_D/V_c \simeq 0.5\ f$) and therefore his figures of $f = .03$ and $e\phi/T_c = 10\%$ are mutually inconsistent according to our analysis. The question is whether this level is likely to be reached before saturation. There is some evidence from computer simulations which casts doubts on the effectiveness of ion turbulence as a means of inhibiting the thermal flux (7.45). These simulations confirmed earlier results by Biskamp and Chodura (7.62) which showed that turbulence levels rose rapidly and then decayed over several hundred wave periods. The results of the Los Alamos workers were best fitted by the following expression for an anomalous collision frequency

$$\frac{\nu^*}{\omega_{pe}} \sim 3 \times 10^{-5} \left(\frac{T_e}{T_i}\right) \left(\frac{v_D}{V_e}\right) \left(\frac{m_e}{m_i}\right)^{\frac{1}{2}}$$

in which v_D is the effective electron drift normalized to the thermal speed V_e and m_j, T_j are the species masses and temperature respectively. This is much less than the theoretical value corresponding to Manheimer's choice of turbulence level of $\sim 10\%$ i.e.

$$\frac{\nu^*}{\omega_{pe}} \sim k\lambda_D \left(\frac{e\phi}{T_e}\right)^2 .$$

For values of $v_D/V_e \sim 0.5$, $T_e/T_i = 100$ used in the simulation and taking $k\lambda_D = 0.5$, $e\phi/T_e = 0.1$ then

$$\left(\frac{\nu^*}{\omega_{pe}}\right)_{\text{theory}} \sim 20 \times \left(\frac{\nu^*}{\omega_{pe}}\right)_{\text{simulation}} .$$

For our parameters, $k\lambda_D = 0.5$, $T_e/T_i = 20$, $v_D/V_e = 0.05$ we predict $e\phi/T_e = 0.01$, hence

$$\left(\frac{\nu^*}{\omega_{pe}}\right)_{\text{theory}} \lesssim 10 \left(\frac{\nu^*}{\omega_{pe}}\right)_{\text{simulation}} .$$

The observed levels of 9% in the experiments of Gray et al was conducted in a Z pinch. It is possible that here alternative sources of free energy exist based on the magnetic field.

The turbulence levels predicted here ought to be regarded as upper limits. Quasi-linear diffusion of the thermal electrons causes their distribution function to evolve to a shape having a reduced slope at the phase velocity i.e. the instability weakens. Also, as ions are heated and tail formation occurs, ion Landau damping increases. These effects bring the system back to marginal stability.

In conclusion, then, we believe that ion wave turbulence is ineffective as a thermal flux inhibitor for the parameters pertaining to recent Rutherford Laboratory experiments.

H.C. Barr and T.J.M. Boyd

7.4.7 Radiation Transport Calculations in Heavy Ion Fusion Targets

The effect of radiation in glass shelled heavy ion fusion targets has been calculated using ANISN an Sn transport code. In order to do this S7 group photon cross-section and source terms have been calculated for the plasma conditions given by the simulation code MEDUSA in each of its mesh intervals. The physical model used includes the effects of Free-Free radiation, and Bound-Free radiation from the K shell electrons of oxygen, silicon, helium and hydrogen. For these effects LTE is assumed so that source terms and cross-section are related by detailed balance. Thomson scattering is also included but approximated by an isotropic scattering term, but Bound-Bound radiation effects are ignored as they are mainly small and extremely difficult to calculate with any accuracy.

As the radiation affects the plasma conditions its effect needs to be found for each MEDUSA timestep. The calculation using ANISN however takes too much time to be used every timestep. A simple radiation routine has therefore been developed for inclusion in MEDUSA, being adjusted to give reasonable agreement with the ANISN calculations. This routine approximates the energy flux from a mesh interval by

$$F(x) = \frac{F(o)}{1 + \Sigma x/C} \qquad (1)$$

where F is the flux, x the distance from the interval, Σ the photon cross-section and C an adjustable constant chosen to give good agreement with ANISN. The cross-section is calculated from the expected total Free-Free radiation produced in an interval and the requirement that if that interval thickness tended to infinity the total radiation loss would be given by blackbody radiation. A temperature dependent adjustment is made to the Free-Free effects to allow for Bound-Free effects.

A comparison is shown in Fig.7.48 of the radiation heating calculated by ANISN with that given by the routine in MEDUSA. The comparison was made for a typical spherical target of 2.5 mm radius with a glass shell 1 mm thick, filled by solid D-T. When the comparison was made the compression shock wave was two thirds the way through the D-T and the glass shell which was absorbing the heavy ions had a maximum temperature of about 600 ev.

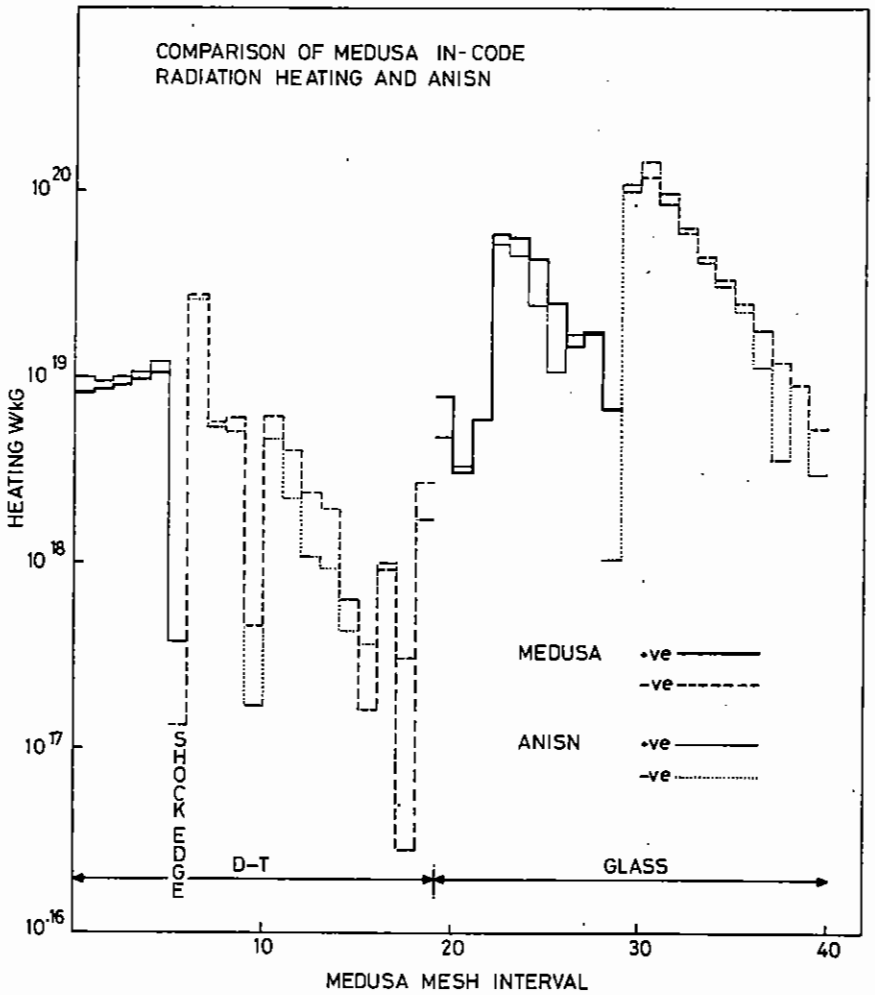

Fig.7.48

T D Beynon, E Smith

CHAPTER 7 REFERENCES

7.01 E K Storm et al, Lawrence Livermore Lab Report UCRL 79788 (1977).

7.02 M D Rosen and J M Nuckolls, P. Fluids 22, 1393 (1979).

7.03 B Ahlborn and M H Key, Rutherford Lab Report RL 79033 (1979).

7.04 B Ahlborn and M H Key, UBC Lab Report 73 (1980), and Bull. Am. Phys. Soc.

7.05 M.H. Key, Proc. SUSSP, Laser Plasma Interactions, Scottish University Press (1980).

7.06 B I Bennet, J D Johnson, G I Kerley and G T Rood, Los Alamos Lab Report LA 7130 (1978).

7.07 D A Kirzhnits, Sov. Phys. JETP 8. 1081 (1958).

7.08 R Latter, Phys. Rev. 99, 1854 (1955).

7.09 S L McCarthy, Lawrence Radiation Laboratory Report UCRL-14364 (1965).

7.10 A Raven, et al, Appl. Phys. Lett. 35, 7, 526 (1979).

7.11 G J Pert, J. of Plasma Phys. 18, 227 (1977).

7.12 J P Christiansen, DETF Ashby and K V Roberts, Com. Phys. Comm. 7, 271 (1974).

7.13 K R Manes, H G Ahlstrom, R A Haas and J F Holtzrichter, J. Opt. Soc. Am. 67, 717 (1977).

7.14 L D Landau and E M Lifchitz, Electrodynamics of Continuous Media, Pergammon, Oxford (1975).

7.15 T W Johnston and J M Dawson, Phys. Fluids 16, 722 (1973).

7.16 See, e.g., V.L. Ginzburg, The Propagation of Electromagnetic Waves in Plasmas, Pergamon, Oxford (1970).

7.17 D T Attwood, D W Sweeney, J M Auerbach and PHY Lee, Phys. Rev. Lett. 40, 184 (1978).

7.18 A Raven and O Willi, Phys. Rev. Lett. 43, 278 (1979).

7.19 See, e.g., A Montes, M Hubbard, C Kler and I Spalding, Appl. Phys. Lett. 36, 652 (1980).

7.20 See, e.g., D W Forslund, J M Kindel and K Lee, Phys. Rev. Lett. 39, 284 (1977) and references therein.

7.21 D Kershaw, UCID preprint 17424 (1977).

7.22 D Kershaw, UCRL preprint 78333 (1977).

7.23 P L Brown and K B Wallick, LASL Report (1975).

7.24 W D Schultz, "Methods in Computational Physics", Academic Press, Vol. 3 (1964).

7.25 Richtmyer and Morton, "Difference Methods in Initial Value Problems, Ch. 12.

7.26 R J Mason, B.A.P.S. 24, 8, 4E1

7.27 N A Tahir, Ph.D. Thesis (1978) (Glasgow University).

7.28 E W Laing and N A Tahir, Rutherford Laboratory Annual Report RL-78-039 (1978).

7.29 N A Tahir, Rutherford Laboratory Annual Report RL-79-036 (1979).

7.30 N A Tahir and E W Laing, Radiation Effects in Laser Compression Simulations (to be published in Plasma Physics).

7.31 J A Stamper and B H Ripin, Phys. Rev. Lett. 34, 138 (1975).

7.32 J A Stamper, E A McLean and B H Ripin, Phys. Rev. Lett. 40, 1177 (1978).

7.33 A Raven, O Willi an P T Rumsby, Phys. Rev. Lett. 41, 554 (1978).

7.34 D G Colombant and N K Winsor, Phys. Rev. Lett. 38, 697 (1977).

7.35 R L Morse and C W Nielson, Phys. Fluid 16, 6, p.909 (1973).

7.36 Rutherford Laboratory Report RL-79-036, Annual Report to the Laser Facility Committee 1979.

7.37 A B Langdon, B F Lasinski, Methods in Comp. Phys. 16, 327 (1976).

7.38 E L Lindman, J. Comp. Phys. 18, 66 (1975).

7.39 C S Cooper, Rutherford Laboratory Report RL-75-138, The DRIO Package Users' Guide.

7.40 HBOOD Users Guide, CERN program library, Y250 and DD/77/9.

7.41 The Problem Program Efficiency package, CIGAR.

7.42 R Decoste and B H Ripin, Phys. Rev. Lett. 40, 34 (1978).

7.43 A V Gurevich, D Anderson and H Wilhelmason, Phys. Rev. Lett. 42, 769 (1979).

7.44 C Joshi, M C Richardson and G D Enright, Appl. Phys. Lett. 34, 625, (1979).

7.45 E L Lindmann, J. de Phys. (Paris), Colloq. 38, C6-9 (1977).

7.46 L M Wickens, J E Allen and P T Rumsby, Phys. Rev. Lett. 41, 243 (1978).

7.47 L M Wickens and J E Allen, J. Plasma Phys., 22, 167 (1979).
7.48 L M Wickens and J E Allen, to be published.

7.49 J E Allen and L M Wickens, J. de Physique 40, supp. No. 7, C7-547 (1979) (Proc. XIVth Ionised Gases Conf.).

7.50 A V Gurevich, L V Pariiskaya and L V Pitaersky, JETP 37, 1071 (1973).

7.51 Ia. B. Zeldovich and Raizer, "Physics of Shock Waves", Vol. 1, Academic Press (1966).

7.52 J J Sanderson and S P Gary, 9th European Conference on Controlled Fusion and Plasma Physics, Oxford, 17 - 21 September, 1979. Contributed papers, p.65.

7.53 R C Malone, R L McCrory and R L Morse, Phys. Rev. Lett. 34, 721 (1975).

7.54 L Spitzer, 'Physics of fully ionised gases (publ. Interscience, New York) (1965).

7.55 D A Tidman and A Eviator, Phys. Fluids 8, 2059 (1965).

7.56 W C Mead, et al, Phys. Rev. Letts. 37, 489 (1976).

7.57 P M Campbell, et al, Phys. Rev. Letts, 39, 274 (1977)

7.58 J D Kilkenny, et al, Rutherford Laboratory Report RL-79-036 (1979).

7.59 R Benattar, et al, Phys. Rev. Letts. 42, 766 (1979).

7.60 H C Barr, Ph.D. Thesis, University of Wales, 1974 (unpublished).

H C Barr and TJM Boyd, J. Plasma Phys. 15, 279 (1976), ibid, 17. 503 (1977).

TJM Boyd, Proc. XIth International Symposium on Shock Waves (Unov. of Washington Press), 156 (1987).

7.61 D Gray, et al, Phys. Rev. Lett. 39, 1270 (1977).

7.62 D Biskamp and R Chodura, 'Plasma Physics and Controlled Nuclear Fusion Research, Vol.II, (I.A.E.A., Vienna), 265 (1971).

7.63 T H Dupree, Phys. Fluids 9, 1773 (1966); ibid, 10, 1049 (1967).

7.64 J Weinstock, Phys. Fluids 12, 1045 (1969); ibid, 13, 2308 (1970).

7.65 W M Manheimer, Phys. Fluids 20, 265 (1977).

APPENDIX

CENTRAL LASER FACILITY PUBLICATIONS

RESEARCH PAPERS

B Ahlborn and M H Key
Scaling laws for the compression of shell targets
Bull Am Phys Soc 24 1008 (1979)

J E Allen and L M Wickens
Hydromagnetic rarefaction waves
J de Physique, Colloque C.7 40 C7-547 (1979)

D Bond et al
A demonstration of resistive inhibition of laser plasma fast electrons by low density gold targets
Phys Rev Lett (to be published)

D D Burgess, D Everett and R W Lee
Suppression of Doppler broadening for XUV transitions in dense plasmas
J Phys B 12 L755 (1979)

R A Cairns
The spectrum of second harmonic emission from a laser produced plasma
J Plasma Physics 22 149 (1979)

P D Carter, S M L Sim, H C Barr and R G Evans
Time resolved observations of the three-halves harmonic spectrum from laser produced plasmas
Phys Review Lett (to be published)

P D Carter, S M I Sim and E R Wooding
Mechanisms for three-halves harmonic emission from laser-produced plasmas
Optics Comm 32 443 (1980)

C B Edwards, M H R Hutchinson, M D Hutchinson and D J Bradley
Repetitive vacuum ultraviolet xenon eximer laser
Rev Sci Inst 50 10 1201

B C Fawcett, A Ridgeley and T P Hughes
Line classifications for Ni XXV and XXVI and new observations of Fe XXIII and XXIV in laser produced spectra
Mon Not Roy Astr Soc 188 365 (1979)

A F Gibson
Laser driven fusion
Phys Educ 15 4 (1980)

A F Gibson and M H Key
High power lasers
Reports on Progress in Physics 43 1 (1980)

A F Gibson and M F Kimmitt
Photon drag detection
Chapter in "Infra red and millimetre waves" Editor K Button
Publ: Academic Press (to be published)

A F Gibson, M F Kimmitt, A O Koohiam, D E Evans and G F D Levy
A study of radiation pressure in a refractive medium
Proc Roy Soc A370 303 (1980)

D R Gray et al
Time-resolved spectroscopic studies of laser produced plasmas
Plasma Phys (to be published)

D R Gray and J D Kilkenny
The measurement of ion accoustic turbulence and reduced thermal conductivity caused by a large temperature gradient in a laser heated plasma
Plasma Phys 22 81 (1980)

J D Hares, J D Kilkenny, M H Key and J G Lunney
Measurement of fast electron energy spectra and preheating in laser irradiated targets
Phys Rev Lett 42 1216 (1979)

R J Hutcheon, G E Bromage, R L Cooke, M H Key and C L S Lewis
2p-4d and 2p-4s transition arrays in F-like Cu XXI to As XXV spectra
J Phys B 13 673 (1980)

R J Hutcheon, L Cooke, M H Key, C L S Lewis and G E Bromage
Neon-like and fluorine-like X-ray emission spectra for elements from Cu to Sr
Physica Scripta 21 89 (1980)

R Illingworth and R K Thareja
Interferometry of laser-created plasmas using a Fresnel bi-prism or bi-mirror
Optics Comm 32 51 (1980)

M H Key
Some topical issues in short pulse laser produced plasma research
Phil Trans Roy Soc (to be published)

M H Key, M J Lamb, C L S Lewis, A Moore and R G Evans
X-ray streak camera study of the dynamics of laser imploded microballoons
Appl Phys Lett 34 550 (1979)

M H Key, C L S Lewis, J G Lunney, A Moore, J M Ward and R L Thareja
Time resolved X-ray spectroscopy of laser produced plasmas
Phys Rev Lett (to be published)

M H Key and R J Hutcheon
Sprectroscopy of laser produced plasma
Advances in Atomic and Molecular Physics. Ed D R Bates
Publ: Academic Press (to be published)

M H Key, J G Lunney, J D Kilkenny and R W Lee
Experimental evidence of hydrodynamic instabilities in laser driven implosions
Appl Phys Lett 36 269 (1980)

J D Kilkenny, R W Lee, M H Key and J G Lunney
The S-ray diagnosis of laser produced plasmas with emphasis on line broadening
Phys Rev (to be published)

R W Lee
Study of the plasma broadening of spectral lines of hydrogenic ions
J Phys B 12 1129 (1979)

R W Lee
Study of ion dynamic effects on Lyman and Balmer hydrogenic lines

R W Lee
Amodel study of non-thermal affects in the plasma broadening of spectral lines
J Phys B 12 1165 (1979)

R W Lee, G E Bromage and A G Richards
Atheoretical study of the plasma broadening of helium-like transitions for high Z emitters
J Phys B 12 3445 (1979)

A Raven, P T Rumsby, J A Stamper, O Willi, R Illingworth and R Thareja
Dependence of spontaneous magnetic fields in laser produced plasmas on target size and structure
Appl Phys Lett 35 526 (1979)

A Raven, P T Rumsby and J Watson
Multichannel digitizer for monitoring of ion emission from laser driven implosions
Rev Sci Inst 51 351 (1980)

A Raven and O Willi
Electron density structures in laser produced plasmas at high irradiances
Phys Rev Lett 43 278 (1979)

M J Shaw
Eximer laser
Prog in Quant Electronics 6 3 (1979)

J G Turner and T J M Boyd
Soliton formation in magnetised Vlasov plasmas
J Plasma Physics 22 121 (1979)

R W Tuxworth, M Lawton and M J Shaw
Operation of discharge excited KrF and XeF lasers at elevated temperatures
J Phys D 13 135 (1980)

M J Webster and M J Shaw
Excitation transfer in the 2p levels of Ne due to collisions with ground state He atoms
J Phys B 12 3521 (1979)

L M Wickens and J E Allen
Free expansion of a plasma with two electron temperatures
J Plasma Physics 22 167 (1979)

O Willi, R G Evans and A Raven
Time resolved density profiles of laser heated plasmas
Phys of Fluids (to be published)

O Willi and A Raven
A holographic microinterferometer to study laser-produced plasmas
Appl Opt 19 192 (1980)

O Willi, A Raven and P T Rumsby
Self generated magnetic fields in laser produced plasmas
Phys Lett 71A 435 (1979)

CONFERENCE CONTRIBUTIONS TO BE PUBLISHED

PROCEEDINGS OF THE FOURTH NATIONAL QUANTUM ELECTRONICS CONFERENCE
(to be published by J Wiley and Sons)

D Bond et al
A parametric investigation of fast electron preheat in laser plasma interactions

T J M Boyd
Laser plasma interactions (invited)

A J Cole et al
Time resolved spectroscopic studies from laser produced plasmas

D Craddock et al
Electron beam excited rare gas halide lasers

R G Evans and A R Bell
Improvements to the equation of state in the Medusa compression simulation

A F Gibson
Lasers for plasma research (invited)

D Gray et al
X-ray diagnosis of the interaction of 0.53 μm radiation with layered targets at 5×10^{14} w cm^{-2}
C L S Lewis et al
Time resolved X-ray shadowgraphy of laser driven ablative implosion

D J Nicholas and C B Edwards
EPIC – a relativistic e-beam depostion code

PROCEEDINGS OF THE NINTH EUROPEAN CONFERENCE ON CONTROLLED FUSION AND PLASMA PHYSICS (to be published by the UKAEA)

J D Kilkenny et at
Energy transport from 1.06 μm and 0.53 μm laser plasma interactions at 10^{14} w cm^{-2}

C L S Lewis et al
Studies of laser driven implosions by time resolved shadowgraphy

J G Lunney et al
X-ray spectrometry of laser compressed microballoons

J J Sanderson and S P Gary
On the transport theory of electrostatic microinstabilities

PROCEEDINGS OF THE 20TH SCOTTISH UNIVERSITIES SUMMER SCHOOL IN PHYSICS
LASER PLASMA INTERACTIONS. Ed R A Cairns and J J Sanderson
(to be published by the SUSSP)

M G Haines
The physics of the coronal region

T P Hughes
Laser plasma absorption processes

M H Key
The physics of the superdense region

N J Peacock
Diagnostics for e-m radiation emissions

G Pert
Computer modelling of laser plasma experiments and fluid codes

PROCEEDINGS OF THE TOPICAL MEETING ON EXIMER LASERS
(to be published by the Optical Society of America)

C B Edwards et al
High efficiency KrF and ArF lasers

PROCEEDINGS OF REAL TIME DATA '79
(to be published by North Holland, Amsterdam)

C J Reason, P Gottfeldt and J G Watson
Control and data acquisition at the Rutherford Laboratory Laser Facility

PROCEEDINGS OF THE FIFTH WORKSHOP ON LASER INTERACTION WITH MATTER
(to be published by Plenum Press)

J D Kilkenny et al
Recent progress in laser interaction and ablative compression experiments
at the Rutherford Laboratory